Exploring the Trans-Neptunian solar system using stellar occultations : application to Triton

Joana Marques Oliveira

THÈSE DE DOCTORAT DE
LE SORBONNE UNIVERSITÉ

Spécialité

Astronomie

École doctorale d'Astronomie et d'Astrophysique d'Ile de France (Paris)

Présentée par

Joana MARQUES OLIVEIRA

Pour obtenir le grade de
DOCTEUR de le SORBONNE UNIVERSITÉ

Sujet de la thèse :

Explorer le système solaire extérieur au-delà de Neptune en utilisant des occultations stellaires : Application à Triton

soutenue le 29 Octobre 2021

devant le jury composé de :

Bruno SICARDY	Directeur de thèse
François FORGET	Présidente du jury
Candice HANSEN	Rapporteur
Pascal RANNOU	Rapporteur
Thierry FOUCHET	Examinateur
Cathy OLKIN	Examinateur
Darrell STROBEL	Examinateur

Acknowledgments

First and foremost, there is one person I want to thank: me. For being brave to travel to a country where I knew no one for a Ph.D., for surviving some horrible moments, and for finishing what I set out to do!

The next person I would like to thank, is the other person that made this thesis possible: my supervisor, Bruno Sicardy. Thank you for all your teachings, patience, and availability!

I would like to thank my thesis committee: François Forget, Candice Hansen, Pascal Rannou, Thierry Fouchet, Cathy Olkin, and Darrell Strobel.

To all my colleagues and friends, new and old, a huge thank you. Sarah, my first friend here in Paris, thank you for accepting my first invitation to hang out, and thank you for all the great Sundays around Paris, and elsewhere! Guga, Helo, Bruno, Fabiola, Thamiris, thank you for the fun times at the residence, for all your help, and all the alcohol and popcorn.

Diogo, thank you for the patience, for waiting for me so we can start our life together, and for supporting me during the worst times.

To my parents, grandmother, and brother, a thank you for the fun video calls and weird messages. And also for the support, of course.

A special thank you to my baby, Lucky, for being the best pet rabbit ever, and for annoying (and keeping company to) my parents for me while I am gone.

I would like to thank the Observatoire de Paris, LESIA, and Université Sorbonne for having me.

This work was supported by the Ph.D. grant provided by Fundação para a Ciência e a Tecnologia (FCT) and European Science Foundation (ESF), reference SFRH/BD/131700/2017, and the European Research Council (ERC) under the European Community's H2020 2014-2021 ERC grant Agreement n. 669416 "Lucky Star".

Contents

Abstract

The stellar occultation technique is a very powerful tool to observe distant and/or small objects in the Solar System. In particular, ground-based occultations can detect tenuous atmospheres, down to a pressure of $\sim$ 10 nbar. Triton's atmosphere can be detected by this technique.

A stellar occultation by Triton was observed on 5 October 2017. 90 positive detections were obtained, 42 of them featuring a central flash detection. Using the Abel inversion and ray-tracing methods, I was able to obtain the density, pressure, and temperature profiles in the altitude range $\sim$ 8 km to $\sim$ 190 km, where a pressure of 1.18 $\pm$ 0.03 μbar was found at a reference radius of 1400 km (47 km altitude).

A novel analysis of the Voyager 2 data was then performed, to directly compare its results to those obtained in 2017. It shows that they are consistent with each other, implying that Triton's atmospheric pressure obtained in 2017 is at its Voyager 2 epoch levels. A survey of stellar occultations obtained between 1989 and 2017 suggests an increase in the atmospheric pressure. This is, however, debatable, due to very few high signal-to-noise ratio light curves and data accessible for reanalysis. Volatile Transport Models examined suggest that any increase during this time frame should be modest, as they do not support a strong increase in the surface pressure.

A central flash analysis allowed the study of the lower atmosphere's shape. It shows that there is no evidence of atmospheric distortion. An upper limit of 0.0011 for the apparent oblateness of the atmosphere near the 8 km altitude is found.

Keywords: Occultations, Trans-Neptunian Objects, Asteroids, Light Curves.

Résumé

Le travail effectué au cours de mon programme de doctorat de quatre ans est principalement axé sur l'occultation stellaire de Triton, qui s'est produit le 5 octobre 2017. Cet événement a eu lieu à peu près au moment où j'ai commencé mon programme de Doctorat, et c'est donc par cet événement que j'ai commencé mes recherches, en travaillant sur la photométrie de certaines des 90 observations positives obtenues. Cette étude n'a cependant pas été le seul travail effectué pendant ces quatre années. J'ai également participé à des occultations d'autres objets, j'ai réduit les données de différentes occultations stellaires, j'ai partagé mes résultats dans plusieurs conférences et séminaires, et j'ai suivi des cours sur divers sujets scientifiques.

Une occultation stellaire se produit lorsqu'un objet planétaire passe devant une étoile, du point de vue d'un observateur, bloquant totalement ou partiellement sa lumière. L'ombre projetée par cet objet, ou trajectoire d'occultation, peut être observée depuis plusieurs endroits, appelés stations, et l'atténuation de l'étoile enregistrée pour une analyse ultérieure. On obtient alors une "corde d'occultation" qui dépend de la durée de l'événement et de la position de la station. Avec plusieurs cordes, nous pouvons construire la géométrie du corps, ainsi qu'une pléthore d'autres propriétés physiques. La technique de l'occultation stellaire est un outil très puissant pour observer des objets lointains et/ou de petite taille dans le système solaire. Les occultations stellaires sont une technique principalement, mais pas exclusivement, basée au sol. L'avantage d'utiliser des observations au sol est un coût plus faible et une plus grande mobilité, puisque de plus petits télescopes peuvent être utilisés, ainsi que l'obtention d'un plus grand nombre de cordes pour un même événement, puisque de nombreuses personnes, astronomes professionnels et non professionnels, peuvent effectuer les observations.

La technique d'occultation stellaire permet, en particulier, de détecter une atmosphère, jusqu'à une pression atmosphérique de 10 nbar, dans un objet planétai-

re. Cela se fait par l'observation de la disparition et de la réapparition progressive de l'étoile (respectivement immersion et émersion) ou par l'étude des flashs centraux. Les occultations stellaires peuvent sonder les atmosphères planétaires pour retrouver les profils de température, de pression et de densité en utilisant la méthode d'inversion (French et al., 1978). Cette méthode suppose que la structure de l'atmosphère est en équilibre hydrostatique. Des informations peuvent également être obtenues en utilisant des modèles qui sont ensuite ajustés aux données (Elliot and Young, 1992). En fonction des données d'occultation disponibles, cette technique peut également être sensible aux variations locales de densité, à l'extinction causée par les molécules et les aérosols, à la période de rotation de l'atmosphère, aux vents zonaux, entre autres propriétés atmosphériques.

Lors d'une occultation stellaire par un objet possédant une atmosphère, le flux de l'étoile occultée s'atténue par réfraction différentielle causée par l'effet de lentille de l'atmosphère, ou par absorption de matière dans l'atmosphère. Si la matière absorbante, telle que les brumes ou les nuages, est absente aux niveaux où la technique d'occultation sonde l'atmosphère, l'atténuation de l'étoile, son flux, est principalement due à la réfraction qui dévie la lumière de l'étoile. Pour ce travail, je me suis concentrée uniquement sur les occultations par réfraction. Si l'atmosphère de l'objet occultant est suffisamment dense, les rayons lumineux qui sondent les couches profondes de l'atmosphère (en passant par la centralité ou à proximité) peuvent être courbés au point de traverser la ligne centrale qui relie l'étoile, l'objet et l'observateur. Si l'atmosphère est transparente, le flux augmente à mesure que l'événement se rapproche du centre de l'ombre. Lorsque l'observateur, l'objet et l'étoile sont parfaitement alignés, on atteint la valeur maximale du flux observé. Dans ce cas, les images stellaires forment un anneau qui entoure l'objet. Si l'atmosphère n'est pas sphérique, les centres de courbure du limbe ne sont pas au centre de l'objet, ils suivent une courbe, la développée du limbe. Les flashs centraux sont extrêmement sensibles à la forme de l'atmosphère. La forme de l'atmosphère est elle-même maintenue par les vents qui peuvent être présents.

Les flashs centraux permettent également la détection, puis l'étude, des brumes. Étant donné que le flash central sonde les couches les plus profondes de l'atmosphère, où les nuages sont le plus susceptibles d'être présents, si tant est qu'ils existent, il s'agit de la partie de la courbe de lumière la plus sensible à ces

brumes. L'étude des flashs centraux dans différentes longueurs d'onde est une méthode de détection. Si deux courbes de lumière prises dans la même station, ou le long de la même corde, enregistrées dans des longueurs d'onde différentes, présentent des flashs centraux avec des pics de valeurs différentes, cela révèle un fort effet chromatique, qui peut contraindre les propriétés optiques des aérosols de la brume (Sicardy et al., 2006). Une autre méthode de détection de la brume est l'amplification du flux stellaire due à la courbure du limbe.

Deux méthodes ont été principalement utilisées pour étudier les courbes de lumière dans mon travail. La méthode d'inversion d'Abel est utilisée pour retrouver la structure atmosphérique à partir des courbes de lumière. En particulier, nous pouvons obtenir les profils atmosphériques de densité, de pression et de température. Il est important de noter que le principal résultat de l'inversion d'Abel est le profil de densité. Le profil de température présente une indétermination mathématique qui est due au fait qu'il est déduit d'une équation différentielle du premier ordre et qu'il nécessite une condition initiale, $T_0 = T(r_0)$. Cela signifie qu'il existe une infinité de profils de température qui peuvent expliquer la même courbe de lumière d'occultation. Le choix de cette condition initiale nécessite une information indépendante, telle que la température dérivée d'un vaisseau spatial au rayon r_0, afin de restreindre les valeurs possibles de $T(r_0)$. L'autre méthode utilisée, le tracé de rayon, est employée dans plusieurs cas. Elle est réalisée sur les courbes de lumière dont le rapport signal/bruit est insuffisant, ou les points de données de la courbe de lumière sont trop espacés dans le temps. Elle est utilisée lorsque la station est très proche de la centralité, et comporte un flash central, car la méthode d'inversion d'Abel ne prend en compte qu'une seule image stellaire. Avec un flash central, les deux images stellaires ont des flux comparables. La méthode de tracé de rayons est principalement sensible au niveau de pénombre, et prend en compte les deux images stellaires, ce qui rend cette méthode idéale pour reproduire et analyser les flashs centraux. Elle est également choisie dans le cas où il y a des brumes qui absorbent une partie du flux, ce qui biaise les profils retrouvés de densité, de pression et de température. Les deux méthodes supposent que l'atmosphère est sphériquement symétrique et qu'elle est transparente.

L'atmosphère de Triton peut être détectée par cette technique, en sondant jusqu'à une altitude de $\sim$ 190 km. Triton est le plus grand satellite de Neptune, découvert le 10 octobre 1846. C'est la septième plus grande lune, avec un

rayon de ∼1353 km, et le plus grand satellite irrégulier du système solaire (Burns, 1986). Triton est un satellite très curieux, et il a été proposé d'être un objet transneptunien capturé, avec certains des arguments soutenant cette théorie étant qu'il présente une excentricité orbitale essentiellement nulle (0,000016), et une orbite rétrograde. Triton est un monde océanique potentiel (Hansen et al., 2021), très actif, et avec une surface jeune. Lors du survol du système neptunien par Voyager 2 de la NASA, des panaches et des geysers jaillissant de la surface de Triton ont été détectés. C'est le seul satellite, après Titan, à posséder une atmosphère significative. Triton est un corps très intéressant. Quelques missions spatiales ont été proposées pour étudier le système neptunien, avec des recherches approfondies sur Triton. Cependant, aucune mission n'a encore été approuvée, ni même lancée, en direction de ce système fascinant, après le survol de Voyager 2 en 1989.

Triton sort actuellement d'un rare "solstice austral extrême", où des latitudes sub-solaires allant jusqu'à 50° S ont été directement et constamment illuminées par le Soleil, une configuration qui se produit tous les ∼ 650 ans en raison d'une combinaison du mouvement héliocentrique de Neptune et de la précession orbitale de Triton.

Après avoir collecté plus de 4700 images CCD de Triton entre 1992 et 2016, un travail astrométrique détaillé a été dérivé, un peu comme dans Assafin et al. (2010) et dans Camargo et al. (2014), et une occultation par Triton a été trouvée. L'événement, avec une étoile de magnitude V = 12,7, G = 12,2 (UCAC4 410-143659 ; *Gaia* DR2 2610107911326516992), se produirait le 5 octobre 2017, traversant l'Europe, l'Afrique du Nord, et atteignant l'est des États-Unis. Entre le 15 et le 23 septembre 2017, un programme de 8 nuits a été mené à l'Observatoire du Pico dos Dias (Brésil) pour améliorer la précision de la prédiction. En utilisant le package PRAIA (Assafin et al., 2011), des réductions ont été faites en utilisant le catalogue *Gaia* DR1. Cela a donné une incertitude d'environ 130 km sur la trajectoire transversale, et d'environ 10 secondes pour le moment de plus courte approche. Le programme couvrait une période complète de Triton, ce qui signifie que le décalage moyen reflète des erreurs dans la position héliocentrique de Neptune et non une erreur neptunocentrique dans les éphémérides de Triton.

Le 30 septembre 2017, l'équipe de *Gaia* a publié un sous-ensemble préliminaire de *Gaia* DR2, avant sa publication officielle en avril 2018 (Gaia Collaboration et al., 2016, 2018), dans le but d'améliorer la prédiction de cet événement. Ce

sous-ensemble comprenait 431 étoiles de magnitudes R = 12-17 qui entouraient la trajectoire de Triton dans le plan du ciel pendant les 8 nuits effectuées. Le catalogue *Gaia* DR2 comprend les mouvements propres des étoiles, ce qui permet d'obtenir une précision de l'ordre de la milliarcseconde (mas) pour les positions stellaires à l'époque. En appliquant ce nouveau catalogue au cycle de 8 nuits, on a constaté que la trajectoire de l'ombre présentait un déplacement significatif d'environ 370 km vers le sud dans le plan du ciel, et d'environ 500-700 km lorsqu'elle est projetée sur la Terre, et que les incertitudes étaient réduites par des facteurs de $\sim 1,5$ et $\sim 2,2$, respectivement. La prédiction actualisée a été communiquée à la communauté scientifique avant l'événement.

Plus de cent stations ont tenté d'observer l'événement. Ensemble, les observateurs d'Europe, d'Afrique du Nord et de l'est des États-Unis ont obtenu un total de 90 courbes de lumière d'occultation. L'analyse des courbes de lumière a montré que l'occultation s'est produite environ 9 s plus tôt, et que le centre de l'ombre se trouvait à 12 km (soit 0.6 mas) au nord de la prédiction finale. Cette différence se situe à un niveau de $\sim$1,3σ, non significatif à notre niveau de précision. Elle montre que l'astrométrie DR2 de *Gaia* a été déterminante dans la prédiction finale. DR2 a joué un rôle clé dans l'obtention d'une prédiction précise, en permettant la détection du flash central dans de nombreuses stations. Pour extraire des informations de la pléthore de données obtenues, nous avons adopté une approche "bootstrap", en itérant entre l'inversion d'Abel et la méthode de traçage de rayons. Ceci a permis de retrouver la densité moléculaire, la pression et la température de l'atmosphère de Triton en fonction de la distance au centre de Triton. Les courbes de La Palma (télescope Liverpool de 2 m, Espagne) et Helmos (télescope Aristarchos de 2,28 m, Grèce) ont été inversées pour obtenir la forme des profils, en utilisant des images de calibration. La courbe de lumière de Calern (télescope C2PU de 1,04 m, France) a été inversée par la suite, pour confirmer la forme trouvée avec les deux autres courbes de lumière.

En partant de la surface, le profil de température obtenu présente un fort gradient de température positif de 5 K km^{-1}. Ce gradient diminue rapidement et la température atteint un maximum d'environ 50 K à $r = 1363$ km (10 km d'altitude), avec un gradient moyen de 1,2 K km^{-1} dans cette partie. Les données indiquent la présence d'une mésosphère avec un gradient négatif (également vu dans Elliot et al., 2003) qui atteint $-0,2$ K km^{-1} à $r = 1375$ km (23 km d'altitude),

avant de se connecter avec le gradient positif de la branche supérieure.

La méthode de traçage de rayons est principalement sensible au niveau de mi-lumière pour l'étoile. Ce niveau correspond à un rayon d'environ 1415 km (altitude ~60 km) et à une pression de ~0,55 μbar. Elle est utilisée une fois que la procédure d'inversion d'Abel a fourni les profils de densité, et qu'un profil de température modèle a été obtenu. Cette méthode génère des courbes de lumière synthétiques qui sont ajustées aux courbes de lumière d'occultation observées, afin de décrire la structure globale de l'atmosphère de Triton. Nous trouvons la valeur la mieux ajustée de $p_{1400} = 1,18 \pm 0,03$, avec sa barre d'erreur de 1σ. La valeur la mieux ajustée de la correction transversale à l'éphéméride $\Delta\rho = -359,3 \pm 1$ km est utilisée pour retrouver la distance de plus courte approche géocentrique entre Triton et l'étoile, projetée dans le plan du ciel, et son temps correspondant.

Une nouvelle analyse des données de Voyager 2 a été réalisée, afin de comparer les données originales de Voyager 2 à nos résultats. J'ai généré, pour comparaison, le retard de phase à 3,6 cm qui serait observé avec nos meilleurs profils de densité, comme s'il avait été obtenu à bord de Voyager 2. Nous estimons une fourchette prudente de $p_{1400,RSS} = 1,0 \pm 0,2$ μbar pour la pression à 1400 km en 1989. En comparant ce résultat à notre résultat au sol de 2017, $p_{1400} = 1,18 \pm 0,03$, ainsi qu'en comparant les pressions de surface, nous ne voyons aucune variation significative de pression entre les résultats de Voyager 2 de 1989 et les résultats déduits de l'occultation au sol de 2017. Il est important de noter que l'expérience radio de Voyager 2 a encore réussi à fournir de nouvelles informations, après toutes ces années, et alors que l'information de ces données ait été considérée comme étant épuisée. En particulier, elle a permis une comparaison directe de la densité, et de la pression, entre les données obtenues en 1989 et nos résultats de 2017. Ce nouveau résultat était crucial pour ce travail, car il a montré que la pression atmosphérique de Triton, en 2017, est revenue au niveau de l'époque de Voyager 2.

Après avoir obtenu les pressions des événements analysés, je me suis mis à la recherche d'autres études qui avaient leur propre déduction de la pression, soit à la surface, soit à $r = 1400$ km, un rayon de référence commun pour déduire la pression atmosphérique de Triton. Comme la valeur originale de Voyager 2 n'est déduite que pour la surface, nous avons extrapolé tous les autres résultats

(en plus de notre propre analyse de Voyager 2) en supposant un rapport constant. Il semble que l'augmentation de pression rapportée dans la littérature au cours des années 1990, par rapport à l'époque de Voyager 2, soit confirmée par notre analyse. Cependant, compte tenu de la rareté des points de données disponibles, et de l'absence d'une analyse totalement cohérente de tous les événements, cette question restera en fait non résolue. Malgré cela, la valeur de la pression que nous avons obtenue en 2017 est beaucoup plus précise et est entièrement compatible avec celle dérivée de l'expérience de Voyager 2. Le point de 2017 se situe dans la barre d'erreur de 1σ de celui de Voyager 2. Cela signifie qu'il n'y a pas de différence notable entre les deux points de données. Donc, soit il n'y a pas eu d'augmentation de la pression entre 1989 et 2017, soit si elle a bien eu lieu, la pression est revenue à son niveau de Voyager 2 en 2017.

Bertrand et al. (2022) ont utilisé les valeurs que nous avons obtenues dans ce travail pour effectuer des simulations avec leur modèle de transport volatil Triton du Laboratoire de Météorologie Dynamique. Leurs résultats suggèrent qu'une calotte polaire septentrionale qui s'étend jusqu'à au moins 45° N - 60° N est nécessaire en 2017 pour garantir que la pression de surface soit à ~14 μbar, soit un retour au niveau de Voyager 2. Si l'on suppose qu'il n'y a pas de calotte septentrionale, la pression de surface modélisée est supérieure à 16 μbar en 2017, mais cela ne correspond pas à nos observations. Il est à noter qu'une forte augmentation de la pression de surface avant 2000 ne peut être obtenue s'il y a de la glace N_2 présente entre 30° S - 0°. Il est également important de mentionner que la pression de surface est toujours supérieure à 5 μbar, même pendant la saison opposée, lorsqu'une calotte septentrionale permanente s'étendant jusqu'à 45° N est simulée. Cela implique que la présence permanente des deux calottes, sud et nord, empêche l'atmosphère de Triton de s'effondrer pendant l'hiver austral.

Parmi les 90 courbes de lumière observées, 42 présentent une augmentation notable du flux stellaire près du point milieu de l'occultation, caractéristique d'un flash central, et 23 ont un rapport signal/bruit suffisamment bon pour nous permettre de les utiliser dans la modélisation du flash central. C'est une occasion unique d'étudier la basse atmosphère de Triton, car de nombreux points de données ont été obtenus. Les résultats de notre méthode de tracé de rayons montrent que le flash central est causé par une couche d'une épaisseur d'environ 2 km, et est située à environ 8 km au-dessus de la surface de Triton, ou à un rayon de ~ 1361 km.

Dans cette gamme d'altitude, et parce que l'image stellaire secondaire le long du limbe de Triton devient de plus en plus significative, la méthode d'inversion d'Abel n'est pas valide. Cette invalidité devient apparente à des niveaux d'altitude d'environ 20 km, ce qui correspond aux couches les plus profondes sondées par la courbe de lumière de La Palma. Par conséquent, le flash central permet une analyse de quelques $\sim$ 12 km plus bas (environ 0,6 hauteur d'échelle), atteignant le niveau d'altitude de $\sim$ 8 km, par rapport à l'inversion d'Abel.

Avec le modèle de température, nous pouvons maintenant supposer une couche causant le flash sphérique. La qualité de l'ajustement, $\chi^2_{\rm dof} = 0,80$, est en accord avec celle obtenue sans les flashs centraux, $\chi^2_{\rm dof} = 0,85$, montrant qu'en effet il n'y a pas de détection d'une déviation par rapport à la sphéricité. Un examen visuel plus approfondi des résidus des éclairs les plus forts avec les meilleurs rapports signal/bruit révèle quelques déviations à l'ajustement mineures et localisées, peut-être dues à des ondes atmosphériques, mais aucune déviation globale au modèle sphérique. En effectuant un ajustement simultané aux seuls flashs centraux, en excluant les parties d'entrée et de sortie des courbes de lumière, on obtient un autre argument en faveur de la sphéricité de l'atmosphère de Triton. Le centre de l'ombre de Triton, dans cet ajustement, coïncide à 0,1 km près avec le centre de l'ombre déterminé par l'ajustement global qui excluait les éclairs centraux. Ce petit décalage est insignifiant, surtout si l'on tient compte du fait que le centre de l'atmosphère dans l'ajustement global a une erreur typique de 1σ de 1 km perpendiculaire au mouvement de Triton. Cela signifie que le centre que nous avons déduit de la couche du flash central, sensible au niveau d'altitude 8 km, correspond très bien au centre récupéré pour le centre de l'ombre globale, sensible seulement au niveau d'altitude 60 km. Il est possible que ces deux niveaux atmosphériques soient proches de la sphéricité, mais déplacés de la même manière par rapport au centre de Triton, cependant, cette configuration semble peu probable.

La possibilité d'un écart par rapport à la sphéricité dans la basse atmosphère de Triton a également été étudiée. Elle a été limitée au modèle simple d'une couche de flash central globalement aplatie. Des formes plus complexes pourront être testées lorsque les modèles climatiques globaux 3D de Triton seront disponibles. Une limite supérieure de 0,0011 pour l'aplatissement apparent de l'atmosphère près de l'altitude de 8 km est trouvée. Ici, on suppose que la forme de la couche d'éclair centrale est entièrement soutenue par les vents zonaux. En particulier,

nous supposons l'absence d'un gradient horizontal de température, de sorte que le niveau isobare correspond également au niveau isopycnique (densité constante). Lors de discussions avec Tanguy Bertrand et François Forget, qui analysent le régime des vents sur Triton par le biais de simulations, nous avons conclu sur certaines informations obtenues en 1989, par Voyager 2, sur la circulation atmosphérique. Alors que les traînées de vent de surface suggéraient des vents rétrogrades en surface entre les latitudes 15° S et 45° S (Hansen et al., 1990), la déviation des panaches laissait supposer que dans l'atmosphère au-dessus d'eux, à 8 km, et près de 49° S et 57° S, le vent était en fait prograde (Hansen et al., 1990; Yelle et al., 1995). D'un point de vue purement théorique, Ingersoll (1990) a suggéré que cela pourrait provenir d'un contraste de température entre le pôle froid couvert de givre et l'équateur chaud sans givre.

Les vents rétrogrades globaux n'ont pas été observés par Voyager 2. Pour obtenir une rotation prograde dans les latitudes mi-sud comme l'indiquent les observations des panaches de Triton par Voyager 2, la condensation inter-hémisphérique doit être faible. Si c'est le cas, un gradient thermique peut créer un faible vent prograde comme suggéré par Ingersoll (1990), atteignant quelques mètres par seconde dans les simulations des modèles climatiques globaux. Cependant, les modèles de Pluton suggèrent qu'un régime de super-rotation (comme sur Vénus ou Titan) peut se produire (Forget et al., 2017). La super-rotation pourrait expliquer la direction des panaches sur Triton. On pense qu'un tel régime dérive, initialement, de la formation d'un jet de haute-moyenne latitude, résultant de l'équilibre thermique entre l'équateur chaud et un pôle plus froid, ou du flux de condensation des basses latitudes vers le pôle. Les ondes barotropes peuvent donc transporter le moment angulaire vers et depuis l'équateur et accélérer l'ensemble de l'atmosphère. Dans leur modèle climatique global de Pluton, Forget et al. (2017) a trouvé un vent zonal équatorial moyen allant jusqu'à 15 m s^{-1}. Ceci, cependant, pourrait dépendre du modèle utilisé. Par conséquent, il n'est pas facile de fixer une limite théorique à cette éventuelle super-rotation. La limite supérieure obtenue en 2017 sur le vent prograde proche de 50 m s^{-1} fournit donc une contrainte faible pour cette super-rotation hypothétique.

Mots clés: Occultations, Objets Trans-Neptuniens, Astéroïdes, Courbes de lumière.

List of Figures

List of Tables

Chapter 1

Introduction

The work performed during the four years of my Ph.D. program had a primary focus on the stellar occultation event of Triton, that occurred on 5 October 2017. This event took place around the time I started my Ph.D. program, and so, it was the event that I started my research with, by working on the photometry of some of the 90 positive observations obtained.

This Triton stellar occultation event was the most recorded occultation event ever for Neptune's biggest satellite. It soon became apparent that Triton was an interesting target to study during my four years of research. I then started on the analysis of Triton's atmosphere from the data obtained. I also gathered more observational data, including Voyager 2's radio science data, obtained on 25 August 1989, where I did some new analysis, in order to compare the results from both events directly. Two more ground-based stellar occultations, obtained in 1997 and 2008, were analysed during this study.

Comparing these results to other observations in the literature I was able to paint a picture of whether Triton's atmospheric pressure increased since Voyager 2's flyby, or if it remained constant during the time that elapsed between these two observations. I also made a study of Triton's lower atmosphere, using a central flash feature that is present in 42 observations of the 5 October 2017 event. Namely, I analysed if atmospheric distortion was present, or any evidence of the atmosphere's departure from sphericity.

The present thesis details the results obtained during this study of Triton's atmosphere.

This study was not the only work done during these four years, however. I also participated in occultation events of other objects, reduced data from differ-

ent stellar occultations, shared my results in several conferences and seminars, and attended some courses about diverse scientific topics. Some of these activities included travelling to San Diego, California, USA, to observe the Pluto occultation event on 15 August 2018, where I observed the event successfully, and reduced the data I obtained. I also reduced data from the (307261) 2002 MS4 event on 8 August 2020. I was involved with managing the camera kits' inventory we have, as well as make sure that all the equipment was in working condition. I gave a small workshop on small telescope assembly to some colleagues, as we were provided with one to use for local stellar occultation events. I will not go into great detail regarding these activities in this thesis, I will focus solely on my main research.

1.1 Structure of this manuscript

This work was conducted thanks to the Ph.D. grant provided by Fundação para a Ciência e a Tecnologia (FCT) and European Science Foundation (ESF), reference SFRH/BD/131700/2017, as well as funding from the European Research Council (ERC) under the European Community's H2020 2014-2021 ERC grant Agreement n. 669416 "Lucky Star", that focuses on the study of small bodies of the outer Solar System using Stellar Occultations.

This thesis is structured as follows:

- Chapter 2 - The Stellar Occultation technique, methods used to analyse light curves, and how the photometry was performed, are introduced.
- Chapter 3 - An overview of Triton, including historically relevant events and some origin theories, is detailed in this Chapter.
- Chapter 4 - The stellar occultation events studied are described, with the results from each presented.
- Chapter 5 - The analysis conducted, with the results obtained, to retrieve the pressure and atmospheric structure of Triton is presented.
- Chapter 6 - Finally, conclusions are drawn, and some future work is mentioned.

Chapter 2

Stellar Occultations

A stellar occultation event occurs when a planetary object passes in front of a star, from the perspective of an observer, blocking its light totally or partially. The shadow projected by this object, or occultation path, can be observed from several locations, referred to as stations, and the dimming of the star recorded, from each station, for further analysis. We then obtain an "occultation chord" that depends on the duration of the event and the position of the station. With multiple chords, we can reconstruct the body's geometry, as well as a plethora of other physical properties that will be mentioned in more detail in Section 2.1. Figure 2.1 shows an illustration of a minor body occulting a star, detectable from Earth.

Stellar occultations are a primarily, but not exclusively, ground-based technique. To name a few examples of non-ground-based observations, the Stratospheric Observatory for Infrared Astronomy (SOFIA), part of a partnership between the National Aeronautics and Space Administration (NASA) and the German Space Agency, is a Boeing 747SP aircraft modified to carry a 2.7 m telescope. SOFIA has observed several high-profile occultations: Pluto, Triton, Titan, and (486958) Arrokoth, are some examples. Spacecrafts, such as NASA's Voyager 2 and New Horizons, may also perform occultations during their missions. The advantage with using ground-based observations is lower cost and higher mobility, as smaller telescopes can be used, as well as obtain more chords for any one event, as many people, both professional and non-professional astronomers, can perform the observations.

In this Chapter, I will explain the stellar occultation technique, in particular its use in studying atmospheres. I will then mention the technical details of the methods used to analyse the data in Section 2.2. Finally, I will show how the pho-

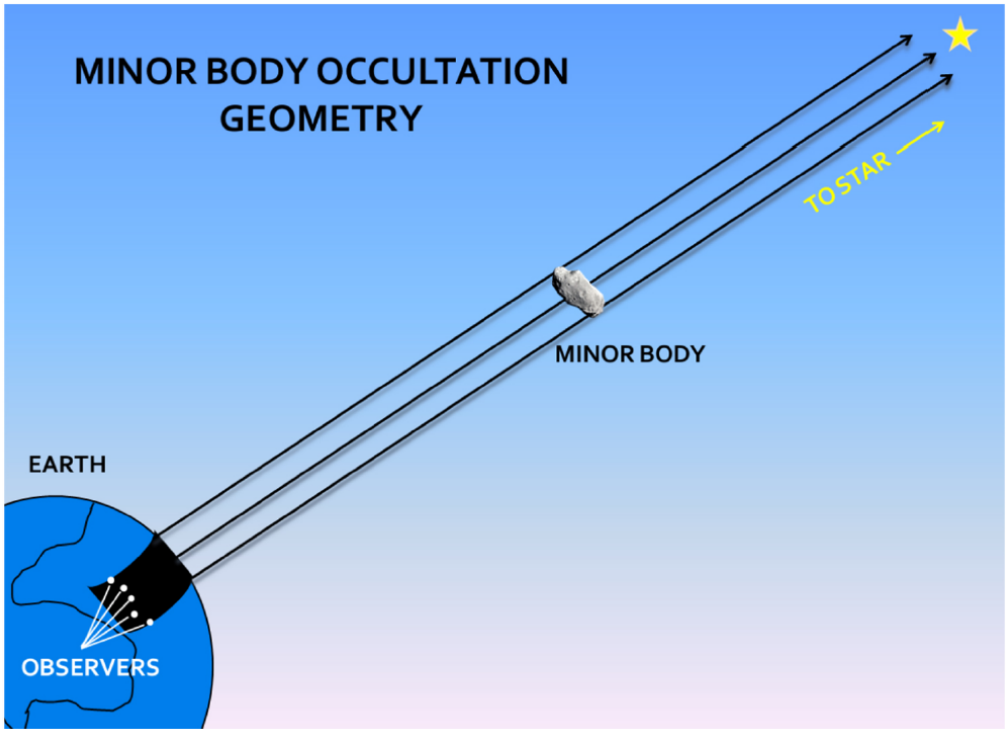

Figure 2.1: A schematic of a stellar occultation of a minor body from the Solar System observable from Earth. Spreading observers throughout the occultation path on Earth allows for the analysis of different parts of the object. Figure from Santos-Sanz et al. (2016).

tometry of the data was made in Section 2.3.

2.1 Technique

From a stellar occultation, we obtain a "light curve", shown as an example in Figure 2.2, and this light curve allows us to study the occulting object. For example, we can obtain information regarding sizes and shapes, more accurately that any other technique (except for spacecraft missions). The size and shape are two basic physical parameters that must be known very accurately in order to characterize an object. With them, densities can be derived. Knowing the density of an object, we can then determine its internal composition, as well as model its internal structure (Carry, 2012). Combining size, shape, and brightness measurements gives

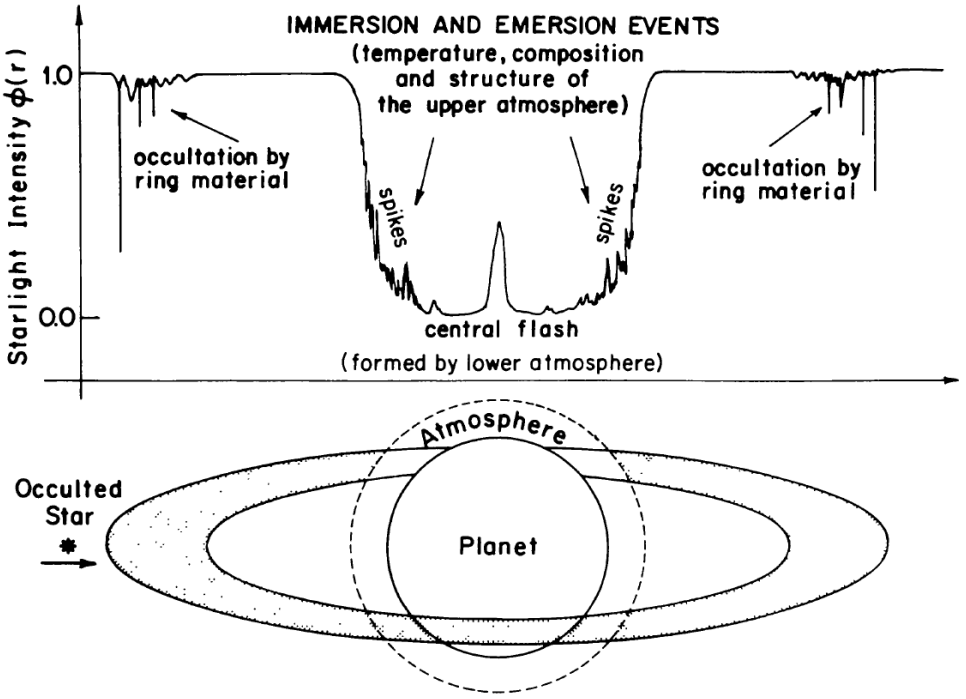

Figure 2.2: Schematic of a stellar occultation of an object with an atmosphere and rings. Shown here is a light curve (above) derived from the stellar occultation of the body below. The star is represented to move behind the body, close to passing through the centre of the object, or close to centrality. The light curve obtained shows the ring features as a drop in flux intensity before and after the main body's occultation. The atmospheric features are shown as the gradual decrease and increase in flux intensity, spikes, and a central flash (discussed in Section 2.1.2). Figure from Elliot (1979).

geometric albedos.

Stellar occultations allow for the detection of dust structures such as rings around the occulting object, a schematic of this is shown in Figure 2.2. One of the most notable historical results obtained are the detection of Uranus' (Millis et al., 1977) and Neptune's (Hubbard et al., 1986; Manfroid et al., 1986) rings. Occultations permitted the detection of rings around the centaur Chariklo (Braga-Ribas et al., 2014), and later the discovery of a ring around the dwarf planet Haumea (Ortiz et al., 2017).

This technique also allows for the detection of an atmosphere, down to an

atmospheric pressure of 10 nbar, in a planetary object, for the best data sets available. This is done by observing the gradual disappearance and reappearance of the star (immersion and emersion, respectively) or through the study of central flashes (Figure 2.2; explained further in Section 2.1.2).

During a stellar occultation by an object that possesses an atmosphere, the flux of the occulted star mainly dims through differential refraction caused by the lensing effect of the atmosphere, or through absorption by haze and/or cloud material in the atmosphere, if any.

Stellar occultations can probe planetary atmospheres to retrieve the temperature, pressure, and number density profiles using the inversion method (French et al., 1978). This assumes that the structure of the atmosphere is in hydrostatic equilibrium. Information may also be obtained using models that are then fit to the data (Elliot and Young, 1992). Depending on the occultation data available, this technique can also be sensible to local density variations, extinction caused by molecules and aerosols, rotation period of the atmosphere, zonal winds, among other atmospheric properties.

2.1.1 Refractive occultations

If absorbing material, such as hazes or clouds, is absent at the levels the occultation technique probed the atmosphere, the dimming of the star, its flux, is due to the refraction bending the starlight. For this work, I focused solely on refractive occultations, the reasoning behind this is explained in Section 5.2.3. Using the equations from Press et al. (1992), and the nomenclature from Vapillon et al. (1973), I will now provide an explanation of the geometry of refractive occultations.

Considering a light ray propagating in a refractive medium with a refraction index $\mu(r)$, defining refractivity as

$$\nu(r) = \mu(r) - 1, \tag{2.1}$$

and the vector $\vec{\tau}$ derived from the unit vector $\hat{u}$ as

$$\vec{\tau} = [1 + \nu(r)]\hat{u}, \tag{2.2}$$

we obtain the Snell-Descartes' refraction law, that shows that the ray is deflected according to

$$\frac{d\vec{\tau}}{ds} = \vec{\nabla}\nu, \tag{2.3}$$

where s is the displacement along the ray, and $\vec{\nabla}$ is the gradient operator. From the refractivity, the molecular density profile can be extracted, using the relation

$$n(r) = \frac{\nu(r)}{K}, \tag{2.4}$$

where K is the molecular refractivity.

Let us consider an atmosphere that refracts light rays coming from a star at infinity, and going towards the observer (assumed to be on Earth), also considered at infinity. This is because distance D between the observer and the object is very large compared to the object's size. This scenario is shown in Figures 2.3 and 2.4.

Outside the atmosphere, $\nu = 0$, so that $\vec{\tau} = \hat{u}$, and the total variation of $\hat{u}$ is

$$\Delta\hat{u} = \int_{-\infty}^{+\infty} \vec{\nabla}\nu \cdot ds, \tag{2.5}$$

providing the total deviation of the light ray, measured by $\|\Delta\hat{u}\|$. This is a small value for ground-based occultations. The deviation angle ω is given by the projection along the vertical axis $0r$ of $\Delta\hat{u}$,

$$\omega = \Delta u = \Delta\hat{u} \cdot \hat{r}, \tag{2.6}$$

where $\hat{r}$ is the unit vector along $0r$.

The bending of the light rays redistributes the initial stellar flux Φ_0, observed outside the event, from a surface element dP at the object's level to a surface element

$$dz = \left[1 + D \cdot \frac{\partial\omega}{\partial r}\right]\left[1 + D \cdot \frac{\partial\omega}{\partial x}\right], \tag{2.7}$$

in the observer plane.

If the atmosphere is transparent, energy is conserved, and the flux Φ received by the observer is given by

$$\frac{1}{\Phi} = \left[1 + D \cdot \frac{\partial\omega}{\partial r}\right]\left[1 + D \cdot \frac{\partial\omega}{\partial x}\right], \tag{2.8}$$

where the unocculted flux is normalized to unity. The first term on the right hand side of Equation 2.8 refers to the defocusing of the light rays as it passes through

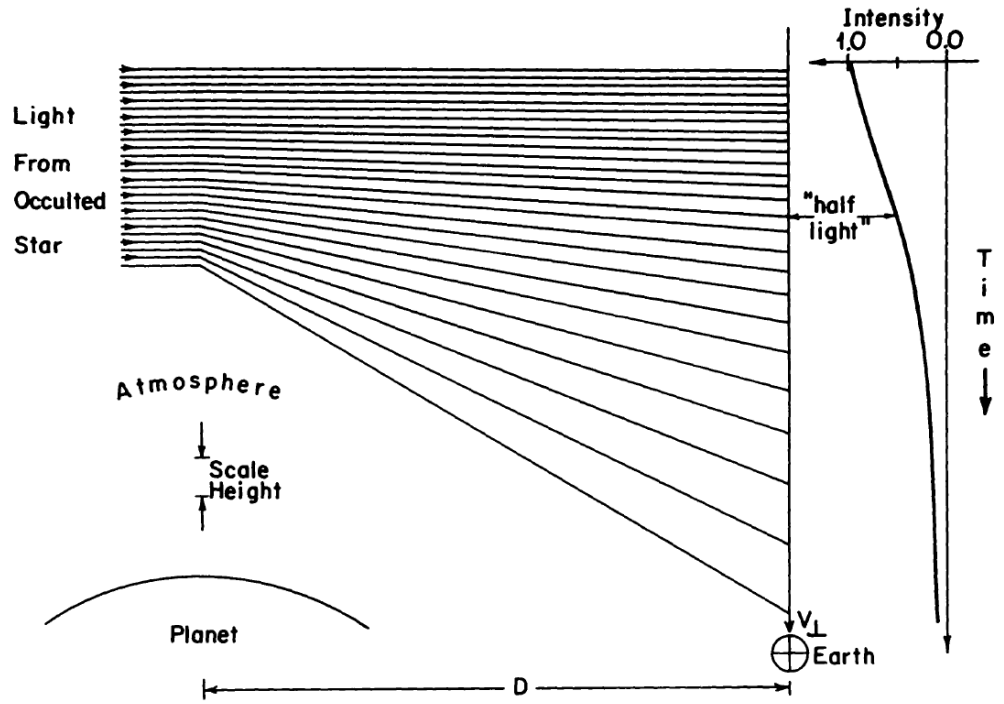

Figure 2.3: Basic geometry of a refractive occultation. Light rays coming from infinity (considered to be parallel) on the left are differentially refracted as they encounter deeper and denser atmospheric layers. The observer notes a decrease of flux with time as the object moves in the observer plane. The half light level is defined as the moment the flux dropped by a factor of two. Figure from Elliot (1979).

the atmosphere, due to the local vertical differential refraction, while the second term on the right side refers to the focusing caused by the curvature of the object's limb.

Absorbing material may influence the incoming flux, decreasing it by a factor of $\exp(-\tau)$, where τ is the optical depth of the material along the line-of-sight. The flux Φ is then obtained using the expression:

$$\Phi = \left(\frac{1}{1 + D \cdot \dfrac{\partial \omega}{\partial r}} \right) \left(\frac{1}{1 + D \cdot \dfrac{\partial \omega}{\partial x}} \right) \exp(-\tau). \tag{2.9}$$

The deviation angle ω is very small for ground-based occultations. In fact, the occulting object's apparent size spans a few arcseconds, giving $\omega \lesssim 10^{-5}$ rad. In

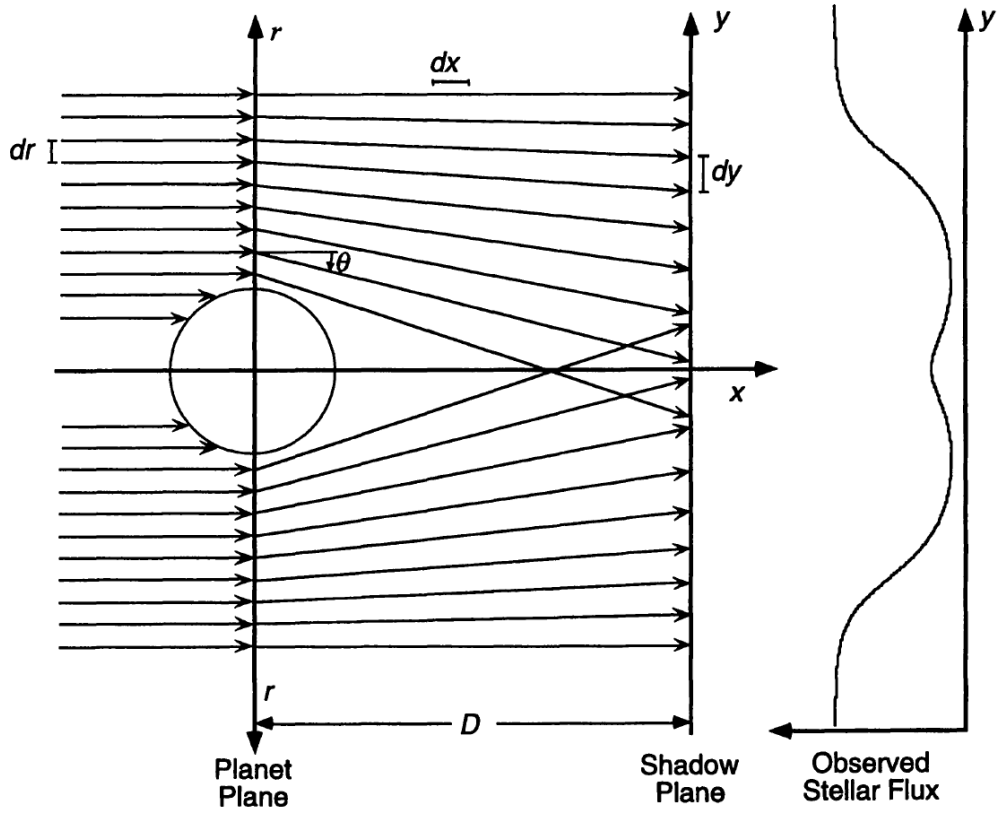

Figure 2.4: In the case of dense atmospheres, light rays can cross the centre line, when the observer is close to centrality, and cause a central flash around the middle of the event. Figure from Elliot and Olkin (1996).

the case of Triton or Pluto, it is actually even less than that, with their apparent sizes of ~ 0.1 arcsec, and an ω in the order of 10^{-7} rad. As a consequence, the light ray suffers a very small shift linearly. The majority of the bending of the ray comes from a length l, of a few hundred kilometers travelled in these types of atmospheres, defined as

$$l \sim \sqrt{2\pi RH}, \tag{2.10}$$

where R is the radius of the object and H is the scale height of its atmosphere. The deviation in the atmosphere is $\sim (l/D)\omega$, a fraction of a metre. This means that we can use a straight line approximation to estimate the integral in Equation 2.5. It is important to note that, because D is very large, the bending of the ray in the observer plane can reach a value of the order of tens of kilometres.

Let us define the scale height as

$$H = -\frac{n(r)}{\frac{\partial n}{\partial r}}, \tag{2.11}$$

ignoring for the moment the curvature of the limb and haze absorption, while assuming that H is roughly constant with altitude, Equation 2.9 gives

$$\frac{1}{\Phi} = 1 - \frac{D\omega}{H} = 1 + \nu\sqrt{\frac{2\pi r D^2}{H^3}}. \tag{2.12}$$

This means that the flux reaches half of its unocculted value, known as "half light level" (denoted with subscript $1/2$), for

$$\omega_{1/2} = -\frac{H}{D}. \tag{2.13}$$

A useful approximation is to consider that the half light ray is bent by one scale height H when it arrives at the observer. This occurs for

$$\nu_{1/2} = \sqrt{\frac{H^3}{2\pi r D^2}}, \tag{2.14}$$

and corresponds to a molecular density

$$n_{1/2} = \frac{\nu_{1/2}}{K}. \tag{2.15}$$

The larger the H, the denser the half light level probed in the atmosphere will be. The larger the D, the smaller $n_{1/2}$ will be. This is the reason why ground-based occultations, despite having incredibly large D, can probe very tenuous atmospheres, with pressures in the order of $\sim \mu$bar, and still observe strong flux drops.

From the definition of the half light level, we have that

$$\begin{aligned} \frac{1}{\Phi} &= 1 + \frac{r - z}{H} \\ 2 &= 1 + \frac{r_{1/2} - z_{1/2}}{H}, \end{aligned} \tag{2.16}$$

which gives

$$\frac{1}{\Phi} - 2 = \frac{r - r_{1/2}}{H} - \frac{\Delta z}{H}, \tag{2.17}$$

where $\Delta z = z - z_{1/2}$. If we now consider that

$$\begin{aligned} \omega &= \nu\sqrt{\frac{2\pi r}{H}} \\ \omega_{1/2} &= \nu_{1/2}\sqrt{\frac{2\pi r_{1/2}}{H}}, \end{aligned} \tag{2.18}$$

we obtain

$$\frac{\omega}{\omega_{1/2}} = \frac{\nu}{\nu_{1/2}} = \exp\left(-\frac{r - r_{1/2}}{H}\right). \tag{2.19}$$

Using Equation 2.12 with ω and $\omega_{1/2}$, we have

$$\frac{1}{\Phi} - 1 = \frac{\omega}{\omega_{1/2}} = \exp\left(-\frac{r - r_{1/2}}{H}\right). \tag{2.20}$$

Now, inputting this equation into Equation 2.17, we obtain the Baum and Code equation (Baum and Code, 1953):

$$\frac{1}{\Phi} + \log\left(\frac{1}{\Phi} - 1\right) - 2 = -\frac{\Delta z}{H}. \tag{2.21}$$

We have that $\Phi = 1/2$ for $\Delta z = 0$, as it was expected. When $\Delta z \gg H$, the edge of the occultation shadow, where

$$\Phi \sim 1 - \exp\left(-\frac{\Delta z}{H}\right), \tag{2.22}$$

we have that at a few scale heights above the half light level, the light curve will tend to unity very rapidly. At that point, the flux drop $\exp(-\Delta z/H)$ will be lost in the noise of the light curve, and we are unable to retrieve any more useful information about the atmosphere. This means that the density can be reliably retrieved up to the level where the flux standard deviation σ_Φ due to photometric noise is comparable to the drop of stellar flux caused by the occultation (Dias-Oliveira et al., 2015). From Equation 2.12, this corresponds to a density of

$$n_{\text{upper}} \sim \frac{\sigma_\Phi}{K}\sqrt{\frac{H^3}{2\pi r D^2}}, \tag{2.23}$$

where n_{upper} denotes the upper limit in the atmosphere where we can still derive the density.

On the other hand, when Δz is negative with a large absolute value, we have

$$\Phi \sim -\frac{H}{\Delta z}, \tag{2.24}$$

where we see that the stellar drop is mild when deep into the occultation shadow. However, this does not account for the curvature of the limb, that causes an increase of the signal near the shadow centre (Eq. 2.9).

2.1.2 Central flashes

If the atmosphere of the occulting object is sufficiently dense, the light rays that probe deep in the atmosphere (passing through or near centrality) may be bent so much that they cross the centre line that connects the star, the object, and the observer, as shown in Figures 2.2 and 2.4. If that is the case, the ray intersects the observer plane at a negative z. This originates the appearance of two stellar images of comparable flux along the limb, and the observation of a central flash. Figure 2.5 shows the two stellar images along the limb of Pluto. The refracted stellar images act as probes of the low atmosphere, close to the surface of the object, and there is the possibility of detecting hazes or even topographic features. Another example is shown in Figure 2.6, where adaptive optics, and the proximity of Titan to Earth, allows the resolution of the object, and the two stellar images.

The second term on the right side of Equation 2.9 comes from the focusing of the light rays caused by the limb of a spherical object. The stellar image is then stretched along the object's limb, much like a microlensing event (Figure 2.7). The difference between these two events is that, in the case of microlensing, this distortion comes from general relativity, and not refraction.

If the atmosphere is transparent, the surfacic flux from the stellar image is constant, and the flux increases as the event approaches the centre of the shadow. When the observer, the object, and the star are perfectly aligned, we reach the maximum value of the observed flux. When this happens, the stellar images form a ring that surrounds the object, with a circumference $2\pi r$ and width Φ_c. Φ_c is the stellar flux Φ at the centre of the shadow without the focusing term, and with $\tau = 0$, in Equation 2.9. Given that two stellar images are present during a central flash,

$$\Phi_{\text{flash max}} = 16\frac{r}{d_*}\Phi_c, \tag{2.25}$$

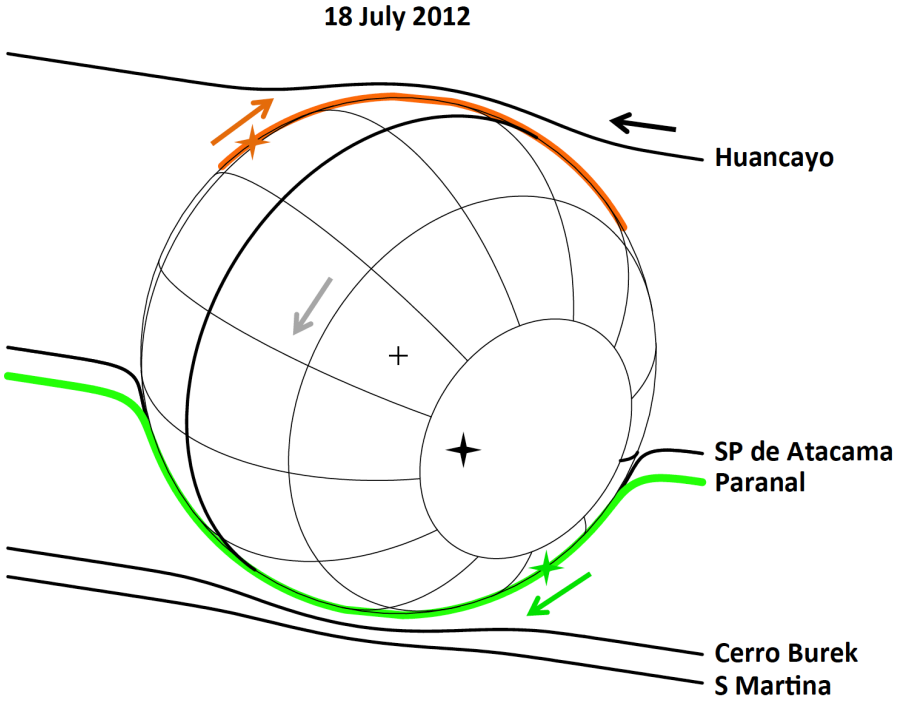

Figure 2.5: Trajectory of the two stellar images created when the shadow path crosses close to centrality from the Pluto occultation observed in 2012. The green curve represents the primary stellar image, while the orange curve corresponds to the secondary stellar image. For a spherical atmosphere, the primary and secondary images (green and orange stars, respectively) are aligned with the position of the star behind the object (black star) and its centre (plus symbol). The gray arrow indicates the direction of the object's rotation, and the other arrows denote the motion of their respective stellar images. The two stellar images always move in opposite directions. Figure from Dias-Oliveira et al. (2015).

where d_* is the diameter of the star projected at the object distance, gives the maximum flux that the central flash can reach. Because r is of the order of $\sim$ 1000 km and $d_* \sim 1$ km, the intensity of the flash may be made larger than the unocculted stellar flux.

If the atmosphere is not spherical, then this not as straight forward. The centres of curvature of the limb are not at the centre of the object, they follow an arrangement, an evolute, of the limb. Figure 2.8 shows a visualisation of such an evolute for an atmosphere with an elliptical shape. This evolute is a diamond-shaped curve, and during an occultation event, observers are able to note a discontinu-

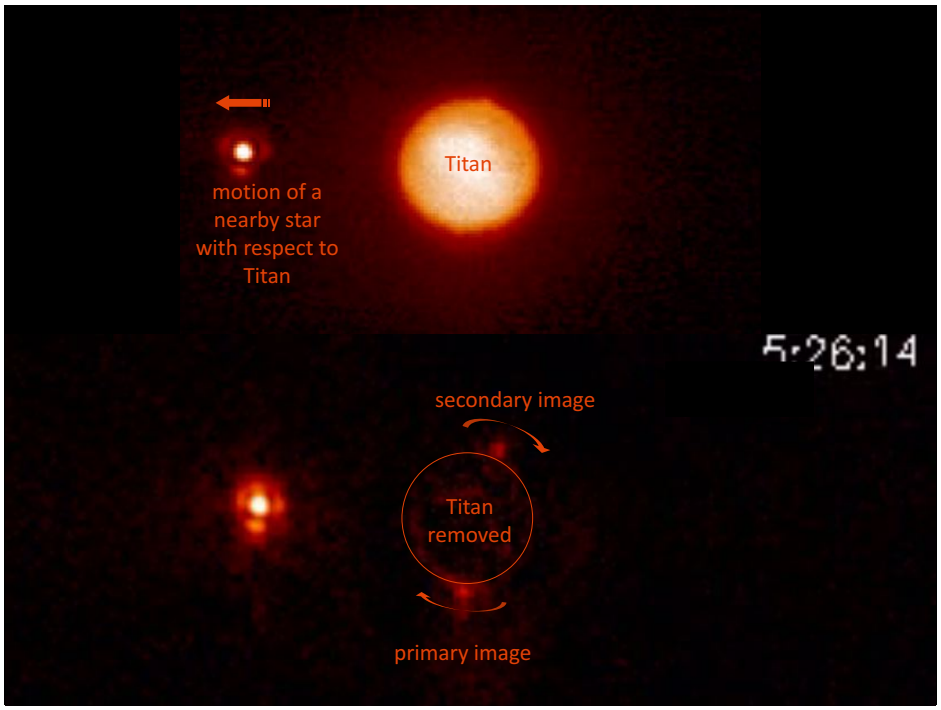

Figure 2.6: Observation of a Titan occultation, on 20 December 2001, where the two stellar images are resolved due to the use of adaptive optics. The 5 m Palomar Hale telescope was used. With Titan's disk image subtracted, it is easy to see the two images created by the occulted star. Figure from Bouchez (2004).

ous increase of the flux caused by the caustics created by the evolute. Figure 2.9 features a real-life example of a complex evolute, as it is the case of Titan's atmosphere (Sicardy et al., 2006).

Central flashes are extremely sensitive to the shape of the atmosphere. The shape of the atmosphere is supported by winds that may be present. Therefore, it is of relevance to introduce some definitions regarding winds. Let us consider only zonal winds, where the wind velocity $\vec{v}$ is directed along a parallel at a constant latitude λ. We then have centrifugal forces that are balanced with a local pressure gradient, defining an isobaric level $r(\lambda)$. If the temperature is constant along this isobar, $r(\lambda)$ defines an isopycnic (constant density) level as well.

Hydrostatic equilibrium requires a balance between gravity, pressure gradient,

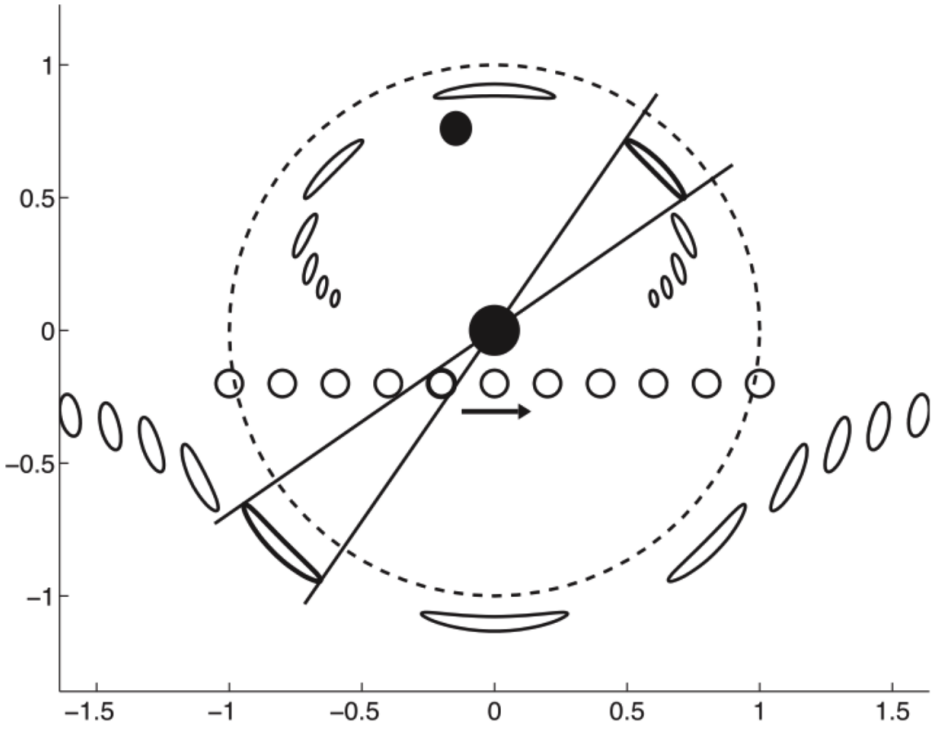

Figure 2.7: The stretching of the stellar images as the star gets closer to the object's centre is a very similar process to that of a microlensing event. In this example, a background star (white dots) presents an elongated image because of the bending that the mass of the foreground star and its planet (large and small black dots, respectively) causes on the light rays. Figure from Abe et al. (2013).

and centrifugal acceleration (Sicardy et al., 2006), so that

$$\vec{\nabla} p = -\rho \left\{ \vec{g} - \left[\frac{v^2(r,\lambda)}{r_\perp} \right] \cdot \hat{u}_\perp \right\}, \tag{2.26}$$

where p is the pressure, ρ is the mass density, $\vec{g}$ is the acceleration of gravity, $v(r,\lambda)$ is the zonal wind velocity, $r_\perp$ is the distance to the planet spin axis, and $\hat{u}_\perp$ is the unit radial vector perpendicular to the planet spin axis. This equation allows the derivation of the shape $r(\lambda)$ of the isobar, provided that the isobaric surface is perpendicular to the vector in Equation 2.26. Therefore, we arrive at

$$\frac{1}{r}\frac{dr}{d\lambda} = -\frac{f \cos\lambda \sin\lambda}{1 - f\cos^2\lambda}, \tag{2.27}$$

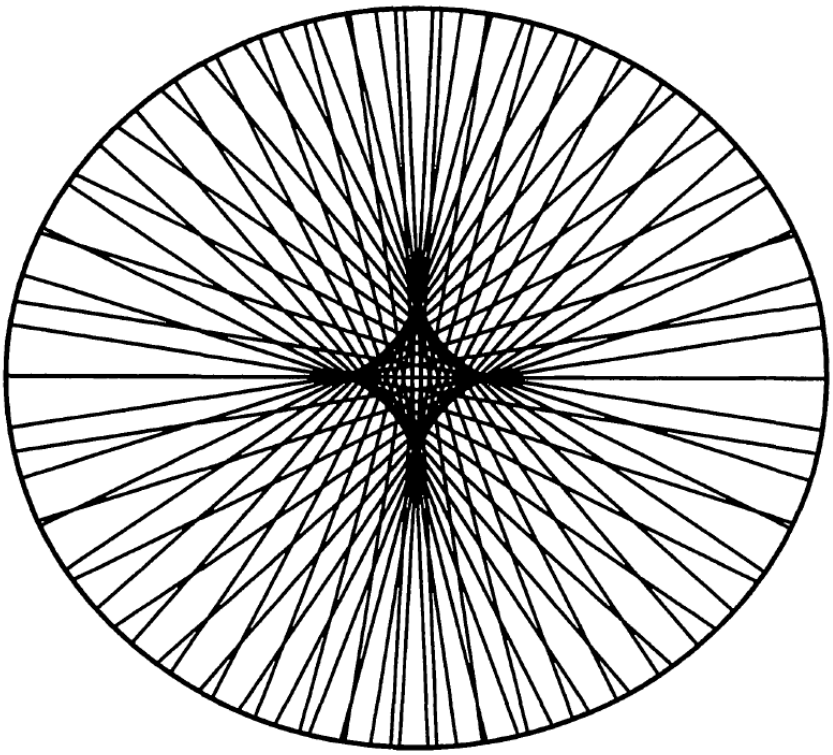

Figure 2.8: A representation of the way the light rays propagate perpendicular to the limb in the shadow of an elliptical atmosphere. The convergence of the light rays close to the centre generates an evolute, which causes caustics where the flux suddenly increases. The oblateness of the atmosphere is exaggerated here to provide a better visualisation of the evolute. Figure from Elliot et al. (1977).

where

$$f = \frac{r^3\Omega^2}{GM} = \frac{rv^2}{GM\cos^2\lambda} \ll 1 \tag{2.28}$$

is the rotation parameter, Ω is the angular velocity of the atmosphere, G is the gravitational constant and M is the mass of the object. Equation 2.27 can be inverted to retrieve the zonal wind velocity (r, λ), when the shape $r(\lambda)$ of the isobaric level is derived from the central flash:

$$v^2 = -gr\frac{dr/d\lambda}{\tan(\lambda) - \dfrac{dr/d\lambda}{r}}. \tag{2.29}$$

Central flashes also allow for the detection, and subsequent study, of hazes. Because the central flash probes the deepest layers in the atmosphere, where hazes

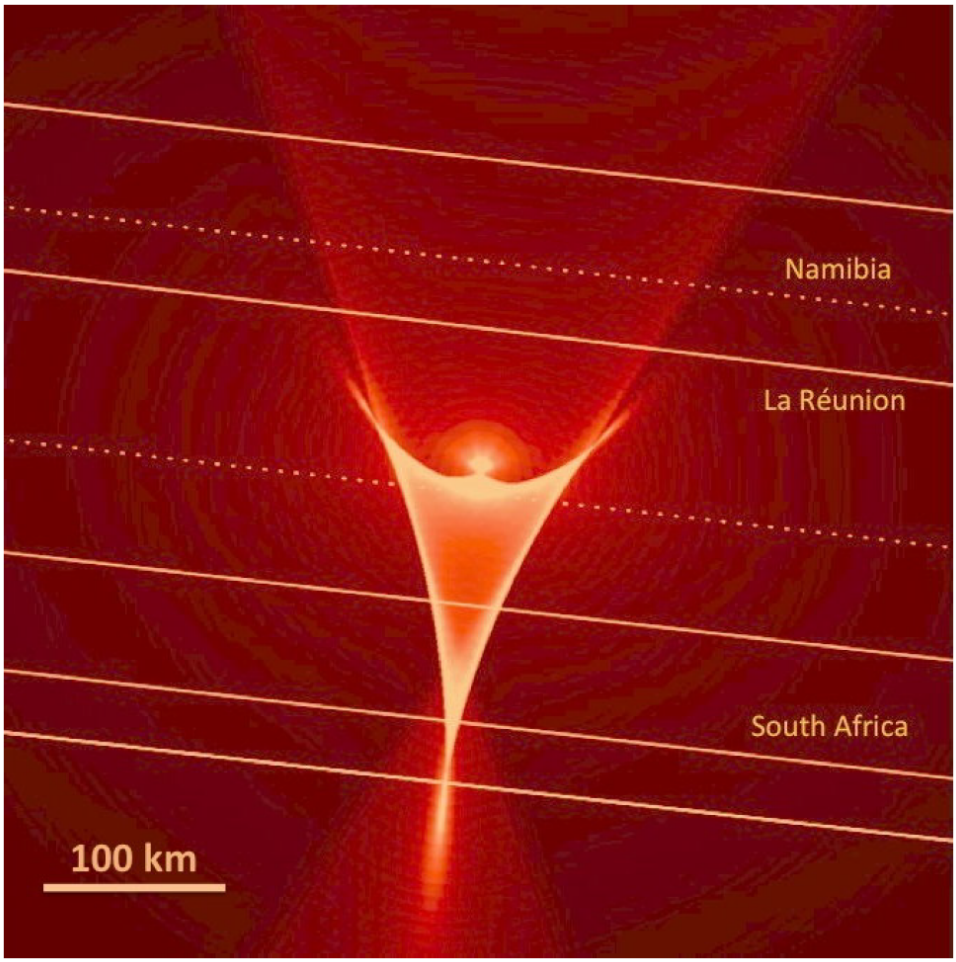

Figure 2.9: Evolute obtained from central flash observations during a Titan occultation on 14 November 2003. If the atmosphere is not elliptical, but presents a more complex shape, the evolute will feature a complex shape as well. Figure from Sicardy et al. (2006).

are most likely to be present, if at all existent, it is the most sensitive part of the light curve to these features. The study of central flashes in different wavelengths is one method of detection. If two light curves taken in the same station, or along the same chord, recorded in different wavelengths, feature central flashes of different flux peaks, that reveals a strong chromatic effect, that can constraint the optical properties of the aerosols of the hazes (Sicardy et al., 2006). Another method of haze detection is the dampening of the stellar flux due to the limb curvature.

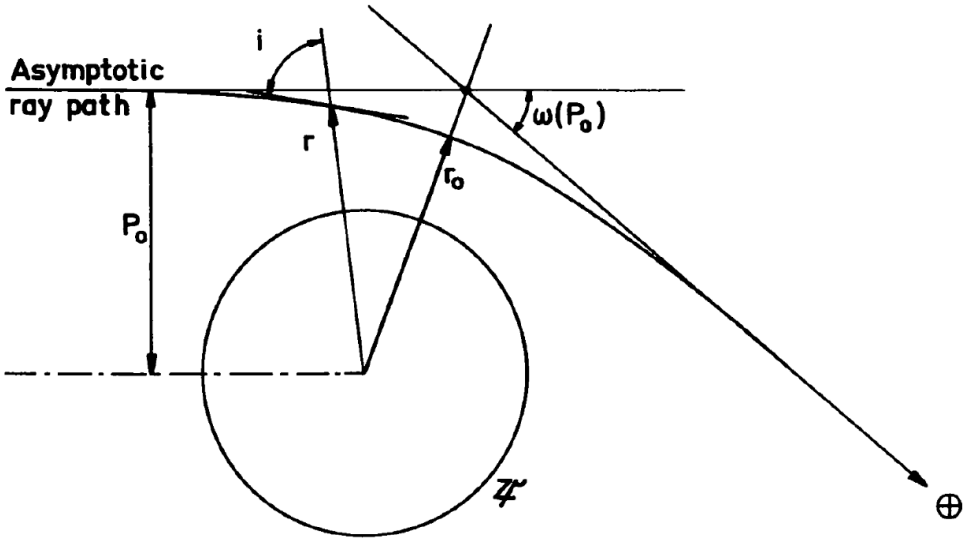

Figure 2.10: Geometry of a stellar occultation involving an object with atmosphere. r is the distance from the centre of the object to an arbitrary point in the atmosphere where the bent ray is passing through, i is the angle between the tangent to the light ray inside the layer and the radial direction of r, and $\omega(P_0)$ is the total bending angle. Figure from Vapillon et al. (1973).

2.2 Methods

Two methods were mainly used to study light curves in my work. They are explained here. Both methods assume that the atmosphere is spherically symmetric and that it is transparent.

2.2.1 Abel inversion

This method is used to retrieve the atmospheric structure from light curves. In particular, we can obtain the density, pressure, and temperature atmospheric profiles. Here I used the equations from Vapillon et al. (1973), but many works have been done on Abel inversions.

The geometry and nomenclature used are shown in Figure 2.10. r_0 is the

radius of closest approach of a light ray to the planetary object. $P_0 = P(r_0)$ is the incoming impact parameter of the light ray. By Bouguer's rule, a version of the Snell-Descartes' law in a spherical atmosphere, P_0 is invariant along a light ray, and we have

$$P_0 = \mu(r) \cdot r \cdot \sin(i) = \mu(r_0) \cdot r_0. \tag{2.30}$$

We now have a relation between the refractive index and the two parameters of a light ray.

Light rays are bent towards the centre of the object, as the index of refraction increases with atmospheric depth. $\omega(P_0)$ is the total deviation angle. Variations in the angle i during the ray propagation are related to variations in $\omega(P_0)$, and we obtain:

$$\omega(P_0) = \int_{r_0}^{\infty} \frac{2p(r)}{\mu(r)} \frac{d\mu(r)}{dr} \frac{dr}{\sqrt{[\mu(r) \cdot r]^2 - [\mu(r_0) \cdot r_0]^2}}. \tag{2.31}$$

This integral can be inverted using an Abel inversion that gives this method its name. We can then obtain the index of refraction $\mu(r_0)$ at closest approach, where the total deviation is ω_0 (Phinney and Anderson, 1968; Fjeldbo et al., 1971):

$$\mu(r_0) = \exp\left\{\frac{1}{\pi}\int_0^{\omega_0} \log\left[\frac{P(\omega)}{P_0} + \sqrt{\left(\frac{p(\omega)}{P_0}\right)^2 - 1}\right] \cdot d\omega\right\}. \tag{2.32}$$

The location of the star in relation to the limb of the object can be described by the observer's motion relative to the occulting body, assuming it is stationary (Figure 2.11). If we assume there is no horizontal gradient of refractivity, then

$$P(t) = R + z_{occ} - z(t) + D[\omega(t) - \omega(t_{occ})], \tag{2.33}$$

where $z(t)$ is measured normally to the star direction, R is the object's radius at this level, D is the distance between the object and the observer, and the time of the half light level is taken as the origin of the time scale.

The bending of the light rays is related to the stellar flux through the equation:

$$\frac{\Phi_0}{\Phi(t)} = -\frac{dz(t)}{dP(t)}, \tag{2.34}$$

where Φ_0 is the flux before the event, and $\Phi(t)$ is the flux as a function of time. Deriving Equation 2.33, using the equality in Equation 2.34, and integrating the result, we obtain:

$$\omega(t) = \frac{1}{D}\int_{-\infty}^{\tau=t} \frac{\Phi_0 - \Phi(\tau)}{\Phi_0} \cdot dz(\tau) \tag{2.35}$$

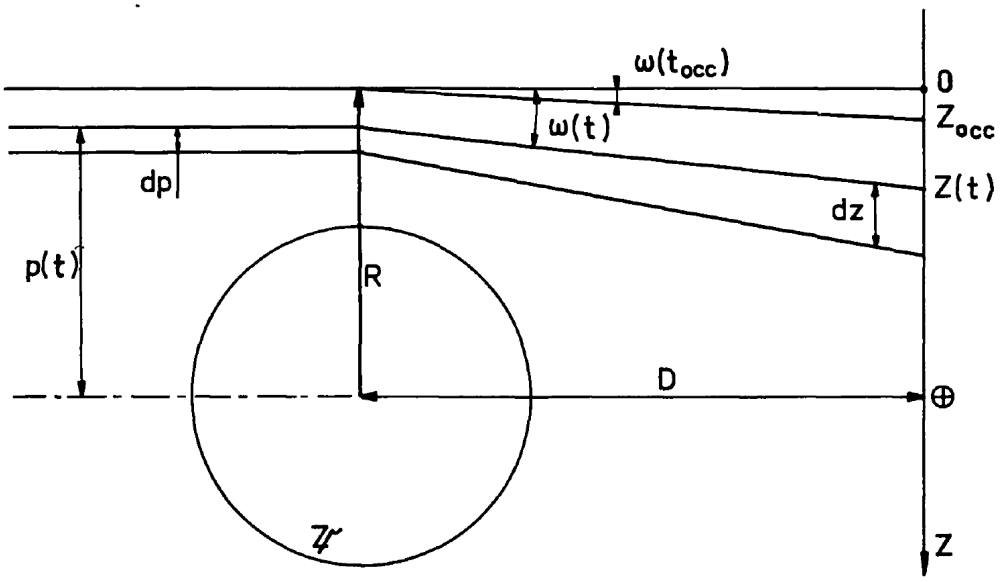

Figure 2.11: Detailed geometry of a stellar occultation involving an object with atmosphere. The axis r has its origin in the centre of the object, and increases radially outward. The axis z is located where the observers are, and has its origin in the centre of the shadow projected there. It increases in the same direction as the axis r. The subscript "occ" refers to the half light level. Figure from Vapillon et al. (1973).

We are now ready to solve Equation 2.32. From it, the molecular density profile can be extracted, using Equation 2.4.

From the $n(r)$ profile, we can derive the pressure $p(r)$, and temperature $T(r)$ profiles using the hydrostatic equation,

$$\frac{\partial p}{\partial r} = -\eta n(r) g(r), \tag{2.36}$$

where η is the molecular mass, and

$$g(r) = \frac{GM}{r^2} \tag{2.37}$$

is the acceleration due to gravity. With the ideal gas equation,

$$p(r) = n(r) k_B T(r), \tag{2.38}$$

where k_B is the Boltzmann constant, we then obtain:

$$\frac{dT}{T(r)} = -\left[\frac{\eta g(r)}{k_B T(r)} + \frac{1}{n(r)}\frac{dn}{dr}\right] \cdot dr. \tag{2.39}$$

It is important to note that the main result of the Abel inversion is the density profile. The temperature profile features a mathematical indetermination that is due to the fact that it is derived from a first-order differential equation, and it needs an initial condition, $T_0 = T(r_0)$. This means that there is an infinity of temperature profiles that can explain the same occultation light curve. The choice of this initial condition requires independent information, such as the temperature derived from a spacecraft at radius r_0, in order to restrict the possible values of $T(r_0)$.

So far, the Abel inversion was described as a method to analyse ray bending. There is, however, other uses of such mathematical property. One of which, also used in this work, is its employment to obtain the refractivity profile $\mu(r)$ from the phase delay $\Delta\phi(r)$ accumulated along the ray that traverses the atmosphere, that may be obtained by a spacecraft's radio science experiment. Again, the Abel inversion provides the refractivity by:

$$\mu(r) = -\frac{\lambda}{2\pi^2}\int_r^{+\infty}\frac{d(\Delta\phi)}{dR}\frac{dR}{\sqrt{R^2-r^2}} = -\frac{\lambda}{2\pi^2}\int_0^{+\infty}\frac{1}{R}\frac{d\Delta\phi}{dR}dl, \tag{2.40}$$

employing the auxiliary variable $l = \sqrt{R^2 - r^2}$ to calculate the integral. This use will be described in more detail in Section 4.2.

2.2.2 Ray-tracing

The other method used, ray-tracing, is employed in several cases. It is a direct method that is used for light curves whose signal-to-noise ratio is insufficient for performing an Abel inversion, or the data points of the light curve are too apart in time, resulting in numerical problems due to coarse sampling. It is used when the station is very close to centrality, and features a central flash, as the Abel inversion method only accounts for one stellar image. With a central flash, the two stellar images have comparable fluxes, as explained in Section 2.1.2. The ray-tracing method is mainly sensitive to the half light level, and accounts for both stellar images, making this method ideal to reproduce and analyse the central flashes. It is also chosen in case there are hazes absorbing part of the flux, biasing the retrieved density, pressure, and temperature profiles.

In many cases, we only need global, and less detailed, parameters than what is obtained using the Abel inversion method. For example, we may be interested in

retrieving the pressure at some fixed radius (surface, for instance), or analyse some simple features of the temperature profile, such as an average temperature gradient in the mesosphere or troposphere, among others. In these cases, we may use the ray-tracing method, as it is a direct method. To use this method, we must have a template temperature profile that can be fit into the light curves, the pressure is fixed at a prescribed radius r_0, employ Equation 2.38 to obtain the density $n(r_0)$, and use Equation 2.39 to retrieve the density profile. Then, from Equation 2.4 we can derive the refractivity profile and its gradient $dv(r)/dr$. Finally, Equation 2.5 can be executed numerically to provide the deviation of the rays, arriving at the synthetic flux through Equation 2.9.

A least-squares fit to the light curves determines the best fitting parameters, such as the pressure at a radius r_0, and the offset perpendicular to the object's apparent motion projected in the sky, $\Delta\rho$, and their respective error bars, through a χ^2 minimization analysis. This method has a small number of free parameters, and weighs each light curve, accounting for the quality of each one. It performs all this using a consistent template model, one of the advantages of this method.

2.3 Photometry

A large part of my Ph.D. was to derive information from the original data obtained by all the observing stations. Therefore, I will explain here how the photometry was performed during this work.

The software ESO-MIDAS, from the European Southern Observatory (ESO), was the image processing tool used. There are some quirks to this software that made each observation require a certain type of attention, always different from one another, in order to have the best photometry possible for each station. The first thing needed was to check if the stars or bodies we may want to use as references were saturated. That is a quick verification using an image visualisation software. In most cases, a renaming of files is necessary to comply with the ESO-MIDAS input format. Moreover, book-keeping of the timings is also required to precisely associate each image with the mid-exposure UTC time. If the observation also includes dark and flat images, these also need to go through the same name changing procedure.

A median of the dark and flat images is made, and the median of the flat images is normalised to unity. A quick verification of the size of the file, telling of how long the program will take to analyse each image, indicates if a trimming of the images is required for run time efficiency, and if so, the area of each cut is defined, so that all the important objects are always in the images, even if the telescope presented some drift, and a large enough background is shown, as it will be necessary in order to remove the background noise from the flux. The median of the dark images is then subtracted from the observation images, and the flat normalisation is divided.

A stacking of some of the observation images before the event is done to reveal faint stars, and the drift of the telescope, if present. We can then check the position of each object, occulted star, and any reference stars or bodies. Offsets from the reference stars or bodies to the occulted star are also determined, as it is important to track it in case the occulted star is too faint for the software to follow, as it runs a gaussian to keep track of the objects' apparent motion on the camera while analysing the images. Finally, some rectangles are positioned (Figure 2.12) to perform a rectangular photometry. The first is the one that will register the flux of all objects throughout the analysis. The second is the rectangle where the software will be looking for the gaussian in order to track its drift throughout the analysis in case the drift is too strong, or there was actual movement to the telescope during the event. If that is the case, these rectangles must be forced into the correct position at certain images, and the software is then allowed to continue its run. The final two rectangles, usually placed above and below the object they correspond to, are used to remove the background from the flux of the object. These rectangles must, therefore, be in background areas, which is the reason why the average is made to reveal faint stars that could influence the flux collected in these rectangles.

When this is all done, the software is ready to run a first time. At this moment, this first run reveals possible errors in the program, or in the positioning of the rectangles. It also allows for the refining of the image interval the software must analyse, to make it less time consuming. If the images are lower quality, the software may lose the occulted star several times, which needs to be corrected by forcing the correct position at the failing image into the program before it is run again. The program displays the image it is analysing in a window, allowing us to track its procedure, and catch if there is any error in the positioning of the

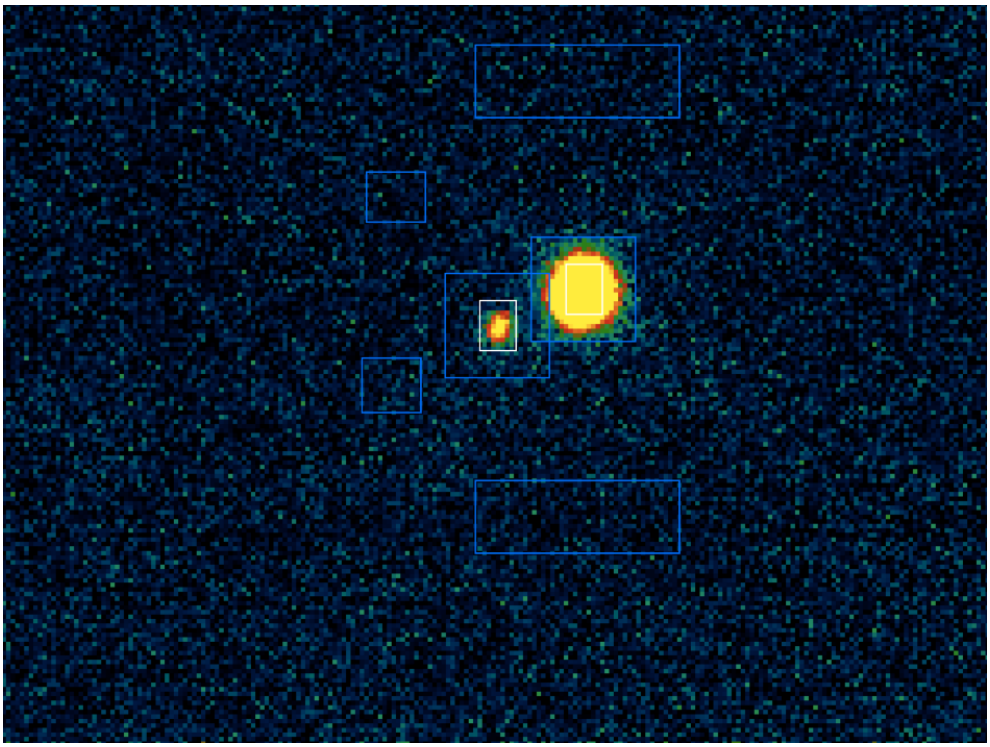

Figure 2.12: Example of the ESO-MIDAS software view during the software's run of the images taken from the Ithaca station for the Triton occultation event on 5 October 2017. The white rectangles are always the same size and record the flux from the occulted star and reference stars or bodies (in this case, Neptune). The blue rectangles just outside these are used to track each object using a gaussian. The other four rectangles are used to subtract the background noise from the flux of the studied objects.

rectangles. Several apertures are also studied in this phase (Figure 2.13), in order to determine the best aperture that yields the highest signal-to-noise ratio in the final light curve.

A Python program that performs a running average on the reference stars or bodies' fluxes is employed once the final version of the photometry is achieved. A ratio between the flux of the occulted star and the reference star or body is the result of this program. This running average is done to eliminate high frequency noise from the reference star's flux, as it would increase the noise of this ratio. The program must analyse several running averages, to determine which would have the highest signal-to-noise ratio. This program also corrects for the time recording

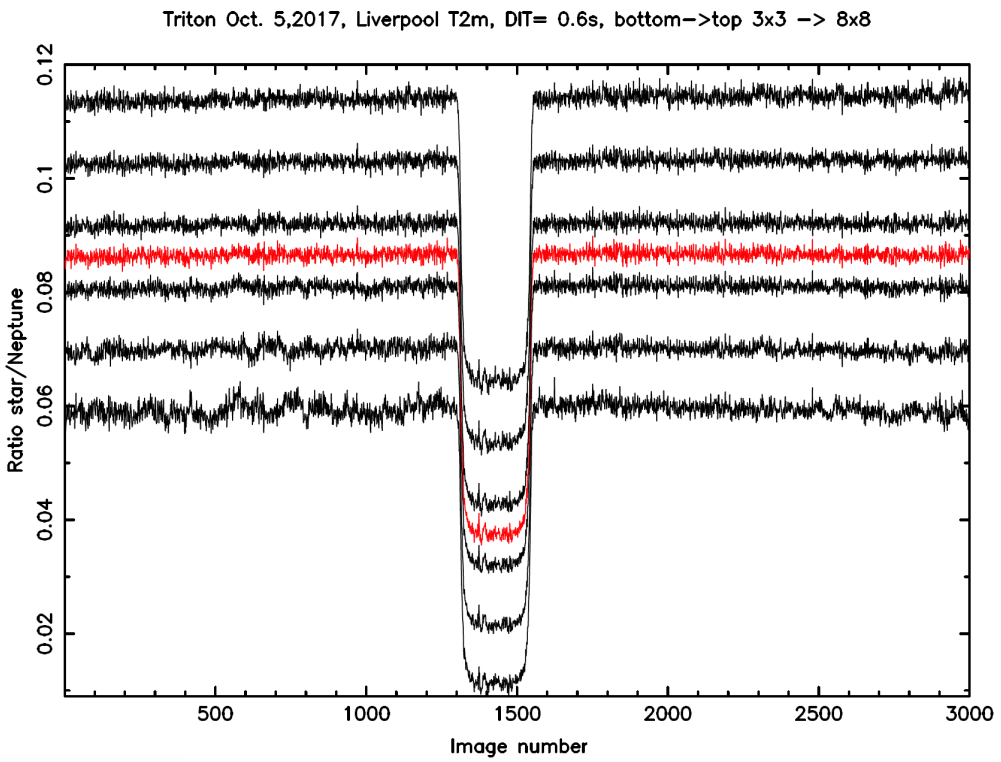

Figure 2.13: Ratio point per point between the fluxes of the occulted star + Triton and the reference star or body (in this case, Neptune) of the La Palma light curve from the Triton occultation event on 5 October 2017. Each of these ratios use different rectangular apertures. The black curves refer to ratios that go from a 3×3 aperture (top-most curve), and it increases until the bottom-most curve with an 8×8 aperture. The red curve shows the best solution for this light curve, with an aperture of 5×6.

of the acquisition cameras, that does not always reflect the mid-integration time. This is not a fixed number, and depends on the type (and even brand) of the camera used. This program is only relevant if at least one of the reference stars or bodies is not saturated. If they are all saturated, or there is no reference star or body in the field, or even if the fluctuations of the reference star or body are unrelated to the occulted star's fluctuations, then the flux of the occulted star is used alone.

We are then ready to normalise the final light curve, obtaining the overall root mean square of the flux fluctuations. The light curve and corresponding root mean square are input into the programs that will perform the ray-tracing. An example of the final light curve, normalised and fit through the ray-tracing code, is shown

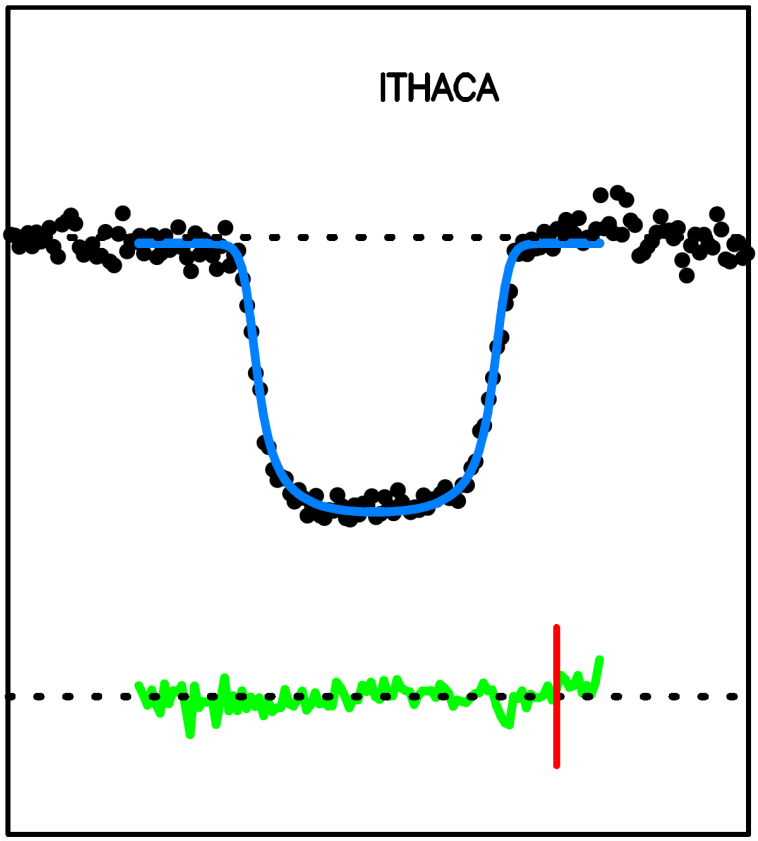

Figure 2.14: Final version of the Ithaca light curve (black dots) from the Triton occultation event on 5 October 2017. The blue line is the fit done using the ray-tracing method with a template temperature model described in Section 4.1.3. The lower and upper horizontal dotted lines refer to the zero-flux level and the total star + Triton unocculted flux (normalised to unity), respectively. The green line is the residuals, and the red line marks 23:55 UTC. The total duration of the panel is five minutes.

in Figure 2.14.

It is important to note the use of rectangular aperture when using the ESO-MIDAS software, rather than a, more common, circular aperture. A comparison has been made between the two types of apertures, with the PRAIA package (Assafin et al., 2011) using a circular aperture. This yielded equivalent results between the two types of apertures.

Chapter 3

Triton

Triton is Neptune's biggest satellite. Discovered on 10 October 1846 (a small history regarding Neptune and Triton's discovery is described in Section 3.1), it is the seventh biggest moon, with a radius of ~1353 km, and the largest irregular satellite in the Solar System (Burns, 1986). Triton is a very curious satellite, and it has been proposed to be a captured Trans-Neptunian Object, discussed in more detail in Section 3.2, with some of the arguments supporting this theory being that it features an eccentricity of essentially zero (0.000016), and a retrograde orbit.

Triton is a potential ocean world (Hansen et al., 2021), highly active, and with a young surface. During NASA's Voyager 2's flyby of the Neptunian system, plumes and geysers erupting from Triton's surface were detected. It is the only satellite, besides Titan, to possess a significant atmosphere, further discussed in Section 3.4.

As we can see, Triton is a very interesting body. A few spacecraft missions have been proposed to study the Neptunian system, with extensive science performed regarding Triton, however, a mission has yet to be approved, or even launched, in the direction of this fascinating system, after Voyager 2's flyby of 1989 (Section 3.3).

Triton is currently exiting its rare "extreme southern solstice", where sub-solar latitudes of up to 50° S were directly and constantly illuminated by the Sun, a configuration that occurs every ~ 650 years (Fig. 3.1) due to a combination of Neptune's heliocentric motion and Triton's orbital precession.

The physical parameters for Triton and its atmosphere that were used in this study are presented in Table 3.1.

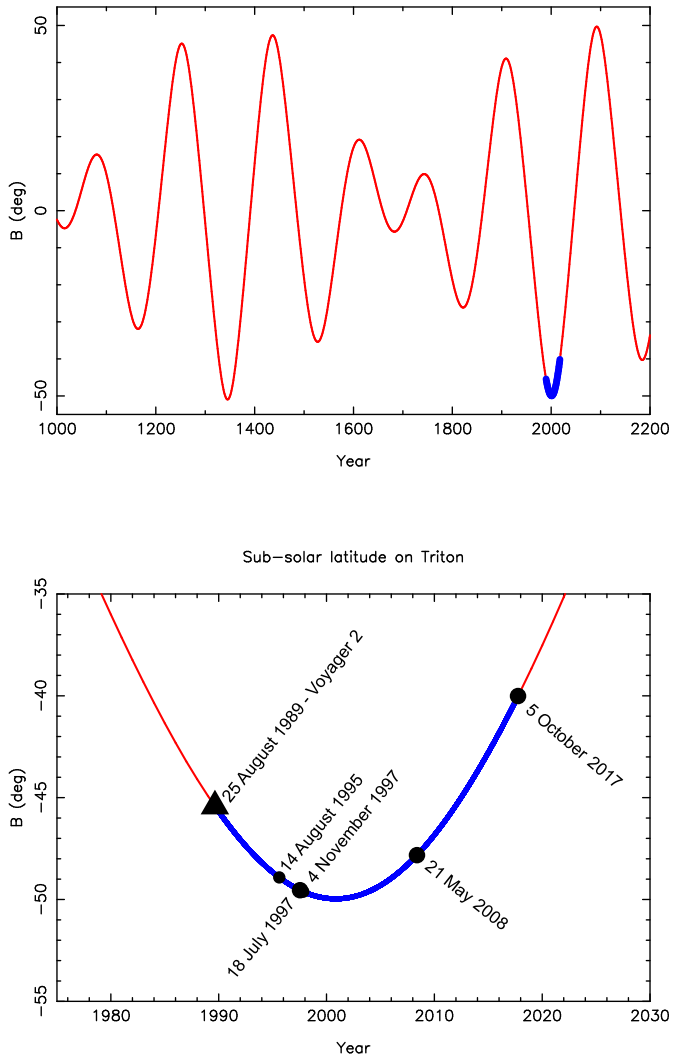

Figure 3.1: The upper panel shows the sub-solar latitude on Triton over time, during the last thousand years. The blue line corresponds to the period of time between Voyager 2's flyby, on 25 August 1989, until the 5 October 2017 stellar occultation. During this time, Triton experienced an extreme summer solstice in its southern hemisphere, with a sub-solar latitude of up to 50° S in 2000. The lower panel is a close up view of the blue line, around the year 2000. The black dots correspond to ground-based occultations observed. The larger dots are from the data that was used in this work. The black triangle is Voyager 2's flyby.

Table 3.1: Adopted physical parameters for Triton and its atmosphere.

Body[a]	
Mass	$GM_T = 1.428 \times 10^{12}$ m^3 s^{-2}
Radius	$R_T = 1353$ km
Atmosphere parameters	
N_2 molecular mass	$\mu = 4.652 \times 10^{-26}$ kg
N_2 specific heat at constant pressure	$c_p = 1.04 \times 10^3$ J K^{-1} kg^{-1}
N_2 molecular refractivity (visible bands[b])	$K = 1.091 \times 10^{-23} + (6.282 \times 10^{-26}/\lambda^2_{\mu\mathrm{m}})$ cm^3 molecule^{-1}
Refractivity at 3.6-cm[c]	$K = 1.0945 \times 10^{-23}$ cm^3 molecule^{-1}
Boltzmann constant	$k_B = 1.380626 \times 10^{-23}$ J K^{-1}

[a] McKinnon et al. (1995), where G is the constant of gravitation.
[b] Washburn (1930).
[c] Gurrola (1995).

3.1 Discovery

Moore (1995) presented a lovely description of the sequence of events leading to the discovery of Neptune and Triton. I will summarize it here to include some of the most important events.

Neptune's story began with the discovery of Uranus, in 1782. Mathematicians found, as early as 1788, that Uranus' orbit was not moving in its predicted path. Observations of the movements of Halley's comet showed that it was also perturbed from its predicted position. Besides these evidences for a Trans-Uranian planet, astronomers also considered that another planet should exist because of Bode's "law".

John Couch Adams was the first to attempt a calculation of this new planet's orbit. He assumed that the distance from the Sun was predicted by Bode's "law", causing the calculation to be incorrect. His estimate of the planet's magnitude, on the other hand, was 8, very close to the actual 7.7. Unfortunately, he did not attempt any observation, as he was not practiced in it, deferring this task to other people.

While Adams was searching for someone that could do the observations, and repeatedly having his requests denied, Urbain Jean Joseph Le Verrier, in France, was also tackling the Uranus problem, challenged by François Arago. His position

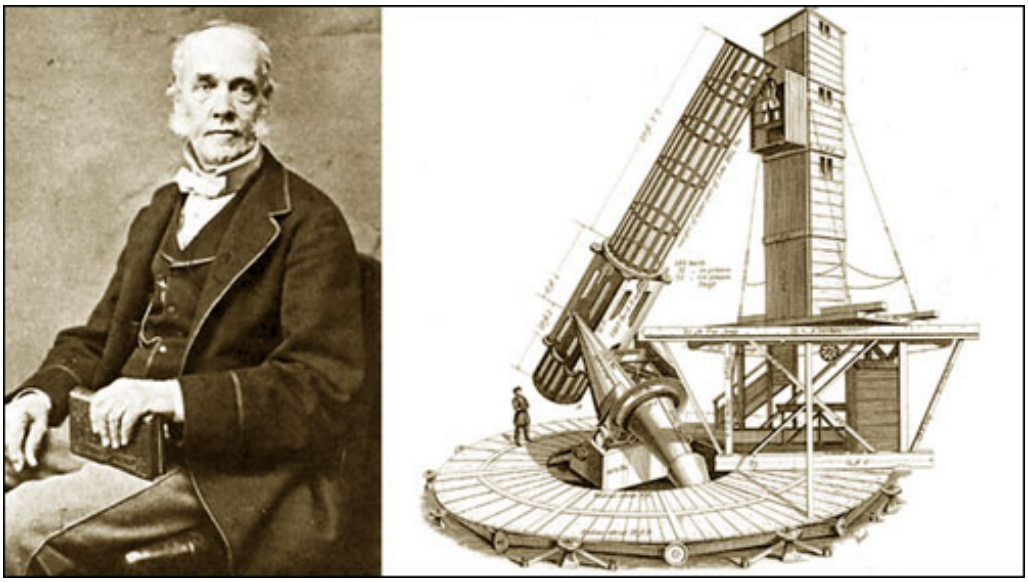

Figure 3.2: English astronomer William Lassell, Triton's discoverer. The 24 inch reflecting telescope depicted here was the instrument used in the discovery. It was completed in 1845, and was the first telescope to be mounted equatorially.

for the planet was in line with Adams' within almost 1°.

On 31 August 1846, Le Verrier provided orbital elements, a position for the planet, and an apparent diameter of about 3.3 arcseconds (the actual value is 2 arcseconds). He expected the observations to be carried out at the Paris Observatory, however, much like with Adam's case, nothing was done. He was not a patient person, so he decided to send a letter to Johann Gottfried Galle, from the Berlin Observatory. Galle received this letter on 23 September 1846, and began the search that very evening. Heinrich D'Arrest, his assistant, suggested to cross-reference the stars observed to a star map: Hora XXI of the Berlin Academy's Star Atlas. Turning the telescope to the position Le Verrier provided, Galle described, within minutes, an 8 magnitude star that D'Arrest noted not to be on the map (Galle, 1846). The find was confirmed the following night, and on 25 September, Galle sent a letter to Le Verrier, relaying the discovery.

On 1 October 1846, John Herschel wrote to William Lassell (Figure 3.2) asking him to search for any satellites of the newly discovered planet. He wasted no time, with his first observation made on 2 October, and on 10 October, only 17 days after Neptune's discovery, he discovered Triton (Lassell, 1846).

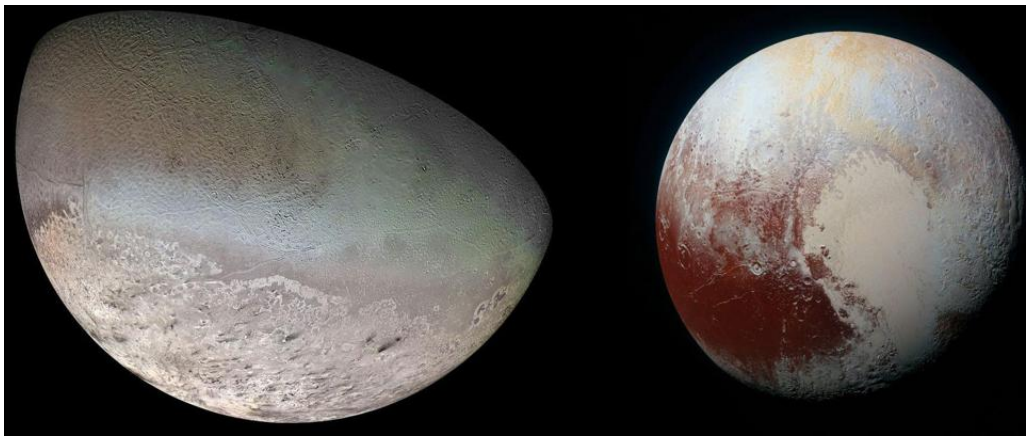

Figure 3.3: Images of Triton (left) and Pluto (right), not to scale. Image data from Voyager 2 and New Horizons (NASA/JPL-Caltech).

3.2 Origin theories

The Neptunian system is unique in the Solar System. It is very unusual, comprised of several small satellites orbiting within 5 Neptune radii (N_R), its biggest satellite, Triton, in a circular, inclined, retrograde orbit at 14.3 R_N, and Nereid, with a semimajor axis of approximately 223 R_N. Nereid features the most eccentric orbit of all of the Solar System's satellites. Triton's orbit places it inside the region that is usually limited to regular satellites, however, its orbit is very inclined and retrograde. It is difficult to explain how one or more protosatellite disks can result in a very compact regular, prograde satellite system with an inclined, retrograde major satellite. Therefore, it is likely that the Neptunian system is not a primordial system, but has been highly evolved or disturbed.

Lyttleton (1936) suggested that Triton and Pluto (Figure 3.3) had the same origin, as Neptune's satellites. He considered that Pluto may have been one of Neptune's satellites, given its proximity to the planet, and the crossing of their orbits. It was then possible that Triton and Pluto had an interaction while they both belonged to the early Neptunian system, and the end result was Pluto's ejection from the system and the reversal of the orbital motion of Triton around the planet. However, when Pluto's orbital resonance with Neptune was discovered,

this hypothesis quickly lost its popularity. This resonance would not allow the two objects to be closer together than they currently are, not in the future nor the past (Cohen and Hubbard, 1965). Many studies were done with a Triton and Pluto as Neptune's satellites configuration, showing that it was highly unlikely for such a configuration to have been the case for these bodies' origin.

A capture hypothesis was first introduced by McCord (1966). Years later, McKinnon (1984) examined constraints regarding the origins of Triton and Pluto, and suggested that Lyttleton's theory should be reversed. Rather than having belonged to the Neptunian system, they both originated as objects with an heliocentric orbit, most likely in the Edgeworth–Kuiper belt. Both of these objects would have been considered dwarf planets, given that Triton's radius (1353 km) is larger than Pluto's (1187 km). Triton was then captured by Neptune. Several hypotheses have been proposed for the specific mechanism that enabled said capture. Two hypotheses seem to be the most favored: collision and gas drag. Triton's capture by the collision scenario is the preferred explanation, but gas drag is possible as well. This preference stems simply from the fact that the collision scenario is simpler to understand and to model. Tidal breaking may also be an important ingredient of Triton's capture (Goldreich et al., 1989; Correia, 2009; Nogueira et al., 2011).

These hypotheses solve many of the mysteries surrounding Triton. They are consistent with Triton's density, surface, atmospheric composition, and geologic history. They also account for Nereid's eccentric, distant orbit, and provide explanations of why there are only small satellites, besides Triton, and why several are in such close proximity to the planet.

Despite the different hypotheses put forward to explain Triton's, and really all of the Neptunian system's, oddity, Triton and Pluto seem to have had the same origin. Either as satellites of Neptune, or dwarf planets formed in the Edgeworth–Kuiper belt, these two bodies seem to be interconnected in their origin. They also have many similarities other than a shared origin. Triton's inferred rock/ice ratio is more in line with Pluto's than any of the other large, regular, icy satellites of the other giant planets (except Europa). Their ice composition is similar, and their thin atmospheres are both in vapour pressure equilibrium with the frost at the surface. There are differences, however, that may derive from the early capture of Triton, and its interaction with Neptune's magnetosphere, or possibly simply due to their size difference.

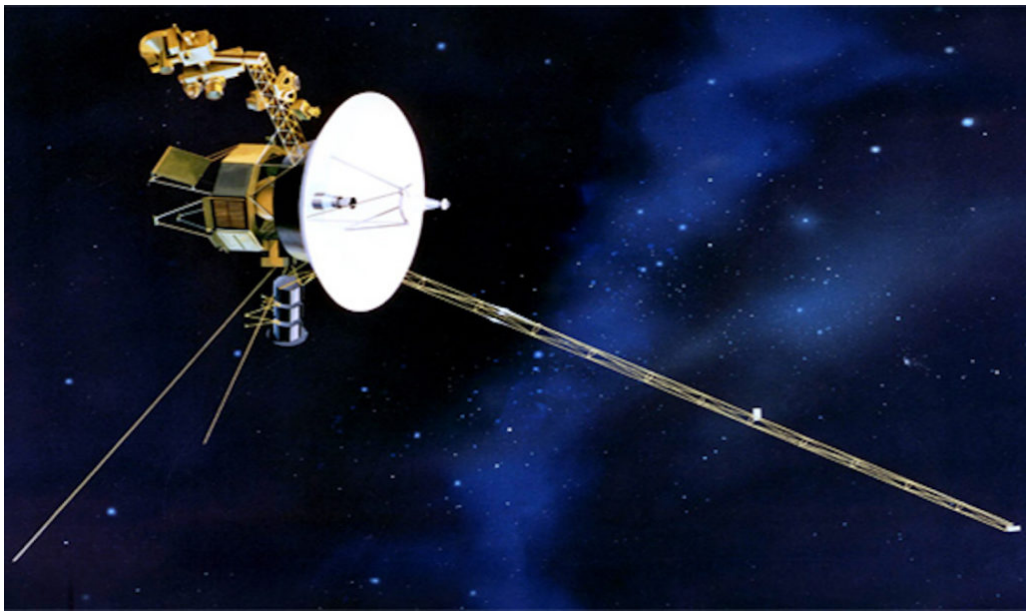

Figure 3.4: An artist's concept of the Voyager 2 spacecraft. Figure from NASA/JPL-Caltech.

3.3 Voyager 2 flyby

Voyager 2's journey, having passed by Jupiter's moons Ganymede and Europa, Saturn's rings and moon Titan, and Uranian system, came to an official end with the flyby of the Neptunian system on 25 August 1989. Voyager 2 (Figure 3.4) was launched on 20 August 1977, before the launch of its twin spacecraft, Voyager 1. Its mission was to fly by Jupiter and Saturn, and, if it survived the crossing of Saturn's rings, would continue on to Uranus and Neptune. The journey was not without its problems, as there was some malfunction in the transmission of the signals after the Saturn ring-plane crossing. Luckily, the problem solved itself, and Voyager 2 continued on, with no more major problems.

As Voyager 2 approached the Neptunian system, data started pouring in, with a pool of images of the system clearer than ever before (or since). A new satellite was discovered one month before the encounter, and days before the encounter, the ring arcs had been detected. Deep inside Neptune's ionosphere, the spacecraft was silent for almost one hour while it passed behind the planet, with the on-

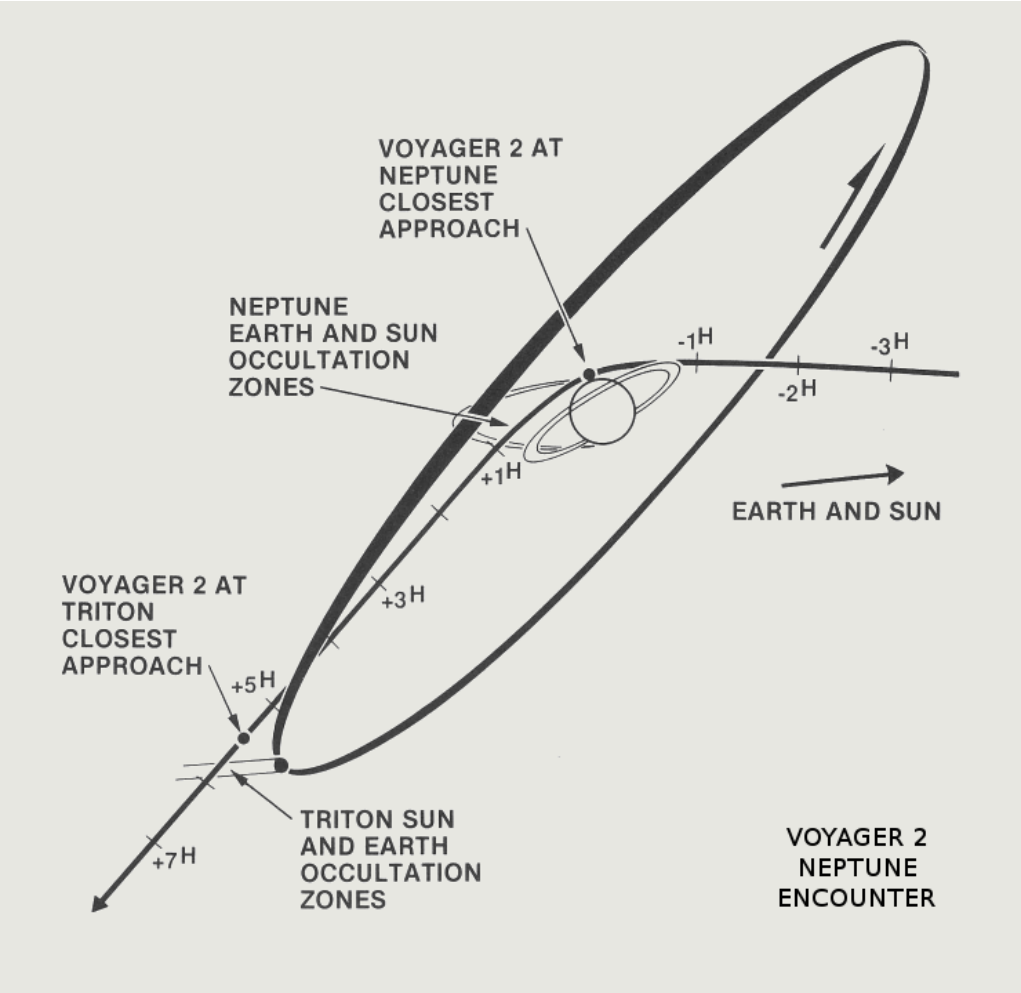

Figure 3.5: Voyager 2's trajectory through the Neptunian system on 25 August 1989. Figure from NASA/JPL-Caltech.

board command sequence taking control of the scan platform and the instruments, sending the data to a tape recorder to relay it later back to Earth. Closest approach occurred at 03:56 UTC, and Voyager 2 was at 29,240 km from the planet's centre (Figure 3.5).

Voyager 2's closest approach to Triton, 39,800 km away from the satellite's centre, occurred 5 hours and 14 minutes after the closest approach to Neptune (Stone and Miner, 1989). Images of its topography, surprisingly young surface, plumes, and clouds were arriving every four or five minutes (Figures 3.6, 3.7, and 3.8). A Radio Science Experiment was conducted on Triton, allowing

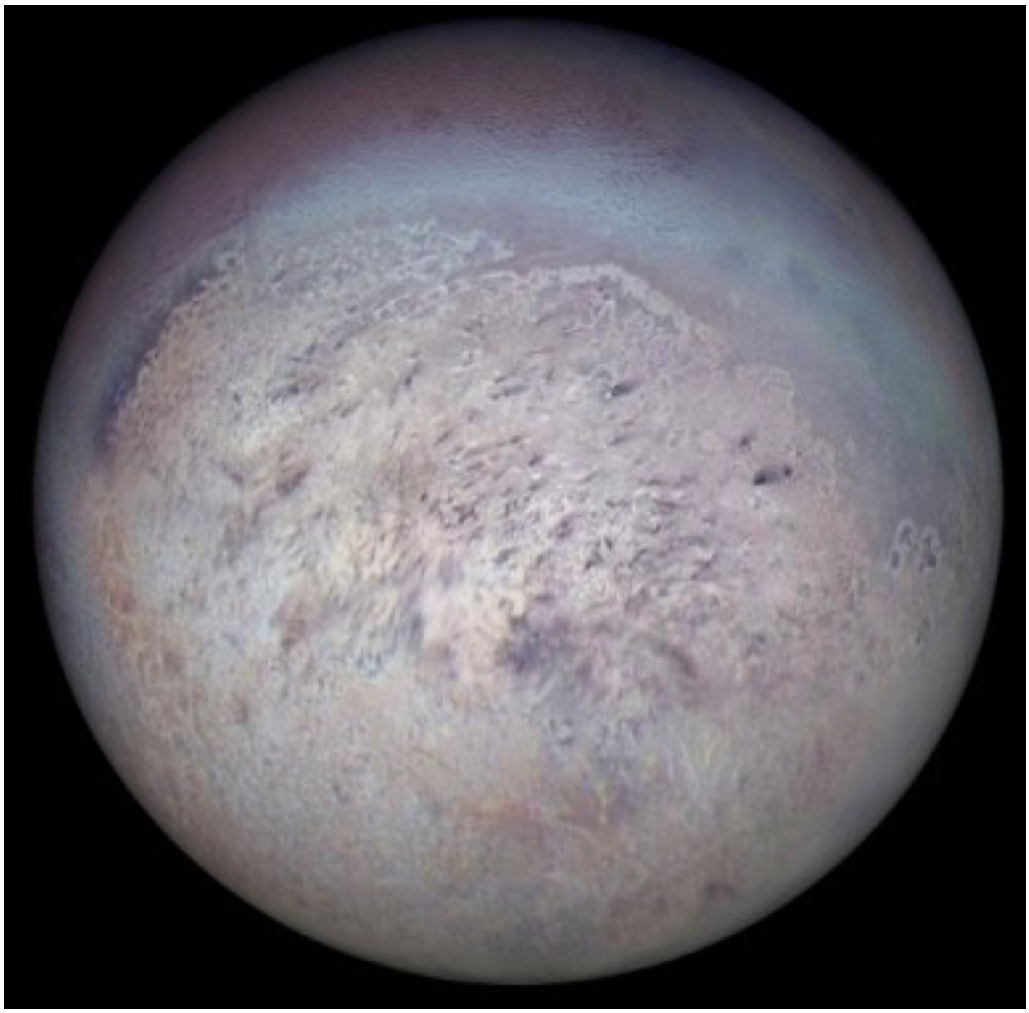

Figure 3.6: Triton's southern hemisphere, revealing an incredible topography, unlike what has been seen on any other rocky or icy moon, and a very young surface. Image data from Voyager 2 (NASA/JPL-Caltech).

for the confirmation of an atmosphere and the obtention of its surface pressure $p_{\text{surf}} = 14 \pm 2$ μbar (Gurrola, 1995). Further description of this experiment is provided in Section 4.2.

After fulfilling its mission successfully, Voyager 2 departed the Neptunian system still recording data, and taking more images of the newly studied planet and its satellite (Figure 3.9). Voyager 2 began its Interstellar Mission extension after leaving the Neptunian system. This mission is currently ongoing. Some of its instruments have been turned off to save power, with the imaging system being the

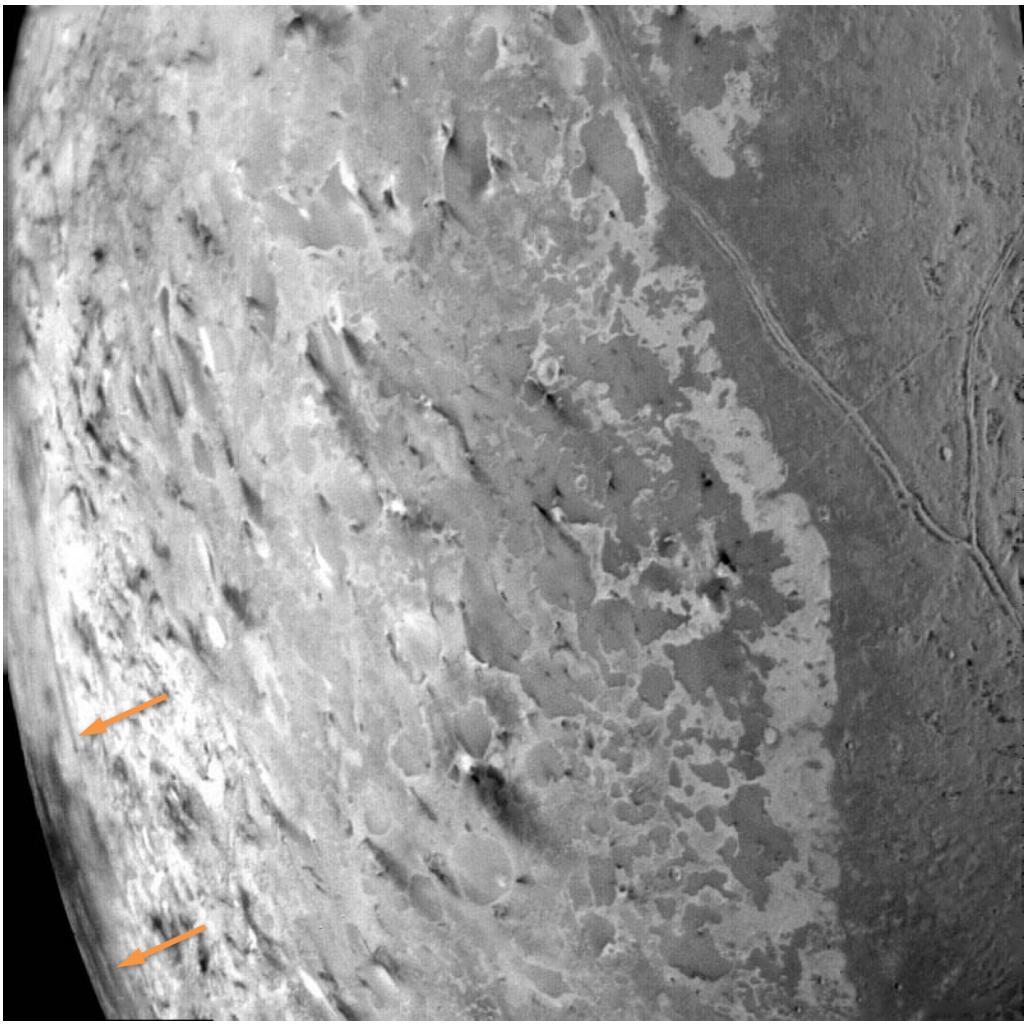

Figure 3.7: Two of Triton's plumes, noted with orange arrows. Image data from Voyager 2 (NASA/JPL-Caltech).

first, in 1989. It has been returning data about cosmic rays and the solar wind ever since. On 5 November 2018, the spacecraft crossed the heliopause. Voyager 2 will continue to return data, this time from interstellar space, until around 2025.

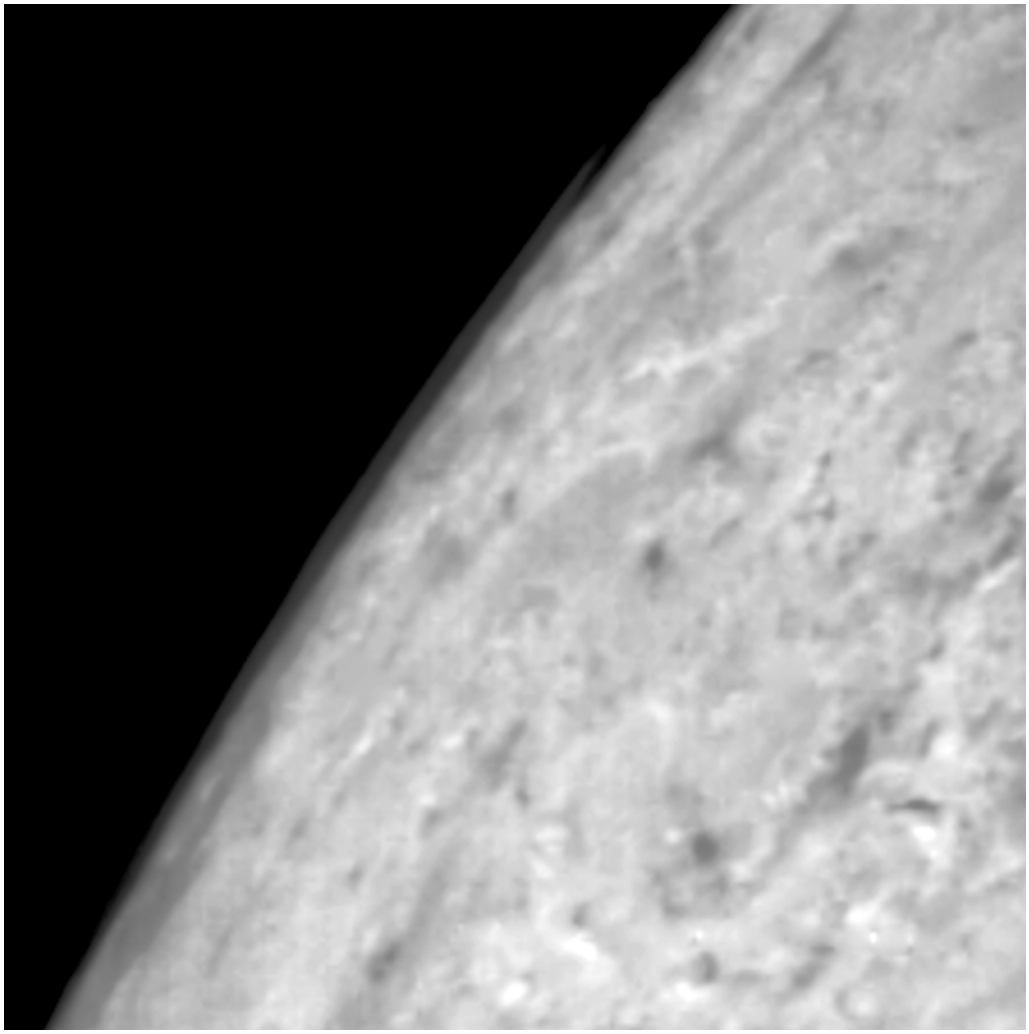

Figure 3.8: Triton's limb, revealing a cloud feature in its atmosphere. Image data from Voyager 2 (NASA/JPL-Caltech).

Figure 3.9: Look back at Neptune and Triton as Voyager 2 was leaving the system, backlit by the Sun. Image data from Voyager 2 (NASA/JPL-Caltech).

3.4 Atmosphere

An atmosphere on Triton was first proposed by Cruikshank and Silvaggio (1979), where they claimed to have detected the spectral signature of gaseous methane (CH_4), however, it has since been shown that these features were due to CH_4 ice on the surface. Regardless, the simple presence of this volatile ice would be indicative of an atmosphere. Ten years later, an atmosphere was confirmed by Voyager 2's flyby. During the flyby, Triton was shown to have a tenuous atmosphere, composed mainly of molecular nitrogen (N_2; Broadfoot et al., 1989), during the Radio Science Subsystem (RSS) occultation, providing its surface density, pressure and temperature (Tyler et al., 1989; Ingersoll, 1990). These results were later improved by Gurrola (1995), who obtained a surface pressure of $p_{\text{surf}} = 14 \pm 2\ \mu\text{bar}$.

As mentioned in Section 3.1, Triton's atmosphere is in vapour pressure equilibrium with the frost at the surface. This happens because, despite its surface being very cold (~38 K), the surface temperature is high enough to partially sublime N_2, CH_4, and carbon monoxide (CO). The abundance of these gases can be calculated using the equations for vapour pressure equilibrium.

Using the nomenclature from Sánchez-Lavega (2010), we start with the Clausius-Clapeyron equation:

$$\frac{dp_{VS}}{dT} = \frac{L_i}{T(V_2 - V_1)}, \tag{3.1}$$

where L_i is the latent heat of the phase transition, $V_i = 1/\rho_i$ is the specific volume (the subscript 1 corresponds to the vapour phase, while 2 corresponds to the liquid or gas phases), and p_{VS} is the saturation vapour pressure in relation to the liquid or solid phases in the vapour pressure equilibrium.

The first law of thermodynamics is the expression of the conservation of energy:

$$\delta Q = dU + \delta W = dU + p \cdot dV, \tag{3.2}$$

where the heat δQ provided to a closed system atmospheric parcel is equal to the increase of its internal energy dU plus the work done on the parcel δW, and V is the volume the parcel occupies.

Using Equations 3.2 and 2.36, and assuming the saturation state and that only one of the components condenses, we get that the amount of heat deposited in the

condensing layer is

$$\delta Q = -L_i \cdot dx_S, \tag{3.3}$$

where dx_S refers to the change in the saturation mixing ratio of the condensable gas, and the first law of thermodynamics can be written as

$$c_p \cdot dT = -g \cdot dr - L_i \cdot dx_S, \tag{3.4}$$

where c_p is the specific heat at constant pressure. From this equation, and using the ideal gas equation and hydrostatic equilibrium, defined in Equations 2.38 and 2.36, it is possible to show (Sánchez-Lavega, 2010) that there are two different adiabatic lapse rates near the surface. One is the "dry" lapse rate:

$$\Gamma_d = \left(\frac{dT}{dr}\right)_d = -\frac{g}{c_p}, \tag{3.5}$$

caused by convective motion near the surface. The other one is the "wet" lapse rate, assuming that the gas is marginally saturated throughout. If the latent heat dominates the kinetic energy of the gas particles, it is:

$$\Gamma_w = \left(\frac{dT}{dr}\right)_w = -\frac{g}{\frac{L_i}{T}}. \tag{3.6}$$

Using parameters of Table 3.1 and $L_i = 2.5 \times 10^5$ J kg^{-1} for N_2, this provides $\Gamma_d = -0.75$ K km^{-1} and $\Gamma_w = -0.11$ K km^{-1}, meaning that $\Gamma_d \sim 6.3\Gamma_w$.

The atmospheric transport of energy in the form of latent heat is efficient, and, therefore, the N_2 frosts are isothermal over the surface. We have that Triton's atmosphere is composed primarily of N_2 gas, comprising 99% of the atmospheric particulates, with traces of CH_4 near the surface with a volume mixing ratio of less than 10^{-3} (Strobel and Summers, 1995; Lellouch et al., 2010). The mole fraction of the surface CH_4 is low enough that it is photochemically destroyed in the lower atmosphere (Strobel and Zhu, 2017).

Voyager 2 revealed clouds in Triton's atmosphere (Figure 3.8), covering 37% of the area poleward of 30°, and stopping at altitudes between 6 and 10 km. Wind regimes were studied using Voyager 2 images of the plumes near Triton's surface (Yelle et al., 1991). The vertical profiles of CH_4 and hazes have been obtained as well using Voyager 2's ultraviolet images (Strobel et al., 1990; Herbert and Sandel, 1991; Krasnopolsky et al., 1993; Krasnopolsky and Cruikshank, 1995; Strobel and Summers, 1995).

Chapter 4

Triton occultation events

In this Chapter, I will present the occultation events studied. In particular, the ground-based occultation event my Ph.D. focused on, that occurred on 5 October 2017, will be described in detail in Section 4.1. I mention the effort made for the prediction of this occultation, the amount of data obtained from a single occultation event, as well as the results obtained, employing the methods shown in Section 2.2.

Three other events were studied and/or reanalysed for this work. Section 4.2 features a new analysis of Voyager 2's Radio Science Subsystem (RSS) occultation, on 25 August 1989, using a new method I made in order to extract more, and new, information from the original data-set. Finally, two other ground-based stellar occultations are described in Section 4.3. These events were all analysed using the same method, employing a template temperature model (described in Section 4.1.3) derived from the results obtained from the 5 October 2017 event, and their respective observations and results are presented.

4.1 5 October 2017

This event was the focus of my four-year Ph.D., taking the bulk of the time to do the photometry of the light curves (described in Section 2.3), and analysing the results retrieved from the data. The event and results obtained are described in detail in this Section. A template temperature model derived from the Abel inversion analysis of this event is provided in Section 4.1.3. I also mention here some

of the difficulties encountered during this study.

4.1.1 Prediction

In the early 2010s, many candidates for occultations by Pluto, large TNOs, and Centaurs were uncovered by surveys made using the Wide Field Imager attached to the 2.2 m Max-Planck ESO telescope (Assafin et al., 2010, 2012; Camargo et al., 2014). These surveys focused on faint stars up to magnitudes of 19 in the R filter. However, no suitable Triton events were found for the interval between 2008 and 2015. This is because Neptune has been crossing a region away from the galactic plane, with little stars.

The problem in predicting occultation events by Triton is two-fold:

- Neptune's orbit could have systematic errors, causing Triton's position to be shifted in relation to the stars;

- Triton's orbit around Neptune may, itself, have systematic errors brought on by the brightness and colour differences between the planet and its satellite, and also from changes in Neptune's magnitude, meaning their relative colour is variable (Schmude et al., 2016).

These two points affect ground-based measurements of Triton and Neptune, and the result is a distorted neptunocentric orbit for Triton. R or I filters can be used to overcome these problems in order to reduce differential refraction during observations. Distributing Triton observations evenly along its neptunocentric orbit, its path can be set by the average ephemeris offsets found for right ascension (α) and declination (δ).

After collecting over 4700 CCD images of Triton between 1992 and 2016 using the 0.6-m B&C and 1.6-m P&E telescopes at Pico dos Dias Observatory (OPD/LNA) in Brazil (IAU code 874), a detailed astrometric work was derived, much like in Assafin et al. (2010) and in Camargo et al. (2014), and an occultation by Triton was found. The event, with a relatively bright star of magnitude V = 12.7, G = 12.2 (UCAC4 410-143659; *Gaia* DR2 2610107911326516992), would occur on 5 October 2017, crossing Europe, northern Africa, and reaching eastern USA.

Between 15 and 23 September 2017, an 8-night run on the OPD/LNA 1.6 m telescope was performed to improve the accuracy of the prediction. Using the PRAIA package (Assafin et al., 2011), reductions were made using the *Gaia* DR1 catalogue. This yielded an uncertainty of about 130 km cross-track, and around 10 seconds for the closest approach. The run covers a full Triton period, meaning that the average offset reflects errors in Neptune's heliocentric position and not a neptunocentric error in Triton's ephemeris.

On 30 September 2017, the *Gaia* team released a preliminary *Gaia* DR2 subset[1], ahead of its official release in April 2018 (Gaia Collaboration et al., 2016, 2018), in an attempt to improve the prediction for this event. This subset featured 431 stars of magnitudes R = 12-17 that surrounded Triton's path in the sky plane during the 8-night run performed at the OPD/LNA. The *Gaia* DR2 catalogue includes star proper motions, allowing for an accuracy at milliarcsecond-level of stellar positions at epoch.

Applying this new catalogue to the 8-night run, it was found that the shadow path showed a significant shift by around 370 km to the south in the sky plane, about 500-700 km when projected on Earth, and reduced the uncertainties by factors of ~ 1.5 and ~ 2.2, respectively.

The updated prediction was released to the scientific community before the event[2]. The map of the shadow track on Earth is displayed in Figure 4.1.

4.1.2 Occultation observations

Over one hundred stations attempted to observe the event. Together, observers in Europe, northern Africa, and eastern USA obtained a total of 90 occultation light curves. Figure 4.2 shows the trajectories of the star relative to Triton (occultation chords) for all positive stations. Appendix A shows the circumstances of observations for all stations involved in this event. Managing over 200 people to give and confirm the information required many working hours and a systematic data organization and communicating with the observers. While many observers provided all the information in the reports, immediately after the event, and were quick to confirm the information, others were unresponsive, and required a number of

[1] https://www.cosmos.esa.int/web/gaia/news_20170930
[2] https://www.cosmos.esa.int/web/gaia/iow_20171005

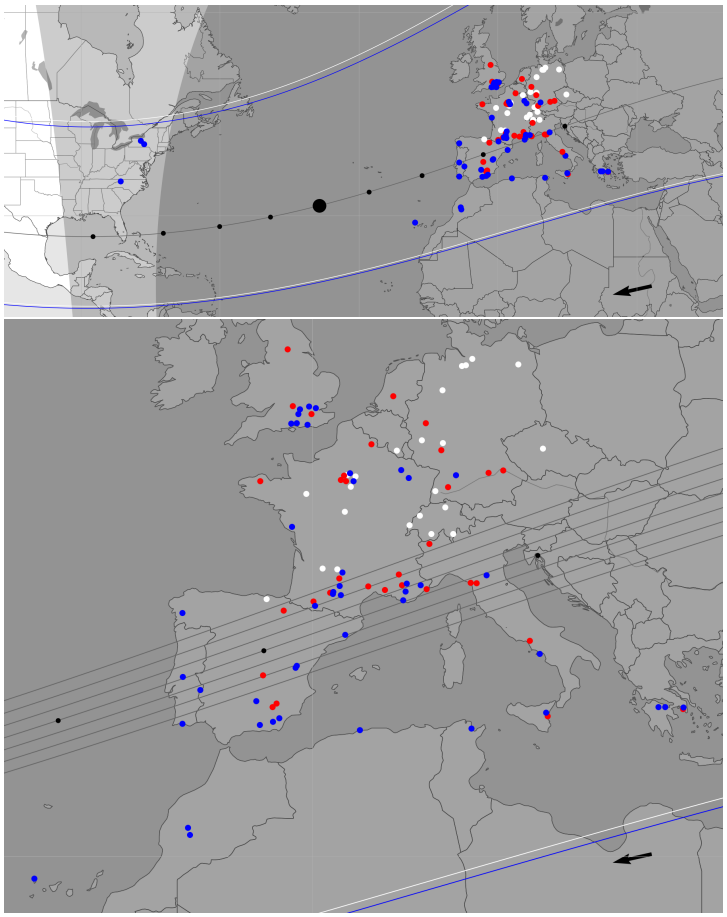

Figure 4.1: Triton's shadow path on 5 October 2017. The biggest black dot along the centre line corresponds to the closest approach of the shadow centre to the geocentre, at around 23h52 UTC. All black dots are spaced by one minute, and the arrow indicates the direction of motion of the shadow. The northern and southern limits of the solid body assuming a radius of 1353 km are represented, showing the predicted path as white lines, and the effective path as blue lines. The dark grey area indicates full astronomical night, and the light grey indicates twilight on Earth. Stations with a successful observation, that have been used in the fit, are represented in blue dots, stations not used are shown as red dots. The white dots are the stations that attempted observation, but were clouded out or had technical difficulties. These images show the amount of observing stations, and therefore, of data obtained from this one event. *Upper panel:* Overview of the observing stations. *Lower panel:* Closer look at the central flash path across Europe. The grey lines around the center line correspond to a spacing of 50 km, once projected in the sky plane.

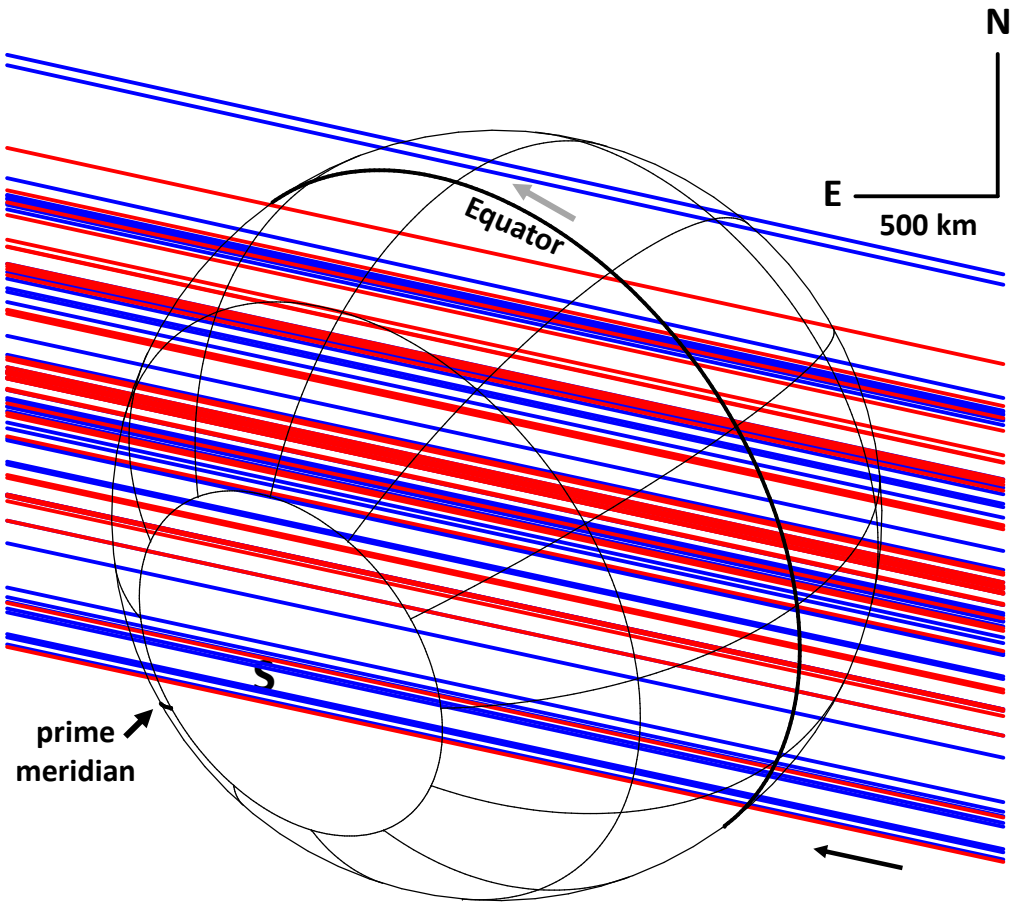

Figure 4.2: Geometry of the 5 October 2017 stellar occultation by Triton, as seen in the sky plane. The J2000 celestial north (N) and east (E) directions and the scale are indicated in the upper right corner. The grey arrow near the equator shows the direction of rotation of the satellite. The Neptune-facing prime meridian is drawn as a thick line, and the south pole is labelled with an S. The inclined lines are the occultation chords as observed from all stations, with the black arrow indicating the direction of motion. A total of 90 occultation light curves were obtained, 52 of them (in blue) were included in a global atmospheric fit, and 38 of them (in red) were not included in the fit.

exchanges to retrieve all the needed information.

All light curves are presented in Appendix B. I derived 18 of the 90 positive light curves, 45 were analysed by various members the Lucky Star group. The remaining 27 were light curves analysed by the observers themselves, and those required some conversion and normalisation to be consistent with the other light

Table 4.1: Triton's geometry on 5 October 2017.

Triton pole position[a] (J2000)	α_p= 20h 09m 29.40s
	δ_p= 20° 25' 34.2"
Sub-solar latitude	40.0° S
Sub-observer latitude	40.5° S
Sub-observer longitude	169.9° E
North pole position angle[b]	305.7°
Geocentric distance	$D = 4.3506 \times 10^9$ km

[a]On 5 October 2017, using Davies et al. (1996), with corrections available at ftp://ftp.imcce.fr/pub/iauwg/poles.pdf.

[b]Position angle of Triton's north pole projected in the sky plane. Counted positively from celestial north to celestial east.

curves. Some stations were analysed by two people from the Lucky Star group in a redundant way, so that I could cross check the consistency of the results obtained. Obtaining the images from all stations was, again, not an easy task. We received images from around half of the stations right away, and these were quickly included in the fit described in Section 4.1.3, provided they had a signal-to-noise ratio of $<\sim 10$ per data point (except for the light curves that presented a strong central flash). However, many observers claimed to have a positive detection but did not provide the data, nor a light curve. Again, a number of exchanges needed to be made to acquire all light curves. At this point, some of them were not included in the fit, even though they had sufficient signal-to-noise ratio, simply because we received their light curve after doing all the analyses. These were, therefore, used only to superimpose the synthetic light curves from the template model discussed in Section 4.1.3.

Table 4.1 lists Triton's geometry for this event. Analysing the light curves (with the methods described in Section 4.1.3), it was shown that the occultation occurred about 9 s earlier, and the shadow centre was 12 km north of the final prediction (shown in Figure 4.1). This difference is at a $\sim 1.3\sigma$-level, insignificant at our accuracy level. It does show that the *Gaia* DR2 astrometry was key in obtaining an accurate prediction, allowing for the detection of the central flash at numerous stations.

4.1.3 Results

To extract information from the plethora of data obtained, we adopted a boot-strap approach, iterating between the Abel inversion and the ray-tracing method (both methods described in Section 2.2). This allowed us to retrieve the molecular density $n(r)$, pressure $p(r)$, and temperature $T(r)$ of Triton's atmosphere as a function of the distance to Triton's centre, r, described as $r = R_T + z$, with z as the altitude from Triton's surface, and R_T as Triton's radius.

This approach assumes that:

- The atmosphere is composed primarily of pure N_2. CH_4, the next most abundant species, has a volume mixing ratio [CH_4/N_2] of less than 10^{-3} (Strobel and Summers, 1995; Lellouch et al., 2010). The ray-tracing code shows that this abundance causes a negligible change (considering the noise level of the data) of the synthetic flux of about 10^{-5} near the half light level.

- The atmosphere is transparent. The deepest layers reached in ground-based occultations of Triton are those of the central flash layer, at an altitude of around 8 km. This assumption will be discussed in Section 5.2.3.

- The upper atmosphere is globally spherical. Section 5.2 shows that the observed central flashes are consistent with a spherical shape, supporting this assumption.

The following discussion explains the results obtained for each method used, and difficulties faced in each of them.

Abel inversion

Inputting the values of K and D listed in Table 3.1 into Equation 2.23, considering that $H \sim 30$ km around $r = 1500$ km, and taking $\sigma_\Phi \sim 0.011$ for our best data set (La Palma station), we find that reliable density values cannot be obtained above $r_{\text{upper}} \sim 1540$ km, where $n \sim 4 \times 10^{11}$ cm^{-3}, corresponding to pressures of a few nbars.

With that in mind, three data sets with the highest signal-to-noise ratio were used in the Abel inversion method (Section 2.2.1). La Palma (2-m Liverpool telescope, Spain) and Helmos (2.28-m Aristarchos telescope, Greece), displayed in

Table 4.2: Local circumstances at the three stations (ingress and egress) used for the Abel inversion analysis.

Site	Time (UTC)[a]	Location on surface	Local solar time[b]
La Palma, ingress	23:48:27	251° E, 10° N	06:36 (sunrise)
La Palma, egress	23:50:52	18° E, 46° S	22:08 (sunset)
Helmos, ingress	23:45:38	254° E, 7° N	06:24 (sunrise)
Helmos, egress	23:47:58	12° E, 47° S	22:32 (sunset)
Calern, ingress	23:46:28	228° E, 32° N	08:08 (sunrise)
Calern, egress	23:49:15	50° E, 30° S	19:00 (sunset)

[a]UTC time at half light level

[b]One "hour" corresponds to a 15° rotation of Triton. Local time before (after) 12 h means morning (evening) limb.

Figure 4.3, were inverted to obtain the shape of the profiles, employing calibration images. The light curve from Calern (1.04-m C2PU telescope, France; Figure 4.4) was inverted later on, to confirm the shape found with the other two light curves, and removing the central flash region of that light curve, as it would influence the inversion process (a secondary image issue is mentioned below). The circumstances of observations for these three stations are shown in Appendix A.

At half light times, and for ingress and egress, these stations probe different locations of Triton's atmosphere. Latitudes, longitudes, and local solar times of the sub-occultation points are shown in Table 4.2. The paths of the stellar images, from these three stations, over Triton's surface are displayed in Figure 4.5.

The first thing to do in order to employ this Abel inversion is to assess Triton's contribution to the total flux in the light curve.

$$\phi_0 = \frac{F_T}{F_S + F_T} \tag{4.1}$$

is the zero stellar flux level in the normalised occultation light curves, where F_T and F_S are the flux coming from Triton and the unocculted star, respectively. Varying ϕ_0 changes primarily the deepest parts of the inverted profiles, as shown in Figure 4.6.

Measuring this value requires images where Triton and the star are angularly separated, in order to have more accurate measurements of each object at the time of the occultation. It is difficult to obtain good calibration images, as the photometric accuracy must be better than 1% to have useful constraints. To get

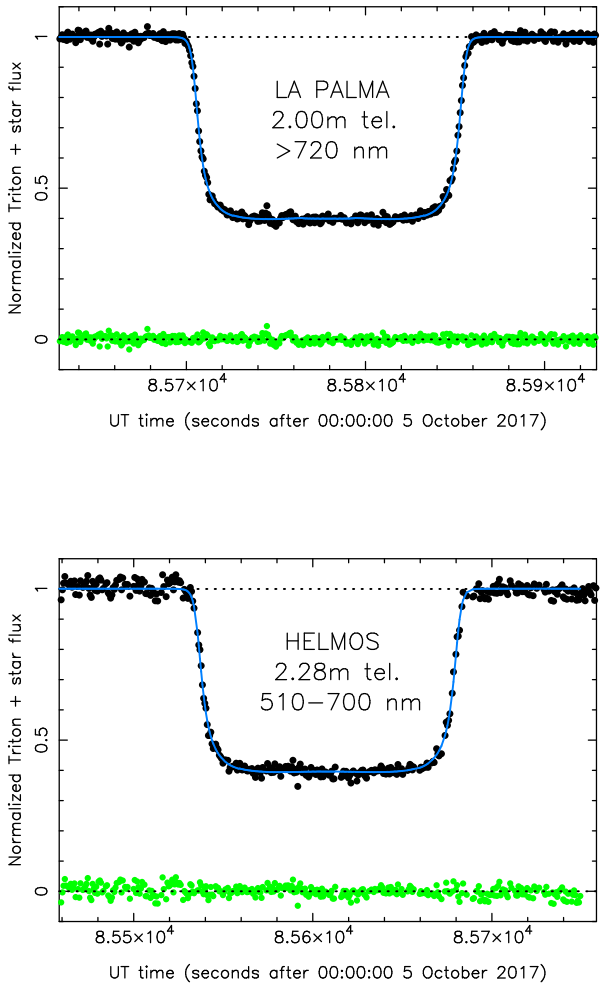

Figure 4.3: The best two light curves obtained (black points), at La Palma and Helmos stations. Both telescopes were equipped with a E2V CCD 47-20 detector with quantum efficiency peaking at 600 nm and reaching zero near 300 and 1000 nm, respectively. The spectral ranges used for each instrument are indicated in the figures (I + z at La Palma and V + R at Helmos). The blues lines are the best simultaneous fits obtained with our ray-tracing approach. The green dots are the residuals of the fits. The panels have a duration of five minutes, centred around the time of closest approach of the station to Triton's shadow centre. *Upper panel*: full resolution light curve (cycle time 0.635 s) for the La Palma station. *Lower panel*: the same for the Helmos station (cycle time 0.674 s).

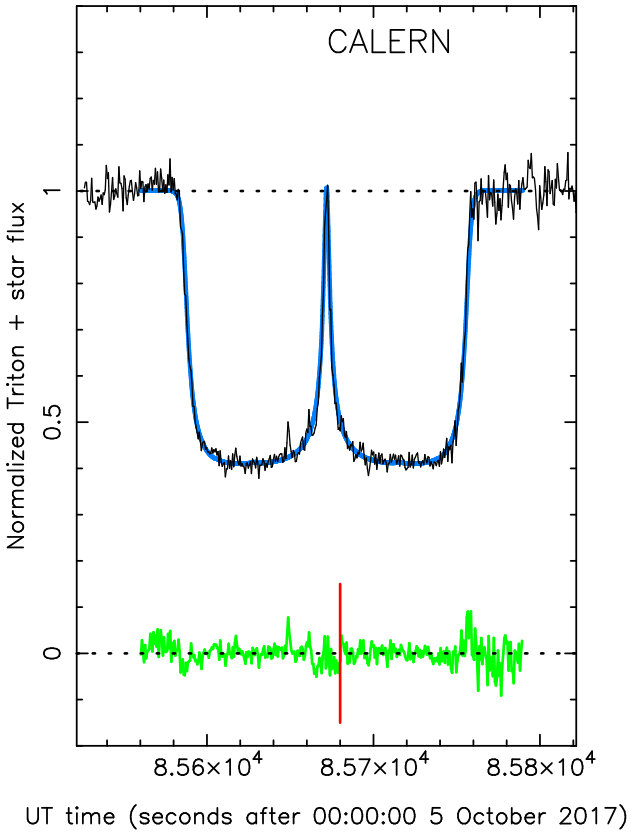

Figure 4.4: Same as Figure 4.3 for the third light curve used in the inversion process, from the Calern station. The blue line is the best simultaneous fit obtained with our ray-tracing method. The black line is the data, and the green curve is the residuals of the fit. The lower and upper horizontal dotted lines mark the zero-flux level and the star + Triton unnoculted flux, respectively. The vertical red line marks the time 23:48 UTC, as reference.

these calibration images, and because Triton and the star have different colours, images must be taken at the same elevation as for the occultation either before or after the event. Having these images taken at the same elevation as the event is meant to minimize differential chromatic effects. It is also preferable to have at

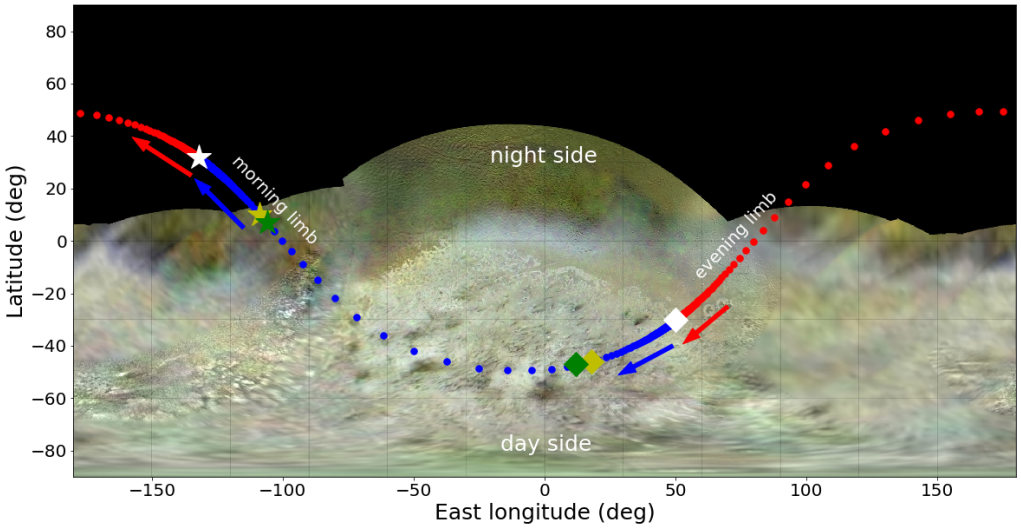

Figure 4.5: Paths of the primary (red dots) and secondary (blue dots) stellar images above Triton's surface, as seen from Constância, plotted every 0.1 s. The junctions between the red and blue paths correspond to ingress (left) and egress (right) for the Constância station. The arrows indicate the direction of the stellar images' path. The regions probed by the central flash are those where the dots are more spaced because the stellar images are then moving faster along Triton's limb. All the other stations probed essentially the same path (or part of it), with the primary and secondary images being swapped (as well as their directions of motion), depending on whether the station probed north or south of the shadow centre. Since the Earth and the Sun are angularly close ($\sim 1^{\circ}$) to each other as seen from Triton, the stellar paths basically mark Triton's terminator, the night side extending above the terminator. The two yellow symbols are for the La Palma station, with ingress plotted as a star and egress plotted as a diamond. The two green symbols are the same for the Helmos station, and the two white symbols for the Calern station, Table 4.2 shows the corresponding values of the latitudes and longitudes. The background image is a global colour map of Triton, produced using Voyager 2 data and orange, green, and blue filter images in order to obtain an approximation of Triton's natural colours. Background image credits: image selection, radiometric calibration, geographic registration and photometric correction, and final mosaic assembly were performed by Dr. Paul Schenk at the Lunar and Planetary Institute, Houston, Texas. Image data from Voyager 2 (NASA, JPL).

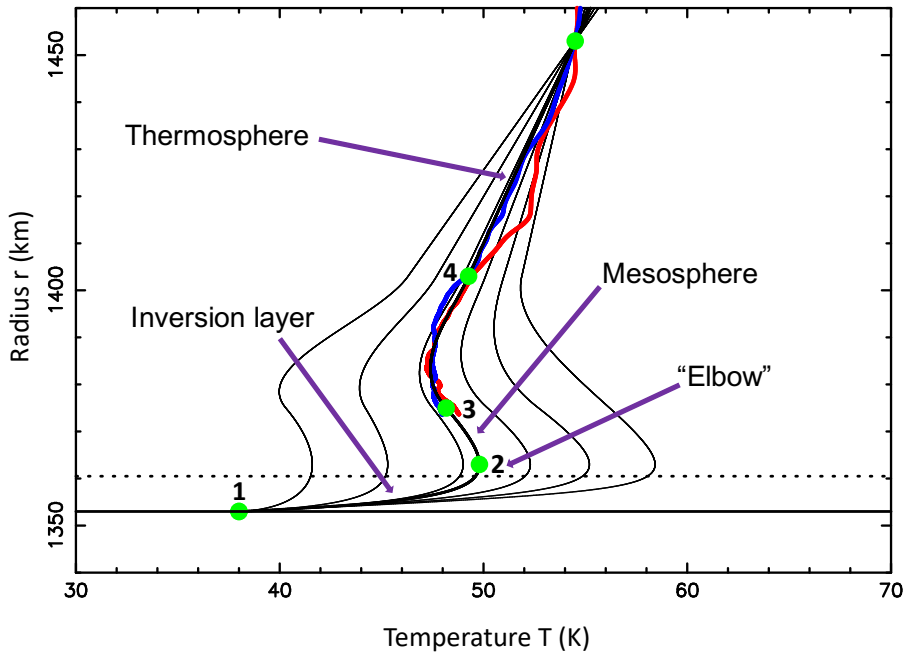

Figure 4.6: Six hypothetical temperature profiles obtained with ϕ_0 = 0.370, 0.365, 0.360, 0.355, 0.350, and 0.3445 (from right to left), for La Palma, represented as the thin black lines. The profile obtained from the calibration images corresponds to ϕ_0 = 0.3445. The best profile found corresponds to ϕ_0 = 0.35885, and the inverted profiles for La Palma are shown in red (ingress) and blue (egress). The green dots labelled 1 through 4 are points specified in Table 4.3 that define the template temperature profile. The horizontal line is the surface, and the dotted line marks the altitude of the central flash layer. The purple arrows denote the different areas of Triton's atmosphere. See also Figure-5.11 for a comparison with the Atacama Large Millimeter/submillimeter Array (ALMA) results.

least one reference star with flux F_R, to see if the following condition is met:

$$\frac{F_S}{F_R} + \frac{F_T}{F_R} = \frac{F_S + F_T}{F_R}. \tag{4.2}$$

If this is not met, it can reveal variabilities in the objects involved, and serve as an estimator of any systematic source of error.

The stations La Palma and Helmos obtained good calibration images, besides being the best data sets in terms of signal-to-noise ratio. The focal lengths

of these telescopes are large, and they can clearly resolve Triton from Neptune and from the occulted star. This avoids, in particular, contamination from the planet to the occultation or calibration light curves. The values obtained were $\phi_0 = 0.3445 \pm 0.0003$ for La Palma, and $\phi_0 = 0.360 \pm 0.013$ for Helmos. It is important to note that ϕ_0 can be different for each station. Observing conditions and instrument filters play an important role in this difference.

The shape of the inverted profile for these two stations can be reconciled by changing the ϕ_0 of one, or both, stations. However, ϕ_0 needs to be changed well outside of the error bars so they match with each other, meaning the values of ϕ_0 for La Palma and Helmos are mutually inconsistent. They provide significantly different bottoms for the temperature profiles. This is especially problematic for La Palma, where the temperature profile peaked at $T \sim 58$ K just above the central flash layer, using the $\phi_0 = 0.3445$ derived from the calibration (right-most profile in Figure 4.6).

Even the synthetic light curve derived from this template temperature profile provided a central flash that was too narrow when compared with the observations, prompting us to think that the temperature profile was different between the northern and the southern hemisphere, or that the inversion layer was even stronger to connect the surface than what we ultimately arrived at.

We could not find an explanation for why the value of ϕ_0 in La Palma was so inconsistent. A number of possibilities were considered. The first was unaccounted light contamination from Neptune, even though this telescope was one of the biggest used in the event, and should not have had this problem. Digital coronagraphy was used to test the effect of this possible contamination. However, there were no significant changes to ϕ_0 by employing this technique. Next, we considered if variations of Triton's flux due to rotational light curves were possible. Considering the low amplitude of said curves (Buratti et al., 2011), and the fact that the calibration images were taken 90 minutes before the event at La Palma, Triton's flux variation should be below the 1% level, with a negligible effect on the value of ϕ_0.

For these reasons, we decided to vary the value of ϕ_0 from the La Palma light curve. Using small incremental steps, the light curve was inverted to obtain the station's temperature profile. The same modelling as in Dias-Oliveira et al. (2015) was used, except that the upper branch of the temperature profile is not isothermal.

Table 4.3: Parameters of the template temperature profile used.

r_1, T_1, $dT/dr(r_1)$	1353 km, 38 K, 5 K km^{-1} (surface)
r_2, T_2, $dT/dr(r_2)$	1363 km, 49.8 K, 1.2 K km^{-1} ("elbow")
r_3, T_3, $dT/dr(r_3)$	1375 km, 48.2 K, -0.2 K km^{-1} (inflexion point)
r_4, T_4, $dT/dr(r_4)$	1403 km, 49.3 K, 0.105 K km^{-1} (upper branch, thermosphere)

It has a constant gradient $dT/dr \sim 0.1$ K km^{-1} to account for a general temperature increase, at the thermosphere level, described in Strobel and Zhu (2017). We find a best fit with $\phi_0 = 0.35885$ for La Palma (thicker line in Figure 4.6), fitting the central flashes well, and remaining within the error bar of Helmos. Using a recent Atacama Large Millimeter/submillimeter Array (ALMA) analysis (Gurwell et al., 2019), we see that this best fit matches with their independent observations. This point is also discussed in Section 5.2.3.

The results of the inversion are shown in Figures 4.7-4.10. Also plotted in these figures are the profiles retrieved from the analysis of the RSS occultation, described in Section 4.2.

Using the notations of Dias-Oliveira et al. (2015), and adopting the parameters of Table 4.3, the template temperature profile was constructed. T and dT/dr profiles are continuous, however, the d^2T/dr^2 profile is not. This discontinuity creates a very small bump at point 3 (in Figure 4.6) in the synthetic light curve, shown in Figure 4.11. This bump is well below the noise level of the observed light curves, and therefore, has a negligible effect to their fit. Figure 4.11 also shows why it is not possible to probe down to the surface of Triton with our stellar occultation data. The point that probes the surface, indicated as point 1, is a very faint signal, and actually gets blended with the stronger signal, meaning we cannot get information below about 8 km altitude.

Starting from the surface, the profile has a strong positive temperature gradient of 5 K km^{-1} (Figure 4.10). This gradient decreases rapidly and the temperature reaches a maximum of about 50 K at $r = 1363$ km (10 km altitude), with an average gradient of 1.2 K km^{-1} in that part. The data show a hint of a mesosphere with a negative gradient (also seen in Elliot et al., 2003) that reaches -0.2 K km^{-1} at $r = 1375$ km (23 km altitude), before connecting with the positive gradient of the upper branch.

The strong surface temperature gradient at the surface derives from the need

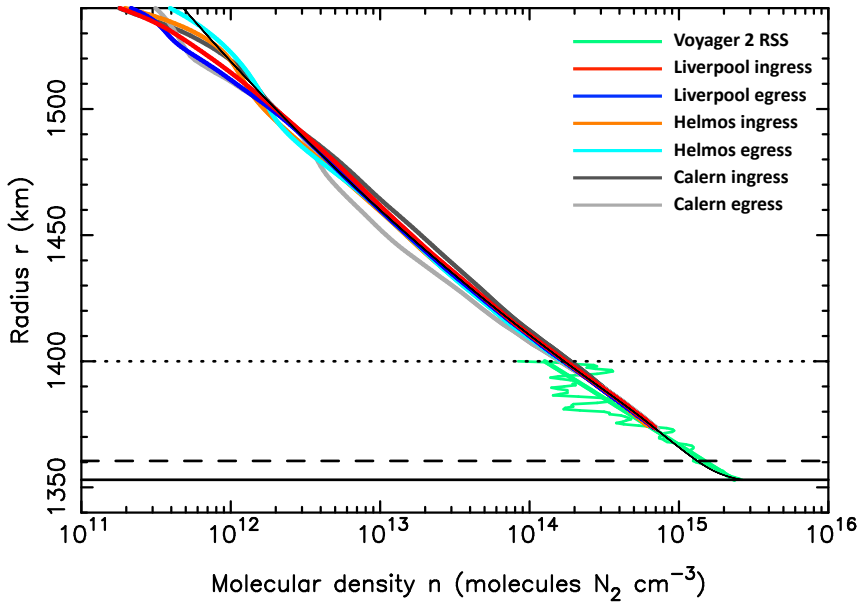

Figure 4.7: Density profiles of Triton's atmosphere as a function of radius r, retrieved by inverting three light curves obtained during the 5 October 2017 occultation and from the Voyager 2 radio phase delay at 3.6 cm. The colour codes are indicated in the upper right part of the plot. The thin black curve is a smooth synthetic density profile that fits the inverted profiles and is extrapolated down to the surface, derived from the smooth temperature profile shown in Figure 4.9. The solid horizontal line marks Triton's surface, the dashed line indicates the central flash layer (around 1360 km), and the dotted horizontal line marks r_{ref}.

to connect our inverted profiles to the surface at 38 K. Since we do not have information in this lower portion of the atmosphere, the simple hyperbolic form of Dias-Oliveira et al. (2015) was employed to connect the template profile to the surface, so that the surface gradient does not necessarily reflect the real value at that level. A different value for the surface temperature would not have an influence on the fit to the data, as the data probe only down to about 8 km. Because of this, even if the surface were warmer than the N_2 surface ice (that is at 38 K), we would not be able to discern anything from our data. Therefore, we decided to stick to the value presented in the literature, and the value for the surface pressure

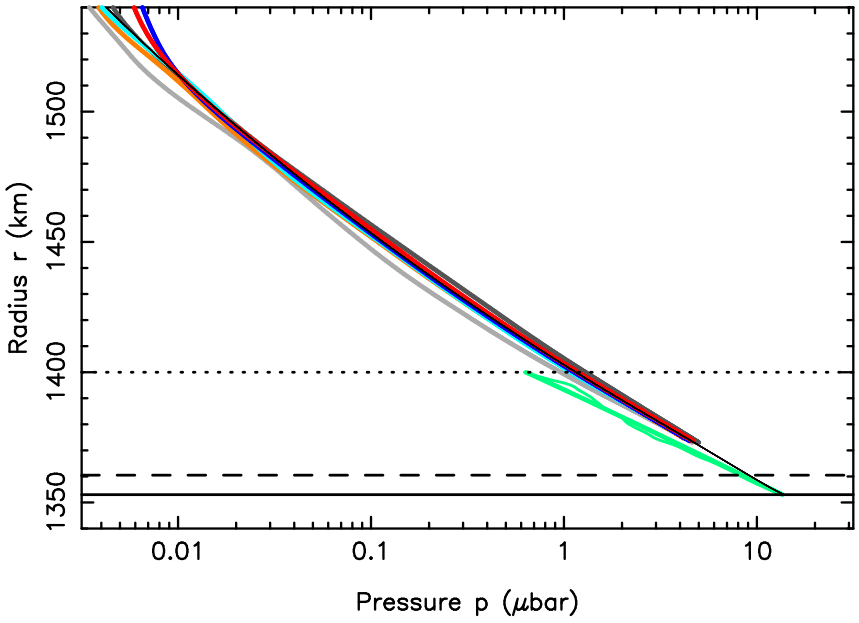

Figure 4.8: Pressure profiles derived from the density profiles (using Equation 2.36) shown in Figure 4.7, using the same colour scheme, and the same line delineation.

equilibrium for N_2 ice.

This general positive gradient can be achieved by considering heating by CH_4 from near-infrared absorbing bands. For instance, a CH_4 volume mixing ratio of 0.0004 yielding $T = 52$ K at 1363 km could explain our result. Strobel and Zhu (2017) ran their model for discrete values of the CH_4 volume mixing ratios not included in their paper and found that a CH_4 surface volume mixing ratio ~0.00015 would be sufficient to support a temperature rise of ~9 K, and a CH_4 surface volume mixing ratio ~0.0004 for a temperature rise of ~12 K, in the first 10 km. Because CH_4 is photochemically destroyed in the lower atmosphere, its scale height is roughly half the N_2 scale height. In terms of CH_4 column density there is the need of a higher surface CH_4 volume mixing ratio to compensate for its smaller scale height. For remote sensing observations, the column density is the important measurement, not just the surface volume mixing ratio. This 0.0004

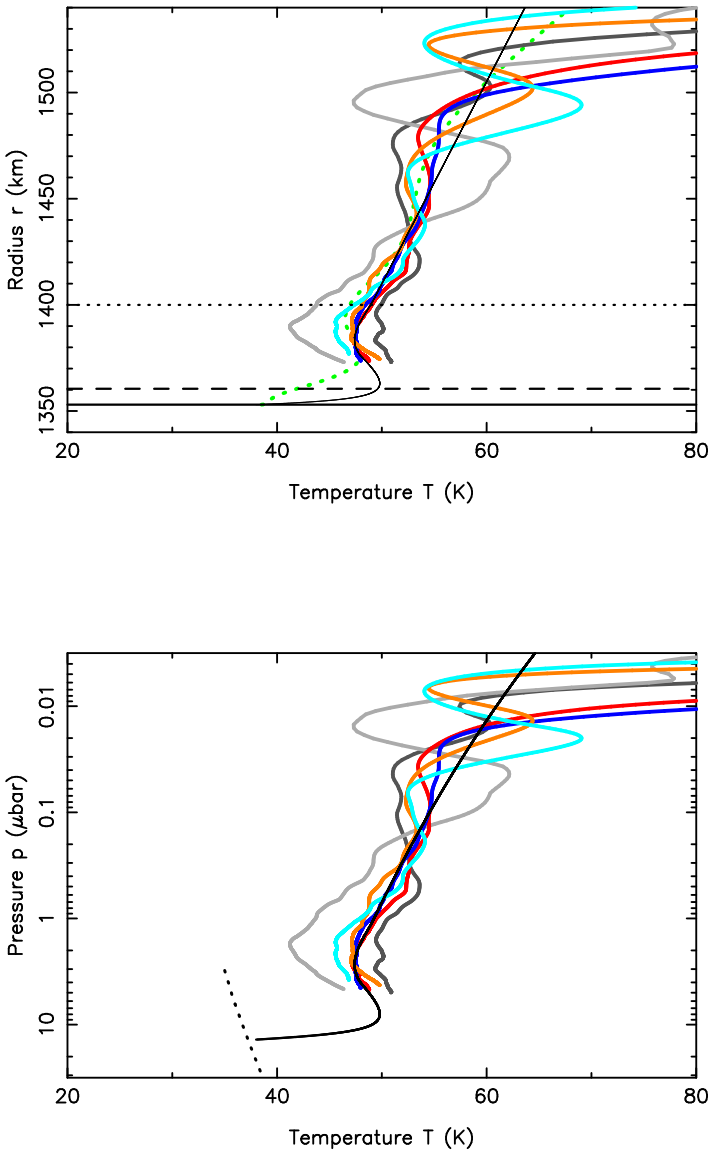

Figure 4.9: Temperature profiles derived from the density and pressure profiles (using Equation 2.38) shown in Figures 4.7 and 4.8 as a function of radius (upper panel) and pressure (lower panel). The oblique dotted line in the lower panel is the wet adiabat (vapour pressure equilibrium line for N_2) taken from Fray and Schmitt (2009).

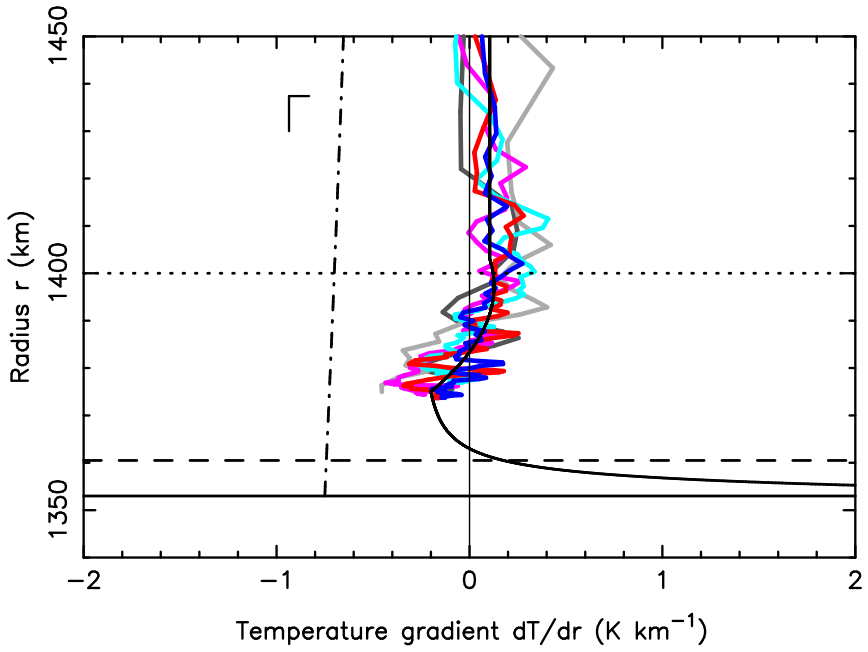

Figure 4.10: Temperature gradient corresponding to the upper panel of Fig. 4.9. The dot-dashed line is the dry adiabatic temperature gradient $\Gamma = -g/c_p$ (the limit of convective instability) where c_p is the specific heat at constant pressure for N_2.

value is smaller than, but roughly consistent with, the range found by Lellouch et al. (2010) for the CH_4 volume mixing ratio, 0.0005-0.0010. A troposphere just above the surface might complicate this picture. So far the presence of such a troposphere is only suggested indirectly through Voyager 2's plumes observations Yelle et al. (1991) up to $\sim$ 10 km altitude. Currently, none of the central flashes that we examined show evidence for a troposphere. If real, the troposphere on Triton has been shown to be controlled by turbulent mixing above the surface, and to be sensitive to surface thermal contrasts between N_2 ice and the volatile free bedrock (due to different surface albedo or thermal inertia, Vangvichith, 2013). On Pluto, climate models showed that the sublimation of cold N_2 ice and subsequent transport of the cold N_2 air in the impact basin Sputnik Planitia yield a km-thick cold troposphere as observed by New Horizons (Forget et al., 2017; Hinson et al., 2017).

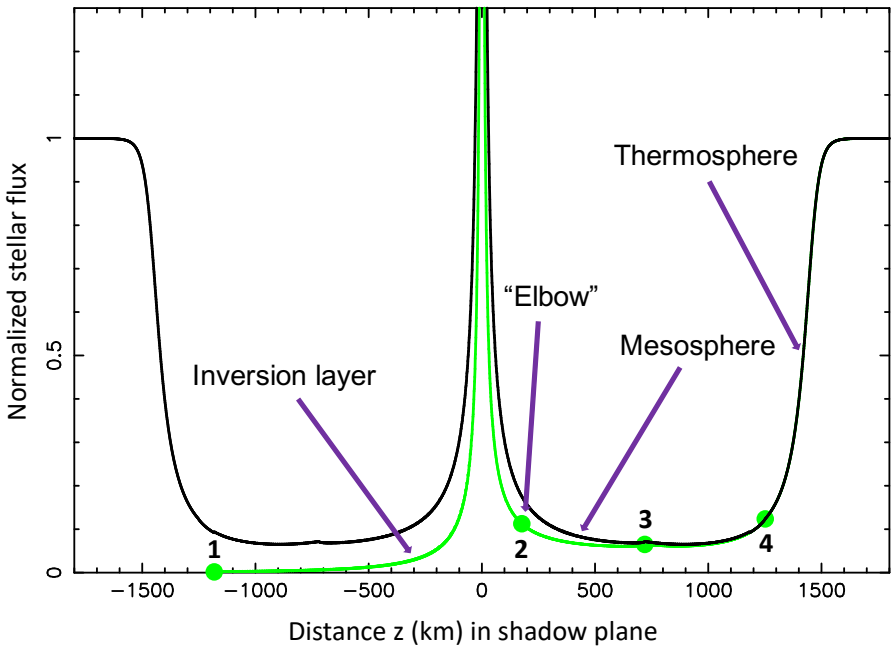

Figure 4.11: Synthetic light curve obtained by applying the ray tracing code to our template temperature profile, with the best fit value of $p_{1400} = 1.18$ μbar. The normalised stellar flux is plotted against the distance to Triton's shadow centre. The green curve represents the flux with only one stellar image. The green dots labelled 1 through 4 correspond to the points in Figure 4.6. The purple arrows denote the different areas of Triton's atmosphere. The black curve is the sum of the green curve and its mirrored version along the $z = 0$ axis, as a mimic of the fluxes from the two stellar images. This curve is then used to fit the observations (blue line in Figure 4.3, for example).

The negative gradient in the mesosphere, reminiscent of the more extended mesosphere on Pluto (Lellouch et al., 2017; Young et al., 2018), calls for the existence of a coolant. It must cool the atmosphere above its peak temperature of ~50 K, as well as radiate away the downward thermal heat flux from the upper atmosphere where $T \sim 100$ K. There are a few candidates for this coolant: haze particles and/or influx of dust particles that may either be pure H_2O ice or with silicate cores and coated with H_2O ice (see Ohno et al., 2020 for more details).

Of course, this is but one template temperature profile that best fits the central

flashes. It is certainly not the only one. However, the template must capture the main properties of the actual profile, with a temperature maximum just above the central flash layer, and a mesosphere with a mild negative gradient above this peak in temperature.

It is also important to discuss that the Abel inversion assumes that only one stellar image, the primary image, contributes to the flux. Triton's atmosphere produces two stellar images, a primary (near-limb) and a secondary (far-limb). The fluxes of both stellar images are added to the light curve. This is a potential source of error, especially in the central flash region, where both images have comparable contributions to the flux.

Tests were performed to assess how this effect could affect the inversion with La Palma's light curve. The station was at ~685 km from the shadow centre at closest approach, meaning it provides information down to ~20 km in altitude (Figure 4.12). A smooth temperature profile is used to generate the synthetic light curves at this station, one using only the flux from the primary image, the other with the sum of fluxes from the primary and secondary images.

Figure 4.12 shows that, as was expected, the inversion of the light curve with only the primary image retrieves the temperature at the 0.2 K accuracy level, and the density and pressure profiles at 0.1% accuracy level. On the other hand, the inversion of the light curve with the two images retrieves the upper parts of the profile properly, but fails in the lower parts. In the latter, at the deepest point reached by La Palma, the temperature is retrieved to within 0.9 K and the pressure at 1% level, a satisfactory result at our accuracy level. This disparity increases in the deeper levels. For example, at $r = 1362$ km (9 km altitude level), where the temperature reaches a maximum, the discrepancy between the template and the retrieved temperature is about 3 K. In this case, the retrieved temperature profile has an unrealistic behaviour, for it extends below the surface of Triton.

The conclusion is that the inversion procedure cannot provide reliable results below the 20 km altitude level. This means that La Palma and Helmos's inversion is not influenced by a spurious increase due to a secondary image contamination, however, the central flash region must not be used in the inversion. In particular, when Calern's light curve was inverted, and because this light curve features a strong central flash (Figure 4.4), the central flash portion of the light curve was removed before proceeding with the inversion.

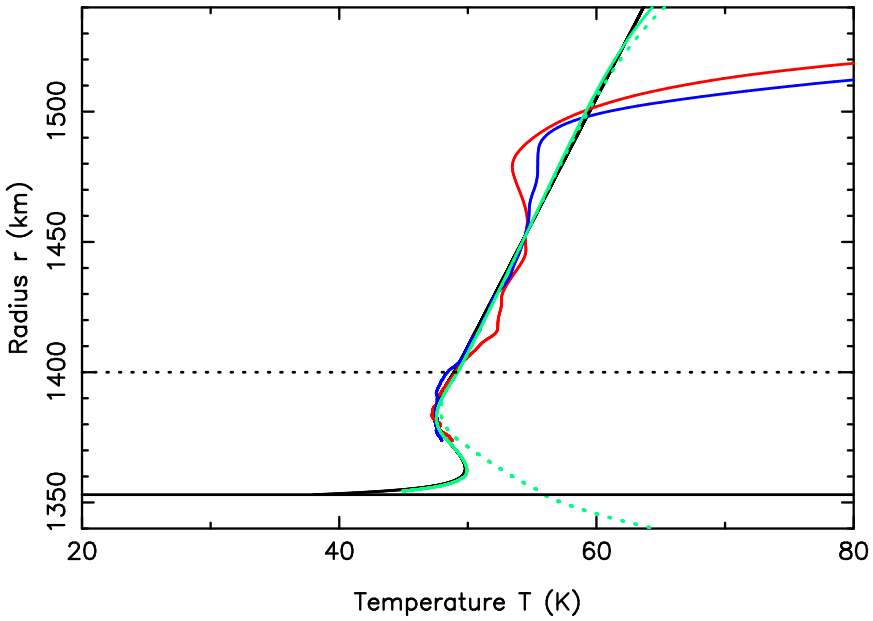

Figure 4.12: Effect of the secondary stellar image on the Abel inversion result for the temperature profile. The red and blue lines are the profiles obtained from the inversion of La Palma's light curve at ingress and egress, respectively. The solid green line is the retrieved temperature profile if only the primary image is considered, while the dotted green line is the retrieved temperature profile where both the primary and the secondary images are added. The black curve is the template temperature profile. The black horizontal solid line marks Triton's surface, while the dotted one is the reference radius (1400 km).

Ray-tracing

The ray-tracing method (Section 2.2.2) is mainly sensitive to the half light level. That level corresponds to a radius of about 1415 km (altitude ~60 km) and a pressure of ~0.55 μbar. It is used once the Abel inversion procedure provided the density profiles, and a template temperature profile has been obtained. This method generates synthetic light curves that are fitted to the observed occultation

light curves, to describe the global structure of Triton's atmosphere.

One result of such fit is the value of the pressure $p_{\rm ref}$ at the reference radius $r_{\rm ref}$ = 1400 km, allowing the comparison with previous results (e.g. Olkin et al., 1997; Elliot et al., 2000b), so that we can detect possible long-term seasonal effects. The pressure at any level can be deduced using the template temperature profile discussed previously. To obtain the surface pressure $p_{\rm surf}$, we can use the relation

$$p_{\rm surf} = 12.0\ p_{1400}. \tag{4.3}$$

This is a relation stemming from the template model that is used to extrapolate p_{1400} from $p_{\rm surf}$ and vice versa.

The other result of this approach is the DE435/NEP081 ephemeris offset perpendicular to its apparent motion projected in the sky, $\Delta\rho$. This location of Triton's centre is then used iteratively with the Abel inversion, improving the accuracy on the altitude scale. The ephemeris offset along Triton's motion is decoupled from this fit, see Dias-Oliveira et al. (2015) for details.

For this analysis, 52 light curves were simultaneously fitted. The other light curves were not considered as they either have lower signal-to-noise ratio, or their data/light curve was provided to us too late to be included in this process. In a first step, light curves that present a strong central flash had their central portion cut to avoid giving too much weight to those parts. The objective here is to obtain the global properties of the atmosphere, and to constrain p_{1400} and $\Delta\rho$. In a second step, the central flashes were fully included in the fit so that we could analyse the deepest atmospheric layers. In particular, we wanted to check if the central flash location coincides with the centre found by the global fit, as well as assess the shape of the atmosphere's deepest layers. This approach includes the primary and secondary images, and it does not have the constraints the Abel inversion method had concerning this point. The decision to remove the central flash part from the light curves that present it is purely for the separate analysis of the global properties of the atmosphere and the deepest atmospheric layers.

For all data sets used, the same procedure as in Dias-Oliveira et al. (2015), consisting of simultaneously fitting the refractive light curves with synthetic profiles generated by the ray-tracing method, was employed. For each station used, a least-squares fit is performed to adjust the synthetic light curve to the observed light curve. ϕ_0 is considered a free parameter when performing these fits, due to

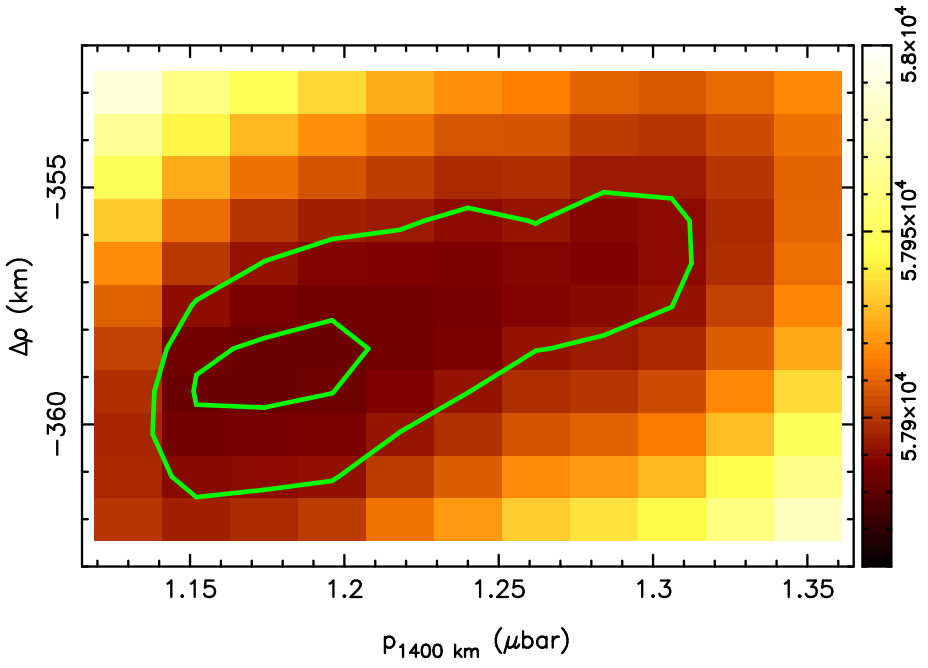

Figure 4.13: χ^2 map obtained from the simultaneous fit of the 52 light curves, using the ϕ_0 corresponding to the template temperature profile. The inner green contour is the 1σ limit of the fit, and the outer green contour is the 3σ limit.

uncertainties in the determination of this value for some stations, as well as the lack of calibration images for the majority of them. This adds one degree of freedom per station to the fit, increasing the error bars on the retrieved atmospheric parameters.

Error bars are obtained from the classical χ^2 function

$$\chi^2 = \sum_{i=1}^{N} \left(\frac{\phi_{\mathrm{i,obs}} - \phi_{\mathrm{i,syn}}}{\sigma_i} \right)^2, \tag{4.4}$$

reflecting the noise level σ_i of each of the N data points, where $\phi_{\mathrm{i,obs}}$ and $\phi_{\mathrm{i,syn}}$ are the observed and synthetic fluxes at the i^{th} data point, respectively.

Figure 4.13 shows the $\chi^2(\Delta\rho, p_{1400})$ map obtained after running a grid of values for $\Delta\rho$ and p_{1400} through the ray-tracing code. A satisfactory fit should provide a minimum value χ^2_{min} close to $N - M$, where M is the number of fitted param-

eters. We also considered ϕ_0 as a free parameter for all light curves, including La Palma's, due to the uncertainty on what causes the big discrepancy between the obtained value and the best value found, as discussed before. Therefore, the fitted parameters are the values of $\Delta\rho$, p_{1400}, and the 52 values of ϕ_0, for a total of $M = 54$ fitted parameters. $N = 68446$ data points were used. We obtain a global value of χ^2 per degree of freedom,

$$\chi^2_{\rm dof} = \frac{\chi^2_{\rm min}}{N - M} = 0.85, \tag{4.5}$$

a satisfactory global fit to the data. Examining the values of $\chi^2_{\rm dof}$ for each individual light curve also show values near unity. Therefore, we do not see significant differences when comparing the synthetic light curves derived from the synthetic density profile shown in Figure 4.7. This confirms that Triton's atmosphere is spherically symmetric on a global scale at our accuracy level. More is discussed in the central flash analysis in Section 5.2.

We then employ the marginal distribution, used when we wish to find the probability of specific variables of a subset without consideration of other variables. We do not consider $\Delta\rho$ to find that the marginal distribution for the 1σ and 3σ error contours on p_{1400} are estimated by tracing the iso-levels $\chi^2_{\rm min} + 1$ and $\chi^2_{\rm min} + 9$, respectively, as shown in Figure 4.13. The internal error bar for our best model provides a pressure of $p_{1400} = 1.18 \pm 0.03$, with its 1σ error bar. The best-fitting value of $\Delta\rho = -359.3 \pm 1$ km (Figure 4.13) is used to retrieve the closest geocentric approach distance between Triton and the star, projected in the sky plane, and its corresponding time.

It is worth noting here that we do not note differences between ingress and egress. With all the observations obtained, spanning Triton almost top to bottom, and covering both morning and evening limbs (Figure 4.2), there is no discernible difference between them.

The best simultaneous fit is displayed in Appendix B for all light curves obtained. The light curves that were not included in this analysis were, nonetheless superimposed with the synthetic light curves, in order to confirm that the template model satisfactorily fits these light curves as well.

4.2 25 August 1989

During its Triton flyby, on 25 August 1989, the Voyager 2 spacecraft sent its radio signal, the RSS experiment, back to Earth as it passed behind the satellite. The main product of this observation was the temperature and pressure at the surface of Triton.

I wondered if this was all the information that could be retrieved from the data, as there was no way of directly comparing this result to ours, always requiring an extrapolation from one of them for the comparison.

I decided to contact Eric Gurrola, asking if he could provide the original data used in Gurrola (1995). It turned out to not be a simple task, as the original data was stored in an old floppy disk that required an adaptor for it to be accessible with modern computers. After much searching on the part of Eric Gurrola, and after a few weeks, I obtained the original data, and started the process of figuring out if there was a way to compare it directly to our data.

4.2.1 Original analysis

We found that, even though the data becomes quite noisy above the 20 km altitude level, the RSS phase delay still provides constraints on Triton's lower atmosphere, with science left to explore. Here I will summarise the work done by Gurrola (1995) to obtain the original surface temperature and pressure. I will mention, in particular, the points that pertain to the comparison effort made.

The Voyager 2 high gain 3.7 m antenna transmitted to Earth two radio signals at 3.6 and 13 cm (X-band and S-band, respectively). The phases in those bands are related to one another by

$$\Delta\phi = \frac{121}{112}(\phi_x - \frac{3}{11}\phi_s), \tag{4.6}$$

ϕ_x is the phase in the X-band, ϕ_s is the phase in the S-band, and $\Delta\phi$ is the corrected radio phase corresponding to the neutral atmosphere at the X-band wavelength. This calculation is done to remove plasma effects on the phase.

Gurrola (1995) used only the egress data for his analysis, because the ingress data presented sudden changes in slope, resulting in a problematic fit.

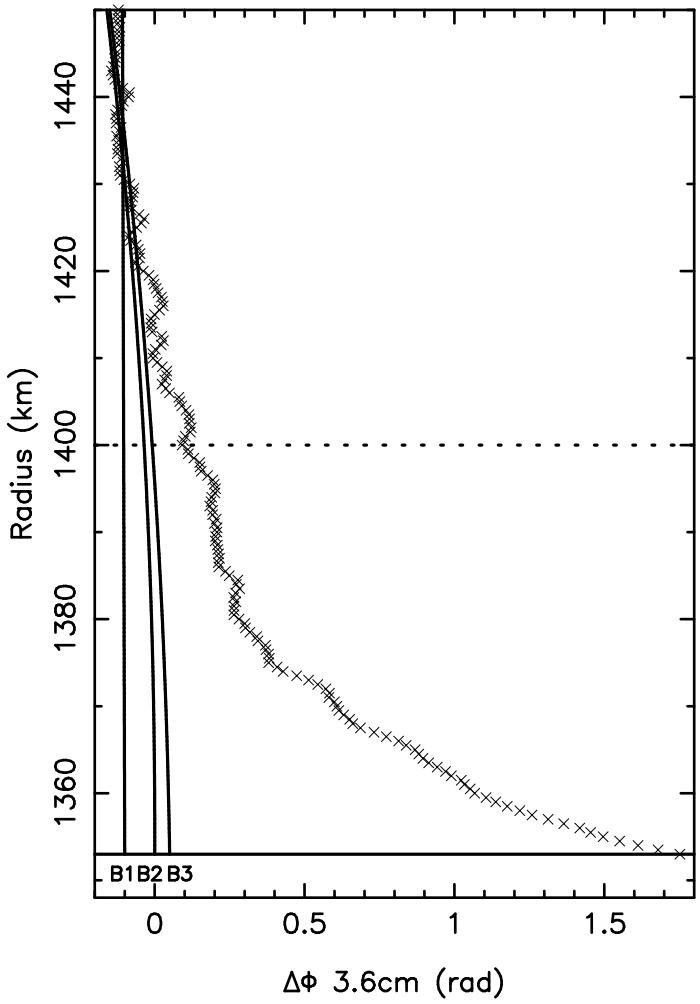

Figure 4.14: Radio phase delay observed during the egress of the Voyager 2 RSS occultation on 25 August 1989, in the 3.6 cm X-band (adapted from Gurrola, 1995). The crosses are the data, and the solid lines (labelled B_1, B_2 and B_3) are the three polynomial modelings of the phase delay baseline.

Gurrola provided us with the corrected radio phase delay $\Delta\phi(r)$ in relation with altitude (Figure 4.14), as well as the results from his models to obtain only the "pure atmosphere phase delay". This corresponds to the phase delay once a

general polynomial trend is subtracted from $\Delta\phi$ to account for thermal noise and instabilities in the frequency reference on board of Voyager 2. These polynomials, referred to as baselines in Gurrola (1995), were designated as B_1, B_2, and B_3 (shown in Figure 4.14).

B_1 is the linear baseline used by Tyler et al. (1989), that was determined using 120 km of the data obtained, which Gurrola (1995) considered insufficient to reliably estimate the drift of the instrument over the atmosphere, as it did not extrapolate from high enough altitudes (in order for the atmosphere to be too thin to affect the signal phase) downwards toward Triton's surface. On the other hand, baselines B_2 and B_3 used about 700 km of the data, and are, respectively, the second and third-order polynomials of the best fit at egress from Gurrola (1995). The preferred solution of this author is B_2.

Using B_2, the $\Delta\phi(r)$ from the original data is displayed in green in Figure 4.15. And I derived the profiles represented by the green curves in Figure 4.7.

4.2.2 Re-analysis

In order to compare the original Voyager 2 data to our results, we generated, for comparison, the phase delay at 3.6 cm that would be observed with our best density profiles (the black line in Figures 4.7 and 4.8) as if it were obtained on board of Voyager 2:

$$\Delta\phi(r) = \frac{2\pi}{\lambda} K \sigma_{N_2}(r), \tag{4.7}$$

λ is the wavelength (3.6 cm), K is the corresponding molecular refractivity of N_2 (see Table 3.1), and $\sigma_{N_2}(r)$ is now the column density stemming from our best model. The resulting $\Delta\phi(r)$ profile is the black line in Figure 4.15, along with the phase delays deduced from the inverted light curves (red line).

Conversely, we used the Voyager 2 corrected X-band radio phase to retrieve the refractivity profile using the Abel inversion given in Equation 2.40. The density profile can then be deduced, employing Equation 2.4. Now, we can directly compare our results to those from Voyager 2. It is important to note that, as we can see in Figures 4.7 and 4.8, the RSS profiles probe an altitude interval that overlaps our ground-based occultation altitude interval. This overlapping region extends from the lowest probed point of the La Palma light curve, $r = 1373$ km (20 km altitude), up to roughly the reference level, $r = 1400$ km (47 km altitude),

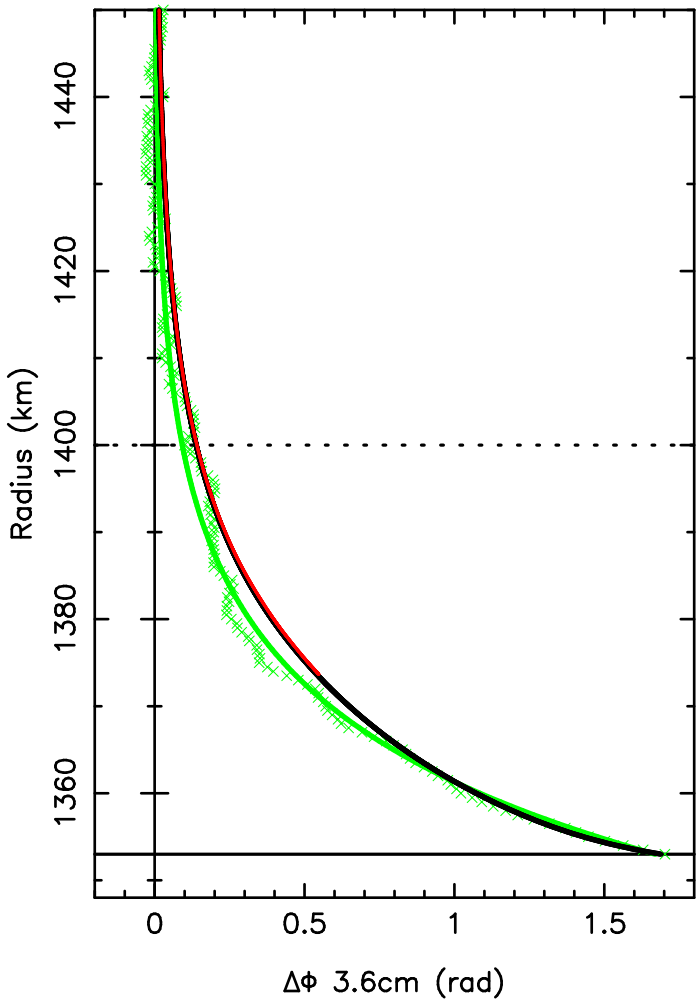

Figure 4.15: Green crosses are the radio phase data after subtracting the B_2 baseline polynomial shown in Figure 4.14, representing the effect of the atmosphere alone. The green line is the smoothed version of this radio phase delay, constructed by Gurrola (1995). The red line is the phase delay that would be observed at 3.6 cm from the retrieved density profile of La Palma at immersion (Figure 4.7). The other phase delay profiles obtained from the inversion would be indistinguishable from this red line, and are, therefore, not plotted here. The black line is the phase delay profile obtained from our template model.

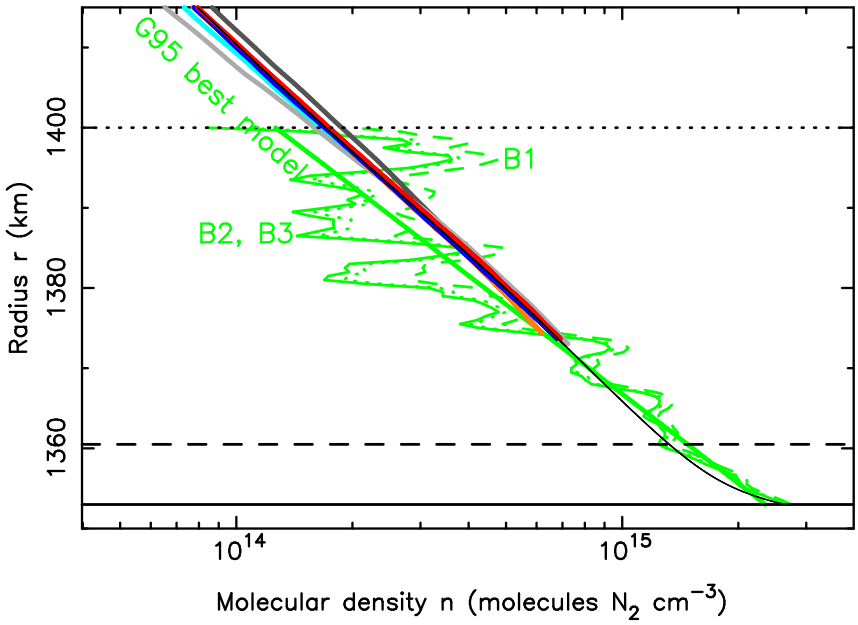

Figure 4.16: Close up view of the low atmosphere in the density profile of Figure 4.7. Several profiles derived from the RSS occultation are shown in green. The dashed green line is the profile retrieved by Tyler et al. (1989), using B_1 to correct for the RSS phase instability. The thin solid green line is the profile retrieved by Gurrola (1995), using B_2, and the dotted green line uses B_3. The thick solid green line is the best model of Gurrola (1995), based on the B_2 profile. The other coloured lines are the result from our inversion, using the same colour coding as in Figure 4.7. The thin black line that connects to the surface is our template model.

at which point the RSS profiles become too noisy to be reliable, reaching a noise factor of about two at this point.

Figure 4.16 shows that no significant difference in density is detected between the two profiles, especially at the connection point, at r = 1373 km. It also shows that the RSS density profile is insensitive to the solution, B_1, B_2, or B_3, chosen to retrieve it.

Integrating the weight of the atmospheric column provides the RSS pressure profile (Figure 4.8). However, this profile includes a contribution of the weight of

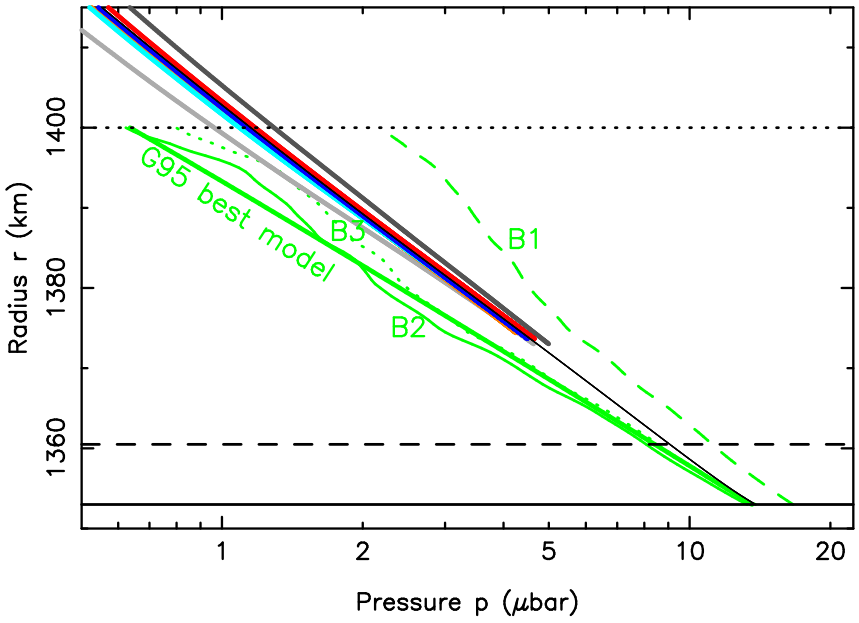

Figure 4.17: Same as Figure 4.16 for the pressure profiles.

the layers above $r = 1400$ km, where the RSS data is very noisy. This is because the integration of the atmospheric column starts from the top of the atmosphere, and integrates as it decreases in altitude. This adds all the noise of the top of the RSS data to the lower layers. Figure 4.17 shows that the B_1 pressure profile is quite offset in slope with respect to the B_2 and B_3 profiles. So, and contrarily to the density profiles, the slope of $\log_{10}(p)$ vs. radius r is sensitive to the choice of the polynomial baseline. Therefore, it is difficult to conclude if the break in slope between the RSS profile and our ground-based results is real or not. The conclusion that can be reached here, the only robust result from the RSS pressure profile, is the difference of pressure between the surface and the lowest point of the La Palma profile at $r = 1373$ km, $p_{\mathrm{surf,RSS}} - p_{1373,\mathrm{RSS}} = 9.82$ μbar.

We decided to approach the search for the surface pressure for Voyager 2's data in a different way. The main result of the inversion from Equation 2.40 is the density profile, and we can translate this into pressure, using an estimate of the

surface temperature T_{surf}, by employing the ideal gas law (Equation 2.38). Using the preferred B_2 model, we obtain $p_{\mathrm{surf,RSS}} = 13.6$ μbar and $p_{1373,\mathrm{RSS}} = 3.77$ μbar for Voyager 2, in 1989. We will now discuss how we arrived at the error bar on $p_{\mathrm{surf,RSS}}$ caused by the uncertainties on T_{surf}.

The value $p_{1373,\mathrm{RSS}} = 3.77$ μbar that we find is 21% smaller than the value we obtained for 2017 at the same level, 4.58 μbar. Propagating this 21% difference to the 1400 km radius then yields $p_{1400,\mathrm{RSS}} = 0.97$ μbar. Estimating the error bar for that value is difficult, because the RSS pressure depends on the pressure values of the atmosphere above, as mentioned earlier. If we adopt the error bar $p_{\mathrm{surf,RSS}} = 14 \pm 2$ μbar of Gurrola (1995) and propagate it upward, this yields $p_{1400,\mathrm{RSS}} = 0.97 \pm 0.14$ μbar.

A more robust way to estimate $p_{\mathrm{surf,RSS}}$ is to use the RSS density profile alone. The caveat here is that we need an independent measurement of the surface temperature T_{surf} in order to derive the pressure. These temperature measurements (given below) are more accurate than the estimation by Gurrola (1995) ($T_{\mathrm{surf}} = 42 \pm 8$ K) and thus reduce the ± 2 μbar uncertainty of the value of $p_{\mathrm{surf,RSS}}$ from Gurrola (1995). However, this approach is valid only if these temperature measurements apply to the N_2 ice surface that the RSS experiment probed, and if vapour pressure equilibrium between the N_2 ice and the gas is achieved.

Estimations of T_{surf} are given by various authors (see also Figure 4.18):

- 38^{+3}_{-4} K (Conrath et al., 1989),
- 38^{+2}_{-1} K (Tryka et al., 1993),
- the range 36.5-41 K (Grundy et al., 1993),
- and 37.5 ± 1 K (Merlin et al., 2018).

Adopting a value of $n_{\mathrm{surf,RSS}} = 2.4 \times 10^{15}$ cm^{-3} derived from the RSS phase delay inversion (Figure 4.16), we find surface pressures of:

- $12.3^{+1.0}_{-1.3}$ μbar,
- $12.3^{+0.6}_{-0.3}$ μbar,
- the range 11.5-13.3 μbar,
- and 12.4 ± 0.3 μbar,

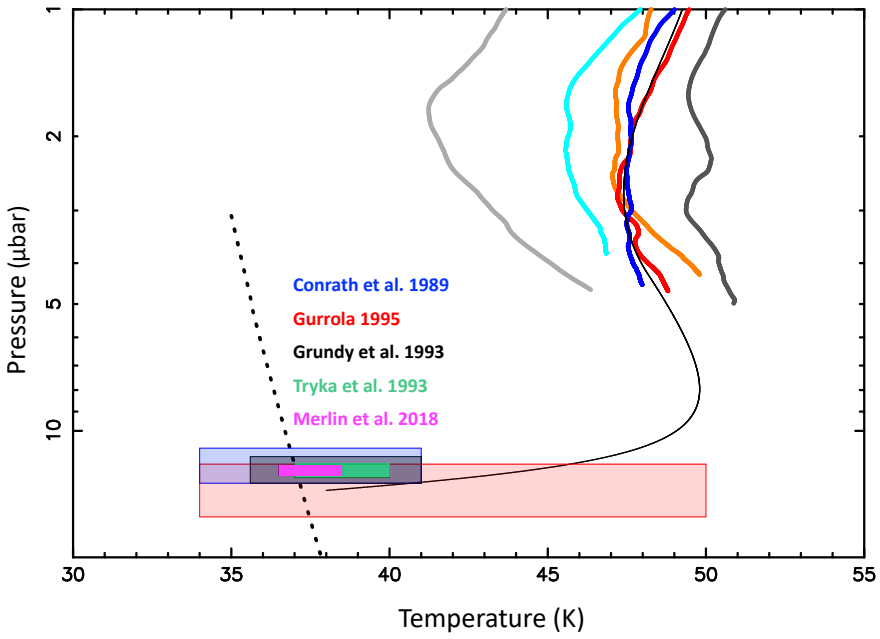

Figure 4.18: Close up view of the lower panel of Figure 4.9. The width of each coloured box is Triton's surface temperature (T_{surf}), as estimated by the various authors mentioned above the boxes. The heights of the boxes are the range of surface pressures p_{surf}.

respectively, for the four choices of surface temperatures. All these values are consistent with a surface in vapour pressure equilibrium with the atmosphere, as shown in Figure 4.18. This supports the hypothesis that the RSS surface density and the estimated surface temperatures are consistent with a pressure being controlled by the N_2 surface ice sublimation.

From the surface temperatures given above, we estimate that a safe surface pressure range of 12.5 ± 0.5 μbar can be derived for the Voyager 2 epoch, fully consistent with the analysis of Gurrola (1995), $p_{\mathrm{surf,RSS}} = 14 \pm 2$ μbar. In our analysis, the error bar essentially stems from the uncertainties of the temperatures. Comparing this value with our own estimation of $p_{\mathrm{surf}} = 14.1 \pm 0.4$ μbar for 2017, and assuming a constant factor (12.5/14.1) throughout the profile, we obtain $p_{1400} = 1.05 \pm 0.04$ μbar in 1989. This is consistent with our estimation made

before, $p_{1400,RSS} = 0.97 \pm 0.14$ μbar. We, therefore, estimate a conservative range of $p_{1400,RSS} = 1.0 \pm 0.2$ μbar for the pressure at 1400 km in 1989. Comparing this to our ground-based result from 2017, $p_{1400} = 1.18 \pm 0.03$, as well as comparing the surface pressures, we see no significant variations of pressure between the RSS results of 1989 and the results derived from the ground-based occultation of 2017.

It is of important note that the RSS experiment still managed to provide new information, after all these years, and after the science from this data was considered exhausted. In particular, it allowed for a direct comparison of the density, and pressure, between the data obtained in 1989 and our results from 2017. This novel result was crucial for this work, as it showed that Triton's atmospheric pressure, in 2017, is back at the Voyager 2 epoch level.

4.3 Other stellar occultation events analysed

Two other events, between 1989 and 2017, were analysed by the Lucky Star group. They are described here in this Section.

We employed our template temperature profile (Table 4.3; black profile in the upper panel of Figure 4.9) to fit the light curves obtained for each of these events, using the ray-tracing approach to retrieve the pressure at the reference radius $r = 1400$ km, p_{1400}. For these events, we vary p_{1400} to fit the synthetic light curves to the data.

4.3.1 18 July 1997

This event involved one station in the USA and three stations in Australia. It was a joint effort between two groups, and, therefore, both have access to the data. The original analysis of this event was done by Elliot et al. (2000a), and they also present more details on the observations.

The circumstances of observations are listed in Appendix A, and the geometry of the event is displayed in Figure 4.19.

Here, we provide the results stemming from our own approach to constrain p_{1400}. As mentioned, we adopt the template temperature profile derived from the

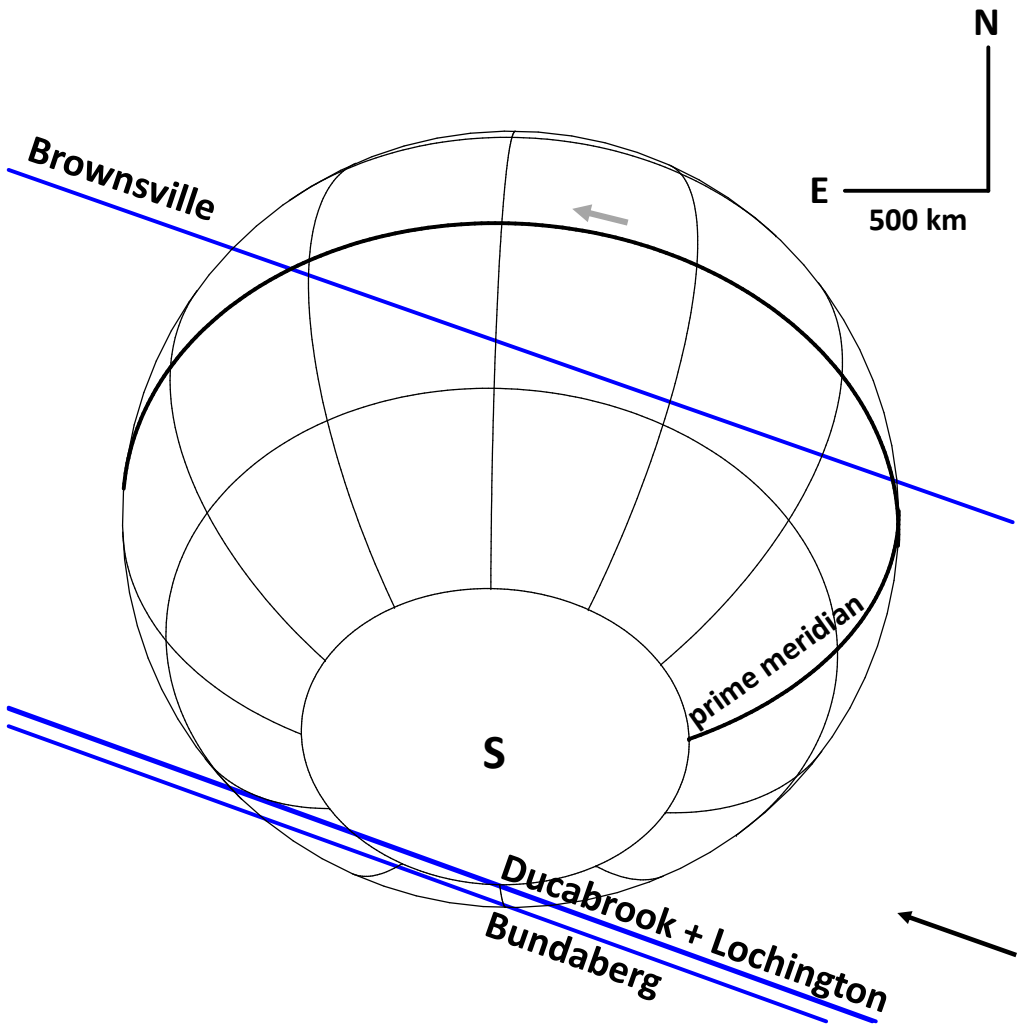

Figure 4.19: Geometry of the 18 July 1997 occultation, with the same conventions as Figure 4.2.

2017 event (Table 4.3; black profile in the upper panel of Figure 4.9), and we vary p_{1400} to fit the synthetic light curves to the data.

The $(\chi^2, \Delta\rho)$ map, resulting from this analysis is displayed in Figure 4.20. The best fit of the light curves is shown in Figure 4.21. We obtain, for the 18 July 1997 event, a pressure at the reference radius of $p_{1400} = 1.90^{+0.45}_{-0.30}$ μbar, with $\chi^2_{\rm dof} = 0.95$, indicating a satisfactory fit. Extrapolating down to the surface, using Equation 4.3, we obtain $p_{surf} = 22.8^{+5.4}_{-3.6}$ μbar.

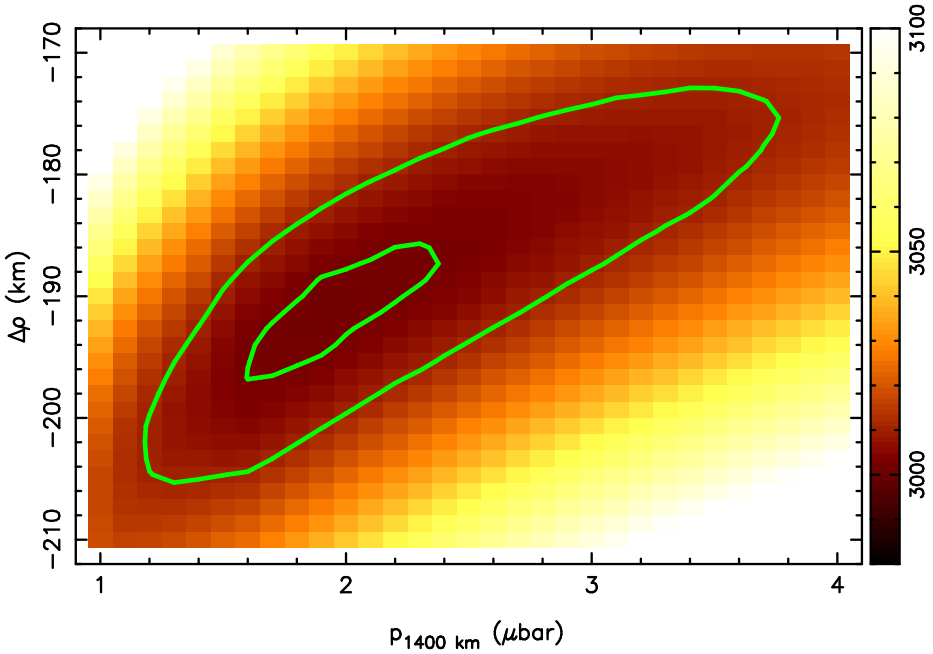

Figure 4.20: Same as Figure 4.13 for the 18 July 1997 occultation.

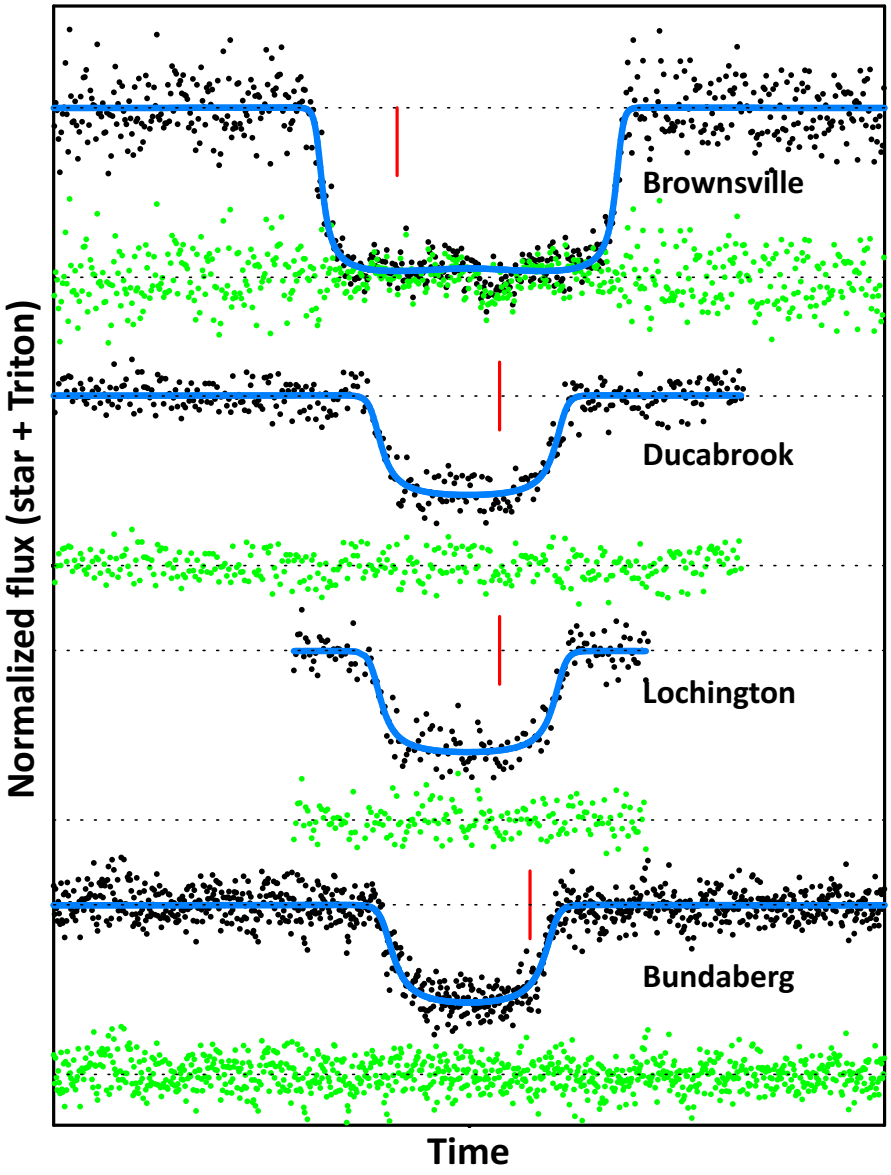

Figure 4.21: Simultaneous fits to the 18 July 1997 light curves. The panel covers 300 seconds. The light curves were shifted so that the mid-occultation times are aligned. The red vertical marks indicate 10:10 UTC at the Brownsville station (USA), and 10:18 UTC for the three Australian stations. The blue lines are the fit to the data (black dots), using the best value found in Figure 4.20, $p_{1400} = 1.9\,\mu$bar, and the template temperature profile shown in Figure 4.9, and Table 4.3. The green dots are the fit residuals. The upper dotted line is the normalised value of the star + Triton flux, and the lower dotted line is the zero flux (no photons received).

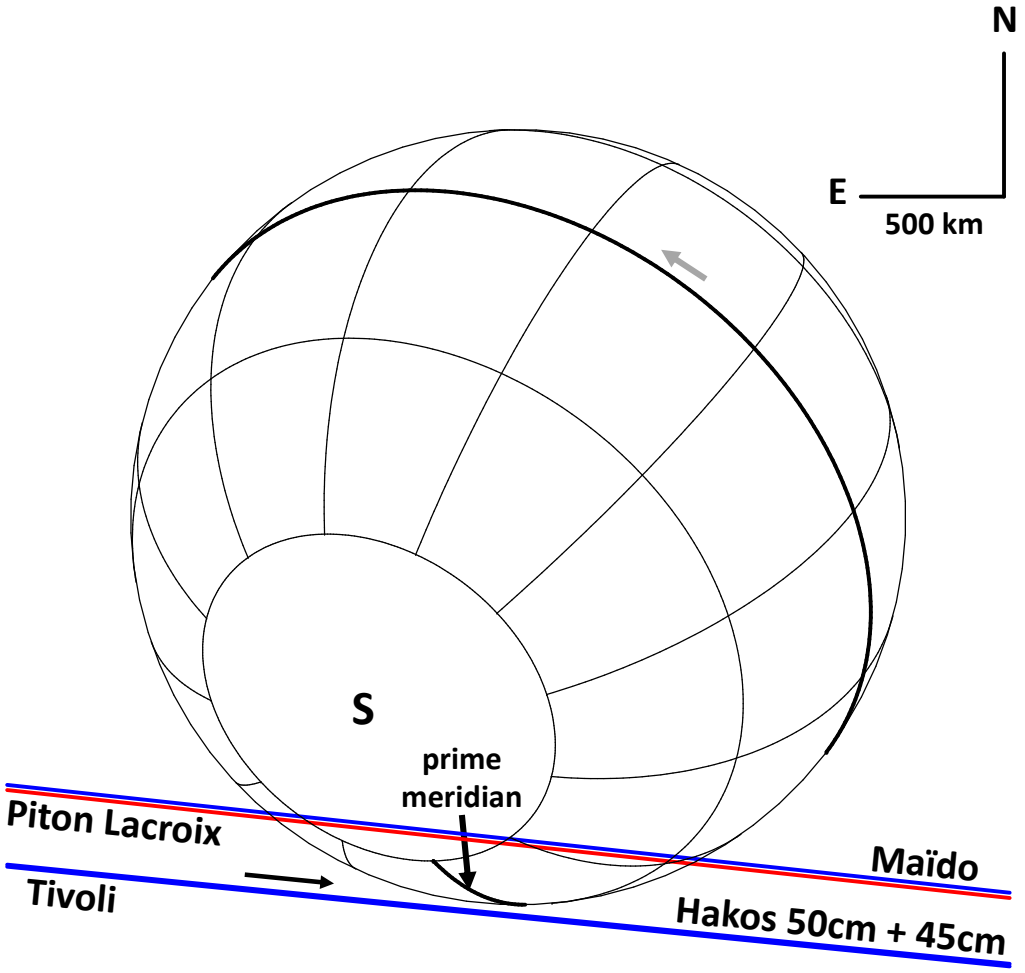

Figure 4.22: Geometry of the 21 May 2008 occultation, with the same conventions as in Figure 4.2.

4.3.2 21 May 2008

This event was observed from Namibia (two stations) and from the La Réunion Island (two stations). The circumstances of observations are listed in Appendix A. Given that each pair of stations are close together, only two effective chords have been obtained, as shown in Figure 4.22.

These chords were grazing. In fact, two of the light curves only probed the very edges of the atmosphere. Because of this, there is a strong correlation between the closest approach distances of the chords to Triton's shadow centre and

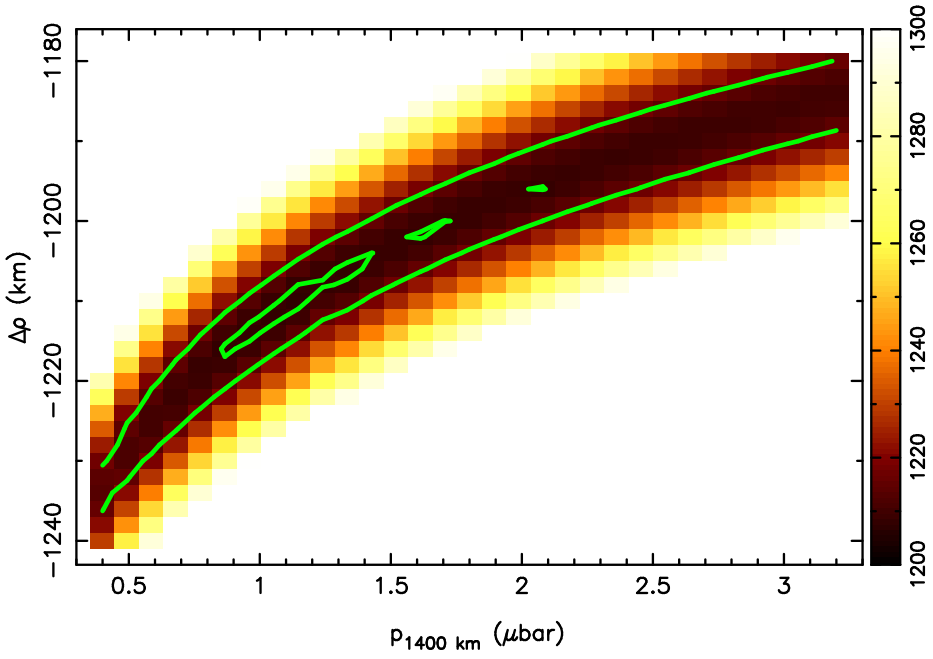

Figure 4.23: Same as Figure 4.13 for the 21 May 2008 occultation.

the retrieved reference pressure p_{1400}, as evidenced in Figure 4.23. The best fit of the light curves is shown in Figure 4.24. As a consequence, the value of p_{1400} is poorly constrained at the 1σ level. We obtained $p_{1400} = 1.15^{+1.03}_{-0.37}$ μbar. At the 3σ level, the value is so unconstrained that it does not bring any information on the temporal evolution of the pressure.

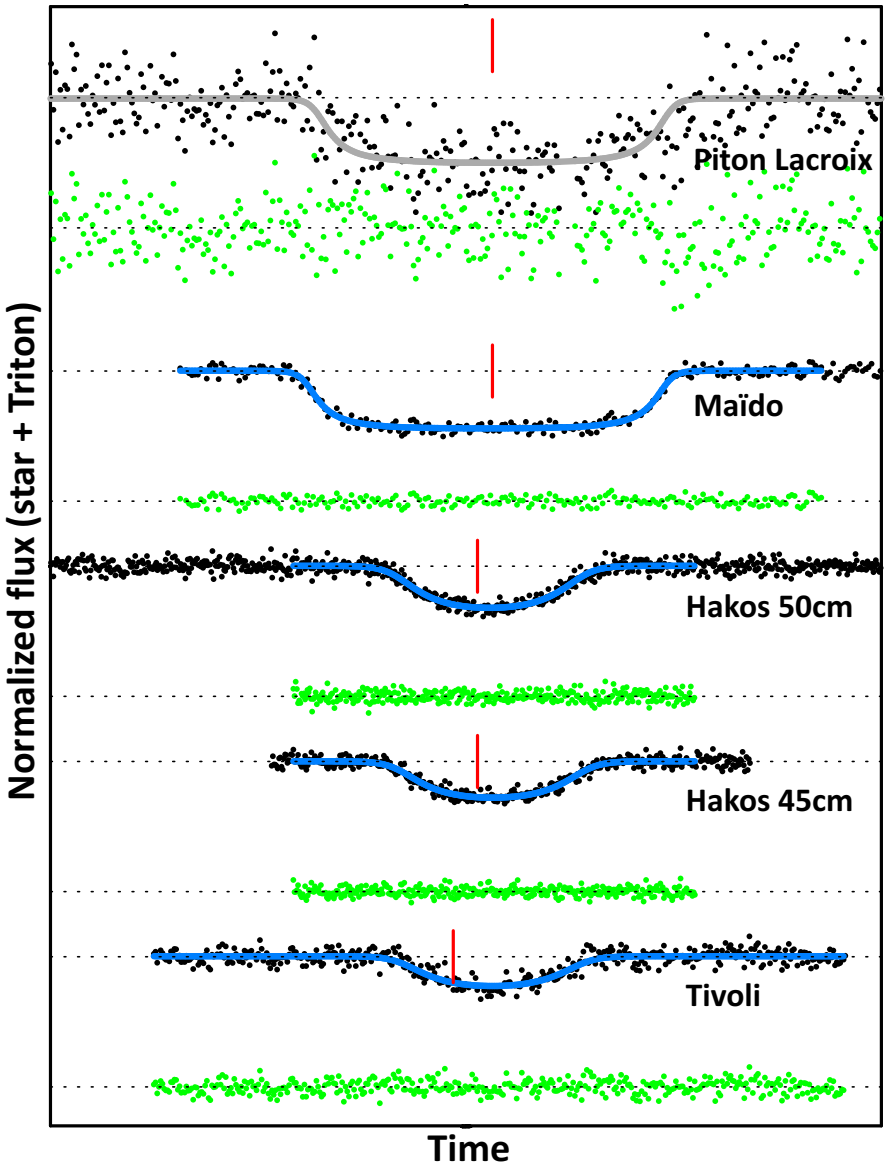

Figure 4.24: Simultaneous fits to the 21 May 2008 light curves. The same conventions as for Figure 4.21 are used, except that the panel now covers 720 seconds. The red vertical marks indicate 01:51 UTC for La Fournaise and Maïdo, and 01:41 UTC for Hakos. The synthetic light curve for La Fournaise is plotted in gray because it is not used in the fit, due to the high noise level.

Chapter 5

Triton's atmospheric evolution and structure

In this Chapter, I will put our findings in context with other works done, namely the evolution of the atmospheric pressure of Triton. A Volatile Transport Model obtained from our analysis by Bertrand et al. (2022) is described here as well.

The final approach to analysing the data will also be discussed. We used the ray-tracing approach to fit the central flashes observed in some light curves, to measure if there is a departure from the spherical shape in Triton's deep atmosphere. This fit also serves to reveal possible absorbing material (by comparing the height of the central flash in stations that provided observations in different wavelengths) along the line-of-sight.

5.1 Pressure evolution

After obtaining the pressures described in Chapter 4, I set out to search for other studies that had their own derivation of the pressure, either at the surface, or at r = 1400 km, a common radius of reference to infer Triton's atmospheric pressure. Because the original Voyager 2 value is derived only for the surface, we extrapolated all other results (besides our own Voyager 2 analysis) assuming a constant ratio (Equation 4.3). Table 5.1 lists the values obtained in this work, as well as values found in the literature. Figure 5.1 plots the values of p_{1400} with time, for a better visual of the evolution of the pressure at r = 1400 km over time.

I will now provide a discussion of the pressure evolution, comparing each

Table 5.1: Atmospheric pressure on Triton.

Date	Pressure at 1400 km p_{1400} (μbar)	Pressure at the surface $p_{\rm surf}$ (μbar)[a]	Fit quality $\chi^2_{\rm dof}$
This work			
25 August 1989	1.0 ± 0.2	12.5 ± 0.5	N/A
18 July 1997	$1.90^{+0.45}_{-0.30}$	$(22.8^{+5.4}_{-3.6})$	0.95
21 May 2008	$1.15^{+1.03}_{-0.37}$	$(13.8^{+12.4}_{-4.4})$	0.93
5 October 2017	1.18 ± 0.03	(14.1 ± 0.4)	0.85
Other works			
25 August 1989[b]	N/A	14 ± 2	N/A
14 August 1995[c]	1.4 ± 0.1	(17 ± 1)	N/A
18 July 1997[d]	2.23 ± 0.28	(26.8 ± 3.4)	N/A
4 November 1997[e]	1.76 ± 0.02	(21.1 ± 0.2)	N/A

[a] The values in parentheses were obtained using Equation 4.3.
[b] Gurrola (1995).
[c] Olkin et al. (1997).
[d] Elliot et al. (2000a, 2003).
[e] Average over ingress and egress obtained by Elliot et al. (2003).

result to the value at the Voyager 2 epoch.

Starting with the value from 14 August 1995, by Olkin et al. (1997), we see a 40% increase in the pressure between 1989 and 1995, but at a low significance level of 1.8σ.

The 18 July 1997 event, with two analyses from different groups, and two different approaches, has the values $p_{1400} = 2.23 \pm 0.28$ μbar from Elliot et al. (2000a), and $p_{1400} = 1.90^{+0.45}_{-0.30}$ μbar from our own study. The two results differ by a factor of 0.85. This stems from the use of a different template temperature model. This difference is at the 0.6σ level and is, therefore, statistically insignificant. Using our value for this event, it indicates a pressure increase by a factor of 1.9 between 1989 and 1997, but it remains at the 2.5σ level, making it marginally significant.

The point obtained on 4 November 1997, $p_{1400} = 1.76 \pm 0.02$ μbar, by Elliot et al. (2000a, 2003), has a very low error bar due to the light curve's high signal-to-noise ratio, as it was recorded by the *Hubble Space Telescope*. This implies an increase in pressure by a factor of 1.76 between 1989 and 1997, at a level of 3.8σ. However, it is not clear how the astrometry of this event was done. We do not

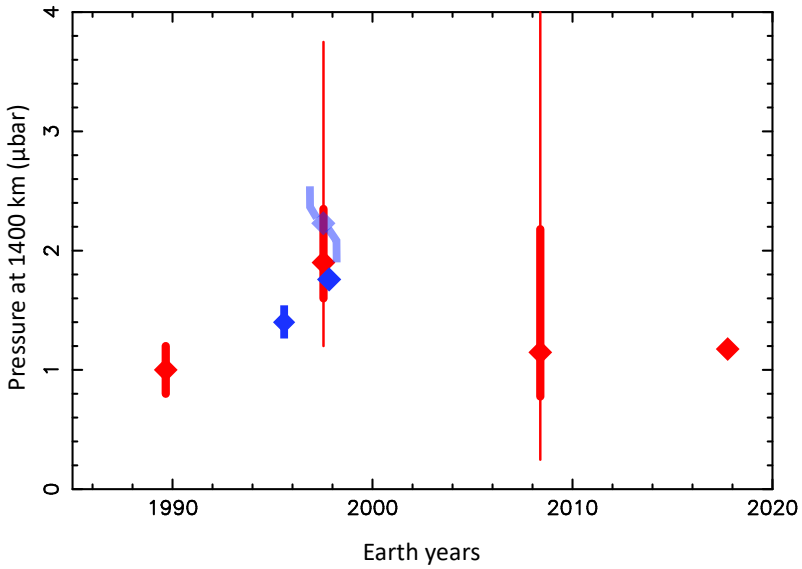

Figure 5.1: Triton's atmospheric pressure evolution. The values are presented in Table 5.1. The points obtained from our analysis are in red, while points taken from the literature are in blue. Because the event on 18 July 1997 has two different values, from our analysis and from Elliot et al. (2000a), the value derived by Elliot et al. (2000a) is plotted in a translucent blue colour, and the error bars are curved. The thick error bars correspond to the 1σ confidence levels. The thin error bars relate to the 3σ confidence levels.

have access to this data as of yet, I am currently in contact with Michael Person that is searching for the original data, so it is impossible to verify if this increase would be present if we analysed it consistently with our methods.

Lastly, the 21 May 2008 event provided only two effective grazing chords, as mentioned in Section 4.3, providing a 3σ error bar that is too large, and gives no new information here. Therefore, no firm conclusion in terms of change of pressure between 1989 and 2008 can be made from this event.

To conclude, it seems that the surge of pressure reported in the literature during the 1990s, when compared to the Voyager 2 epoch, is confirmed by our analysis. However, considering the paucity of data points available, and the lack of a fully consistent analysis of all the events, it shall remain generally unsolved. Despite

this, the value of the pressure we obtained in 2017 is much more accurate and is fully compatible with the one derived from the Voyager 2 RSS experiment. From Figure 5.1, and Table 5.1, we can see that the 2017 point is within the 1σ error bar of Voyager 2's. This means that there is no increase to be claimed between the two data points. So, either there was no surge in pressure between 1989 and 2017, or if it did indeed occur, the pressure is back to its Voyager 2 level in 2017.

In this analysis, we used pressures from the literature that were derived from stellar occultations, in an attempt to have a more consistent comparison. This way, we were comparing the same type of measurements with each other. There is, however, one value found in the literature, not from a stellar occultation, that is highly quoted to be the evidence for the increase of pressure in Triton's atmosphere. This point was obtained from high-resolution spectroscopy in July 2009, by Lellouch et al. (2010). They obtained the first detection of CH_4 gas in Triton's atmosphere since Voyager 2, and the first CO gas detection. The analysis provided a CH_4 gas number density at the surface that is $4.0^{+5.0}_{-2.5}$ times larger than what was inferred by Voyager 2 (Herbert and Sandel, 1991; Strobel and Summers, 1995). Assuming that the N_2 pressure would follow a similar evolution, Lellouch et al. (2010) estimated a 40 μbar global atmospheric pressure. This value, that does not represent a direct measurement of the N_2 pressure, is clearly outside the 3σ error bar of the 21 May 2008 point in Figure 5.1 and Table 5.1. We may obtain no new information from the 21 May 2008, as mentioned previously, but we are able to use it to exclude the inference of this large 40 μbar pressure.

Bertrand et al. (2022) performed numerical simulations of N_2 and CH_4 volatile transport on Triton, constraining it using the surface pressure derived from the 2017 stellar occultation presented here. In their simulations, they account for a small amount of pure CH_4 at the surface, along with N_2:CH_4 mixtures (Merlin et al., 2018). In the simulation where this pure CH_4 ice is located at the South pole, and covers 2% of the visible projected disk of Triton's surface, they obtain a large increase in the CH_4 gas abundance between 1990 and 2005, without observing any change to the N_2 surface pressure.

Given that CH_4 is not completely mixed in with the N_2 ice, this implies that the large increase of the CH_4, when compared to Voyager 2, reported by Lellouch et al. (2010) can be decoupled from the N_2 evolution. Therefore, the value reported by Lellouch et al. (2010) does not represent a measurement of the global

pressure of Triton's atmosphere.

5.1.1 Volatile Transport Model

Bertrand et al. (2022) used the values we obtained in this work to run simulations with their Triton volatile transport model of the Laboratoire de Météorologie Dynamique (LMD). I will describe some of their work and how it is relevant to the study we performed here.

The Triton volatile transport model is a 2D (latitude × longitude) surface thermal model adapted from the LMD Pluto volatile transport model. For this simulation, only the volatile cycle of N_2 (insolation, surface thermal balance, condensation-sublimation; Bertrand and Forget, 2016), and the seasonal variation of the subsolar point (Forget et al., 2000) are taken into account. Much like the Pluto volatile transport model, it was considered that Triton's atmosphere is thin and transparent. That implies that the atmosphere has negligible influence on the surface's thermal balance, besides condensation, sublimation, and exchanges of latent heat. The atmospheric transport of N_2 is parametrized using a simple global mixing function. The topography in the model is assumed to be flat.

These simulations are performed on a horizontal grid of 32×24 points, corresponding to a grid-point spacing of 11.25° in longitude and 7.5° in latitude (around 270 km and 180 km at the equator, respectively). Performing these simulations over around 10,000 years, fixing the artificially-prescribed N_2 ice reservoirs at the poles, the evolution of surface pressure in the current season resulting from these distributions of N_2 ice is analysed. N_2 is only allowed to sublime and condense within these fixed reservoirs, with no interaction with the bedrock.

The N_2 cycle is very sensitive to the N_2 ice bond albedo, A_{N_2}, and emissivity, ε_{N_2}. The globally averaged energy balance for the N_2 ice on Triton can be simplified to first order by the equation

$$\varepsilon_{N_2}\sigma T^4 \approx (1 - A_{N_2})\frac{F}{4}, \tag{5.1}$$

where F is the solar constant at Triton and σ is the Stefan-Boltzmann constant. This assumes a spatially uniform and isothermal ice with a flat topography, an efficient global transport of N_2, and neglects thermal inertia and the global average

of latent heat exchanges. The result is that the N_2 ice equilibrium temperature, and the N_2 surface pressure, depend on $(1 - A_{N_2})/\varepsilon_{N_2}$.

In these simulations, the emissivity is fixed to a high value $\varepsilon_{N_2} = 0.8$, in line with recent Pluto volatile transport model works (Bertrand and Forget, 2016; Meza et al., 2019; Johnson et al., 2020), just above the estimated values from Voyager 2's data ($0.7 < \varepsilon_{N_2} < 0.77$; Stansberry et al., 1992), and close to the upper value estimated for Pluto from a surface energy balance model ($0.47 < \varepsilon_{N_2} < 0.72$; Lewis et al., 2021). This would correspond to large centimetre sized N_2 ice grains (Stansberry et al., 1996).

The N_2 ice albedo is adjusted to insure the surface pressure hits 14 μbar in 1989, the original result from Voyager 2 (Gurrola, 1995). A high seasonal thermal inertia was assumed in the sub-surface for this ice, fixed at 1000 J $s^{-1/2}$ m^{-2} K^{-1}, as has been suggested on Pluto (Bertrand and Forget, 2016; Johnson et al., 2020). The diurnal thermal inertia for all ices was set to 20 J $s^{-1/2}$ m^{-2} K^{-1}. Even though this value has never been measured on Triton, it was set in analogy to Pluto (Lellouch et al., 2011, 2016).

The surface pressure stays at ~5 μbar during the opposite season if a North polar cap (acting as a buffer, see below) extends down to 60° N and if the South polar cap extends up to 0°. The amplitude of the peak in the pressure is dampened if the N_2 ice deposits remains between 30° S - 0°. This would happen because these latitudes are dominated by condensation, and not sublimation, after the year 2000.

In these simulations, the surface pressure peak occurs just after the southern summer solstice, happening between the years 2000-2010 (Figure 5.2). The surface pressure results obtained are similar to those obtained by Spencer and Moore (1992). They artificially maintained a permanent large southern cap of bright N_2 ice (as shown in their Figure 7).

If the northern cap is large, it can serve as a condensation area and buffer the N_2 sublimation in the southern hemisphere better than if it is small. This results in a lower surface pressure peak, and it also occurs sooner.

These results suggest that a northern polar cap that extends down to at least 45° N - 60° N is required in 2017 to ensure that the surface pressure is at ~14 μbar, back to the Voyager 2 level. If no northern cap is assumed, the modelled surface pressure is higher than 16 μbar in 2017, but that is inconsistent with our observa-

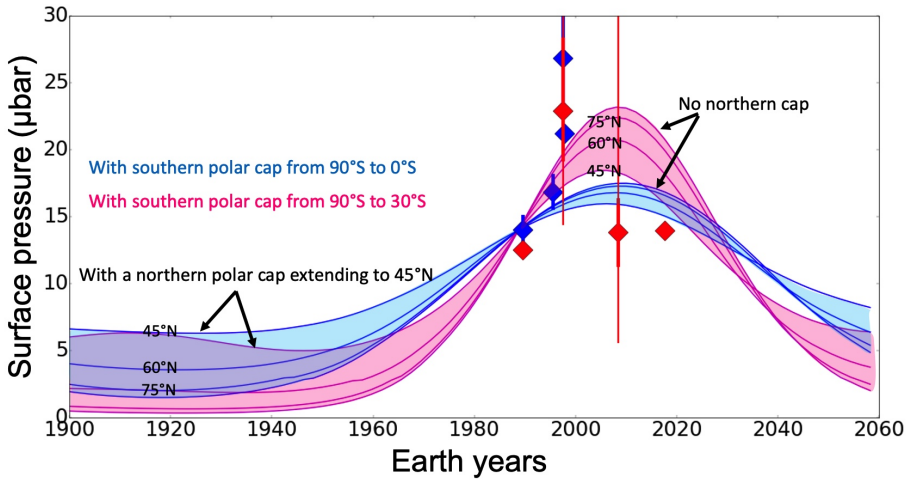

Figure 5.2: Surface pressure evolution on Triton, as simulated by the volatile transport model. It assumes different fixed N_2 ice distributions on both hemispheres. The blue lines refer to a southern cap extending up to the equator. The pink lines refer to a southern cap extending up to only 30° S. The points are the same as shown in Figure 5.1, and are presented in Table 5.1. Each of the lines are marked with their corresponding values, and they refer to different extensions of the northern cap: 45° N, 60° N, 75° N, and no cap.

tions. It is of note that a strong increase in surface pressure before 2000 cannot be obtained if there is N_2 ice present between 30° S - 0°. Also important to refer is that the surface pressure is always greater that 5 μbar, even during the opposite season, when a permanent northern cap extending down to 45° N is simulated. This implies that the permanent presence of both southern and northern caps is preventing Triton's atmosphere from collapsing during the southern winter.

5.2 Lower atmosphere

As I already mentioned in Section 4.1, a central flash was detected on the 5 October 2017 occultation. Among the 90 light curves observed, shown in Appendix B, 42 show evidence of the tell-tale sign of the stellar flux increase near the mid-occultation point characteristic of a central flash, and 23 have good enough signal-to-noise ratio that allows us to use them in the central flash modelling. Two of the

centre-most stations, Le Beausset and Felsina Observatory, were used in this fit, despite of their lower signal-to-noise ratio, simply because their central flash is so large, I deemed them important to study the deepest layers of Triton's atmosphere. This is a unique opportunity to study the lower atmosphere of Triton, as many data points were obtained. The central flash passed over Europe along the lines shown in black in Figure 4.1.

The results of our ray-tracing method show that the central flash is caused by a layer with a thickness of about 2 km, and is located at around 8 km above Triton's surface, or at a radius of $\sim$ 1361 km. In this altitude range, and because the secondary stellar image along Triton's limb (Figure 4.12) becomes increasingly significant, the Abel inversion method is not valid, as already mentioned in Section 4.1.3. This invalidity becomes apparent at altitude levels of about 20 km, which corresponds to the deepest layers probed by La Palma's light curve. Therefore, the central flash permits an analysis of some further $\sim$ 12 km down (about 0.6 scale height), hitting the $\sim$ 8 km altitude level, compared to the Abel inversion. The ray-tracing method provides the refraction angle corresponding to each image (primary and secondary), allowing to determine their positions along Triton's limb at any time, and can then be projected onto its surface, as shown in Figure 4.5.

In Figure 5.3, we see the reconstructed intensity map of Triton's shadow for the 2017 event, with a bright dot near the shadow centre, characteristic of a central flash. It is apparent that the flux reaches a minimum of about 7% of the unocculted flux inside the shadow and then increases rapidly at the centre of the shadow. To provide a few examples, at Calar Alto, passing at about 300 km from the shadow centre at closest approach, the increase of stellar flux is barely a bump, while at Calern, passing at 29 km, the flux reaches the full unocculted stellar flux. At Constância, with a closest approach of 8.4 km, the maximum of the flash reaches three times the unocculted stellar flux, and around 3.4 times at Le Beausset (the closest of all stations, with a closest approach of 6.7 km). The central flashes, along with their best fits, are shown in Figures 5.4-5.6.

5.2.1 Spherical fit

As I mentioned before, in Section 4.1.3, the first employment of the ray-tracing code excluded the central flashes. This time, in order to study the lower atmo-

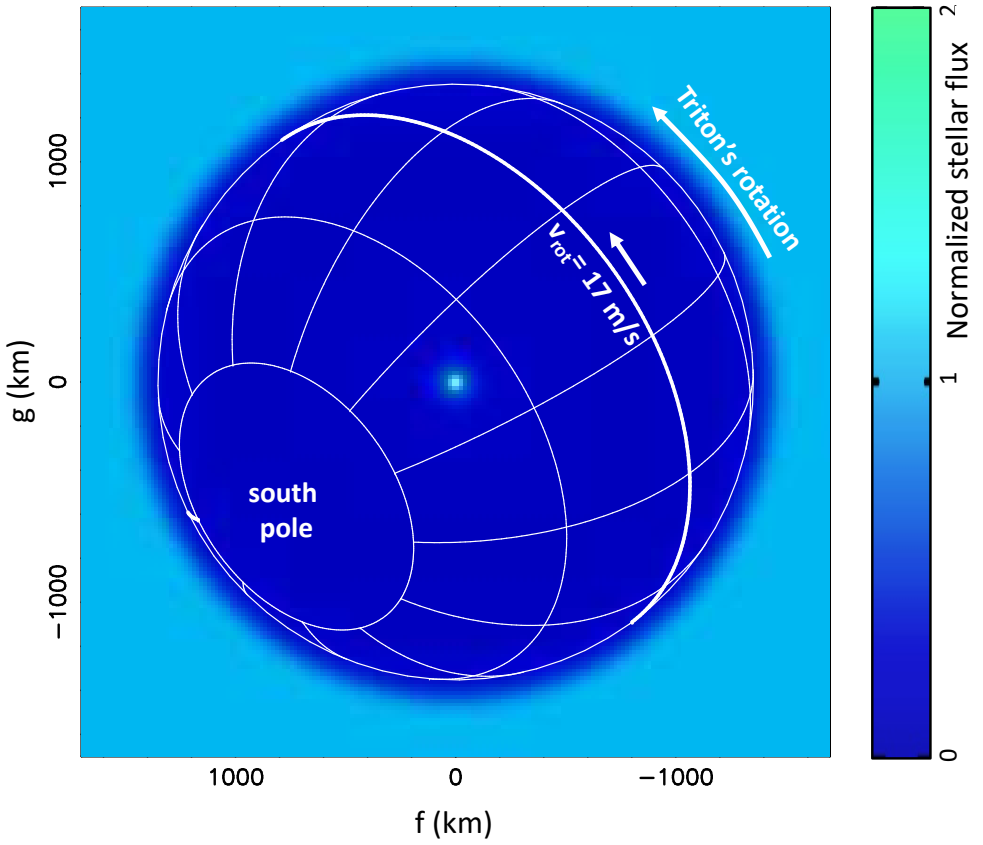

Figure 5.3: Stellar flux in Triton's shadow for the 5 October 2017 stellar occultation, normalised to unity outside the body (light-blue area). The direction of Triton's rotation is indicated by the arrows. Its equatorial rotation velocity in an inertial frame $v_{\rm rot}$ = 17 m s^{-1} is also shown.

sphere, I have included them, assuming a transparent atmosphere. A departure from sphericity of the layer responsible for the flash is now allowed (see Sicardy et al., 2006 for more details). This layer was the source for the assumption that two different template temperature models, one for the northern hemisphere and one for the southern hemisphere, as already mentioned in Section 4.1.3. The error was corrected when I noticed that the synthetic central flashes were too narrow, and did not fit any of the light curves that probed this layer. Some tests were made on the Abel inversion of the La Palma light curve, and another inversion was performed, using the Helmos light curve. Finally, the Calern light curve was inverted without the central flash layer to confirm the shape of the models.

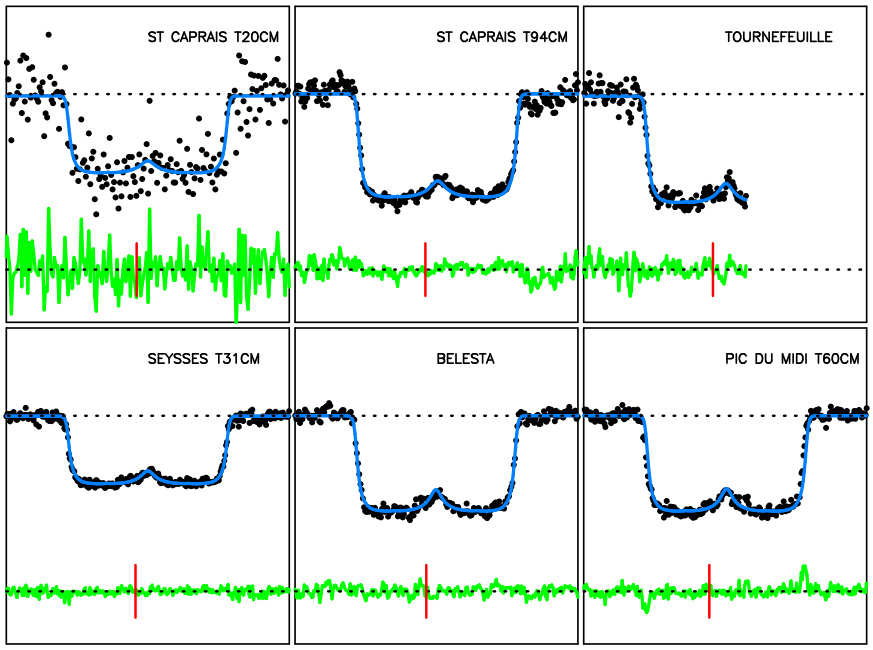

Figure 5.4: Simultaneous fits of the data (black dots) with the template temperature model described in Table 4.3. The blue lines are the synthetic light curves fitted to the data. The stations are sorted from left to right and top to bottom starting at the northernmost station (Saint Caprais) to the southernmost station (Calar Alto). Stations with exposure times smaller than 1 s were smoothed to have a sampling time close to 1 s, to make for easier signal-to-noise ratio comparison of all data sets. The green curves are the residuals of the fit. The lower and upper dashed lines correspond to the zero-flux level and the total star + Triton unocculted flux, respectively. Each panel has a duration of five minutes and is centred around the time of closest approach of the station to Triton's shadow centre. The vertical red line marks the time 23:48 UTC, for reference.

With the template temperature model derived, we can now assume a spherical flash layer, and we obtain the best simultaneous fits displayed in Figures 5.4-5.6. The quality of the fit, $\chi^2_{\rm dof} = 0.80$, is in line with that obtained without the central flashes, $\chi^2_{\rm dof} = 0.85$, showing that indeed there is no detection of a departure from sphericity. A more detailed discussion on the upper limit of such a departure of the sphericity is provided in Section 5.2.2. Taking a closer visual examination of the residuals of the strongest flashes with the best signal-to-noise ratios does reveal some minor and localised features, possibly atmospheric waves (Figures 5.7 and

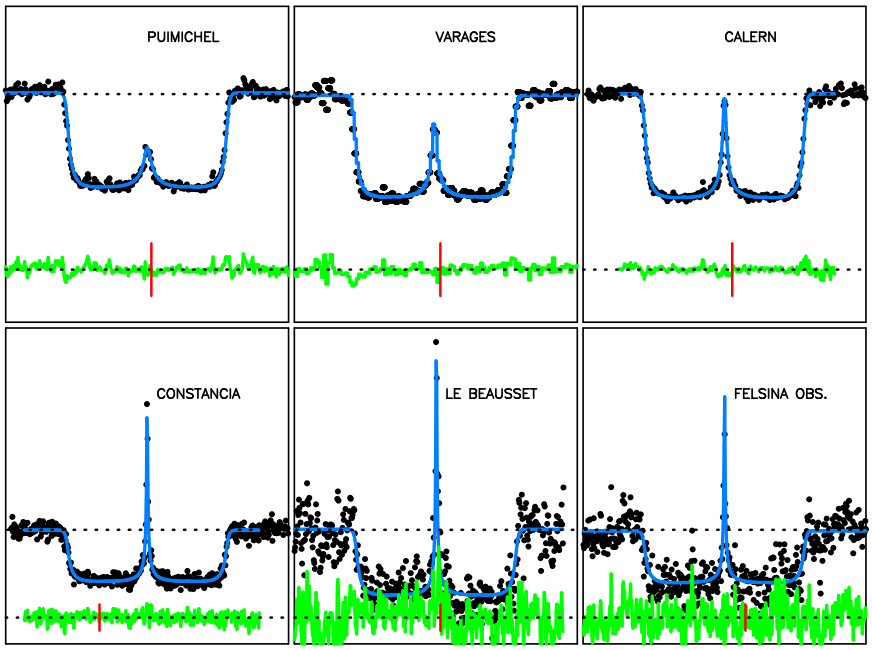

Figure 5.5: Continuation of Figure 5.4. In the case of Constância, Le Beauset, and Felsina Observatory, the light curves were not smoothed, and kept at their original sampling time, so that the full resolution of their strong central flashes are displayed here. These stations are plotted at a different vertical scale from the others, to show their peak.

5.8), but no global deviation from the spherical model.

Doing a simultaneous fit to the central flashes alone, excluding the ingress and egress portions of the light curves, yields another argument in support of the sphericity of Triton's atmosphere. The centre of Triton's shadow, in this fit, coincides to within 0.1 km with the shadow centre determined by the global fit that excluded the central flashes. This small offset is insignificant, especially when taken into account that the atmosphere's centre in the global fit has a typical 1σ error of 1 km cross-track (Fig. 4.13). This means that the centre we retrieved of the central flash layer, sensitive down to the 8 km altitude level, matches very well with the centre retrieved for the global shadow centre, sensitive only to the 60 km altitude level. It is possible that both of these atmospheric levels are near sphericity, but displaced in the same way in relation to Triton's centre, however, this configuration seems less likely to be the case.

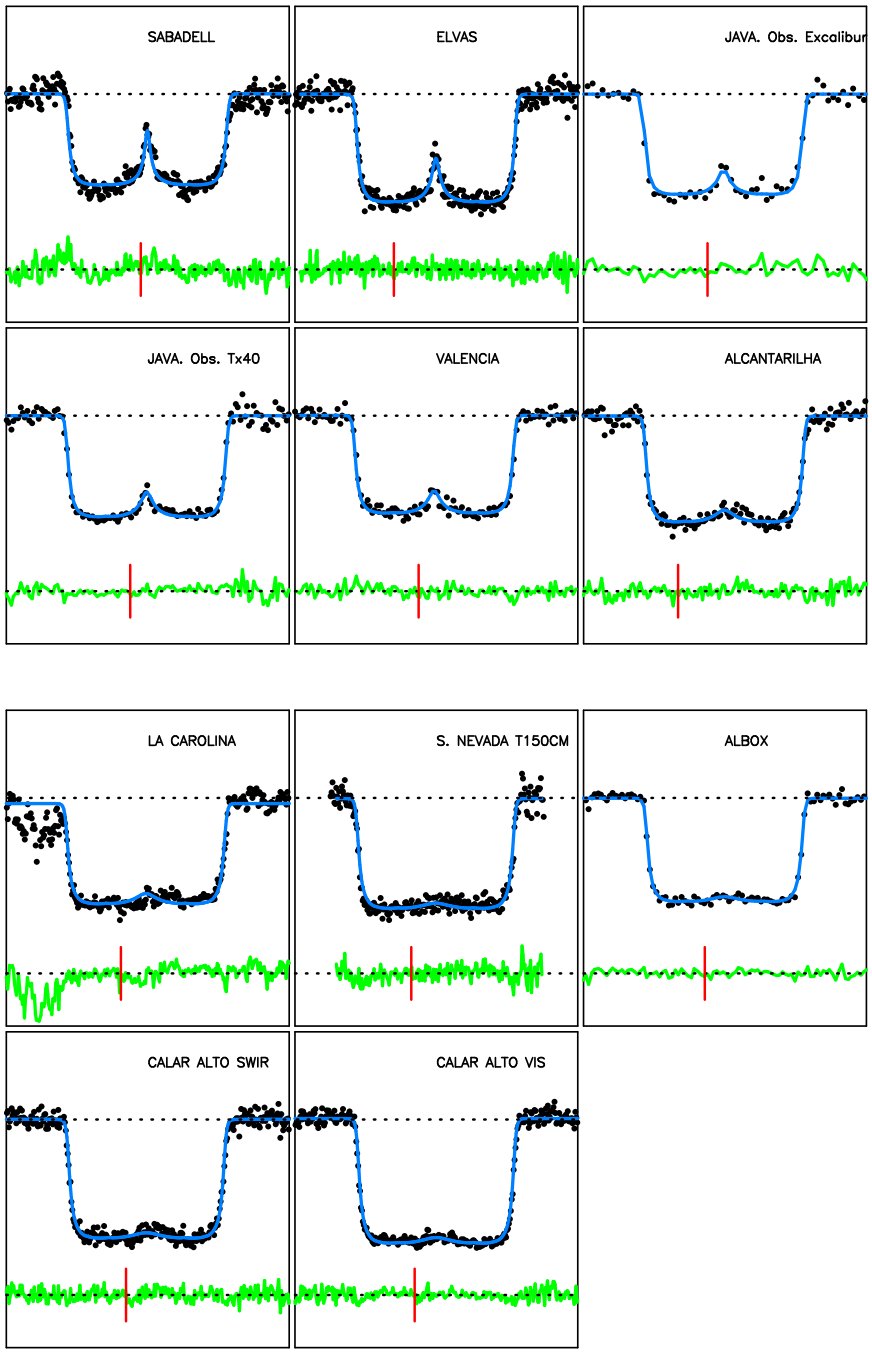

Figure 5.6: Continuation of Figure 5.5. "JAVA." is the abbreviation of Javalambre, used so that the name of the station fits into the plot.

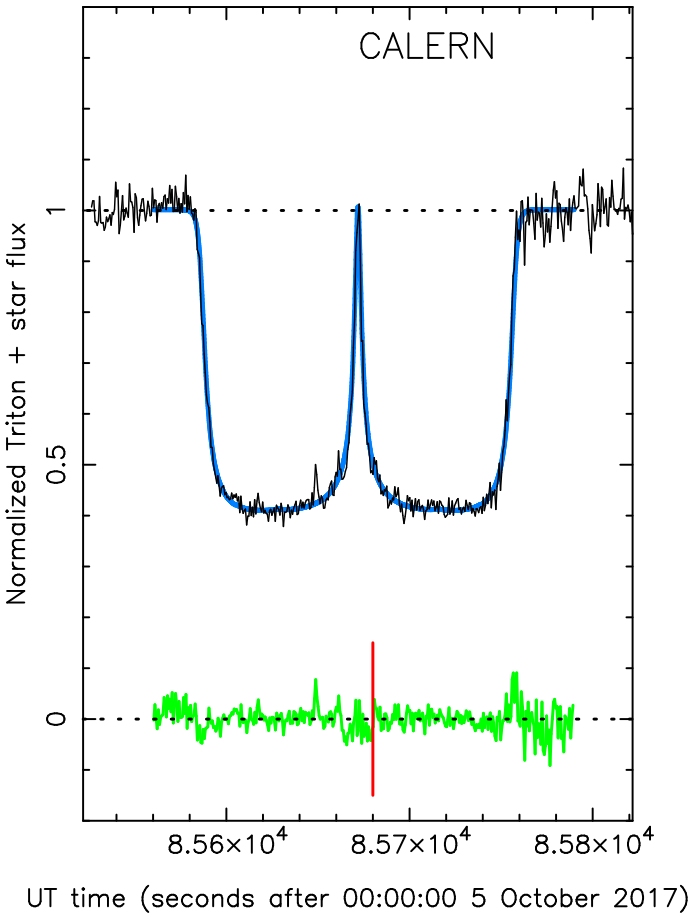

Figure 5.7: More detailed view taken of the flash observed at Calern, with the same setup as in Figures 5.4-5.6.

5.2.2 Atmospheric distortions and winds

Let us now discuss the possibility of a departure from sphericity in Triton's lower atmosphere. I shall restrict it to the simple model of a globally oblate central flash layer. More complex shapes may be tested once Triton's 3D Global Climate Models become available. Projected in the sky plane, an oblate layer appears to be an

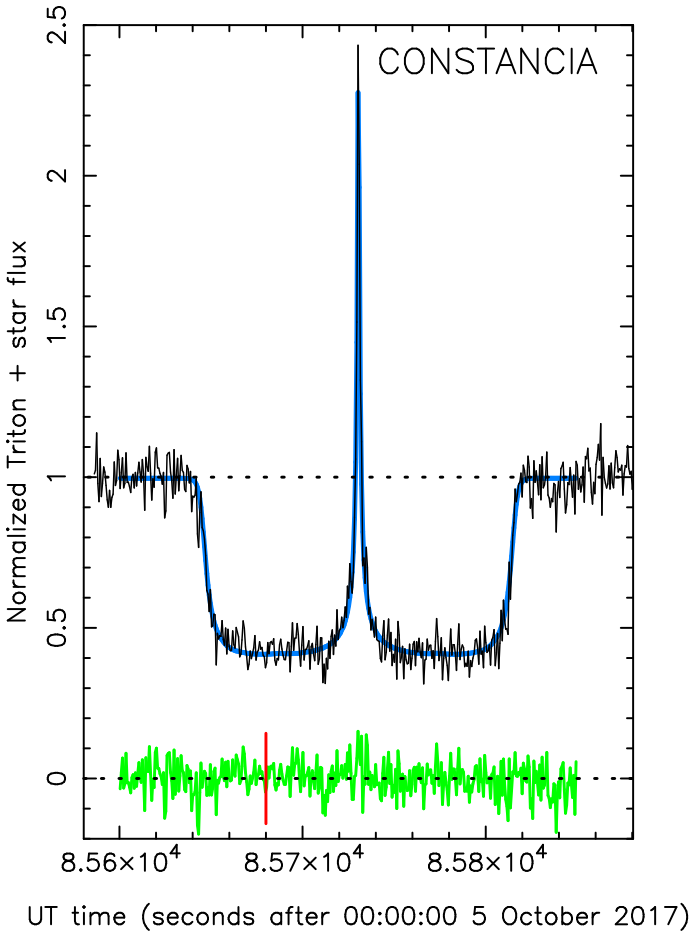

Figure 5.8: More detailed view taken of the flash observed at Constância, with the same setup as in Figures 5.4-5.6.

ellipse with apparent semi-major and semi-minor axes a' and b', respectively. The centre of curvature of said ellipse forms a diamond shaped caustic curve (Figure 2.8) where strong flux variations can be observed, as shown, for example, in Figures 5.9 and 5.10. The equation of the caustic (Elliot et al., 1977) is

$$(a'x)^{2/3} + (b'y)^{2/3} = (a'^2 - b'^2)^{2/3}, \tag{5.2}$$

where Oxy is a Cartesian reference system, with its origin O fixed at the ellipse centre, and Ox (respectively Oy) is aligned with a' (respectively b'). We have

$a' \sim 1360$ km, because the central flash layer is at ~ 8 km altitude. The orientations of the a' and b' axes are still to be specified.

The apparent oblateness of the central flash layer is defined as

$$\epsilon' = \frac{a' - b'}{a'}. \tag{5.3}$$

We explored different values of ϵ' starting at zero (spherical central flash layer), and tracked the variations of the χ^2 for each from the simultaneous fits of the central flashes. For this study, we considered only the central flashes from the stations at Varages, Calern, Constância, Le Beausset, and Felsina Observatory, the stations whose light curves present the strongest central flashes. The other stations cannot constrain ϵ' as they are too far away from centrality or have lower quality. The four cusps of the diamond-shaped caustic curve extend up to $\sim 2\epsilon' a$ from the shadow centre, according to Equation 5.2. As upper limits of $\sim$0.002 for ϵ' are obtained, we get $2\epsilon' a <\sim 5$ km for $a \sim 1360$ km. Therefore, only in the vicinity of the shadow centre, less than ~ 20 km, is sensitive to any departure from sphericity. Stations that are more distant essentially probe central flashes that provide no information on the sphericity, as they are indistinguishable from a spherical solution.

First, the semi-minor axis b' is assumed to be aligned with Triton's poles. This corresponds to an oblate central flash layer that is being maintained by an axisymmetric zonal wind regime. Said wind has a constant angular velocity around the b' axis. Using the $\chi^2 < \chi^2_{\rm min} + 1$ and $\chi^2 < \chi^2_{\rm min} + 9$ criteria, we find the 1σ-level and 3σ-level, respectively, upper limits of $\epsilon' < 0.0011$ and $\epsilon' < 0.0014$, respectively, for the apparent oblateness of the central flash layer. This limit's central flash intensity map is displayed in Figure 5.9. This apparent oblateness can be deprojected to retrieve the actual oblateness ϵ through the relation

$$\epsilon = 1 - \frac{\sqrt{(1-\epsilon')^2 - \sin^2 B}}{\cos B} \sim \frac{\epsilon'}{\cos^2(B)}, \tag{5.4}$$

where $B = 40.5°$ S is the sub-observer latitude (Table 4.1), and where the approximation holds for $\epsilon' \ll 1$. Using the result obtained, $\epsilon' < 0.0011$, yields a 1σ-level upper limit $\epsilon < 0.0019$ for the deprojected oblateness. This corresponds to a difference between the equatorial and polar radii, r_e and r_p respectively, of the layer of $r_{\rm e} - r_{\rm p} \sim 3$ km, using $r_e = a' = 1360$ km.

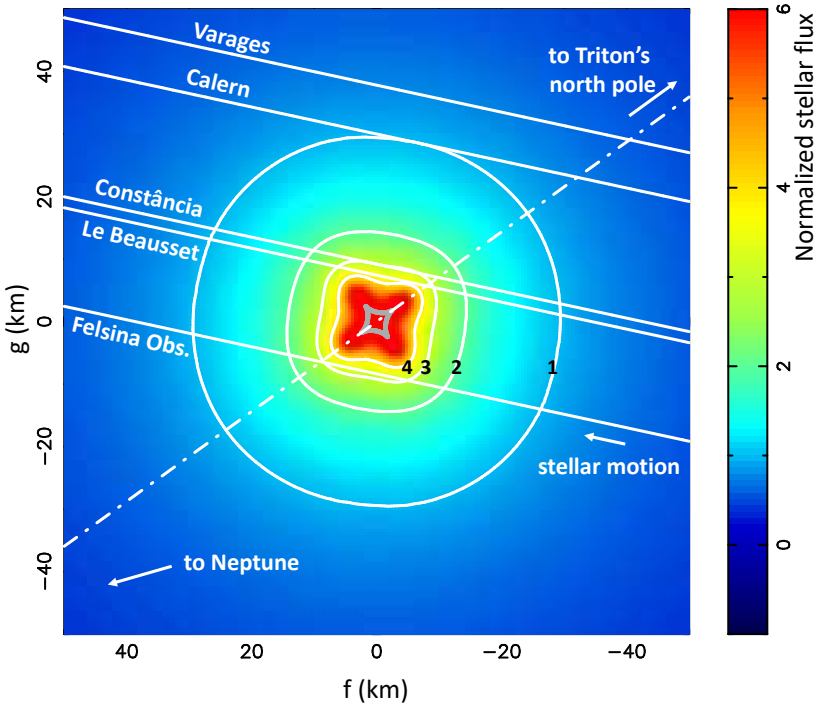

Figure 5.9: Map of the central flash intensity. The 1σ upper limit $\epsilon' = 0.0011$ is adopted for the apparent oblateness of the central flash layer (corresponding to a deprojected oblateness $\epsilon = 0.0019$). The numbers 1-4 along the iso-intensity contours refer to the received stellar flux in units of its unocculted value. The grey diamond-shaped feature around the centre is the caustic curve described by Equation 5.2 and corresponds to $\epsilon' = 0.0011$. The dash-dotted line indicates the apparent direction of Triton's poles. Neptune's direction is determined from the position angle 286° of Triton with respect to the planet at the moment of the occultation.

Here, it is assumed that the central flash layer shape is entirely supported by the zonal winds. In particular, we assume the absence of a horizontal temperature gradient, so that the isobar level also corresponds to the isopycnic (constant density) level. The radius r of the central flash layer is given as a function of the latitude φ by the equation (Hubbard et al., 1993; Sicardy et al., 2006):

$$\frac{1}{r}\frac{dr}{d\varphi} = -\frac{f\cos(\varphi)\sin(\varphi)}{1 - f\cos^2(\varphi)}, \tag{5.5}$$

where

$$f = \frac{rv^2(\varphi)}{GM_T\cos^2(\varphi)}. \tag{5.6}$$

This equation states that the isobar is locally perpendicular to the effective gravity field, where both the gravity field of the body and centrifugal forces are accounted for. Including in Equation 5.5 the polar equation of an oblate central flash layer,

$$r = \frac{r_e r_p}{[r_e^2 \sin^2(\varphi) + r_p^2 \cos^2(\varphi)]^{1/2}}, \tag{5.7}$$

it is obtained to lowest order in $\epsilon = (r_e - r_p)/r_e$ the velocity

$$v = \sqrt{\epsilon}\sqrt{\frac{2GM_T}{r_e}}\cos\varphi \sim 1450\sqrt{\epsilon}\cos\varphi \ \text{ m s}^{-1}, \tag{5.8}$$

with the value of GM_T listed in Table 3.1. Using $\epsilon < 0.0019$, we obtain a 1σ level upper limit for the zonal wind at the equator of $|v_e| < 63$ m s^{-1}.

This motion can be prograde, represented with a positive sign in Equation 5.8, or retrograde, represented with a negative sign, and it is measured in an inertial frame. Therefore, having v'_e as the zonal wind in a frame rotating with Triton, allowing for the measurement of the atmospheric circulation at that level, we have

$$v_e = v'_e + v_{rot}, \tag{5.9}$$

where $v_{rot} = 17$ m s^{-1} is the equatorial velocity imposed from Triton's rotation, shown in Figure 5.3. A retrograde zonal wind regime ($v'_e < 0$) implies the 1σ limit to be $|v'_e| < 63 + 17 = 80$ m s^{-1}, and a prograde regime ($v'_e > 0$) implies $v'_e < 63 - 17 = 46$ m s^{-1}. These values are 87 m s^{-1}, and 53 m s^{-1} respectively, if we consider the 3σ upper limit.

In discussions with Tanguy Bertrand and François Forget, who are analysing the wind regime on Triton through simulations, we concluded on some information obtained in 1989, by Voyager 2, about the atmospheric circulation. While surface wind streaks suggested retrograde surface winds between the latitudes 15° S and 45° S (Hansen et al., 1990), the deflection of plumes hinted that in the atmosphere above them, at 8 km, and near 49° S and 57° S, the wind was actually prograde (Hansen et al., 1990; Yelle et al., 1995). From a purely theoretical standpoint, Ingersoll (1990) suggested that this could stem from a contrast in temperature between the cold frost-covered pole and the warm frost-free equator.

Vangvichith (2013) provided some Global Climate Models simulations, including the N_2 condensation-sublimation cycle. Other simulations have been made to explore the circulation on Pluto, relevant here because it is similar to

Triton where it relates to rotation rate and atmospheric composition (Forget et al., 2021 and references therein). These simulations show that if N_2 sublimes significantly in the southern hemisphere, the circulation would be dominated by a retrograde wind resulting from the conservation of angular momentum of the flow, with velocities that must be equal or lower than the rotation of the object (17 m s^{-1}). This, however, is much less than the upper limits that were derived from the observations.

As already mentioned, global retrograde winds were not observed by Voyager 2. To obtain a prograde rotation in the mid-southern latitudes as indicated by Voyager 2's observations of Triton's plumes, the inter-hemispheric condensation must be weak. If that is the case, a thermal gradient can create a weak prograde wind as suggested by Ingersoll (1990), reaching a few metres per second in Global Climate Model simulations. However, models of Pluto suggest that a regime of super-rotation (much like on Venus or Titan) may occur (Forget et al., 2017). Super-rotation could explain the direction of the plumes on Triton. Such a regime is thought to derive, initially, from the formation of a high-mid latitude jet, resulting from the thermal balance between the warm equator and a colder pole, or from the condensation flow from low latitudes to the pole. Barotropic waves can, then, transport angular momentum to and from the equator and accelerate the entire atmosphere. In their Pluto Global Climate Model, Forget et al. (2017) found a mean equatorial zonal wind of up to 15 m s^{-1}. This, however, could be dependent on the model used. Therefore, it is not an easy task to set a theoretical limit to this possible super-rotation. The upper limit obtained in 2017 on the prograde wind near 50 m s^{-1} provides a constraint for this hypothetical super-rotation.

I studied other orientations for the central flash layer, as projected in the sky plane, in order to analyse if there is an asymmetry along the b' axis. This is done by relaxing the condition that b' should be aligned with Triton's pole. We decided to do such an analysis because this might be the case if there are other causes of distortion other than zonal winds, such as tidal forces from Neptune or Triton's potential anomalies. These orientations provide stricter upper limits for the apparent oblateness ϵ' since the cusps of the caustic are allowed to get closer to the paths of the central-most stations (Figure 5.9). As an example, rotating the caustic by 45° imposes the 1σ upper limit of $\epsilon < 0.00074$, instead of 0.0019. This requires an equatorial wind of $\sim$ 40 m s^{-1}, still much larger than the values

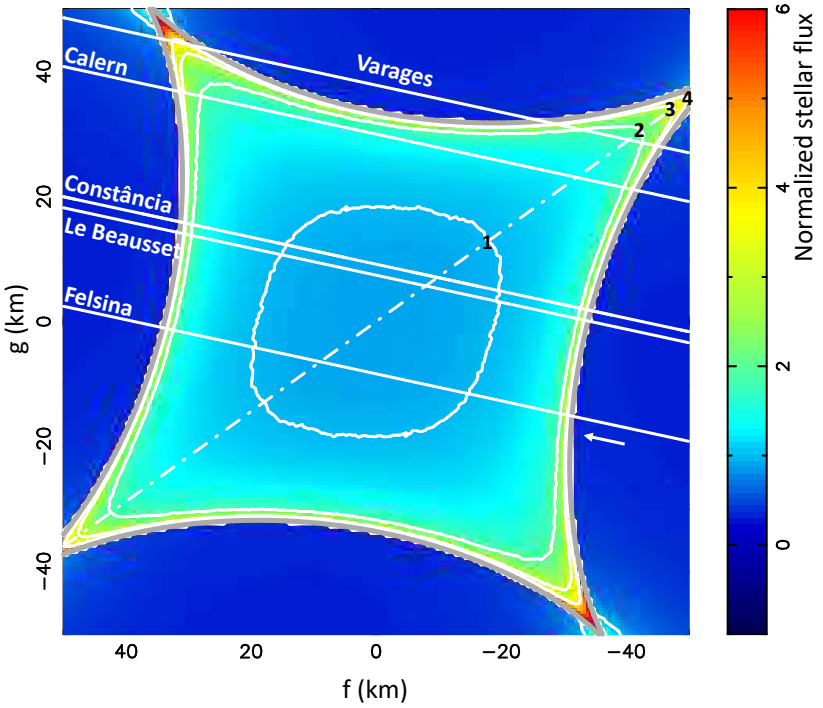

Figure 5.10: Same as Figure 5.9, adopting the oblate solution $\epsilon = 0.042$ found by Elliot et al. (1997) from the shape of a central flash observed during the 14 August 1995 occultation.

of $\sim$ 10 m s^{-1} expected from Global Climate Models, and therefore, the value we obtained is not a constraining limit as far as the Global Climate Models are concerned.

I searched the literature for other solutions found for ϵ, and uncovered the value obtained by Elliot et al. (1997) from a single cut inside the central flash region during the 14 August 1995 occultation. Two solutions are considered by the authors, an oblate central flash layer with $\epsilon = 0.042$ and a prolate central flash layer with $\epsilon = -0.032$. Adopting the $\epsilon = 0.042$ value, the map of the central flash intensity in Figure 5.10 is extracted. This value implies that the five stations analysed here, shown in the map, would cross the caustic, and present strong flux variations at those crossings that are not observed in the data, as shown in Figures 5.7 and 5.8, for instance. A similar conclusion is obtained if the prolate value $\epsilon = -0.032$ of Elliot et al. (1997) is adopted. It is of note that the closest approach distance to the shadow centre for the observation of 1995 was about 100 km, well

outside the diamond-shaped caustic displayed in Figure 5.10. Therefore, caustic crossings could not be tested for the observations in 1995.

The problem with these large oblateness values is that they require unrealistically high wind velocities in order for the atmosphere to maintain these strong distortions. As an example, $\epsilon = 0.042$ results in an equatorial wind velocity of $v_e \sim 300$ m s^{-1}, more than double the sonic velocity near Triton's surface (~ 130 m s^{-1} at ~ 40 K) and is a much larger result than those predicted by Global Climate Models, as mentioned previously. One possibility, provided by Elliot et al. (1997), is that Triton's atmospheric distortion was local and not global, being restricted only to the mid-latitude regions. This allows for lower wind speeds, 110-170 m s^{-1}, depending on which solution, prolate or oblate, is considered. Such velocity is still supersonic, or very close to it, and is, again, not expected in Global Climate Models. Also, this distortion would have been detected in our data set, that sampled the central flash region quite heavily, but it was not found in our observations.

Another explanation proposed by the authors is that the presence of hazes, that absorbed part of the stellar flux at some locations along the limb, would change the shape of the central flash. However, according to the authors, neither the optical depth obtained for the hazes at the corresponding altitude levels, nor their wavelength dependence, were consistent with the results from Voyager 2. I will discuss hazes further in Section 5.2.3.

The shape of Triton's solid body, as observed by Voyager 2, indicates an oblateness no larger than 0.0014 (Thomas, 2000), too small to explain the incredibly large distortions by Elliot et al. (1997). Non-radial components of Triton's inner gravitational field may also cause atmospheric distortions. Such distortions would be permanent, and therefore, should have been present and observable in 2017.

Taking all this discussion into consideration, we reached the conclusion that the large oblatenesses reported by Elliot et al. (1997) are both theoretically unexpected and inconsistent with our observations.

We think that the differences between the flash models and its observation in 1995 (as well as small departures from our spherical model in Figures 5.7 and 5.8) could be caused by small local corrugations of the flash layer induced by gravity waves. These atmospheric waves present themselves as small fluctuations, with

little effect on the overall light curve shape, and therefore, were not studied in detail. Given that the caustic is the focus point of the limb centre of curvatures, its shape is very sensitive to local (but small) corrugations of that layer. Examples of these effects have been investigated to explain flash shapes, deviating from sphericity, in stellar occultations by Neptune (Hubbard et al., 1988) and Titan (Sicardy et al., 2006). The study of these corrugations was not performed for Triton, as it was for Titan (Sicardy et al., 2006), however, we know that these fluctuations are much smaller than 300 m, as we do not see the same type of features that Titan presents. As long as zonal wind and gravity wave regimes are not available for Triton's lower atmosphere, this is as far as we can go in this study regarding this topic.

5.2.3 Hazes and clouds

Throughout my work, we assumed that Triton's atmosphere is clear, transparent, free of absorbing material. However, Voyager 2's observations revealed both hazes and clouds in the lower atmosphere, two types of absorbing features. They were detected in the visible wavelengths through the mission's imaging system (Rages and Pollack, 1992), as well as during the ultraviolet occultation experiment (Krasnopolsky et al., 1992, 1993; Krasnopolsky and Cruikshank, 1995).

Yelle et al. (1995) reviewed Voyager 2's observations. They explain that the hazes were detected up to an altitude of about 30 km, observed around the entirety of Triton's limb, except for a small region near east longitude 280° and between latitudes 4° and 18° S. These features should also be present during the occultation event of 5 October 2017, unless a drastic change occurred, pertaining to the formation of the hazes. The cloud feature is observed closer to the surface when compared to hazes. They stay below an altitude of $\sim$ 8 km. Unlike hazes, clouds exhibit a patchier distribution along Triton's limb.

Absorbing material should be detected best in the central flash structures, caused by a layer at about 8 km altitude, because of their lower altitudes, and since the central flash probes to about that altitude level. Estimations of the hazes' integrated, down to Triton's surface, vertical optical depth at 0.47 μm is $\tau_{\rm vis} = 0.005 \pm 0.001$, with a typical scale height of $H_{\rm h} \sim 12$ km (Krasnopolsky et al., 1993; Rages and Pollack, 1992). Therefore, the integrated vertical

optical depth down to the 8 km altitude level should be reduced by a factor of $\exp(-8/H_{\rm h}) \sim 0.5$. Together with a factor of $\sqrt{2\pi R_T/H_{\rm h}} \sim 27$ due to the amplification of the slant (along the line-of-sight) optical depth, we obtain a slant optical depth of the hazes at 8 km in the order of

$$0.005 \sqrt{\frac{2\pi R_T}{H_{\rm h}}} \exp\left(\frac{-8}{H_{\rm h}}\right) \sim 0.07. \tag{5.10}$$

Consequently, the slant optical depth of the hazes at the central flash layer is expected to be in the range 0.05-0.10, a reduction of the flash amplitude by 5-10%, if no changes occurred since 1989.

Clouds are much denser features than hazes. Their vertical optical depth down to the surface is 0.1 or higher. Cloud particles have a vertical distribution with a scale height $H_{\rm c}$ comparable to or larger than the atmospheric scale height of about 20 km. Therefore, the slant optical depth of the clouds at 8 km should be in the order of

$$0.1 \sqrt{\frac{2\pi R_T}{H_{\rm c}}} \exp\left(\frac{-8}{H_{\rm c}}\right) \sim 1.4 \tag{5.11}$$

or larger. This corresponds to a decrease of the flash amplitude by a factor of 4 or more.

It is expected that hazes have a mild effect on the overall height of the central flashes, with an expected reduction of only 5-10%. As shown in Section 5.2.1, we do not see any departure from the template temperature model, assumed as spherical, on the highest central flash observations from the 5 October 2017 event. We also do not detect any trends on the observed central flash amplitudes regarding different wavelengths. For example, the central flash at Constância, in Figure 5.8, observed at an effective wavelength of $\sim$0.6 μm and agrees with the template temperature model at the same satisfaction level as the Varages central flash, observed at $\sim$1.3 μm, in Figure 5.5. A study in different wavelengths is also possible at Calar Alto, a station with two simultaneous observations used in our fits, one in the visible (0.4-1.0 μm) and another in the near-infrared (1.0-1.7 μm), shown in Figure 5.6 and Appendix A. A central flash is observed at this station, however, it is too faint to uncover a difference between the two observations. There is another station that made two observations that were used in the fit, Kryoneri, in the R and I bands, but this station was too far away from the centre to exhibit a central flash. It does not show any significant differences in the fit of the synthetic light curve (Appendix B).

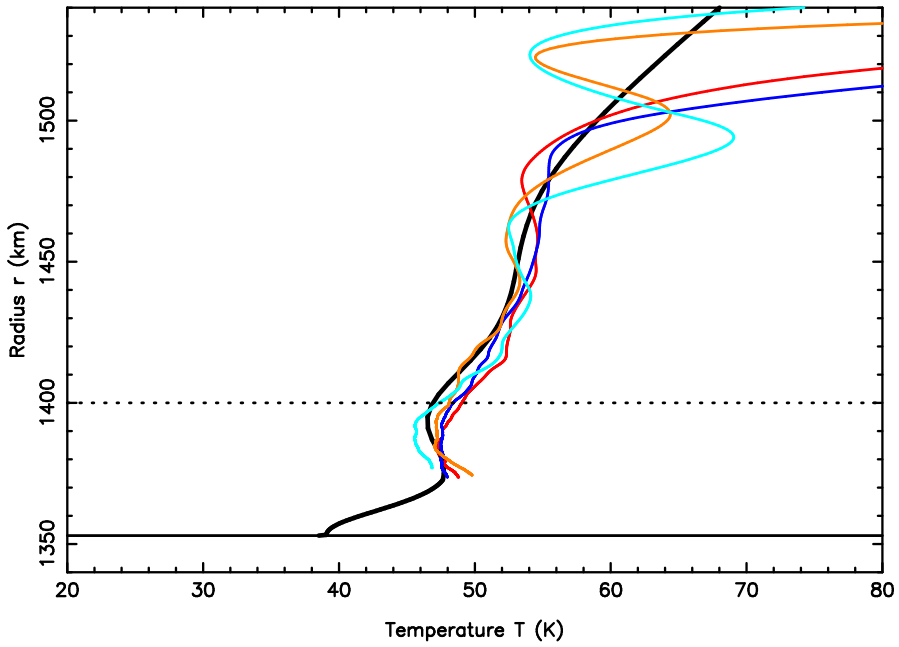

Figure 5.11: Comparison between the temperature profiles obtained from the inversion of La Palma and Helmos' light curves (using the same colour coding as in Figure 4.7) and ALMA observations of CO (black curve) by Gurwell et al. (2019).

These results seem to indicate that the hazes have no detectable effect on our central flash shapes. This result is also true for the cloud features, since they would reduce the central flash amplitudes by a factor of at least 4, something not observed in the data. Meaning that our template temperature model consistently explains all observations, including the central flashes, using a clear, transparent, atmosphere.

There is, however, a caveat. The height of the central flash actually depends on the assumed template temperature model. In order to separate the haze from the temperature effects, independent information on the thermal profile of the lower atmosphere is required. Gurwell et al. (2019) compared their temperature profile to ours, and they are consistent with each other (Figure 5.11), meaning that our template temperature model should be sound.

5.2.4 Troposphere

It is important to mention that Yelle et al. (1991) inferred a troposphere from the Voyager 2 observations of geysers and clouds. We do not observe such a troposphere, as our deepest layer probed, at the central flash level, coincide with the expected altitude of the tropopause. Therefore, our model is consistent with our central flashes, as discussed in Section 5.2.1, and we saw no real need to include a troposphere to accommodate for the data. However, this of course does not mean that we can exclude a troposphere as we do not have information down to this part of the lower atmosphere.

Chapter 6

Conclusions

Triton possesses a thin atmosphere, that is in vapour pressure equilibrium with the satellite's surface. As a possible captured Trans-Neptunian Object, Triton may provide insight into the region beyond Neptune, including the study of its twin atmosphere of Pluto. The knowledge of this atmosphere is yet underdeveloped, as theoretical models are only now being developed for Triton. While Global Climate Models are not fully developed, observational constraints are being collected, and will be used to test and validate these models.

To probe Triton's atmosphere, I took advantage of the stellar occultation technique, where I analysed data from 1989 up to 2017. In this work, I:

- Derived 18 light curves obtained during the Triton stellar occultation on 5 October 2017;
- Analysed the data from the 90 positive observations obtained during this event, using the Abel inversion and ray-tracing direct methods;
- Studied the central flash feature present in 42 light curves from this event, to study the atmosphere's sphericity and distortion;
- Performed a novel analysis of the Voyager 2 data, obtained on 25 August 1989, in order to compare directly those results to ours;
- Used the template temperature model derived from the Abel inversion to fit the light curves obtained from two other stellar occultations;
- And analysed the evolution of Triton's atmospheric pressure.

The main results are summarised in this Chapter.

6.1 Findings

The 5 October 2017 Triton stellar occultation event was the most recorded event of this type to ever observe the satellite. The event crossed Europe, northern Africa, and eastern USA. It yielded 90 positive observations, with 42 presenting a central flash feature.

After performing the photometry of three of the best light curves in terms of signal-to-noise ratio, an Abel inversion method was used to retrieve the density, pressure, and temperature profiles. Further study was required at this step, as there seemed to be a problem with the calibration of the best light curve. Using independent observations, as well as using the other two light curves' inversion to confirm the result, I was able to obtain the final version of the template model. This template model is a synthetic and smoothed model of the results derived in this process and it extrapolates the density, pressure, and temperature down to the surface.

There is a hint of a mild negative temperature gradient (reaching -0.2 K km^{-1}) at the deepest part probed by these stations, below the altitude of $\sim$30 km. This indicates the presence of a mesosphere just above an expected positive temperature gradient, a stratosphere, that connects the atmosphere to the cold surface.

Using the template temperature model obtained from the Abel inversion, a ray-tracing method was then used to perform a global fit of 52 light curves, where a pressure $p_{1400} = 1.18 \pm 0.03$ μbar at radius 1400 km was obtained.

A novel analysis of the Voyager 2 radio experiment was made, where I was able to retrieve useful information extracted from the surface up to $\sim$ 1400 km. This shows that the pressure obtained in the 2017 event is consistent with the pressure obtained in 1989. And it provides a new way to directly compare results obtained from ground-based stellar occultations, as occultations derive the pressure at a standard reference radius of 1400 km, while Voyager 2's results were, historically, only of the surface pressure.

A survey of pressure values obtained between 1989 and 2017, from stellar occultations, was conducted. The two past occultations, from 1997 and 2008, re-

analysed using our template temperature model, indicate that the surface pressure reported in the 1990s is real, but it remains debatable due to the scarcity of high signal-to-noise ratio light curves and the lack of a fully consistent analysis of all past occultations.

The pressure obtained from the 2017 event is consistent with the results retrieved from the Voyager 2 data, meaning that the pressure in 2017 was back to the level of 1989. The Volatile Transport Models explored do not support a strong increase of the surface pressure occurring between 1989 and 2017, and seem to point to a modest increase. These Volatile Transport Models also show that a strong increase in surface pressure before 2000 cannot occur if N_2 is present between latitude 30° S - 0°, and that a northern polar cap should extend down to at least 45° N - 60° N in 2017 in order for the pressure to be back at Voyager 2 epoch levels.

Central flash analysis does not show evidence of atmospheric distortion nor the presence of hazes near the 8 km altitude level. The atmosphere appears to be globally spherical, with a 1σ upper limit of 0.0011 for its apparent oblateness near the 8 km altitude. This corresponds to a global difference of less than 1.5 km between the largest and smallest atmospheric radii at that altitude, much smaller than values reported in the literature.

6.2 Perspectives

On 6 October 2022, another stellar occultation by Triton will take place (Figure 6.1), the first since 2017. The path is expected to cross most of Asia, with a bright star being occulted. This occultation will be extremely important, as it will add one more data point in the atmospheric pressure evolution of this satellite. There is the possibility to plan a "picket-fence" approach and dual observations of the central flashes, in order to obtain more information regarding hazes and the lower atmosphere as a whole.

Once Global Climate Models are fully developed, testing using these findings will also be possible. It will allow us to tackle in depth the presence (or absence) of hazes and of a troposphere just above Triton's surface, as well as the possible detection of gravity waves. An analysis of the possibility of a troposphere is worth

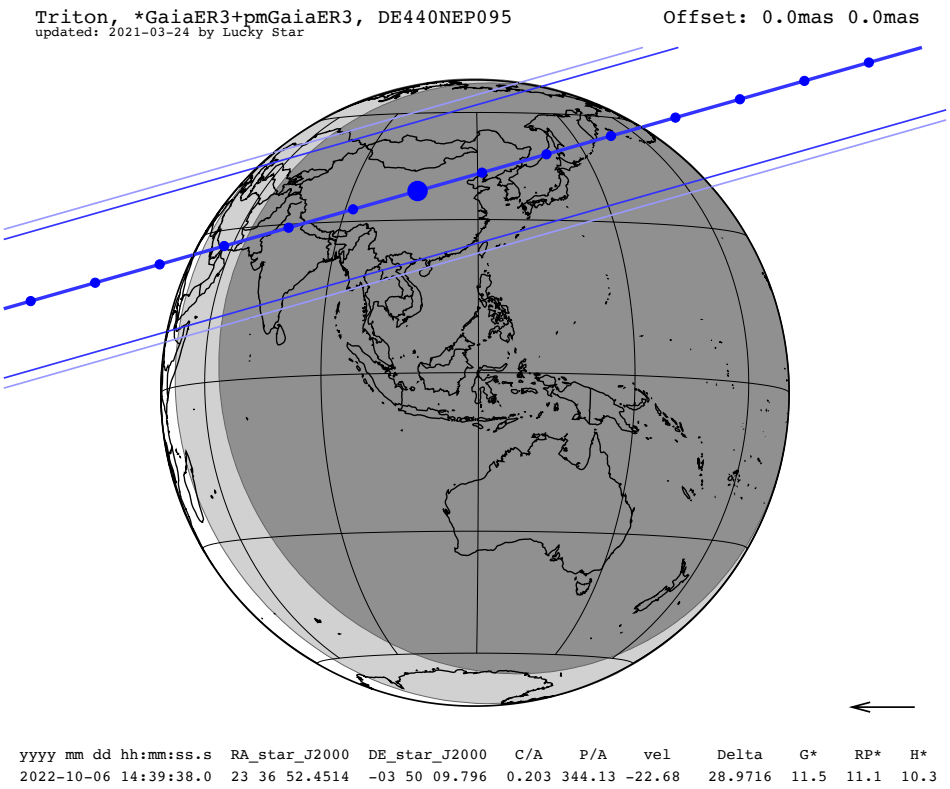

Figure 6.1: Prediction of Triton's stellar occultation occurring on 6 October 2022, crossing most of Asia.

an effort for future studies of our central flash data. We can also test haze models, when available.

There has been several proposals for new spacecraft missions to visit the Neptunian system, after Voyager 2. Recently, the *Trident* concept mission for a flyby was submitted, as part of the Discovery 15 and 16 in NASA's Discovery Program. Thus far, however, no proposal has been approved. A new concept mission, Neptune Odyssey, for an orbiter and entry probe, is currently under development, with Dr. Abigail Rymer as the principal investigator (Rymer et al., 2020). It is expected to incorporate NASA's 2023-2032 Planetary Science and Astrobiology Decadal Survey. The launch proposal is in 2033, with an arrival at the Neptunian system in 2049, and a mission length of five years.

Appendix A

Circumstances of observations

In this Appendix the circumstances of observations for all stations that attempted an observation for the occultation events studied are presented.

Tables A.1-A.6 list the stations from the 5 October 2017 event that were used in the simultaneous fit to the template temperature model.

Tables A.7-A.11 list the stations from the 5 October 2017 event that were not used in the fit, either because the light curves had insufficient signal-to-noise ratios to provide relevant contribution to the fit, or they were provided to us too late to be included.

Tables A.12-A.14 list the stations from the 5 October 2017 event that could not gather data due to bad weather or technical problems, but were otherwise involved in the campaign.

Table A.15 lists all the stations from the 18 July 1997 event.

Tables A.16 and A.17 list all the stations from the 21 May 2008 event.

Table A.1: Circumstances of observations for the 5 October 2017 event.

Site	**Coordinates Altitude (m)**	**Telescope aperture (m) Instrument/filter**	**Exp. Time/Cycle (s)**	**Observers**
Observations that provided light curves that are used in Triton's atmospheric fit				
Agerola	40 37 26.2 N	0.28	0.86/0.86	L. Morrone
Italy	14 33 50.6 E	CCD/clear		
	660.0			
Albox	37 24 20.0 N	0.41	2.00/3.34	J. L. Maestre García
Spain	02 09 07.0 W	CCD/clear		
	485.0			
Alcantarilha	37 07 58.8 N	0.36	0.33/0.64	F. Marques Dias
Portugal	08 21 54.0 W	CCD/red		
	65.0			
Algiers	36 47 52.1 N	0.81	0.04/0.04	D. Baba Aissa,
Algeria	03 01 56.2 E	video/clear		Z. Grigahcene
	331.0			
Ariana	36 53 03.0 N	0.20	0.50/0.60	S. Kamoun
Tunisia	10 11 42.0 E	CCD/clear		
	5.0			
Athens	37 58 06.8 N	0.40	1.00/3.50	K. Gazeas,
Greece	23 47 00.1 E	CCD/clear		E. Karampotsiou,
	250.0			L. Tzouganatos
Belesta	43 26 39.4 N	0.30	0.64/0.64	P. André,
France	01 48 58.6 E	video/clear		M. Llibre,
	235.0			F. Pailler
Boissettes	48 31 41.0 N	0.30	0.50/0.50	M. Irzyk
France	02 37 28.0 E	CCD/clear		
	75.0			

Table A.2: Circumstances of observations for the 5 October 2017 event - continuation.

Site	**Coordinates Altitude (m)**	**Telescope aperture (m) Instrument/filter**	**Exp. Time/Cycle (s)**	**Observers**
Calar Alto	37 13 24.7 N	1.23	VIS: 0.063/0.063	R. Hueso,
(2 channels)	02 32 44.9 W	SCMOS/VIS: (0.4-1.0 μm)	SWIR: 0.11/0.11	S. Pérez-Hoyos,
Spain	2160.0	SWIR: (1.0-1.7 μm)		A. Sánchez-Lavega
Calern	43 45 13.2 N	1.04	0.10/0.11	J. Ferreira, P. Machado,
France	06 55 22.4 E	CCD/I'		P. Tanga, J.-P. Rivet
	1268.0			
Catania	37 41 35.8 N	0.80	0.80/1.70	G. Leto,
Italy	14 58 29.1 E	CCD/clear		R. Zanmar Sanchez,
	1725.0			P. Bruno, G. Occhipinti
Clanfield	50 56 19.2 N	0.61	0.16/0.16	D. Briggs,
England	01 01 10.6 W	video/clear		S. Broadbent
	155.0			
Constância	39 29 41.6 N	0.51	0.64/0.64	R. Gonçalves,
Portugal	08 19 25.2 W	video/clear		M. Ferreira
	147.0			
Côtes de Meuse	49 00 07.2 N	0.83	0.06/0.06	S. Renner,
France	05 41 06.6 E	EMCCD/clear		M. Kaschinski
	284.0			
Cuq les Vielmur	44 29 05.0 N	0.20	2.00/4.00	A. Cailleau,
France	01 55 05.0 E	CCD/clear		V. Pic,
	300.0			L. Granier
Dark Sky Obs.	36 15 09.6 N	0.36	1.50/2.50	J. Pollock,
United States	81 25 01.2 W	CCD/clear		D. B. Caton
	960.0			V. Kouprianov

Table A.3: Circumstances of observations for the 5 October 2017 event - continuation.

Site	**Coordinates Altitude (m)**	**Telescope aperture (m) Instrument/filter**	**Exp. Time/Cycle (s)**	**Observers**
Elvas	38 50 47.6 N	0.27	0.30/0.30	W. Beisker
Portugal	07 12 27.4 W	CCD/clear		
	285.0			
Felsina Obs.	44 21 22.0 N	0.40	0.64/0.64	R. Di Luca,
Italy	11 09 09.0 E	video/clear		D. Alboresi
	652.0			
Forcarei	42 36 38.4 N	0.51	0.64/0.64	R. Iglesias-Marzoa,
Spain	08 22 15.1 W	video/clear		H. González
	673.0			
Hartley Wintney	51 18 23.2 N	0.36	1.00/3.31	G. Thurston
England	00 54 44.9 W	CCD/Johnson V		
	65.0			
Helmos	37 59 08.1 N	2.28	0.60/0.674	E. M. Xilouris, I. Alikakos,
Greece	22 11 54.6 E	CCD/V+R		A. Gourzelas,
	2323.0			V. Charmandaris
Hornchurch	51 33 06.4 N	0.24	0.64/0.64	P. Denyer
England	00 11 38.8 E	video/clear		
	14.0			
Ithaca	42 27 29.4 N	0.60	0.20/0.36	J. Lloyd,
United States	76 23 05.5 W	CCD/clear		M. El Moutamid,
	530.0			C. Lamarche
Javalambre Astrophys.	40 02 30.6 N	0.40 Tx40 CCD/clear	2.00/2.50	R. Iglesias-Marzoa,
Obs. (2 telescopes)	01 00 57.6 W	0.28 Excalibur CCD/clear	2.00/3.00	J. Abril Ibáñez,
Spain	1955.0			M. Chioare Díaz Martín

Table A.4: Circumstances of observations for the 5 October 2017 event - continuation.

Site	**Coordinates Altitude (m)**	**Telescope aperture (m) Instrument/filter**	**Exp. Time/Cycle (s)**	**Observers**
Kryoneri	37 58 19.0 N	1.20	0.19/0.20	E. M. Xilouris,
(2 channels)	22 37 07.0 E	sCMOS/R and I		A. Liakos,
Greece	930.0			V. Charmandaris
La Palma	28 45 43.2 N	2.00	0.6/0.635	J. Marchant,
Spain	17 52 39.3 W	Liverpool Tel.		B. Sicardy
	2340.0	CCD/I+Z		
La Carolina	38 16 27.0 N	0.64	0.15/0.15	S. Alonso,
Spain	03 36 55.0 W	CCD/clear		A. Román Reche
	595.0			
La Roche-Sur-Yon	46 32 48.4 N	0.40	0.20/0.20	J. Desmars,
France	01 19 37.8 W	CMOS/clear		R. Tanguy,
	48.0			J. David
Le Beausset	43 11 38.1 N	0.25	0.64/0.64	S. Lisciandra,
France	05 48 05.9 E	video/clear		J. F. Coliac
	197.0			
Marrakech	31 35 16.2 N	0.60	2.5/5.5	A. Daassou, K. Barkaoui,
Morocco	08 00 46.9 W	CCD/clear		Z. Benkhaldoun,
	494.0			M. Guennoun, J. Chouqar
Nancy	48 39 51.6 N	0.25	1.50/2.10	D. Lavandier,
France	06 09 28.7 E	CCD/luminance		D. Walliang
	284.0			
Newark	43 00 23.7 N	0.25	0.53/0.53	B. Timerson
United States	77 07 06.5 W	video/clear		
	165.0			

Table A.5: Circumstances of observations for the 5 October 2017 event - continuation.

Site	**Coordinates Altitude (m)**	**Telescope aperture (m) Instrument/filter**	**Exp. Time/Cycle (s)**	**Observers**
Oukaïmeden	31 12 23.0 N	0.50	2.00/6.80	C. Rinner
Morocco	07 51 59.0 W	CCD/clear		
	2727.0			
Paris	48 52 17.0 N	0.15	0.25/0.25	R. Chauvet
France	02 23 07.0 E	CCD/clear		
	92.0			
Pic du Midi Obs.	42 56 12.0 N	0.60	0.05/0.05	D. Berard
France	00 08 31.9 E	EMCCD/visible		
	2862.0			
Puimichel	43 58 53.1 N	0.60	0.10/0.10	S. Moindrot
France	06 02 10.0 E	EMCCD/visible		
	714.0			
Reading	51 30 23.8 N	0.30	0.64/0.64	T. V. Haymes
England	00 48 58.1 W	video/red		
	80.0			
Sabadell	41 33 00.2 N	0.50	0.16/0.16	A. Selva,
Spain	02 05 24.8 E	video/clear		C. Perello,
	224.0			V. Cabedo
Saint Caprais	43 52 25.9 N	0.20 CCD/Johnson V	1.00/1.58	A. Klotz,
(2 telescopes)	01 43 05.8 E	0.94 SWIR/clear	0.05/0.08	Y. Rieugnie,
France	185.0			A. N. Klotz
Seysses	43 30 06.3 N	0.31	0.32/0.32	M. Boutet
France	01 17 20.3 E	video/UV-IR block		
	183.0			

Table A.6: Circumstances of observations for the 5 October 2017 event - continuation.

Site	**Coordinates Altitude (m)**	**Telescope aperture (m) Instrument/filter**	**Exp. Time/Cycle (s)**	**Observers**
Sierra Nevada	37 03 51.0 N	1.50	0.04/0.04	J. L. Ortiz,
Spain	03 23 05.0 W	video/clear		P. Santos-Sanz,
	2925.8			V. Casanova
Southampton	50 55 18.9 N	0.40	0.25/0.25	N. J. Haigh
England	01 22 28.1 W	CMOS/clear		
	16.0			
Sternwarte Stuttgart	48 46 56.7 N	0.41	0.64/0.64	A. Eberle
Germany	09 11 47.4 E	video/clear		K. Rapp
	346.0			
Steyning	50 53 16.0 N	0.28	2.00/4.00	N. Quinn
England	00 19 57.0 W	CCD/luminance		
	20.0			
Tournefeuille	43 34 58.8 N	0.32	0.25/0.25	M. Delcroix
France	01 19 35.4 E	CCD/clear		
	163.0			
UCL Obs.	51 36 47.6 N	0.35	1.00/2.38	S. J. Fossey,
London	00 14 32.3 W	CCD/luminance		C. Arena
England	82.0			
Valencia	39 56 42.0 N	0.50	1.00/2.50	V. Peris,
Spain	01 06 05.4 W	CCD/clear		O. Brevia
	1280.0			
Varages	43 36 44.6 N	0.50	2.30/2.30	F. Jabet
France	05 57 49.1 E	InGaAs/RG1000		
	300.0	(effective λ=1.3 μm)		

Table A.7: Circumstances of observations for the 5 October 2017 event - continuation.

Site	**Coordinates Altitude (m)**	**Telescope aperture (m) Instrument/filter**	**Exp. Time/Cycle (s)**	**Observers**
Observations that provided light curves that are not used in Triton's atmospheric fit				
Abingdon	51 37 53.1 N	0.30	0.16/0.16	J. Talbot
England	01 16 55.2 W	video/clear		
	59.0			
Agerola	40 37 26.2 N	0.50	0.50/0.50	A. Noschese,
Italy	14 33 50.6 E	CMOS/clear		A. Vecchione
	660.0			
Calar Alto	37 13 24.7 N	0.36	1.00/1.00	J. F. Rojas,
Spain	02 32 44.9 W	CCD/clear		A. Sánchez-Lavega
	2160.0	SWIR		
Caserta	41 16 11.3 N	0.24	2.00/2.46	L. Cupolino
Italy	13 56 28.9 E	CCD/clear		
	407.0			
Catania	37 30 24.0 N	0.28	0.64/0.64	C. Scalia,
Italy	15 05 35.5 E	video/clear		R. Lo Savio,
	50.0			G. Giardina
Charles Fehrenbach	50 05 01.5 N	0.36	0.28/0.30	P. Morel
Obs., La Biette	03 46 34.4 E	CCD/clear		
France	191.0			
Glyfada-Athens	37 52 33.6 N	0.35	1.00/1.15	E. I. Kardasis,
Greece	23 46 12.0 E	CCD/clear		A. Christou
	100.0			
Guirguillano	42 42 42.2 N	0.31	2.56/2.56	I. Ordóñez-Etxeberria,
Spain	01 51 54.3 W	video/clear		P. Martorell,
	595.0			J. Salamero

Table A.8: Circumstances of observations for the 5 October 2017 event - continuation.

Site	**Coordinates Altitude (m)**	**Telescope aperture (m) Instrument/filter**	**Exp. Time/Cycle (s)**	**Observers**
Hamsey Green	51 19 09.4 N	0.28	1.00/1.00	M. Jennings
England	00 04 01.4 W	video/clear		
	170.0			
Houten	52 01 59.3 N	0.36	0.41/0.41	J. Sussenbach
Netherlands	05 09 44.2 E	CCD/		
	2.0	685 nm long pass		
La Hita Obs.	39 34 06.8 N	0.77 CCD/luminance	1.00/3.55	N. Morales, J. L. Ortiz,
(2 telescopes)	03 11 09.5 W	0.40 video/clear	0.30/0.30	F. Organero, L. Ana,
Spain	695.0			F. Fonseca, P. Santos-Sanz
Lamandine	44 12 35.0 N	0.30	0.06/0.06	M. Miniou
France	01 42 01.7 E	CCD/clear		
	297.0			
La Sagra Obs.	37 58 58.1 N	0.36 each	1.00/3.79 (tetra1)	N. Morales,
(4 telescopes)	02 34 05.1 W	tetra1, tetra2: CCD/clear	1.00/3.56 (tetra2)	J. L. Ortiz,
Spain	1530.0	tetra3, tetra4: video/clear	0.20/0.20	P. Santos-Sanz
Leeds	53 50 15.6 N	0.20	1.28/1.28	A. Pratt
England	01 36 27.8 W	video/IR-UV block		
	113.0			
Lias	43 33 33.3 N	0.40	0.13/0.13	F. Metz,
France	01 06 34.4 E	CCD/clear		D. Erpelding,
	300.0			J.-P. Nougayrède
Louargat	48 32 16.7 N	0.30	0.20/0.20	B. Reginato,
France	03 21 30.5 W	CMOS/L		E. Reginato
	196.0			

Table A.9: Circumstances of observations for the 5 October 2017 event - continuation.

Site	**Coordinates Altitude (m)**	**Telescope aperture (m) Instrument/filter**	**Exp. Time/Cycle (s)**	**Observers**
Massa	44 01 17.2 N	0.20	5.12/5.12 (1st half)	P. Baruffetti
Italy	10 07 56.7 E	video/clear	2.56/2.56 (2nd half)	
	30.0			
Montigny le	48 45 54.0 N	0.28	0.50/0.51	O. Dechambre
Bretonneux	02 00 52.0 E	CCD/clear		
France	168.0			
Mount Agliale Obs.	43 59 43.1 N	0.50	1.50/3.23	F. Ciabattari
Italy	10 30 53.8 E	CCD/clear		
	750.0			
Nerpio	38 09 56.0 N	0.32	1.00/16.11	E. Briggs
Spain	02 19 35.0 W	CCD/clear		
	1650.0			
Neutraubling	48 59 23.1 N	0.28	0.16/0.16	B. Kattentidt
Germany	12 12 57.3 E	video/clear		
	333.0			
Nice	43 43 32.9 N	0.13	2.00/2.00	M. Conjat
France	07 17 59.4 E	video/clear		
	350.0			
Obs. de Biscarmiau	43 08 40.4 N	0.31	0.64/0.64	G. Vaudescal
France	00 03 31.8 E	video/clear		
	488.0			
Obs. des Baronnies	44 24 29.7 N	0.80	2.00/2.00	M. Bretton
Provençales	05 30 54.4 E	CCD/clear		
France	820.0			

Table A.10: Circumstances of observations for the 5 October 2017 event - continuation.

Site	**Coordinates Altitude (m)**	**Telescope aperture (m) Instrument/filter**	**Exp. Time/Cycle (s)**	**Observers**
Obs. Monplaisir	43 40 58.3 N	0.28	1.03/1.49	J. Ardissone
France	04 38 32.6 E	CCD/clear		
	5.0			
Orcemont	48 35 28.0 N	0.10	10.00/10.15	P. Delay
France	01 48 45.0 E	CCD/IR cut		
	165.0			
Overath	50 57 11.4 N	0.20	0.32/0.32	B. Klemt
Germany	07 14 53.1 E	video/clear		
	200.0			
Pfünz	48 53 26.0 N	0.28	1.00/1.20	B. Gährken
Germany	11 16 23.0 E	CCD/clear		
	488.0			
Pic du Midi Obs.	42 56 12.0 N	1.05	0.10/0.10	F. Colas
France	00 08 31.9 E	sCMOS/clear		
	2862.0			
Rosenfeld-Brittheim	48 17 17.8 N	0.80	0.40/0.40	S. Kowollik,
Germany	08 40 38.9 E	CMOS/UV-IR block		R. Bitzer
	700.0			
Saint Chéron	48 32 16.6 N	0.18	0.08/0.08	J. Berthier
France	02 07 51.7 E	video/clear		
	160.0			
Saint-Maurice-	43 50 39.3 N	0.21	0.64/0.64	J. Lecacheux
-Navacelles	03 33 47.3 E	CCD/clear		
France	583.0			

Table A.11: Circumstances of observations for the 5 October 2017 event - continuation.

Site	**Coordinates Altitude (m)**	**Telescope aperture (m) Instrument/filter**	**Exp. Time/Cycle (s)**	**Observers**
Saint Michel	43 54 23.3 N	0.60	0.05/0.05	E. Meza,
France	05 43 34.7 E	EMCCD/clear		O. Labrevoir
	564.0			
Selztal Obs.	49 50 00.0 N	0.51	0.8/0.8	G. M. Piehler
Friesenheim	08 15 00.0 E	CMOS/clear		
Germany	110.0			
Seysses	43 30 06.3 N	0.23	0.32/0.32	J. Sanchez
France	01 17 20.3 E	video/UV-IR block		
	183.0			
Sierra Nevada	37 03 51.0 N	0.90	1.00/3.33	J. L. Ortiz,
Spain	03 23 05.0 W	CCD/clear		P. Santos-Sanz,
	2925.8			V. Casanova
Valle d'Aosta	45 47 23.1 N	0.81	0.2/0.2	D. Cenadelli,
Italy	07 28 42.3 E	EMCCD/clear		J.-M. Christille,
	1675.0			B. Sicardy

Table A.12: Circumstances of observations for the 5 October 2017 event - continuation.

Site	Coordinates Altitude (m)	Telescope aperture (m) Instrument/filter	Exp. Time/Cycle (s)	Observers
Stations with technical or weather problems that provided no light curves				
Bilbao Spain	43 15 43.6 N 02 56 54.6 W 47.0	0.5 CCD/clear		S. Pérez-Hoyos, A. Sánchez-Lavega
Buthiers France	48 17 30.0 N 02 26 18.0 E 87.0	0.59 CMOS/L	0.10/0.10	J. L. Dauvergne
Cavarc Obs. France	44 40 35.2 N 00 37 43.1 E 100.0	0.50 CMOS/clear		J. Rudelle, B. Tregon
Comthurey Germany	53 15 57.8 N 13 11 24.6 E 74.0	0.18		K. Guhl
Emmendingen Germany	48 06 14.2 N 07 51 28.6 E 210.0	0.18 CMOS/clear	3.00/3.33	K.-L. Bath
Eppstein-Bremthal Germany	50 08 17.4 N 08 21 50.4 E 256.0	0.25 video/clear		O. Klös
Gnosca Switzerland	46 13 53.2 N 09 01 26.5 E 260.0	0.40		S. Sposetti
Grapfontaine Belgium	49 48 54.2 N 05 23 57.5 E 445.0	0.28 video/clear		F. Van Der Abbeel

Table A.13: Circumstances of observations for the 5 October 2017 event - continuation.

Site	**Coordinates Altitude (m)**	**Telescope aperture (m) Instrument/filter**	**Exp. Time/Cycle (s)**	**Observers**
Hamburg-Bergedorf	53 28 50.0 N	0.60		V. Perdelwitz
Germany	10 14 29.0 E	CCD/clear		
	25.0			
Handeloh	53 14 06.4 N	0.35		K. von Poschinger
Germany	09 49 46.7 E	CCD/clear		
	60.0			
Observatory Hoher	50 09 42.0 N	1.00		M. Miller, G. Herzogenrath,
List, Eifel	06 50 55.0 E	CCD/clear		D. Frangenberg, L. Brandis,
Germany	549.0			I. Pütz
Labastide-Murat	44 38 43.2 N	0.20	0.32/0.32	E. Frappa
France	01 34 13.9 E	video/clear		
	445.0			
Lauenbrück	53 12 26.6 N	0.50		M. Kretlow
Germany	09 34 36.1 E	CCD/clear		
	31.0			
Malvilliers	47 01 58.5 N	0.30		L. Falco
Switzerland	06 52 03.0 E	CCD/clear		R. Leiva
	845.0			
EXPO Obs.	52 15 45.0 N	1.12	0.04/0.04	P. Riepe,
Melle	08 20 12.0 E	video/clear		E. Bredner
Germany	185.0			
Meudon	48 48 18.3 N	1.00		T. Widemann, W. Thuillot,
France	02 13 51.6 E	CMOS/clear		D. Hestroffer,
	157.6			E. Lellouch

Table A.14: Circumstances of observations for the 5 October 2017 event - continuation.

Site	**Coordinates Altitude (m)**	**Telescope aperture (m) Instrument/filter**	**Exp. Time/Cycle (s)**	**Observers**
Ondřejov	49 54 33.8 N	0.50	0.04/0.04	M. Jelínek,
Czech Republic	14 46 52.9 E	EMCCD/R		J. Štrobl
	530.0			
Saint-Luc	46 13 41.8 N	0.30		E. Bouchet,
Obs. F.-X. Bagnoud	07 36 45.6 E	CCD/clear		M. Cottier
Switzerland	2200.0			
Saulges	47 59 02.0 N	0.25	0.20/0.20	T. Midavaine
France	00 24 30.0 W	video/clear		
	97.0			
TRAPPIST-North	31 12 22.0 N	0.60		E. Jehin
Oukaïmeden	07 51 59.0 W	CCD/clear		
Morocco	2751.0			
Uranoscope	48 44 32.0 N	0.28 video/clear	0.25/0.25	A. Leroy,
(2 telescopes)	02 44 32.0 E	0.36 CMOS/clear	0.25/0.25	S. Bouley
France	110.0			
Valée de Joux	46 37 06.0 N	0.61	1.00/1.15	R. Barbosa,
Switzerland	06 13 10.0 E	CMOS/clear		R. Behrend
	1145.0			M. Spano
Vierzon	47 13 23.7 N	0.25		L. Rousselot
France	02 03 09.8 E	CMOS/clear		
	97.0			
Zurich	47 24 27.8 N	0.50	2.00/4.00	S. Gallego,
Switzerland	08 30 39.5 E	CCD/Johnson R		L. Tortorelli
	553.0			

Table A.15: Circumstances of observations for the event 18 July 1997.

Site	**Coordinates Altitude (m)**	**Telescope aperture (m) Instrument/filter**	**Exp. Time/Cycle (s)**	**Observers**
Observations that provided light curves that are used in Triton's atmospheric fit				
Brownsville	25 58 40.9 N	0.35	0.5/0.5	W. B. Hubbard,
United States	97 32 11.3 W	CCD/clear		H. J. Reitsema,
	9.0			R. Hill
Bundaberg	24 56 37.5 S	0.48	0.33/0.33	E. Hummel, M. Moy,
Australia	152 22 35.4 E	CCD/clear		I. Pink, R. Walters
	10.0			
Ducabrook	23 53 55.0 S	0.35	0.66/0.66	L. Ball,
Australia	147 26 40.0 E	CCD/clear		G. Neilsen
	320.0			
Lochington	23 56 42.5 S	0.35	0.66/0.66	W. Beisker,
Australia	147 31 24.8 E	CCD/clear		S. Hutcheon
	270.0			
Observations that provided data that are not used in Triton's atmospheric fit				
Ballandean	28 49 05.0 S	0.48		K. Lay
Australia	151 48 36.0 E	Visual		
	710.0			
Ipswich	~27 38 S	0.30	10	B. Downs
Australia	~152 45 E	CCD/clear	grazing	
	~40			
The Gap	27 27 42.3 S	0.40		P. Anderson
Australia	152 55 58.0 E	Visual		
	176.0			

Table A.16: Circumstances of observations for the 21 May 2008 event.

Site	**Coordinates Altitude (m)**	**Telescope aperture (m) Instrument/filter**	**Exp. Time/Cycle (s)**	**Observers**
Observations that provided light curves that are used in Triton's atmospheric fit				
Hakos	23 14 11.0 S	0.5	0.67/1.49	K.-L. Bath
Namibia	16 21 41.5 E	CCD/clear		
	1825.0			
Hakos	23 14 11.0 S	0.45	0.84/1.0	B. Sicardy
Namibia	16 21 41.5 E	CCD/clear		
	1825.0			
Maïdo	21 04 15.5 S	0.23	2.56/2.56	J. Lecacheux
La Réunion Island	55 23 14.2 E	CCD/clear		T. Payet
France	2200.0			
Tivoli	23 27 40.2 S	0.35	1.48/1.48	H.-J. Bode
Namibia	18 01 01.2 E	CCD/clear		
	1344			
Observations that provided light curves that are not used in Triton's atmospheric fit				
Piton Lacroix	21 12 54.4 S	0.28	2/2	E. Frappa
La Réunion Island	55 38 38.5 E	CCD/clear		
France	2330.0			

Table A.17: Circumstances of observations for the 21 May 2008 event - continuation.

Site	**Coordinates Altitude (m)**	**Telescope aperture (m) Instrument/filter**	**Exp. Time/Cycle (s)**	**Observers**
Grünau	~27 44 S	0.30	clouded out	W. Beisker
Namibia	~18 23 E			
	~1100			
Hakos	23 14 11.0 S	0.28	?/?	C. Boissel
Namibia	16 21 41.5 E	(IOC?)		A. Doressoundiram
	1825			
Les Makes	21 11 57.4.0 S	0.35	clouded out	B. Payet
La Réunion Island	55 24 34.5.0 E	CCD/clear		
France	972			
Maïdo	21 04 15.5 S	0.30	wind shaking	J. Françoise
La Réunion Island	55 23 14.2 E	video/clear		B. Mondon
France	2200.0			
Piton Lacroix	21 12 52.0 S	0.28	moisture	A. Peyrot
La Réunion Island	55 38 35.0 E	CCD/clear		J.-P. Teng-Chuen-Yu
France	2350.0			
Springbok	29 39 40.3 S	0.30	clouded out	T. Widemann
South Africa	17 52 58.9 E	CCD/clear		
	951			
Sutherland	32 22 43.8 S	1.0	outside shadow	G. Blanchard
South Africa	20 48 42.0 E	CCD/clear		M. Castets
	1760			F. Colas
Tivoli	23 27 40.2 S	0.27	?/?	B. Thome
Namibia	18 01 01.2 E	CCD/clear		
	1344			

Appendix B

Fit to the light curves from the 5 October 2017 event

All 90 occultation light curves from the 5 October 2017 event are presented here.

Figures B.1-B.5 correspond to the light curves that were used in the simultaneous fit to the template temperature model. Figures B.6-B.9 correspond to the light curves that were not used in the fit, either because they had insufficient signal-to-noise ratios to provide relevant contribution to the fit, or they were provided to us too late to be included. The best synthetic models expected for these light curves are fully consistent with the observations, in the limit of the noise level.

For all images, the black dots correspond to the data, and the green dots are the residuals of the fits. The lower and upper horizontal dotted lines mark the zero-flux level and the total star + Triton unocculted flux, respectively. For reference, the vertical red lines mark 23:48 UTC for the European and African stations, and 23:55 UTC for the US stations (Newark, Ithaca, and Dark Sky Obs.).

Each panel has a duration of five minutes and is centred around the time of closest approach, the mid-occultation time, of the station to Triton's shadow centre. The stations with exposure times smaller than 1 second have been smoothed to have a sampling time close to 1 second, allowing a direct visual comparison of signal-to-noise ratio of the various data sets. Constância, Le Beausset, and Felsina Obs. are plotted at a different vertical scale to accommodate the presence of a strong central flash. The stations are sorted from left to right and top to bottom from the northern-most track (Newark) to the southern-most track (Athens), projected on Triton in the sky plane (Figure 4.2).

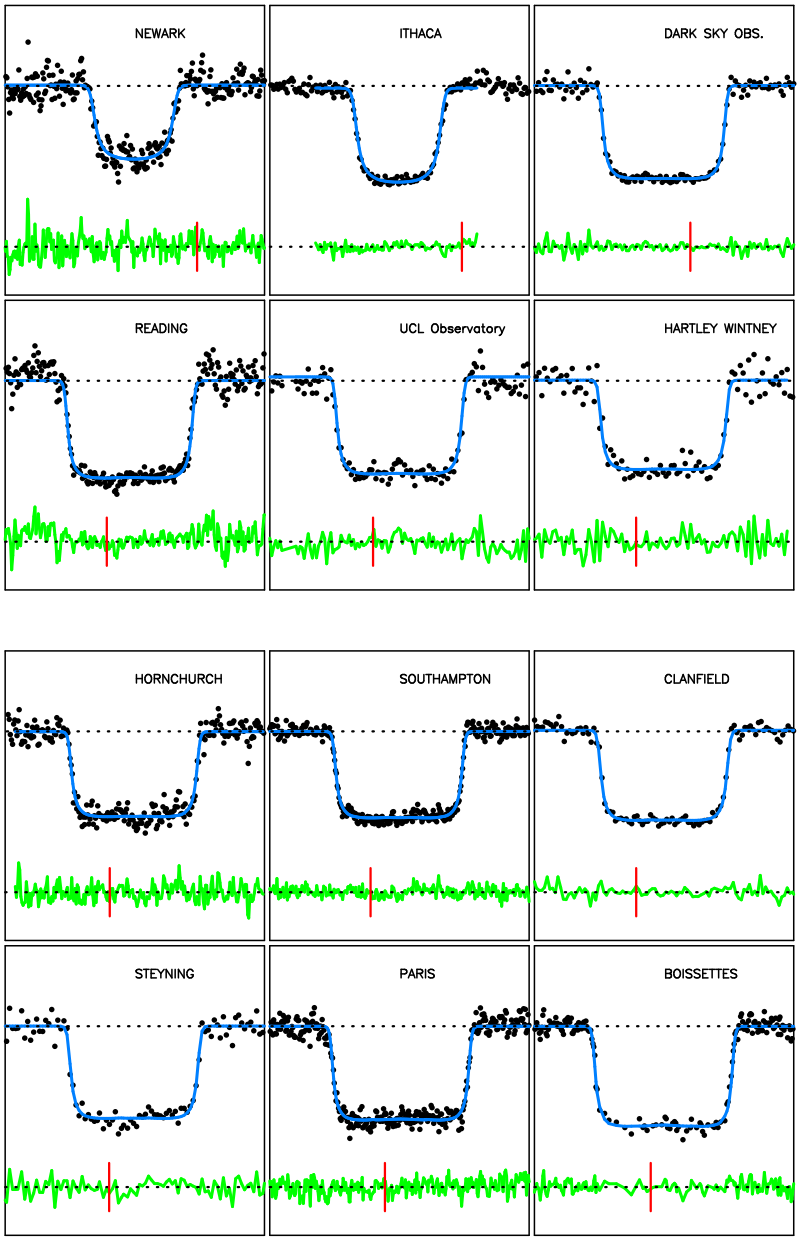

Figure B.1: The data (black dots) have been fitted simultaneously with synthetic light curves, represented by the blue lines. The central flash regions have been excluded from the fit, so that we obtain a global fit that is not influenced by the deepest atmospheric layers.

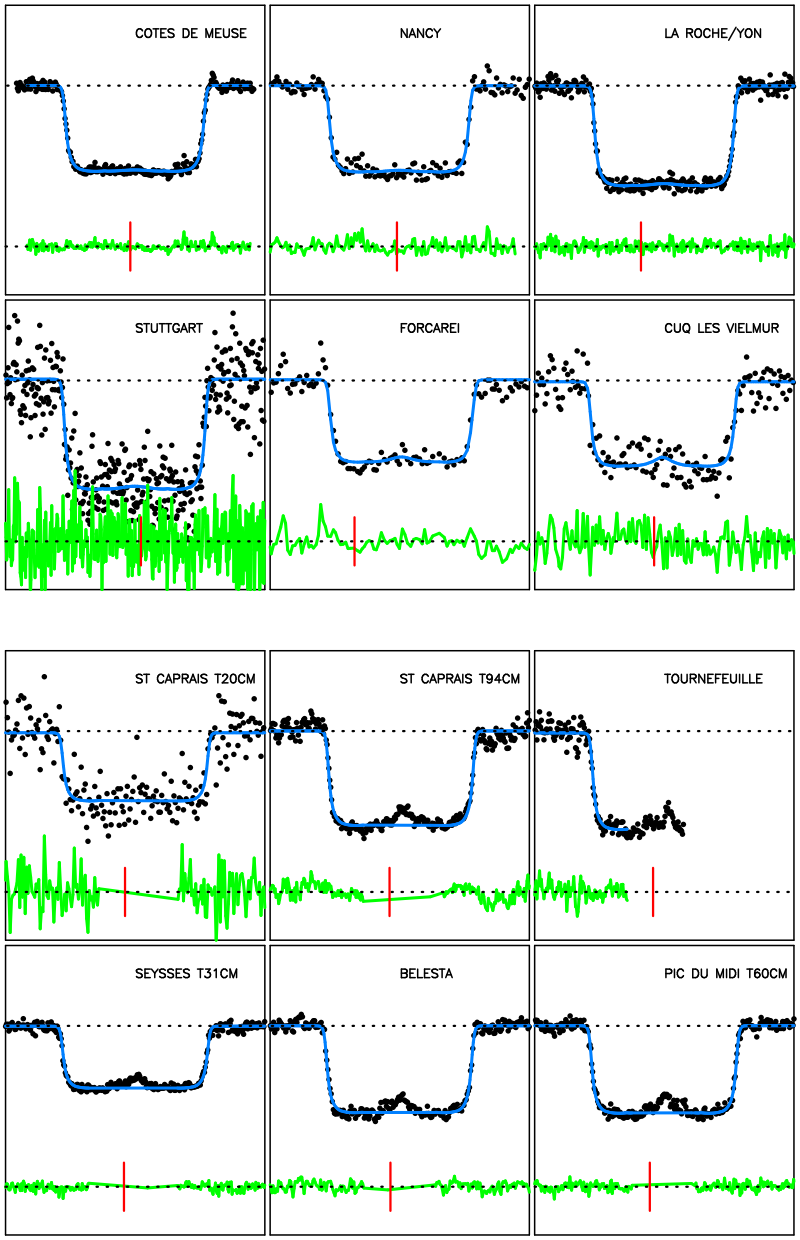

Figure B.2: Continuation of Figure B.1.

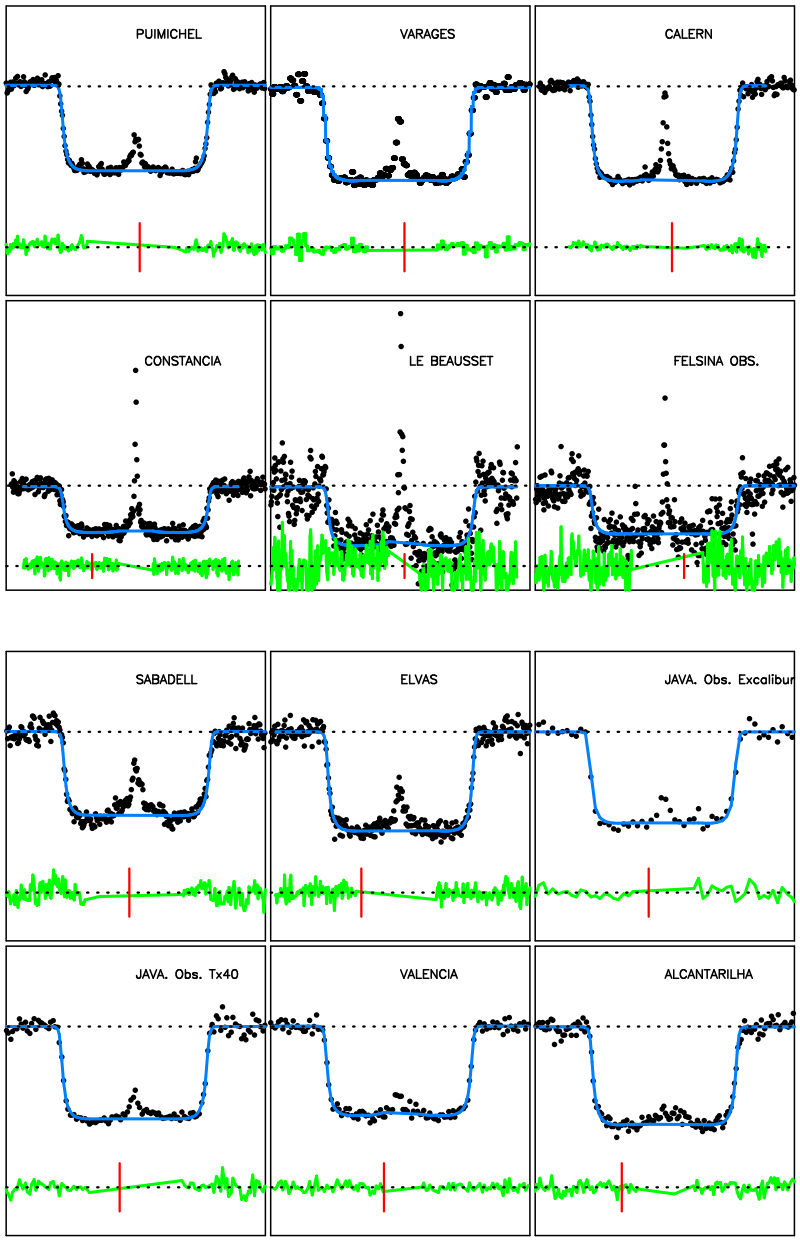

Figure B.3: Continuation of Figure B.2. "JAVA." is the abbreviation of Javalambre, used so that the name of the station fits into the plot.

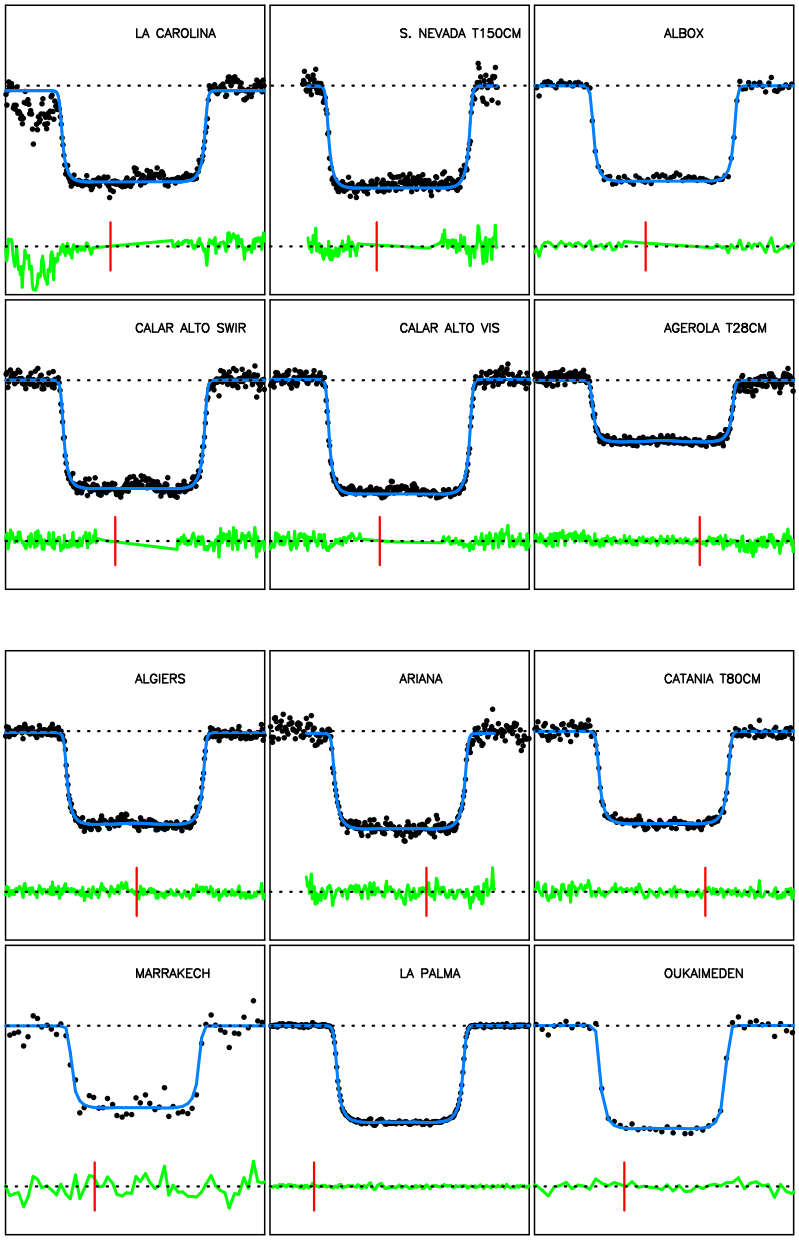

Figure B.4: Continuation of Figure B.3.

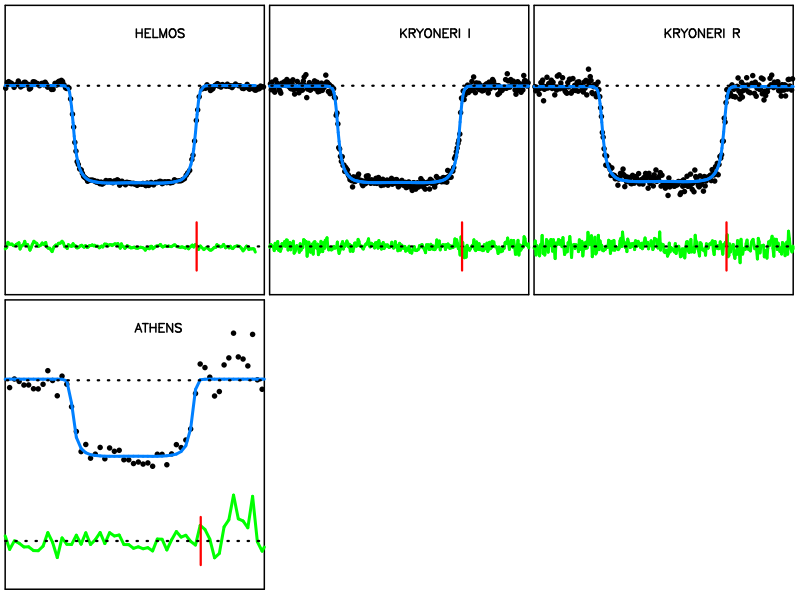

Figure B.5: Continuation of Figure B.4.

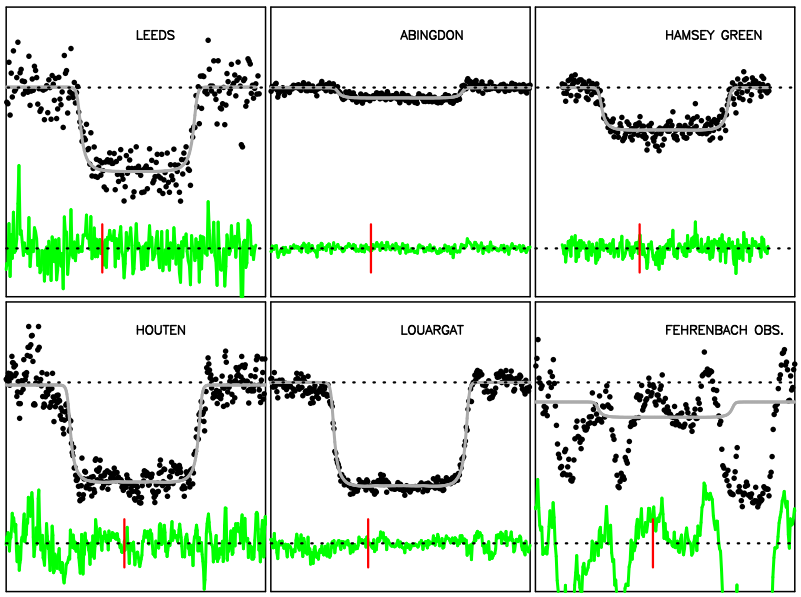

Figure B.6: Same as Figures B.1-B.5, but for stations that were not used in the simultaneous fit. The synthetic light curves are now represented by gray lines.

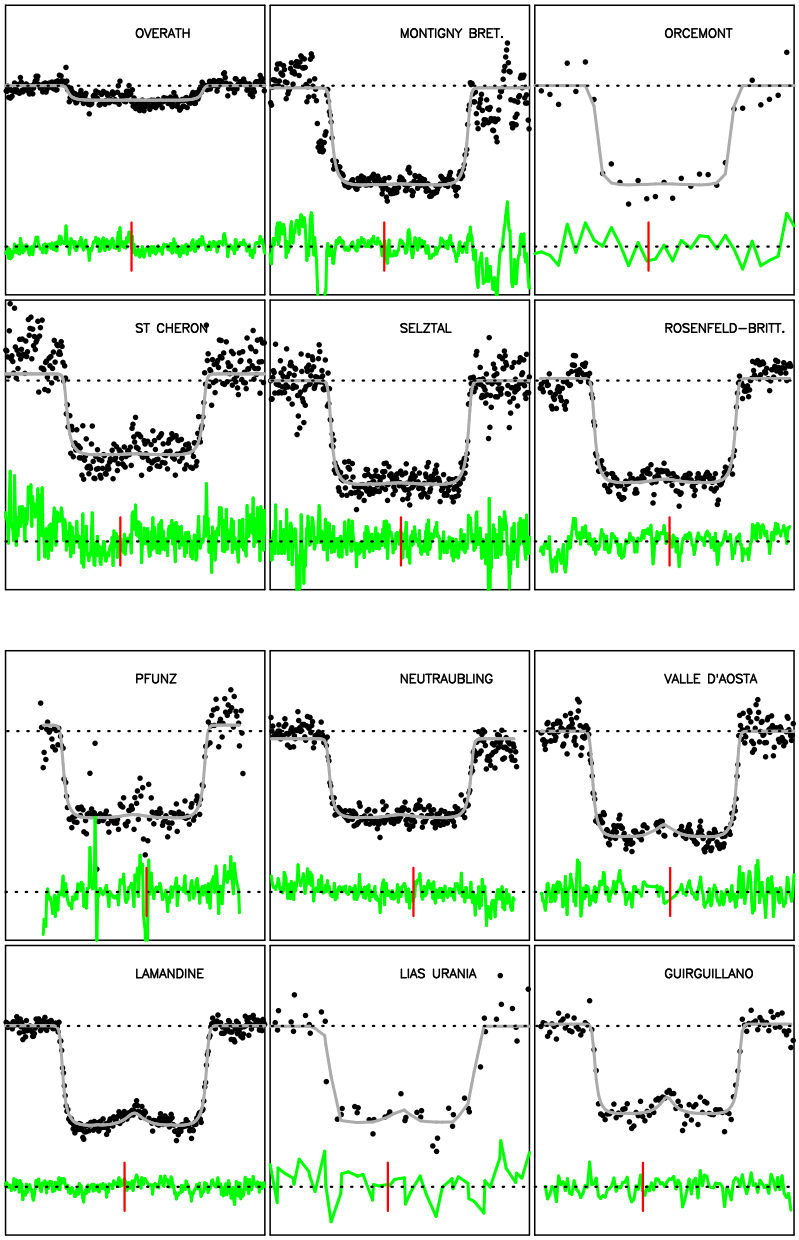

Figure B.7: Continuation of Figure B.6.

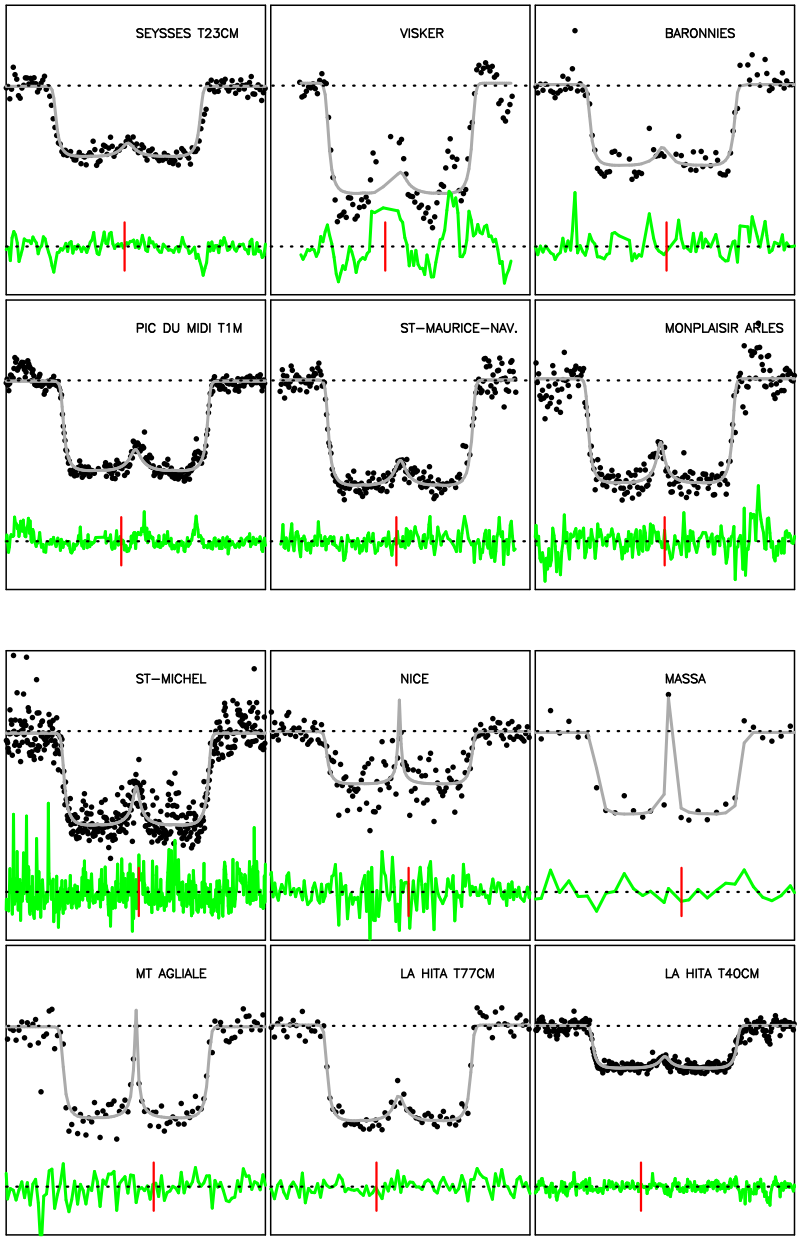

Figure B.8: Continuation of Figure B.7.

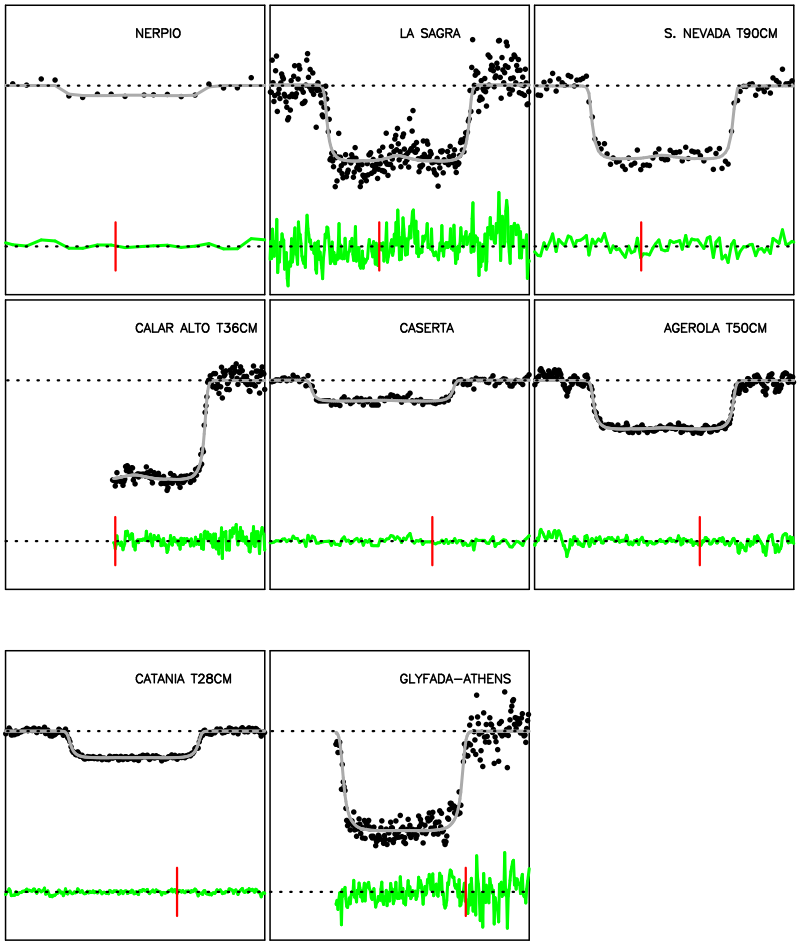

Figure B.9: Continuation of Figure B.8.

Appendix C

Articles

This Appendix features the Marques Oliveira et al. paper that was submitted to the journal *Astronomy & Astrophysics*. It has been accepted to be published, and is currently under editing. This paper summarizes the findings in Chapters 4 and 5.

Meza et al. (2019) is my first contributed paper, and is the second article in this Appendix.

Bertrand et al. (2022) is my second contributed paper, and is the third article in this Appendix. It is accepted to be published in the journal *Icarus*.

There are other studies currently under way where I am contributing, but no other is published/accepted as of yet.

Astronomy & Astrophysics manuscript no. output
November 15, 2021

Constraints on the structure and seasonal variations of Triton's atmosphere from the 5 October 2017 stellar occultation and previous observations

J. Marques Oliveira[1], B. Sicardy[1], A. R. Gomes-Júnior[2,3], J. L. Ortiz[4], D. F. Strobel[5], T. Bertrand[1,6], F. Forget[7], E. Lellouch[1], J. Desmars[8,9], D. Bérard[1], A. Doressoundiram[1], J. Lecacheux[1], R. Leiva[10,11], E. Meza[12,13], F. Roques[1], D. Souami[1,14], T. Widemann[1], P. Santos-Sanz[4], N. Morales[4], R. Duffard[4], E. Fernández-Valenzuela[15,4], A. J. Castro-Tirado[4], F. Braga-Ribas[16,1,17,3], B. E. Morgado[17,1,3], M. Assafin[18,3], J. I. B. Camargo[17,3], R. Vieira-Martins[17,3,9], G. Benedetti-Rossi[1,3,2], S. Santos-Filho[18,3], M. V. Banda-Huarca[17,3], F. Quispe-Huaynasi[17], C. L. Pereira[17,3], F. L. Rommel[17,3], G. Margoti[16], A. Dias-Oliveira[19], F. Colas[9], J. Berthier[9], S. Renner[9,20], R. Hueso[21], S. Pérez-Hoyos[21], A. Sánchez-Lavega[21], J. F. Rojas[21], W. Beisker[22,23], M. Kretlow[4,22,23], D. Herald[24,25], D. Gault[24], K.-L. Bath[22,23], H.-J. Bode[22,23,⋆], E. Bredner[23,26,27,28], K. Guhl[29,23], T. V. Haymes[30,23], E. Hummel[23], B. Kattentidt[23], O. Klös[23], A. Pratt[23,30], B. Thome[23], C. Avdellidou[31], K. Gazeas[32], E. Karampotsiou[32], L. Tzouganatos[32], E. Kardasis[33], A. A. Christou[34], E. M. Xilouris[35], I. Alikakos[35], A. Gourzelas[35], A. Liakos[35], V. Charmandaris[36,37], M. Jelínek[38], J. Štrobl[38], A. Eberle[39], K. Rapp[39], B. Gährken[40], B. Klemt[41], S. Kowollik[42], R. Bitzer[42], M. Miller[43], G. Herzogenrath[43], D. Frangenberg[43], L. Brandis[43], I. Pütz[43], V. Perdelwitz[44,45], G. M. Piehler[46], P. Riepe[26,47], K. von Poschinger[48], P. Baruffetti[49], D. Cenadelli[50], J.-M. Christille[50], F. Ciabattari[51], R. Di Luca[52], D. Alboresi[52], G. Leto[53], R. Zanmar Sanchez[53], P. Bruno[53], G. Occhipinti[53], L. Morrone[54], L. Cupolino[55], A. Noschese[56], A. Vecchione[56], C. Scalia[57,58,53], R. Lo Savio[57], G. Giardina[57], S. Kamoun[59], R. Barbosa[60], R. Behrend[61], M. Spano[62], E. Bouchet[63], M. Cottier[63], L. Falco[64], S. Gallego[65], L. Tortorelli[66], S. Sposetti[67], J. Sussenbach[68], F. Van Den Abbeel[69], P. André[70], M. Llibre[70], F. Pailler[70], J. Ardissone[71], M. Boutet[72], J. Sanchez[72], M. Bretton[73], A. Cailleau[74], V. Pic[74], L. Granier[74], R. Chauvet[75], M. Conjat[76], J. L. Dauvergne[77], O. Dechambre[78], P. Delay[79,80], M. Delcroix[81], L. Rousselot[81], J. Ferreira[82,10], P. Machado[82], P. Tanga[10], J.-P. Rivet[10], E. Frappa[83], M. Irzyk[84], F. Jabet[85], M. Kaschinski[86], A. Klotz[87], Y. Rieugnie[88], A. N. Klotz[89,90], O. Labrevoir[91], D. Lavandier[92], D. Walliang[92], A. Leroy[93], S. Bouley[94], S. Lisciandra[95,⋆⋆], J.-F. Coliac[95,96], F. Metz[97], D. Erpelding[97], P. Nougayrède[97], T. Midavaine[27], M. Miniou[98], S. Moindrot[99], P. Morel[100,101], B. Reginato[102], E. Reginato[103,104], J. Rudelle[105], B. Tregon[106], R. Tanguy[107], J. David[107], W. Thuillot[9], D. Hestroffer[9], G. Vaudescal[108], D. Baba Aissa[109], Z. Grigahcene[109], D. Briggs[110,30], S. Broadbent[110,30,111], P. Denyer[30], N. J. Haigh[30], N. Quinn[30], G. Thurston[30,112], S. J. Fossey[113], C. Arena[113], M. Jennings[114], J. Talbot[115], S. Alonso[116], A. Román Reche[117], V. Casanova[4], E. Briggs[118], R. Iglesias-Marzoa[119,120], J. Abril Ibáñez[119], M. C. Díaz Martín[119], H. González[121], J. L. Maestre García[122], J. Marchant[123], I. Ordonez-Etxeberria[124], P. Martorell[124], J. Salamero[124], F. Organero[125], L. Ana[125], F. Fonseca[125], V. Peris[126], O. Brevia[126], A. Selva[127], C. Perello[127], V. Cabedo[128,129], R. Gonçalves[130], M. Ferreira[131], F. Marques Dias[132], A. Daassou[133,134], K. Barkaoui[134,135], Z. Benkhaldoun[134], M. Guennoun[136], J. Chouqar[134], E. Jehin[137], C. Rinner[138], J. Lloyd[139], M. El Moutamid[140], C. Lamarche[141], J. T. Pollock[142], D. B. Caton[142], V. Kouprianov[143,144], B. W. Timerson[25,⋆⋆⋆], G. Blanchard[145], B. Payet[146], A. Peyrot[146], J.-P. Teng-Chuen-Yu[146], J. Françoise[147], B. Mondon[147], T. Payet[147], C. Boissel[148], M. Castets[149], W. B. Hubbard[150], R. Hill[150], H. J. Reitsema[151], O. Mousis[152], L. Ball[153], G. Neilsen[153], S. Hutcheon[153], K. Lay[153,⋆⋆⋆⋆], P. Anderson[153], M. Moy[153,†], M. Jonsen[154], I. Pink[154], R. Walters[154,‡], and B. Downs[155]

(Affiliations can be found after the references)

Received mm:dd, yyyy; accepted mm:dd, yyyy

ABSTRACT

Context. A stellar occultation by Neptune's main satellite, Triton, was observed on 5 October 2017 from Europe, North Africa, and USA. We derived 90 light curves from this event, 42 of them yielding a central flash detection.

Aims. We aim at constraining Triton's atmospheric structure and the seasonal variations of its atmospheric pressure since the Voyager 2 epoch (1989). We also derive the shape of the lower atmosphere from central flash analysis.

Methods. We used Abel inversions and direct ray-tracing code to provide the density, pressure, and temperature profiles in the altitude range ~ 8 km to ~ 190 km, corresponding to pressure levels from 9 μbar down to a few nbar.

Results. (*i*) A pressure of 1.18 ± 0.03 μbar is found at a reference radius of 1400 km (47-km altitude). (*ii*) A new analysis of the Voyager 2 radio science occultation shows that this is consistent with an extrapolation of pressure down to the surface pressure obtained in 1989. (*iii*) A survey of occultations obtained between 1989 and 2017 suggests an enhancement in surface pressure as reported during the 1990s might be real, but debatable, due to very few high SNR light curves and data accessible for reanalysis. The Volatile Transport Model analysed supports a moderate increase in surface pressure, with a maximum value around 2005-2015 no higher than 23 μbar. The pressures observed in 1995-1997 and 2017 appear mutually inconsistent with the Volatile Transport Model presented here. (*iv*) The central flash structure does not show evidence of an atmospheric distortion. We find an upper limit of 0.0011 for the apparent oblateness of the atmosphere near the 8-km altitude.

Key words. methods: data analysis, observational – planets and satellites: atmospheres, physical evolution – techniques: photometric

1. Introduction

The large satellite Triton was discovered in 1846, only 17 days after the discovery of its planet, Neptune. An atmosphere was first speculated by Cruikshank & Silvaggio (1979), with the claimed detection of gaseous CH_4 spectral signature, although in retrospect the features were due to methane ice on the surface. In any case, the presence of this volatile ice did suggest the existence of an atmosphere. This was to be confirmed ten years later, as the NASA Voyager 2 (V2) spacecraft flew by the Neptunian system in August 1989. During this flyby, Triton's tenuous atmosphere (mainly nitrogen N_2) was detected during the Radio Science Subsystem (RSS) occultation, providing its surface density, pressure and temperature (Tyler et al. 1989). These results were later improved by Gurrola (1995) (G95 herein), who derived a surface pressure of $p_{\rm surf} = 14 \pm 2$ μbar. These studies using RSS data did not provide, however, a thermal profile. Dynamical aspects, such as wind regimes, were studied using V2 images of plumes near Triton's surface (Yelle et al. 1991), as well as vertical profiles of methane and hazes using V2's UV images (Strobel et al. 1990; Herbert & Sandel 1991; Krasnopolsky et al. 1993; Krasnopolsky 1993; Krasnopolsky & Cruikshank 1995; Strobel & Summers 1995).

Triton is currently experiencing a rare "extreme southern solstice", a configuration that occurs every ~ 650 years (Fig. 1). In particular, the sub-solar latitude on the satellite reached about 50° S in 2000. The various measurements of Triton's atmospheric pressure using occultations bracket that epoch, from the RSS results in 1989 to the ground-based stellar occultation of 2017 discussed here. In this context, it is interesting to look for ongoing seasonal effects (if any) occurring in Triton's atmosphere, especially large pressure variations in the last three decades. Such seasonal variations (or its absence) can then constrain Global Climate Models (GCMs) and Volatile Transport Models (VTMs) that account for volatile transport induced by insolation changes.

Since 1989, only a handful of Earth-based stellar occultations have been observed, as well as spectroscopic studies with the detection of CO and CH_4 in the near-IR (Lellouch et al. 2010) and CO and HCN with ALMA in the mm (Gurwell et al. 2019). As discussed later, the deepest layers accessible during Triton Earth-based occultations (when a central flash[1] is observed) lie at typically 8 km altitude (~ 9 μbar pressure level). Conversely, the best light curves can provide information up to an altitude of about 190 km, corresponding to a few nanobars.

Here, we report on results obtained from the 5 October 2017 ground-based stellar occultation. This rare event was attempted from more than 100 sites in Europe, Northern Africa, and Eastern USA. We extracted 90 occultation light curves from this campaign, among which 42 show a central flash. This is by far the most observed stellar occultation by Triton ever monitored (and among the most observed event of its kind, all solar system objects combined) both in terms of latitudinal coverage of the satellite and central flash sampling.

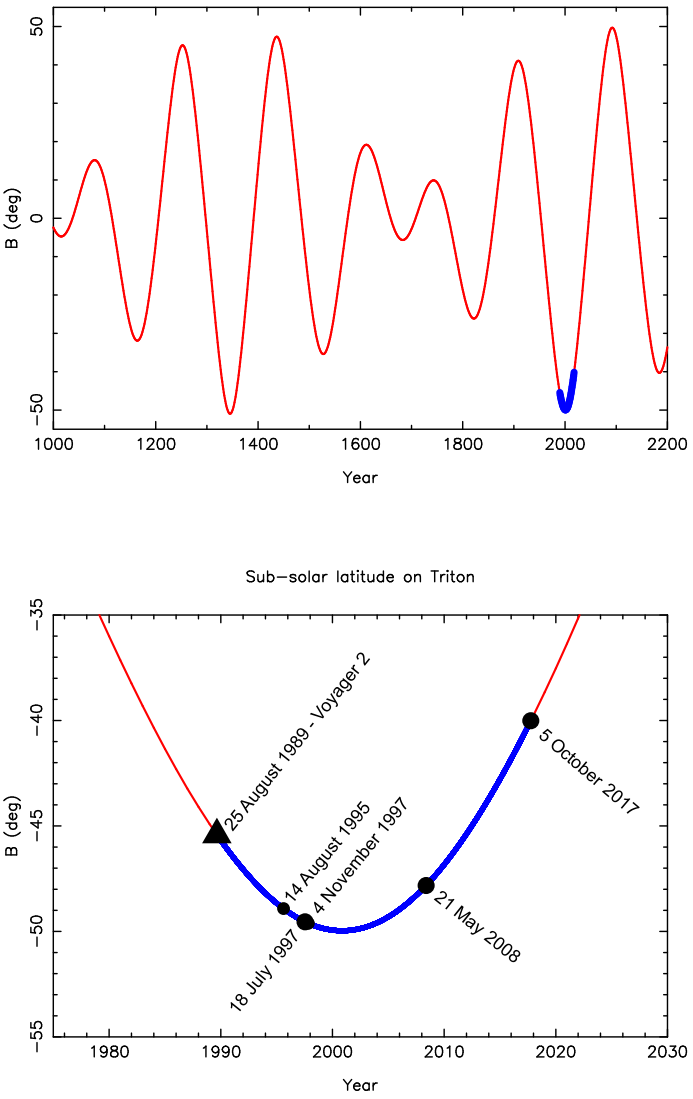

Fig. 1. *Upper panel:* The sub-solar latitude on Triton vs. time during the last millennium. The blue part corresponds to the period from the V2 encounter (August 1989) to the 5 October 2017 stellar occultation. It shows that during this interval, Triton experienced an extreme summer solstice in its southern hemisphere, with a minimum sub-solar latitude of 50° S in 2000. *Lower panel:* Close up view of the upper panel around the year 2000. The black points correspond to occultations observed, distinguishing from the black triangle (V2 RSS experiment). The larger symbols are from the data that we use in this paper.

Our goals are to (1) provide Triton's atmospheric profiles (density, pressure, temperature) derived from this event, (2) compare the results with those obtained from previous occultations, including the V2 RSS experiment, (3) constrain the seasonal variations of Triton's atmosphere, (4) compare the results with current GCMs, (5) and derive the shape of the central flash layer.

The 5 October 2017 event is discussed in Section 2. The methods used are given in Section 3, and in Section 4 we present the results. We reanalyse previous events, including a new approach to retrieve new information from the V2 experiment in Section 5. In Section 6 we discuss the atmospheric seasonal variations, using pressure values from our work and from other

⋆ Deceased
⋆⋆ Deceased
⋆⋆⋆ Deceased
⋆⋆⋆⋆ Deceased
† Deceased
‡ Deceased

[1] A central flash is a sharp increase in the intensity of the stellar light observed during a stellar occultation. It is observed near the central path of the occultation shadow and produced by the refraction of light in the atmosphere of the occulting object.

works. Section 7 focuses on the analysis of the central flashes. We mention some issues that are to be addressed at a future date in Section 8. Concluding remarks are provided in Section 9.

2. The 5 October 2017 stellar occultation

2.1. Prediction

In the past two decades, Neptune has been crossing regions with low surface-density of stars. In the early 2010s, faint star surveys up to R = 19 were made using the Wide Field Imager attached to the 2.2 m Max-Planck ESO telescope (Assafin et al. 2010, 2012; Camargo et al. 2014). They provided many candidates for occultations by Pluto, large Trans-Neptunian Objects and Centaurs, but no suitable Triton events for 2008-2015.

Predicting occultations by Triton is problematic for two reasons: (1) Neptune's orbit may have systematic errors, causing a systematic shift of Triton's position with respect to the stars; (2) Triton's neptunocentric orbit may have systematic errors due to the large brightness and colour differences between Neptune and Triton, and also from changes in Neptune's magnitude, making their relative colour variable (Schmude et al. 2016). Both points affect differently the ground-based measurements of Triton and Neptune, resulting in a distorted neptunocentric orbit for the satellite. A way to overcome these problems is to use R or I filters to minimise differential refraction during observations and distribute Triton observations evenly along its orbit around Neptune. Triton's path is then set by the average ephemeris offsets found for right ascension (α) and declination (δ).

In this context, we gathered more than 4700 CCD images of Triton in R between 1992 and 2016 with the 0.6-m B&C and 1.6-m P&E telescopes at Pico dos Dias Observatory (OPD) in Brazil (IAU code 874). The observations were reduced with the best available astrometric catalogue at that time, the UCAC4 (Zacharias et al. 2013), following the same procedures described in Gomes-Júnior et al. (2015). From the average ephemeris offsets of many nights, and after sigma-clipping, we found an overall offset $(\Delta\alpha\cos\delta, \Delta\delta) = (+1 \pm 45, -16 \pm 45)$ milliarcsec (mas), with error bars at 1σ level, with respect to the DE435/NEP081 JPL ephemeris. Applying this offset and searching for post-2015 events, we uncovered the promising occultation by Triton of a relatively bright star with V=12.7, G=12.2 (UCAC4 410-143659; *Gaia* DR2 2610107911326516992) that was to occur on 5 October 2017, crossing all Europe, northern Africa, and reaching eastern USA.

Closer in time to the event, a dedicated 8-night run on the OPD 1.6 m telescope was conducted between 15 and 23 September 2017 to further improve the accuracy of the prediction, in particular to pin down the path of the central flash. The field of view of the images was $6.1' \times 6.1'$ with a pixel scale of 180 mas/pixel. At that point, digital coronography (Assafin et al. 2009; Camargo et al. 2015), that mitigates Neptune's scattered light, proved to be unnecessary. Chromatic refraction corrections to Triton's position were carried out, but proved to be negligible too, as the observations were made in I band. Observations from two nights were discarded due to bad weather, but we were able to cover a complete orbit of Triton around Neptune (about 6 days) with more than 1000 images.

Prior to the *Gaia* DR2 release in April 2018 (Gaia Collaboration et al. 2016, 2018), the *Gaia* team[2] released a preliminary *Gaia* subset DR2 with 431 stars (R = 12-17) surrounding Triton's path in the sky plane during the 8 nights of our run. The main improvement with respect to DR1 is the inclusion of the stars' proper motions, leading to mas-level accuracy of stellar positions at epoch. Using these reference stars and the PRAIA package (Assafin et al. 2011), we obtained a mean offset $(\Delta\alpha\cos\delta, \Delta\delta) = (+7.8 \pm 5.4, -17.6 \pm 2.6)$ mas with respect to the JPL DE435/NEP081 ephemeris. The corresponding prediction uncertainty was about 60 km cross-track and 8 seconds in time. Fig. 2 displays the mean offset $(\Delta\alpha\cos\delta, \Delta\delta)$ for the 8 nights, using the *Gaia* DR2 catalogue. This is a large improvement from a prediction using only the *Gaia* DR1 catalogue, shifting the shadow path about 370 km to the south in the sky plane, or some 500-700 km when projected on Earth, depending on the station considered, as well as reducing the offsets uncertainties by factors of about 1.5 and 2.2, respectively. Since the run covers a full synchronous revolution/rotational period of Triton, the average offset reflects an error in Neptune's heliocentric position rather than a neptunocentric error in Triton's ephemeris.

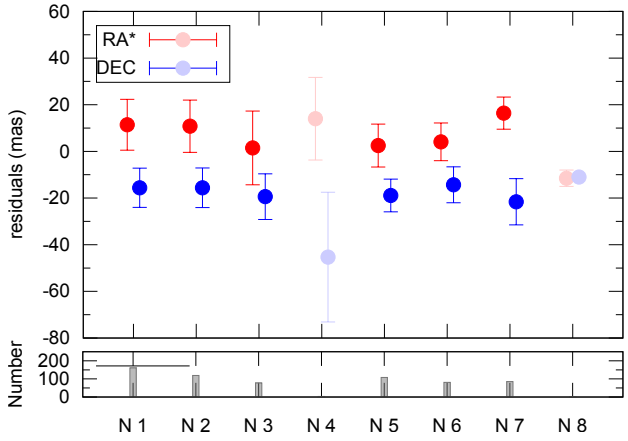

Fig. 2. Average offsets in (α, δ) mas of the 8 nights of OPD observations using the preliminary *Gaia* DR2 catalogue for the astrometric reduction. Positions in lighter colours were not accounted for to compute the average offset, due to lower quality associated with poor weather conditions. The lower panel refers to the number of images taken for each night.

The ±60 km cross-track uncertainty on the prediction was essential for better planning observations of the central flash, keeping in mind that the width of the region where that central flash is significant (say more than 20% of the unocculted stellar flux, see Figs. 23-24) spans typically ±100 km in the sky plane.

Combining the pre-event Triton's ephemeris offset with the geocentric astrometric *Gaia* DR2 position of the occulted star[3], we obtained the parameters describing the nominal prediction listed in Table 1. This updated prediction was promptly released to the scientific community before the event[4] and the corresponding map of the shadow track on Earth is displayed in Fig. 3.

2.2. Observations of the occultation

The event was attempted from over one hundred stations in Europe, northern Africa and eastern USA, resulting in a total of 90 occultation light curves. Fig. 4 displays the corresponding occultation chords and Table 5 lists the circumstances of observations for the respective sites.

The first part of this table lists the stations that were eventually used in a simultaneous fit to a Triton's atmospheric template model. The second part of the table lists other stations that were

[2] https://www.cosmos.esa.int/web/gaia/news_20170930

[3] https://www.cosmos.esa.int/web/gaia/news_20170523

[4] https://www.cosmos.esa.int/web/gaia/iow_20171005

Table 1. Occultation prediction using the *Gaia* DR2 position for the star and JPL DE435/NEP081 for Neptune's and Triton's ephemerides and the additional offset deduced from the OPD observations (see text for details).

Occultation circumstances (5 October 2017)	
Predicted time of geocentric closest approach	23h51m38.0s ± 8 s UTC
Predicted geocentric closest approach Triton-star	196 mas
Position angle between Triton and star at closest approach	347.51 deg
Geocentric shadow velocity at closest approach	16.80 km s^{-1}
Retrieved time of geocentric closest approach	23h51m28.92s ± 0.02 s UTC
Retrieved geocentric Triton-star closest approach	196.58 ± 0.05 mas
Occulted Star (from *Gaia* DR2)	
Star source ID (stellar catalogue)	2610107911326516992
Geocentric star position (ICRF) at epoch	α = 22h54m18.4364s ± 0.2 mas, $\delta = -08°00'08.318"$ ± 0.2 mas
G-mag / RP mag	12.5 / 12.0
Stellar diameter projected at Triton's distance[1]	0.65 km

Notes. [(1)] Using van Belle (1999)'s formulae and magnitudes B= 13.305, V= 12.655 (AAVSO photometric survey) and K= 11.080 (2mass) for the star, see http://vizier.u-strasbg.fr/viz-bin/VizieR

not used because the light curves had insufficient signal-to-noise ratios (SNR) to provide relevant contribution to that fit. The last part of the table provides information on the sites that were involved in the campaign, but could not gather data due to bad weather or technical problems.

The rule we used for deciding to include or not a light curve in the global fit is as follows. The SNR was first estimated by calculating the standard deviation σ of the flux outside the occultation. The resulting SNR $1/\sigma$ per data point was then re-calculated for a fixed time interval of one second. Assuming a gaussian noise, this implies a multiplicative factor of $\sqrt{1/\text{exposure time}}$ to be applied to the SNR obtained above. Finally, the noise level must be compared to the 'useful' information, i.e. the actual drop of signal caused by the occultation, not the total signal. This implies a new multiplicative factor of $\Delta\phi$ applied to the SNR per second obtained above, where $\Delta\phi$ is the flux drop observed during the occultation. Consequently, some light curves were eliminated due to a low contrast caused by light contamination from Neptune, see for instance the Abington, Caserta, Agerola 50 cm or Catania 28 cm light curves in Figs. B.6-B.9.

The normalization described above then allows us to compared consistently the various data sets. We used a normalized SNR cut-off of ten prior to the global fit. There are a few exceptions to that rule for light curves containing a strong central flash, see for instance the Le Beausset and Felsina data in Fig. B.3. They have a poor overall SNR, but we have kept them in the global fit (without flash, Section 4.2) to test the effect of the central flash inclusion, see Fig. 23 and Section 7.2. This approach allowed us to ensure that the central flashes provide a shadow centre witch is consistent with, but more accurate than the one given by the global fit, see Section 7.2.

This said, the cut-off of ten remains somehow arbitrary. We have tested other cut-off values, and we did not obtain any significant changes in the results of the fits presented in the rest of the paper.

The analysis of the light curves (as described in the next Section) allowed us to reconstruct the geometry of the event by providing Triton's position with respect to the occulted star, see Table 1. The reconstructed geometry of the occultation implies a shift of $(\Delta\alpha\cos\delta, \Delta\delta) = (-7.2, +0.6)$ mas of Triton's position with respect to the latest prediction described in the previous Section. This means that the occultation occurred about 9 s earlier than expected, and that the shadow centre was 12 km north of the predicted path in the sky plane.

This mismatch between observation and prediction is at a $\sim 1.3\sigma$-level, and is thus insignificant at our accuracy level. It shows in particular that the *Gaia* DR2 astrometry was crucial in getting an accurate prediction that allowed the detection of the central flash at various stations.

2.3. Occultation light curves

All our occultation light curves are displayed in Figs. B.1-B.5 and Figs. B.6-B.9. As was done in Table 5, the first group of figures corresponds to light curves that had sufficient SNR to be used in Triton's atmospheric fit, while the second group is for light curves with lower SNR that were not used in the fit. Note, however, that the best synthetic models expected for those light curves (plotted in grey in Figs. B.6-B.9) are fully consistent with the observations, in the limit of the noise level.

Among those light curves, three were used for obtaining atmospheric profiles from an Abel inversion procedure, see Section 4. Two of them (La Palma and Helmos) are displayed in Fig. 5, and the third one (Calern) is shown in the upper panel of Fig. 25.

3. Retrieving Triton's atmospheric structure

3.1. Methodology

We first adopt a boot-strap method to retrieve the molecular density $n(r)$, pressure $p(r)$, and temperature $T(r)$ of Triton's atmosphere as a function of the distance to Triton's centre, r. To do so, one approach is the Abel inversion of our refractive occultation light curves that have the highest SNR. Its primary result is the density profiles $n(r)$, from which the $p(r)$ and $T(r)$ profiles are derived by using the hydrostatic and ideal gas equations.

The other approach is a direct one. It is used once the inversion procedures have provided the density profiles $n(r)$. These profiles are smoothed and parameterised according to physical arguments (discussed later). Then, a ray-tracing scheme generates synthetic light curves that are fitted to the occultation light curves, thus describing the global structure of Triton's atmosphere, as illustrated in Fig. 4. One product of this fit is the location of Triton's centre, that is used iteratively with the Abel inversion, thus improving the accuracy on the altitude scale. The other product of our approach is the value of the pressure at a

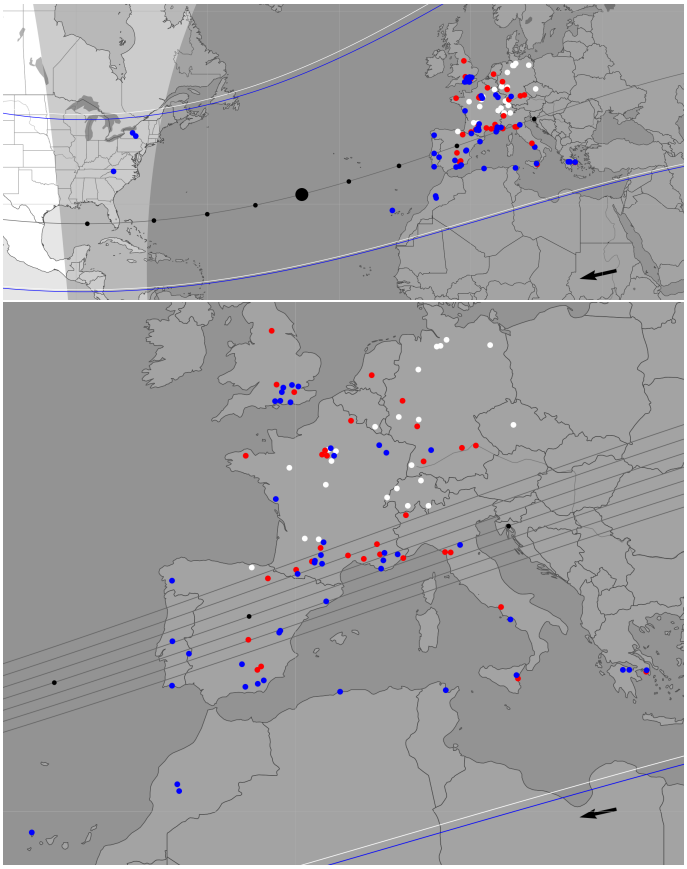

Fig. 3. Triton's shadow path on 5 October 2017. The black dots are spaced by one minute, the arrow indicating the direction of motion of the shadow. The northern and southern limits of the solid body assuming a radius of 1353 km are also represented, with the predicted path as the white lines, and the effective path as the blue lines. The grey area represents night on Earth (dark grey for full astronomical night and light grey for twilight). Stations with a successful observation, that have been used in our fit, are represented by blue dots, while the ones that were not used are shown as red dots. The white dots are the stations that attempted observation, but were clouded out or had technical difficulties. *Upper panel:* Overview of all observing stations. The larger black dot along the black line corresponds to the closest approach of the shadow centre to the geocentre, at around 23h52 UTC (see Table 1). *Lower panel:* Closer look at the central flash path across Europe. The grey lines around the centre-most line correspond to a spacing of 50 km (corresponding to about 2.5 mas), once projected in the sky plane.

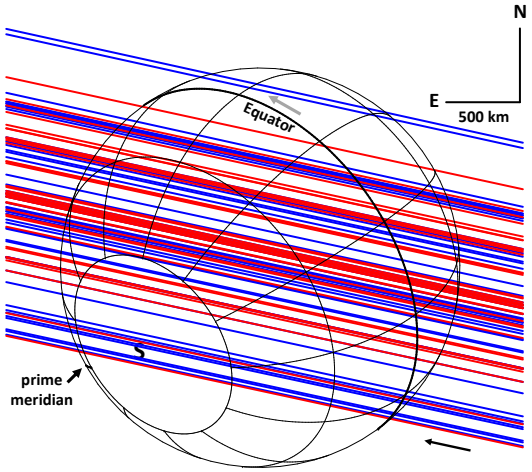

Fig. 4. Geometry of the 5 October 2017 stellar occultation by Triton, as seen in the sky plane. The J2000 celestial north (N) and east (E) directions and the scale are indicated in the upper right corner. Triton's radius is fixed at R_T = 1353 km and the grey arrow near the equator shows the direction of rotation of the satellite. The (Neptune-facing) prime meridian is drawn as a thicker line compared to the other meridians, and the south pole is marked by the label S. The inclined lines are the trajectories of the star relative to Triton (or "occultation chords") as observed from various stations, with the black arrow indicating the direction of motion. We have gathered a total of 90 occultation light curves, 52 of them (corresponding to the blue colour, as in Fig. 3) having sufficient SNR to be included in a global atmospheric fit, and 38 of them (red colour) with lower SNR, that are not included in the fit.

prescribed radius for comparison with previous results, aimed at detecting possible long-term seasonal effects.

The final approach is to fit the central flashes observed in some light curves, to measure the departure (if any) from the spherical shape of Triton's deep atmosphere, eventually used to constrain its wind regime. The other goal of this fit is to reveal possible absorbing material (by comparing the height of the central flash in stations that provided observations in different wavelengths) along the line of sight, such as hazes just above Triton's surface.

Technical details on the inversion technique are given in Vapillon et al. (1973), ray-tracing schemes and central flash fitting are described in Sicardy et al. (1999), and applications to Pluto's atmosphere are presented in Dias-Oliveira et al. (2015) (DO15 hereafter), and Meza et al. (2019). Numerical values used in both our inversion and ray-tracing codes are summarised in Table 2.

3.2. Assumptions

Our inversion and ray-tracing schemes assume that:
(1) The atmosphere is composed of pure N_2. The next most abun-

Table 2. Adopted physical parameters for Triton and its atmosphere

Triton's body	
Mass[1]	$GM_T = 1.428 \times 10^{12}$ m^3 s^{-2}
Radius[1]	R_T = 1353 km
Triton's geometry on 5 October 2017	
Triton pole position[2]	α_p= 20h 09m 29.40s
(J2000)	δ_p= 20° 25' 34.2"
Sub-solar latitude	40.0° S
Sub-observer latitude	40.5° S
Sub-observer longitude	169.9° E
N. pole position angle[3]	305.7°
Geocentric distance	$D = 4.3506 \times 10^9$ km
Triton's atmosphere parameters	
N_2 molecular mass	$\mu = 4.652 \times 10^{-26}$ kg
N_2 specific heat	$c_p = 1.04 \times 10^3$ J K^{-1} kg^{-1}
at constant pressure	
N_2 molecular	$K = 1.091 \times 10^{-23}$
refractivity	$+(6.282 \times 10^{-26}/\lambda_{\mu m}^2)$
(visible bands[4])	cm^3 molecule^{-1}
Refractivity at 3.6-cm[5]	$K = 1.0945 \times 10^{-23}$ cm^3 molecule^{-1}
Boltzmann constant	$k_B = 1.380626 \times 10^{-23}$ J K^{-1}

Notes. [(1)] McKinnon et al. (1995), where G is the constant of gravitation. [(2)] On 5 October 2017, using Davies et al. (1996), with corrections available at ftp://ftp.imcce.fr/pub/iauwg/poles.pdf. [(3)] Position angle of Triton's north pole projected in the sky plane. Counted positively from celestial north to celestial east. [(4)] Washburn (1930). [(5)] G95.

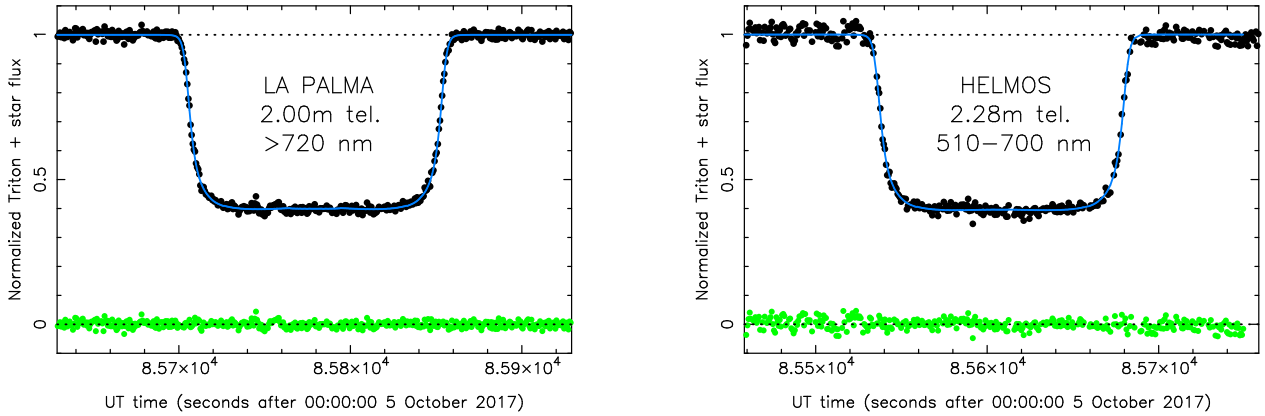

Fig. 5. The best two light curves obtained during the Triton occultation of 5 October 2017, at La Palma and Helmos stations (see details in Table 1). Both telescopes were equipped with the same E2V CCD 47-20 detector with quantum efficiency peaking at 600 nm and reaching zero near 300 and 1000 nm, respectively. *Left panel*: full resolution light curve (cycle time 0.635 s) for the La Palma station. *Right panel*: the same for the Helmos station (cycle time 0.674 s). The spectral ranges used for each instrument are indicated in the figures (I+z at La Palma and V+R at Helmos). The blue lines are the best simultaneous fits obtained with our ray-tracing approach, see Section 4.

dant species (CH_4) has a volume mixing ratio (hereafter referred to as mixing ratio) [CH_4/N_2] of less than 10^{-3} (Strobel & Summers 1995; Lellouch et al. 2010). Our ray-tracing code shows that such abundance causes a fractional change of the synthetic flux of about 10^{-5} near the half-light level, these effects are negligible considering the noise level of the data.
(2) The atmosphere is transparent. The deepest layers reached during Earth-based occultations are those that cause the central flash, at an altitude of about 8 km, see Section A. The validity of this assumption will be discussed in Section 8.
(3) The upper atmosphere is globally spherical. This hypothesis is supported by the fact that the observed central flashes are consistent with a spherical shape (Section 7). Small departures from the spherical model, however, are observed in some central flash shapes, and are discussed in Section 7.

The limitations of our approach described above are presented in Appendix A.

4. Results

4.1. Inverted profiles

We used the three data sets with highest SNR to perform our inversion method, more precisely the light curves from La Palma (2-m Liverpool telescope, Spain), Helmos (2.28-m Aristarchos telescope, Greece) and Calern (1.04-m C2PU telescope, France), see Table 5. At half-light times (where the star flux has been reduced by 50%) and for ingress and egress, each of these stations probe different locations in Triton's atmosphere. The corresponding latitudes, longitudes, and local solar times of the sub-occultation points are provided in Table 3. The paths of the stellar images over Triton's surface as seen from these stations are plotted in Fig. 6.

The results of the inversions are displayed in Figs. 7-9. We also plot in these figures the profiles retrieved from our analysis of the RSS occultation (see Section 5.1 for more details, as well as a discussion on the connection of these profiles with our results). Noteworthy features are:

1. All six $n(r)$ and $p(r)$ inverted profiles are very similar, showing that the stations at La Palma, Helmos and Calern probed essentially identical atmospheric layers at their ingress and egress points. No significant variations vs. local time and latitude are observed.
2. In their common range of probed altitudes, our density profiles and the RSS profile coincide, to within the noise level of the RSS experiment (the noise level in our retrieved profiles being much smaller).
3. The pressure profiles from RSS and from our inversions are also close to each other. However, contrary to the density profile, some small differences appear. This is discussed in Section 5.
4. The general positive gradient in the upper parts of our retrieved thermal profiles is a mere result of the choice of our initial conditions. This is intended to match the general temperature profiles obtained independently by Strobel & Zhu (2017) which were constrained by the RSS occultation data taken in 1989, see Appendix A.
5. However, all of our six retrieved thermal profiles show a marked turning point in their deepest parts, where the temperature gradient becomes negative. This gradient is always well below (in absolute value) the local dry adiabatic gradient, so that the atmosphere is convectively stable in those parts (Fig. 9).

4.2. Ray-tracing approach

For all the data sets used here, we employed the same procedure as in DO15 which consists of simultaneously fitting the refractive occultation light curves with synthetic profiles generated by the ray-tracing code. For each station, a least-squares fit is performed to adjust the synthetic light curve to the observation. Due to the uncertainties in the determination of ϕ_0 (the fraction of the flux attributed to Triton, see Appendix A) for some stations, and the lack of calibration for most of them, we considered ϕ_0 as a free parameter when performing these fits. Note that this adds one degree of freedom per station to the fit, and thus increases the error bars on the retrieved atmospheric parameters.

Table 3. Local circumstances at the three stations (ingress and egress) used for the Abel inversion analysis.

Site	Time (UT)[1]	Location on surface	Local solar time[2]
La Palma, ingress	23:48:27	251°E, 10°N	06:36 (sunrise)
La Palma, egress	23:50:52	18°E, 46°S	22:08 (sunset)
Helmos, ingress	23:45:38	254°E, 7°N	06:24 (sunrise)
Helmos, egress	23:47:58	12°E, 47°S	22:32 (sunset)
Calern, ingress	23:46:28	228°E, 32°N	08:08 (sunrise)
Calern, egress	23:49:15	50°E, 30°S	19:00 (sunset)

Notes. [(1)] UTC time at half-light level, 5 October 2017 [(2)] One "hour" corresponds to a 15° rotation of Triton. A local time before (resp. after) 12.0 h means morning (resp. evening) limb.

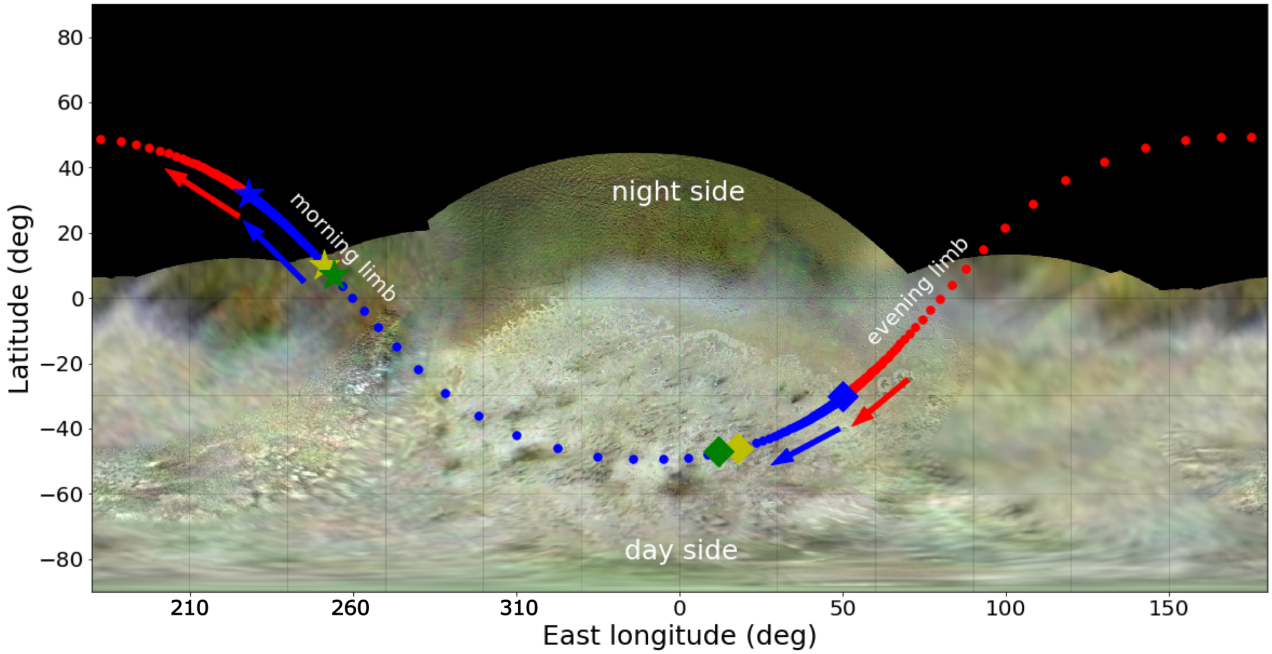

Fig. 6. Tracks of the primary (red dots) and secondary (blue dots) stellar images above Triton's surface, as seen from Constância, plotted every 0.1 s. The junctions between the red and blue paths correspond to ingress (left) and egress (right) points for the Constância station. The arrows show the direction of the stellar images' path. The regions probed by the central flash are those where the dots are more spaced. All the other stations probed essentially the same path (or part of it), with the primary and secondary images being swapped (as well as their directions of motion), depending on whether the station probed north or south of the shadow centre. Since the Earth and the Sun are angularly close (∼ 1°) to each other as seen from Triton, the stellar paths essentially mark Triton's terminator, the night side extending above the terminator in this figure. The two yellow symbols are for La Palma station, with ingress plotted as a star and egress plotted as a diamond. The two green symbols are the same for Helmos station, and the two white symbols for Calern station, see Table 3 for the corresponding values of the latitudes and longitudes. The background image is a global colour map of Triton, produced using V2 data and orange, green, and blue filter images in order to obtain an approximation of Triton's natural colours. Background image credits: Image selection, radiometric calibration, geographic registration and photometric correction, and final mosaic assembly were performed by Dr. Paul Schenk at the Lunar and Planetary Institute, Houston, Texas. Image data from Voyager 2 (NASA, JPL).

Our ray-tracing method is mainly sensitive to the half-light level. It corresponds to a radius of about 1415 km in Triton's atmosphere (altitude ∼60 km) and a pressure level of ∼0.55 μbar. For a prescribed temperature profile $T(r)$, this method returns two best fitting parameters. One parameter is the pressure $p_{\rm ref}$ at a reference radius, here $r_{\rm ref}$ = 1400 km. This particular choice stems from the fact that this reference radius has been used in previous works (e.g. Olkin et al. 1997; Elliot et al. 2000b), thus allowing consistent comparisons.

To proceed forward, we have defined a template $T(r)$ profile that matches the inverted profiles obtained at the station with the best SNR (La Palma). It has the same functional variation with altitude as in Dias-Oliveira et al. (2015), where it was applied to Pluto's atmosphere, except for the upper branch which is not isothermal, but rather has a constant thermal gradient that connects the lower atmosphere to an upper thermosphere. The adopted parameters for the template profile $T(r)$ are provided in Appendix A.2.

The lower part of the profile has been adjusted so as to fit the central flashes, see Appendix A.2 for details. That adjustment provides constraints on the thermal profile between the lowest inverted point of La Palma (∼20 km altitude) down to the central

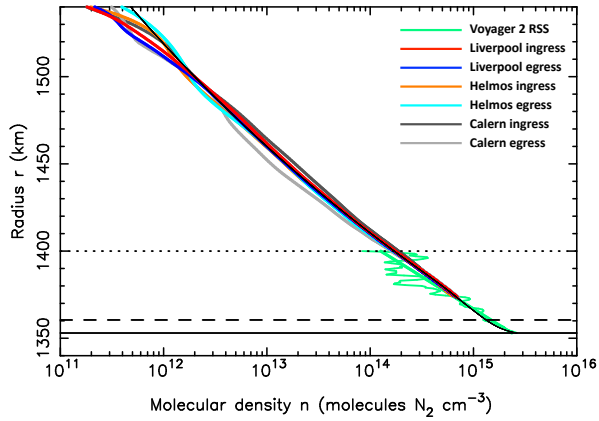

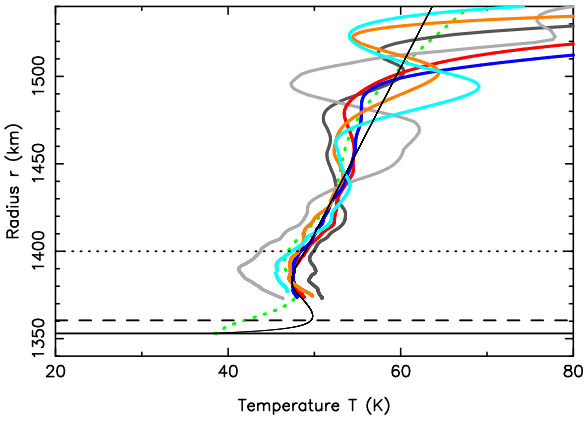

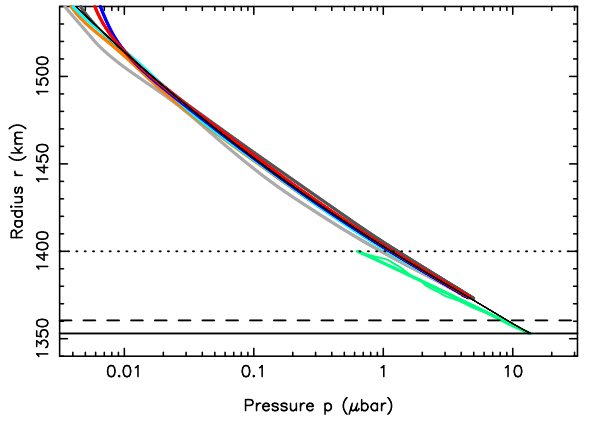

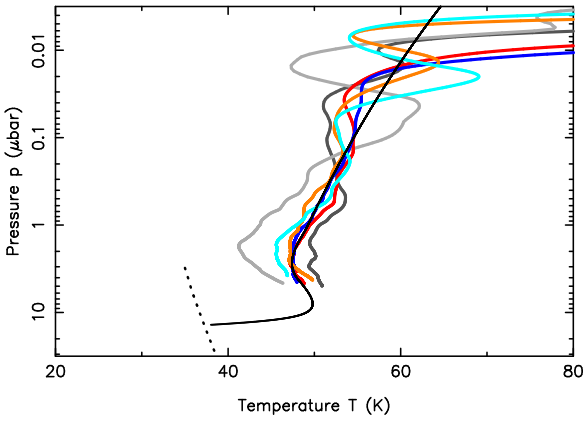

Fig. 7. *Upper panel:* Density profiles of Triton's atmosphere as a function of radius r (the distance to Triton's centre), retrieved by inverting three light curves obtained during the 5 October 2017 occultation and from the V2 radio phase delay at 3.6-cm. The colour codes are indicated in the upper right part of the plot. The same codes are used in Figs. 8-9 and Figs. 12-13. The thin black curve is a smooth synthetic density profile that fits the inverted profiles and is extrapolated down to the surface. It is derived from the smooth temperature profiles shown in Fig. 8. The solid horizontal line marks Triton's surface (at radius R_T = 1353 km), the dashed line indicates the central flash layer (near 1360 km), while the dotted horizontal line marks the reference radius $r_{\rm ref}$ = 1400 km. *Lower panel:* the corresponding pressure profiles.

Fig. 8. The temperature profiles as a function of radius (upper panel) and pressure (lower panel). The oblique dotted line in the lower panel is the wet adiabat, i.e. the vapour pressure equilibrium line for N_2, taken from Fray & Schmitt (2009).

flash level (~8 km altitude). Finally, below 8 km, the profile has been connected to the surface's temperature at 38 K. This is a "blind part" of the profile, as it does not contribute significantly to the refracted stellar flux received on Earth.

The resulting synthetic temperature profile is shown as a thin black line in Fig. 8. Starting from the surface, the profile first has a strong positive temperature gradient of 5 K km^{-1}. This gradient decreases rapidly (Fig. 9) and the temperature reaches a maximum value of about 50 K at r = 1363 km (10 km altitude), thus implying an average gradient of 1.2 K km^{-1} in that lower part. Our data show a hint of a mesosphere with a negative gradient (also seen in Elliot et al. 2003) that reaches −0.2 K km^{-1} at r = 1375 km (23 km altitude), before connecting with the general positive gradient of the upper branch.

The strong surface temperature gradient at the surface derives from the need to connect our inverted profiles to the surface at 38 K. Since we do not have information in this lower portion of the atmosphere, we employed the simple hyperbolic form of DO15 to connect our profile to the surface, so that our surface gradient does not necessarily reflect the real value at that level.

This said, the general positive gradient can be achieved by considering the heating by CH_4 stemming from near IR absorbing bands. For instance, we estimate that a CH_4 mixing ratio of 0.0004 yields T = 52 K at 1363 km, and thus could explain our result. Strobel & Zhu (2017) ran their model for discrete values of the CH_4 mixing ratios not included in their paper and found that a CH_4 surface mixing ratio ~ 0.00015 would suffice to support a temperature rise ~ 9 K, and a CH_4 surface mixing ratio ~ 0.0004 a temperature rise ~ 12 K, in the first 10 km. Because CH_4 is photochemically destroyed in the lower atmosphere, its scale height is roughly half the N_2 scale height and in terms of CH_4 column density one needs a higher surface CH_4 mixing ratio to compensate for its smaller scale height. For remote sensing observations it is the column density that is important and not just the surface mixing ratio that is relevant. Note

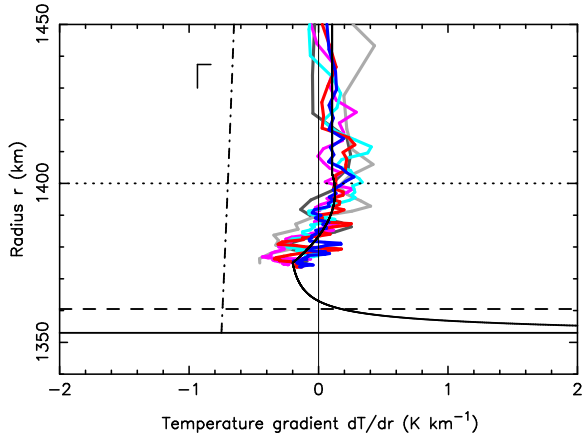

Fig. 9. The temperature gradient corresponding to the upper panel of Fig. 8. The dot-dashed line is the dry adiabatic temperature gradient $\Gamma = -g/c_p$, i.e. the limit of convective instability, where c_p is the specific heat at constant pressure for N_2 and $g = GM_T/r^2$ is the acceleration due to gravity.

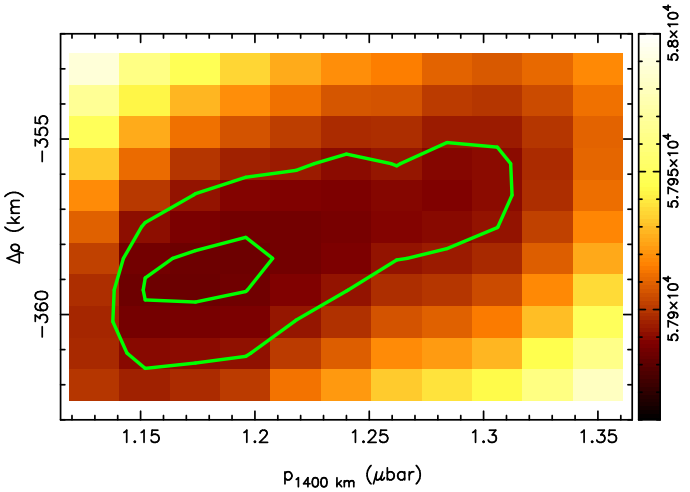

Fig. 10. The χ^2 map for the simultaneous fit of 52 light curves obtained during the occultation of 5 October 2017, using the ϕ_0 corresponding to the temperature profile in Fig. 8. The inner green line contour is the 1σ limit of the fit, while the outer green line is the 3σ limit.

that the 0.0004 value is smaller than, but roughly consistent with the range found by Lellouch et al. (2010) for the CH_4 mixing ratio, 0.0005-0.0010. Moreover, some complications may arise, like the existence of a troposphere.

The troposphere on Triton has been shown to be controlled by turbulent mixing above the surface, and to be sensitive to surface thermal contrasts between N_2 ice and the volatile free bedrock (due to different surface albedo or thermal inertia, Vangvichith 2013). On Pluto, climate models showed that the sublimation of cold N_2 ice and subsequent transport of the cold N_2 air in the impact basin Sputnik Planitia yield a km-thick cold troposphere as observed by New Horizons Forget et al. (2017); Hinson et al. (2017).

The negative gradient in the mesosphere, reminiscent of the more extended mesosphere on Pluto (Lellouch et al. 2017; Young et al. 2018), calls for the existence of a coolant. It must cool the atmosphere above its peak temperature of $\sim$ 50 K, as well as radiate away the downward thermal heat flux from the upper atmosphere where $T \sim 100$ K. There are a few candidates for this coolant: haze particles and/or influx of dust particles that may either be pure H_2O ice or with silicate cores and coated with H_2O ice (see Ohno et al. 2020 for more details).

The pressure at any level can then be deduced by using the temperature template described above. In particular, the surface pressure $p_{\rm surf}$ can be obtained by the relation $p_{\rm surf} = 12.0 \times p_{1400}$. This ratio will be used to extrapolate p_{1400} from $p_{\rm surf}$ or vice versa. The other fitted parameter is Triton's DE435/NEP081 ephemeris offset perpendicular to its apparent motion projected in the sky, $\Delta\rho$. Note that the ephemeris offset along Triton's motion is decoupled from that fit, see DO15 for details.

Error bars are obtained from the classical function $\chi^2 = \sum_1^N [(\phi_{\rm i,obs} - \phi_{\rm i,syn})/\sigma_i]^2$, which reflects the noise level σ_i of each of the N data points, where $\phi_{\rm i,obs}$ and $\phi_{\rm i,syn}$ are the observed and synthetic fluxes at the $i^{\rm th}$ data point, respectively.

We simultaneously fitted a selected pool of 52 light curves obtained during the 5 October 2017 occultation. Other light curves were not considered at this stage because they are affected by higher or non-normal noise that would degrade the global fit. In a first step, we excluded from the fit the parts of the light curves where a strong central flash is present. This is to avoid giving too much weight to those parts, while they reflect only the properties of the deepest atmospheric layers. So, the goal of this fit is to get the global properties of the atmosphere, and in particular, to constrain p_{1400} and the location of the shadow centre with respect to the occultation chords. In a second step, we included the central flashes in the fit to assess the shape of Triton's atmosphere and to check if the central flash location coincides with the centre found by the global approach.

After exploring a grid of values for $\Delta\rho$ and p_{1400}, we obtained the $\chi^2(\Delta\rho, p_{1400})$ map displayed in Fig. 10. A satisfactory fit should provide a minimum value $\chi^2_{\rm min}$ close to $N - M$, where M is the number of fitted parameters. Besides p_{1400} and $\Delta\rho$, we considered Triton's contribution to the light curve (ϕ_0) as a free parameter for all light curves. This is because no satisfactory values of ϕ_0 have been obtained for any of the light curves, see Appendix A.2. Thus, the fitted parameters are the values of $\Delta\rho$ and p_{1400}, plus the 52 values of the ϕ_0, i.e. a total of $M = 54$ fitted parameters. On the other hand, we used $N = 68446$ data points. We then obtain a global value of χ^2 per degree of freedom, $\chi^2_{\rm dof} = \chi^2_{\rm min}/(N - M) = 0.85$, indicating a satisfactory global fit to the data. An examination of values of $\chi^2_{\rm dof}$ for individual light curves also show values near unity for all of them. Thus, none of our light curves show significant discrepancies when compared to the synthetic light curves derived from the synthetic density model shown in Fig. 7. This confirms the spherical symmetry of Triton's atmosphere on a global scale.

Without considering $\Delta\rho$, the marginal distribution[5] for 1σ and 3σ error contours on p_{1400} are estimated by tracing the isolevels $\chi^2_{\rm min} + 1$ and $\chi^2_{\rm min} + 9$, respectively, as shown in Fig. 10. The best-fitting value of p_{1400}, its 1σ error bar and the quality of the fit, $\chi^2_{\rm dof}$, are listed in Table 4. The best-fitting value of $\Delta\rho$ (-359.3±1 km, Fig. 10) is used to retrieve the closest geocentric

[5] The marginal distribution is used when we wish to find the probability of specific variables of a subset without consideration of other variables.

approach distance between Triton and the star (projected in the sky plane) and its corresponding time, see Table 1.

Finally, the best simultaneous fit corresponding to the minimum of χ^2 is displayed in Figs. B.1-B.5. For the sake of completeness, Figs. B.6-B.9 show the synthetic light curves superimposed on the light curves that have *not* been included in the fit. Although they have poorer SNR, they all confirm that our global model satisfactorily fits these data.

5. Reanalysis of results from previous events

5.1. The Voyager 2 radio occultation

During its Triton flyby on the 25 August 1989, the V2 spacecraft sent its radio signal (RSS experiment) back to Earth as it passed behind the satellite. Details on the gathering of the V2 RSS data are given in G95.

The main product of this observation was the temperature and pressure at Triton's surface. However, although it becomes quite noisy above the 20-km altitude level, the RSS phase delay still provides useful constraints on Triton's lower atmosphere, with some science left to explore. Here, we give a summary of Gurrola's work, and describe how we use the V2 phase delay to retrieve Triton's atmospheric structure in the 10-20 km above the surface.

The V2 high gain 3.7-m antenna transmitted to Earth two radio signals at 3.6 and 13 cm (X-band and S-band, respectively). The phases in these bands are related to one another by

$$\Delta\phi = \frac{121}{112}(\phi_x - \frac{3}{11}\phi_s), \tag{1}$$

where, ϕ_x is the phase in the X-band, ϕ_s is the phase in the S-band, and $\Delta\phi$ is the corrected radio phase corresponding to the neutral atmosphere at the X-band wavelength. This calculation is done to remove plasma effects on the phase.

Due to problems in fitting the ingress data, as there seemed to be sudden changes in slope, G95 used only the egress data for his analysis.

Gurrola provided us with the corrected phase delay $\Delta\phi(r)$ vs. altitude above Triton's surface, as well as the results from his models to obtain only the "pure atmosphere phase delay". This corresponds to the phase delay once a general polynomial trend has been subtracted from $\Delta\phi$ to account for thermal noise and instabilities in the frequency reference on board V2. These polynomials, referred to as baselines in G95, were designated as B_1, B_2, and B_3. B_1 is the linear baseline used by Tyler et al. (1989), determined using 120 km of the data obtained. G95 considered this insufficient to reliably estimate the drift of the instrument over the atmosphere, as it did not extrapolate from high enough altitudes (so that the atmosphere is too thin to affect the signal phase) downwards toward Triton's surface. On the other hand, baselines B_2 and B_3 used about 700 km of the data, and are, respectively, the second and third-order polynomials of G95's best fit at egress. The preferred solution of this author is B_2. The resulting $\Delta\phi(r)$ is displayed in green in Fig. 11.

Using the B_2 solution, we derive the profiles displayed as green curves in Fig. 7. In order to compare this result to ours, we generated for comparison the phase delay at 3.6-cm that would be observed with our best profiles $n(r)$ (the black line in Fig. 7) as if it were obtained by V2:

$$\Delta\phi(r) = \frac{2\pi}{\lambda} K \sigma_{N_2}(r), \tag{2}$$

where λ is the wavelength (3.6-cm), K is the corresponding molecular refractivity of N_2 (see Table 2), and $\sigma_{N_2}(r)$ is now the column density stemming from our best model. The resulting $\Delta\phi(r)$ profile is shown in black in Fig. 11, together with the phase delays deduced from the inversions of La Palma and Helmos' light curves (in colours).

Conversely, we used the V2 corrected X-band radio phase to retrieve the refractivity profile from the Abel inversion

$$\nu(r) = -\frac{\lambda}{2\pi^2}\int_r^{+\infty} \frac{d(\Delta\phi)}{dR}\frac{dR}{\sqrt{R^2-r^2}} = -\frac{\lambda}{2\pi^2}\int_0^{+\infty} \frac{1}{R}\frac{d\Delta\phi}{dR}dl, \tag{3}$$

using the auxiliary variable $l = \sqrt{R^2 - r^2}$ to calculate the integral. Finally, the density profile $n(r) = \nu(r)/K$ can be deduced.

With this, we can directly compare our results to those of V2. Note that the RSS profiles probe altitude interval levels that overlap our ground-based occultation levels. This overlapping region extends from the lowest inverted points of the La Palma station, $r = 1373$ km (20 km altitude), up to roughly the reference level, $r = 1400$ km (47 km altitude), at which point the RSS profiles become too noisy to be reliable, reaching a factor of about two at that level.

The examination of the upper panel of Fig. 12 shows that no significant difference in density is detected between the 1989 and 2017 profiles, especially at the "junction level" at $r = 1373$ km. Note that the RSS density profile is rather insensitive to the particular solution B_1, B_2 or B_3 chosen to retrieve $n(r)$.

Integrating the weight of the atmospheric column provides the RSS pressure profile (lower panel of Fig. 7). However, this profile includes a contribution of the weight of the layers above $r = 1400$ km, where the RSS phase delay is very noisy. Note that the B_1 pressure profile is quite offset in slope with respect to the B_2 and B_3 solutions (lower panel of Fig. 12). So, and contrarily to the density profiles, the general slope of $\log_{10}(p)$ vs. radius r is quite sensitive to the particular choice of the polynomial baseline. In this context, it is difficult to conclude if the break in slope between the RSS profile and our ground-based results of 2017 is real or not.

Using the preferred B_2 model, and using the Abel inversion (Eq. 3), we obtain $p_{\mathrm{surf,RSS}} = 13.6\,\mu$bar and $p_{1373,\mathrm{RSS}} = 3.77\,\mu$bar as of 1989. The main result of the inversion is the density profile; to translate this into pressure, we need an estimate of the surface temperature T_{surf}. The error bar on $p_{\mathrm{surf,RSS}}$ caused by the uncertainties on T_{surf} will be discussed next.

In any instance, our results are consistent with the analysis of G95, $p_{\mathrm{surf,RSS}} = 14 \pm 2\,\mu$bar. This is also fully consistent with our estimation of the surface pressure as of 2017, $14.1 \pm 0.3\,\mu$bar (Table 4). Thus, no significant variations of surface pressure is found when comparing the RSS results of 1989 and the results derived from the ground-based occultation of 2017.

The value $p_{1373,\mathrm{RSS}} = 3.77\,\mu$bar that we find is 21% smaller than the value we obtained in 2017 at that level, 4.58 μbar. Propagating this 21% difference to the 1400 km radius then yields $p_{1400,\mathrm{RSS}} = 0.97\,\mu$bar. Estimating the error bar on that value is difficult, because the RSS pressure depends on the (noisy) pressure values obtained above, as mentioned earlier. If we adopt the error bar $p_{\mathrm{surf,RSS}} = 14 \pm 2\,\mu$bar of G95 and propagate it upward, this yields $p_{1400,\mathrm{RSS}} = 0.97 \pm 0.14\,\mu$bar.

Another, more robust way to estimate $p_{\mathrm{surf,RSS}}$ is to use the RSS density profile alone. The counterpart is that we need an independent measurement of the surface temperature T_{surf} in order to derive the pressure from the ideal gas equation $p_{\mathrm{surf,RSS}} = n_{\mathrm{surf,RSS}} k_B T_{\mathrm{surf}}$. These temperature measure-

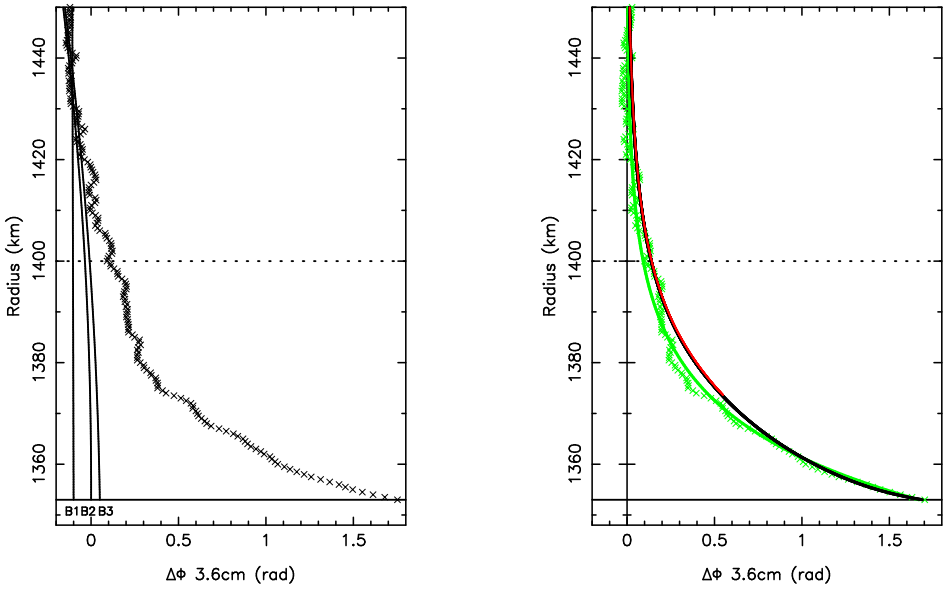

Fig. 11. *Left panel:* The radio phase delay observed during the egress of the V2 RSS occultation on the 25 August 1989, in the 3.6-cm X-band (adapted from G95). The crosses are the data and the three solid lines (labelled B_1, B_2 and B_3) are three polynomial modellings of the phase delay baseline. As discussed by G95, the preferred baseline solution is B_2. *Right panel:* Green crosses: the radio phase after subtraction of the B_2 baseline polynomial shown in the left panel, thus representing the effect of the atmosphere only. Green line: the smooth version of that radio phase delay, as constructed by G95. The red profile is the phase delay that would be observed at 3.6-cm from the retrieved density profile of La Palma at immersion, see Fig. 7. Other phase delay profiles obtained from La Palma (emersion) and Helmos would be indistinguishable from the red profile, and are not plotted here for sake of clarity. The black profile is the phase delay obtained from our best model of Triton's atmosphere, see text for details.

ments (given below) are more accurate than G95's estimation ($T_{\rm surf}$ = 42 ± 8 K) and thus reduce the ±2 μbar uncertainty of G95's value of $p_{\rm surf,RSS}$. However, this approach is valid only if these temperature measurements apply to the N_2 ice surface that the RSS experiment probed, and if the vapour pressure equilibrium between the N_2 ice and the gas is achieved.

Estimations of $T_{\rm surf}$ are given by various authors (see also Fig. 13): 38^{+3}_{-4} K (Conrath et al. 1989), 38^{+2}_{-1} K (Tryka et al. 1993), the range 36.5-41 K (Grundy et al. 1993) and 37.5 ± 1 K (Merlin et al. 2018). Adopting a value of $n_{\rm surf,RSS} = 2.4 \times 10^{15}$ cm^{-3} derived from our RSS phase delay inversion (Fig. 12), we find surface pressures of $12.3^{+1.0}_{-1.3}$ μbar, $12.3^{+0.6}_{-0.3}$ μbar, a range 11.5 − 13.3 μbar and 12.4 ± 0.3 μbar, respectively, for the four choices of surface temperatures. Note that all these values are consistent with the surface being in vapour pressure equilibrium with the atmosphere, as shown in Fig. 13. This supports the hypothesis that the reported temperatures are indeed representative of the N_2 ice surface.

In summary, we estimate from the surface temperatures given above, a safe surface pressure range of 12.5 ± 0.5 μbar can be derived at the V2 epoch. In this case, the error bar essentially stems from the uncertainties on the temperatures. Comparing this value with our estimation $p_{\rm surf}$ = 14.1 ±0.4 μbar in 2017 (Table 4), and assuming a constant factor (12.5/14.1) throughout the profile, we formally obtain p_{1400} = 1.05 ± 0.04 μbar in 1989. This is consistent with our estimate made above, $p_{1400,RSS}$ = 0.97 ± 0.14 μbar. We thus estimate a conservative range of $p_{1400,RSS}$ = 1.0 ± 0.2 μbar for the pressure at 1400 km in 1989.

5.2. The 18 July 1997 stellar occultation

This campaign involved one station in the USA and three stations in Australia. It was a joint effort between two groups, and, therefore, both have access to the data. The circumstances of observations are listed in Table 5 and the geometry of the event is displayed in Fig. 14. More details on these observations and their analysis are given in Elliot et al. (2000a).

Here we provide the results of our own approach to constrain p_{1400}. In particular, we adopt the same temperature profile $T(r)$ as for 2017 (see Fig. 8), but varying p_{1400} to fit the synthetic light curves to the data. The $(\chi^2, \Delta\rho)$ map is displayed in Fig. 15 and the best fit is shown in Fig. 16. This yields $p_{1400} = 1.90^{+0.45}_{-0.30}$ μbar and $\chi^2_{\rm dof} = 0.95$, indicating a satisfactory fit.

5.3. The 21 May 2008 stellar occultation

This event was observed from Namibia (two stations) and from La Réunion Island (two stations), see Table 5. Given that each pair of stations are close together, only two effective chords have been obtained, see Fig. 17. Moreover, these chords being grazing, there is a strong correlation between the closest approach distances of the chords to Triton's shadow centre and the retrieved reference pressure p_{1400}, see Fig. 18. The best fit is also shown in Fig. 19. As a consequence, the value of p_{1400} is poorly constrained at the 1σ level, $p_{1400} = 1.15^{+1.03}_{-0.37}$ μbar. At the 3σ level, the value is so unconstrained that it does not bring any information on the temporal seasonal variations of the pressure (Fig. 20).

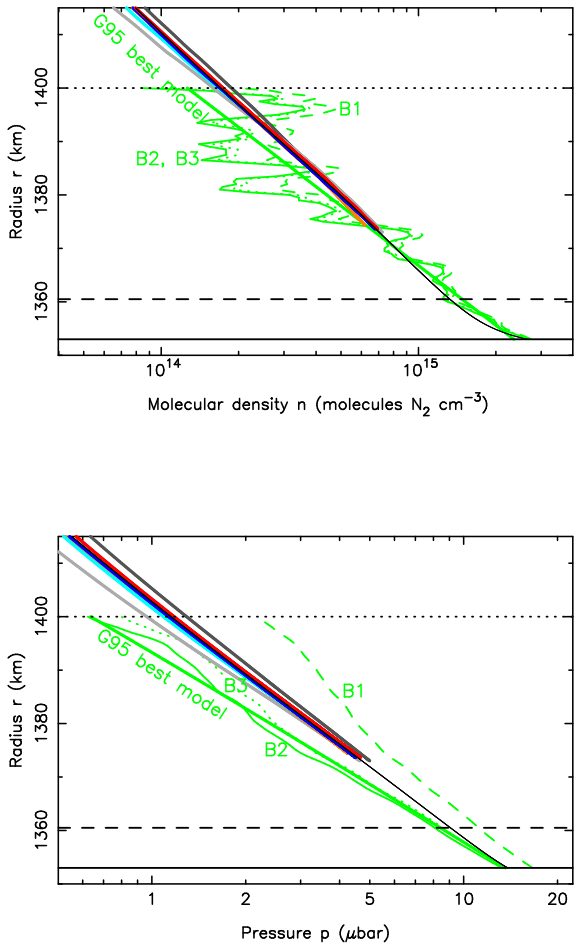

Fig. 12. *Upper panel:* close up view of the upper panel of Fig. 7. Various profiles derived from the RSS occultation are shown in green. Dashed line: the profile retrieved by Tyler et al. (1989), using a polynomial extrapolation B_1 to correct for the RSS phase instability. Thin solid line: the profile retrieved by G95, using the polynomial extrapolation B_2. Dotted line: the same by G95, but using the polynomial extrapolation B_3. The thick solid line is the best model of G95, based on the B_2 profile. *Lower panel:* The same for the pressure profiles.

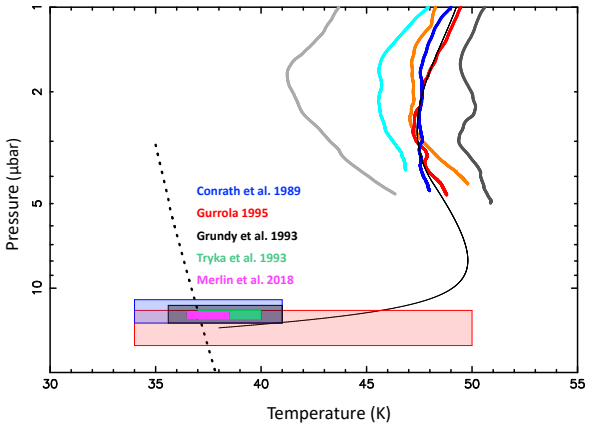

Fig. 13. A close up view of lower panel of Fig. 8. The width of each coloured box is Triton's surface temperature ($T_{\rm surf}$), as estimated by the various authors mentioned just above the boxes, see text for details. The heights of the boxes are the range of surface pressures $p_{\rm surf}$, using the ideal gas law $p_{\rm surf} = n_{\rm surf,RSS} k_B T_{\rm surf}$, where $n_{\rm surf,RSS} = 2.4 \times 10^{15}$ cm^{-3} is the surface molecular nitrogen density derived from our inversion of the RSS data, see text. Note that all the boxes intersect the vapour pressure equilibrium plotted as a dotted line. This shows that the RSS surface density and the estimated surface temperatures are mutually consistent with a pressure being controlled by the N_2 ice sublimation.

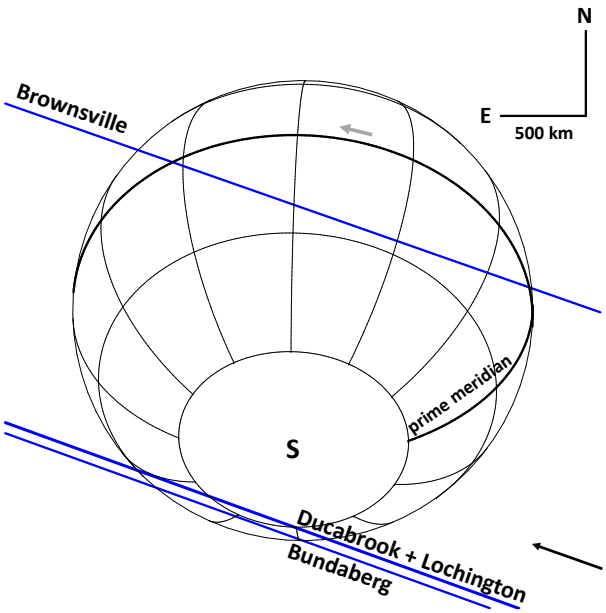

Fig. 14. Geometry of the 18 July 1997 occultation, with the same conventions as in Fig. 4.

6. Atmospheric seasonal variations

6.1. Occultation results

Table 4 lists our values of p_{1400} at various epochs, as well as values taken from other works. Extrapolations to the surface have also been included, assuming a constant ratio $p_{\rm surf}/p_{1400} = 12.0$. The corresponding seasonal variations of p_{1400} with time is displayed in Fig. 20.

The value of Olkin et al. (1997) indicates a 40% increase of pressure between 1989 and 1995, but at a low significance level of 1.8σ. From the 18 July 1997 event, Elliot et al. (2000a) obtained $p_{1400} = 2.23 \pm 0.28$ μbar, whereas with the same data set, we obtain $p_{1400} = 1.90^{+0.45}_{-0.30}$ μbar. The difference between the two results amounts to a factor of 0.85 and stems from the use of a different template model $T(r)$. This said, this difference remains at the 0.6σ level and is statistically insignificant. Using our value of p_{1400} for 1997 indicates a pressure increase by a factor of 1.9 between 1989 and 1997, but at a marginally significant 2.5σ level only.

The 4 November 1997 value obtained by Elliot et al. (2000a, 2003), $p_{1400} = 1.76 \pm 0.02$ μbar, has a much lower error bar due to the high SNR of the light curve, obtained with the *Hubble Space Telescope*. Taken at face value, this implies an increase of pressure by a factor 1.76 between 1989 and 1997, at a 3.8σ level. However, this observation was a single-chord event, and a model was used to retrieve the astrometry of this event. Consequently, there is an uncertainty that was not accounted for. Since

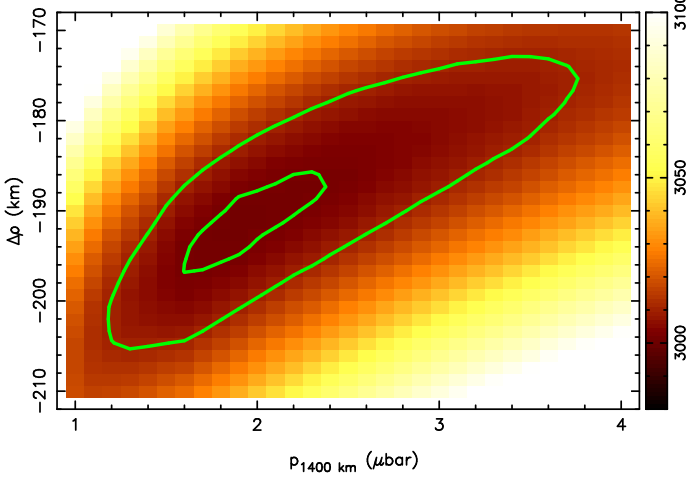

Fig. 15. Same as Fig. 10 for the 18 July 1997 occultation.

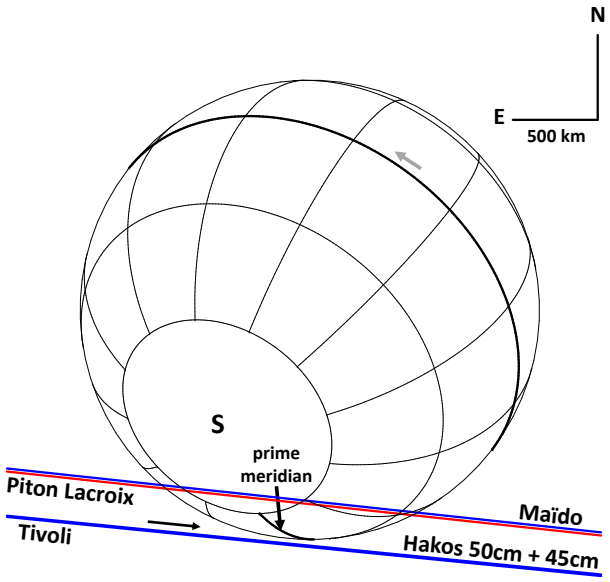

Fig. 17. Geometry of the 21 May 2008 occultation, with the same conventions as in Fig. 4.

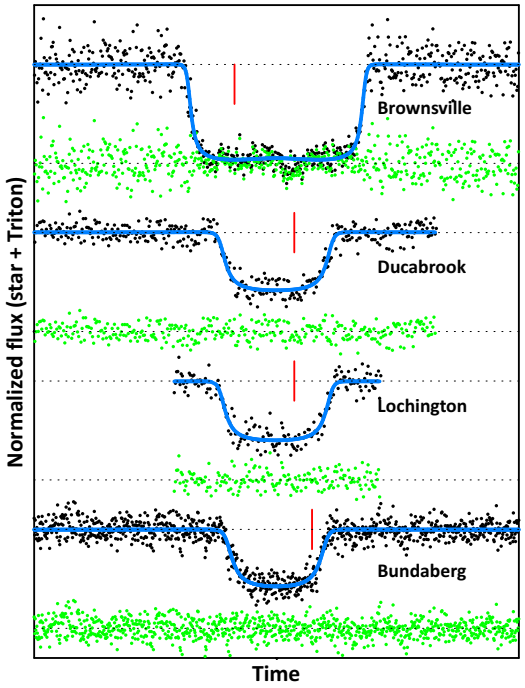

Fig. 16. Simultaneous fits to the 18 July 1997 light curves. The panel covers 300 seconds in time. All the light curves have been shifted so that the mid-occultation times are aligned. The red vertical tick marks indicate 10:10 UTC at the Brownsville station (USA), and 10:18 UTC for the three Australian stations. The blue lines are simultaneous fits to the data (black dots), using the best value found in Fig. 15, p_{1400} = 1.9 μbar, and the temperature profile shown in Fig. 8. The green dots are the fit residuals. For each light curve, the upper dotted line is the normalised value of the star + Triton flux, and the lower dotted line is the background flux. Note that the data from the Brownsville station has been normalised during the event, as shown in Elliot et al. 2000a.

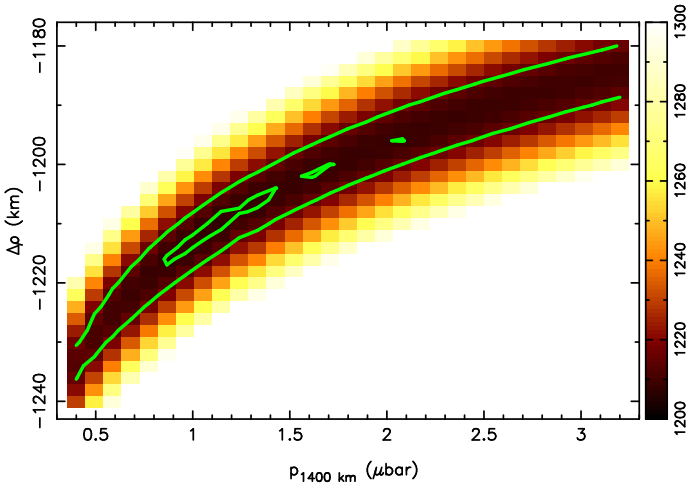

Fig. 18. Same as Fig. 10 for the 21 May 2008 occultation.

we do not have access to this data, it is impossible for us to verify their result using our own methods, and therefore, confirm this increase.

Finally, the 21 May 2008 event provided only two grazing chords, bringing no new information, so that no firm conclusion can be drawn on any change of pressure between 1989 and 2008.

In summary, we estimate that the surge of pressure reported in the 1990s (compared to the V2 epoch) seems to be confirmed by our own analysis, but it remains debatable considering the paucity of data points available, and the lack of a fully consistent analysis of all the observed events. Note that the 2017 data rules out the concept of a monotonic increase in Triton's pressure over time, but does not rule out the observed increase in 1995-1997. Regardless, the much more accurate value of p_{1400} that we obtain in 2017 is fully compatible with that derived from the V2 RSS experiment. If we consider the 3σ level, Fig. 20 shows that no increase can be claimed between the two measurements. So either no surge occurred between 1989 and 2017, or if it happened, the pressure has been back to its V2 value in 2017.

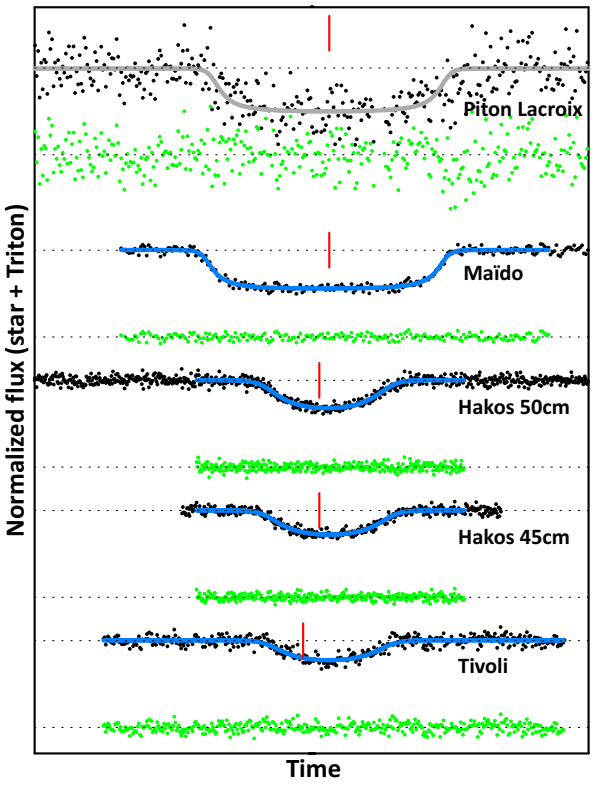

Fig. 19. Fit to the 21 May 2008 light curves. The same conventions as for Fig. 16 are used, except that the panel now covers 720 seconds in time. The synthetic light curve for Piton Lacroix is plotted in grey because it is not used in the fit, due to the high noise level. The red vertical tick marks indicate 01:51 UTC for Piton Lacroix and Maïdo, and 01:41 UTC for Hakos.

From high-resolution spectroscopy in July 2009, Lellouch et al. (2010) obtained the first detection of methane gas in Triton's atmosphere since V2, and the first CO gas detection. Their analysis yielded a CH_4 gas number density at the surface $4.0^{+5.0}_{-2.5}$ larger than inferred from V2 (Herbert & Sandel 1991; Strobel & Summers 1995). Assuming that the N_2 pressure would qualitatively follow a similar seasonal variation, they estimated a 40 μbar pressure in 2009. This value (which did not represent a direct measurement of the N_2 pressure) is clearly at odds with the picture shown in Fig. 20, in particular with the 21 May 2008 point.

Table 4. Atmospheric pressure on Triton

Date	Pressure at 1400 km p_{1400} (μbar)	Pressure at the surface p_{surf} (μbar)[1]	Fit quality[2] χ^2_{dof}
This work			
25 August 1989[3]	1.0 ± 0.2	12.5 ± 0.5	N/A
18 July 1997	$1.90^{+0.45}_{-0.30}$	$(22.8^{+5.4}_{-3.6})$	0.95
21 May 2008	$1.15^{+1.03}_{-0.37}$	$(13.8^{+12.4}_{-4.4})$	0.93
5 October 2017	1.18 ± 0.03	(14.1 ± 0.4)	0.85
Other works			
25 August 1989[4]	N/A	14 ± 2	N/A
14 August 1995[5]	1.4 ± 0.1	(17 ± 1)	N/A
18 July 1997[6]	2.23 ± 0.28	(26.8 ± 3.4)	N/A
4 November 1997[7]	1.76 ± 0.02	(21.1 ± 0.2)	N/A

Notes. [(1)] The values in parentheses assume a constant ratio of 12.0 between the pressures at the surface and at 1400 km, as derived from our best model (Fig. 8). [(2)] See discussion in Section 4.2. [(3)] Using our own inversion of the V2 RSS phase delay profile, see text. [(4)] G95. [(5)] Olkin et al. (1997). [(6)] Elliot et al. (2000a, 2003) [(7)] This value is the average over ingress and egress obtained by Elliot et al. (2003).

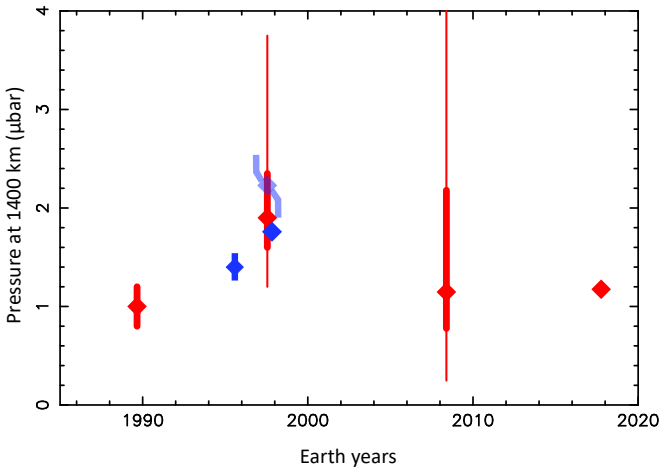

Fig. 20. Triton's atmospheric pressure seasonal variations with time, using the values from Table 4. Our results are in red, values taken from other works are plotted in blue. For better viewing, the value derived by Elliot et al. (2000a) from the 18 July 1997 occultation is plotted in a semi-transparent blue colour, using the same data set as we are using here for that date, and providing our red diamond-shaped point just below it. For all points, the thick error bars correspond to 1σ confidence levels. Note that for the 4 November 1997 and 5 October 2017 values, the 1σ error bar is smaller than the diamond-shaped symbol, and therefore is not visible. For the 18 July 1997 and 21 May 2008 events, we have also plotted for information our 3σ error bars as thinner lines, see text for discussion.

6.2. Climatic context from numerical volatile transport modelling

The climatic context of Triton is described and analysed in detail in a recent paper by Bertrand et al. (2022). Bertrand et al. (2022) employed the volatile transport model (VTM) of Triton, developed at the Laboratoire de Météorologie Dynamique (LMD), to investigate the long-term and seasonal volatile cycles of N_2 and CH_4 on Triton. Their simulations are constrained by the surface pressure derived from the stellar occultations presented in this paper. In this Section, we summarise the main results of this paper that are relevant for the interpretation of our observations.

In VTM simulations, the surface pressure peak occurs slightly after the southern summer solstice (2000) between years 2000-2010 (see Fig. 21). The surface pressure seasonal variations obtained by Bertrand et al. (2022) is similar to that obtained by Spencer & Moore (1992), when they artificially maintained a permanent large southern cap of bright N_2 (see their Fig. 7). The larger the northern cap, the more it can serve as a condensation area and buffer N_2 sublimation in the southern hemisphere, which results in a lower and earlier surface pressure peak. The

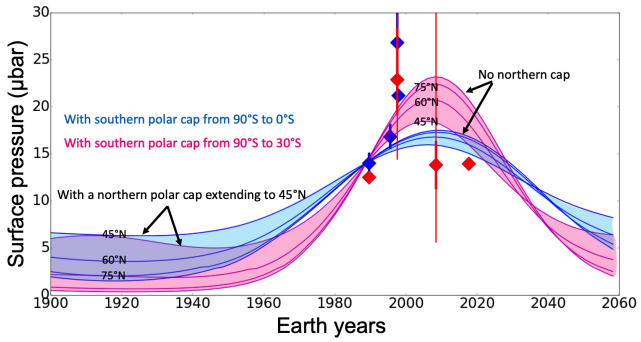

Fig. 21. Surface pressure cycle on Triton as simulated with the VTM assuming different fixed N_2 ice distribution in both hemispheres. A thermal inertia of 1000 J $s^{-1/2}$ m^{-2} K^{-1} (SI) was assumed. Bertrand et al. (2022) include more simulations in their paper, and their Fig. 9 show cases with different thermal inertias. It is of note that their simulations show that a lower thermal inertia would delay the peak of the surface pressure, in opposition with the occultation data points. The blue lines refer to a southern cap extending to the equator, while the pink lines are for a southern cap extending to 30° S. Each line, marked with its corresponding value, refer to a different extension of the northern cap: 45° N, 60° N, 75° N, and no cap.

amplitude of the surface pressure peak is strongly attenuated if N_2 ice remains between 30° S - 0°, because condensation will dominate over sublimation between the years 1980-2020.

According to the model, Triton's atmospheric surface pressure will remain at 5 μbar during the next solstice season if the North polar cap extends to 60° N and the South polar cap extends to 0°. The amplitude of the pressure peak is attenuated if N_2 ice deposits remain between 30° S - 0° because these latitudes are dominated by condensation rather than sublimation after the year 2000.

These results suggest that a northern cap extending down to at least 45° N – 60° N is needed in 2017 to restore the surface pressure back to the V2 measured value ~ 14 μbar. Otherwise, the surface pressure will remain higher than 16 μbar in 2017 with no northern cap. A strong increase in surface pressure cannot occur before 2000 if N_2 ice remains between 30° S - 0°. To ensure that the surface pressure remains greater than 5 μbar during the opposite season (southern winter) a permanent northern cap extending down to 45° N is required.

In their simulations, Bertrand et al. (2022) also investigated the CH_4 cycle by taking into account a small amount of pure CH_4 ice at the surface in addition to the N_2-rich mixture (Merlin et al. 2018). In the case where this pure CH_4 ice is placed at the South pole of Triton, covering 2% of the surface of the visible projected disk, they obtain a large increase in the CH_4 gas abundance from 1990 to 2005, without any significant change in N_2 surface pressure. Since CH_4 is not completely mixed with N_2 ice, it implies that the large increase of CH_4 (with relation to V2) reported by Lellouch et al. 2010 could be decoupled from the N_2 seasonal variations and, therefore, does not necessarily represent a measurement of the global pressure of the atmosphere.

For more details on the N_2 and CH_4 seasonal variations as simulated by the VTM, the reader is referred to Bertrand et al. (2022).

7. Triton's lower atmosphere: central flash

The detection of a central flash during the 5 October 2017 occultation offered a unique opportunity to study Triton's lower atmosphere. Our ray-tracing code shows that the flash is caused by a layer having a typical thickness 2 km, lying at about 8 km above Triton's surface (radius of 1361 km). In that altitude range, the Abel inversion method is no longer valid, due to the co-existence of two stellar images along Triton's limb, see Fig. A.2. This problem arises at altitude levels of about 20 km, corresponding to the deepest layers probed by the light curve obtained at La Palma. Consequently, the central flash allows us to gain about 12 km downward (about 0.6 scale height) compared to the inversion method. The explanation for this is shown in Fig. A.1 and further detailed in Appendix A.2.

7.1. The central flash: observations

The central flash swept Europe along the lines shown in grey in Fig. 3. Among the 90 light curves shown in Figs. B.1-B.5 and Figs. B.6-B.7, 42 show evidence of a stellar flux increase near mid-occultation, and 23 of them have enough SNR to be used in the central flash modelling.

Fig. 22 displays the reconstructed intensity map of Triton's shadow, with in particular the presence of a bright dot (central flash) near the shadow centre.

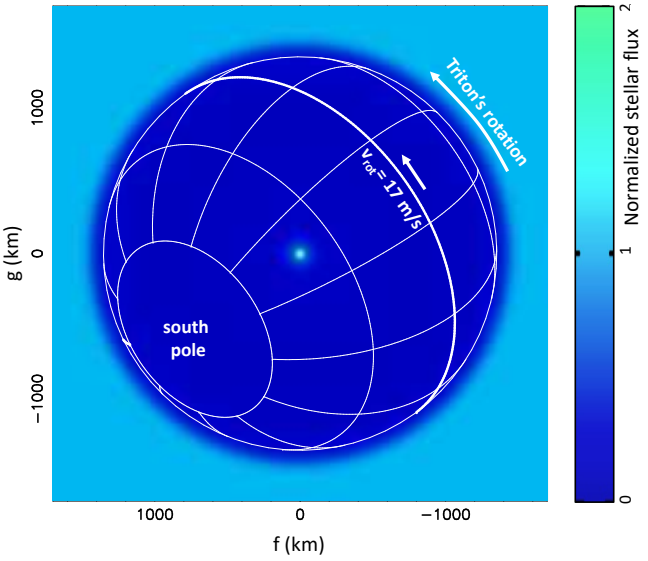

Fig. 22. The stellar flux in Triton's shadow for the 5 October 2017 event, normalised to unity outside the body (light-blue region). The flux reaches a minimum of about 7% of the unocculted flux inside the shadow, and then rises sharply at the shadow centre. The direction of Triton's rotation is indicated, as well as the equatorial rotation velocity v_{rot} = 17 m s^{-1} (in a inertial frame), using the parameters of Table 2.

At Calar Alto, which passed at about 300 km from the shadow centre at closest approach (C/A), the increase of stellar flux is barely noticeable (Fig. 24), while it reaches the full unocculted stellar flux at Calern, which passed at 29 km from the centrality. At Constância (C/A 8.4 km), the maximum of the flash peaks at three times the unocculted stellar flux, and about 3.4 times the unocculted flux at Le Beausset (C/A 6.7 km, the closest of all stations), see Figs. 23 and 25.

The fit of the central flash is described in Section 4.2, except that we now allow a departure from sphericity of the layer responsible for the flash (see Sicardy et al. 2006 for details). Note that the ray tracing code accounts for both the primary and secondary stellar images. Thus, we are not restricted in using this

code as would be the case for the Abel inversion scheme (Section A.3).

7.2. The central flash: spherical fit

Assuming a spherical flash layer, we obtain the best simultaneous fits (now including the central flashes) displayed in Figs. 23-24. The quality of the fit ($\chi^2_{\rm dof} = 0.80$) is comparable to the quality obtained without the flashes ($\chi^2_{\rm dof} = 0.85$), showing that no departure from sphericity is detected. A more quantitative assessment for the upper limit for such departure (some 1.5 km along the limb, as projected in the sky plane) is provided in the next subsection. A closer visual examination of the residuals for the strongest flashes with best SNR reveal, however, some minor and localised features, possibly due to atmospheric waves (Fig. 25), but no global departure from the spherical model.

There is another argument supporting the spherical nature of Triton's atmosphere. The centre of Triton's shadow, as determined by the simultaneous fit to all the flashes, while excluding the ingress and egress parts of the light curves, coincides to within 0.1 km with the shadow centre determined by a global fit to all 52 light curves, by excluding the central flashes but including the ingress and egress parts. This 0.1-km offset is not significant, considering that the global fit centre has a typical 1σ error of 1 km cross-track (Fig. 10). In other words, the centre of the central flash layer, which is sensitive to the 8-km altitude level, coincides with the global shadow centre, which is sensitive to the 60-km altitude level. It could be that both atmospheric levels are close to spherical, but displaced in the same way with respect to Triton's centre, but this configuration seems unlikely.

7.3. The central flash: limit on atmospheric distortions and winds

We now assess a possible departure of Triton's lower atmosphere from sphericity, restricting ourselves to the simple model of a globally oblate flash layer. Testing more complex shapes will be performed once Triton's 3D GCMs are available, something which is beyond the scope of this paper. Once projected in the sky plane, an oblate layer appears as an ellipse with apparent semi-major and semi-minor axes a' and b', respectively. The centres of curvature of that ellipse form a diamond-shaped caustic curve where abrupt flux variations are observed, see examples in Fig. 26. The equation of the caustic is (Elliot et al. 1977):

$$(a'x)^{2/3} + (b'y)^{2/3} = (a'^2 - b'^2)^{2/3}, \quad (4)$$

where Oxy is a Cartesian reference system whose origin O is fixed at the ellipse centre, and where Ox (resp. Oy) is aligned with a' (resp. b'). Since the flash layer lies at $\sim$ 8 km altitude, we have $a' \sim 1360$ km. Note that the orientations of the a' and b' axes are still to be specified.

We define the apparent oblateness of the flash layer as $\epsilon' = (a' - b')/a'$. We have explored values of ϵ' from zero (i.e. a spherical flash layer) to some maximum value, and tracked the corresponding variations of χ^2 stemming from a simultaneous fit to central flashes. In this study, only the central flashes of Varages, Calern, Constância, Le Beausset, and Felsina Obs. have been considered. The other stations are too far away from centrality and/or with lower quality to usefully constrain ϵ'. This is because the four cusps of the diamond-shaped caustic curve extend up to $\sim 2\epsilon' a$ from the shadow centre according to Equation 4. As we obtain upper limits of ~0.002 for ϵ' (see below), we have $2\epsilon' a <\sim 5$ km for $a \sim 1360$ km. Thus, only the immediate vicinity of the shadow centre (typically less than 20 km) is sensitive to departures from sphericity. More distant stations essentially probe flashes that are indistinguishable from a spherical solution.

We first assume that the semi-minor axis b' is aligned with Triton's pole. This corresponds to an oblate flash layer maintained by an axisymmetric zonal wind regime that has a constant angular velocity around that axis. By using the $\chi^2 < \chi^2_{\rm min} + 1$ (resp. $\chi^2 < \chi^2_{\rm min} + 9$) criterion, we find 1σ-level (resp. 3σ-level) upper limits of

$$\epsilon' < 0.0011 \ \ (\text{resp. } \epsilon' < 0.0014),$$

for the apparent oblateness of the flash layer. The flash intensity map corresponding to this limit is displayed in Fig. 26. This apparent oblateness must be "deprojected" to obtain the actual oblateness ϵ through the relation

$$\epsilon = 1 - \frac{\sqrt{(1-\epsilon')^2 - \sin^2 B}}{\cos B} \sim \frac{\epsilon'}{\cos^2(B)},$$

where $B = 40.5°$ S is the sub-observer latitude (Table 2), and where the approximation holds for $\epsilon' \ll 1$. Using $\epsilon' < 0.0011$, this yields a 1σ-level upper limit $\epsilon < 0.0019$ for the deprojected oblateness. This corresponds to a difference between the equatorial and polar radii r_e and r_p of the layer, respectively, of $r_{\rm e} - r_{\rm p} \sim 3$ km, using $r_e = a' = 1360$ km.

We assume that the flash layer shape is entirely supported by zonal winds. In particular, we assume the absence of a horizontal temperature gradient, so that the isobar level also corresponds to the isopycnic (constant density) layer. The radius r of the flash layer is given as a function of the latitude φ by the equation (Hubbard et al. 1993; Sicardy et al. 2006)

$$\frac{1}{r}\frac{dr}{d\varphi} = -\frac{f\cos(\varphi)\sin(\varphi)}{1 - f\cos^2(\varphi)},$$

where $f = rv^2(\varphi)/GM\cos^2(\varphi)$. This equation states that the isobar is locally perpendicular to the effective gravity field, where both the gravity field of the (spherical) body and centrifugal forces are accounted for. Introducing in that expression the polar equation of an oblate flash layer:

$$r = \frac{r_{\rm e} r_{\rm p}}{[r_{\rm e}^2 \sin^2(\varphi) + r_{\rm p}^2 \cos^2(\varphi)]^{1/2}},$$

we obtain to lowest order in $\epsilon = (r_{\rm e} - r_{\rm p})/r_e$ the velocity

$$v = \sqrt{\epsilon}\sqrt{\frac{2GM_T}{r_{\rm e}}}\cos\varphi \sim 1450\sqrt{\epsilon}\cos\varphi \ \ \text{m s}^{-1}, \quad (5)$$

the value of GM_T is listed in Table 2. Using $\epsilon < 0.0019$, this provides a 1σ-level upper limit for the zonal wind at the equator of $|v_{\rm e}| < 63$ m s^{-1}.

Note that this motion can be prograde (positive sign) or retrograde (negative sign), and that it is measured in an inertial frame. Thus, noting $v'_{\rm e}$ the zonal wind in a frame rotating with Triton (which thus measures the atmospheric circulation at that level), we have $v_{\rm e} = v'_{\rm e} + v_{\rm rot}$, where $v_{\rm rot} = 17$ m s^{-1} is the equatorial velocity stemming from Triton's rotation, see Fig. 22. Consequently, a retrograde zonal wind regime ($v'_{\rm e} < 0$) implies a 1σ limit $|v'_{\rm e}| < 63 + 17 = 80$ m s^{-1}, while a prograde regime ($v'_{\rm e} > 0$) implies $v'_{\rm e} < 63 - 17 = 46$ m s^{-1}. Those values are respectively 87 m s^{-1} and 53 m s^{-1} if the 3σ upper limit is considered.

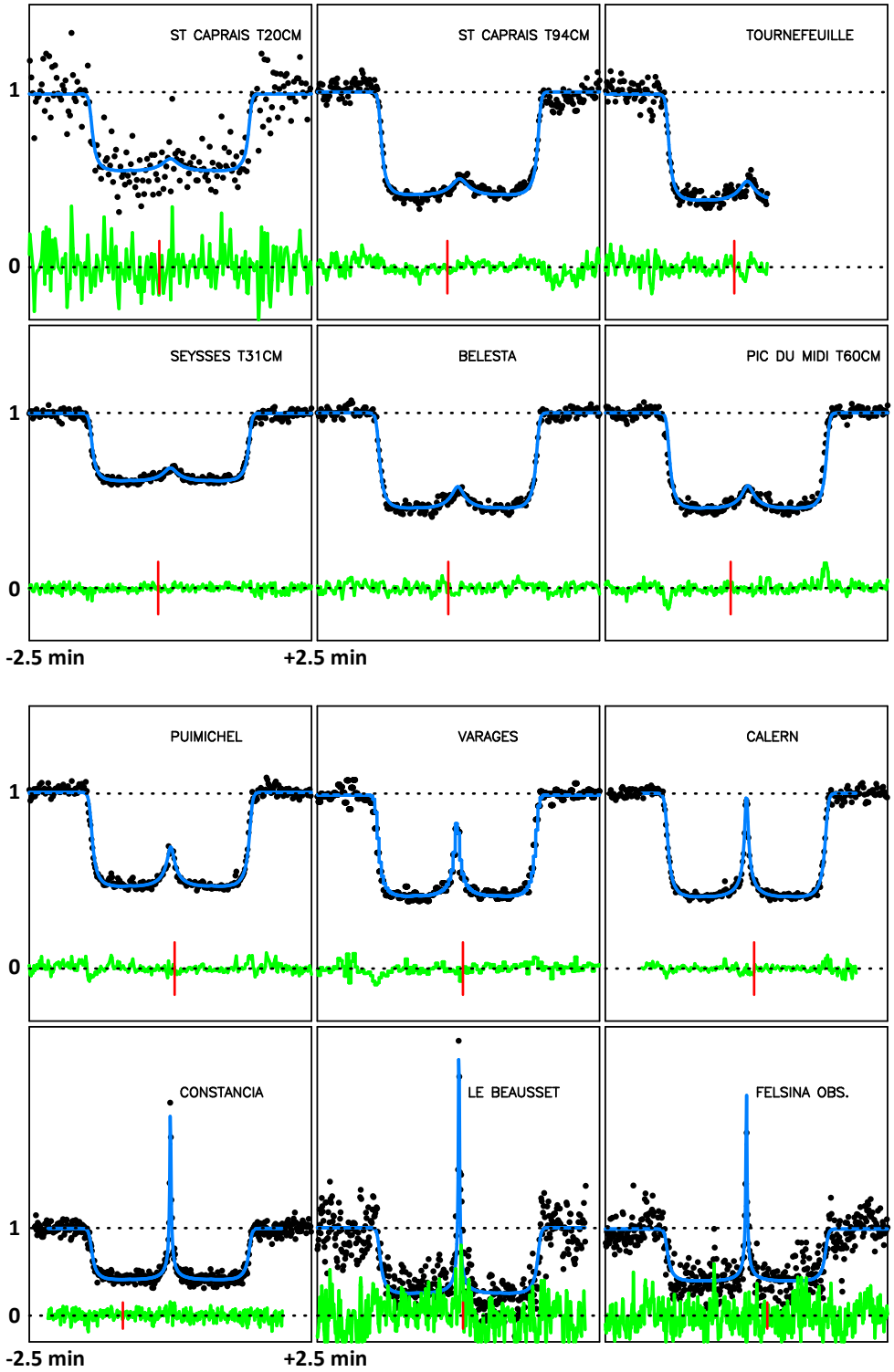

Fig. 23. Simultaneous fits of the data (black dots) by synthetic light curves (blue lines), based on the temperature profile displayed in Fig. 8 (black line) and the pressure boundary condition $p_{1400} = 1.18\,\mu$bar (Table 4). The green curves are the residuals of the fits. The lower and upper horizontal dotted lines mark the zero-flux level and the total star+Triton unocculted flux, respectively. Note also that the three bottom light curves are plotted at a different vertical scale from the others, to accommodate for the presence of a strong central flash. The stations are sorted from left to right and top to bottom from the northernmost track (St Caprais) to the southernmost track (Calar Alto, see next figure). Each panel has a duration of five minutes and is centred around the time of closest approach (or mid-occultation time) of the station to Triton's shadow centre, as indicated under the lower left panel in each block of six light curves. For reference, the vertical red line marks the time 23:48 UTC. The stations with exposure times smaller than 1 s have been smoothed to have a sampling time as close as possible close to 1 s, for easier SNR comparison of the various data sets. Note that in this approach, the sampling of the Constância, Le Beausset and Felsina Observatory light curves (0.64 s) is kept at its original value, so that full resolution versions of the corresponding strong flashes at those stations are displayed here. The same kind of plots showing all the stations, but with the flashes excluded from the fits, are displayed in Figs. B.1-B.5.

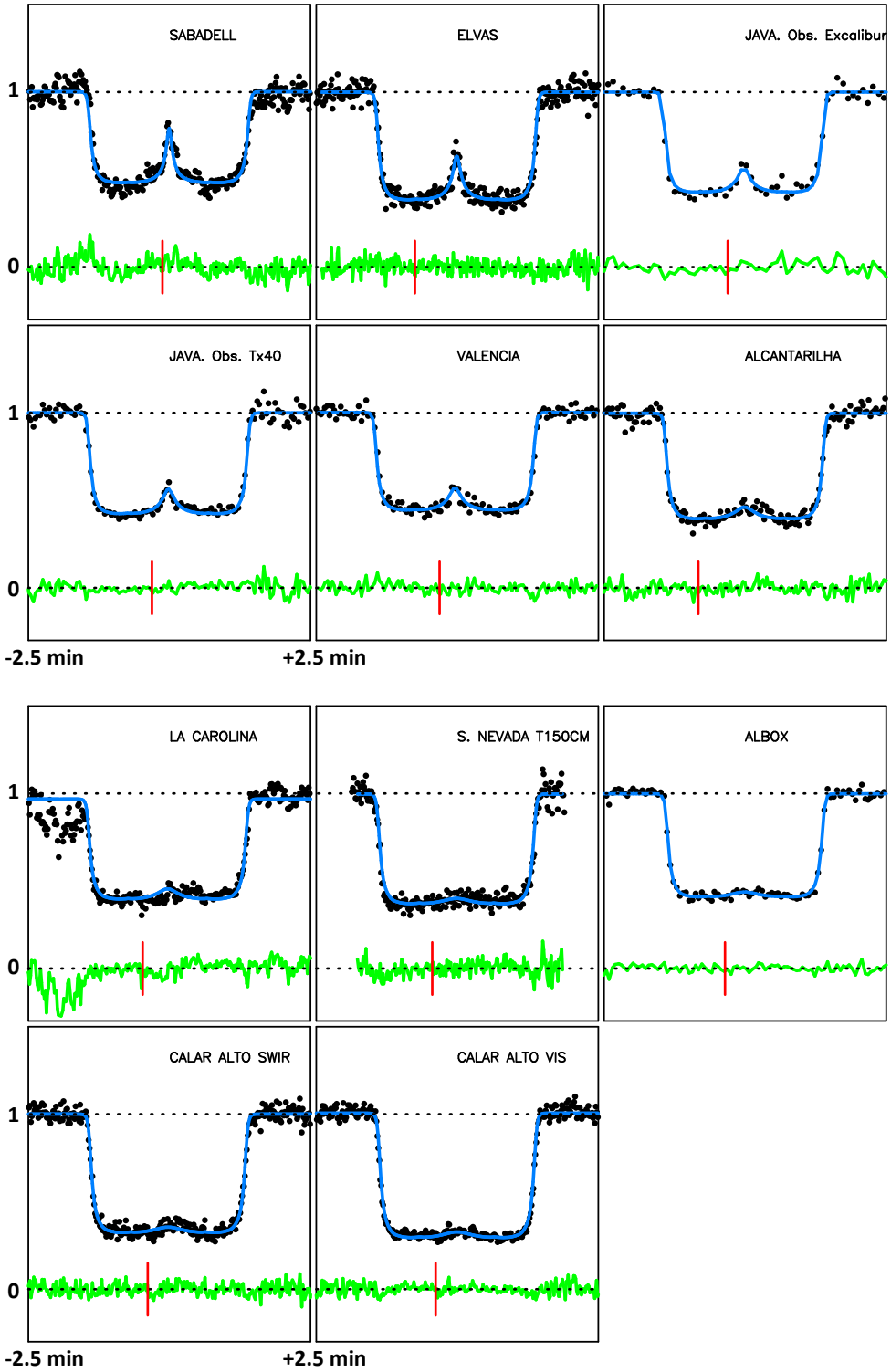

Fig. 24. Continuation of Fig. 23. NB. "JAVA." is the abbreviation of Javalambre, used so that the name of the station fits into the plot.

Information on the atmospheric circulation of Triton was obtained in 1989 by V2: while surface wind streaks suggested eastward surface winds between latitudes of 15° S and 45° S (Hansen et al. 1990), the deflection of plumes showed that in the atmosphere above, at 8 km near 49° S and 57° S, the wind was westward and prograde (Hansen et al. 1990; Yelle et al. 1995). On the basis of theoretical consideration, Ingersoll (1990) proposed that this could result from a temperature contrast between the cold frost-covered pole and the warm unfrosted equator. More realistic GCMs simulations, including the N_2 condensation-sublimation cycle, have been reported in Vangvichith (2013), and additional relevant simulations have been performed to explore the circulation on Pluto, which is similar to Triton in terms of rotation rate and atmospheric composition (see Forget et al. 2021 and reference therein). These models show that if N_2 significantly sublimes in the southern hemisphere and condenses in

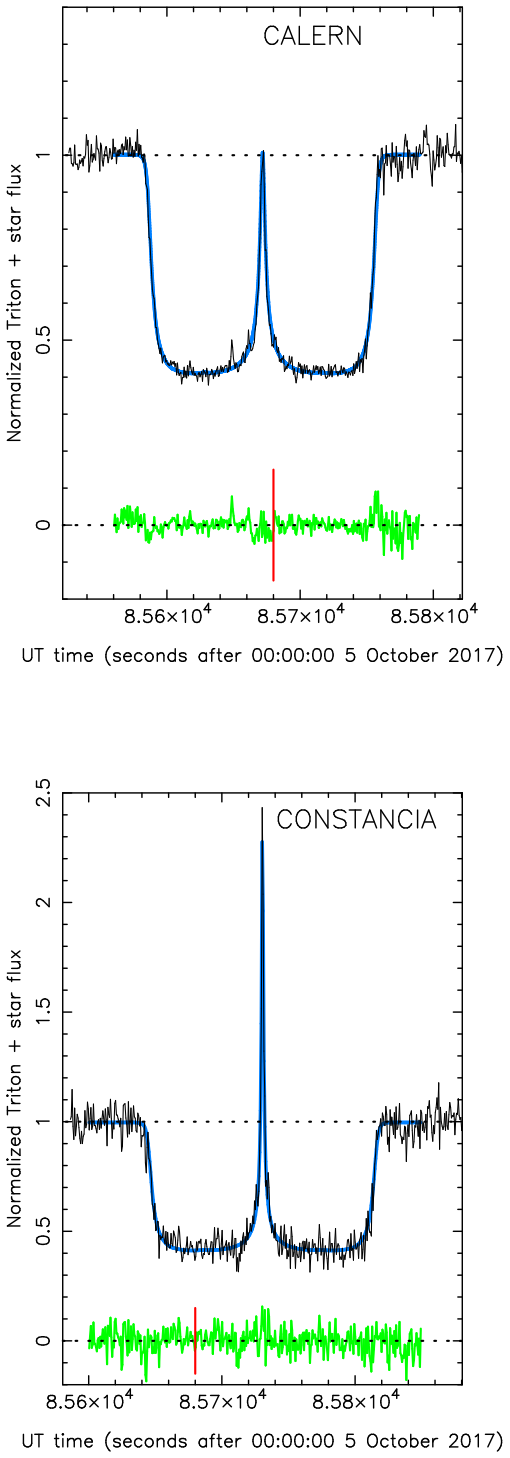

Fig. 25. More detailed views taken of the flashes observed at Calern (top panel) and Constância (bottom panel), with the same setup as in the previous figure.

the northern hemisphere, the circulation should be dominated by a retrograde circulation resulting from the conservation of angular momentum of the flow, with velocities that cannot be higher than the rotation of the planet (17 m s^{-1}). This is significantly less than the upper limits that we derive from our observations. In any case, as mentioned above, global retrograde winds were not observed in 1989: to get prograde rotation in the mid southern latitude as suggested by the V2 plume observations, the interhemispheric condensation must be weak. In that case a thermal gradient could create a weak prograde wind as suggested by Ingersoll (1990), reaching a few metres per second in GCM simulations. However, modelling Pluto suggests that in some conditions a regime of super-rotation (like on Venus or Titan) could occur (Forget et al. 2017). This could explain the plume direction on Triton. Such a superrotation is thought to initially result from the formation of a high-mid latitude jet (due to thermal balance between a warm equator and a colder pole, or condensation flow from low latitudes to the pole). Then barotropic waves can transport angular momentum to and from the equator and seriously accelerate the entire atmosphere. In their Pluto GCM, Forget et al. (2017) found mean equatorial zonal wind up to 15 m s^{-1}. However this could be model-dependant. It is not easy to set a theoretical limit to such a superrotation. Our upper limit on prograde wind near 50 m s^{-1} provides a constraint for such a hypothetical superrotation in 2017.

We have considered other orientations for the central flash layer, as projected in the sky plane, by relaxing the condition that b' should be aligned with Triton's pole. This might be the case if other causes of distortion than zonal winds are at work, e.g. tidal forces from Neptune or Triton's potential anomalies. Those orientations provide more stringent upper limits of the apparent oblateness ϵ' because the cusps of the caustic can then get closer to the paths of the central-most stations (Fig. 26). For instance, rotating the caustic by 45 degrees imposes the more stringent 1σ upper limit, $\epsilon < 0.00074$ (instead of 0.0019). This requires an equatorial wind of $\sim$ 40 m s^{-1}, which is still quite larger than the values $\sim$ 10 m s^{-1} expected from GCMs, and thus not a constraining limit as far as GCMs are concerned.

We now compare our upper limit for the deprojected oblateness of the central flash layer ($\epsilon < 0.0024$) with the value obtained by Elliot et al. (1997) from a single cut inside the central flash region during the 14 August 1995 occultation. Two solutions are considered by those authors, an oblate flash layer with $\epsilon = 0.042$ and a prolate one with $\epsilon = -0.032$. Adopting the $\epsilon = 0.042$ value, we obtain the central map displayed in the right panel of Fig. 26. This would imply the crossing of the caustic by the five stations shown in the map, and result in strong flux variations at those crossings that are not observed in the data, see Fig. 25. A similar conclusion would be drawn by adopting the prolate value $\epsilon = -0.032$ of Elliot et al. (1997). Note that the closest approach distance to the shadow centre during the central observation flash of 1995 was about 100 km, i.e. well outside the diamond-shaped caustic displayed in the right panel of Fig. 26. Thus, caustic crossings could not be tested at that epoch.

The main problem of the large oblateness values obtained by Elliot et al. (1997) is that they imply unrealistically large wind velocities to maintain such distortions. For instance, taken at face value, $\epsilon = 0.042$ results in an equatorial wind velocity of $v_e \sim 300$ m s^{-1}, more than twice the sonic velocity near Triton's surface ($\sim$ 130 m s^{-1} at $\sim$ 40 K), and much larger than predicted by GCMs, see above. A possibility considered by Elliot et al. (1997) was that Triton's atmospheric distortion was restricted to mid-latitude regions, i.e. were local rather than global. This permits lower values of wind speeds (110-170 m s^{-1}) depending on whether prolate or oblate solutions are considered. This is still essentially supersonic and not expected from circulation models. Moreover, this distortion would also be detected in our data set which densely sampled the central flash region.

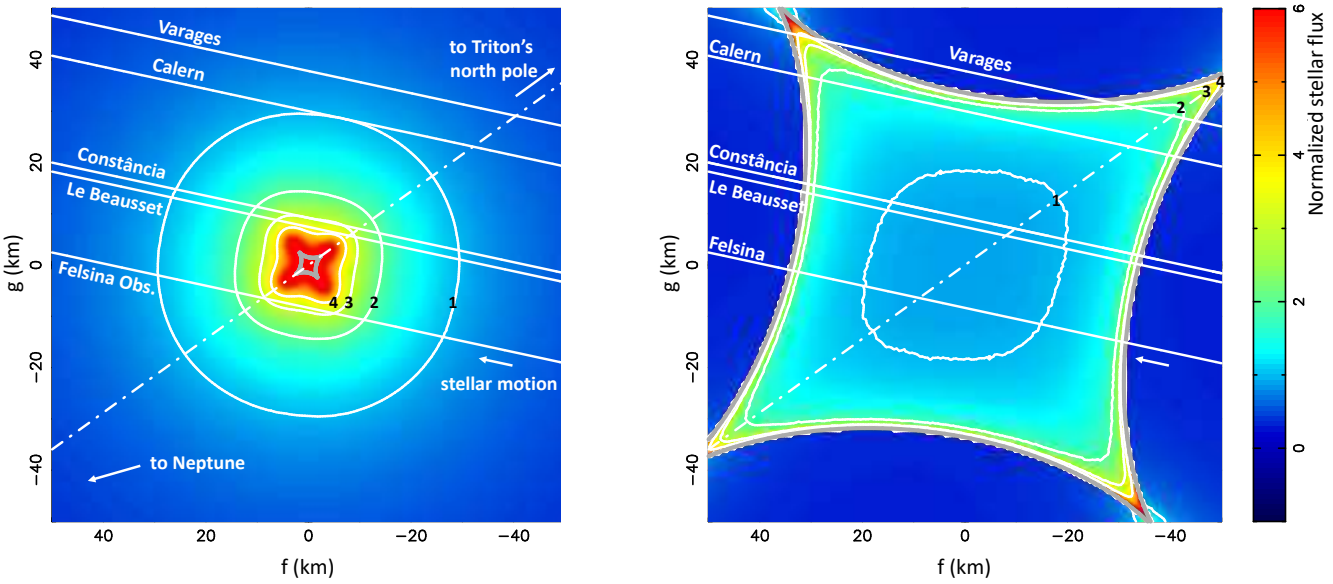

Fig. 26. *Left panel:* The map of the central flash intensity, adopting the 1σ upper limit $\epsilon' = 0.0011$ for the apparent oblateness of the flash layer (corresponding to a deprojected oblateness $\epsilon = 0.0019$), see text for details. The black labels along the iso-intensity contours (in curves) indicate the received stellar flux in units of its unocculted value. The grey diamond-shaped feature near the centre is the caustic curve described by Eq. 4 and corresponding to $\epsilon' = 0.0011$. In the case considered here, the flash layer is assumed to be aligned with the apparent direction of Triton's poles, indicated by the dash-dotted line. Neptune's direction is determined from the position angle 286° of Triton with respect to the planet at the moment of the occultation. *Right panel:* The same, adopting the oblate solution $\epsilon = 0.042$ found by Elliot et al. (1997) from the shape of a central flash observed during the 14 August 1995 occultation.

An alternative explanation proposed by Elliot et al. (1997) is the presence of hazes that absorbed part of the stellar flux at some specific locations along Triton's limb, thus altering the central flash shape. However, according to those authors, neither the optical depth obtained for those hazes at the corresponding altitude levels, nor its dependence with wavelength, were consistent with the V2 results. The haze problem is discussed in more detail in Section 8.

Finally, the shape of Triton's solid body as observed in V2 images indicates an oblateness smaller than 0.0014 (Thomas 2000), which is too small to explain the claimed distortions. Moreover, non-radial components of Triton's inner gravitational field might also cause atmospheric distortions, but they would then be permanent and thus, should be observed also in 2017.

From all this, we conclude that the large oblatenesses reported by Elliot et al. (1997) are both theoretically unexpected and inconsistent with our observations.

At this point, we think that the mismatches between the flash models and its observation in 1995 (as well as small departures from our spherical model in Fig. 25) could be caused by small local corrugations of the flash layer induced by gravity waves. As the caustic is the locus of the limb centre of curvatures, its shape is very sensitive to local (but small) corrugations of that layer. Examples of such effects have been investigated for explaining flash shapes in the cases of stellar occultations by Neptune (Hubbard et al. 1988) and Titan (Sicardy et al. 2006). As mentioned earlier, this approach remains beyond the scope of this paper, as long as zonal wind and gravity wave regimes are not available for Triton's lower atmosphere.

8. Pending issues

8.1. Hazes

In the present work, we assumed that Triton's atmosphere is clear, i.e. free of absorbing material. However, V2 observations in 1989 revealed two kind of absorbing features in the lower atmosphere: hazes and clouds. These features were detected in the visible through the imaging system (Rages & Pollack 1992) and during the UV occultation experiment (Krasnopolsky et al. 1992, 1993; Krasnopolsky & Cruikshank 1995).

The general picture that emerges from the V2 observations is reviewed in Yelle et al. (1995) and is described as follows: hazes are detected up to an altitude of about 30 km, they were observed around the entire Triton's limb, except for a small clear region near east longitude 280° and between latitudes 4 and 18° S. Thus, unless drastic changes in haze formation occurred, they should also be present during our observation of 5 October 2017. Clouds are observed closer to the surface compared to hazes, i.e. below an altitude level of about 8 km. Contrary to hazes, they exhibit a more patchy distribution along the limb.

Due to their low altitudes, absorbing materials should be best detected in the central flash structures, caused by a layer at about 8 km altitude. Estimation of the integrated (down to the surface) vertical optical depth of the hazes at 0.47 μm is $\tau_{\rm vis} = 0.005 \pm 0.001$, with a typical scale height of $H_{\rm h} \sim 12$ km (Krasnopolsky et al. 1993; Rages & Pollack 1992). Thus, the integrated vertical optical depth down to the 8 km altitude level should be reduced by a factor of $\exp(-8/H_{\rm h}) \sim 0.5$. Moreover, the slant (along the line-of-sight) optical depth is amplified by a factor of $\sqrt{2\pi R_T/H_{\rm h}} \sim 27$, yielding a slant optical depth of hazes at 8 km in the order of $0.005\ \sqrt{2\pi R_T/H_{\rm h}}\ \exp(-8/H_{\rm h}) \sim 0.07$, and a reduction of the flash amplitude by 5-10% if no changes occurred since 1989.

Clouds are much denser than hazes, with vertical optical depth to the surface of 0.1 or higher. Cloud particles have a vertical distribution with a scale height H_c comparable to or larger than the atmospheric scale height (about 20 km). Thus, the slant optical depth of clouds at 8 km should be in the order of $0.1\ \sqrt{2\pi R_T/H_c}\ \exp(-8/H_c)\ \sim\ 1.4$ or larger, corresponding to a decrease of the flash amplitude by a factor of 4 or more.

To summarize, hazes are expected to have a mild effect on the central flash heights, with an expected reduction of only 5-10%. We do not see any departure from the model at that level on the best flash profiles. Moreover, we do not detect trends on the observed flash amplitudes vs. wavelength. For instance, the strong flash at Constância (Fig. 25) observed at an effective wavelength of ∼0.6 μm agrees with the model at the same satisfaction level as the Varages flash, observed at ∼1.3 μm (Fig. 23). The same is true with the Calar Alto observation, that was made simultaneously in the visible (0.4-1.0 μm) and the near IR (1.0-1.7 μm), see Fig. 24 and Table 5. A flash is observed at that station, but it is too faint to reveal a difference between the two channels. Finally, the dual observation made at Kryoneri (R and I bands) was too far away from the centre line to show a central flash, but does not show significant differences anyway in the fits by the synthetic light curve (Fig. B.5).

Taken at face value, these results indicate that hazes have no detectable effect on the flash shapes. This result is true *a fortiori* for the clouds, that would reduce the flash amplitudes by a factor of 4 or greater which is not observed in the data. In other words, our model consistently explains all the flashes using a clear atmosphere.

However, a difficulty arises at this point since the height of the flash actually depends on the assumed template temperature profile. In order to disentangle the haze vs. temperature effects, independent information on the thermal profile of the lower atmosphere is required. This requirement could be met with the ALMA results reported by Gurwell et al. (2019). This issue remains, for the moment, beyond the scope of the present paper.

8.2. Troposphere

Yelle et al. (1991) inferred a troposphere from the V2 observations of geysers and clouds. We do not observe this, as our deepest layer probed, at the central flash level, which coincides with the expected altitude of the tropopause. Therefore, our model is consistent with our central flashes, as discussed in Section 7, and there is no need to include a troposphere to accommodate for the data. However, this does not mean that we can exclude a troposphere as we do not have information down to this part of the lower atmosphere.

The absorption, caused by hazes and clouds, impacts our data and the model. For a troposphere to be included, we need independent measurements of the lower atmosphere.

8.3. Gravity waves

In Section 7 and Fig. 25 we mention that the residuals in these light curves show minor features that are probably attributed to atmospheric waves. They present themselves as small fluctuations, with little effect on the overall light curve shape, and therefore we did not study them in detail. This topic needs further analysis that is beyond the scope of the present paper.

8.4. ϕ_0 of inverted profiles

The determinations of the baseline levels ϕ_0 used for inverting the profiles of La Palma and Helmos remain an open issue, as they provide inconsistent results in the deepest parts of the $T(r)$ profiles (Appendix A.2). This matter must be analysed further and needs independent results, in particular from ALMA, to confirm which ϕ_0 should be used.

9. Concluding remarks

In this paper, we present results obtained from the ground-based stellar occultation by Triton observed on 5 October 2017. The main goals were (*i*) retrieve the general structure of Triton's atmosphere between altitude levels of ∼8 km (∼9 μbar) and ∼190 km (few-nanobar level) and (*ii*) compare these results with other ground-based occultations and the Voyager 2 radio occultation, to assess a pressure seasonal variation in the last three decades.

The 2017 event yielded 90 positive observations, 42 showing a central flash. We used Abel inversions to retrieve density, pressure, and temperature profiles from our three best SNR light curves. We find a hint of a mild negative temperature gradient (reaching -0.2 K km^{-1}) at the deepest part of our profiles, i.e. below the altitude ∼30 km. This constitutes a mesosphere just above an expected stratosphere with a positive temperature gradient that connects the atmosphere to the cold surface.

A ray-tracing approach was used to a global fit to the best 52 light-curves, providing a pressure $p_{1400} = 1.18 \pm 0.03$ μbar at radius 1400 km. It also provides a synthetic and smoothed model to extrapolate the density, pressure, and temperature down to the surface.

A new analysis of the V2 radio experiment, with useful information extracted from the surface up to around 1400 km, shows that the pressure retrieved in the 2017 event is consistent with the pressure obtained in 1989.

A survey of pressure values obtained between 1989 and 2017 was conducted. The two past occultations (in 1997 and 2008), reanalyzed using our methods, indicate that the surface pressure reported in the 1990's is real, but remains debatable due to the scarcity of high SNR light curves and the lack of a fully consistent analysis of the best data sets used by other teams.

The pressure that we obtain from the 2017 occultation is consistent with that derived from the Voyager radio experiment, meaning that the pressure is back to its level of 1989. Results from a volatile transport model (VTM) of Triton, described in detail in a paper by Bertrand et al. (2022), do not support a strong increase of surface pressure in the last decades, but instead a modest increase with a surface pressure reaching up to 20 μbar in the intervening 28 years. The VTM simulations also suggest that (1) a strong increase in surface pressure before 2000 cannot be obtained if N2 is present between latitude 30° S - 0°, and (2) a northern polar cap should extend down to at least 45° N - 60° N in 2017 to have the surface pressure back at the V2 level of 1989.

Finally, the central flash analysis does not reveal any evidence of an atmospheric distortion. The atmosphere appears as globally spherical, with a 1σ upper limit of 0.0011 for its apparent oblateness near the 8 km altitude. This corresponds to a global difference of less than 1.5 km between the largest and smallest atmospheric radii at that altitude. This is much smaller than values reported in the literature. In particular, this does not support the existence of supersonic winds previously claimed by Elliot et al. (1997).

Open issues, requiring a more specific analysis of our data set, will be addressed elsewhere. This includes the possible presence (or absence) of hazes and of a troposphere just above Triton's surface, as well as the possible detection of gravity waves.

Acknowledgements. J.M.O. acknowledges financial support from the Portuguese Foundation for Science and Technology (FCT) and the European Social Fund (ESF) through the PhD grant SFRH/BD/131700/2017. The work leading to these results has received funding from the European Research Council under the European Community's H2020 2014-2021 ERC grant Agreement n° 669416 "Lucky Star". We thank S. Para who supported some travels to observe the 5 October 2017 occultation. T.B. was supported for this research by an appointment to the National Aeronautics and Space Administration (NASA) Post-Doctoral Program at the Ames Research Center administered by Universities Space Research Association (USRA) through a contract with NASA. We acknowledge useful exchanges with Mark Gurwell on the ALMA CO observations. This work has made use of data from the European Space Agency (ESA) mission *Gaia* (`https://www.cosmos.esa.int/gaia`), processed by the *Gaia* Data Processing and Analysis Consortium (DPAC, `https://www.cosmos.esa.int/web/gaia/dpac/consortium`). Funding for the DPAC has been provided by national institutions, in particular the institutions participating in the *Gaia* Multilateral Agreement. J.L.O., P.S.-S., N.M. and R.D. acknowledges financial support from the State Agency for Research of the Spanish MCIU through the "Center of Excellence Severo Ochoa" award to the Instituto de Astrofísica de Andalucía (SEV-2017-0709), they also acknowledge the financial support by the Spanish grant AYA-2017-84637-R and the Proyecto de Excelencia de la Junta de Andalucía J.A. 2012-FQM1776. The research leading to these results has received funding from the European Union's Horizon 2020 Research and Innovation Programme, under Grant Agreement no. 687378, as part of the project "Small Bodies Near and Far" (SBNAF). P.S.-S. acknowledges financial support by the Spanish grant AYA-RTI2018-098657-J-I00 "LEO-SBNAF". The work was partially based on observations made at the Laboratório Nacional de Astrofísica (LNA), Itajubá-MG, Brazil. The following authors acknowledge the respective CNPq grants: F.B.-R. 309578/2017-5; R.V.-M. 304544/2017-5, 401903/2016-8; J.I.B.C. 308150/2016-3 and 305917/2019-6; M.A. 427700/2018-3, 310683/2017-3, 473002/2013-2. This study was financed in part by the Coordenação de Aperfeiçoamento de Pessoal de Nível Superior - Brasil (CAPES) - Finance Code 001 and the National Institute of Science and Technology of the e-Universe project (INCT do e-Universo, CNPq grant 465376/2014-2). G.B.R. acknowledges CAPES-FAPERJ/PAPDRJ grant E26/203.173/2016 and CAPES-PRINT/UNESP grant 88887.571156/2020-00, M.A. FAPERJ grant E-26/111.488/2013 and A.R.G.Jr. FAPESP grant 2018/11239-8. B.E.M. thanks CNPq 150612/2020-6 and CAPES/Cofecub-394/2016-05 grants. Part of the photometric data used in this study were collected in the frame of the photometric observations with the robotic and remotely controlled telescope at the University of Athens Observatory (UOAO; Gazeas 2016). The 2.3 m Aristarchos telescope is operated on Helmos Observatory by the Institute for Astronomy, Astrophysics, Space Applications and Remote Sensing of the National Observatory of Athens. Observations with the 2.3 m Aristarchos telescope were carried out under OPTICON programme. This project has received funding from the European Union's Horizon 2020 research and innovation programme under grant agreement No 730890. This material reflects only the authors views and the Commission is not liable for any use that may be made of the information contained therein. The 1.2 m Kryoneri telescope is operated by the Institute for Astronomy, Astrophysics, Space Applications and Remote Sensing of the National Observatory of Athens. The Astronomical Observatory of the Autonomous Region of the Aosta Valley (OAVdA) is managed by the Fondazione Clément Fillietroz-ONLUS, which is supported by the Regional Government of the Aosta Valley, the Town Municipality of Nus and the "Unité des Communes valdôtaines Mont-Émilius". The 0.81 m Main Telescope at the OAVdA was upgraded thanks to a Shoemaker NEO Grant 2013 from The Planetary Society. D.C. and J.M.C. acknowledge funds from a 2017 'Research and Education' grant from Fondazione CRT-Cassa di Risparmio di Torino. P.M. acknowledges support from the Portuguese Fundação para a Ciência e a Tecnologia ref. PTDC/FISAST/29942/2017 through national funds and by FEDER through COMPETE 2020 (ref. POCI010145 FEDER007672). F.J. acknowledges Jean Luc Plouvier for his help. S.J.F. and C.A. would like to thank the UCL student support observers: Helen Dai, Elise Darragh-Ford, Ross Dobson, Max Hipperson, Edward Kerr-Dineen, Isaac Langley, Emese Meder, Roman Gerasimov, Javier Sanjuan, and Manasvee Saraf. We are grateful to the CAHA, OSN and La Hita Observatory staffs. This research is partially based on observations collected at Centro Astronómico Hispano-Alemán (CAHA) at Calar Alto, operated jointly by Junta de Andalucía and Consejo Superior de Investigaciones Científicas (IAA-CSIC). This research was also partially based on observation carried out at the Observatorio de Sierra Nevada (OSN) operated by Instituto de Astrofísica de Andalucía (CSIC). This article is also based on observations made with the Liverpool Telescope operated on the island of La Palma by Liverpool John Moores University in the Spanish Observatorio del Roque de los Muchachos of the Instituto de Astrofisica de Canarias with financial support from the UK Science and Technology Facilities Council. Partially based on observations made with the Tx40 and Excalibur telescopes at the Observatorio Astrofísico de Javalambre in Teruel, a Spanish Infraestructura Cientifico-Técnica Singular (ICTS) owned, managed and operated by the Centro de Estudios de Física del Cosmos de Aragón (CEFCA). Tx40 and Excalibur are funded with the Fondos de Inversiones de Teruel (FITE). A.R.R. would like to thank Gustavo Román for the mechanical adaptation of the camera to the telescope to allow for the observation to be recorded. R.H., J.F.R., S.P.H. and A.S.L. have been supported by the Spanish projects AYA2015-65041-P and PID2019-109467GB-100 (MINECO/FEDER, UE) and Grupos Gobierno Vasco IT1366-19. Our great thanks to Omar Hila and their collaborators in Atlas Golf Marrakech Observatory for providing access to the T60cm telescope. TRAPPIST is a project funded by the Belgian Fonds (National) de la Recherche Scientifique (F.R.S.-FNRS) under grant PDR T.0120.21. TRAPPIST-North is a project funded by the University of Liège, and performed in collaboration with Cadi Ayyad University of Marrakesh. E.J. is a FNRS Senior Research Associate.

References

Assafin, M., Camargo, J. I. B., Vieira Martins, R., et al. 2010, A&A, 515, A32
Assafin, M., Camargo, J. I. B., Vieira Martins, R., et al. 2012, A&A, 541, A142
Assafin, M., Vieira-Martins, R., Braga-Ribas, F., et al. 2009, AJ, 137, 4046
Assafin, M., Vieira Martins, R., Camargo, J. I. B., et al. 2011, in Gaia follow-up network for the solar system objects : Gaia FUN-SSO workshop proceedings, 85–88
Bertrand, T., Lellouch, E., Holler, B. J., et al. 2022, Icarus, 373, 114764
Buratti, B. J., Bauer, J. M., Hicks, M. D., et al. 2011, Icarus, 212, 835
Camargo, J. I. B., Magalhães, F. P., Vieira-Martins, R., et al. 2015, A&A, 582, A8
Camargo, J. I. B., Vieira-Martins, R., Assafin, M., et al. 2014, A&A, 561, A37
Conrath, B., Flasar, F. M., Hanel, R., et al. 1989, Science, 246, 1454
Cruikshank, D. P. & Silvaggio, P. M. 1979, ApJ, 233, 1016
Davies, M. E., Abalakin, V. K., Bursa, M., et al. 1996, Celestial Mechanics and Dynamical Astronomy, 63, 127
Dias-Oliveira, A., Sicardy, B., Lellouch, E., et al. 2015, ApJ, 811, 53
Elliot, J. L., French, R. G., Dunham, E., et al. 1977, ApJ, 217, 661
Elliot, J. L., Person, M. J., McDonald, S. W., et al. 2000a, Icarus, 148, 347
Elliot, J. L., Person, M. J., & Qu, S. 2003, AJ, 126, 1041
Elliot, J. L., Stansberry, J. A., Olkin, C. B., Agner, M. A., & Davies, M. E. 1997, Science, 278, 436
Elliot, J. L., Strobel, D. F., Zhu, X., et al. 2000b, Icarus, 143, 425
Forget, F., Bertrand, T., Hinson, D., & Toigo, A. 2021, in Pluto System After New Horizons
Forget, F., Bertrand, T., Vangvichith, M., et al. 2017, Icarus, 287, 54, special Issue: The Pluto System
Fray, N. & Schmitt, B. 2009, Planet. Space Sci., 57, 2053
Gaia Collaboration, Brown, A. G. A., Vallenari, A., et al. 2018, A&A, 616, A1
Gaia Collaboration, Prusti, T., de Bruijne, J. H. J., et al. 2016, A&A, 595, A1
Gazeas, K. 2016, in Revista Mexicana de Astronomia y Astrofisica Conference Series, Vol. 48, 22–23
Gomes-Júnior, A. R., Assafin, M., Vieira-Martins, R., et al. 2015, A&A, 580, A76
Grundy, W. M., Schmitt, B., & Quirico, E. 1993, Icarus, 105, 254
Gurrola, E. M. 1995, PhD thesis, Stanford University.
Gurwell, M., Lellouch, E., Butler, B., et al. 2019, in EPSC-DPS Joint Meeting 2019, Vol. 2019, EPSC–DPS2019–806
Hansen, C. J., McEwen, A. S., Ingersoll, A. P., & Terrile, R. J. 1990, Science, 250, 421
Herbert, F. & Sandel, B. R. 1991, J. Geophys. Res., 96, 19241
Hinson, D. P., Linscott, I. R., Young, L. A., et al. 2017, Icarus, 290, 96
Hubbard, W. B., Lellouch, E., Sicardy, B., et al. 1988, ApJ, 325, 490
Hubbard, W. B., Sicardy, B., Miles, R., et al. 1993, A&A, 269, 541
Ingersoll, A. P. 1990, Nature, 344, 315
Krasnopolsky, V. A. 1993, J. Geophys. Res., 98, 17123
Krasnopolsky, V. A. & Cruikshank, D. P. 1995, J. Geophys. Res., 100, 21271
Krasnopolsky, V. A., Sandel, B. R., & Herbert, F. 1992, J. Geophys. Res., 97, 11695
Krasnopolsky, V. A., Sandel, B. R., Herbert, F., & Vervack, R. J. 1993, J. Geophys. Res., 98, 3065
Lellouch, E., de Bergh, C., Sicardy, B., Ferron, S., & Käufl, H. U. 2010, A&A, 512, L8
Lellouch, E., Gurwell, M., Butler, B., et al. 2017, Icarus, 286, 289
McKinnon, W. B., Lunine, J. I., & Banfield, D. 1995, in Neptune and Triton, 807–877
Merlin, F., Lellouch, E., Quirico, E., & Schmitt, B. 2018, Icarus, 314, 274
Meza, E., Sicardy, B., Assafin, M., et al. 2019, A&A, 625, A42

Ohno, K., Zhang, X., Tazaki, R., & Okuzumi, S. 2020, arXiv e-prints, arXiv:2012.11932
Olkin, C. B., Elliot, J. L., Hammel, H. B., et al. 1997, Icarus, 129, 178
Rages, K. & Pollack, J. B. 1992, Icarus, 99, 289
Schmude, Richard W., J., Baker, R. E., Fox, J., et al. 2016, arXiv e-prints, arXiv:1604.00518
Sicardy, B., Colas, F., Widemann, T., et al. 2006, Journal of Geophysical Research (Planets), 111, E11S91
Sicardy, B., Ferri, F., Roques, F., et al. 1999, Icarus, 142, 357
Spencer, J. R. & Moore, J. M. 1992, Icarus, 99, 261
Strobel, D. F. & Summers, M. E. 1995, in Neptune and Triton, 1107–1148
Strobel, D. F., Summers, M. E., Herbert, F., & Sandel, B. R. 1990, Geophys. Res. Lett., 17, 1729
Strobel, D. F. & Zhu, X. 2017, Icarus, 291, 55
Thomas, P. C. 2000, Icarus, 148, 587
Tryka, K. A., Brown, R. H., Anicich, V., Cruikshank, D. P., & Owen, T. C. 1993, Science, 261, 751
Tyler, G. L., Sweetnam, D. N., Anderson, J. D., et al. 1989, Science, 246, 1466
van Belle, G. T. 1999, PASP, 111, 1515
Vangvichith, M. 2013, PhD thesis, Ecole Polytechnique France, available online at http://www.sudoc.fr/17695547X
Vapillon, L., Combes, M., & Lecacheux, J. 1973, A&A, 29, 135
Washburn, E. W. 1930, International Critical Tables of Numerical Data: Physics, Chemistry and Technology, Vol. 7 (McGraw-Hill, New York)
Yelle, R. V., Lunine, J. I., & Hunten, D. M. 1991, Icarus, 89, 347
Yelle, R. V., Lunine, J. I., Pollack, J. B., & Brown, R. H. 1995, in Neptune and Triton, 1031–1105
Young, L. A., Kammer, J. A., Steffl, A. J., et al. 2018, Icarus, 300, 174
Zacharias, N., Finch, C. T., Girard, T. M., et al. 2013, AJ, 145, 44

[1] LESIA, Observatoire de Paris, Université PSL, CNRS, Sorbonne Université, 5 place Jules Janssen, 92190 Meudon, France
e-mail: Joana.Oliveira@obspm.fr
[2] UNESP - São Paulo State University, Grupo de Dinâmica Orbital e Planetologia, Guaratinguetá, SP, 12516-410, Brazil
[3] Laboratório Interinstitucional de e-Astronomia - LIneA, Rua Gal. José Cristino 77, Rio de Janeiro, RJ, 20921-400, Brazil
[4] Instituto de Astrofísica de Andalucía (IAA-CSIC). Glorieta de la Astronomía s/n. 18008-Granada, Spain
[5] Departments of Earth & Planetary Sciences and Physics & Astronomy, Johns Hopkins University, 3400 N. Charles Street, Baltimore, MD 21218, United States
[6] National Aeronautics and Space Administration (NASA), Ames Research Center, Space Science Division, Moffett Field, CA 94035, USA
[7] Laboratoire de Météorologie Dynamique, IPSL, Université PSL, CNRS, Sorbonne Université, 4 place Jussieu, 75005 Paris, France
[8] Institut Polytechnique des Sciences Avancées IPSA, 63 boulevard de Brandebourg, F-94200 Ivry-sur-Seine, France
[9] IMCCE/Observatoire de Paris, Université PSL, CNRS, Sorbonne Université, Univ. Lille - 77 Avenue Denfert Rochereau, 75014 Paris, France
[10] Université Côte d'Azur, Observatoire de la Côte d'Azur, CNRS, Laboratoire Lagrange, Bd de l'Observatoire, CS 34229, 06304, Nice cedex 4, France
[11] Departamento de Astronomía, Universidad de Chile, Camino del Observatorio 1515, Las Condes, Santiago, Chile
[12] Comisión Nacional de Investigación y Desarrollo Aeroespacial del Perú - CONIDA
[13] Observatorio Astronómico de Moquegua
[14] naXys, University of Namur, 8 Rempart de la Vierge, Namur, B-5000, Belgium
[15] Florida Space Institute, University of Central Florida, 12354 Research Parkway, Partnership 1, Orlando, FL, USA
[16] Federal University of Technology-Paraná (UTFPR / DAFIS), Curitiba, Brazil
[17] Observatório Nacional/MCTIC, Rio de Janeiro, Brazil
[18] Universidade Federal do Rio de Janeiro - Observatório do Valongo, Ladeira Pedro Antônio 43, CEP 20.080-090 Rio de Janeiro - RJ, Brazil
[19] Polo Educacional Sesc, Av. Ayrton Senna, 5677, Jacarepaguá, Rio de Janeiro CEP 22775-004, Brazil
[20] Université de Lille, Observatoire de Lille, 1, impasse de l'Observatoire, F-59000 Lille, France
[21] Dpto. Física Aplicada, Escuela de Ingeniería de Bilbao, Universidad del País Vasco (UPV/EHU), Plaza Ingeniero Torres Quevedo 1, 48013, Bilbao, Spain
[22] Internationale Amateursternwarte (IAS) e. V., Mittelstr. 6, D-15749 Mittenwalde, Germany
[23] International Occultation Timing Association - European Section (IOTA/ES), Am Brombeerhag 13, D-30459 Hannover, Germany
[24] Trans-Tasman Occultation Alliance (TTOA) P.O. Box 2241, Wellington, New Zealand
[25] International Occultation Timing Association (IOTA), PO Box 7152, Kent, WA 98042, USA
[26] Vereinigung der Sternfreunde e.V. (VdS)
[27] Club Eclipse
[28] DOA
[29] Archenhold Sternwarte, Alt-Treptow 1, 12435 Berlin, Germany
[30] British Astronomical Association, Burlington House, Piccadilly, London, W1J 0DU, UK
[31] European Space Agency ESA, ESTEC SCI-S, Keplerlaan 1, NL 2201 AZ Noordwijk, The Netherlands
[32] Section of Astrophysics, Astronomy and Mechanics, Department of Physics, National and Kapodistrian University of Athens, GR-15784, Zografos, Athens, Greece
[33] Hellenic Amateur Astronomy Association, Athens, Greece
[34] Armagh Observatory and Planetarium, Northern Ireland, UK
[35] Institute for Astronomy, Astrophysics, Space Applications and Remote Sensing, National Observatory of Athens, P. Penteli, GR-15236 Athens, Greece
[36] Department of Physics, University of Crete, GR-71003 Heraklion, Greece
[37] Institute of Astrophysics, Foundation for Research and Technology-Hellas, GR-70013 Heraklion, Greece
[38] Astronomical Institute of the Czech Academy of Sciences, Fričova 298, 25165 Ondřejov, Czech Republic
[39] Sternwarte Stuttgart, Germany
[40] Hieronymusstr. 15b, 81241 Munich/München, Germany
[41] Astronomische Arbeitsgemeinschaft Wanne-Eickel / Herne e.V.
[42] Observatory: Sternwarte Zollern-Alb, Rosenfeld-Brittheim e.V., Germany
[43] AVV (Astronomische Vereinigung Vulkaneifel) Astronomical Society Volcano Eifel
[44] Department of Physics, Ariel University, Ariel, 40700, Israel
[45] Hamburger Sternwarte, Gojenbergsweg 112, 21029 Hamburg, Germany
[46] Selztal Observatory
[47] Bochumer Herbsttagung der Amateuratsronomen (BoHeTa)
[48] Gesellschaft für volkstümliche Astronomie e.V. Hamburg, Hamerichstraße 5, 22605 Hamburg, Germany
[49] Gruppo Astrofili Massesi, EURASTER
[50] Astronomical Observatory of the Autonomous Region of the Aosta Valley, Nus (AO) I-11020 Italy
[51] Mount Agliale Observatory
[52] AAB - Associazione Astrofili Bolognesi, Bologna, Italy
[53] INAF - Osservatorio Astrofisico di Catania, Via S. Sofia 78, 95123 Catania, Italy
[54] via Radicosa 44, 80051 Agerola, Italy
[55] Associazione Astrofili Aurunca, 1,Via Giordano Bruno - 81037 Sessa Aurunca, Italy
[56] Astrocampania Associazione - Osservatorio Salvatore di Giacomo - Agerola (NA) - Italy
[57] Gruppo Astrofili Catanesi, via Milo 28, 95125 Catania, Italy
[58] Università di Catania, Dipartimento di Fisica e Astronomia, Sezione Astrofisica, Via S. Sofia 78, 95123 Catania, Italy
[59] Astronomical Society of Tunisia
[60] Société Astronomique de Genève, Switzerland
[61] Observatoire de Genève, CH-1290 Sauverny, Switzerland
[62] AstroVal, Observatoire de la Vallée de Joux, CH-1347 Le Solliat, Switzerland

[63] Observatoire François-Xavier Bagnoud, CH-3961 St-Luc, Switzerland
[64] Société Neuchâteloise d'Astronomie, Switzerland
[65] Department of Physics, ETH Zurich, Wolfgang-Pauli-strasse 27, 8093 Zurich, Switzerland
[66] Institute for Particle Physics and Astrophysics, ETH Zurich, Wolfgang-Pauli-strasse 27, 8093 Zurich, Switzerland
[67] CH-6525 Gnosca, Switzerland
[68] Meekrap-oord 3, 3991 VE Houten, The Netherlands
[69] Observatoire Centre-Ardenne, 6840 Grapfontaine, Belgique
[70] ADAGIO, Belesta observatory (A05: MPC code), Belesta en Lauragais 31 - France
[71] 13200 Arles, France
[72] Observatoire les Pléiades, Latrape, France
[73] Observatoire des Baronnies Provençales, 05150 Moydans, France
[74] Association Photographie Astronomie Montredonnaise (APAM)
[75] 75000 Paris, France
[76] Observatoire de la Côte d'Azur (OCA)
[77] Ciel et Espace
[78] 78180 Montigny le Bretonneux, France
[79] Albireo78 Association, Yvelines, France
[80] Sadr Association
[81] Société Astronomique de France, Paris, France
[82] Instituto de Astrofísica e Ciências do Espaço (IA), Universidade de Lisboa, Tapada da Ajuda - Edifício Leste - 2º Piso 1349-018 Lisboa, Portugal
[83] Euraster, 1 rue du Tonnelier, 46100 Faycelles, France
[84] 77350 Le Mée-sur-Seine, France
[85] Airylab, 04800 Greoux les Bains, France
[86] Observatoire des Côtes-de-Meuse, 8 Place de Verdun, F-55210 Viéville-sous-les-Côtes, France
[87] Observatoire Midi-Pyrénées et Université Toulouse-III, IRAP, 31400 Toulouse, France
[88] Observatoire de Saint-Caprais, 81800 Rabastens, France
[89] Institut Supérieur de l'Aéronautique et de l'Espace, ISAE-SUPAERO, Toulouse University, Toulouse, France
[90] Université Toulouse-III, FSI, 31400 Toulouse, France
[91] Centre d'Astronomie, 04870 Saint-Michel-l'Observatoire, France
[92] 93 Société Lorraine d'Astronomie, Vandoeuvre-lès-Nancy, France
[93] Uranoscope de l'Ile de France, Gretz Armainvilliers, UAI A07
[94] GEOPS – Géosciences Paris Sud, Univ. Paris-Sud, CNRS, Université Paris-Saclay, Orsay, France
[95] Association Marseillaise d'Astronomie (AMAS)
[96] O.A.B.A.C. - Observatoire Astronomique du Beausset André Coliac
[97] Astroclub Urania 31
[98] 28800 Sancheville, France
[99] Observatoire de Puimichel, 04700 Puimichel, France
[100] Observatoire Charles Fehrenbach
[101] Astro Club de France
[102] 22540 Louargat, France
[103] Université Grenoble Alpes, Inria, 38000 Grenoble, France
[104] Université Paris-Saclay, Université Paris-Sud, 91400, Orsay, France
[105] SAS Les Pleiades (Opticiens)
[106] LOMA CNRS-Université de Bordeaux UMR5798
[107] Vendéen Astronomical Center
[108] Association Dinastro
[109] Center of Research in Astronomy, Astrophysics and Geophysics (CRAAG) - Algiers Observatory - Algeria
[110] Hampshire Astronomical Group
[111] Royal Astronomical Society
[112] American Association of Variable Star Observers
[113] UCL Observatory, Dept. of Physics and Astronomy, University College London, Gower St., London WC1E 6BT, UK
[114] CR2 9BF, UK
[115] Reading Astronomical Society, Earley, Reading RG6 1EY, UK
[116] Dept. of Software Engineering, University of Granada, Spain
[117] SAG, Sociedad Astronómica de Granada, Spain
[118] Puckett Observatory, P.O. BOX 818 Ellijay, Ga. 30540 USA
[119] Centro de Estudios de Física del Cosmos de Aragón, Plaza San Juan 1, 44001 Teruel, Spain
[120] Astrophysics Department, Universidad de La Laguna, 38205 La Laguna, Tenerife, Spain
[121] Observatorio de Forcarei
[122] Observatorio Astronómico de Albox - C/ Poeta Martin Torregrosa nº8 2ºA - 04800 Albox - Almeria, Spain
[123] Liverpool Telescope Group, Astrophysics Research Institute, Liverpool John Moores University, UK
[124] Observatorio Astronómico de Guirguillano, Navarra, Spain
[125] Observatorio Astronómico La Hita, 45850 La Villa de Don Fadrique, Toledo, Spain
[126] Observatorio Astronómico, Universidad de Valencia, Valencia, Spain
[127] Agrupacio Astronomica de Sabadell, Occultation's Group, C/. Prat de la Riba, s/n., 0/8203, Sabadell, Barcelona, Spain
[128] Astrophysics department, CEA/DRF/IRFU/DAp, Université Paris Saclay, UMR AIM, F-91191 Gif-sur-Yvette, France
[129] Institut de Ciències del Espai, Campus UAB, Carrer de Can Magrans, s/n, 08193, Barcelona, Spain
[130] Instituto Politécnico de Tomar, CI2 e U.D. Matemática e Física, Portugal
[131] Observatório Astronómico, Centro Ciência Viva de Constância, Portugal
[132] Centro Ciência Viva do Algarve, Faro, Portugal
[133] Fundamental and Applied Physics Laboratory - Safi, Physics Department, Polydisciplinary Faculty, Safi, Cadi Ayyad University, Morocco
[134] Oukaimeden Observatory, High Energy Physics and Astrophysics Laboratory, FSSM, Cadi Ayyad University, Marrakech, Morocco
[135] Astrobiology Research Unit, Université de Liège, 19C Allèe du 6 Août, 4000 Liège, Belgium
[136] Laboratory of High Energy Physics and Astrophysics, Physics department, Cadi Ayad University, PB 2390, Marrakech 40000, Morocco
[137] STAR Institute, Université de Liège, Allée du 6 août, 19C, 4000 Liège, Belgium
[138] 68490 Ottmarsheim, France
[139] Department of Astronomy and Carl Sagan Institute, Cornell University, Space Sciences Building, Ithaca, NY 14853, USA
[140] Cornell Center for Astrophysics and Planetary Science, Carl Sagan Institute, Cornell University, Space Sciences Building, Ithaca, NY 14853, USA
[141] Department of Physics and Astronomy, University of Toledo, 2801 West Bancroft Street, Toledo, OH 43606, USA
[142] Department of Physics and Astronomy, Appalachian State University, Boone, North Carolina, United States
[143] Department of Physics and Astronomy, University of North Carolina, Chapel Hill, North Carolina, United States
[144] Central (Pulkovo) Observatory of the Russian Academy of Sciences, 196140, 65/1 Pulkovskoye Ave., Saint Petersburg, Russia
[145] 78 rue de la tombe Issoire, 75014 Paris, France
[146] Association de Gestion de l'Observatoire Réunionais d'Astronomie (AGORA), Observatoire des Makes, La Réunion Island, France
[147] Association Réunionnaise pour l'Etude du Ciel Austral (ARECA), La Réunion Island, France
[148] Planétarium de Vaulx-en-Velin, Place de la Nation, 69120 Vaulx-en-Velin, France
[149] Association AT60, Observatoire du Pic du Midi, France
[150] Lunar and Planetary Laboratory, University of Arizona, Tucson, Arizona 85721, USA
[151] Reitsema Enterprises Inc, 1584 Waukazoo Drive Holland, MI 49424, USA
[152] Aix Marseille Univ, CNRS, CNES, LAM, Marseille, France
[153] Astronomical Association of Queensland, St. Lucia, Queensland, Australia
[154] Bundaberg Astronomical Society Inc., Bundaberg, Australia
[155] Brisbane Astronomical Society, Australia

10. Circumstances of observations

Appendix A: Retrieval of atmospheric structure

Here we discuss some limitations and caveats associated with the approach mentioned in the main text.

Appendix A.1: Upper and lower limits of probed atmosphere

The density $n(r)$ is reliably retrieved up to the level where the flux standard deviation σ_Φ due to photometric noise is comparable to the drop of stellar flux caused by the occultation (DO15). This corresponds to a density of

$$n_{\rm upper} \sim \frac{\sigma_\Phi}{K}\sqrt{\frac{H^3}{2\pi r D^2}}, \quad (A.1)$$

where K is the molecular refractivity of N_2, $H = -n/(dn/dr)$ is the scale-height and D is Triton's geocentric distance.

Using the values of K and D listed in Table 2, considering that $H \sim 30$ km around $r = 1500$ km, and taking $\sigma_\Phi \sim 0.011$ for our best data set (La Palma station), we find that reliable density values cannot be obtained above $r_{\rm upper} \sim 1540$ km, where $n \sim 4\times10^{11}$ cm^{-3}, corresponding to pressures of a few nanobars.

The relative error on $n(r)$ reduces as $\exp[-(r-r_{\rm up})/H]$ when deeper levels are probed. In practice, only the inversion of the best light curves provide useful retrieved profiles. In our case, this concerns the light curves from La Palma and Helmos stations, providing the profiles displayed in Figs. 7-9.

The deepest layers probed when inverting an occultation light curve are those corresponding to the closest approach of the observing station to Triton's shadow centre. In our case, La Palma's light curve provides data down to a radius of about $r = 1375$ km (i.e. just above the 20 km altitude level). However, the central flashes provide constraints that go further down, typically just under the 8-km altitude level, see Section 7.

Appendix A.2: Constructing the temperature profile template

A difficulty encountered during the inversion of the light curves is the assessment of Triton's contribution to the total flux. Let us define $\phi_0 = F_T/(F_S + F_T)$, where F_T (resp. F_S) is the flux coming from Triton (resp. the unocculted star). Thus, ϕ_0 corresponds to the zero stellar flux level in the normalised occultation light curves. Changing its value mainly changes the deepest parts of the retrieved profiles, see Fig. A.1.

Measuring ϕ_0 relies on images where Triton and the star are angularly separated. It is generally a difficult task, since a photometric accuracy of better that 1% is necessary to bring useful constraints. To mitigate differential chromatic effects (as the star and Triton have different colours), images were taken at the same elevation as for the occultation, either during the same nights or during nights before or after the event. As a sanity check, it is also desirable to use another reference star with flux F_R, and see if the sum of the ratios F_S/F_R and F_T/F_R outside the event matches the ratio $(F_S + F_T)/R_R$ during the event. Mismatches may then reveal possible variabilities in any of the objects involved (the target and reference stars, and/or Triton), and serve as an estimator of systematic sources of errors.

Such calibration images were acquired at the La Palma and Helmos sites, which provided the best data sets in terms of SNR. The focal lengths of those two telescopes are large enough to clearly resolve Triton from Neptune and from the occulted star, and avoid in particular flux contamination from the planet in the occultation light curve.

The calibration results are self-consistent for both instruments, with small internal error bars on ϕ_0, i.e. $\phi_0 = 0.3445 \pm 0.0003$ for La Palma and $\phi_0 = 0.360 \pm 0.013$ for Helmos. Note that there is no reason why the ϕ_0 should be the same for the two stations, as different filters were used: I+z (>720 nm) at La Palma and V+R at Helmos. Also, different observing conditions were prevailing at the two stations. In particular, the different airmasses (1.3 and 2.4 at La Palma and Helmos, respectively) may also affect the flux ratios star/Triton. However, the different values of ϕ_0 at La Palma and Helmos are mutually inconsistent (to within error bars) in the sense that they provide significantly different bottom parts for the $T(r)$ profiles.

This is particularly problematic for La Palma, where we obtain a temperature profile that peaks at $T \sim 58$ K just above the flash layer, using the value $\phi_0 = 0.3445$ derived from the calibration (Fig. A.1). This imposes a strong inversion layer in order to connect the temperature profile 38 K at the surface, see Fig. 13 and associated discussion. When used in our ray tracing code, this profile yields inconsistent synthetic central flashes when compared with observations (Figs. 23-24). In particular, it is not possible to fit simultaneously the flashes lying north and south of the shadow centre.

We have no satisfactory explanations for the inconsistencies induced by the photometric calibration, i.e. by the retrieved values of ϕ_0. It could stem from unaccounted light contamination from Neptune, although the biggest telescopes should be free of this problem, as mentioned above. We have tested the effect of digital coronography to remove such possible contamination. However, no significant changes of ϕ_0 are obtained with and without the use of coronography. Possible variations of Triton's flux due to rotational light curves of the satellite have also been considered. However, considering the low amplitude of those rotational curves (Buratti et al. 2011), and the fact that calibrations were made about 90 minutes before the occultation at La Palma, Triton's flux variation should be well below the 1% level, and thus have a negligible effect on the retrieved value of ϕ_0.

In these conditions, we have opted for another approach. We have varied the value of ϕ_0 for the best data set, i.e. the La Palma light curve. For each value, we have inverted the light curve to obtain $T(r)$, and then derived a template temperature profile using the Dias-Oliveira et al. (2015) modelling, except that the upper branch of $T(r)$ is not isothermal, but has a constant gradient $dT/dr \sim 0.1$ K km^{-1} to account for the general temperature increase (thermosphere) described in Strobel & Zhu (2017).

Each particular value of ϕ_0 provides a set of prescribed $T(r)$ boundary conditions (the green dots in Fig. A.1). Then it is possible to interpolate those prescribed values for any ϕ_0 using smooth polynomial functions, and finally get a one-parameter family of $T(r)$ profiles depending only on ϕ_0.

The main goal here is to find the value of ϕ_0 that best matches all the central flashes, thus constraining the deepest part of the $T(r)$ profile. The best $T(r)$ profile (with $\phi_0 = 0.35885$) is shown as a thicker line in the upper panel of Fig. A.1, and is adopted throughout this paper every time we use our ray tracing code. An example of an output of our tracing code is displayed in the lower panel of Fig. A.1.

Using the notations of Dias-Oliveira et al. (2015), the $T(r)$ profile is constructed by adopting the parameters of Table A.1. Note that although both the T and dT/dr profiles are continuous, the d^2T/dr^2 profile is not. This is evident in Fig. 9 at the inflexion point labelled "3" in Fig. A.1. The discontinuity of d^2T/dr^2 creates a very small kink at the corresponding point in the synthetic light curve, see lower panel of Fig. A.1. This kink is well below the noise level of all the observed light curves, and thus, has a negligible effect on the fit to the data.

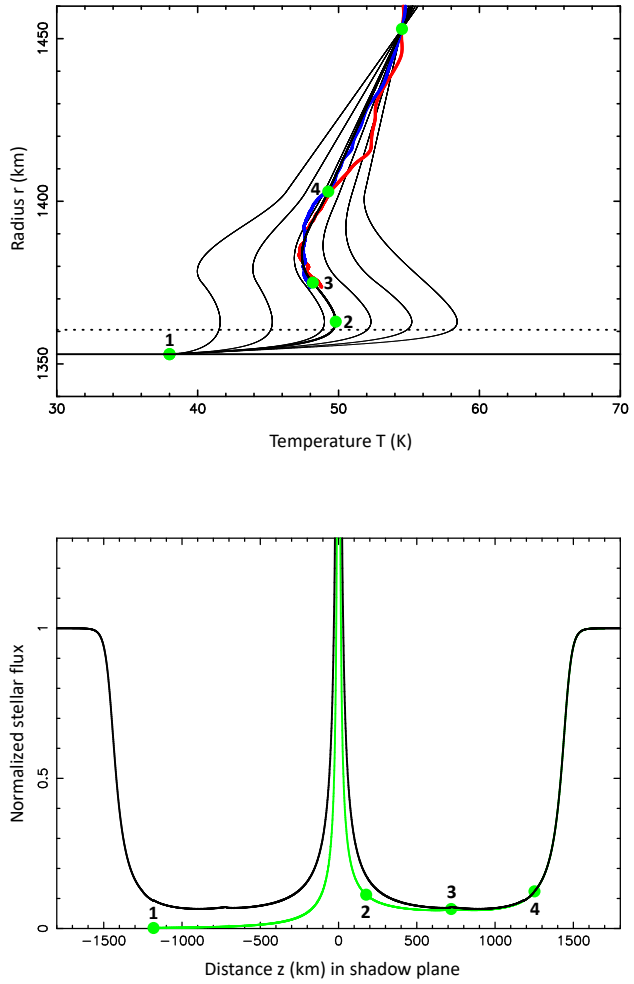

Fig. A.1. *Upper panel:* Thin black lines: six template temperature profiles obtained taking values ϕ_0 = 0.370, 0.365, 0.360, 0.355, 0.350 and 0.3445 (from left to right) of Triton's contribution to the normalised occultation light curve at La Palma. The right-most profile (corresponding to ϕ_0 = 0.3445) is the profile obtained from the calibration images taken before the event. Exploring ϕ_0 with small incremental steps, we find a best fit to the central flash for ϕ_0 = 0.35885, see the thicker black template profile, where the green dots labelled 1 to 4 are prescribed particular points in the Dias-Oliveira et al. (2015) model, as specified in Table A.1. Note that all the profiles go through the boundary condition T = 54.5 K at r = 1453 km (100 km altitude, upper green dot). The inverted profiles for La Palma corresponding to ϕ_0 = 0.35885 are shown in red (ingress) and blue (egress). The horizontal dotted line marks the altitude of the central flash layer. *Lower panel:* The result of the ray tracing code, using the best $T(r)$ profile of the upper panel, and the best fit value of p_{1400} = 1.18 μbar (Table 4). The normalised stellar flux is plotted against the distance to Triton's shadow centre. The green curve represents the flux if only one stellar image is present, and the green dots show the correspondence with the points labelled 1 to 4 in the upper panel. The black curve is the sum of the fluxes from two stellar images, i.e. the sum of the green curve and its mirrored version with respect to the z = 0 axis. This black curve is then used to fit the observations.

Admittedly, there is not a unique way to find a template $T(r)$ model that best fits the flashes. However, our solution should capture the main properties of the real profile, with a temperature maximum reached just above the central flash layer, and a mesosphere with a mild negative temperature gradient above that temperature peak. Note that the inversion layer connecting the profile to the surface at 38 K (i.e. below the temperature peak) has a vanishing effect on the synthetic light curve as the surface is approached, thus defining a "blind zone" as far as our data are concerned.

Table A.1. Parameters of the temperature template profile.

r_1, T_1, $dT/dr(r_1)$	1353 km, 38 K, 5 K km^{-1} (surface)
r_2, T_2	1363 km, 49.8 K ("elbow")
r_3, T_3	1375 km, 48.2 K (inflexion point)
r_4, T_4, $dT/dr(r_4)$	1403 km, 49.3 K, 0.105 K km^{-1} (upper branch, thermosphere)

Appendix A.3: The secondary stellar image issue

The Abel inversion assumes that only one stellar image (the near-limb, or primary refracted image) contributes to the recorded flux. In reality, Triton's atmosphere also produces a far-limb (secondary) stellar image whose flux is added to the light curve[6]. This is a source of error, especially in the central flash region, where the primary and secondary images have comparable fluxes, see for instance the lower panel of Fig. A.1.

We have performed tests to assess this effect on La Palma's light curve. At closest approach, the station was at about 685 km from the shadow centre, providing information down to the ∼20 km altitude level (Fig A.2). A smooth $T(r)$ profile is used to generate synthetic light curves at this station, one with the flux of the primary image only, and one with the sum of the fluxes of the primary and secondary images.

As expected, the inversion of the one-image light curve correctly retrieves the temperature at the 0.2 K accuracy level (Fig A.2), and the density and pressure profiles at the 0.1% accuracy level. Conversely, the inversion of the two-image light curve correctly retrieves the upper parts of the profiles, but it fails in reproducing the lower parts. For instance, at the deepest point reached by La Palma's light curve, the primary flux is 0.061 (normalizing the unocculted stellar flux to unity), while the secondary flux is 0.0072, about 8.5 times fainter than the primary flux. At that point, the temperature is retrieved to within 0.9 K and the pressure at the 1% level, a satisfactory result at our accuracy level.

However, this discrepancy rapidly increases as deeper levels are probed. For instance at r = 1362 km (9 km altitude level, where the temperature locally reaches a maximum, see upper panel of Fig. A.2), the discrepancy between the original and retrieved temperature is about 3 K. Note also that in this case, the retrieved temperature profile has an unrealistic behaviour as it extends below Triton's surface. Although the pressure profile is satisfactorily retrieved even if the secondary image is present, it suffers nevertheless the same unrealistic behaviour as $T(r)$, as it also extends below Triton's surface (lower panel of Fig. A.2).

In summary, the inversion procedure cannot provide reliable results below the 20-km altitude level. In particular the central flash region cannot be used in the inversion procedure. Note however that the direct (ray-tracing) approach does include the primary and secondary fluxes, and as such, it can be used to constrain the atmospheric profiles in the central flash region.

[6] More images can be produced in the central flash region for a non-spherical atmosphere.

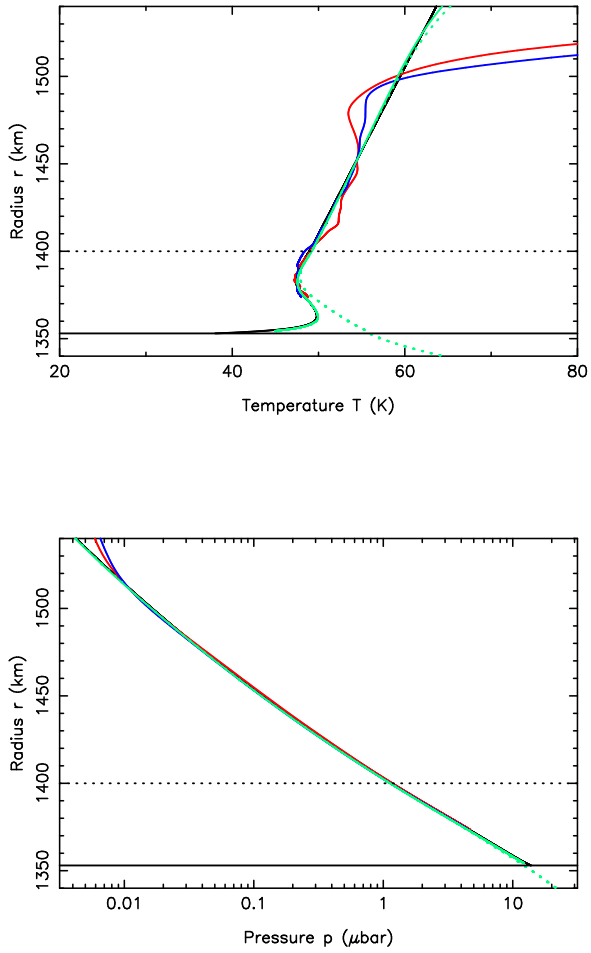

Fig. A.2. *Upper panel:* Retrieving the temperature profiles: effect of the secondary stellar image on the inversion results. The smooth black line connects these profiles to the surface at 38 K, where the pressure is set to 14 μbar. The resulting density profile is used to generate synthetic light curves that feed the Abel inversion procedure. Solid green line: the retrieved $T(r)$ profile with only the primary image accounted for. Green dotted line: the retrieved profile where the primary and secondary images have been added. The profiles obtained from the inversion of La Palma's light curve at ingress and egress (in red and blue, respectively) are shown for comparison, see also Figs. 7-9. Black horizontal solid and dotted lines: Triton's surface and reference radius (1400 km). *Lower panel:* The same with the pressure profiles.

Appendix B: Fit to the data

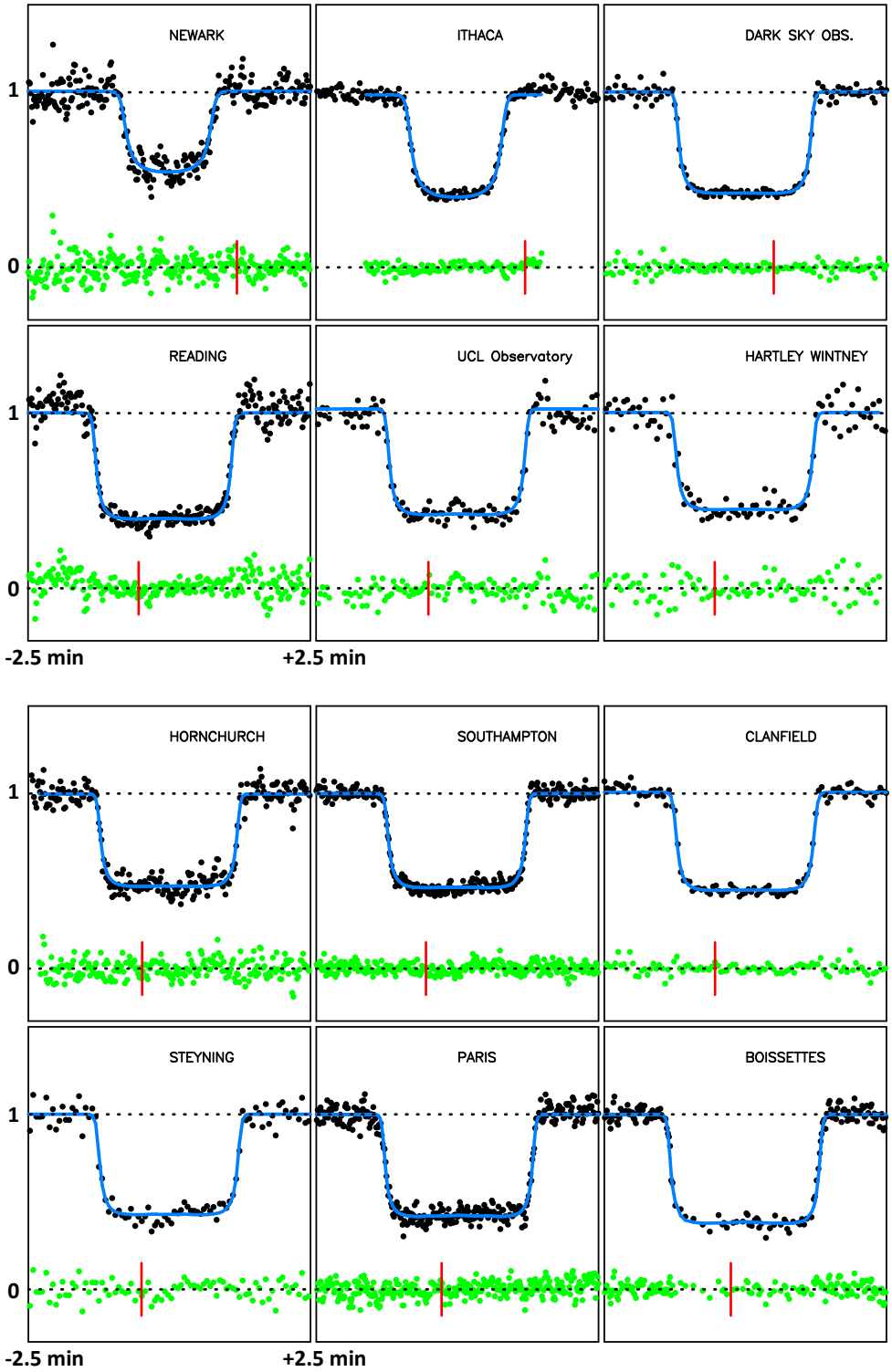

Fig. B.1. The data (black dots) have been fitted simultaneously with synthetic light curves (blue lines), based on the temperature profile displayed in Fig. 8 (black line) and the pressure boundary condition $p_{1400} = 1.18$ μbar (Table 4). The green dots are the residuals of the fits. Note that the central flash regions have been excluded from the fit, so that we obtain a global fit that is not influenced by the deepest atmospheric layers. The stations with exposure times smaller than 1 s have been smoothed to have a sampling time close to 1 s, allowing a direct visual comparison of SNR of the various data sets. The lower and upper horizontal dotted lines mark the zero-flux level and the total star+Triton unocculted flux, respectively. Note that the three central-most stations (Constância, Le Beausset and Felsina Obs., in Fig. B.3) are plotted at a different vertical scale to accommodate the presence of a strong central flash. Each panel has a duration of five minutes and is centred around the time of closest approach (or mid-occultation time) of the station to Triton's shadow centre. The stations are sorted from left to right and top to bottom from the northern-most track (Newark) to the southern-most track (Athens, see Fig. B.5), projected on Triton in the sky plane (Fig. 4). For reference, the vertical red lines mark 23:48 UTC for the European and African stations, and 23:55 UTC for the US stations (Newark, Ithaca, and Dark Sky Obs.).

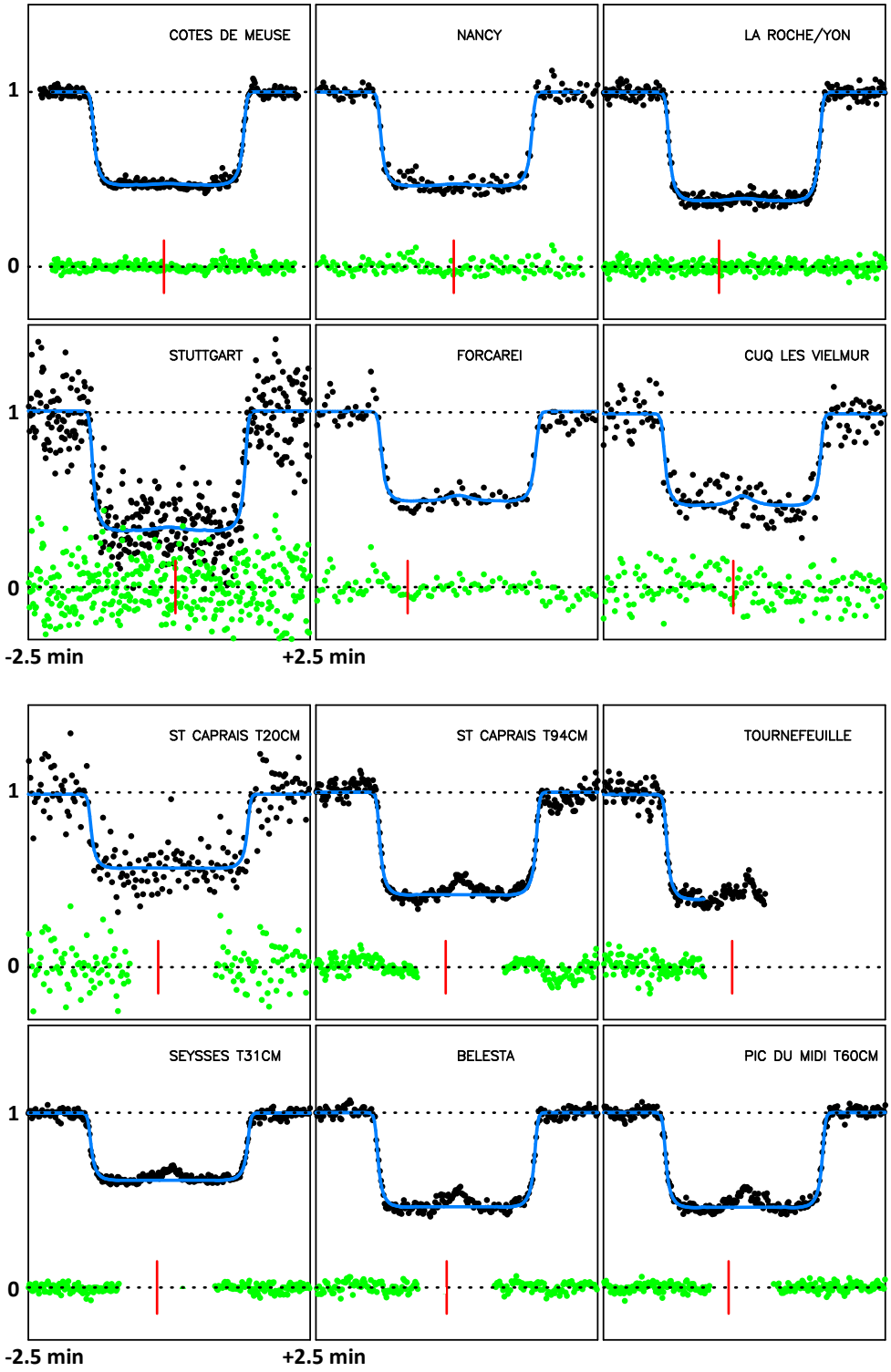

Fig. B.2. Continuation of Fig. B.1.

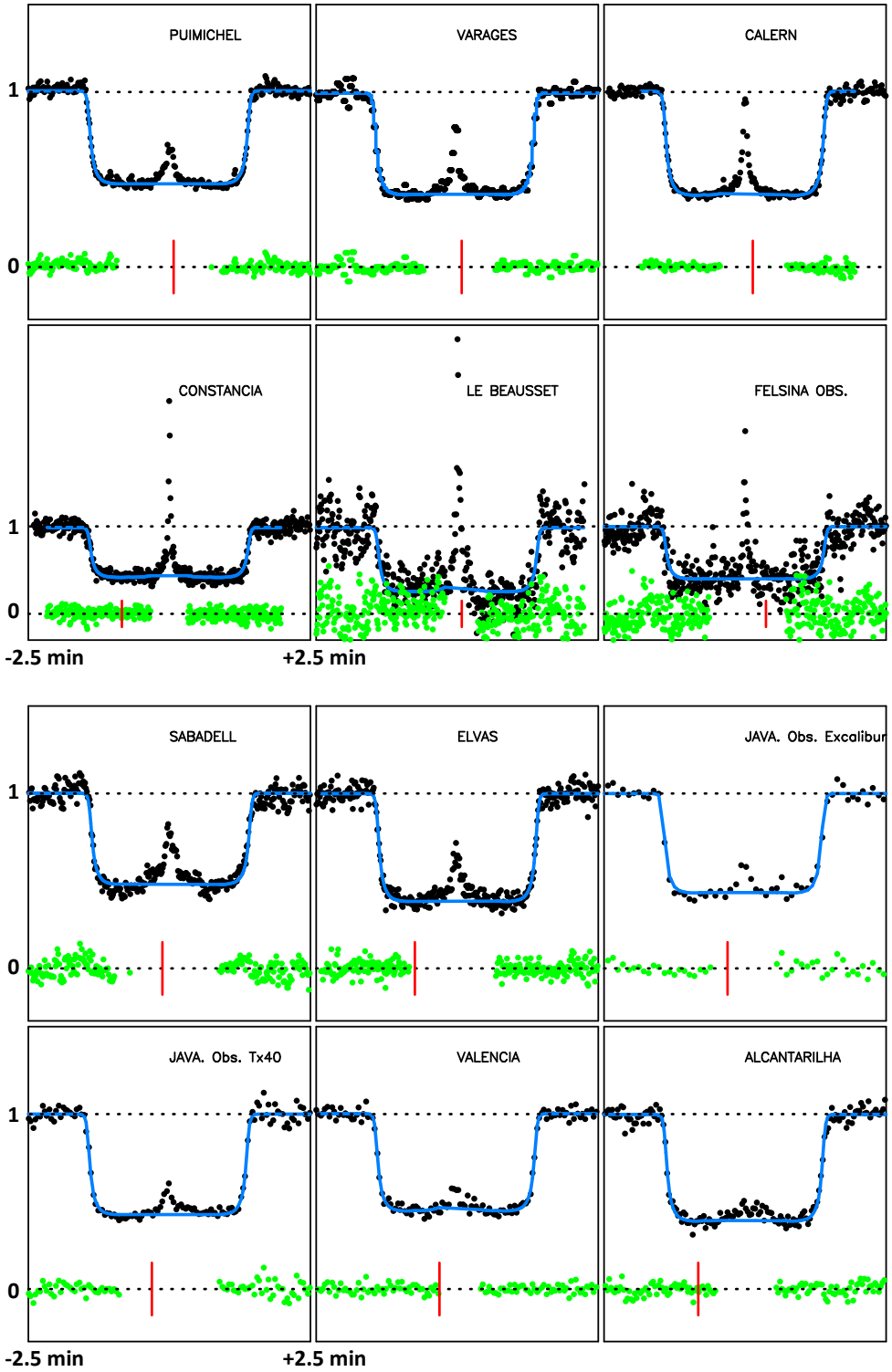

Fig. B.3. Continuation of Fig. B.2. NB. “JAVA." is the abbreviation of Javalambre, used so that the name of the station fits into the plot.

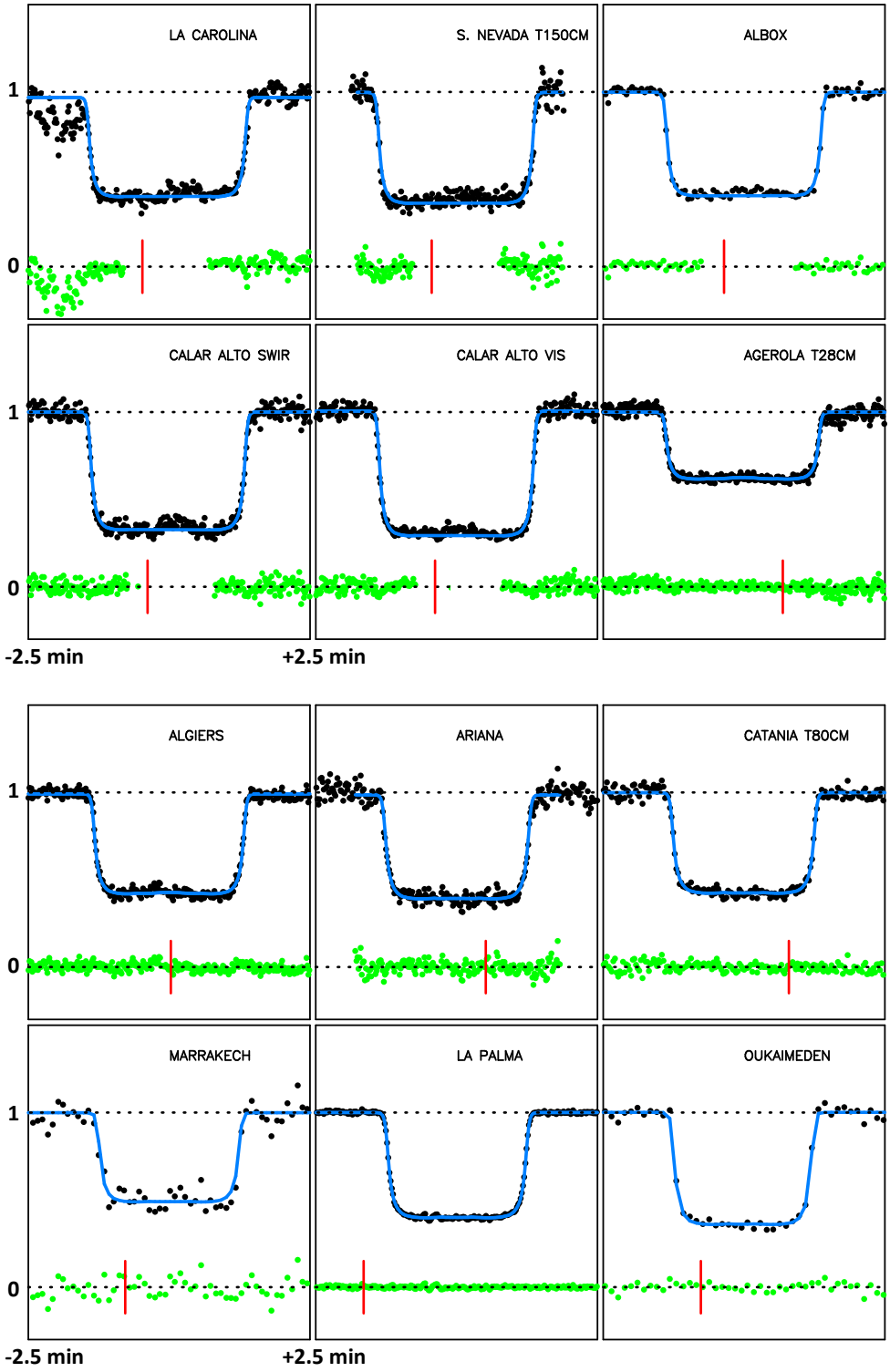

Fig. B.4. Continuation of Fig. B.3.

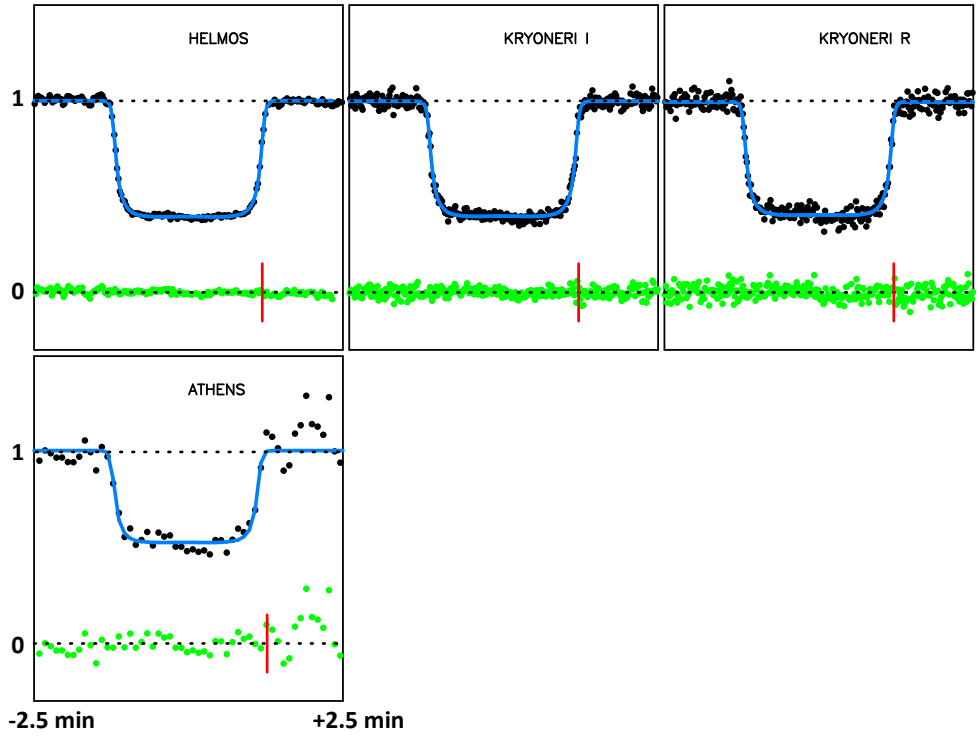

Fig. B.5. Continuation of Fig. B.4.

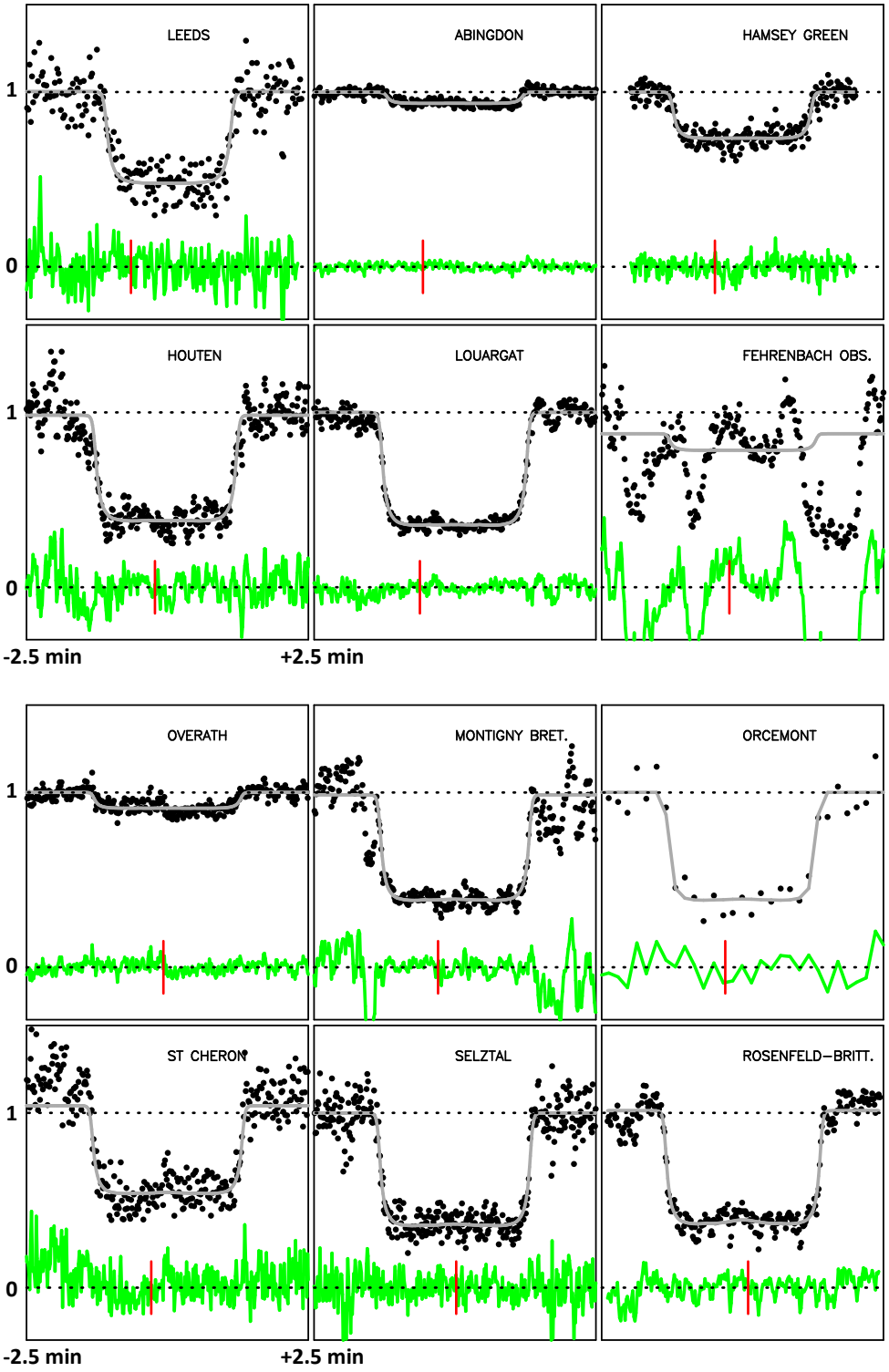

Fig. B.6. The same as Figs. B.1-B.5, but for stations that were *not* used in the simultaneous fit.

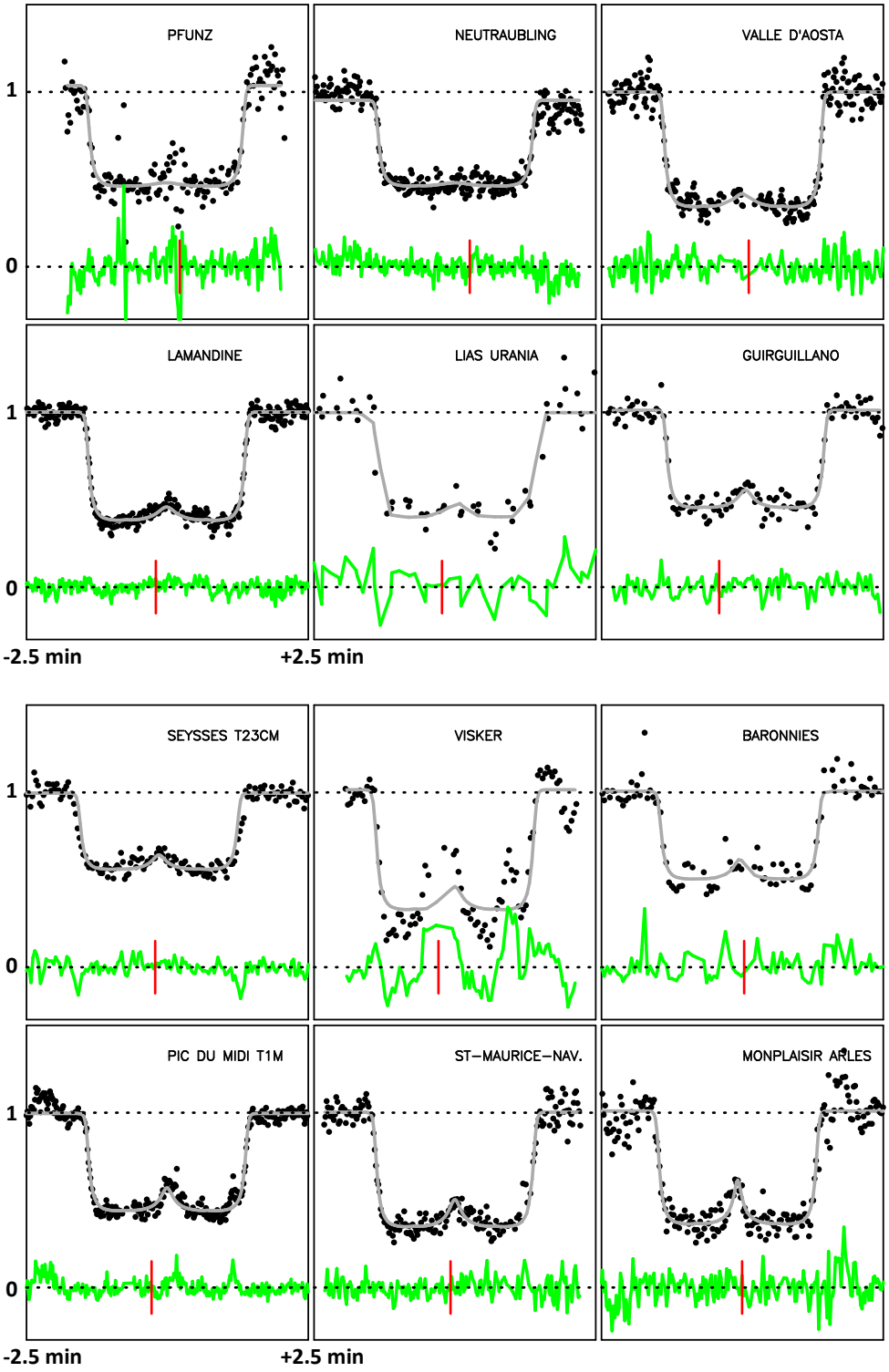

Fig. B.7. Continuation of Fig. B.6.

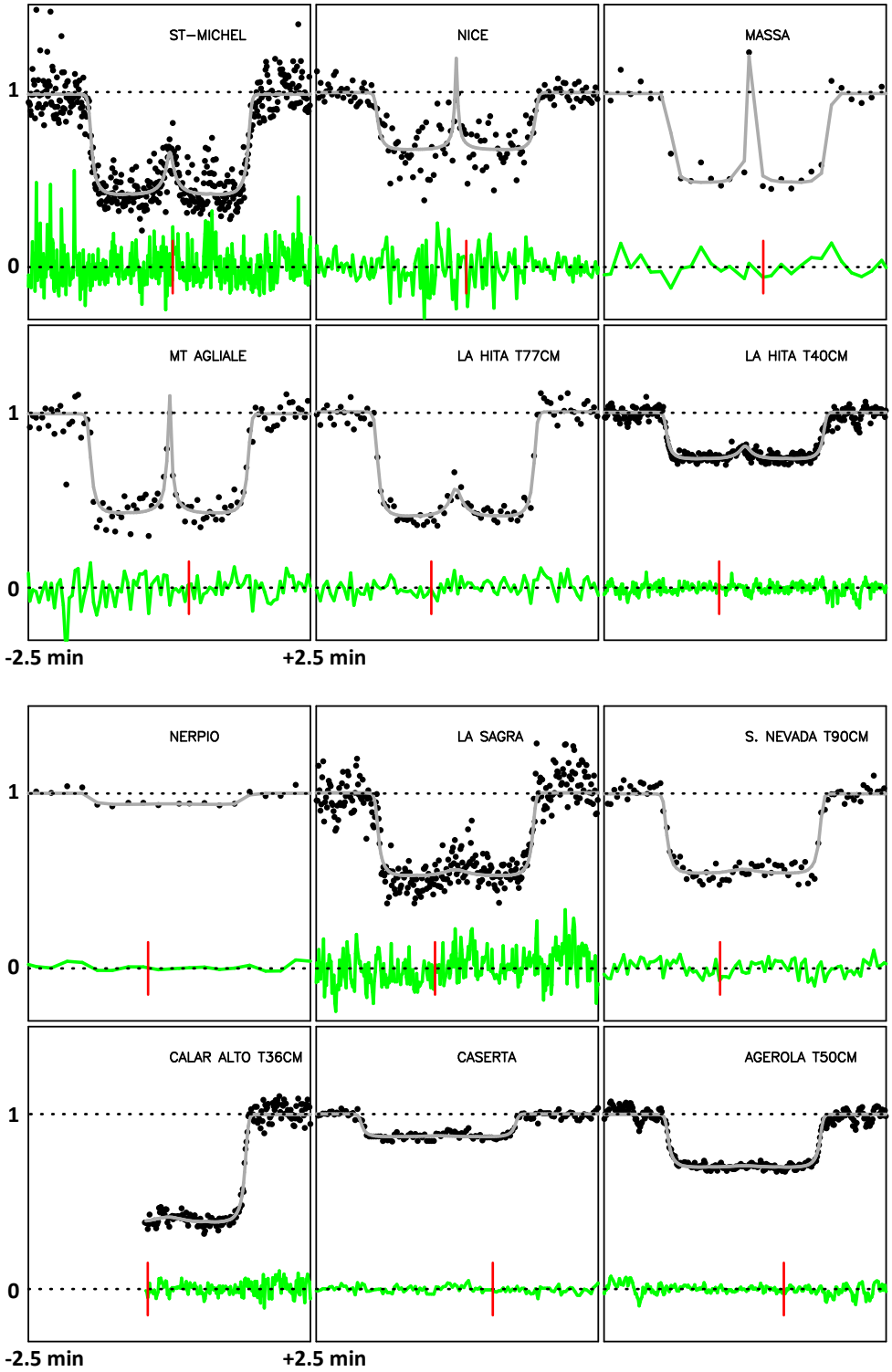

Fig. B.8. Continuation of Fig. B.7.

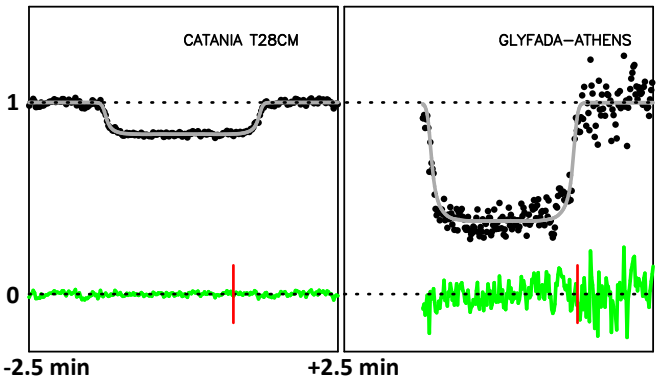

Fig. B.9. Continuation of Fig. B.8.

Table 5. Circumstances of Observations

Site	Coordinates Altitude (m)	Telescope aperture (m) Instrument/filter	Exp. Time/Cycle (s)	Observers
Observations that provided light curves that are used in Triton's atmospheric fit				
Agerola Italy	40 37 26.2 N 14 33 50.6 E 660.0	0.28 CCD/clear	0.86/0.86	L. Morrone
Albox Spain	37 24 20.0 N 02 09 07.0 W 485.0	0.41 CCD/clear	2.00/3.34	J. L. Maestre García
Alcantarilha Portugal	37 07 58.8 N 08 21 54.0 W 65.0	0.36 CCD/red	0.33/0.64	F. Marques Dias
Algiers Algeria	36 47 52.1 N 03 01 56.2 E 331.0	0.81 video/clear	0.04/0.04	D. Baba Aissa, Z. Grigahcene
Ariana Tunisia	36 53 03.0 N 10 11 42.0 E 5.0	0.20 CCD/clear	0.50/0.60	S. Kamoun
Athens Greece	37 58 06.8 N 23 47 00.1 E 250.0	0.40 CCD/clear	1.00/3.50	K. Gazeas, E. Karampotsiou, L. Tzouganatos
Belesta France	43 26 39.4 N 01 48 58.6 E 235.0	0.30 video/clear	0.64/0.64	P. André, M. Llibre, F. Pailler
Boissettes France	48 31 41.0 N 02 37 28.0 E 75.0	0.30 CCD/clear	0.50/0.50	M. Irzyk
Calar Alto (2 channels) Spain	37 13 24.7 N 02 32 44.9 W 2160.0	1.23 SCMOS/VIS: (0.4-1.0 μm) SWIR: (1.0-1.7 μm))	VIS: 0.063/0.063 SWIR: 0.11/0.11	R. Hueso, S. Pérez-Hoyos, A. Sánchez-Lavega
Calern France	43 45 13.2 N 06 55 22.4 E 1268.0	1.04 CCD/I'	0.10/0.11	J. Ferreira, P. Machado, P. Tanga, J.-P. Rivet
Catania Italy	37 41 35.8 N 14 58 29.1 E 1725.0	0.80 CCD/clear	0.80/1.70	G. Leto, R. Zanmar Sanchez, P. Bruno, G. Occhipinti
Clanfield England	50 56 19.2 N 01 01 10.6 W 155.0	0.61 video/clear	0.16/0.16	D. Briggs, S. Broadbent
Constância Portugal	39 29 41.6 N 08 19 25.2 W 147.0	0.51 video/clear	0.64/0.64	R. Gonçalves, M. Ferreira
Côtes de Meuse France	49 00 07.2 N 05 41 06.6 E 284.0	0.83 EMCCD/clear	0.06/0.06	S. Renner, M. Kaschinski
Cuq les Vielmur France	44 29 05.0 N 01 55 05.0 E 300.0	0.20 CCD/clear	2.00/4.00	A. Cailleau, V. Pic, L. Granier
Dark Sky Obs. United States	36 15 09.6 N 81 25 01.2 W 960.0	0.36 CCD/clear	1.50/2.50	J. Pollock, D. B. Caton V. Kouprianov
Elvas Portugal	38 50 47.6 N 07 12 27.4 W 285.0	0.27 CCD/clear	0.30/0.30	W. Beisker
Felsina Obs. Italy	44 21 22.0 N 11 09 09.0 E 652.0	0.40 video/clear	0.64/0.64	R. Di Luca, D. Alboresi
Forcarei Spain	42 36 38.4 N 08 22 15.1 W 673.0	0.51 video/clear	0.64/0.64	R. Iglesias-Marzoa, H. González
Hartley Wintney	51 18 23.2 N	0.36	1.00/3.31	G. Thurston

Continued on next page

Table 5 – *Continued from previous page*

Site	Coordinates Altitude (m)	Telescope aperture (m) Instrument/filter	Exp. Time/Cycle (s)	Observers
England	00 54 44.9 W 65.0	CCD/Johnson V		
Helmos Greece	37 59 08.1 N 22 11 54.6 E 2323.0	2.28 CCD/V+R	0.60/0.674	E. M. Xilouris, I. Alikakos, A. Gourzelas, V. Charmandaris
Hornchurch England	51 33 06.4 N 00 11 38.8 E 14.0	0.24 video/clear	0.64/0.64	P. Denyer
Ithaca United States	42 27 29.4 N 76 23 05.5 W 530.0	0.60 CCD/clear	0.20/0.36	J. Lloyd, M. El Moutamid, C. Lamarche
Javalambre Astrophysical Observatory (2 telescopes) Spain	40 02 30.6 N 01 00 57.6 W 1955.0	0.40 Tx40 CCD/clear 0.28 Excalibur CCD/clear	2.00/2.50 2.00/3.00	R. Iglesias-Marzoa, J. Abril Ibáñez, M. Chioare Díaz Martín
Kryoneri (2 channels) Greece	37 58 19.0 N 22 37 07.0 E 930.0	1.20 sCMOS/R and I	0.19/0.20	E. M. Xilouris, A. Liakos, V. Charmandaris
La Palma Spain	28 45 43.2 N 17 52 39.3 W 2340.0	2.00 Liverpool Tel. CCD/I+Z	0.6/0.635	J. Marchant, B. Sicardy
La Carolina Spain	38 16 27.0 N 03 36 55.0 W 595.0	0.64 CCD/clear	0.15/0.15	S. Alonso, A. Román Reche
La Roche-Sur-Yon France	46 32 48.4 N 01 19 37.8 W 48.0	0.40 CMOS/clear	0.20/0.20	J. Desmars, R. Tanguy, J. David
Le Beausset France	43 11 38.1 N 05 48 05.9 E 197.0	0.25 video/clear	0.64/0.64	S. Lisciandra, J. F. Coliac
Marrakech Morocco	31 35 16.2 N 08 00 46.9 W 494.0	0.60 CCD/clear	2.5/5.5	A. Daassou, K. Barkaoui, Z. Benkhaldoun, M. Guennoun, J. Chouqar
Nancy France	48 39 51.6 N 06 09 28.7 E 284.0	0.25 CCD/luminance	1.50/2.10	D. Lavandier, D. Walliang
Newark United States	43 00 23.7 N 77 07 06.5 W 165.0	0.25 video/clear	0.53/0.53	B. Timerson
Oukaïmeden Morocco	31 12 23.0 N 07 51 59.0 W 2727.0	0.50 CCD/clear	2.00/6.80	C. Rinner
Paris France	48 52 17.0 N 02 23 07.0 E 92.0	0.15 CCD/clear	0.25/0.25	R. Chauvet
Pic du Midi Obs. France	42 56 12.0 N 00 08 31.9 E 2862.0	0.60 EMCCD/visible	0.05/0.05	D. Berard
Puimichel France	43 58 53.1 N 06 02 10.0 E 714.0	0.60 EMCCD/visible	0.10/0.10	S. Moindrot
Reading England	51 30 23.8 N 00 48 58.1 W 80.0	0.30 video/red	0.64/0.64	T. V. Haymes
Sabadell Spain	41 33 00.2 N 02 05 24.8 E 224.0	0.50 video/clear	0.16/0.16	A. Selva, C. Perello, V. Cabedo
Saint Caprais (2 telescopes) France	43 52 25.9 N 01 43 05.8 E 185.0	0.20 CCD/Johnson V 0.94 SWIR/clear	1.00/1.58 0.05/0.08	A. Klotz, Y. Rieugnie, A. N. Klotz
Seysses	43 30 06.3 N	0.31	0.32/0.32	M. Boutet

Continued on next page

Table 5 – *Continued from previous page*

Site	Coordinates Altitude (m)	Telescope aperture (m) Instrument/filter	Exp. Time/Cycle (s)	Observers
France	01 17 20.3 E 183.0	video/UV-IR block		
Sierra Nevada Spain	37 03 51.0 N 03 23 05.0 W 2925.8	1.50 video/clear	0.04/0.04	J. L. Ortiz, P. Santos-Sanz, V. Casanova
Southampton England	50 55 18.9 N 01 22 28.1 W 16.0	0.40 CMOS/clear	0.25/0.25	N. J. Haigh
Sternwarte Stuttgart Germany	48 46 56.7 N 09 11 47.4 E 346.0	0.41 video/clear	0.64/0.64	A. Eberle K. Rapp
Steyning England	50 53 16.0 N 00 19 57.0 W 20.0	0.28 CCD/luminance	2.00/4.00	N. Quinn
Tournefeuille France	43 34 58.8 N 01 19 35.4 E 163.0	0.32 CCD/clear	0.25/0.25	M. Delcroix
UCL Observatory London England	51 36 47.6 N 00 14 32.3 W 82.0	0.35 CCD/luminance	1.00/2.38	S. J. Fossey, C. Arena
Valencia Spain	39 56 42.0 N 01 06 05.4 W 1280.0	0.50 CCD/clear	1.00/2.50	V. Peris, O. Brevia
Varages France	43 36 44.6 N 05 57 49.1 E 300.0	0.50 InGaAs/RG1000 (effective λ=1.3 μm)	2.30/2.30	F. Jabet
Observations that provided light curves that are not used in Triton's atmospheric fit				
Abingdon England	51 37 53.1 N 01 16 55.2 W 59.0	0.30 video/clear	0.16/0.16	J. Talbot
Agerola Italy	40 37 26.2 N 14 33 50.6 E 660.0	0.50 CMOS/clear	0.50/0.50	A. Noschese, A. Vecchione
Calar Alto Spain	37 13 24.7 N 02 32 44.9 W 2160.0	0.36 CCD/clear SWIR	1.00/1.00	J. F. Rojas, A. Sánchez-Lavega
Caserta Italy	41 16 11.3 N 13 56 28.9 E 407.0	0.24 CCD/clear	2.00/2.46	L. Cupolino
Catania Italy	37 30 24.0 N 15 05 35.5 E 50.0	0.28 video/clear	0.64/0.64	C. Scalia, R. Lo Savio, G. Giardina
Charles Fehrenbach Observatory, La Biette France	50 05 01.5 N 03 46 34.4 E 191.0	0.36 CCD/clear	0.28/0.30	P. Morel
Glyfada-Athens Greece	37 52 33.6 N 23 46 12.0 E 100.0	0.35 CCD/clear	1.00/1.15	E. I. Kardasis, A. Christou
Guirguillano Spain	42 42 42.2 N 01 51 54.3 W 595.0	0.31 video/clear	2.56/2.56	I. Ordóñez-Etxeberria, P. Martorell, J. Salamero
Hamsey Green England	51 19 09.4 N 00 04 01.4 W 170.0	0.28 video/clear	1.00/1.00	M. Jennings
Houten Netherlands	52 01 59.3 N 05 09 44.2 E 2.0	0.36 CCD/ 685 nm long pass	0.41/0.41	J. Sussenbach
La Hita Observatory (2 telescopes) Spain	39 34 06.8 N 03 11 09.5 W 695.0	0.77 CCD/luminance 0.40 video/clear	1.00/3.55 0.30/0.30	N. Morales, J. L. Ortiz, F. Organero, L. Ana, F. Fonseca, P. Santos-Sanz

Continued on next page

Table 5 – *Continued from previous page*

Site	Coordinates Altitude (m)	Telescope aperture (m) Instrument/filter	Exp. Time/Cycle (s)	Observers
Lamandine	44 12 35.0 N	0.30	0.06/0.06	M. Miniou
France	01 42 01.7 E	CCD/clear		
	297.0			
La Sagra Observatory	37 58 58.1 N	0.36 each	1.00/3.79 (tetra1)	N. Morales,
(4 telescopes)	02 34 05.1 W	tetra1, tetra2: CCD/clear	1.00/3.56 (tetra2)	J. L. Ortiz,
Spain	1530.0	tetra3, tetra4: video/clear	0.20/0.20	P. Santos-Sanz
Leeds	53 50 15.6 N	0.20	1.28/1.28	A. Pratt
England	01 36 27.8 W	video/IR-UV block		
	113.0			
Lias	43 33 33.3 N	0.40	0.13/0.13	F. Metz,
France	01 06 34.4 E	CCD/clear		D. Erpelding,
	300.0			J.-P. Nougayrède
Louargat	48 32 16.7 N	0.30	0.20/0.20	B. Reginato,
France	03 21 30.5 W	CMOS/L		E. Reginato
	196.0			
Massa	44 01 17.2 N	0.20	5.12/5.12 (1st half)	P. Baruffetti
Italy	10 07 56.7 E	video/clear	2.56/2.56 (2nd half)	
	30.0			
Montigny le Bretonneux	48 45 54.0 N	0.28	0.50/0.51	O. Dechambre
France	02 00 52.0 E	CCD/clear		
	168.0			
Mount Agliale Observatory	43 59 43.1 N	0.50	1.50/3.23	F. Ciabattari
Italy	10 30 53.8 E	CCD/clear		
	750.0			
Nerpio	38 09 56.0 N	0.32	1.00/16.11	E. Briggs
Spain	02 19 35.0 W	CCD/clear		
	1650.0			
Neutraubling	48 59 23.1 N	0.28	0.16/0.16	B. Kattentidt
Germany	12 12 57.3 E	video/clear		
	333.0			
Nice	43 43 32.9 N	0.13	2.00/2.00	M. Conjat
France	07 17 59.4 E	video/clear		
	350.0			
Observatoire de Biscarmiau	43 08 40.4 N	0.31	0.64/0.64	G. Vaudescal
France	00 03 31.8 E	video/clear		
	488.0			
Observatoire des	44 24 29.7 N	0.80	2.00/2.00	M. Bretton
Baronnies Provençales	05 30 54.4 E	CCD/clear		
France	820.0			
Observatoire Monplaisir	43 40 58.3 N	0.28	1.03/1.49	J. Ardissone
France	04 38 32.6 E	CCD/clear		
	5.0			
Orcemont	48 35 28.0 N	0.10	10.00/10.15	P. Delay
France	01 48 45.0 E	CCD/IR cut		
	165.0			
Overath	50 57 11.4 N	0.20	0.32/0.32	B. Klemt
Germany	07 14 53.1 E	video/clear		
	200.0			
Pfünz	48 53 26.0 N	0.28	1.00/1.20	B. Gährken
Germany	11 16 23.0 E	CCD/clear		
	488.0			
Pic du Midi Obs.	42 56 12.0 N	1.05	0.10/0.10	F. Colas
France	00 08 31.9 E	sCMOS/clear		
	2862.0			
Rosenfeld-Brittheim	48 17 17.8 N	0.80	0.40/0.40	S. Kowollik,
Germany	08 40 38.9 E	CMOS/UV-IR block		R. Bitzer
	700.0			
Saint Chéron	48 32 16.6 N	0.18	0.08/0.08	J. Berthier
France	02 07 51.7 E	video/clear		
	160.0			

Continued on next page

Table 5 – *Continued from previous page*

Site	Coordinates Altitude (m)	Telescope aperture (m) Instrument/filter	Exp. Time/Cycle (s)	Observers
Saint-Maurice-Navacelles France	43 50 39.3 N 03 33 47.3 E 583.0	0.21 CCD/clear	0.64/0.64	J. Lecacheux
Saint Michel France	43 54 23.3 N 05 43 34.7 E 564.0	0.60 EMCCD/clear	0.05/0.05	E. Meza, O. Labrevoir
Selztal Obs. Friesenheim Germany	49 50 00.0 N 08 15 00.0 E 110.0	0.51 CMOS/clear	0.8/0.8	G. M. Piehler
Seysses France	43 30 06.3 N 01 17 20.3 E 183.0	0.23 video/UV-IR block	0.32/0.32	J. Sanchez
Sierra Nevada Spain	37 03 51.0 N 03 23 05.0 W 2925.8	0.90 CCD/clear	1.00/3.33	J. L. Ortiz, P. Santos-Sanz, V. Casanova
Valle d'Aosta Italy	45 47 23.1 N 07 28 42.3 E 1675.0	0.81 EMCCD/clear	0.2/0.2	D. Cenadelli, J.-M. Christille, B. Sicardy
Stations with technical or weather problems that provided no light curves				
Bilbao Spain	43 15 43.6 N 02 56 54.6 W 47.0	0.5 CCD/clear		S. Pérez-Hoyos, A. Sánchez-Lavega
Buthiers France	48 17 30.0 N 02 26 18.0 E 87.0	0.59 CMOS/L	0.10/0.10	J. L. Dauvergne
Cavarc Observatory France	44 40 35.2 N 00 37 43.1 E 100.0	0.50 CMOS/clear		J. Rudelle, B. Tregon
Comthurey Germany	53 15 57.8 N 13 11 24.6 E 74.0	0.18		K. Guhl
Emmendingen Germany	48 06 14.2 N 07 51 28.6 E 210.0	0.18 CMOS/clear	3.00/3.33	K.-L. Bath
Eppstein-Bremthal Germany	50 08 17.4 N 08 21 50.4 E 256.0	0.25 video/clear		O. Klös
Gnosca Switzerland	46 13 53.2 N 09 01 26.5 E 260.0	0.40		S. Sposetti
Grapfontaine Belgium	49 48 54.2 N 05 23 57.5 E 445.0	0.28 video/clear		F. Van Den Abbeel
Hamburg-Bergedorf Germany	53 28 50.0 N 10 14 29.0 E 25.0	0.60 CCD/clear		V. Perdelwitz
Handeloh Germany	53 14 06.4 N 09 49 46.7 E 60.0	0.35 CCD/clear		K. von Poschinger
Observatory Hoher List Eifel Germany	50 09 42.0 N 06 50 55.0 E 549.0	1.00 CCD/clear		M. Miller, G. Herzogenrath, D. Frangenberg, L. Brandis, I. Pütz
Labastide-Murat France	44 38 43.2 N 01 34 13.9 E 445.0	0.20 video/clear	0.32/0.32	E. Frappa
Lauenbrück Germany	53 12 26.6 N 09 34 36.1 E 31.0	0.50 CCD/clear		M. Kretlow
Malvilliers Switzerland	47 01 58.5 N 06 52 03.0 E	0.30 CCD/clear		L. Falco R. Leiva

Continued on next page

Table 5 – *Continued from previous page*

Site	Coordinates Altitude (m)	Telescope aperture (m) Instrument/filter	Exp. Time/Cycle (s)	Observers
	845.0			
EXPO Observatory	52 15 45.0 N	1.12	0.04/0.04	P. Riepe,
Melle	08 20 12.0 E	video/clear		E. Bredner
Germany	185.0			
Meudon	48 48 18.3 N	1.00		T. Widemann, W. Thuillot,
France	02 13 51.6 E	CMOS/clear		D. Hestroffer,
	157.6			E. Lellouch
Ondřejov	49 54 33.8 N	0.50	0.04/0.04	M. Jelínek,
Czech Republic	14 46 52.9 E	EMCCD/R		J. Štrobl
	530.0			
Saint-Luc	46 13 41.8 N	0.30		E. Bouchet,
Obs. F.-X. Bagnoud	07 36 45.6 E	CCD/clear		M. Cottier
Switzerland	2200.0			
Saulges	47 59 02.0 N	0.25	0.20/0.20	T. Midavaine
France	00 24 30.0 W	video/clear		
	97.0			
TRAPPIST-North	31 12 22.0 N	0.60		E. Jehin
Oukaïmeden	07 51 59.0 W	CCD/clear		
Morocco	2751.0			
Uranoscope	48 44 32.0 N	0.28 video/clear	0.25/0.25	A. Leroy,
(2 telescopes)	02 44 32.0 E	0.36 CMOS/clear	0.25/0.25	S. Bouley
France	110.0			
Valée de Joux	46 37 06.0 N	0.61	1.00/1.15	R. Barbosa,
Switzerland	06 13 10.0 E	CMOS/clear		R. Behrend
	1145.0			M. Spano
Vierzon	47 13 23.7 N	0.25		L. Rousselot
France	02 03 09.8 E	CMOS/clear		
	97.0			
Zurich	47 24 27.8 N	0.50	2.00/4.00	S. Gallego,
Switzerland	08 30 39.5 E	CCD/Johnson R		L. Tortorelli
	553.0			
Previous occultations				
18 July 1997				
Brownsville	25 58 40.9 N	0.35	0.5/0.5	W. B. Hubbard,
United States	97 32 11.3 W	CCD/clear		H. J. Reitsema,
	9.0			R. Hill
Bundaberg	24 56 37.5 S	0.48	0.33/0.33	E. Hummel, M. Moy,
Australia	152 22 35.4 E	CCD/clear		I. Pink, R. Walters
	10.0			
Ducabrook	23 53 55.0 S	0.35	0.66/0.66	L. Ball,
Australia	147 26 40.0 E	CCD/clear		G. Neilsen
	320.0			
Lochington	23 56 42.5 S	0.35	0.66/0.66	W. Beisker,
Australia	147 31 24.8 E	CCD/clear		S. Hutcheon
	270.0			
Observations that provided data that are not used in Triton's atmospheric fit				
Ballandean	28 49 05.0 S	0.48		K. Lay
Australia	151 48 36.0 E	Visual		
	710.0			
Ipswich	~27 38 S	0.30	10	B. Downs
Australia	~152 45 E	CCD/clear	grazing	
	~40			
The Gap	27 27 42.3 S	0.40		P. Anderson
Australia	152 55 58.0 E	Visual		
	176.0			
21 May 2008				
Hakos	23 14 11.0 S	0.5	0.67/1.49	K.-L. Bath
Namibia	16 21 41.5 E	CCD/clear		

Continued on next page

Table 5 – *Continued from previous page*

Site	Coordinates Altitude (m)	Telescope aperture (m) Instrument/filter	Exp. Time/Cycle (s)	Observers
	1825.0			
Hakos	23 14 11.0 S	0.45	0.84/1.0	B. Sicardy
Namibia	16 21 41.5 E	CCD/clear		
	1825.0			
Maïdo	21 04 15.5 S	0.23	2.56/2.56	J. Lecacheux
La Réunion Island	55 23 14.2 E	CCD/clear		T. Payet
France	2200.0			
Tivoli	23 27 40.2 S	0.35	1.48/1.48	H.-J. Bode
Namibia	18 01 01.2 E	CCD/clear		
	1344			
Observations that provided light curves that are not used in Triton's atmospheric fit				
Piton Lacroix	21 12 54.4 S	0.28	2/2	E. Frappa
La Réunion Island	55 38 38.5 E	CCD/clear		
France	2330.0			
Stations with technical or weather problems that provided no light curves				
Grünau	~27 44 S	0.30	clouded out	W. Beisker
Namibia	~18 23 E			
	~1100			
Hakos	23 14 11.0 S	0.28	?/?	C. Boissel
Namibia	16 21 41.5 E	(IOC?)		A. Doressoundiram
	1825			
Les Makes	21 11 57.4.0 S	0.35	clouded out	B. Payet
La Réunion Island	55 24 34.5.0 E	CCD/clear		
France	972			
Maïdo	21 04 15.5 S	0.30	wind shaking	J. Françoise
La Réunion Island	55 23 14.2 E	video/clear		B. Mondon
France	2200.0			
Piton Lacroix	21 12 52.0 S	0.28	moisture	A. Peyrot
La Réunion Island	55 38 35.0 E	CCD/clear		J.-P. Teng-Chuen-Yu
France	2350.0			
Springbok	29 39 40.3 S	0.30	clouded out	T. Widemann
South Africa	17 52 58.9 E	CCD/clear		
	951			
Sutherland	32 22 43.8 S	1.0	outside shadow	G. Blanchard
South Africa	20 48 42.0 E	CCD/clear		M. Castets
	1760			F. Colas
Tivoli	23 27 40.2 S	0.27	?/?	B. Thome
Namibia	18 01 01.2 E	CCD/clear		
	1344			

A&A 625, A42 (2019)
https://doi.org/10.1051/0004-6361/201834281

Astronomy & Astrophysics

Lower atmosphere and pressure evolution on Pluto from ground-based stellar occultations, 1988–2016

E. Meza[1,⋆], B. Sicardy[1], M. Assafin[2,3], J. L. Ortiz[4], T. Bertrand[5], E. Lellouch[1], J. Desmars[1], F. Forget[6], D. Bérard[1], A. Doressoundiram[1], J. Lecacheux[1], J. Marques Oliveira[1], F. Roques[1], T. Widemann[1], F. Colas[7], F. Vachier[7], S. Renner[7,8], R. Leiva[9], F. Braga-Ribas[1,3,10], G. Benedetti-Rossi[3], J. I. B. Camargo[3], A. Dias-Oliveira[3], B. Morgado[3], A. R. Gomes-Júnior[3], R. Vieira-Martins[3], R. Behrend[11], A. Castro Tirado[4], R. Duffard[4], N. Morales[4], P. Santos-Sanz[4], M. Jelínek[12], R. Cunniffe[13], R. Querel[14], M. Harnisch[15,16], R. Jansen[15,16], A. Pennell[15,16], S. Todd[15,16], V. D. Ivanov[17], C. Opitom[17], M. Gillon[18], E. Jehin[18], J. Manfroid[18], J. Pollock[19], D. E. Reichart[20], J. B. Haislip[20], K. M. Ivarsen[20], A. P. LaCluyze[21], A. Maury[22], R. Gil-Hutton[23], V. Dhillon[24,25], S. Littlefair[24], T. Marsh[26], C. Veillet[27], K.-L. Bath[28,29], W. Beisker[28,29], H.-J. Bode[28,29,†], M. Kretlow[28,29], D. Herald[15,30,31], D. Gault[15,32,33], S. Kerr[15,34], H. Pavlov[30], O. Faragó[29,†], O. Klös[29], E. Frappa[35], M. Lavayssière[35], A. A. Cole[36], A. B. Giles[36], J. G. Greenhill[36,†], K. M. Hill[36], M. W. Buie[9], C. B. Olkin[9], E. F. Young[9], L. A. Young[9], L. H. Wasserman[37], M. Devogèle[37], R. G. French[38], F. B. Bianco[39,40,41,42], F. Marchis[1,43], N. Brosch[44], S. Kaspi[44], D. Polishook[45], I. Manulis[45], M. Ait Moulay Larbi[46], Z. Benkhaldoun[46], A. Daassou[46], Y. El Azhari[46], Y. Moulane[18,46], J. Broughton[15], J. Milner[15], T. Dobosz[47], G. Bolt[48], B. Lade[49], A. Gilmore[50], P. Kilmartin[50], W. H. Allen[15], P. B. Graham[15,51], B. Loader[15,30], G. McKay[15], J. Talbot[15], S. Parker[52], L. Abe[53], Ph. Bendjoya[53], J.-P. Rivet[53], D. Vernet[53], L. Di Fabrizio[54], V. Lorenzi[25,54], A. Magazzú[54], E. Molinari[54,55], K. Gazeas[56], L. Tzouganatos[56], A. Carbognani[57], G. Bonnoli[58], A. Marchini[29,58], G. Leto[59], R. Zanmar Sanchez[59], L. Mancini[60,61,62,63], B. Kattentidt[29], M. Dohrmann[29,64], K. Guhl[29,64], W. Rothe[29,64], K. Walzel[64], G. Wortmann[64], A. Eberle[65], D. Hampf[65], J. Ohlert[66,67], G. Krannich[68], G. Murawsky[69], B. Gährken[70], D. Gloistein[71], S. Alonso[72], A. Román[73], J.-E. Communal[74], F. Jabet[75], S. deVisscher[76], J. Sérot[77], T. Janik[78], Z. Moravec[78], P. Machado[79], A. Selva[29,80], C. Perelló[29,80], J. Rovira[29,80], M. Conti[81], R. Papini[29,81], F. Salvaggio[29,81], A. Noschese[29,82], V. Tsamis[29,83], K. Tigani[83], P. Barroy[84], M. Irzyk[84], D. Neel[84], J. P. Godard[84], D. Lanoiselée[84], P. Sogorb[84], D. Vérilhac[85], M. Bretton[86], F. Signoret[87], F. Ciabattari[88], R. Naves[29], M. Boutet[89], J. De Queiroz[29], P. Lindner[29], K. Lindner[29], P. Enskonatus[29], G. Dangl[29], T. Tordai[29], H. Eichler[90], J. Hattenbach[90], C. Peterson[91], L. A. Molnar[92], and R. R. Howell[93]

(Affiliations can be found after the references)

Received 19 September 2018 / Accepted 1 March 2019

ABSTRACT

Context. The tenuous nitrogen (N_2) atmosphere on Pluto undergoes strong seasonal effects due to high obliquity and orbital eccentricity, and has recently (July 2015) been observed by the New Horizons spacecraft.
Aims. The main goals of this study are (*i*) to construct a well calibrated record of the seasonal evolution of surface pressure on Pluto and (*ii*) to constrain the structure of the lower atmosphere using a central flash observed in 2015.
Methods. Eleven stellar occultations by Pluto observed between 2002 and 2016 are used to retrieve atmospheric profiles (density, pressure, temperature) between altitude levels of ∼5 and ∼380 km (i.e. pressures from ∼10 μbar to 10 nbar).
Results. (*i*) Pressure has suffered a monotonic increase from 1988 to 2016, that is compared to a seasonal volatile transport model, from which tight constraints on a combination of albedo and emissivity of N_2 ice are derived. (*ii*) A central flash observed on 2015 June 29 is consistent with New Horizons REX profiles, provided that (a) large diurnal temperature variations (not expected by current models) occur over Sputnik Planitia; and/or (b) hazes with tangential optical depth of ∼0.3 are present at 4–7 km altitude levels; and/or (c) the nominal REX density values are overestimated by an implausibly large factor of ∼20%; and/or (d) higher terrains block part of the flash in the Charon facing hemisphere.

Key words. methods: observational – methods: data analysis – planets and satellites: atmospheres – techniques: photometric – planets and satellites: physical evolution – planets and satellites: terrestrial planets

⋆ Partly based on observations made with the Ultracam camera at the Very Large Telescope (VLT Paranal), under program ID 079.C-0345(F), the ESO camera NACO at VLT, under program IDs 079.C-0345(B), 089.C-0314(C) and 291.C- 5016, the ESO camera ISAAC at VLT under program ID 085.C-0225(A), the ESO camera SOFI at NTT Paranal, under program ID 085.C-0225(B), the WFI camera at 2.2 m La Silla, under program ID's 079.A-9202(A), 075.C-0154, 077.C-0283, 079.C-0345, 088.C-0434(A), 089.C-0356(A), 090.C-0118(A) and 091.C-0454(A), the Laboratório Nacional de Astrofísica (LNA), Itajubá – MG, Brazil, the Southern Astrophysical Research (SOAR) telescope, and the Italian Telescopio Nazionale *Galileo* (TNG).

† Deceased.

1. Introduction

The tenuous atmosphere of Pluto was glimpsed during a ground-based stellar occultation observed on 1985 August 19 (Brosch 1995), and fully confirmed on 1988 June 9 during another occultation (Hubbard et al. 1988; Elliot et al. 1989; Millis et al. 1993) that provided the main features of its structure: temperature, composition, pressure, and density; see the review by Yelle & Elliot (1997).

Since then, Earth-based stellar occultations have been a highly efficient method to study the atmosphere of Pluto. They yield, in the best cases, information from a few kilometers above the surface (pressure ∼10 μbar) up to 380 km in altitude (∼10 nbar). As Pluto moved in front of the Galactic center, the yearly rate of stellar occultations dramatically increased during the 2002–2016 period, yielding a few events per year that greatly improved our knowledge of the atmospheric structure and evolution of this planet.

Ground-based occultations also provided a decadal monitoring of the atmosphere. Pluto has a large obliquity (∼120°, the axial inclination to its orbital plane) and high orbital eccentricity (0.25) that takes the dwarf planet from 29.7 to 49.3 AU during half of its 248-year orbital period. Northern spring equinox occurred in January 1988 and perihelion occurred soon after in September 1989. Consequently, our survey monitored Pluto as it receded from the Sun while exposing more and more of its northern hemisphere to sunlight. More precisely, as of 2016 July 19 (the date of the most recent occultation reported here), the heliocentric distance of Pluto has increased by a factor of 1.12 since perihelion, corresponding to a decrease of about 25% in average insolation. Meanwhile, the subsolar latitude has gone from 0° at equinox to 54° north in July 2016. In this context, dramatic seasonal effects are expected, and observed.

Another important aspect of ground-based occultations is that they set the scene for the NASA New Horizons mission (NH hereafter) that flew by the dwarf planet in July 2015 (Stern et al. 2015). A fruitful and complementary comparison between the ground-based and NH results ensued – another facet of this work.

Here we report results derived from eleven Pluto stellar occultations observed between 2002 and 2016, five of them yet unpublished, as mentioned below. We analyze them in a unique and consistent way. Including the 1988 June 9 occultation results, and using the recent surface ice inventory provided by NH, we constrain current seasonal models of the dwarf planet. Moreover, a central flash observed during the 2015 June 29 occultation is used to compare the lower atmosphere structure of Pluto derived from the flash with profiles obtained by the Radio Science EXperiment instrument (REX) on board NH below an altitude of about 115 km.

Observations, data analysis, and primary results are presented in Sect. 2. Implications for volatile transport models are discussed in Sect. 3. The analysis of the 2015 June 29 central flash is detailed in Sect. 4, together with its consequences for Pluto's lower atmosphere structure. Concluding remarks are provided in Sect. 5.

2. Observations and data analysis

2.1. Occultation campaigns

Table A.1 lists the circumstances of all the Pluto stellar occultation campaigns that our group organized between 2002 and 2016. The first part of this table lists the eleven events that were used in the present work. In a second part of the table, we list other campaigns that were not used because the occultation light curves had insufficient signal-to-noise ratios (S/Ns) and/or because of deficiencies in the configuration of the occulting chords (grazing chords or single chord) and as such, do not provide relevant measurements of the atmospheric pressure.

Table 1. Adopted physical parameters for Pluto.

Mass [(a)]	$GM_P = 8.696 \times 10^{11}$ m^3 s^{-2}
Radius [(a)]	$R_P = 1187$ km
N_2 molecular mass	$\mu = 4.652 \times 10^{-26}$ kg
N_2 molecular	$K = 1.091 \times 10^{-23}$
Refractivity [(b)]	$+(6.282 \times 10^{-26}/\lambda^2_{\mu m})$ cm^3 molecule^{-1}
Boltzmann constant	$k = 1.380626 \times 10^{-23}$ J K^{-1}
Pluto pole position [(c)]	α_p= 08h 52 m 12.94 s
(J2000)	$\delta_p = -$06d 10′ 04.8″

Notes. [(a)]Stern et al. (2015), where G is the constant of gravitation. [(b)]Washburn (1930). [(c)]Tholen et al. (2008).

Details on the prediction procedures can be found in Assafin et al. (2010, 2012) and Benedetti-Rossi et al. (2014). Some of those campaigns are already documented and analyzed in previous publications, namely the 2002 July 20, 2002 August 21, 2007 June 14, 2008 June 22, 2012 July 18, 2013 May 4, and 2015 June 29 events. They were used to constrain Pluto's global atmospheric structure and evolution (Sicardy et al. 2003, 2016; Dias-Oliveira et al. 2015; French et al. 2015; Olkin et al. 2015), the structure and composition (CH_4, CO and HCN abundances) of the lower atmosphere by combination with spectroscopic IR and sub-millimeter data (Lellouch et al. 2009, 2015, 2017), the presence of gravity waves (Toigo et al. 2010; French et al. 2015), and Charon's orbit (Sicardy et al. 2011). Finally, one campaign that we organized is absent from Table A.1 (2006 April 10). It did not provide any chord on Pluto, but was used to put an upper limit on its rings (Boissel et al. 2014).

We note that five more (yet unpublished) data sets are included here that were obtained on the following dates: 2008 June 24, 2010 February 14, 2010 June 4, 2011 June 4, and 2016 July 19.

2.2. Light-curve fitting

For all the eleven data sets used here, we used the same procedure as in Dias-Oliveira et al. (2015; DO15 hereafter) and in Sicardy et al. (2016). The procedure consists of simultaneously fitting the refractive occultation light curves by synthetic profiles generated by a ray-tracing code that uses the Snell–Descartes law. The physical parameters adopted in this code are listed in Table 1.

We note in particular that our adopted radius for Pluto is taken from Stern et al. (2015), who use a global fit to full-disk images provided by the Long-Range Reconnaissance Imager (LORRI) of NH to obtain $R_P = 1187 \pm 4$ km. Nimmo et al. (2017) improve that value to $R_P = 1188.3 \pm 1.6$ km. However, we kept the 1187 km value because it is very close to the deepest level reached by the REX experiment, near the depression Sputnik Planitia; see Sect. 4. Consequently, it is physically more relevant here when discussing the lower atmospheric structure.

We assume a pure N_2 atmosphere, which is justified by the fact that the next most important species (CH_4) has an abundance

of about 0.5% (Lellouch et al. 2009, 2015; Gladstone et al. 2016), resulting in negligible effects on refractive occultations.

We also assume a transparent atmosphere, which is supported by the NH findings. As discussed in Sect. 4, the tangential (line-of-sight) optical depth of hazes found by NH for the rays that graze the surface is $\tau_T \sim 0.24$, with a scale height of ~50 km (Gladstone et al. 2016; Cheng et al. 2017). As our fits are mainly sensitive to levels around 110 km (see below), this means that haze absorption may be neglected in our ray-tracing approach. We return to this topic in Sect. 4.3, which considers the effect of haze absorption on the central flash, possibly caused by the deepest layers accessible using occultations.

Moreover, we take a global spherically symmetric atmosphere, which is again supported by the NH results, at least above the altitude ~35 km; see Hinson et al. (2017) and Sect. 4. This is in line with global climate models (GCMs), which predict that wind velocities in the lower atmosphere should not exceed $v \sim$1–10 m s^{-1} (Forget et al. 2017). If uniform, this wind would create an equator-to-pole radius difference of the corresponding isobar level of at most $\Delta r \sim (R_P v)^2/4GM_P < 0.1$ km, using Eq. (7) of Sicardy et al. (2006) and the values in Table 1. This expected distortion is too small to significantly affect our synthetic profiles.

Finally, the temperature profile $T(r)$ is taken to be constant. Here, the radius r is counted from the center of Pluto, while the radius found by NH is 1187 km (Table 1). This is the reference radius from which we calculate altitudes. Fixing the pressure at a prescribed level (e.g., the surface) then entirely defines the density profile $n(r)$ to within a uniform scaling factor for all radii r, using the ideal gas equation, hydrostatic equilibrium assumption, and accounting for the variation of gravity with altitude.

Taking $T(r)$ to be constant with time is justified by the fact that the pressure is far more sensitive to surface temperature – through the vapor pressure equilibrium equation – than is the profile $T(r)$ to seasonal effects and heliocentric distance, at least from a global point of view. For instance, an increase of 1 K of the free N_2 ice at the surface is enough to multiply the equilibrium pressure by a factor of 1.7 (Fray & Schmitt 2009). We note that this is not inconsistent with our assumption that $T(r)$ is time-independent. In fact, the overall atmospheric pressure is controlled by the temperature a few kilometers above the surface, while our fits use a global profile $T(r)$ well above the surface.

Pluto ground-based stellar occultations probe, for the best data sets, altitudes from ~5 (pressure level ~10 μbar) to ~380 km (~10 nbar level); see DO15. Rays coming from below ~5 km are detectable only near the shadow center (typically within 50 km) where the central flash can be detected. The analysis is then complicated by the fact that double (or multiple) stellar images contribute to the flux. Moreover, the possible presence of hazes and/or topographic features can reduce the flux; see Sect. 4.

Conversely, rays coming from above 380 km cause stellar drops that are too small (<~1%) to be of any use under usual ground-based observing conditions. That said, our ray-tracing method is mainly sensitive to the half-light level, where the star flux has been reduced by 50%. This currently corresponds to a radius of about 1295 km (or an altitude ~110 km and pressure ~1.6 μbar).

2.3. Primary results

The ray-tracing code returns the best fitting parameters, in particular the pressure at a prescribed radius (e.g., the pressure p_{surf} at the surface, at radius $R_P = 1187$ km) and the ephemeris offset of Pluto perpendicular to its apparent motion, $\Delta\rho$. The ephemeris offset along the motion is treated separately; see DO15 for details. Error bars are obtained from the classical function $\chi^2 = \sum_1^N [(\phi_{i,obs} - \phi_{i,syn})/\sigma_i]^2$ which reflects the noise level σ_i of each of the N data points, where $\phi_{i,obs}$ and $\phi_{i,syn}$ are the observed and synthetic fluxes, respectively. An example of a $\chi^2(\Delta\rho, p_{surf})$ map is displayed in Fig. 1, using a simultaneous fit to the 2015 June 29 occultation light curves. It shows a satisfactory fit for that event, $\chi^2_{dof} \sim 1.06$. Table 2 lists the values of χ^2_{dof} for the other occultations, also showing satisfactory fits. We note the slightly higher values obtained for the 2002 August 21 and

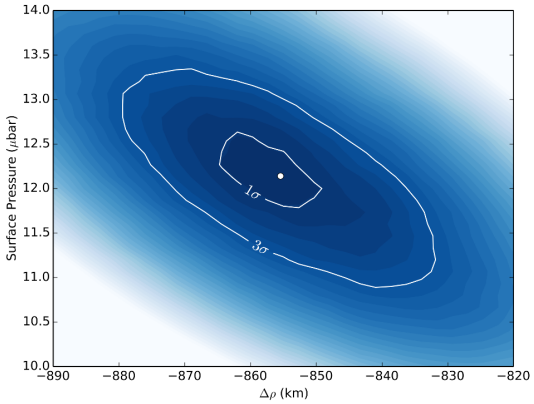

Fig. 1. Example of a $\chi^2(\Delta\rho, p_{surf})$ map derived from the simultaneous fit to the light curves obtained during the 2016 July 19 occultation. The quantity $\Delta\rho$ is the ephemeris offset of Pluto (expressed in kilometers) perpendicular to its apparent motion, as projected in the sky plane. The other parameter (p_{surf}) is the surface pressure of the DO15 atmospheric model. The white dot marks the best fit, where the minimum value χ^2_{min} of χ^2 is reached. The value $\chi^2_{min} = 4716$, using 4432 data points, indicates a satisfactory fit with a χ^2 per degree of freedom of $\chi^2_{dof} \sim 4716/4432 \sim 1.06$. The best fit corresponds to $p_{surf} = 12.04 \pm 0.41$ μbar (1-σ level). The error bar is derived from the 1-σ curve that delineates the $\chi^2_{min} + 1$ level. The 3-σ level curve (corresponding to the $\chi^2_{min} + 9$ level) is also shown.

Table 2. Atmospheric pressure on Pluto.

Date	Surface pressure p_{surf} (μbar)	Pressure at 1215 km p_{1215} (μbar)	Fit quality χ^2_{dof}
1988 Jun. 09	4.28 ± 0.44	2.33 ± 0.24 [(a)]	NA
2002 Aug. 21	8.08 ± 0.18	4.42 ± 0.093	1.52
2007 Jun. 14	10.29 ± 0.44	5.6 ± 0.24	1.56
2008 Jun. 22	11.11 ± 0.59	6.05 ± 0.32	0.93
2008 Jun. 24	10.52 ± 0.51	5.73 ± 0.21	1.15
2010 Feb. 14	10.36 ± 0.4	5.64 ± 0.22	0.98
2010 Jun. 04	11.24 ± 0.96	6.12 ± 0.52	1.02
2011 Jun. 04	9.39 ± 0.70	5.11 ± 0.38	1.04
2012 Jul. 18	11.05 ± 0.08	6.07 ± 0.044	0.61
2013 May 04	12.0 ± 0.09	6.53 ± 0.049	1.20
2015 Jun. 29	12.71 ± 0.14	6.92 ± 0.076	0.84
2016 Jul. 19	12.04 ± 0.41	6.61 ± 0.22	0.86

Notes. [(a)]The value p_{1215} is taken from Yelle & Elliot (1997). The ratio $p_{surf}/p_{1215} = 1.84$ of the fitting model of DO15 was applied to derive p_{surf}. Thus, the surface pressures (and their error bars) are mere scalings of the values at 1215 km. They do not account for systematic uncertainties caused by using an assumed profile (DO15 model); see discussion in Sect. 3.2. The qualities of the fits (values of χ^2_{dof}) are commented on in Sect. 2.3.

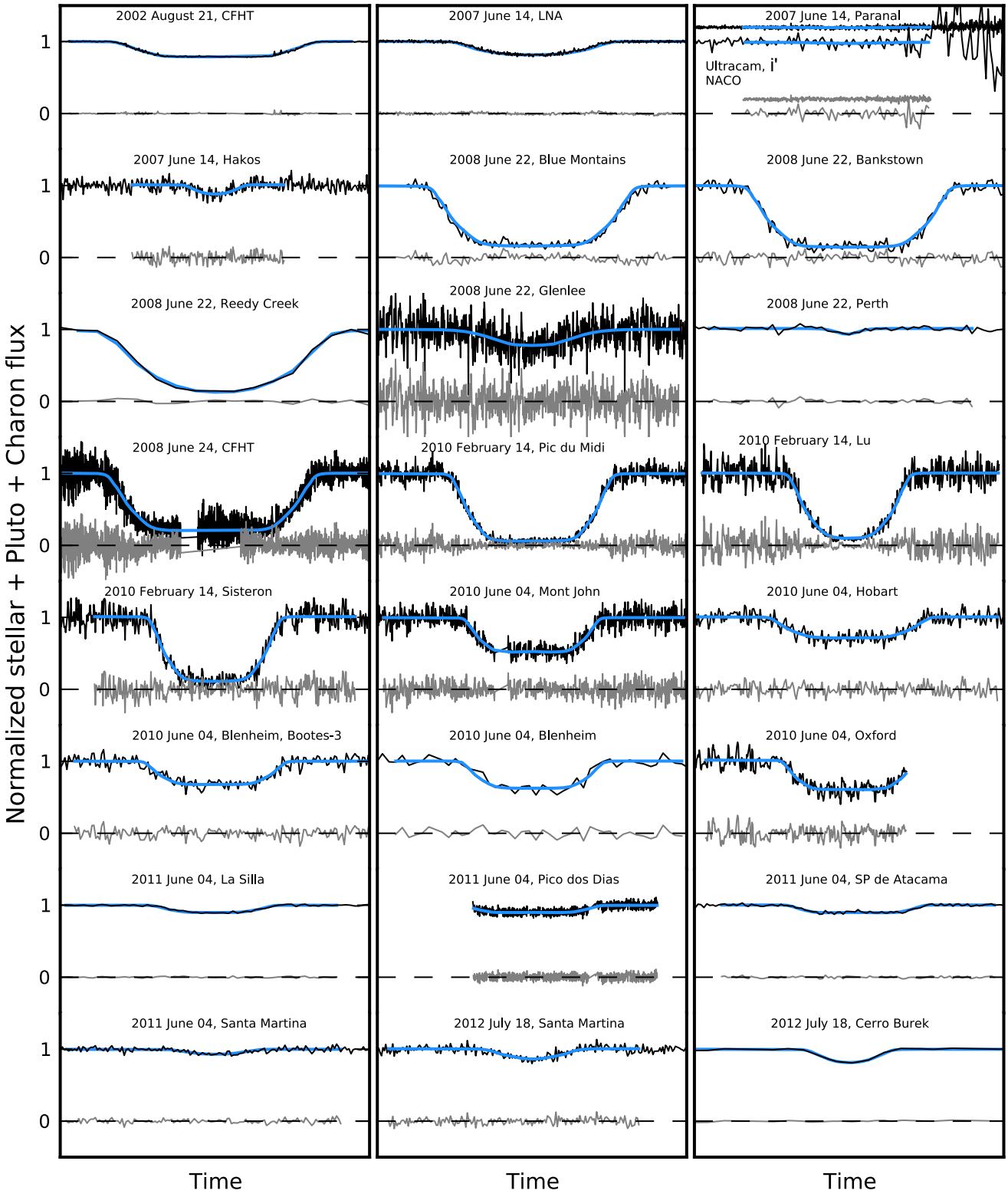

Fig. 2. Pluto occultation light curves obtained between 2002 and 2012. Blue curves are simultaneous fits (for a given date) using the DO15 temperature-radius $T(r)$ model; see text. The residuals are plotted in gray under each light curve.

2007 June 14 events (1.52 and 1.56, respectively). The presence of spikes in the light curve for the 2002 August 21 event (on top of the regular photometric noise) explains this higher value; see Fig. 2. From the same figure, we see that the 2007 June 14 light curves at Paranal were contaminated by clouds, also resulting in a slightly higher value of $\chi^2_{\rm dof}$. All together, those values validate a posteriori the assumptions of pure N_2, transparent, spherical atmosphere with temperature profile constant in time.

In total, we collected and analyzed in a consistent manner 45 occultation light curves obtained from eleven separate ground-based stellar occultations in the interval 2002–2016 (Table A.1). The synthetic fits to the light curves are displayed in Figs. 2

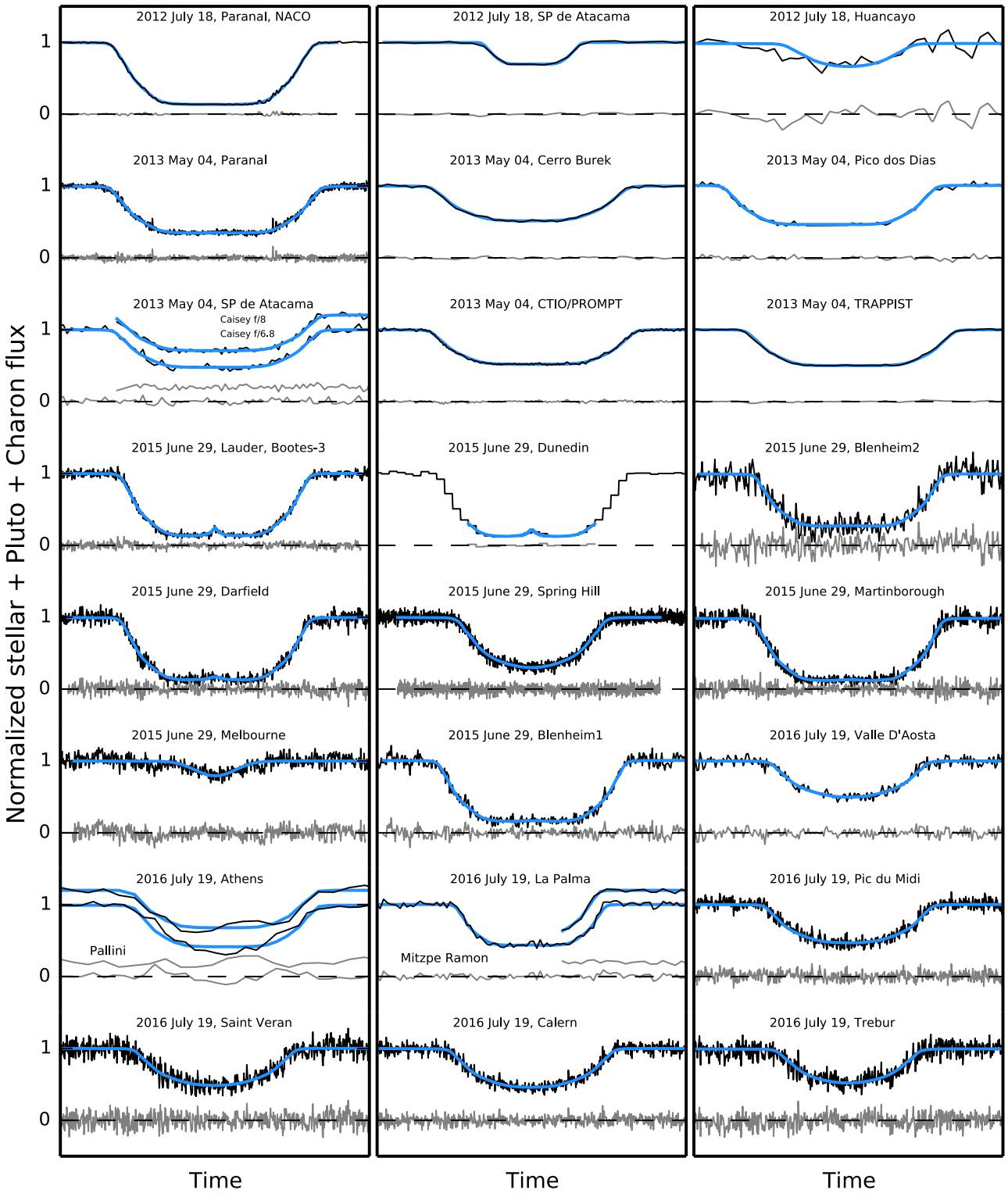

Fig. 3. As in Fig. 2 for the 2012–2016 period.

and 3. Figure B.1 shows the occulting chords and the aspect of Pluto for each event as seen from Earth.

Two main consequences of those results are now discussed in turn: (1) the temporal evolution of atmospheric pressure on Pluto; (2) the structure of its lower atmosphere using the central flash of 2015 June 29. A third product of these results is the update of the ephemeris using the occultation geometries between 2002 and 2016. This latter will be presented in a separate paper (Desmars et al. 2019).

3. Atmospheric evolution

3.1. Constraints from occultations

In 2002, a ground-based stellar occultation revealed that the atmospheric pressure on Pluto had increased by a factor of almost two compared to its value in 1988 (Elliot et al. 2003; Sicardy et al. 2003), although Pluto had receded from the Sun, thus globally cooling down. Models using global volatile

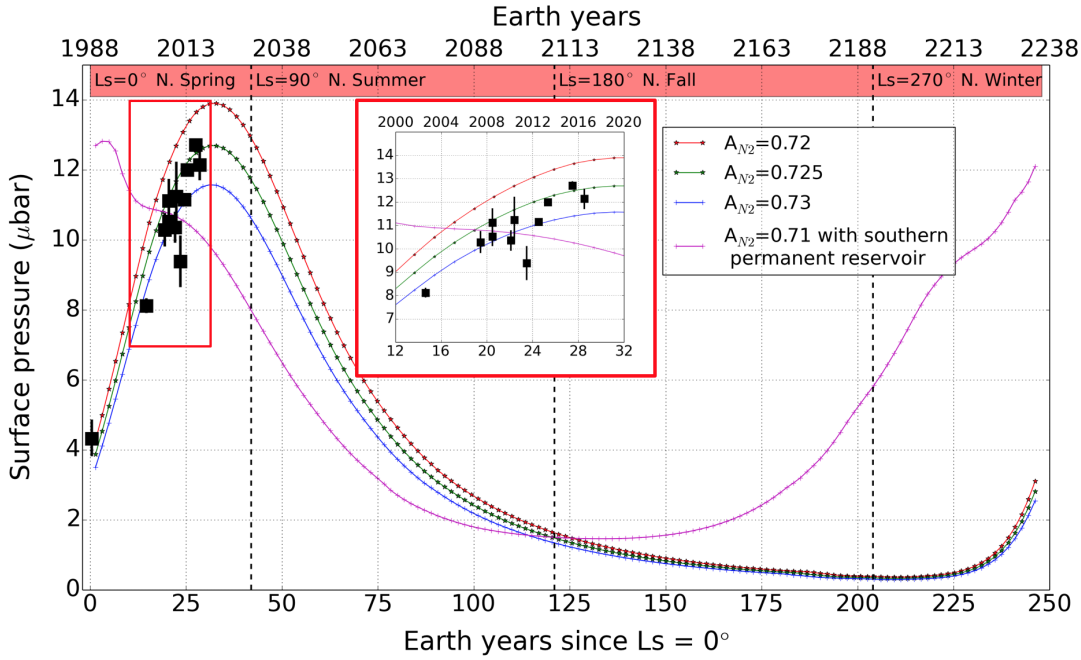

Fig. 4. Typical modeled annual evolution of surface pressure obtained with LMD Pluto volatile transport model, assuming permanent deposits of N_2 ice inside Sputnik Planitia and in the depression of mid-northern latitudes, a uniform soil seasonal thermal inertia of 800 J $s^{-1/2}$ m^{-2} K^{-1}, an emissivity ϵ_{N2} = 0.8 and albedo range A_{N2} = 0.72–0.73 for N_2 ice, chosen to yield a surface pressure near 10–11 μbar in July 2015. The black dots with error bars show the surface pressure (p_{surf}) inferred from stellar occultation pressure measurements (see Table 2). The curve in magenta corresponds to a similar simulation but assuming a permanent N_2 ice reservoir in the south hemisphere between 52.5 and 67.5° S, which leads to a pressure peak in 1990.

transport predicted this seasonal effect, among different possible scenarios (Binzel 1990; Hansen & Paige 1996).

Those models explored nitrogen cycles, and have subsequently been improved (Young 2012, 2013; Hansen et al. 2015). Meanwhile, new models have been developed to simulate possible scenarios for changes over seasonal (248 yr) and astronomical (30 Myr) time scales, accounting for topography and ice viscous flow, as revealed by the NH flyby in July 2015 (Bertrand & Forget 2016; Forget et al. 2017; Bertrand et al. 2018).

The measurements obtained here provide new values of pressure versus time, and are obtained using a unique light curve fitting model (taken from DO15), except for the 1988 occultation; see Table 2. This model may introduce systematic biases, but it can nevertheless be used to derive the relative evolution of pressure from date to date, and thus discriminates the various models of the current seasonal cycle of Pluto. In any case, the DO15 light-curve-fitting model appears to be close to the results derived from NH (see Hinson et al. 2017 and Sect. 4) meaning that those biases remain small. We note that other authors also used stellar occultations to constrain the pressure evolution since 1988 (Young et al. 2008; Bosh et al. 2015; Olkin et al. 2015), but with less comprehensive data sets. We do not include their results here, as they were obtained with different models that might introduce systematic biases in the pressure values.

3.2. Pressure evolution versus a volatile transport model

Table 2 provides the pressure derived at each date, at the reference radius r = 1215 km (altitude 28 km), their scaled values at the surface using the DO15 model, as well as the pressure previously derived from the 1988 June 09 occultation. Figure 4 displays the resulting pressure evolution during the time span 1988–2016. As discussed in the previous section, even if the use of the DO15 model induces biases on p_{surf}, it should be a good proxy for the global evolution of the atmosphere, and as such, provides relevant constraints on seasonal models.

We interpret our occultation results in the frame of the Pluto volatile transport model developed at the Laboratoire de Météorologie Dynamique (LMD). The model is designed to simulate the volatile cycles over seasonal and astronomical timescales on the whole planetary sphere (Bertrand & Forget 2016; Forget et al. 2017; Bertrand et al. 2018). We use the latest, most realistic version of the model featuring the topography map of Pluto (Schenk et al. 2018a) and large ice reservoirs (Bertrand et al. 2018). In particular, we place permanent reservoirs of nitrogen ice in the Sputnik Planitia basin and in the depressions at mid-northern latitudes (30°N, 60°N), as detected by NH (Schmitt et al. 2017) and modeled in Bertrand et al. (2018).

Figure 4 shows the annual evolution of surface pressure obtained with the model compared to the data. This evolution is consistent with the continuous increase of pressure observed since equinox in 1988, reaching an overall factor of almost three in 2016. This results from the progressive heating of the nitrogen ice in Sputnik Planitia and in the northern mid-latitudes, when those areas were exposed to the Sun just after the northern spring equinox in 1988, and close in time to the perihelion of 1989, as detailed in Bertrand & Forget (2016).

The model predicts that the pressure will reach its peak value and then drop in the next few years, due to: the orbitally driven decline of insolation over Sputnik Planitia and the northern mid-latitude deposits; and the fact that nitrogen condenses more intensely in the colder southern part of Sputnik Planitia, thus precipitating and hastening the pressure drop. The climate model has several free parameters: the distribution of nitrogen ice, its Bond albedo and emissivity, and the thermal inertia of

the subsurface (soil). However, the large number of observation points and the recent NH observations provide strong constraints for those parameters, leading to an almost unique solution.

First, our observations restrict the possible N_2 ice surface distribution. Indeed, the southern hemisphere of Pluto is not expected to be significantly covered by nitrogen ice at the present time, because otherwise the peak of surface pressure would have occurred much earlier than 2015, as suggested by the model simulations (Fig. 4). With our model, we obtain a peak of pressure after 2015 only when considering small mid-latitudinal nitrogen deposits (or no deposit at all) in the southern hemisphere.

In our simulation, nitrogen does not condense significantly in the polar night (outside Sputnik Planitia), in spite of the length of the southern fall and winter. This is because in Pluto conditions, depending of the subsurface thermal inertia, the heat stored in the southern hemisphere during the previous southern hemisphere summer can keep the surface temperature above the nitrogen frost point throughout the cold season, or at least strongly limit the nitrogen condensation.

Consequently, the data points provide us with a second constraint, which is a relatively high subsurface thermal inertia preventing massive condensation in the southern polar night. Using a thermal inertia between 700 and 900 J $s^{-1/2}$ m^{-2} K^{-1} permits us to obtain a surface pressure ratio ($p_{\rm surf,2015}/p_{\rm surf,1988}$) of around 2.5–3, as observed. Higher (resp. lower) thermal inertia tends to lower (resp. increase) this ratio, as shown in Fig. 2a of Bertrand & Forget (2016).

Finally, the nitrogen cycle is very sensitive to the nitrogen ice Bond albedo $A_{\rm N2}$ and emissivity $\epsilon_{\rm N2}$, and only a small range for these parameters allows for a satisfactory match to the observations. Figure 4 illustrates that point. To understand it, one can do the thought experiment of imagining Pluto with a flat and isothermal surface at vapor pressure equilibrium. A rough estimate of the equilibrium temperature is provided by the classical equation:

$$\epsilon_{\rm N2}\sigma T^4 = (1 - A_{\rm N2})\,\frac{F}{4},$$

where F is the solar constant at Pluto and $\sigma = 5.67 \times 10^{-8}$ W m^{-2} K^4 is the Stefan–Boltzmann constant. The surface pressure $p_{\rm surf}$ is then estimated from the surface temperature $T_{\rm surf}$ assuming N_2 vapor pressure equilibrium (Fray & Schmitt 2009). Consequently, the surface pressure data set inferred from stellar occultations provide us with a constraint on $(1 - A_{\rm N2})/\epsilon_{\rm N2}$. In practice, in the model, we assume large grains for N_2 ice and we fix the emissivity at a relatively high value $\epsilon_{\rm N2} = 0.8$ (Lellouch et al. 2011). Taking $F = 1.26$ W m^{-2} (in 2015) and assuming $A_{\rm N2} = 0.72$, we find $T_{\rm surf} = 37.3$ K, and a corresponding vapor pressure $p_{\rm surf} = 14.8$ μbar for the N_2 ice at the surface. With $A_{\rm N2} = 0.73$, we obtain $T_{\rm surf} = 37.0$ K and $p_{\rm surf} = 12.0$ μbar. Thus, the simple equation above provides pressure values that are consistent with the volatile transport model displayed in Fig. 4. It can then be used to show that decreasing the nitrogen ice albedo by only 0.01 leads to an increase of surface pressure in 2015 by the large amount of 25%.

4. Lower atmosphere of Pluto

4.1. The 2015 June 29 occultation

The 2015 June 29 event provided seven chords across the atmosphere of Pluto; see Table A.1 and Fig. B.1. A first analysis of this event was presented in Sicardy et al. (2016). The two southernmost stations (Bootes-3 and Dunedin) probed the central flash region (Fig. 5). This was a unique opportunity to study the lower atmosphere a mere fortnight before the NH flyby (2015 July 14). During this short time lapse, we may assume that the atmosphere did not suffer significant global changes.

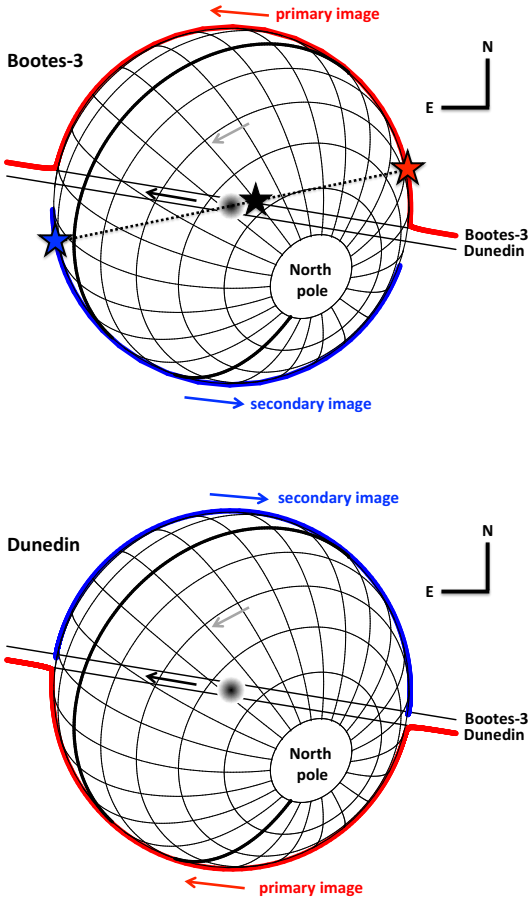

Fig. 5. The reconstructed geometry of the 2015 June 29 Pluto stellar occultation. Celestial north is at the top and celestial east to the left; see labels N and E. The equator and prime meridian (facing Charon) are drawn as thicker lines. The direction of planet rotation is along the gray arrow. In the two panels, the stellar motion relative to Pluto is shown as black solid lines as seen from the Bootes-3 and Dunedin stations, with direction of motion marked by the black arrow. The shaded region at the center roughly indicates the zone where a central flash could be detected. In the upper panel, the red and blue lines are the trajectories of the primary and secondary stellar images, respectively, as seen from Bootes-3. In the lower panel, the same is shown as in the upper panel but for the stellar images as seen from Dunedin. For a spherical atmosphere, the position of the star in the sky plane, the center of Pluto and the two images are aligned, as shown in the upper panel (see the dotted line connecting the star symbols).

For a spherical atmosphere, there are two stellar images at any moment, a primary (near limb) image and a secondary (far limb) image that are aligned with the center of the planet and the star position, as projected in the sky plane; see Fig. 5. Since the ray-tracing code provides the refraction angle corresponding to each image, their positions along the limb of Pluto can be determined at any time (Fig. 5) and then projected onto its surface (Fig. 6).

4.2. Comparison with the REX results

The REX instrument recorded an uplinked 4.2 cm radio signal sent from Earth. The phase shift due to the neutral atmosphere

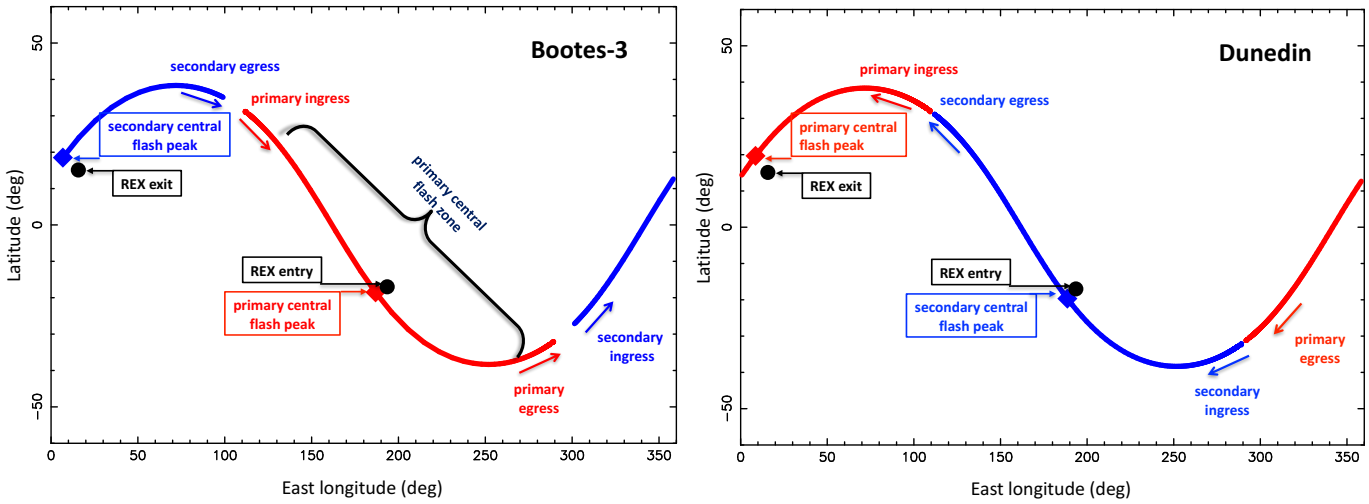

Fig. 6. *Left panel*: traces of the primary (red) and secondary (blue) stellar images observed at Bootes-3, as deduced from Fig. 5. The arrows indicate the direction of motion. "Ingress" (resp. "egress") refers to the disappearance (resp. re-appearance) of the images into the atmosphere of Pluto. The diamond-shaped symbols mark the positions of the image at the peak of the flash, corresponding to the time of closest approach of the respective station to the shadow center. In total, the primary image scanned longitudes from 120 to 270°, while the secondary image scanned longitudes from 310 to 360° and then from 0 to 70°. The brace indicates the total duration of the primary flash (~15 s, see Sect. 4) at Bootes-3, covering a relatively large region of more than 120° in longitude. A similar extension applies to the secondary flash, but the brace has not been drawn for sake of clarity. The black bullets are the locations of the REX measurements at entry and exit (Hinson et al. 2017). We note the casual proximity of the REX points and the 2015 June 29 flash peaks. *Right panel*: same as in left panel but for the Dunedin station, where the brace has not been repeated. We note that the tracks and motions of the primary and secondary images are essentially swapped between the two stations.

Table 3. Regions probed by the central flash (2015 June 29) and REX experiment (2015 July 14.).

	Time (UT) [a]	Location on surface	Local solar time [b]
June 29, 2015			
Bootes-3, primary image	16:52:54.8	186.8°E, 18.5°S	7.67 (sunrise)
Bootes-3, secondary image	16:52:54.8	6.8°E, 18.5°N	19.67 (sunset)
Dunedin, primary image	16:52:56.0	8.6°E, 19.7°N	19.79 (sunset)
Dunedin, secondary image	16:52:56.0	188.6°E, 19.7°S	7.79 (sunrise)
NH radio experiment (REX), July 14, 2015			
Entry	12:45:15.4	193.5°E, 17.0°S	16.52 (sunset)
Exit	12:56:29.0	15.7°E, 15.1°N	4.70 (sunrise)

Notes. [a]For the ground-based observations, this is the time of closest approach to shadow center (Sicardy et al. 2016), for the REX experiment, this the beginning and end of occultation by the solid body (Hinson et al. 2017). [b]One "hour" corresponds to a rotation of Pluto of 15°. A local time before (resp. after) 12.0 h means morning (resp. evening) limb.

was then used to retrieve the $n(r)$, $p(r)$, and $T(r)$ profiles through an inversion method and the usual ideal gas and hydrostatic assumptions (Hinson et al. 2017). The REX radio occultation probed two opposite points of Pluto as the signal disappeared behind the limb (entry) and re-appeared (exit); see Fig. 6. We note that the REX entry point is at the southeast margin of Sputnik Planitia, a depression that is typically 4 km below the surrounding terrains; see Hinson et al. (2017) for details.

We also note the (serendipitous) proximity of the regions scanned by the 2015 June 29 central flash and the two zones probed by REX at entry and exit. This permits relevant tests of the REX profiles against the central flash structure. The local circumstances on Pluto for the central flash and the REX occultation are summarized in Table 3. However, the local times are swapped between our observations and REX suboccultation points: the sunrise regions of one being the sunset places of the other and vice versa; see the discussion below.

The REX profiles are in good general agreement with those derived by Sicardy et al. (2016) – based itself on the DO15 procedure – between the altitudes of 5 and 115 km (Figs. 7 and 8), thus validating our approach. However, we see discrepancies at altitudes below ~25 km ($r < 1212$ km), in the region where the REX entry and exit profiles diverge from one another.

Part of those differences may stem from the swapping of the sunrise and sunset limbs between the REX measurements and our observations, and from the fact that a diurnal sublimation/condensation cycle of N_2 occurs over Sputnik Planitia. In fact, lower temperatures just above the surface are expected at the end of the afternoon in that region, after an entire day of sublimation (Hinson et al. 2017). Conversely, a warmer profile could prevail at sunrise, after an entire night of condensation.

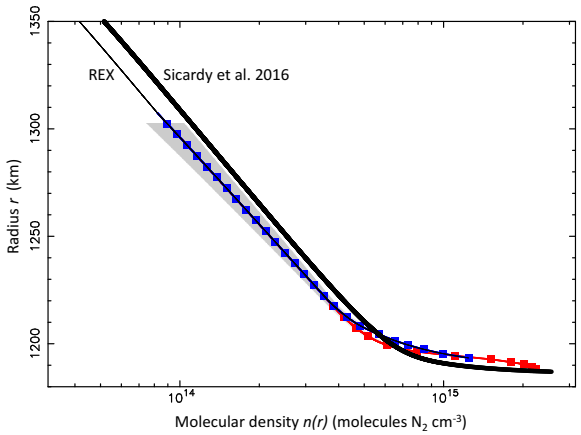

Fig. 7. Red and blue squares: the REX radio occultation N_2 density profiles, with the shaded area indicating the 1-σ error bar domain (Hinson et al. 2017). Below 1220 km, the errors decrease and become unnoticeable in this plot. The entry (resp. exit) profile is given from r = 1188.4 km (resp. 1193.4 km), up to 1302.4 km, where the error bars become too large for a reliable profile to be retrieved. We note that by construction, the REX entry and exit profiles are identical for $r > 1220$ km. Below that radius, the two profiles diverge significantly, due to different physical conditions of the boundary layer just above the surface (Fig. 8). The solid red and blue lines connecting the squares are spline interpolations of the REX profiles that are used in our ray-tracing code; see text. The REX profile is extended above r = 1302.4 km as a thin solid line, by adopting a scaled version of the 2015 June 29 profile (i.e., a mere translation of the thick solid line in this $(\log_{10}(n), r)$ plot), while ensuring continuity with the REX profile. Thick solid line: the profile derived by Sicardy et al. (2016) using the DO15 light-curve-fitting model. The formal 1-σ error bar of this profile is smaller than the thickness of the line, but does not account for possible biases; see text.

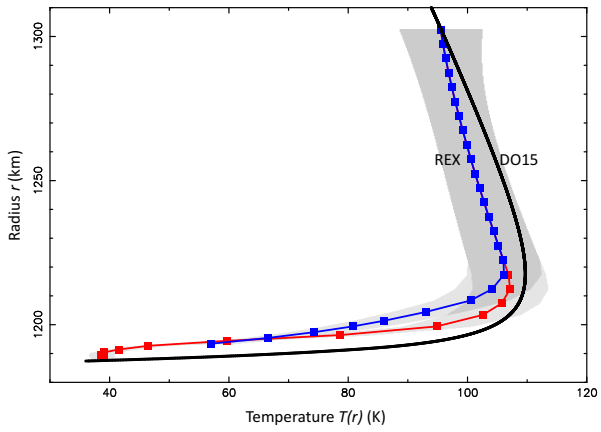

Fig. 8. As in Fig. 7 but for the temperature profiles $T(r)$. By construction, the REX profile uses a boundary condition T_b = 95.5 K at the reference radius r_b = 1302.4 km in order to connect it to the DO15 profile (solid black line). Thus, the intersection of the REX and DO15 profiles at r_b is a mere result of the choice of T_b, and is not a measurement. There are no formal error bars on the temperature profile of Sicardy et al. (2016), as most of the errors come in this case from biases; see text.

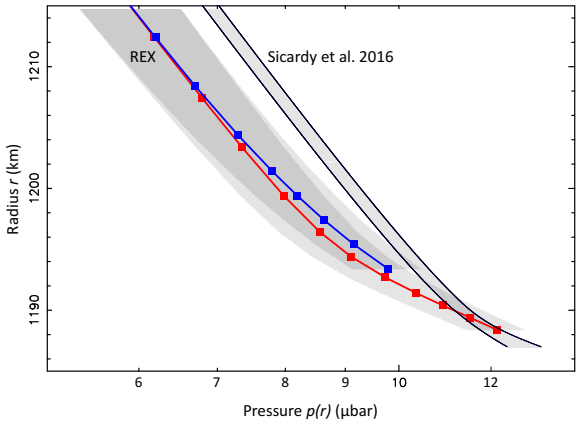

Fig. 9. As in Fig. 7, but for the pressure profiles $p(r)$. The gray region encompassing the profile of Sicardy et al. (2016) and delimited by thin solid lines is the uncertainty domain discussed by those authors.

This warmer profile would then be more in agreement with the DO15 temperature profile.

However, the difference between the REX (red) and DO15 (black) profiles in Fig. 8 remains large (more than 20 K at a given radius). This is much larger than expected from current GCMs (e.g. Forget et al. 2017, Fig. 7), which predict diurnal variations of less than 5 K at altitude levels 1–2 km above Sputnik Planitia, and less than 1 K in the ∼4–7 km region that causes the flash (Sicardy et al. 2016). In practice, Forget et al. (2017) predict that above 5 km, the temperature should be uniform over the entire planet at a given radius. This is in contrast to REX observations that reveal different temperature profiles below 25 km (Fig. 8). Thus, ingredients are still missing to fully understand REX observations, for instance the radiative impact of organic hazes, an issue that remains out of the scope of this paper.

We note that the entry REX profile goes deeper than the exit profile. This reflects the fact that the nominal radii of Pluto are at 1187.4 ± 3.6 km at entry and 1192.4 ± 3.6 km at exit (Hinson et al. 2017). This discrepancy is not significant considering the uncertainties on each radius. However, the examination of Fig. 9 shows that the most probable explanation of this mismatch is that REX probed higher terrains at exit than at entry, then providing the same pressure at a given planetocentric radius. This is the hypothesis that we adopt here, which is furthermore supported by the fact that the REX entry point is actually near the depressed region Sputnik Planitia. More precisely, the REX solution for the radius at entry (1187.4 ± 3.6 km) is fully consistent with the radius derived from NH stereo images at the same location, 1186.5 ± 1.6 km (Hinson et al. 2017). That said, we note that our data do not have enough sensitivity to constrain the absolute vertical scale of the density profiles at a better level than the REX solution (±3.6 km); see following section.

4.3. The 2015 June 29 central flash

The REX profiles extend from the surface (with pressures of 12.8 ± 0.7 and 10.2 ± 0.7 μbar at entry and exit, respectively) up to about 115 km, where the pressure drops to ∼1.2 μbar. Meanwhile, Sicardy et al. (2016) derive a consistent surface pressure of 12.7 μbar, with error domains that are discussed later.

Nevertheless, the DO15-type thermal profile for the stratosphere (also called inversion layer) that extends between the surface and the temperature maximum at r = 1215 km is assumed to have a hyperbolic shape. The DO15 profile stops at its bottom at the point where it crosses the vapor pressure equilibrium line, thus defining the surface (assuming no troposphere). While the adopted functional form captures the gross structure of the thermal profile, it remains arbitrary. In fact, as the error bars of the REX profiles decrease with decreasing altitude, it becomes clear that the DO15 profile overestimates the temperature by tens of degrees (compared to REX) in the stratosphere as one

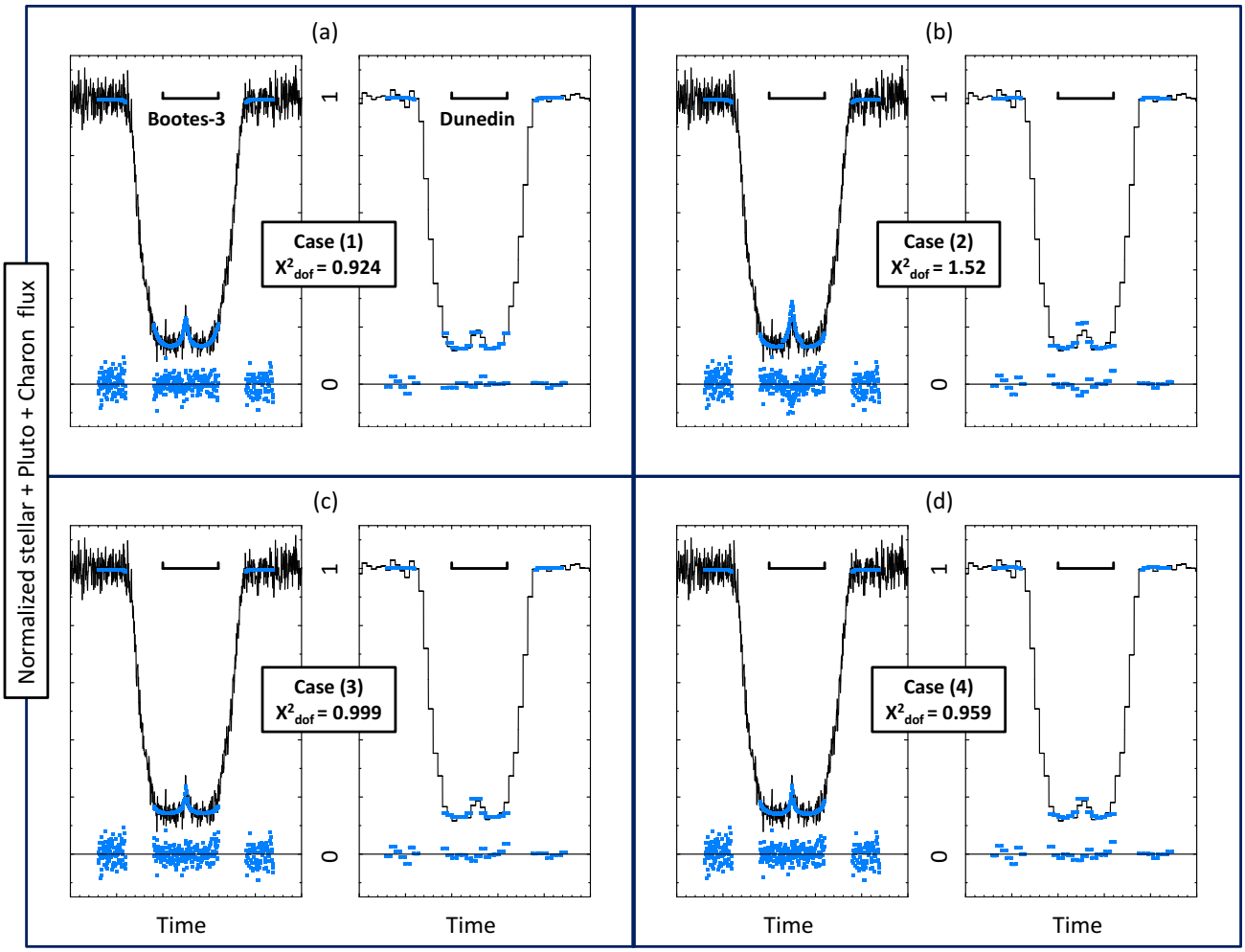

Fig. 10. In each panel, the synthetic fits to the Bootes-3 (*left*) and Dunedin (*right*) observations of 2015 June 29 shown as blue points, together with the residuals (observations minus model) under each light curve, for each of the cases discussed in the text. The tick marks on the time axis are plotted every 10 s, and the horizontal bars above each curve show the one-minute interval from 16h 52 m30 to 16h 53 m30s UT. (*a*) Best fits to the Bootes-3 and Dunedin light curves using the DO15 light curve fitting model (Sicardy et al. 2016); see also Figs. 7 and 8. (*b*) As in panels a but using the nominal REX density profile. We note that the synthetic flashes are too high at both stations. (*c*) As in (a) and (b) but after multiplying the REX density profiles by a factor $f = 0.805$ and moving the shadow of Pluto 17 km north of the solution of Sicardy et al. (2016). (*d*) As in panels c using the nominal REX profiles, but with a topographic feature of height $h = 1.35$ km that blocks the stellar image during part of its motion along the southern Pluto limb (Fig. 5); the shadow has now been moved by 19.5 km north of the solution of Sicardy et al. (2016). In each panel, the value of the χ^2 function per degree of freedom ($\chi^2_{\rm dof}$) provides an estimation of the quality of the fit; see text for discussion.

approaches the surface. Also, it ends up at the surface with a thermal gradient (16 K km^{-1}, see Fig. 8) that is much stronger than in the REX profiles, where it is always less that 10 K km^{-1} in the stratosphere. As discussed in the previous section however the N_2 diurnal cycle might induce a warmer temperature profile (after nighttime condensation) at an altitude of a few kilometres above Sputnik Planitia. This would result in a larger thermal gradient that would be closer to the DO15 profile, but still too far away from it according to GCM models, as discussed previously.

In this context, we have tested the REX profiles after modifying our ray-tracing procedure to generate new synthetic central flashes. We now account for the fact that the two stellar images that travel along the limb of Pluto probe different density profiles. To simplify the problem as much as possible, we assume that the stellar images that follow the northern and southern limbs probe an atmosphere that, respectively, has the entry and exit REX density profiles, in conformity with the geometry described in Fig. 6. This is an oversimplified approach as the stellar images actually scan relatively large portions of the limb, not just the REX entry and exit points (Fig. 6). However, this exercise allows us to assess how different density profiles may affect the shape of the central flash. To ensure smooth synthetic profiles, the discrete REX points have been interpolated by spline functions, using a vertical sampling of 25 m. Finally, above the radius $r = 1302.4$ km, the REX profiles have been extrapolated using a scaled version of the DO15 profile (see details in Fig. 7).

Because we want to test the shape of the central flash only, we restrict the generation of the synthetic light curves to the bottom parts of the occultation. We also include in the fit two intervals that bracket the event outside the occultation, where we know that the flux must be unity (Fig. 10). Those external parts do not discriminate the various models, but serve to properly scale the general stellar drop. Thus, the steep descents and ascents of the occultation light curves are avoided, as they would provide too much weight to the fits. Finally, since no calibrations of the light curves are available to assess the contribution ϕ_P of Pluto

to the observed flux, a linear least-square fit of the synthetic flux to the data was performed before calculating the residuals. This introduces a supplementary adjustable parameter, ϕ_P to the fits.

Four simple scenarios are considered: (1) We first use the original model of Sicardy et al. (2016) to generate the light curves. (2) We take the REX density profiles at face value and use the modified ray-tracing model described above, fixing the ephemeris offset of Pluto as determined in Case (1). (3) We apply an adjustable, uniform scaling factor f to the two REX density profiles (which also applies to the pressure profile since the temperature is fixed), and we adjust the ephemeris offset accordingly. (4) Turning back to the REX density profiles of Case (2), we assume that a topographic feature of height h (on top of the REX exit radius, 1192.4 km) blocks the stellar image generated by the REX exit profile, that is, that the stellar image that travels along the southern limb (Fig. 5) is turned off below a planetocentric radius 1192.4 + h km.

It should be noted that the amplitude of the synthetic flash is insensitive to the absolute altitude scale that we use for the REX density profiles, to within the ±3.6 km uncertainty discussed in the previous section. For instance, displacing the REX entry profile downward by 1 km, while displacing the exit profile upward by the same amount (because the two errors and anticorrelated; see Hinson et al. 2017) changes the relative amplitude of the flash by a mere 10^{-3}, well below the noise level of our observations (Fig. 10). In other words, our central flash observations cannot pin down the absolute vertical scales of the profiles to within the ±3.6 km REX uncertainty.

The fits are displayed in Fig. 10. Their qualities are estimated through the χ^2 value. Depending on the fits, there are M = 1–3 free parameters (the pressure at a prescribed level, off-track displacement of Pluto with respect to its ephemeris, and its contribution ϕ_P to the flux). In all the fits, there are N = 217 adjusted data points. We note that the value of h in Case (4) has been fixed to 1.35 km, i.e., it is not an adjustable parameter. This is discussed further in the points below:

1. The nominal temperature profile $T(r)$ of Sicardy et al. (2016) with surface pressure p_{surf} = 12.7 μbar provides a satisfactory fit with χ^2 = 198 ($\chi^2_{dof} = \chi^2/(N - M)$ = 0.924 per degree of freedom). In this case, the Bootes-3 and Dunedin stations passed 46 km north and 45 km south of the shadow center, respectively.

2. The nominal REX profiles result in flashes that are too high compared to the observations, as noted by a visual inspection of Fig. 10 (and from χ^2 = 326, χ^2_{dof} = 1.52). This can be fixed by introducing haze absorption. A typical factor of 0.7 must be applied to the Bootes-3 synthetic flash in order to match the data, while a typical factor of 0.76 must be applied to the Dunedin synthetic flash. This corresponds to typical tangential optical depths (along the line of sight) in the range τ_T = 0.27–0.35, for rays that went at about 8 km above the REX 1187.4 km radius. Changing the off-track offset of Pluto does not help in this case, as one synthetic flash increases while the other decreases. This could be accommodated by adjusting accordingly the optical depths τ_T, but this introduces too many adjustable parameters to be relevant.

3. A satisfactory best fit is obtained (χ^2 = 214, χ^2_{dof} = 0.999) by uniformly reducing the REX density profiles by a factor of 0.805 and by moving the shadow center cross-track of Pluto by 17 km north with respect to Case (1), the Bootes-3, and Dunedin stations passing 29 km north and 62 km south of the shadow center, respectively. This displacement corresponds to a formal disagreement at 3-σ level for the center position of Pluto between Cases (1) and (3), when accounting for the noise present in the central flashes (Fig. 10). Thus, such a difference remains marginally significant. We also note that a satisfactory fit to the Bootes-3 flash is obtained, while the Dunedin synthetic flash remains slightly too high. As mentioned again below however, a reduction of the density profile by a factor of 0.805 is implausible considering the error bars of the REX profiles.

4. Using again the nominal REX profiles of Case (2), but imposing a topographic feature of height h = 1.35 km on top of the REX exit radius of 1192.4 km, a satisfactory fit to the Bootes-3 flash is obtained (χ^2 = 205, χ^2_{dof} = 0.959); in fact the best of all fits for that station. Meanwhile, the Dunedin synthetic flash remains slightly too high compared to observations. In this model, the center of the shadow of Pluto has been moved cross-track by 19.5 km north with respect to the first model, meaning that the Bootes-3 and Dunedin stations passed 26.5 km north and 64.5 km south of the shadow center, respectively. Again the discrepancy relative to the center solution of Case (1) is at 3-σ level, and is thus marginally significant. The particular choice of h = 1.35 km stems from the fact that lower values would increase the Dunedin flash even more, while higher values would decrease the Bootes-3 flash too much. We have not explored further values of h by tweaking the density profiles. Therefore, this is again an exercise to show that reasonably high topographic features may explain the observed flash.

5. Concluding remarks

5.1. Global atmospheric evolution of Pluto

Figure 4 summarizes our results concerning the evolution of the atmospheric pressure of Pluto with time. It shows that the observed trend can be explained by adjusting the physical parameters of the planet in a rather restrictive way.

As noted in Sect. 3, this evolution is consistent with the continuous increase of pressure observed since 1988 (a factor of almost three between 1988 and 2016). It results from the heating of the nitrogen ice in Sputnik Planitia and in the northern mid-latitudes, when the areas are exposed to the Sun (just after the northern spring equinox in 1989) and when Pluto is near the Sun (Bertrand & Forget 2016). The model also predicts that atmospheric pressure is expected to reach its peak and drop in the next few years, due to (1) the orbitally driven decline of insolation over Sputnik Planitia and the northern mid-latitude deposits, and (2) the fact that nitrogen condenses more intensely in the colder southern part of Sputnik Planitia, thus precipitating and hastening the pressure drop.

In that context, it is important to continue the monitoring of the atmosphere of Pluto using ground-based stellar occultations. Unfortunately, as Pluto moves away from the Galactic plane, such occultations will become increasingly rare.

5.2. Lower atmosphere of Pluto

The models presented in the Sect. 4 and illustrated in Fig. 10 are not unique and not mutually exclusive. For instance, one can have at the same time a topographic feature blocking the stellar rays, together with some haze absorption. Also, hazes, if present, will not be uniformly distributed along the limb. Similarly, topographic features will probably not be uniformly distributed along the limb, but will rather have a patchy structure that complicates our analysis. In spite of their limitations, the simple scenarios presented above teach us a few lessons:

1. Although satisfactory in terms of flash fitting, the nominal temperature profile of Sicardy et al. (2016) seems to be ruled out below the planetocentric radius ~1215 km, since it is clearly at variance with the REX profiles (Fig. 8), while probing essentially the same zones on the surface of the dwarf planet (Fig. 6). As discussed in Sect. 4.2 however, diurnal changes occurring over Sputnik Planitia might explain this discrepancy, with a cooler (sunset) REX temperature profile and a warmer (sunrise) profile more in line with the DO15 solution. However, current GCM models predict that these diurnal changes should occur below the 5 km altitude level, and not as high as the 25 km level observed here. This issue remains an open question that would be worth investigating in future GCM models.

2. The REX profiles taken at face value cannot explain the central flashes observed at Bootes-3 and Dunedin, unless hazes are present around the ~8 km altitude level, with optical depths along the line of sight in the range $\tau = 0.27$–0.35. This is higher but consistent with the reported value of $\tau \sim 0.24$ derived from NH image analysis (Gladstone et al. 2016; Cheng et al. 2017). In fact, the two values are obtained by using quite different methods. Cheng et al. (2017) assume tholin-like optical constant, which is not guaranteed. Moreover, their 0.24 value is the scattering optical depth, while we measure the aerosol extinction (absorption plus scattering). Chromatic effects might also be considered to explain those discrepancies, as the Bootes-3, Dunedin, and the NH instruments have different spectral responses. Our data are too fragmentary however to permit such a discussion.

3. An alternative solution is to uniformly reduce the REX density profiles by a factor 0.805. However, this would induce a large disagreement (8-σ level) on the REX density profile at 7 km altitude, and thus appears to be an unrealistic scenario. Moreover, the underdense versions of the REX profiles would then formally disagree (i.e., beyond the internal error bars of the DO15 light-curve-fitting model) when extrapolated to the overlying half-light level around $r = 1300$ km. A remedy would be to patch up profiles derived from ground-based measurements with the underdense REX profiles, and re-run global fits. This remains out of the scope of the present analysis.

4. The topographic feature hypothesis remains an attractive alternative, as it requires modest elevation (a bit more than 1 km) above the REX exit region, which is known to be higher than the entry region, Sputnik Planitia. A more detailed examination of the elevation maps of Pluto, confronted with the stellar paths shown in Fig. 6, should be undertaken to confirm or reject that hypothesis. That said, such ± 1 km topographic variations are actually observed all over the surface of the planet (Schenk et al. 2018b).

As a final comment, we reiterate that the flashes were generated by assuming a spherical atmosphere near the surface of Pluto. There is no sign of distortion of the Bootes-3 or Dunedin flashes suggesting a departure from sphericity. It would be useful however to assess such departures, or at least establish an upper limit for them in future works.

Acknowledgements. This article is dedicated to the memory of H.-J. Bode, J. G. Greenhill and O. Faragó for their long-standing support and participation to occultation campaigns. The work leading to these results has received funding from the European Research Council under the European Community's H2020 2014-2020 ERC Grant Agreement n° 669416 "Lucky Star". E.M. thanks support from Concytec-Fondecyt-PE and GA, FC-UNI for providing support during the 2012 July 18 occultation. B.S. thanks S. Para for partly supporting this research though a donation, J. P. Beaulieu for helping us accessing to the Hobart Observatory facilities and B. Warner, B. L. Gary, C. Erickson, H. Reitsema, L. Albert, P. J. Merritt, T. Hall, W. J. Romanishin, Y. J. Choi for providing data during the 2007 March 18 occultation. M.A. thanks CNPq (Grants 427700/2018-3, 310683/2017-3 and 473002/2013-2) and FAPERJ (Grant E-26/111.488/2013). J.L.O. thanks support from grant AYA2017-89637-R. P.S.S. acknowledges financial support from the European Union's Horizon 2020 Research and Innovation Programme, under Grant Agreement no 687378, as part of the project "Small Bodies Near and Far" (SBNAF). J.L.O., R.D., P.S.S. and N.M. acknowledge financial support from the State Agency for Research of the Spanish MCIU through the "Center of Excellence Severo Ochoa" award for the Instituto de Astrofísica de Andalucía (SEV-2017-0709). F.B.R. acknowledges CNPq support process 309578/2017-5. G.B.R. thanks support from the grant CAPES-FAPERJ/PAPDRJ (E26/203.173/2016). J.I.B.C. acknowledges CNPq grant 308150/2016-3. R.V.M. thanks the grants: CNPq-304544/2017-5, 401903/2016-8, and Faperj: PAPDRJ-45/2013 and E-26/203.026/2015. B.M. thanks the CAPES/Cofecub-394/2016-05 grant and CAPES/Brazil – Finance Code 001. B.M. and A.R.G.J. were financed in part by the Coordenação de Aperfeiçoamento de Pessoal de Nível Superior - Brasil (CAPES) – Finance Code 001. TRAPPIST-North is a project funded by the University of Liège, in collaboration with Cadi Ayyad University of Marrakech (Morocco). TRAPPIST-South is a project funded by the Belgian Fonds (National) de la Recherche Scientifique (F.R.S.-FNRS) under grant FRFC 2.5.594.09.F, with the participation of the Swiss National Science Foundation (FNS/SNSF). VSD, SPL, TRM and ULTRACAM are all supported by the STFC. K.G. acknowledges help from the team of Archenhold-Observatory, Berlin, and A.R. thanks G. Román (Granada) for help during the observation of the 2016 July 19 occultation. A.J.C.T. acknowledges support from the Spanish Ministry Project AYA2015-71718-R (including EU funds). We thank Caisey Harlingten for the repeated use of his 50 cm telescopes in San Pedro de Atacama, Chile. We thank the Italian Telescopio Nazionale *Galileo* (TNG), operated on the island of La Palma by the Fundación Galileo Galilei of the INAF (Istituto Nazionale di Astrofisica) at the Spanish Observatorio del Roque de los Muchachos of the Instituto de Astrofísica de Canarias. L.M. acknowledges support from the Italian Minister of Instruction, University and Research (MIUR) through FFABR 2017 fund and support from the University of Rome Tor Vergata through "Mission: Sustainability 2016" fund. The Astronomical Observatory of the Autonomous Region of the Aosta Valley (OAVdA) is managed by the Fondazione Clément Fillietroz-ONLUS, which is supported by the Regional Government of the Aosta Valley, the Town Municipality of Nus and the "Unité des Communes valdôtaines Mont-Émilius". The research was partially funded by a 2016 "Research and Education"s grant from Fondazione CRT. We thank D.P. Hinson for his constructive and detailed comments that helped to improve this article.

References

Assafin, M., Camargo, J. I. B., Vieira Martins, R., et al. 2010, A&A, 515, A32
Assafin, M., Camargo, J. I. B., Vieira Martins, R., et al. 2012, A&A, 541, A142
Benedetti-Rossi, G., Vieira Martins, R., Camargo, J. I. B., Assafin, M., & Braga-Ribas, F. 2014, A&A, 570, A86
Bertrand, T., & Forget, F. 2016, Nature, 540, 86
Bertrand, T., Forget, F., Umurhan, O. M., et al. 2018, Icarus, 309, 277
Binzel, R. P. 1990, BAAS, 22, 1128
Boissel, Y., Sicardy, B., Roques, F., et al. 2014, A&A, 561, A144
Bosh, A. S., Person, M. J., Levine, S. E., et al. 2015, Icarus, 246, 237
Brosch, N. 1995, MNRAS, 276, 571
Cheng, A. F., Summers, M. E., Gladstone, G. R., et al. 2017, Icarus, 290, 112
Desmars, J., Meza, E., Sicardy, B., et al. 2019, A&A, 625, A43
Dias-Oliveira, A., Sicardy, B., Lellouch, E., et al. 2015, ApJ, 811, 53
Elliot, J. L., Dunham, E. W., Bosh, A. S., et al. 1989, Icarus, 77, 148
Elliot, J. L., Ates, A., Babcock, B. A., et al. 2003, Nature, 424, 165
Forget, F., Bertrand, T., Vangvichith, M., et al. 2017, Icarus, 287, 54
Fray, N., & Schmitt, B. 2009, Planet. Space Sci., 57, 2053
French, R. G., Toigo, A. D., Gierasch, P. J., et al. 2015, Icarus, 246, 247
Gladstone, G. R., Stern, S. A., Ennico, K., et al. 2016, Science, 351, aad8866
Hansen, C. J., & Paige, D. A. 1996, Icarus, 120, 247
Hansen, C., Paige, D., & Young, L. 2015, Icarus, 246, 183
Hinson, D. P., Linscott, I. R., Young, L. A., et al. 2017, Icarus, 290, 96
Hubbard, W. B., Hunten, D. M., Dieters, S. W., Hill, K. M., & Watson, R. D. 1988, Nature, 336, 452
Lellouch, E., Sicardy, B., de Bergh, C., et al. 2009, A&A, 495, L17
Lellouch, E., Stansberry, J., Emery, J., Grundy, W., & Cruikshank, D. P. 2011, Icarus, 214, 701
Lellouch, E., de Bergh, C., Sicardy, B., et al. 2015, Icarus, 246, 268
Lellouch, E., Gurwell, M., Butler, B., et al. 2017, Icarus, 286, 289
Millis, R. L., Wasserman, L. H., Franz, O. G., et al. 1993, Icarus, 105, 282
Nimmo, F., Umurhan, O., Lisse, C. M., et al. 2017, Icarus, 287, 12
Olkin, C. B., Young, L. A., Borncamp, D., et al. 2015, Icarus, 246, 220
Schenk, P., Beyer, R., Moore, J., et al. 2018a, Lunar Planet. Sci. Conf., 49, 2300
Schenk, P. M., Beyer, R. A., McKinnon, W. B., et al. 2018b, Icarus, 314, 400
Schmitt, B., Philippe, S., Grundy, W., et al. 2017, Icarus, 287, 229

Sicardy, B., Widemann, T., Lellouch, E., et al. 2003, Nature, 424, 168
Sicardy, B., Colas, F., Widemann, T., et al. 2006, J. Geophys. Res. (Planets), 111, E11S91
Sicardy, B., Bolt, G., Broughton, J., et al. 2011, AJ, 141, 67
Sicardy, B., Talbot, J., Meza, E., et al. 2016, ApJ, 819, L38
Stern, S. A., Bagenal, F., Ennico, K., et al. 2015, Science, 350, aad1815
Tholen, D. J., Buie, M. W., Grundy, W. M., & Elliott, G. T. 2008, AJ, 135, 777
Toigo, A. D., Gierasch, P. J., Sicardy, B., & Lellouch, E. 2010, Icarus, 208, 402
Washburn, E. W. 1930, International Critical Tables of Numerical Data: Physics, Chemistry and Technology (New York: McGraw-Hill), 7
Yelle, R. V., & Elliot, J. L. 1997, Atmospheric Structure and Composition: Pluto and Charon, eds. S. A. Stern & D. J. Tholen (Tucson: University of Arizona Press), 347
Young, L. A. 2012, Icarus, 221, 80
Young, L. A. 2013, ApJ, 766, L22
Young, E. F., French, R. G., Young, L. A., et al. 2008, AJ, 136, 1757

[1] LESIA, Observatoire de Paris, PSL Research University, CNRS, Sorbonne Université, Université Paris Diderot, Sorbonne Paris Cité, France
e-mail: bruno.sicardy@obspm.fr
[2] Observatório do Valongo/UFRJ, Ladeira Pedro Antonio 43, Rio de Janeiro, RJ 20080-090, Brazil
[3] Observatório Nacional/MCTIC, Laboratório Interinstitucional de e-Astronomia-LIneA and INCT do e-Universo, Rua General José Cristino 77, Rio de Janeiro CEP 20921-400, Brazil
[4] Instituto de Astrofísica de Andalucía (IAA-CSIC). Glorieta de la Astronomía s/n. 18008-Granada, Spain
[5] National Aeronautics and Space Administration (NASA), Ames Research Center, Space Science Division, Moffett Field, CA 94035, USA
[6] Laboratoire de Météorologie Dynamique, IPSL, Sorbonne Université, UPMC Université de Paris 06, CNRS, 4 place Jussieu, 75005 Paris, France
[7] IMCCE/Observatoire de Paris, CNRS UMR 8028, 77 Avenue Denfert Rochereau, 75014 Paris, France
[8] Observatoire de Lille, Université de Lille, 1, impasse de l'Observatoire, 59000 Lille, France
[9] Southwest Research Institute, Department of Space Studies, 1050 Walnut Street, Suite 300, Boulder, CO 80302, USA
[10] Federal University of Technology – Paraná (UTFPR/DAFIS), Rua Sete de Setembro 3165, CEP 80230-901 Curitiba, Brazil
[11] Geneva Observatory, 1290 Sauverny, Switzerland
[12] Astronomical Institute (ASÚ AVČR), Fričova 298, Ondřejov, Czech Republic
[13] Institute of Physics (FZÚ AVČR), Na Slovance 2, Prague, Czech Republic
[14] National Institute of Water and Atmospheric Research (NIWA), Lauder, New Zealand
[15] Occultation Section of the Royal Astronomical Society of New Zealand (RASNZ), Wellington, New Zealand
[16] Dunedin Astronomical Society, Dunedin, New Zealand
[17] ESO (European Southern Observatory) – Alonso de Cordova 3107, Vitacura, Santiago, Chile
[18] Space sciences, Technologies & Astrophysics Research (STAR) Institute, University of Liège, Liège, Belgium
[19] Physics and Astronomy Department, Appalachian State University, Boone, NC 28608, USA
[20] Department of Physics and Astronomy, University of North Carolina – Chapel Hill, NC 27599, USA
[21] Department of Physics, Central Michigan University, 1200 S. Franklin Street, Mt Pleasant, MI 48859, USA
[22] San Pedro de Atacama Celestial Explorations, San Pedro de Atacama, Chile
[23] Grupo de Ciencias Planetarias, Departamento de Geofísica y Astronomía, Facultad de Ciencias Exactas, Físicas y Naturales, Universidad Nacional de San Juan and CONICET, Argentina
[24] Department of Physics and Astronomy, University of Sheffield, Sheffield S3 7RH, UK
[25] Instituto de Astrofísica de Canarias, C/ Vía Láctea, s/n, 38205 La Laguna, Spain
[26] Department of Physics, University of Warwick, Coventry CV4 7AL, UK
[27] Large Binocular Telescope Observatory, 933 N Cherry Avenue, Tucson, AZ 85721, USA
[28] Internationale Amateursternwarte (IAS) e. V., Bichler Straße 46, 81479 München, Germany
[29] International Occultation Timing Association – European Section (IOTA-ES), Am Brombeerhag 13, 30459 Hannover, Germany
[30] International Occultation Timing Association (IOTA), PO Box 7152, Kent, WA 98042, USA
[31] Canberra Astronomical Society, Canberra, ACT, Australia
[32] Western Sydney Amateur Astronomy Group (WSAAG), Sydney, NSW, Australia
[33] Kuriwa Observatory, Sydney, NSW, Australia
[34] Astronomical Association of Queensland, QLD, Australia
[35] Euraster, 1 rue du Tonnelier 46100 Faycelles, France
[36] School of Physical Sciences, University of Tasmania, Private Bag 37, Hobart, TAS 7001, Australia
[37] Lowell Observatory, 1400 W Mars Hill Rd, Flagstaff, AZ 86001, USA
[38] Department of Astronomy, Wellesley College, Wellesley, MA 02481, USA
[39] Department of Physics and Astronomy, University of Delaware, Newark, DE 19716, USA
[40] Joseph R. Biden, Jr. School of Public Policy and Administration, University of Delaware, Newark, DE 19716, USA
[41] Data Science Institute, University of Delaware, Newark, DE 19716, USA
[42] Center for Urban Science and Progress, New York University, 370 Jay St, Brooklyn, NY 11201, USA
[43] SETI Institute, Carl Sagan Center, 189 Bernardo Avenue, Mountain View, CA 94043, USA
[44] School of Physics & Astronomy and Wise Observatory, Tel Aviv University, Tel Aviv 6997801, Israel
[45] Department of Earth and Planetary Sciences and Department of Particle Physics and Astrophysics, Weizmann Institute of Science, Rehovot 0076100, Israel
[46] Oukaimeden Observatory, LPHEA, FSSM, Cadi Ayyad University, Marrakech Morocco
[47] Bankstown, 115 Oxford Avenue, Sydney 2200, New South Wales, Australia
[48] Craigie, 295 Camberwarra Drive, West Australia 6025, Australia
[49] Stockport Observatory, Astronomical Society of South Australia, Stockport, SA, Australia
[50] Mt. John Observatory, University of Canterbury, PO Box 56, Lake Tekapo 7945, New Zealand
[51] Wellington Astronomical Society (WAS), Wellington, New Zealand
[52] BOSS – Backyard Observatory Supernova Search, Southland Astronomical Society, New Zealand
[53] Observatoire de la Côte d'Azur, Université Côte d'Azur, CNRS, Laboratoire Lagrange, Bd de l'Observatoire CS 34229, 06304 Nice, Cedex 4, France
[54] INAF – Telescopio Nazionale Galileo, Rambla J.A. Fernández Pérez, 7, 38712 Breña Baja, Spain
[55] INAF Osservatorio Astronomico di Cagliari, Via della Scienza 5, 09047 Selargius CA, Italy
[56] Section of Astrophysics, Astronomy and Mechanics, Department of Physics, National and Kapodistrian University of Athens, 15784 Zografos, Athens, Greece
[57] Astronomical Observatory of the Autonomous Region of the Aosta Valley, Aosta, Italy
[58] Astronomical Observatory, Dipartimento di Scienze Fisiche, della Terra e dell'Ambiente, University of Siena, Italy
[59] INAF – Catania Astrophysical Observatory, Italy
[60] Department of Physics, University of Rome Tor Vergata, Via della Ricerca Scientifica 1, 00133 Roma, Italy
[61] Max Planck Institute for Astronomy, Königstuhl 17, 69117 Heidelberg, Germany

[62] INAF – Astrophysical Observatory of Turin, Via Osservatorio 20, 10025 Pino Torinese, Italy
[63] International Institute for Advanced Scientific Studies (IIASS), Via G. Pellegrino 19, 84019 Vietri sul Mare (SA), Italy
[64] Archenhold Sternwarte, Alt-Treptow 1, 12435 Berlin, Germany
[65] Schwäbische Sternwarte e.V., Zur Uhlandshöhe 41, 70188 Stuttgart, Germany
[66] Astronomie Stiftung Trebur, Fichtenstr. 7, 65468 Trebur, Germany
[67] Technische Hochschule Mittelhessen, University of Applied Sciences, Wilhelm-Leuschner-Straße 13, 61169 Friedberg, Germany
[68] Roof Observatory Kaufering, Lessingstr. 16, 86916 Kaufering, Germany
[69] Gabriel Murawski Private Observatory (SOTES), Poland
[70] Hieronymusstr. 15b, 81241, München, Germany
[71] Stallhofen Observatory, Graz, Austria
[72] Software Engineering Department, University of Granada, Fuente Nueva s/n 18071 Granada, Spain
[73] Sociedad Astronómica Granadina (SAG), Apartado de Correos 195, 18080 Granada, Spain
[74] Raptor Photonics Llt, Willowbank Business Park, Larne Co. Antrim BT40 2SF, Northern Ireland
[75] AiryLab SARL, 34 rue Jean Baptiste Malon, 04800 Gréoux Les Bains, France
[76] Gamaya S.A. Batiment C, EPFL innovation park, 1015 Lausanne, Switzerland
[77] 49 bd François Mitterrand, Université Clermont-Auvergne, CS 60032, 63001 Clermont-Ferrand, France
[78] Teplice Observatory, Písečný vrch 2517, 415 01 Teplice, Czech Republic
[79] Institute of Astrophysics and Space Sciences, Observatório Astronómico de Lisboa, Ed. Leste, Tapada da Ajuda, 1349-018 Lisbon, Portugal
[80] Agrupación Astronómica de Sabadell, Carrer Prat de la Riba, s/n, 08206 Sabadell, Catalonia, Spain
[81] Astronomical Observatory, University of Siena, 53100 Siena, Italy
[82] Osservatorio Elianto, Astrocampania, via Vittorio Emanuele III, 84098 Pontecagnano, Italy
[83] Ellinogermaniki Agogi School Observatory (MPC C68), Dimitriou Panagea str, Pallini 15351, Greece
[84] Télescope Jean-Marc Salomon, Planète Sciences, 77060 Buthiers, France
[85] Club Astro de Mars, Maison communale 07320 Mars, France
[86] Observatoire des Baronnies Provençales, 05150 Moydans, France
[87] GAPRA, 2 rue Marcel Paul, 06160 Antibes, France
[88] Osservatorio Astronomico di Monte Agliale, Cune, 55023 Borgo a Mozzano, Lucca, Italy
[89] Balcon des Étoiles du pays toulousain, observatoire des Pléiades, 31310 Latrape, France
[90] Beobachtergruppe Sternwarte Deutsches Museum, Museumsinsel 1, 80538 München, Germany
[91] Cloudbait Observatory, CO, USA
[92] Calvin College, MI, USA
[93] Department of Geology and Geophysics, University of Wyoming, Laramie, WY 82071, USA

Appendix A: Circumstances of observations

Table A.1. Circumstances of observations.

Site	Coordinates altitude (m)	Telescope instrument/filter	Exp. time/cycle (s)	Observers
		DATE		
		2002 August 21		
CFHT Hawaii	19 49 30.88 N 155 28 07.52 W 4200	3.6 m I (0.83 ± 0.1 μm)	1/1.583	C. Veillet
		2007 June 14		
Pico dos Dias Brazil	22 32 7.80 S 45 34 57.70 W 1864	1.6 m CCD/clear	0.4/0.4	F. Braga-Ribas, D. Silva Neto
Hakos Namibia	23 14 50.4 S 16 21 41.5 E 1825.	IAS 0.5 m TC245 IOC/clear	1.373/1.373	M. Kretlow
Paranal Chile	24 37 39.44 S 70 24 18.27 W 2635	UT1 8.2 m Ultracam/u', g', i'	0.1/0.1	V. Dhillon, S. Littlefair, A. Doressoundiram
Paranal Chile	29 15 16.59 S 70 44 21.82 W 2315.	VLT Yepun 8.2 m NACO/Ks	1/1	B. Sicardy
		2008 June 22		
Bankstown Australia	33 55 56 S 151 01 45 E 24.9	0.275 m video/clear	1.28/1.28	T. Dobosz
Blue Mountains Australia	33 39 51.9 S 150 38 27.9 E 286	0.25 m video/clear	1.28/1.28	D. Gault
Reedy Creek Australia	28 06 29.9 S 153 23 52.0 E 65	0.25 m CCD/clear	6.30/8.82	J. Broughton
Glenlee Australia	23 16 09.6 S 150 30 00.8 E 50	0.30 m video/clear	0.12/012	S. Kerr
Perth Australia	31 47 21.5 S 115 45 31.3 E 45	0.25 m CCD/clear	2.0 6.0	G. Bolt
		2008 June 24		
CFHT Hawaii	19 49 30.88 N 155 28 07.52 W 4200	3.6 m Wircam/K	0.065/0.065	L. Albert
		2010 February 14		
Pic du Midi France	42 56 12.0 N 00 08 31.9 E 2862	T1 m CCD/clear	0.32/0.32	J. Lecacheux
Lu Switzerland	46 37 26.3 N 10 22 00.3 E 1933	0.35 m video/clear	0.35/0.50	C. Olkin, L. Wasserman
Sisteron France	44 05 18.20 N 05 56 16.3 E 634	0.3 m Watec 120/clear	0.64/0.64	F. Vachier
		2010 June 04		
Mt John New Zealand	43 59 13.6 S 170 27 50.2 E 1020	1 m CCD/clear	0.32/0.32	B. Loader, A. Gilmore, P. Kilmartin

Table A.1. continued.

Site	Coordinates altitude (m)	Telescope instrument/filter	Exp. time/cycle (s)	Observers
		DATE		
		2010 June 04		
Hobart Australia	42 50 49.83 S 147 25 55.32 E 38	1 m Raptor/I	1/1	J. G. Greenhill, S. Mathers
Blenheim New Zealand	41 29 36.3 S 173 50 20.7 E 37.5	Bootes-3 0.6 m CCD/r'	0.50/1.75	W. H. Allen
Blenheim New Zealand	41 29 36.3 S 173 50 20.7 E 37.5	0.4 m CCD/clear	2.5/6	W. H. Allen
Oxford New Zealand	43 18 36.78 S 172 13 07.8 E 221	0.3 m Video/clear	0.64/0.64	S. Parker
		2011 June 04		
Santa Martina Chile	33 16 09.0 S 45 34 57.70 W 1450	0.4 m EMCCD/clear	2/2	R. Leiva
La Silla Chile	29 15 16.59 S 70 44 21.82 W 2315	TRAPPIST S 0.6 m CCD/clear	3/4.4	E. Jehin
San Pedro de Atacama, Chile	22 57 12.3 S 68 10 47.6 W 2397	Caisey 0.5 m CCD/clear	2/2.87	A. Maury
Pico dos Dias Brazil	22 32 7.80 S 45 34 57.70 W 1864	1.6 m CCD/clear	0.1/0.1	M. Assafin
		2012 July 18		
Santa Martina Chile	33 16 09.0 S 45 34 57.70 W 1450	0.4 m CCD/clear	1/1	R. Leiva
Cerro Burek Argentina	31 47 12.4 S 69 18 24.5 E 2591	ASH 0.45 m CCD/clear	13/15.7	N. Morales
Paranal Chile	24 37 31.0 S 70 24 08.0 W 2635	VLT Yepun 8.2 m NACO/H	0.2/0.2	J. Girard
San Pedro de Atacama, Chile	22 57 12.3 S 68 10 47.6 W 2397	ASH2 0.4 m CCD/clear	13/15.44	N. Morales
Huancayo Peru	12 02 32.2 S 75 19 14.7 W 3344	0.20 m CCD/clear	10.24/10.24 5.12/5.12	E. Meza
		2013 May 04		
Pico dos Dias Brazil	22 32 07.8 S 45 34 57.7 W 1,811	B&C 0.6 m CCD/I	4.5/6	M. Assafin, A. R. Gomes-Júnior
Cerro Burek Argentina	31 47 14.5 S 69 18 25.9 W 2591	ASH 0.45 m CCD/clear	6/8	J.L. Ortiz
Cerro Tololo Chile	30 10 03.36 S 70 48 19.01 W 2207	PROMPT 0.4 m P1, P3, P4, P5 CCD/clear	5/8 P3 offset 2 sec P4 offset 4 sec P5 offset 6 sec	J. Pollock
La Silla Chile	29 15 21.276 S 70 44 20.184 W 2336	Danish 1.54 m Lucky Imager/Z (>650n m CCD/iXon response)	Lucky Imager 0.1/0.1	L. Mancini

Table A.1. continued.

Site	Coordinates altitude (m)	Telescope instrument/filter	Exp. time/cycle (s)	Observers
		DATE		
		2013 May 04		
La Silla Chile	29 15 16.59 S 70 44 21.82 W 2315	TRAPPIST S 0.6 m CCD/clear	4.5/6	E. Jehin
Cerro Paranal Chile	24 37 31.0 S 70 24 08.0 W 2635.43	VLT Yepun 8.2 m NACO/H	0.2/0.2	G. Hau
San Pedro de Atacama, Chile	22 57 12.3 S 68 10 47.6 W 2397	Caisey 0.5 mf/8 CCD/V	3/4.58	A. Maury
San Pedro de Atacama, Chile	22 57 12.3 S 68 10 47.6 W	Caisey 0.5 mf/6.8 CCD/B	4/4.905	L. Nagy
		2015 June 29		
Lauder New Zealand	45 02 17.39 S 169 41 00.88 W 382	Bootes-3/YA 0.60 m EMCCD/clear	0.05633/0.05728	M. Jelínek *central flash detected*
Dunedin New Zealand	45 54 31 S 170 28 46 E 136	0.35 m CCD/clear	5.12/5.12	A. Pennell, S. Todd, M. Harnisch, R. Jansen *central flash detected*
Darfield New Zealand	43 28 52.90 S 172 06 24.40 E 210	0.25 m CCD/clear	0.32/0.32	B. Loader *central flash detected*
Blenheim 1 New Zealand	41 32 08.60 S 173 57 25.10 E 18	0.28 m CCD/clear	0.64/0.64	G. McKay
Blenheim 2 New Zealand	41 29 36.27 S 173 50 20.72 E 38	0.4 m CCD/clear	0.32/0.32	W. H. Allen
Martinborough New Zealand	41 14 17.04 S 175 29 01.18 E 73	0.25 m CCD/B	0.16/0.16	P. B. Graham
Greenhill Obs. Australia	42 25 51.80 S 147 17 15.80 E 641	1.27 m EMCCD/B	0.1/0.1	A. A. Cole, A. B. Giles, K. M. Hill
Melbourne Australia	37 50 38.50 S 145 14 24.40 E 110	0.20 m CCD/clear	0.32/0.32	J. Milner
		2016 July 19		
Pic du Midi France	42 56 12.0 N 00 08 31.9 E 2862	1 m EMCCD/clear	0.3/0.3	F. Colas, E. Meza
Valle d'Aosta Italy	45 47 22.00 N 7 28 42.00 E 1674	0.81 m EMCCD/clear	1/1	B. Sicardy, A. Carbognani
La Palma Spain	28 45 14.4 N 17 53 20.6 E 2387.2	TNG 3.58 m EMCCD/clear	1/5	L. di Fabrizio, A. Magazzú, V. Lorenzi, E. Molinari
Saint Véran France	44 41 49.88 N 06 54 25.90 E 2936	0.5 m EMCCD/clear 0.62 m near IR camera/ RG 850 long pass	0.3/0.3 0.2/0.2	J.-E. Communal, S. de Visscher, F. Jabet, J. Sérot
Calern France	43 45 13.50 N 06 55 21.80 E 1264	C2PU T1m EMCCD/clear	0.3/0.3	D. Vernet, J.-P. Rivet, Ph. Bendjoya, M. Devogèle

Table A.1. continued.

Site	Coordinates altitude (m)	Telescope instrument/filter	Exp. time/cycle (s)	Observers
		DATE		
		2016 July 19		
Mitzpe Ramon Israel	30 35 44.40 N 34 45 45.00 E 862	Jay Baum Rich Telescope 0.7 m CCD/clear	1/2.5	S. Kaspi, D. Polishook, N. Brosh, I. Manulis
Trebur Germany	49 55 31.6 N 08 24 41.1 E 90	T1T 1.2 m CMOS/clear	0.3/0.3	J. Ohlert
Athens Greece	37 58 06.8 N 23 47 00.1 E 250	0.4 m CCD/clear	2/4.5	K. Gazeas, L.Tzouganatos
Ellinogermaniki Agogi, Pallini Greece	37 59 51.7 N 23 58 36.2 E 169	0.4 m CCD/clear	7/11	V. Tsamis, K.Tigani
		Data sets not included in this work		
		2002 July 20		
Arica Chile	18 26 53.8 S 69 45 51.5 W 2500	0.3 m CCD/clear	2/2	F. Colas
		2006 June 12		
Stockport Australia	34 19 55.31 S 138 43 45.38 E 24	0.50 m CCD/clear	1.5/2	B. Lade
Blue Mountains Australia	33 39 51.9 S 150 38 27.9 E 286	0.25 m CCD/clear	1/2	D. Gault
Hobart Australia	42 50 49.83 S 147 25 55.32 E 38	0.4 m	1.6/1.6	W. Beisker, A. Doressoundiram, S. W. Dieters, J. G. Greenhill
		2007 March 18		
Catalina Mts. USA	32 25 00 N 110 43 57 W 2790	Kuiper 1.53 m CCD/clear	0.68/0.68	T. Widemann
Palmer Divide USA	39 05 05 N 104 45 04 W 2302	0.35 m CCD/clear	16.9/16.9	B. Warner
Calvin Rehoboth USA	35 31 32 N 108 39 23 W 2024	0.4 m CCD/I	8.5/8.5	L. A. Molnar
Cloudbait USA	38 47 10 N 105 29 01 W 2767	0.305 m CCD/clear	29/29	C. Peterson
Hereford USA	31 27 08 N 110 14 16 W 1420	0.36 m CCD/clear	3/5.1	B. Gary
Oklahoma USA	35 12 09 N 97 26 39 W 382	0.4 m CCD/R+I	4/6.2	W. Romanishin
		2007 March 18		
Mt Lemmon USA	32 26 32 N 110 47 19 W 2776	Kasi 1 m CCD/I	17.6/17.6	Y.-J. Choi

Table A.1. continued.

Site	Coordinates altitude (m)	DATE Telescope instrument/filter	Exp. time/cycle (s)	Observers
		2007 June 09		
Cerro Pachón Chile	30 14 16.80 S 70 44 1.35 W 2715	SOAR 4.1 m CCD/dual B & R	0.66/0.66	W. Beisker
		2008 August 25		
Lick USA	37 20 24.6 121 38 43.8 1281	Shane 3.0 m IR mosaic/K	0.8/0.8	F. Marchis
Grands Rapids USA	42 55 50 N 85 35 18 W 253	0.4 m CCD/I	10/13.3	L. A. Molnar
		2010 May 19		
Paranal Chile	24 37 36.64 S 70 24 16.32 W 2635	VLT Melipal 8.2 m ISAAC/Ks	0.5/0.5	B. Sicardy
La Silla Chile	29 15 32.1 S 70 44 0.15 W 2375	NTT 3.58 m SOFI/Ks	0.5/0.5	V. D. Ivanov
Cerro Pachón Chile	30 14 16.80 S 70 44 1.35 W 2715	SOAR 4.1 m CCD/clear	2.5/3.5	M. Assafin
		2011 June 23		
San Pedro Mártir Mexico	31 02 39 N 115 27 49 W 2800 m	2.1 m IR mosaic/K	1/1.52	R. Howell
San Pedro Mártir Mexico	31 02 43.1 N 115 27 57.7 W 2811 m	0.84 m CCD/clear	0.35/0.35	R. French
Hale A'a BB	19 09 29.6 N 155 45 19.1 W 1509 m	0.6 m CCD/clear	1/1	E. Young
Hale A'a CE	19 09 29.6 N 155 45 19.1 W 1509 m	0.4 m CCD/clear	1/1	C. Erickson
Haleakala	20 42 27.0 N 156 15 21.0 W 3055 m	FTN 2 m CCD/I	0.093/0.09974	F. Bianco
Kekaha	21 58 15.15 N 159 43 21.558 W 20 m	0.4 m CCD/clear	0.3/0.3	T. Widemann, M. Buie, T. Hall
KEASA	21 59 05.7 N 159 45 09.8 W 10 m	0.35 m CCD/clear	0.333/0.333	J. Merrit
Maui	20 54 43.2 N 156 41 28.9 W 47 m	0.35 m CCD/clear (partly cloudy)	1/1	H.-J. Bode
Majuro	07 04 06.6 N 171 17 39.8 W 8 m	0.4 m CCD/I	0.8/0.8	C. Olkin, H. Reitsema

Table A.1. continued.

Site	Coordinates altitude (m)	Telescope instrument/filter	Exp. time/cycle (s)	Observers
		DATE		
		2012 June 14		
Marrakech Morocco	31 35 16.2 N 08 00 46.9 W 494 m	0.6 m EMCCD/clear	0.5/0.5	S. Renner, Z. Benkhaldoun, M. Ait Moulay Larbi, A. Daassou, Y. El Azhari
Sierra Nevada Obs., Spain	37 03 51 N 03 23 49 W 2925	1.52 m CCD/clear	1.5/2	J. L. Ortiz
		2016 July 14		
Oukameïden Morocco	31 12 23.2 N 07 51 59.3 W 2720 m	TRAPPIST N 0.6 m CCD/clear	2/3	E. Jehin
Sierra Nevada Obs., Spain	37 03 51 N 03 23 49 W 2925	0.9 m CCD/clear	2/3.5	J. L. Ortiz
Granada Spain	36 59 33.2 N 03 43 19.9 W 1130	Dobson 0.6 m CCD/clear	3.5/3.5	S. Alonso, D. Bérard, A. Román

Appendix B: Reconstructed geometries of the occultations

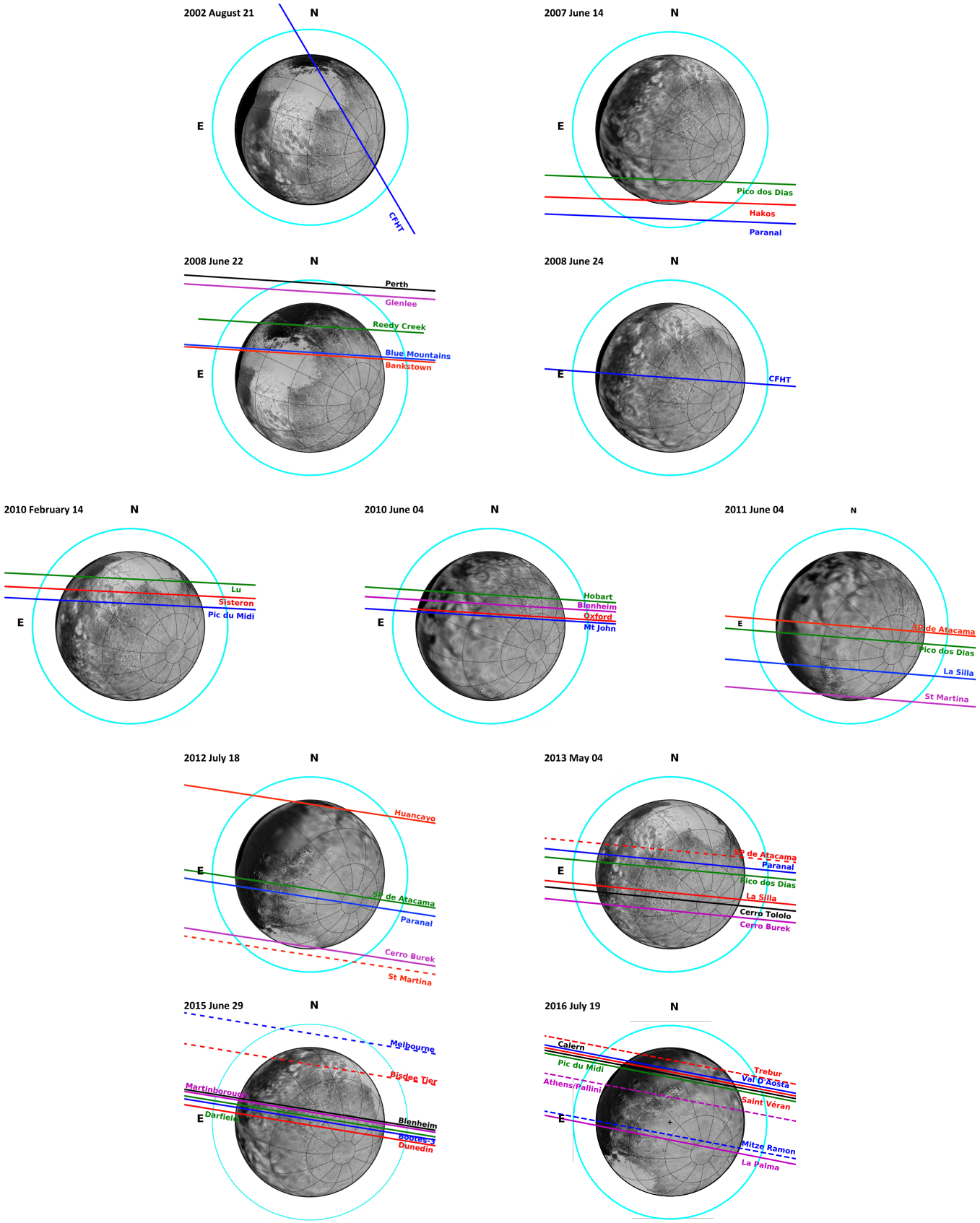

Fig. B.1. The occultation geometries reconstructed from the fits shown in Figs. 2 and 3. Labels N and E show the J2000 celestial north and east directions, respectively. The cyan circle corresponds to the 1% stellar drop, the practical detection limit for the best data sets. The purpose of the dashed lines is to distinguish between lines with the same color, and have no other meaning. In the background, a Pluto map taken by NH during its flyby.

Volatile transport modeling on Triton with new observational constraints

T. Bertrand[1,2], E. Lellouch[1], B. J. Holler[3], L. A. Young[4], B. Schmitt[5], J. Marques Oliveira[1], B. Sicardy[1], F. Forget[6], W. M. Grundy[7], F. Merlin[1], M. Vangvichith[6], E. Millour[6], P. Schenk[8], C. Hansen[9], O. White[2], J. Moore[2], J. Stansberry[3], A. Oza[10,11], D. Dubois[2], E. Quirico[5], D. Cruikshank[2]

[1] Laboratoire d'Etudes Spatiales et d'Instrumentation en Astrophysique (LESIA), Observatoire de Paris, Université PSL, CNRS, Sorbonne Université, Univ. Paris Diderot, Sorbonne Paris Cité, 5 place Jules Janssen, 92195 Meudon, France. tanguy.bertrand@obspm.fr

[2] Ames Research Center, Space Science Division, National Aeronautics and Space Administration (NASA), Moffett Field, CA, USA

[3] Space Telescope Science Institute, Baltimore, MD, USA

[4] Southwest Research Institute, Boulder, CO 80302

[5]. Univ. Grenoble Alpes, CNRS, Institut de Planétologie et d'Astrophysique de Grenoble (IPAG), 38000 Grenoble, France

[6] Laboratoire de Météorologie Dynamique, IPSL, Sorbonne Universités, UPMC Université Paris 06, CNRS, Paris, France

[7] Lowell Observatory, 1400 W. Mars Hill Rd., Flagstaff, AZ 86001.

[8] Lunar and Planetary Institute, Houston, TX 77058, USA

[9] Planetary Science Institute, 1700 E. Fort Lowell, Suite 106, Tucson, AZ 85719, United States of America

[10] Jet Propulsion Laboratory, California Institute of Technology, Pasadena, CA, USA

[11] Physikalisches Institut, Universität Bern, Bern, Switzerland 3012

Abstract

Neptune's moon Triton shares many similarities with Pluto, including volatile cycles of N_2, CH_4 and CO, and represents a benchmark case for the study of surface-atmosphere interactions on volatile-rich Kuiper Belt objects. The observations of Pluto by New Horizons acquired during the 2015 flyby and their analysis with volatile transport models (VTMs) shed light on how volatile sublimation-condensation cycles control the climate and shape the surface of such objects. Within the context of New Horizons observations as well as recent Earth-based observations of Triton, we adapt a Plutonian VTM to Triton, and test its ability to simulate its volatile cycles, thereby aiding our understanding of its climate.

Here we present numerical VTM simulations exploring the volatile cycles of N_2, CH_4 and CO on Triton over long-term and seasonal timescales (cap extent, surface temperatures, surface pressure, sublimation rates) for varying model parameters (including the surface ice reservoir, albedo, thermal inertia, and the internal heat flux). We explore what scenarios and model parameters allow for a best match of the available observations. In particular, our set of

observational constraints include Voyager 2 observations (surface pressure and cap extent), ground-based near-infrared (0.8 to 2.4 μm) disk-integrated spectra (the relative surface area of volatile vs. non-volatile ice) and the evolution of surface pressure as retrieved from stellar occultations.

Our results show that Triton's poles act as cold traps for volatile ices and favor the formation of polar caps extending to lower latitudes through glacial flow or through the formation of thinner seasonal deposits. As previously evidenced by other VTMs, North-South asymmetries in surface properties can favor the development of one cap over the other. Our best-case simulations are obtained for a bedrock surface albedo of 0.6-0.7, a global reservoir of N_2 ice thicker than 200 m, and a bedrock thermal inertia larger than 500 SI (or smaller but with a large internal heat flux). The large N_2 ice reservoir implies a permanent N_2 southern cap (several 100 m thick) extending to the equatorial regions with higher amounts of volatile ice at the south pole, which is not inconsistent with Voyager 2 images but does not fit well with observed full-disk near-infrared spectra. Our results also suggest that a small permanent polar cap exists in the northern (currently winter) hemisphere if the internal heat flux remains relatively low (e.g. radiogenic, < 3 mW m^{-2}). A non-permanent northern polar cap was only obtained in some of our simulations with high internal heat flux (30 mW m^{-2}). The northern cap will possibly extend to 30°N in the next decade, thus becoming visible by Earth-based telescopes. On the basis of our model results, we also discuss the composition of several surface units seen by Voyager 2 in 1989, including the bright equatorial fringe and dark surface patches.

Finally, we provide predictions for the evolution of ice distribution, surface pressure and CO and CH_4 atmospheric mixing ratios in the next decades. According to our model, the surface pressure should slowly decrease but remain larger than 0.5 Pa by 2060. We also model the thermal lightcurves of Triton for different climate scenarios in 2022, which serve as predictions for future James Webb Space Telescope observations.

1. Introduction

The largest satellite of Neptune, Triton, is often described as Pluto's sibling, as the two bodies share similar sizes, densities, ices (non-volatile H_2O and volatile N_2, CH_4, CO, Cruikshank et al. 1993, 2000, Quirico et al. 1999, De Meo et al., 2010, Merlin et al., 2018), and currently similar heliocentric distances, surface pressures and temperatures, and atmosphere composition (N_2 with traces of CH_4 and CO). Its climate and albedo patterns are therefore expected to be dominated by long-term and seasonal volatile condensation-sublimation cycles. However, the geological history (and by extension, interior thermal history) of the two bodies differ: the portion of Triton seen by Voyager 2 during the 1989 flyby has extremely flat topography (vs. dramatic topography of Pluto, Schenk et al., 2018, 2021), an uncratered (geologically young) surface with a globally high Bond albedo (~0.6-0.8, McEwen, 1990, Hillier et al., 1994) without low-albedo red areas, and active geysers (Soderblom et al., 1990). Other differences between the two bodies include the lower amount of atmospheric CH_4 and the colder temperatures in the lower (< 200 km) atmosphere of Triton, ultimately related to the ~10x lower abundance of CH_4 in the ice on Triton, the presence of CO_2 ice on Triton (forming the surface bedrock along with H_2O ice, Quirico et al., 1999, Grundy et al., 2010, Merlin et al. 2018) and the location of the main volatile ice reservoir (Sputnik Planitia on Pluto vs possibly an extended southern cap on Triton, Stern et al., 2015, Smith et al., 1989).

These differences may be related to the fact that Triton is thought to be a captured Kuiper Belt object (McKinnon, 1984; Agnor and Hamilton, 2006, Li et al., 2020) as it has a retrograde, highly inclined orbit, with a differentiated interior possibly heated by tidal braking. This peculiar orbit

leads to complex seasons and possibly to strong obliquity tides and subsequent resurfacing processes (e.g., cryovolcanism, Nimmo and Spencer, 2015). Consequently, Triton is a benchmark case of a dwarf planet that is tidally activated by a giant planet and offers new insights into the surface-atmosphere interactions controlling the climate of large volatile-rich objects of the Kuiper Belt (including Pluto, and others that may exhibit a similar atmosphere near perihelion, e.g. Eris and Makemake).

The flyby of Pluto by New Horizons in July 2015 highlighted the extraordinary complexity of the best studied icy body of the Kuiper Belt (Stern et al., 2015). In particular, volatile transport models (VTMs) of Pluto, constrained by the New Horizons observations, shed light on how the volatile sublimation-condensation cycles can shape the surface of such a planetary body (Bertrand et al., 2016, 2018, 2019, 2020a, 2020b, Johnson et al., 2020). In addition, the correlation of volatile ice deposition with the large global topographic variability of Pluto's surface (total relief exceeding 10 km, with a standard deviation of 1.1 km, Schenk et al., 2018) also indicated the importance of elevation in volatile ice transport on icy bodies with thin atmospheres (Trafton et al., 1998, Bertrand and Forget, 2016). Within the context of New Horizons observations as well as recent Earth-based observations of Triton, it is a natural step to adapt these better-constrained VTMs to Triton and test their ability to simulate its volatile cycles, thereby aiding our understanding of its climate.

Many fundamental issues remain unsolved regarding the climate and the volatile cycles on Triton, which may shape Triton's surface as they do on Pluto. For instance, how do seasonal cycles affect the volatile ice surface distribution, and over what temporal and spatial scales? Is the southern cap seasonal or permanent? Does the winter hemisphere act as a sink for volatile ices? If so, what is the extent and the nature (seasonal vs permanent) of the northern cap, considering that Moore and Spencer (1990) suggested a long term net transfer of N_2 ice from the north to the south and thus a more extended southern vs northern cap? Where are N_2 and CH_4 currently sublimating and condensing? What are the properties of the volatile ices (thermal inertia, reservoir, etc.)? How will the surface pressure, and CO and CH_4 gas abundances evolve? The cases of Spencer and Moore (1992) that best match occultations had a non-global atmosphere in the 1960's, so does Triton's atmosphere collapse (become non-global)? Near-infrared (NIR) rotational lightcurves suggest the latitudes south of 60°S are bare of N_2 (or at least of large-grained N_2, e.g. Grundy et al., 2010, Holler et al., 2016), but what could explain a difference in composition between high southern latitudes and southern mid-latitudes? Finally, how do the volatile cycles on Triton compare with those on Pluto?

Here we present numerical simulations designed to model the evolution of Triton's volatiles (surface ice distribution, surface pressure, and atmospheric abundances) over millions of years on the basis of universal physical equations put into practice with some hypotheses. Our main goal is to investigate where the volatile ices tend to accumulate and sublimate on Triton as the seasons change, and compare our results with the available observations. In particular, we investigate if a perennial northern cap of nitrogen ice can form, and whether our simulations can produce results that are consistent with Earth-based spectroscopic and stellar occultation observations, as well as the observations of the surface by Voyager 2.

Section 2 gives an overview of the past observations of Triton relevant to volatile transport. Section 3 describes the model used, the model parameters, the settings of the reference simulations and defines what the best-case simulations would be. Section 4 discusses the sensitivity of bedrock surface temperatures on Triton to several model parameters. Section 5 presents long-term volatile transport simulations performed over several millions of Earth years (Myrs) and explores the impact of North-South asymmetries in internal heat flux, topography and N_2 ice albedo on the ice distribution. Section 6 presents short-term volatile transport simulations performed over several seasonal cycles with fixed N_2 ice reservoirs and explores the sensitivity

of the surface pressure cycle to different model parameters, including the ice distribution. Section 7 presents a large range of simulation results performed with the full volatile transport model and explores what scenarios and model parameters allow for a best match of the available observations. We discuss these results in Section 8 and provide predictions of Triton's climate for the next decades and future observations with the James Webb Space Telescope (JWST).

2. Background: observations and characteristics of the volatile cycle on Triton

2.1 Triton's orbit and seasons

Triton is moving in a retrograde and circular orbit with an orbital inclination with respect to Neptune of 157°, that is 23° above the planet's equator. It is tidally locked to Neptune with a rotation period of 5.877 days. The combination of this inclination with Neptune's obliquity of 28° leads to complex seasonal cycles, oscillating between low (~5° latitude), moderate (~20° latitude) and extreme (~50° latitude) summer solstices (Trafton, 1984, also see Appendix) over a period of 140-180 years. Each season on Triton lasts ~35-45 terrestrial years. The recent epoch lasting from 1980–2020, during which the highest quality observations of Triton were gathered, corresponds to a period of intense summer in Triton's southern hemisphere (in particular at the south pole), as the subsolar latitude of Triton reached ~50°S in 2000 (Figure 1), and follows a relatively intense winter. At present, the subsolar latitude is rapidly migrating toward the equator. For instance, in 2021, the subsolar latitude will be 36°S and previously unseen regions in the northern hemisphere will come into view (up to 54°N).

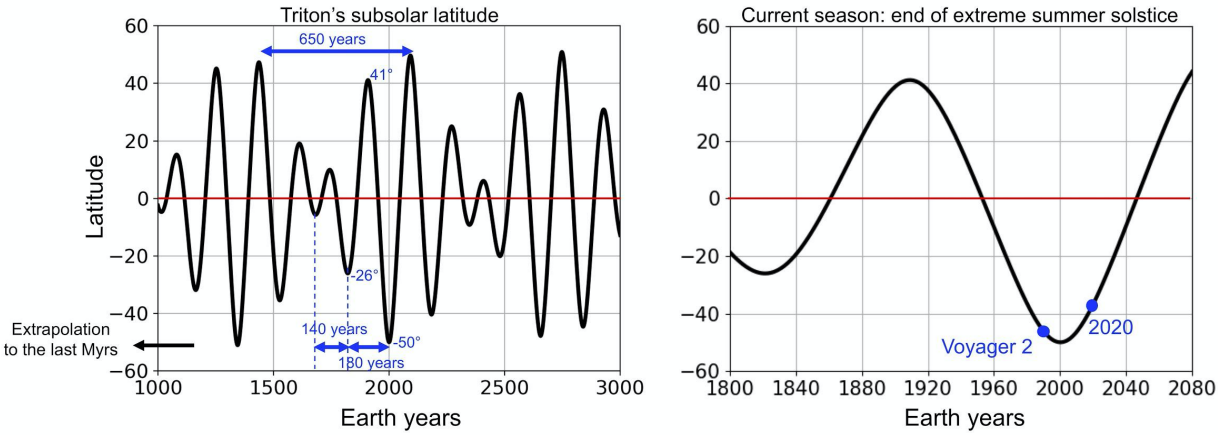

Figure 1: Variation of the subsolar latitude on Triton over time. Triton experiences periods with low (e.g., years 2300-2400), moderate (e.g., years 1500-1650) and intense seasons (e.g., years 1850-2200).

2.2 Surface albedo, color and texture

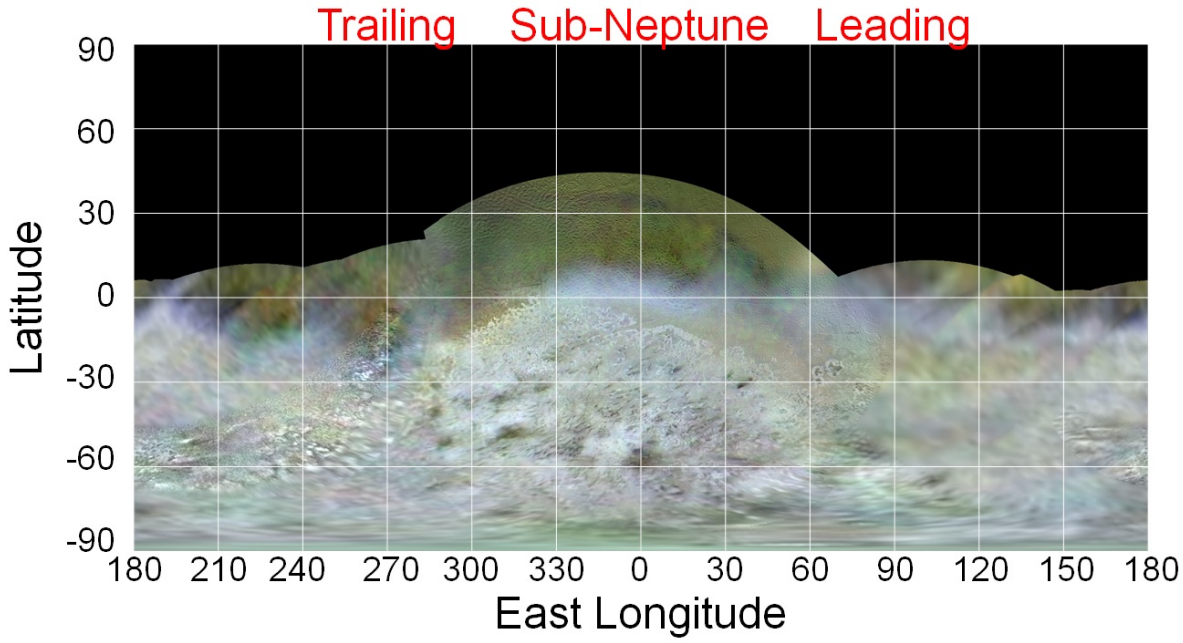

Figure 2: Global color map mosaic of Triton (simple cylindrical projection) at 0.35 km/pixel, as seen by Voyager 2 (color-composite uses orange, green and UV filters in the red, green and blue colors; Schenk et al., 2021). 0°E, 90°E, 180°E, 270°E correspond to the sub-Neptune, leading, anti-Neptune and trailing longitudes respectively.

In 1989, the Voyager 2 flyby of Triton revealed an amazing world with a geologically young (<100 Myr), diverse and active surface as suggested by the presence of plumes (evidence of resurfacing processes), tectonic structures, and very few impact craters (Smith et al., 1989, Croft et al., 1995, Stern and McKinnon, 2000, Schenk and Zahnle, 2007). Figure 2 shows a map of Triton as seen by Voyager 2. Only ~60% of the surface has been imaged (including half of that at relatively high resolution), as much of the northern hemisphere was hidden in the polar night. The northern and southern hemispheres display different terrains in color, albedo, and texture, suggestive of distinct compositions (Cruikshank et al., 1993, McEwen, 1990). Unfortunately, Voyager 2 lacked spectral measurements in the near-infrared, and therefore the exact composition of the different regions remains uncertain.

Triton is uniformly very bright, with a normal reflectance of the surface that varies between ~0.7 and ~1 (Hillier et al., 1994) and a Bond albedo of ~0.85 (Hillier et al., 1991), with a higher reflectance in the southern hemisphere. Estimates of surface emissivities from Voyager 2 data range from 0.3 to 0.8 (Hillier et al., 1991, Stansberry et al., 1996a ; see Section 3.4.1). The Voyager 2 observations suggest that the southern hemisphere is covered by a bright cap of volatile ice (likely N_2 mixed with CH_4 and CO, see Section 2.3), extending to the equator, whereas the observed part of the northern hemisphere may be volatile-free (e.g., Stone and Miner, 1989; Moore and Spencer, 1990). In the absence of spectral measurements, this is supported by the observations of many local dark areas on the bright ice resembling sublimation patterns on Mars (e.g. Mangold, 2011) and on Pluto (e.g. White et al., 2017, Howard et al., 2017) and by the volatile ice longitudinal variability observed from Earth-based near-infrared spectroscopy (see Section 2.3). In this paper, we refer to this geologic terrain as the southern cap (it can include permanent

and seasonal volatile deposits), although we note that other types of terrains and ices may be present at the surface in the southern hemisphere. We do not use the term “polar cap” since the caps tend to extend outside the polar regions down to mid-latitudes and to the equator, but both northern and southern caps mentioned in this paper are centered at the pole. In Voyager 2 images, the northern latitudes seem to be depleted in volatile ice, based on the albedo, geology and texture of these terrains, and should therefore consist of Triton's exposed “bedrock” (CO_2 and/or H_2O). Alternatively, the northern hemisphere could be covered by a thin transparent slab of N_2 ice, so that the albedo of the underlying bedrock is not significantly altered. This has been suggested by Lee et al. (1992), who performed photometric analyses of Voyager 2 high-resolution images and revealed unexpected scattering properties of the surface in the northern hemisphere.

Another region of interest is the blue and very bright equatorial fringe of frost seen between 325°E and 30°E in the close encounter images (Smith et al., 1989, McEwen, 1990). A bluer surface is interpreted as a younger, fresher surface where recent deposition of volatiles has occurred. This is due to a shorter period of exposure to radiation and cosmic rays that tends to redden planetary surfaces. More specifically, the blue (or less red) fringe seen by Voyager 2 has been interpreted to be freshly deposited seasonal N_2 (e.g. Lunine and Stevenson, 1985; Zent 1989).

Photometric observations of Triton have been performed since the 1950s and revealed changes in surface color with time, possibly due to seasonal volatile transport of N_2, CO and CH_4. In particular, the surface became bluer (less red) between 1979 and the Voyager 2 flyby in 1989 (Smith et al., 1989; Buratti et al., 1994; Brown et al., 1995). Whether these bluer regions were brought into view by changing viewing geometry or were created by deposition of volatiles on the already visible hemisphere of Triton is unknown. Possible direct evidence for volatile transport between the Voyager 2 flyby and 2005 was reported by Bauer et al. (2010). They used visible images of Triton obtained with the Hubble Space Telescope (HST) in 2005 to construct visible albedo maps and lightcurves to compare with Voyager 2’s observations. Rotational and regional changes in surface albedo were identified, with an overall brightening in the equatorial regions, suggesting recent deposition there, and a darker anti-Neptune hemisphere. Photometry of Triton for the 1992–2004 period found that the color of the surface was similar to that of the 1950–1974 period (Buratti et al., 1994, Buratti et al., 2011), thus suggesting that Triton reddened since 1989 (assuming it became bluer before 1989). This may be due to the plume activity occurring over the southern cap which tends to redden the ice (wind streaks appear darker and redder than the surrounding deposits, McEwen, 1990) and therefore the global color of Triton (the observed global reddening of Triton’s surface could not be linked to insolation changes, Buratti et al., 2011).

2.3 Earth-based surface spectroscopic observations

In addition to the Voyager data, several ground-based spectroscopic observations of Triton’s surface have been performed, leading to different scenarios for the surface distribution of the volatile and non-volatile ices. The volatile ices N_2, CO, CH_4 and non-volatile CO_2 and H_2O ices have been detected by Cruikshank et al. (1993, 2000), with the non-volatile ices forming Triton's bedrock being at the estimated mean surface temperature of ~40-50 K (Broadfoot et al., 1989; Gurrola, 1995). The surface temperature of N_2 ice was estimated to be 38 ± 1K in 1993 (Tryka et al., 1994), and 37.5 ± 1K for the 2010–2013 epoch (Merlin et al., 2018). It was demonstrated that CO and most of the CH_4 are diluted in N_2 ice with ice mixing ratios relative to N_2 of ~0.05% (Cruikshank et al. 1993; Quirico et al. 1999; Grundy et al. 2010, Merlin et al., 2018), with a small fraction of CH_4-rich ice being present elsewhere (Quirico et al., 1999, Merlin et al., 2018). Tegler et al. (2019) also showed that CO and N_2 molecules on Triton are intimately mixed in the ice rather than existing as separate regions.

During the 2002-2014 period, ground-based infrared (0.8 to 2.4μm) spectroscopic observations performed using the SpeX instrument at NASA’s Infrared Telescope Facility (IRTF) showed a

general increase in N_2 and CH_4 band absorption during this period (Holler et al., 2016). Recent IRTF/SpeX results indicate that they are continuing to increase (Young, L. A.,, personal communication). These trends can be indicative of volatile transport although the monotonic increase in CH_4 absorption could be due to a change in viewing geometry only, if southern high latitudes are deficient in CH_4.

Observations of Triton with IRTF/SpeX showed variability in spectral band depth suggesting longitudinal variability of the ice distribution (Grundy and Young 2004, Grundy et al., 2010, Holler et al., 2016). N_2 and CO spectra displayed a peak absorption at the same longitudes in the sub-Neptune hemisphere, confirming that the two species form a molecular solution. This longitudinal variability for N_2 and CO likely results from variations in surface ice coverage, although variations in other physical parameters of the ice (e.g., particle size, vertical segregation, etc.) may also be at work. There is a certain degree of consistency with the Voyager images showing a southern cap (likely N_2 + diluted CO and CH_4) roughly extending to the equator on the sub-Neptune hemisphere and ~30°S in the opposite hemisphere (Figure 2), which suggests that the longitudinal variation of the spectrum has not changed much since the Voyager 2 flyby (more N_2 ice in the sub-Neptune hemisphere). However, the marked rotational variation of the N_2 and CO spectra also suggests that the very southernmost latitudes are free of detectable N_2 and CO.

The same observations also showed longitudinal variability for CH_4, with an offset of 90° compared to that of N_2 and CO. All the CH_4 bands (weak and strong) were observed in phase, with a maximum absorption near 300°E, but the longitudinal variability decreased from weak to strong CH_4 bands (Grundy et al., 2010, Merlin et al., 2018), suggesting localized regions around 300°E with CH_4-rich ice (and thus with larger optical path lengths in CH_4 and a spectral effect most evident in the weakest CH_4 bands).

The CO_2 and H_2O spectra showed little longitudinal variability, which means that the equatorial and low latitudes are either CO_2 and H_2O free, or have uniform longitudinal coverage of CO_2 and H_2O. In the former case, it has been suggested that CO_2 and H_2O are exposed at the south pole (roughly between 90°S-60°S), which would thus be devoid of volatile ice during the 2002-2014 period (Grundy et al., 2010, Holler et al., 2016). This scenario also has a certain degree of consistency with the observed longitudinal variation of N_2 ice with IRTF/SpeX, whose amplitude would be too shallow if N_2 ice was present at the south pole, according to the near-IR modeling of Grundy et al. (2010). We discuss further this scenario in Section 8.

New near-IR observations performed with SINFONI on the Very Large Telescope (VLT) for the 2010-2013 period obtain similar variabilities for the band areas and support a spatial configuration involving two main units: one dominated by N_2 (with diluted trace amounts of CO and CH_4), but also including CO_2 ice as small grains, and the other dominated by H_2O and CO_2, but also including a few percent of CH_4-rich ice (Merlin et al., 2018). Note that Merlin et al. (2018) did not detect H_2O ice directly (the absorption bands are not seen entirely or are hidden by CH_4 absorption bands), but their model results remain consistent with little longitudinal variability for H_2O and CO_2 ice.

The modeling of the near-IR disk integrated spectrum of Triton's surface also provided constraints on the relative surface area (projected on the visible disk) covered or not covered by CH_4 ice (including CH_4-rich or diluted in N_2 ice, so by extension, the method constrains the fractional area volatile ice/non-volatile ice, e.g. Quirico et al. 1999, Merlin et al. 2018). For instance, Quirico et al. (1999) found for 1995 a volatile/non-volatile fractional area of 55%/45% (see their table IV) whereas Merlin et al. (2018) found for the 2010-2013 period a volatile/non-volatile fractional area of 60-70%/30-40% (see their Table 9), although they note that these results remain model-dependent. The coverage of CH_4-rich ice during this period is estimated to represent 2–3% of the observed surface (i.e. the surface projected on the visible disk) and to be larger in the anti-

Neptune hemisphere, whereas Quirico et al. (1999) estimated a maximum of 10% for 1995. However, the latitudinal distribution of these units remains uncertain.

2.4 Atmospheric surface pressure

Triton's atmosphere is mainly N_2 and is in solid-gas equilibrium with the surface N_2 ice (Tyler et al., 1989). A comprehensive dataset of Triton's surface pressure is detailed in Marques Oliveira et al. (2021) (see their Table 4, and their Section 5 and 6). On August 25, 1989, the Voyager 2 spacecraft flew by Triton and sent its radio signal (RSS experiment) back to Earth as it passed behind Triton. The analysis of the phases and amplitudes of the recorded radio waves provided the line-of-sight column density of the N_2 atmosphere, and an estimation of the surface pressure of ~1.4 ± 0.2 Pa (Broadfoot et al., 1989; Gurrola, 1995).

Different sets of ground-based stellar occultation observations were obtained in the following years. Stellar occultations do not probe the same altitude as RSS, and the methods and assumptions used to retrieve atmospheric pressure vary from one group to another. Consequently, careful comparisons between stellar occultation observations must be made. The first stellar occultation observations performed after Triton's flyby were interpreted as showing that the atmospheric pressure doubled during the 1989–1997 period (Olkin et al., 1997, Elliot et al., 1998). Olkin et al. (1997) derived a surface pressure of 1.7 ± 0.1 Pa for 1995, i.e. a 40% increase since 1989, but at a low 1.8-σ significance level. Elliot et al. (2000) and Marques Oliveira et al. (2021) derived a surface pressure of 2.68 ± 0.34 Pa and $2.28^{+5.4}_{-3.6}$ for the same event (but using different analysis methods) in 1997 (July 18th), respectively, i.e. a 60-90% increase since 1989. It is possible that this dramatic increase in surface pressure is related to the sublimation of the N_2 southern cap. However, in the analysis from Marques Oliveira et al. (2021), no increase can be claimed between the 1989 and the 1995-1997 epochs at a 3-σ significance level. The 4 November 1997 value of Elliot et al. (2003) has a much lower error bar, and at face value does indicate an increase of pressure by a factor 1.76 between 1989 and 1997 (Ps = 2.11 ± 0.02 Pa). This was a single-chord event but with a central flash (chord close to central). The 21 May 2008 event provided only two grazing chords, making it difficult to infer any change of pressure between 1989 and 2003. Finally, a stellar occultation by Triton was observed on 5 October 2017 and provided 90 chords, 25 of them showing a central flash near the shadow center, from which a surface pressure of 1.41 ± 0.04 Pa was derived (Marques Oliveira et al., 2021). This value for 2017 is similar to that measured during the Voyager 2 flyby, which suggests (although at a small confidence level) a pressure maximum around years 2000-2010 and a recent decrease in pressure related to N_2 ice deposition in the northern hemisphere or in the equatorial regions (deposition at the South polar region is ruled out as it remained under continuous daylight). This is also consistent with the N_2 ice temperature of 37.5 ± 1K measured for the 2010–2013 epoch from spectral analyses of the N_2 band shape~~s~~ and position~~s~~ (Merlin et al., 2018), which suggests a $1.6^{+1.6}_{-0.7}$ Pa pressure for this period.

2.5 Atmospheric abundances of CO and CH_4

Triton's atmosphere contains traces of CO and CH_4. In 1989, the Ultraviolet Spectrometer (UVS) on-board Voyager 2 measured a partial pressure of CH_4 of 2.45×10^{-4} Pa (2.45 nbar) from a solar occultation (Herbert and Sandel, 1991, Strobel & Summers, 1995) and a surface pressure of ~1.4 Pa, which gives a CH_4 atmospheric volume mixing ratio of ~0.03% near the surface. This is the only direct measurement of the CH_4 mixing ratio on Triton (since both surface pressure and CH_4 partial pressure were precisely measured at the same time).

Lellouch et al. (2010) reported in 2009 the first detection of CH_4 in the infrared (IR) and the first ever detection of CO in Triton's atmosphere. They found that the partial pressure of CH_4 had increased to $9.8 \pm 3.7 \times 10^{-4}$ Pa (fourfold increase compared to the 1989 value) and estimated the

partial pressure of CO to be about $2.4x10^{-3}$ Pa (24 nbar) with a factor 4 uncertainty. However, they did not measure the surface pressure. If we assume a constant surface pressure of 1.4 Pa for this period (resp. 1.8 Pa), these values correspond to an atmospheric volume mixing ratio for CH_4 of ~0.08%-0.17% (resp. 0.06%-0.13%) and for CO of ~0.17% (resp. 0.13%). This corresponds to a fourfold increase in CH_4 mixing ratio since 1989.

These values are higher than what was anticipated on the basis of Raoult equilibrium and an ideal N_2-CH_4-CO mixture ((of the order of 10^{-5} %, Trafton et al., 1998). A first explanation for that calls for the presence of relatively pure icy patches on Triton's surface (Stansberry et al., 1996b, Lellouch et al. 2010) which have been indeed identified in small amount at the surface of Triton by near-infrared observations (Quirico et al., 1999, Merlin et al., 2018). It has been demonstrated that it is a plausible mechanism for CH_4 ice (Lellouch et al., 2010, Merlin et al., 2018; note that it has clearly been observed on Pluto, e.g. Schmitt et al., 2017), but not for CO, which cannot thermodynamically separate itself from N_2 (Prokhvatilov and Yantsevich, 1983, Vetter et al., 2007, Tan and Kargel, 2018). A second explanation, which applies to CO, is that the seasonal volatile cycles lead to the formation of enriched layers of CO on top of the surface according to the "detailed balancing model" (Trafton, 1984, Lellouch et al., 2010). Note however that based on recent (2017) mm-observations with ALMA, Gurwell et al. (2019) reported a ~100 ppm (~0.01%) CO mixing ratio for an assumed 1.7 Pa atmosphere. This leads to a $1.7x10^{-4}$ Pa CO partial pressure, sharply inconsistent (more than a factor 10 lower) with the IR-derived value from Lellouch et al. (2010). These differences remain to be investigated and understood in more detail, especially given the fact that IR and mm-observations of CO in Pluto's atmosphere give very consistent results on the CO abundance (Lellouch et al. 2011, 2017).

2.6 Seasonal volatile transport: expectations and modeling

As described in the previous sections, several pre- and post-Voyager 2 datasets show changes in Triton's surface albedo patterns, spectra, color and optical light curve that aren't completely due to changes in viewing geometry, but instead could be due to volatile ice migration driven by seasonal insolation changes. The last decades on Triton's southern hemisphere correspond to a period of intense summer, with a subsolar point poleward of 40˚S (Figure 1). Volatile sublimation in the southern hemisphere is therefore expected and several observations support the fact that the bright southern cap, usually presumed to be mostly made of N_2 ice, is currently sublimating away. First, Voyager 2 images of the equatorial regions show local dark areas on the bright ice (on the sub-Neptune hemisphere), which suggest that erosion due to sublimation of N_2 ice was already significant in 1989, when the subsolar latitude was 46°S (Smith et al., 1989). Second, spectral observations showed a tentative seasonal reduction (at 2-σ) in Triton's N_2 ice absorption during the 2000-2009 period (Grundy et al., 2010). The longitudinal pattern of this decline is consistent with a textural reduction in optical path length in N_2 ice, which suggests N_2 ice sublimation but not a retreat of the N_2 ice southern cap (although this is not a unique interpretation, as complex and poorly known microphysical processes are at play). Third, Triton's global color has become redder during the 1992-2004 period, possibly due to plume activity and deposition of dark reddish material over the southern cap, associated with the rapid sublimation of the cap that also concentrates at the surface non-volatile particles included in the ice (McEwen, 1990, Buratti et al., 2011).

Volatile transport models have been developed to investigate the seasonal variations in surface ice distribution on Triton due to the migration of the subsolar point. Stansberry et al. (1990) and Spencer (1990) (superseded by Moore & Spencer 1990, and again by Spencer and Moore 1992) developed zonally-averaged models of the N_2 seasonal cycle and investigated how N_2 ice could evolve and be transported. The former model assumed that N_2 ice is brighter than the underlying bedrock while the latter assumed that fresh N_2 ice is relatively dark and gets brighter with time

and insolation, in a similar way than what has been observed on Mars (Paige 1985). However, both models met limited success in reproducing the observed surface albedo. Most importantly, they did not take into account heat conduction in the subsurface, which has a significant impact on the behavior of the seasonal ice on Mars and on Pluto (Wood and Paige 1992, Bertrand and Forget, 2016, Bertrand et al., 2018, 2019).

Hansen and Paige (1992) investigated both scenarios of bright and dark N_2 ice with a thermal model of the N_2 cycle which included conduction in the subsurface. Their best agreement between the model results and the available observations at that time was obtained with a relatively dark or transparent frost. However, in light of the occultation observations in the 1990s and in 2017, it seems that their scenario with a bright frost now gives a better agreement. They also found that the southern cap is likely to be a large permanent deposit of N_2 ice, otherwise it could not have been extended to the equator in 1989 as seen by Voyager 2. Brown and Kirk (1994) also developed a volatile transport model for Triton, and coupled it with an internal heat flow. They showed that an anisotropic internal heat flow could produce permanent caps of considerable latitudinal extent. Other volatile transport modeling studies showed that a bright permanent N_2 cap (with a reduced N_2 ice reservoir) can also be produced and/or maintained by (a permanent albedo difference between the northern (bedrock) and southern hemispheres (N_2 ice caps) which affects the radiative balance (the “Koyaanismuuyaw” hypothesis, Moore and Spencer 1990, Spencer and Moore, 1992), or by changes in radiative properties of N_2 ice as it goes through the alpha-beta phase transition (this would not produce an asymmetry but would instead help maintain one, Eluszkiewicz, 1991, Duxbury and Brown, 1993, Tryka et al, 1993).

A difference in bedrock topography could also trigger an asymmetry between northern and southern N_2 deposits. On Pluto, N_2 ice tends to accumulate and be more stable in topographic basins, where the surface pressure and therefore the equilibrium ice temperature is higher. This is because the warmer N_2 ice deposits at lower altitudes radiate more heat to space, which is balanced by latent heat of sublimation through increased N_2 deposition rates in order to maintain local conservation of energy, vapor-pressure equilibrium, and hydrostatic equilibrium (Trafton et al. 1998, Trafton & Stansberry 2015, Bertrand & Forget 2016, Bertrand et al. 2018, 2019, and Young et al 2017). This atmospheric-topographic process could also apply to Triton, although the surface (at least the portion imaged by Voyager 2) seems to be much flatter than Pluto’s (Schenk et al., 2021).

In addition to the volatile cycles, Triton's surface activity may be (globally or locally) impacted by the formation of active geysers, such as those observed at the south pole by Voyager 2. Such processes could act to darken the ice, increase the ice sublimation rates, and thus affect volatile transport. The formation of complex chemical molecules (whose spectral properties in the visible range are fairly reproduced by tholin materials formed in the laboratory, Materese et al., 2015, Auge et al., 2016, Jovanovic et al., 2020), through volatile photochemistry occurring in the atmosphere (Krasnopolsky and Cruikshank, 1999), or through direct volatile irradiation at the surface (Moore and Hudson, 2003), could play a similar role at a more global scale.

Finally, complex evolution of N_2:CO:CH_4 mixtures that result in compositional stratification and formation of a bright lag deposit of CH_4 can occur on Triton, in particular where the N_2 sublimation is more intense (Grundy and Fink, 1991, Cruikshank et al, 1991, Quirico et al., 1999). For instance, on Pluto, the northern edge of the N_2 ice sheet Sputnik Planitia is enriched in CH_4 due to intense N_2 sublimation at these latitudes (Protopapa et al., 2017, Schmitt et al., 2017, Bertrand et al., 2018). This could affect the ice and atmospheric mixing ratio of the volatile species.

2.7 Reservoirs of volatile ice and internal heat flow

Triton's orbital elements likely indicate that it is a captured Trans-neptunian Object (e.g., McCord, 1966; McKinnon, 1984; Agnor and Hamilton, 2006, Li et al., 2020), sharing a common volatile origin as the Kuiper Belt Objects (Johnson et al. 2015). Tidal interactions associated with its capture and subsequent circularization around Neptune should have heated its interior significantly (McKinnon et al., 1995, Correia, 2009; Nogueira et al., 2011). Remnant heat stemming from these interactions may have persisted to the present day, as suggested by recent studies showing that the heat flow on Triton should be around 10-100 mW m^{-2} (Ruiz, 2003, Martin-Herrero et al., 2018). These values are much larger than those obtained by assuming only radiogenic production and tidal dissipation for fixed orbital eccentricities (2-4 mW m^{-2}, Gaeman et al. 2012, Brown et al. 1991, Hussmann et al. 2006). The large heat flow could also be produced by internal ocean tidal heating due to Triton's orbit obliquity (Chen et al., 2014; Nimmo and Spencer, 2015; Dubois et al., 2017).

3. The Triton Volatile Transport Model: description and simulation settings

3.1 Model description: the Pluto VTM legacy

We use the latest version of the Triton volatile transport model (VTM) of the Laboratoire de Météorologie Dynamique (LMD). The Triton VTM is a 2D surface thermal model derived from the LMD Pluto VTM, taking into account the volatile cycles of N_2, CH_4, and CO (insolation, surface thermal balance, condensation-sublimation, Bertrand and Forget, 2016), a glacial flow scheme for N_2 ice (Bertrand et al., 2018; based on the equations presented in Umurhan et al., 2017), and the seasonal variation of the subsolar point specific to Triton. The calculations of this complex variation is detailed in the Appendix.

As in the Pluto VTM, we consider that Triton's atmosphere is very thin, almost transparent and thus has a negligible influence on the surface thermal balance aside from the condensation, sublimation and exchanges of latent heat with the surface (this is even more true than for Pluto, given the 10x lower CH_4 abundance, and more tenuous haze). We parametrize the atmospheric transport using a simple global mixing function for N_2, CH_4, and CO in place of 3D atmospheric transport and dynamics, with a characteristic time τ for the redistribution of the surface pressure and trace species, based on reference 3D global climate model simulations of Triton. Tests done with the 3D model determined the timescales for atmospheric transport of CH_4 (10^7 s, i.e., about 4 Earth months),N_2 (1 s, instantaneous mixing) and CO (1 s; CO is well mixed in the atmosphere in 3D global climate model simulations) used in the VTM (the same values were used on Pluto, Bertrand et al., 2019). The topography in the model is controlled by the amount of volatile ice on the surface, but we use a flat topography for the non-volatile bedrock.

3.2 General simulation settings and paleoclimate algorithm

The simulations of this paper are performed on a horizontal grid of 32×24 points, which corresponds to a grid-point spacing of 11.25° in longitude and 7.5° in latitude (about 270 km and 180 km at the equator, respectively). We use 96 timesteps per Triton day. At each time step the local solar insolation is calculated taking into account the variation of the subsolar point, the distance Triton-Sun, and the diurnal cycle. In Sections 5 and 7, we perform simulations over several million years (Myrs) using the paleoclimate and ice equilibration algorithm described in detail in Bertrand et al. (2018):

Typically, the model is first run over ~4,000 Earth years to capture several seasonal cycles of Triton so that the ice distribution and surface pressure reach an equilibrium. We consider that the first ~2,000 Earth years correspond to a spin up time and we use the last seasonal cycles covering ~2,000 Earth years to estimate the mean sublimation-condensation rates over that period (which is also largely enough to capture several seasonal cycles). These mean sublimation-condensation rates are used to calculate the new amounts of ice over a paleo-timestep of Δt=20,000 Earth years, and finally the topography is updated according to the new amounts of volatile ice. These steps are repeated so that the simulation covers at least 2 Myrs, which is enough for large and small N_2 ice reservoirs, glacial flow, and surface and subsurface temperatures to reach a steady state insensitive to the initial state. Consequently, in this paper, the distribution of surface ices and subsurface temperatures of all the simulations (unless stated otherwise) are the outcome of several Myrs of evolution.

Note that here we neglect any change over time in obliquity (with respect to Triton's orbit around Neptune) and orbital parameters, which is valid over the relatively short timescales of a few Myrs (the obliquity of Neptune is suggested to be primordial, Laskar and Robutel, 1993).

Also note that the numerical model only applies to global atmospheres (we neglect the effects of local atmospheres). For Pluto, the approximate limit at which point the atmosphere is non-global is 0.006 Pa (Johnson et al., 2021, Spencer et al., 1997). For Triton, the rescaled threshold is 0.009 Pa (owing to the larger size and gravity constant). In this paper, most of our simulations do not reach that threshold. A few of them do, but over an extremely short range of time, and therefore we do not expect this process to impact the results significantly (it involves very slow sublimation and condensation rates).

3.3 Hypothesis and initial state of the different simulation cases

Section	Simulation type	Initial State	Model parameters
4	Bedrock surface thermal balance only Several seasonal cycles (~10 000 Earth years)	Bedrock only, no volatile ice	**Fixed:** A_{bed}=0.6, ε_{bed}=0.8 **Variable:** TI=500-2000 SI, HF = 0-30 mW m^{-2}
5	Full volatile transport Long term (~7 Myrs) with viscous flow North-South asymmetries in heat flux (HF), topography (TP) and N_2 ice albedo (A_{N2})	Global and uniform cover of 300 m of N_2 ice	**Fixed:** A_{bed}=0.7, ε_{bed}=0.8, A_{N2}=0.7, ε_{N2}=0.8 **Asymmetry HF:** ΔF=5-45 mW m^{-2}, TI=1000 SI **Asymmetry TP:** Δh=2-8 km, TI=500-2000 SI **Asymmetry A:** ΔA_{N2}=0.04-0.1, TI=500-2000 SI
6	Volatile transport limited to fixed N_2 reservoirs Different polar cap extensions Several seasonal cycles (~10 000 Earth years) Including current seasonal cycle (1900-2100)	Fixed and infinite N_2 reservoirs (no glacial flow, flat topography) N_2 albedo adjusted by model	**Fixed:** ε_{N2}=0.8 **Variable:** TI=500-2000 SI **S. PC size:** 90°S-30°S, 90°S-0°, 80°S-0° **N. PC size:** No cap, 90°-75°N, 60°N, 45°N
7	Full volatile transport Long term with viscous flow Including current seasonal cycle (1900-2100) North-South asymmetries in N_2 ice albedo	N_2 ice initially confined to the south pole (90°S-50°S) Northern hemisphere initially volatile-free and warm (T~100 K) N_2 albedo adjusted by model	**Fixed:** ε_{bed}=0.8, ε_{N2}=0.8, TI_{N2}=1000 SI **Variable:** A_{bed}=0.1-0.9, TI_{bed}=100-2000 SI, ΔF=0-30 mW m^{-2}, R_{N2}=0.3-650 m **Asymmetry in N_2 ice albedo:** ΔA_{N2} = 0-0.1

Table 1: Summary of the simulation types, initial states and parameters presented in this paper (see text): albedo (A), emissivity (ε), seasonal thermal inertia (TI) in J s$^{-0.5}$ m^{-2} K^{-1} (SI), internal heat flux (HF), topography (TP), pole-to-pole internal flux, topography gradient and N_2 albedo difference (ΔF, Δh, ΔA_{N2}). S. and N. PC are the southern and northern polar caps.

In this paper, we postulate that the bright terrains observed by Voyager 2 in the southern hemisphere correspond to a N_2 ice southern cap (mixed with CH_4 and CO ices), based on Voyager images and Earth-based spectroscopic observations. As described in Section 2.3, some Earth-based spectroscopic observations suggest that N_2 is not exposed or not detectable at the very southernmost latitudes (i.e. the south pole, Grundy & Young 2004, Grundy et al. 2010, Holler et al. 2016). Note that this does not necessarily means that N_2 ice is not present at the south pole (see further discussions on this topic in section 8.3). In general, we leave the model calculate the surface distribution, but we also added simulation cases in which we force the south pole to be depleted in N_2 ice.

Since 1989, the southern cap has been under constant illumination and is likely dominated by N_2 ice sublimation. Under these conditions, the evolution of surface pressure depends on the N_2 condensation in the northern polar night. Table 1 summarizes the different simulations performed in this paper.

In Section 4, we run the subsurface and surface thermal balance model without volatile ice in order to estimate the mean surface temperatures of the bedrock, for different values of the thermal inertia and internal heat flow. The bedrock albedo is fixed to 0.6. Note that throughout this paper, the "albedo" in the VTM refers to a Bond albedo.

In Section 5, we run long term simulations of the N_2 cycle to explore how North-South asymmetries in internal heat flux, surface N_2 ice albedo and topography lead to asymmetries in the northern and southern cap extents. All simulations start with a global and uniform cover of 300 m of N_2 ice.

In Section 6, we run the model over the last seasonal cycles with artificially-prescribed fixed N_2 ice distributions in the northern and southern hemispheres. We use a flat topography, no glacial flow, and volatile transport is limited to these artificially-prescribed N_2-covered regions (no formation of seasonal frost outside these regions). We analyze the evolution of the surface pressure that results from these specific latitudinal distributions of N_2 ice and compare to observations.

In Section 7, we simulate the full volatile transport over the last 4 Myrs, exploring a large range of parameters (bedrock albedo, thermal inertia, N_2 ice reservoir, internal heat flux, and North-South asymmetry). In these simulations, the ice is initially placed southward of 50˚S and the northern hemisphere is warm and volatile-free with its surface and subsurface temperatures initialized to an extremal value of 100 K. This is to demonstrate that the end state of the simulation and any formation of a northern (polar) cap is independent of the initial ice distribution and surface and subsurface temperatures (see discussions in Section 5 and Section 7). The bedrock topography is flat, so the surface topography is equal to the thickness of N_2 ice lying on top.

Note that in Section 5, Section 6, and Section 7, the N_2 ice albedo in the simulations is not a free model parameter but instead is constrained by the 1989's surface pressure: it is automatically adjusted by the model during the first seasonal cycles of the simulation (spin-up time) so that the calculated surface pressure converges toward ~1.4 Pa in 1989, as observed by Voyager 2 (see Section 3.4.1).

3.4 Surface properties

3.4.1. Albedos and emissivities

As on Pluto, the nitrogen cycle on Triton is very sensitive to the nitrogen ice Bond albedo A_{N2} and emissivity ε_{N2}. The local energy balance on a N_2-covered surface on Triton can be written, to first order (assuming a spatially uniform and isothermal ice with a flat topography, an efficient global transport of N_2, and neglecting thermal inertia and latent heat exchanges) by the classical equation $\varepsilon_{N2}\boldsymbol{\sigma}T^4 \approx (1 - A_{N2})\, F/4$, where F is the solar constant at Triton, $\boldsymbol{\sigma}$ is the Stefan-Boltzmann

constant, and the factor ¼ comes from global averaging. As a result, the N_2 ice equilibrium temperature and therefore the N_2 surface pressure, depend on $(1 - A_{N2})/\varepsilon_{N2}$ (Spencer, 1990). On Pluto, the surface pressure dataset inferred from stellar occultations give a strong constraint on the combination of A_{N2} and ε_{N2} ; only a small range for these parameters allows for a satisfactory match to the observations (Bertrand et al., 2016, Meza et al., 2018, Johnson et al., 2020). In this paper, we intend to apply this study to Triton. We assume a fixed and relatively high emissivity of ε_{N2}=0.8, as in the Pluto VTM (it would correspond to large cm-sized N_2 ice grains, Stansberry et al., 1996a). This value is consistent with the values estimated for Triton from Voyager 2 data ($0.7 < \varepsilon_{N2} < 0.77$, Stansberry et al., 1992), and remains within 10% of the upper value estimated on Pluto from a surface energy balance model ($0.47 < \varepsilon_{N2} < 0.72$, Lewis et al., 2021). However, we note that Hillier et al. (1991) derived a lower surface emissivity of 0.46 ± 0.16, which could be consistent with smaller grain sizes of ~1 mm (Stansberry et al., 1996a). Consequently, in Section 7.3.2, we briefly explore the model sensitivity to lower emissivities than 0.8 (fixed ε_{N2}=0.3 and ε_{N2}=0.5). In addition, since the emissivity of N_2 ice is also thought to vary with the ice temperature, being lower in its α-phase than that in its β-phase (Stansberry and Yelle, 1999; Lellouch et al., 2011b), we also explore the case of a temperature dependent emissivity.

For practical reasons, A_{N2} is automatically calculated by the model so that the surface pressure is close to 1.4 Pa in 1989, as measured by Voyager 2 (tuning manually A_{N2} would be extremely expensive in time and computing resources). In all simulations of this paper, A_{N2} is initially fixed to 0.75, and then the model increments or decrements A_{N2} by steps of 0.005 during each extreme southern summer (at subsolar latitude 45°S corresponding to that of Voyager 2's flyby) so that the surface pressure converges towards 1.4 Pa at this season. Typically, it takes less than 10,000 Earth years for A_{N2} to reach a stable value in the model and thus for the pressure cycle to be consistent with the observed surface pressure in 1989. Since all our simulations of the present-day Triton climate are the results of Myrs of simulations, this means that the convergence occurs quickly at the beginning of the simulations (spin-up time) We ensured that our model results are not sensitive to the initial N_2 ice albedo value and that all our simulations reach a steady state for A_{N2} and surface pressure. By contrast, the albedo of the bedrock A_{bed} is a free parameter of the model and we tested the sensitivity of the results to several values ranging from 0.1 to 0.9.

3.4.2. Thermal inertia (TI)

We assume a high seasonal thermal inertia in the sub-surface for N_2 ice, fixed to 800 J $s^{-1/2}$ m^{-2} K^{-1} (or SI) as has been suggested on Pluto (Bertrand et al., 2016, Johnson et al., 2020). A high thermal inertia was also inferred by Spencer and Moore (1992), and, in retrospect, their high thermal inertia models are more in agreement with the later observed pressure evolution. Note that to first order, this parameter does not significantly impact the N_2 cycle (see Section 2.2 in Bertrand et al., 2018). The diurnal thermal inertia (for all ices) is set to 20 SI by analogy to Pluto (Lellouch et al. 2011, 2016). Note that Pluto has large areas covered by tholins-like dark materials, which are expected to have low diurnal thermal inertias as they form very porous layers of very small grains. They may have played a significant role in the retrieval of thermal inertia values on Pluto (the lightcurves are mostly sensitive to the thermal inertia of the tholins), so the values on Triton could be higher. More thermal observations of Triton's surface are needed to constrain this parameter. For the bedrock (assumed to be water ice or CO_2 ice, but here in this paper it is only characterized by its albedo, emissivity and thermal inertia), we explored the sensitivity of the VTM results to low and high values of seasonal thermal inertia ranging from 200 to 2000 SI.

The thermal skin depth is defined as $\delta = TI/C \times \sqrt{(P/\pi)}$ with TI the thermal inertia, C the ground volumetric specific heat (assumed to be 10^6 J m−3 K−1) and P the period (s) of the thermal wave. With this definition, the diurnal skin depth for 20 SI of ~8 mm and a seasonal skin depth for 200 SI and 2000 SI of ~8 m and 80 m respectively. As in the Pluto VTM, the subsurface is divided into

24 discrete layers, with a geometrically stretched distribution of layers with higher resolution near the surface to capture the short period diurnal thermal waves (the depth of the first layer is z_1 = 1.4×10^{-4} m) and a coarser grid for deeper layers and long seasonal thermal waves (the deepest layer depth is near 1000 m). Note that when a N_2 ice deposit (e.g., 300 m thick) is present at the surface, we assume a subsurface seasonal thermal inertia of 800 SI in the subsurface levels that correspond to the thickness of the deposits (e.g., down to 300 m) and then the seasonal thermal inertia of the bedrock down to the deepest level.

3.4.3. N_2 ice reservoir and internal heat flux

Previous volatile transport modeling on Triton only used low N_2 ice reservoirs (R_{N2} = 0.2-2 m, Moore and Spencer, 1990, Hansen and Paige, 1992, Spencer and Moore, 1992) and thus were limited to the simulation of seasonal frost. Spencer and Moore (1992) also tested simulations in which a permanent southern cap is artificially and indefinitely maintained to a large size, with the aim of reproducing to first order the effect of large reservoir and viscous spreading of N_2 ice from the pole to the equatorial regions. In retrospect, these simulation cases (e.g. case “L” in Spencer and Moore, 1992) are in relatively better agreement with the later observed pressure evolution. Here, on the basis of these results, we used different N_2 ice reservoirs R_{N2} ranging from 1 m to 650 m in global surface coverage, thus exploring both small and large reservoirs. With large N_2 ice reservoirs, the model is able to self-consistently simulate the formation of thick perennial deposits and their viscous flow.

At the deepest subsurface level of the model, there may be a positive heat flow, which is balanced by upward thermal conduction from a negative thermal gradient (-k dT/dz) as in Bertrand et al. (2018, 2019). The reference simulations are performed assuming no internal heat flux, but we also explored the effect of assuming an internal heat flux of 30 mW m^{-2}.

3.4.4. Assumptions on the state of N_2 and CH_4 ice in the model

N_2, CH_4, and CO ices easily mix together and are not expected to exist in perfectly pure states on Triton. Instead, they should form non-ideal solid solutions whose phases follow ternary phase equilibria (Trafton, 2015; Tan and Kargel, 2018). Complex mixtures have been revealed on Pluto’s surface by the analyses of New Horizons observations, with N_2:CH_4 (N_2-rich mixtures, e.g., Sputnik Planitia) and CH_4:N_2 (CH_4-rich mixtures, e.g., the north pole) solid solutions involving different molecular mixing ratios (Grundy et al., 2016; Protopapa et al., 2017; Schmitt et al., 2017). Observations also suggest mixtures of both N_2-rich + CH_4-rich ice phases at some locations, although the exact 'organization' (i.e. intimately mixed and/or vertically stratified) of these deposits remains uncertain (Protopapa et al., 2017; Schmitt et al., 2017).

We note that sophisticated equations of state exist for the N_2–CH_4 and N_2–CH_4–CO systems under surface conditions (surface pressure and temperature) similar to that of Triton (CRYOCHEM, Tan and Kargel, 2018). Although these ternary and binary systems, when applied to Pluto, give results relatively consistent with the diversity of phases seen on Pluto’s surface, it remains unclear how they would apply to the case of Triton. In fact, on Triton, despite a surface pressure and temperatures similar to that of Pluto, the observed mole fraction of CH_4 in N_2-rich ice is ~0.05-0.11% (Quirico et al., 1999, Merlin et al., 2018), which is 5-10 times less than on Pluto (Douté et al. 1999; Merlin, 2015). In addition, the mechanisms controlling the formation and evolution of such mixtures remain largely unknown.

In this context, and given a certain lack of data on the ice mixtures on Triton, the model presented in this paper is rather simple and sticks to the available observations. As in previous VTM studies (Bertrand and Forget, 2016, Bertrand et al., 2018, 2019, 2020a), for simplicity in coding with a VTM, the model does not compute any evolution of ice mixing ratio and adopts Raoult’s law to

describe the solid-gas equilibria. In the simulations, the surface is either volatile-free, covered by pure CH_4 ice or by N_2:CH_4 ice. When both CH_4 and N_2 ices are present on the surface, we assume that CH_4 is diluted in a solid solution N_2:CH_4 with 0.05% of CH_4, as retrieved from the last telescopic observations (Merlin et al., 2018), but we also explored the addition of small areas of CH_4-rich ice (see Section 7.4.2). For CO concentration, we used 0.04% (close to the 0.05% reported by Quirico et al., 1999) and also explored 0.08% to bracket the values 0.04-0.08% suggested by Merlin et al., 2018 (see Section 7.4.1). The modeled N_2:CH_4 ice sublimates by conserving the 0.05% of diluted CH_4. We make the approximation that CH_4-rich ice behaves almost like pure CH_4 ice (Tan and Kargel, 2018), in terms of temperature and vapor pressure at saturation of CH_4, as CH_4-rich ice can contain only up to 3% N_2 around 40K (Prokhvatilov and Yantsevich 1983). It can form after sublimation of N_2 ice (in which CH_4 was trapped before) or directly on a volatile-free surface. In the next sections of this paper, we refer to this phase as CH_4 ice. The formation and evolution of other types of binary or ternary phases is out of the scope of this paper, and we neglect their effect in the model (although we acknowledge that it could lead to some unevaluated uncertainties in N_2-rich and CH_4 solid-phase stability).

3.5 Observational constraints for the definition of best-case simulations

As detailed in Section 3.4.1, the simulations are constrained by one unique observation: the surface pressure of ~1.4 Pa in 1989. The N_2 ice albedo is automatically adjusted by the model during the spin up time to match this constraint.

The other available observational constraints, presented in this section, are not explicitly included in the numerical calculations but are considered when interpreting the simulation results and when looking for the best-case simulations. We search for simulations including (1) an ice distribution consistent with Voyager 2 observations and ground-based near-infrared hemispheric spectra (the relative surface area of volatile vs. non-volatile ice), and (2) an evolution of surface pressure consistent with that retrieved from stellar occultations.

3.5.1. Constraints from the ground-based near-IR spectroscopy

As detailed in Section 2.3, near-IR ground-based spectroscopy of Triton's surface provides a relatively good constraint on the relative surface area (projected on the visible disk) covered or not covered by volatile ice. Based on the results from Quirico et al. 1999 and Merlin et al. 2018 for 1995 and 2010-2013, respectively, we assume with some margin that the volatile/non-volatile fractional area is 45-65%/35-55% in 1995 and 55-75%/25-45% in 2010. To take these constraints into account, we used the calculation in the appendix of Holler et al. (2016) to project our VTM-modeled surface on the visible disk at the time of observation (subsolar latitude 49°S and 46°S for 1995 and 2010, respectively). Note, that, in 2010, 60-70% of the disk-projected surface covered by N_2 would correspond to a southern cap extending from 90°S to ~20°S, or 80°S to ~15°S, or 60°S to ~0°.

3.5.2. Constraints from Voyager 2 images and infrared surface emission measurements

Based on the Voyager 2 images, we assume that the bright southern cap is made of N_2-rich ice, and that its northern edge extends to 30°S-0° in 1989. Note that the volatile/non-volatile fractional area derived from near-IR surface spectroscopy, detailed in Section 3.5.1, is a stronger constraint and is given more weight when interpreting the results because it is a more direct observation (Voyager 2 did not carry any IR spectrometer). We do not make any assumption regarding whether the southernmost latitudes are covered by N_2-rich ice or not. Our model self-consistently calculates the surface ice distribution and we consider that the best-case simulations should have a N_2-rich southern cap (with or without N_2-rich ice at the very pole) with a northern edge extending to 30°S-0° in 1989. In practice, as shown in Section 5 and Section 7, the south pole is always the

most efficient cold trap for N_2 ice in seasonal average and all our simulations present a perennial N_2-rich deposit at the south pole (except in the cases where N_2 is artificially removed from the south pole). This point is further discussed in Section 8.3.

We assume that the northern (polar) cap, if it exists, was in winter night and therefore not seen by Voyager 2 in 1989, implying that it did not extend to latitudes southward of 45°N. Based on the analysis of Voyager 2 images (McEwen, 1990), we also assume that the albedo of all terrains is higher than 0.6.

The Infrared Interferometer Spectrometer (IRIS) instrument on-board Voyager 2 measured the infrared radiation emitted by Triton's surface. The spectra were relatively noisy and the surface emission was mostly detected at the longest wavelengths of the IRIS spectral range (i.e., ~40-50 μm). From these measurements, Conrath et al. (1989) and Stansberry et al. (2015) derived a full-disk averaged surface temperature of Triton in 1989 ranging from 37-44 K, depending on the emissivity of the different surface units. We use this range of surface temperature to constrain the best-case simulations. In fact, most simulations satisfying the previous albedo constraint of > 0.6 fall in this range.

3.5.3. Constraints from the surface pressure from Voyager 2 and stellar occultations

Section 2.4 summarizes the different observations that provide estimates of Triton's surface pressure. Table 2 gives the surface pressure data points used in this paper. Based on the analysis of an extremely high-quality occultation dataset from 2017, and the re-analysis of earlier occultation curves, Marques Oliveira et al. (2021) conclude that the increase in surface pressure reported in 1995-1997 (compared to the Voyager 2 value in 1989) remains elusive (as the data are not available for reanalysis using an approach consistent with theirs), but that the 2017 value has been obtained at a high significance level and is fully compatible with that measured by the Voyager 2 RSS experiment.

Consequently, in this paper, we consider the values reanalyzed by Marques Oliveira et al. (2021) as the strongest observational constraints of surface pressure for our volatile transport simulations, but we will also assess if the model can predict an increase in surface pressure maximum in the 1990s, as suggested by the other values. We also note that the 2017 event and the Voyager pressure are the best quality datasets among the analyzed events.

Date	Surf. Pressure (Pa)	Reference
25 Aug. 1989	1.4 ± 0.2	Gurrola et al., 1995
14 Aug. 1995	1.7 ± 0.1	Olkin et al., 1997
18 Jul. 1997	$2.28^{+0.54}_{-0.36}$ 2.68 ± 0.34	Marques Oliveira et al., 2021 Elliot et al., 2000
4 Nov. 1997	2.11 ± 0.02	Elliot et al., 2003
21 May 2008	$1.38^{+1.24}_{-0.44}$	Marques Oliveira et al., 2021
5 Oct. 2017	1.41 ± 0.04	Marques Oliveira et al., 2021

Table 2: Surface pressures on Triton derived from different observations and detailed in Marques Oliveira et al. (2021).

4. Bedrock surface temperatures on Triton

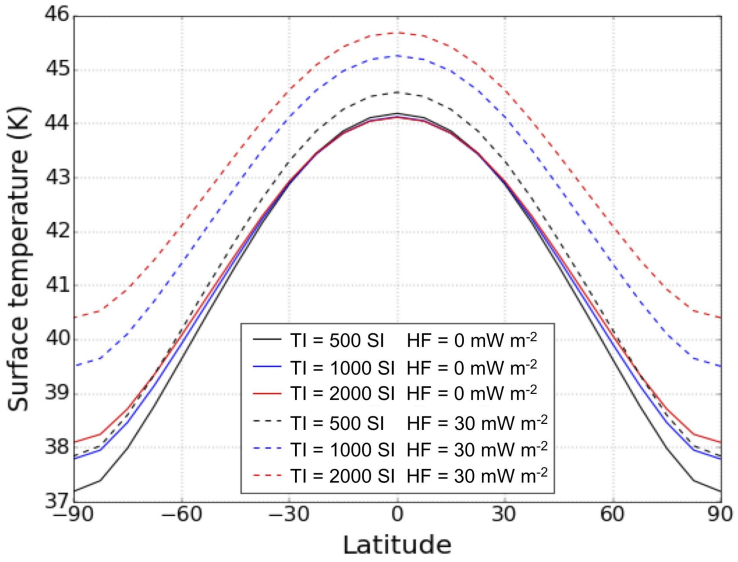

Figure 3: Zonal mean surface temperatures of the bedrock of Triton (assumed to be water ice, no volatile ice) averaged over several seasonal cycles (~10,000 Earth years), with subsurface thermal inertias within 500-2000 SI and internal heat fluxes 0 and 30 mW m^{-2}. The bedrock albedo is fixed to 0.6 and its emissivity to 0.8.

On average over one or several seasonal cycles the poles on Triton receive less insolation flux than the equator. As a result, the poles are colder than the equatorial regions, as shown by Figure 3. High subsurface thermal inertia allows the subsurface to store more heat accumulated during extreme summer and release it during winter, thus dampening and delaying the response of the surface temperatures to insolation (Spencer, 1989) and raising the mean temperatures (the poles are ~1 K warmer with high thermal inertia than with low thermal inertia, on average). While on Pluto, high subsurface thermal inertia allows the poles to be as warm or warmer than the equator on annual or multi-annual average (see Fig. 3 and 4 in Bertrand et al., 2018), on Triton, the poles remain colder than the equator by 5-6 K on average because they receive much less flux (~0.25 W m^{-2}) than the equator (~0.44 W m^{-2}) on average over several seasonal cycles (the subsolar point never reaches high enough latitudes to make the poles warmer than the equator on average, and extreme summers are not occurring every seasonal cycle). For a subsurface (i.e., H_2O ice) TI of 1000 SI, a bedrock surface albedo of 0.6 and no internal flux, maximum and minimum bedrock surface temperatures are respectively ~49 K and ~33 K at the poles (during extreme seasons) and respectively ~45 K and ~43 K at the equator.

Volatile ice would therefore accumulate at the poles on Triton, and form a cold trap. Due to the very low eccentricity of Neptune's orbit and the circular orbit of Triton around Neptune, the northern and southern latitudes of Triton undergo the same seasons over several seasonal cycles (with the same insolation and heliocentric distances). Figure 3 shows that both poles on Triton are symmetric in terms of insolation and surface temperatures, on average over several seasonal cycles. Under these conditions, the volatile transport model would simulate the formation of symmetric southern and northern caps if all ice and surface properties were constant and uniform.

However, in reality, it is likely that one cap "wins" over the other (see Section 5). For instance, Figure 3 shows that an internal heat flux of 30 mW m^{-2} would raise the bedrock surface temperatures by up to ~2 K (for high subsurface thermal inertias), and could locally prevent N_2 condensation at the locations where such a flux reaches the surface.

5. Long-term VTM simulation of the N_2 cycle with North-South asymmetries

As discussed in Section 2.6, the Voyager 2 observations suggest that a southern cap (presumably made of N_2 ice) extends to the equator. It is not clear whether a north (polar) cap exists on Triton, as Voyager 2 did not detect it outside the polar night (southward of 45°N) in 1989. If it does exist, it must therefore be smaller than the southern cap. In Section 2.6, we listed several mechanisms that have been proposed to explain this asymmetry between the northern and southern caps, including the asymmetry in internal heat flux and in surface ice albedo, explored in detail by Brown and Kirk (1994) and Moore and Spencer (1990), respectively.

In this section, we use our volatile transport model to test how the N_2 ice deposits evolve when we set a North-South asymmetry in internal heat flux, surface N_2 ice albedo, and topography. All simulations start with a global and uniform cover of 300 m of N_2 ice, take into account glacial viscous flow of N_2 ice (Umurhan et al., 2017), and are run over 9 Myrs, which is long enough so that the surface and subsurface reach a steady state. Other simulation parameters and settings are summarized in Table 1.

5.1 North-South asymmetry in internal heat flux

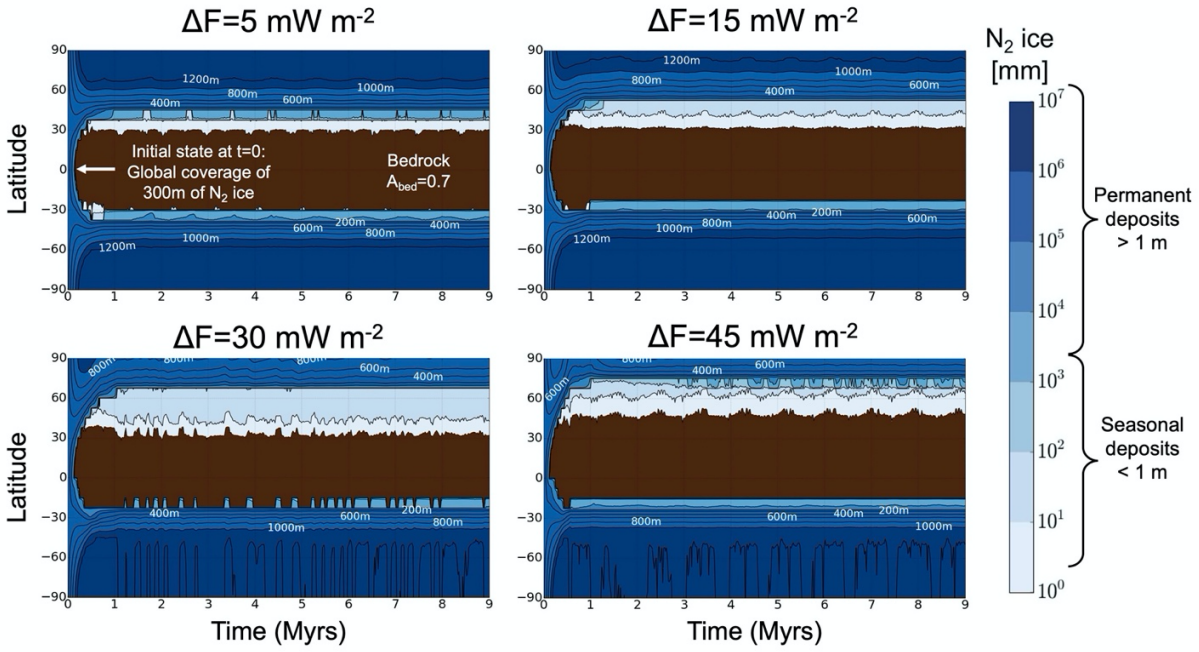

Figure 4: Annual mean evolution of nitrogen ice thickness (in zonal mean) throughout entire VTM simulations (from t=0 to t=9 Myrs), assuming an internal heat flux in the northern hemisphere only

(uniform from 0°N to 90°N) of 5, 15, 30 and 45 mW m^{-2}, and a subsurface bedrock thermal inertia of 1000 SI. Deposits thinner than 1 m tend to be seasonal. The N_2 ice albedo obtained at equilibrium is 0.755, 0.785, 0.790, and 0.795, respectively.

Brown and Kirk (1994) showed that Triton's internal heat source could significantly affect volatile transport and that asymmetries in its latitudinal distribution (possibly driven by volcanic activity or internal convection) could result in permanent caps of unequal latitudinal extent, including the case with only one permanent cap. As expected, we find similar results when we test this scenario in our volatile transport model.

Figure 4 shows the annual mean evolution of N_2 ice thickness when we assume an internal heat flux of 5, 15, 30 and 45 mW m^{-2} in the northern hemisphere only (the internal heat flux is set to 0 mW m^{-2} in the southern hemisphere). In the northern hemisphere, the internal heat flux transferred to the surface N_2 ice is consumed through the latent heat of sublimation of N_2 ice and the maintenance of vapor pressure equilibrium. This leads to enhanced N_2 sublimation rates and reduced N_2 condensation rates and thus favors a larger southern N_2 ice cap.

Our results show that a permanent northern cap, centered at the pole with a thickness of at least a few hundred meters, forms in all cases. In all cases there is also a southern permanent cap, that is at least a kilometer thick at the pole and hundreds of meters thick at ~30°S, in agreement with our interpretation of Voyager 2 observations.

Figure 4 shows that a heat flux difference of at least +15 mW m^{-2} between both hemispheres is necessary for permanent N_2 ice deposits (>1 m) in the northern cap to remain confined poleward of 45°N (and therefore be hidden in the polar night during the Voyager 2 flyby). For example, if the difference reaches +45 mW m^{-2}, then the permanent northern cap is very small and only extends down to 80°N, according to our model. We note that in all cases, mm-to-m thick seasonal deposits extend to 30°N-45°N.

5.2 North-South asymmetry in topography

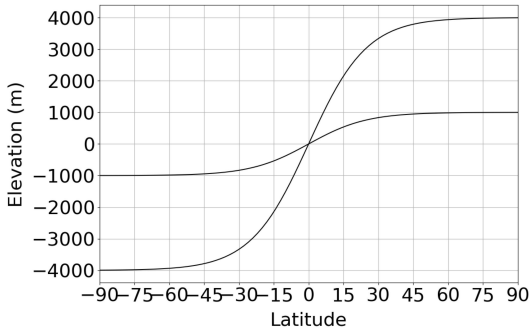

Figure 5: Topography of the bedrock for the simulations described in Section 5.2, with a North-South asymmetry of ± 1 and ± 4 km.

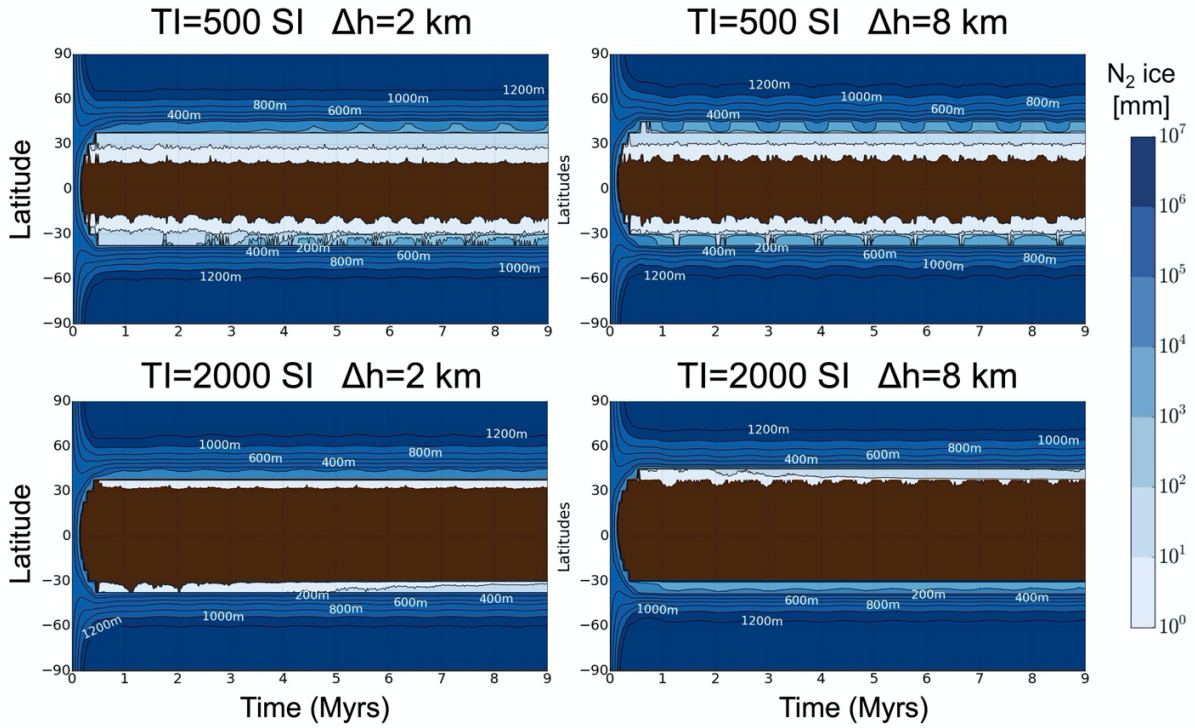

Figure 6: Annual mean evolution of nitrogen ice thickness (in zonal mean) assuming a North-South asymmetry in topography (as shown on Figure 5, with a pole-to-pole difference of 2 and 8 km), and a subsurface thermal inertia of 500-2000 SI. The N_2 ice albedo obtained at equilibrium is 0.740 and 0.750 (for TI=500 SI), and 0.740, and 0.745 (for TI=2000 SI), respectively.

As detailed in Section 2.6, the main reservoir of N_2 ice on Pluto is confined within the massive topographic basin of Sputnik Planitia (estimated to be as much as ~10 km deep, McKinnon et al., 2016) due to (1) its location in the equatorial regions (long-term cold traps induced by the high obliquity cycles) and (2) higher condensation rates in the basin induced by higher surface pressure and infrared cooling of the ice. This atmospheric-topographic process is expected to apply on Triton too, and one could imagine that a North-South topographic asymmetry would favor the formation of a permanent cap of N_2 ice in the lower-elevation hemisphere. Voyager stereo and limb observations of Triton's topography (Schenk et al., 2021) are much more limited than for Pluto, but indicate that topographic amplitudes of the areas observed (<25% of the surface) are only ~1 km or less, including the bright deposits of the southern hemisphere. Although topographic data were lacking over large areas, Schenk et al. (2021) concluded from the lack of discrete large bright or dark patches similar to Sputnik Planitia that Triton also lacked deep basins or high plateaus of similar scale. Unresolved basins and plateaus and local extremes of ~1 km scale are possible in these areas, however.

We tested the above scenario by performing simulations with a North-South asymmetry in bedrock topography, as shown by Figure 5, with a high-standing northern hemisphere and low-standing southern hemisphere of ± 1 and ± 4 km (the former case is well within the current limited constraints while the latter case is extremely unrealistic but provides insights into the magnitudes and extents of the processes involved). Figure 6 shows the annual mean evolution of N_2 ice thickness resulting from this model configuration and for different subsurface thermal inertias.

Our results show that the topography asymmetry does not have a strong effect on reducing the extent of the northern cap, even in the extreme case with a pole-to-pole dichotomy of 8 km. In this scenario, the low-elevated N_2 ice in the southern hemisphere is ~1 K warmer than the high-elevated N_2 ice in the northern hemisphere. As a result, the N_2 condensation rates should always be larger during southern winter than during northern winter. However, as N_2 ice extends to lower latitudes in the southern hemisphere (and because this is maintained by glacial flow in the model), more N_2 ice is available for sublimation during southern summer, which counteracts this difference. This allows for a permanent northern cap of N_2 ice to form in all cases and to be stable with an expansion of N_2 deposits to relatively low latitudes (40°N-50°N) while the permanent southern cap extends to 30°S. We also note that low TI allows for more seasonal deposits forming at the edge of the permanent deposits.

5.3 North-South asymmetry in nitrogen ice albedo

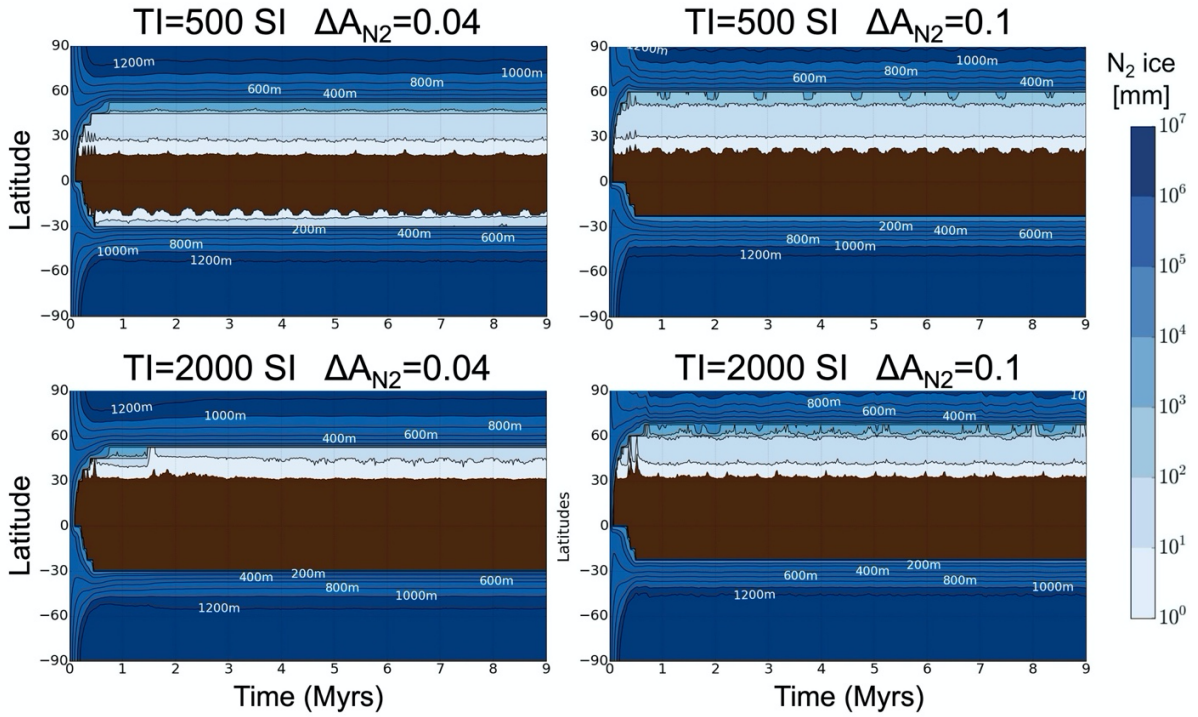

Figure 7: Annual mean evolution of nitrogen ice thickness (in zonal mean) assuming a North-South asymmetry in N_2 ice albedo and a subsurface thermal inertia of 500-2000 SI. The N_2 ice albedo in the southern hemisphere is automatically changed by the model so that it quickly converges toward a value allowing a surface pressure of ~1.4 Pa during the season of the Voyager 2 flyby (see Section 3.4.1). The N_2 ice albedo in the northern hemisphere remains always lower than that in the southern hemisphere by 0.04 (left panels) and 0.1 (right panels). The N_2 ice albedo obtained at equilibrium is 0.765 and 0.775 (for TI=500 SI), and 0.795, and 0.775 (for TI=2000 SI), respectively.

Volatile transport modeling performed by Moore and Spencer (1990) showed that a permanent North-South albedo dichotomy should result in a net, long-term transfer of N_2 from one cap to the other.

Here we tested this scenario with our volatile transport model by performing simulations with a North-South asymmetry in nitrogen ice albedo and we obtained similar results. Figure 7 shows the annual mean evolution of N_2 ice thickness predicted by our model when the N_2 ice albedo in the northern hemisphere is lower by 0.04 (left panels) and 0.1 (right panels) than in the southern hemisphere (where the albedo is calculated by the model so that P1989~1.4 Pa), for thermal inertia TI=500 SI (top) and 2000 SI (bottom).

A permanent northern cap forms in all cases, but extends to 45-55°N (with mm-to-m thick seasonal deposits extending to 30°N if TI is low) while the permanent southern cap extends to 30°S.

5.4 Discussions about the North-South asymmetry

We tested the scenarios of a North-South asymmetry in heat flux, topography, and N_2 ice albedo, and our results are consistent with previous work (Brown and Kirk, 1994, Moore and Spencer, 1990).

We note that:

(1) We used a large global N_2 reservoir of 300 m, which is required for the expansion of the southern cap to 30°S-0°, as observed by Voyager 2.

(2) As described in Brown and Kirk (1994), this N_2 inventory is significantly larger than needed to supply volatile transport. Viscous flow of N_2 ice from the poles (where N_2 condensation is more intense) toward low latitudes balances the net sublimation-condensation flow. On average over several seasonal cycles, net N_2 condensation occurs at the poles and net sublimation occurs in the warm tropical regions, where viscous flow from the pole to the equator ensures that N_2 ice remains available for sublimation. This favors the formation of a permanent northern cap and its expansion to relatively low latitudes.

(3) North-South asymmetries in internal heat flux and in surface ice albedo are efficient means to limit the extent of the permanent northern cap to latitudes northward of 45°N. On average over several seasonal cycles, the N_2 condensation rates at the south pole are larger than those at the north pole by a factor ~8 if the surface N_2 ice albedo is 0.6 in the northern hemisphere vs 0.7 in the southern hemisphere (Figure 7), or if the internal heat flux is 45 W m^{-2} in the northern hemisphere vs 0 W m^{-2} in the southern hemisphere (Figure 4). The asymmetry in topography does not produce a significant asymmetry in cap extents. Even in the case of a topography gradient of 8 km between both poles (Figure 6), the surface temperature gradient is less than 1 K (the ice is warmer in the modeled depression at the south pole) and the condensation rates are larger at the south pole by only a factor of ~1.4. In other words, our results remain quantitatively sensitive to the ice properties (albedo, thermal inertia, N_2 reservoir), and insensitive to topography differences, even those that are larger than expected based on Voyager 2 imagery (although this is true for large N_2 reservoirs only, see below).

(4) The northern and southern permanent caps simulated with our model quickly reach a steady state after ~1 Myrs and then remain relatively stable over time. If we assume an initially warm volatile-free northern hemisphere, it could take a few Myrs longer, but the end result would remain the same. Note that the timescale associated with viscous flow relaxation is ~1 Myrs for a relatively flat bedrock, a layer of 100 m of N_2 ice, and a characteristic length scale for the southern cap of 1000 km (calculated for Triton as detailed in Umurhan et al., 2017, see their Fig. 9b).

(5) Figure 8 shows a few simulation results performed with lower reservoirs (30 m and 100 m). Due to the lower reservoirs, the southern and northern caps are smaller in size and

thickness, but the general tendencies observed for the simulations with 300 m remain valid. As in Spencer (1990), Stansberry et al. (1990), Hansen and Paige (1992) and Spencer and Moore (1992), simulations performed with very low global N_2 reservoirs (e.g. 1 m, not shown) show that most of Triton's N_2 inventory accumulates at the south pole (favored by a North-South asymmetry), and after several seasonal cycles, forms a small southern permanent deposit confined to the south pole and a few meters thick (referred as the problem of ever-shrinking permanent polar caps in Spencer and Moore, 1992). Due to the low amounts of N_2 ice involved, the ice does not flow, and the polar cap never extends to the mid-to-equatorial regions. Thin seasonal deposits can form at the north pole during winter. The topography, albedo and internal flux differences between both poles becomes a more significant driver for N_2 ice migration in these low reservoir cases.

(6) Brown and Kirk (1994) and Moore and Spencer (1990) state that an albedo asymmetry between the northern and southern hemispheres is unlikely to be maintained over a long-term period due to (1) seasonal deposition of meter-thick frost layers each winter in the low-albedo hemisphere, possibly brightening the surface except if the layers are transparent enough to have no significant effect on the albedo of the substrate (which remains unlikely), and (2) an increase in albedo as the ice is fractured by passage through the α-β phase transition (Scott, 1976, Duxbury and Brown, 1993). On the other hand, pole-to-pole difference in ice contamination by dark material, sensible heat flux from the atmosphere or positive feedbacks on the surface (shown to have a non-significant effect on Pluto's ice, Bertrand et al., 2020a) may help maintaining an albedo asymmetry, but these processes would need to be investigated in more detail on Triton.

(7) Amongst the simulations explored here, we do not get any case with N_2 ice at southern low- and mid-latitude but no N_2 ice at the south pole, as suggested by Earth-based spectroscopic observations (see Section 2.3).

(8) Many other processes could explain the asymmetry between the caps. The reader is referred to Section 2.6 and previous work by Brown and Kirk (1994) and Moore and Spencer (1990) for more detail about this topic. Constraining the composition of the ices on both hemispheres will be key to distinguishing between these alternatives.

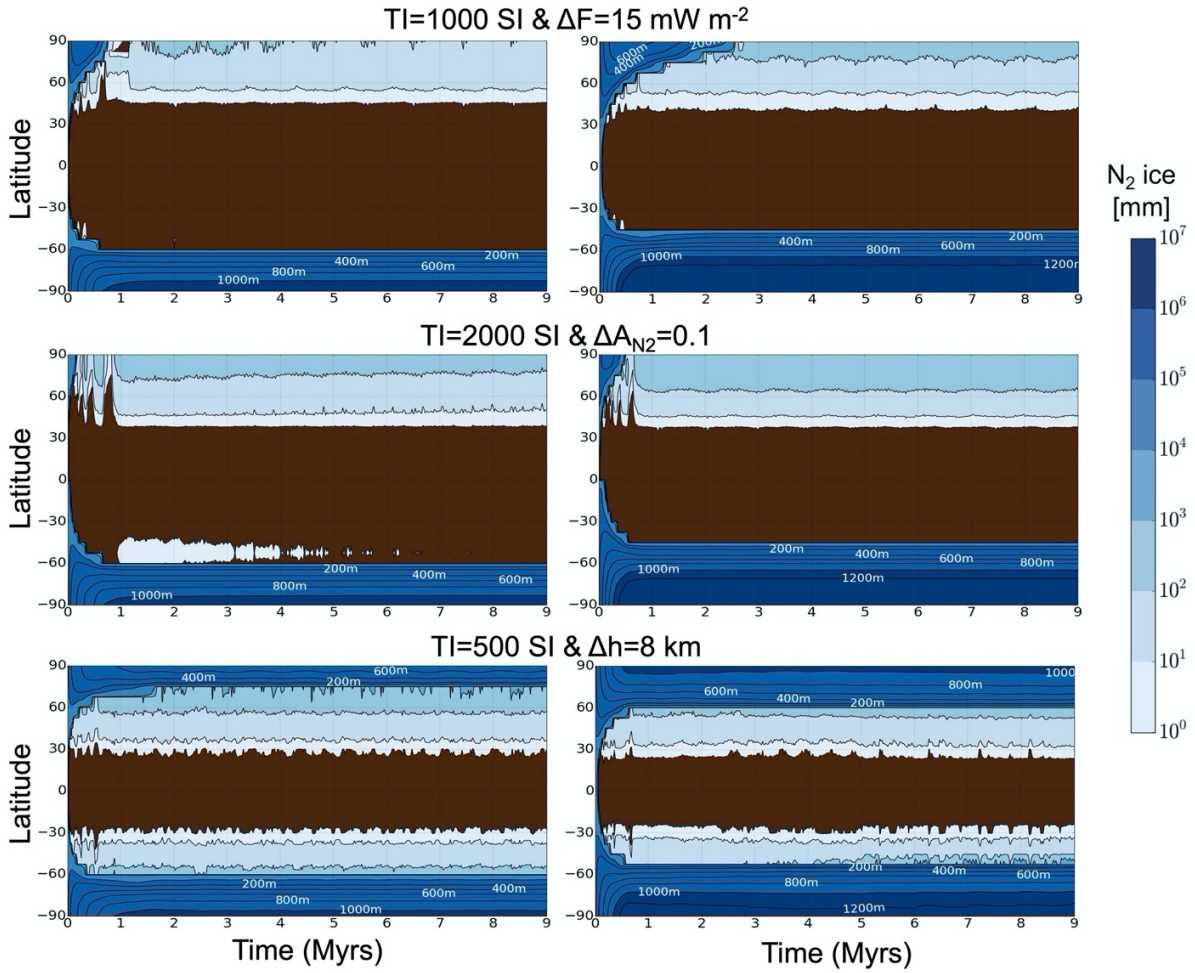

Figure 8: As for previous figures but for a global N_2 reservoir R=30 m (left) and R=100 m (right). The N_2 ice albedo obtained at equilibrium is 0.775, 0.750 and 0.720 (for R=30 m), and 0.790, 0.765 and 0.745 (for R=100 m), respectively.

6. Surface pressure cycle assuming fixed N_2 ice distribution

As shown in Section 5, the permanent (i.e., non seasonal) northern and southern caps remain relatively stable over time (if we assume the seasonal changes in insolation as described in Section 2.1) but their latitudinal extents depend on the model parameters such as albedo, thermal inertia, and N_2 ice reservoir.

In this section, we explore how fixed N_2 ice distributions on Triton and surface properties affect the current surface pressure cycle. For sake of simplicity, and in order to understand the impact of each parameter one after another, we neglect the impact of seasonal deposits and therefore we only use fixed volatile ice distribution (more realistic simulations with full, i.e., self-consistent, volatile transport including seasonal deposits are presented in Section 7). We use the stellar occultation datasets to constrain the properties of the northern and southern caps.

6.1 Initial state of the simulations with fixed N_2 ice distribution

Table 1 summarizes the settings of the volatile transport simulations presented in this section. We place fixed and infinite N_2 reservoirs (no glacial flow, flat topography) confined to 90°S-30°S, 90°S-0°, or 80°S-0° in the southern hemisphere, and to 90°N-75°N, 90°N-60°N or 90°N-45°N in the northern hemisphere (including the case without a northern cap). We limit the volatile transport to these reservoirs (no seasonal frost can form). Consequently, the simulation results are independent of the bedrock surface properties (albedo and emissivity). The simulations are performed over several seasonal cycles (covering ~10 000 Earth years) in order to reach a steady state. The N_2 ice albedo is automatically adjusted by the model so that the surface pressure reaches ~1.4 Pa in 1989, as observed (see Section 3.4.1).

6.2 Simulation results with fixed N_2 ice distribution

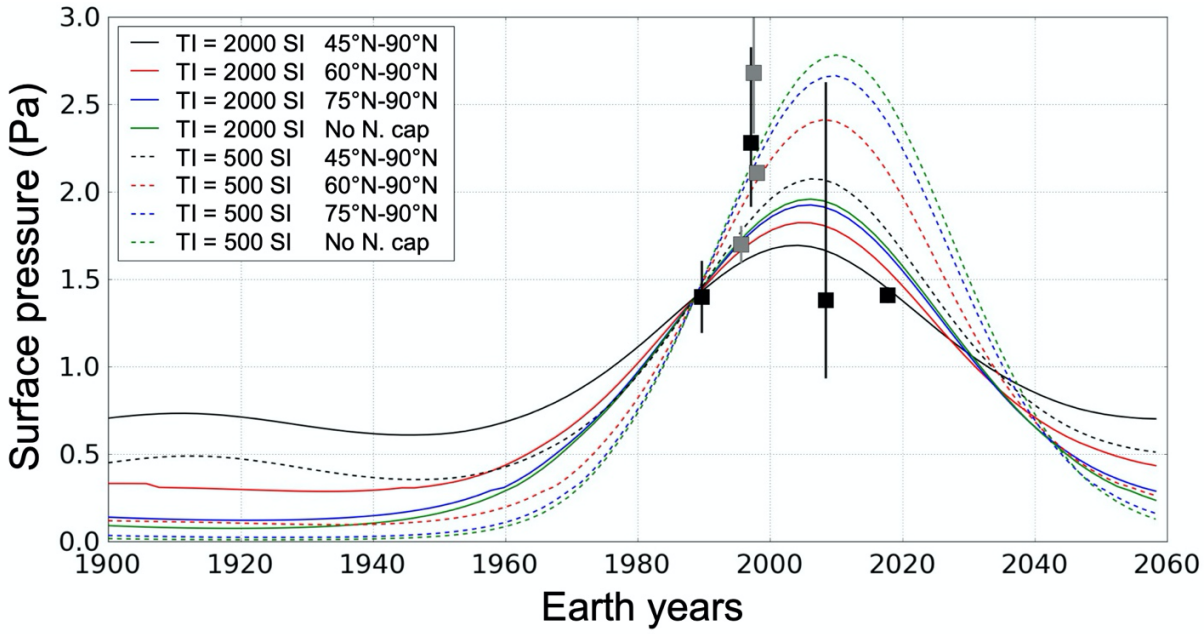

Figure 9: Surface pressure on Triton for the period 1900-2060 as predicted by the model when we assume a fixed N_2 ice distribution with a southern cap placed between 90°S-30°S and a northern cap placed between 90°N-45°N (black), 90°N-60°N (red), 90°N-75°N (blue) or no northern cap (green). The seasonal thermal inertia of N_2 ice is set to 2000 SI (solid lines) or 500 SI (dotted lines). Black and grey data points and 3-σ error bars represent the pressure observations as presented in Table 2 (black are for the data points that we consider are the strongest observational constraints).

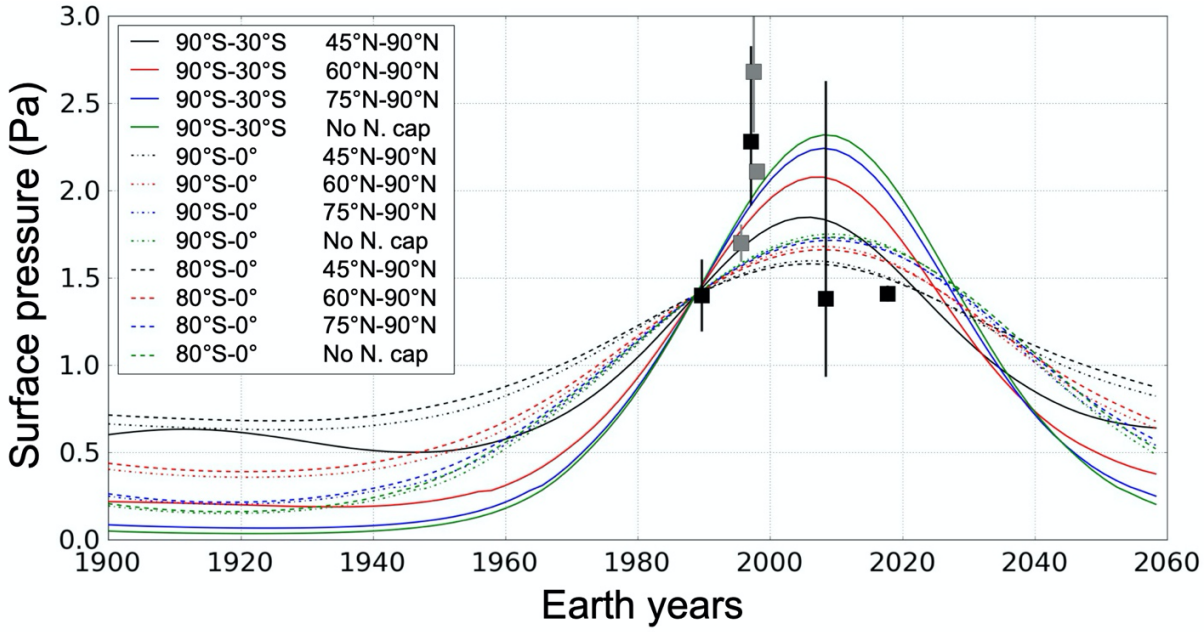

Figure 10: As Figure 9 but for different fixed N_2 ice distributions in the southern and northern hemisphere. The seasonal thermal inertia is set to 1000 SI.

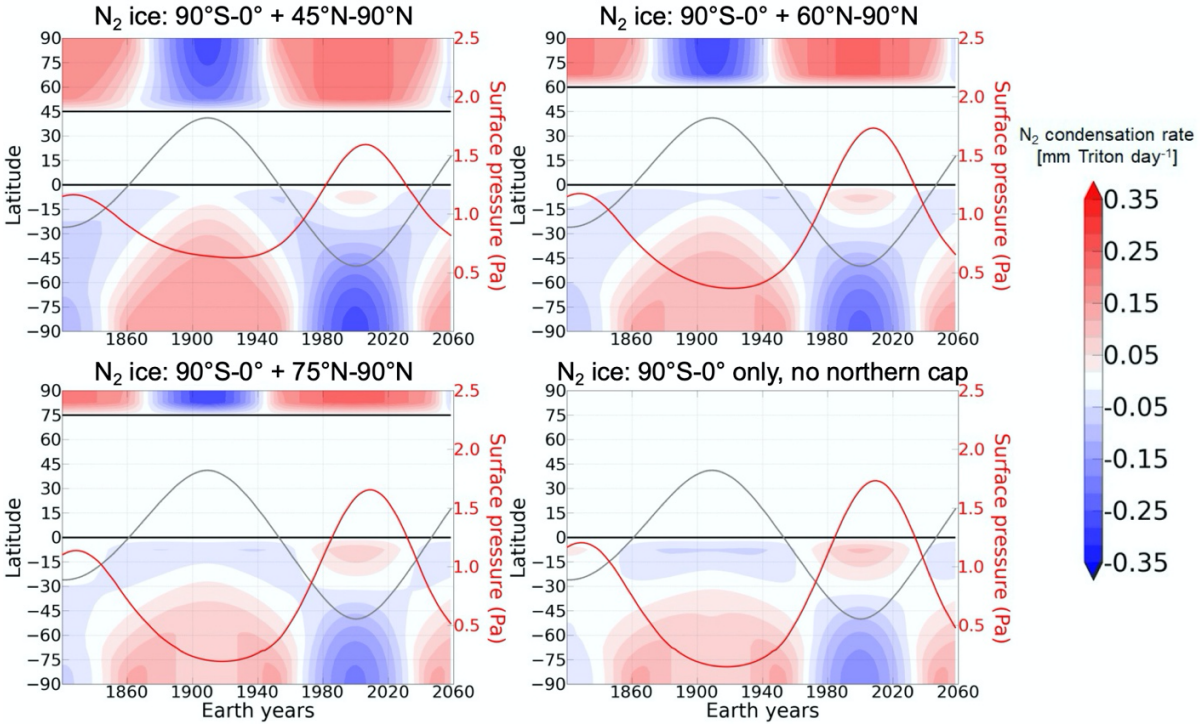

Figure 11: Zonal and diurnal mean N_2 condensation-sublimation rate (mm per Triton day) during the period 1820-2060 as obtained in the model for the cases of fixed N_2 ice distributions: 90°S-0° + 45°N-90°N (top left), 90°S-0° + 60°N-90°N (top right), 90°S-0° + 70°N-90°N (bottom left), 90°S-0° and no northern cap (bottom right). The seasonal N_2 ice thermal inertia is set to 1000 SI. The

thin black contour indicates the extent of the caps. The red line indicates the surface pressure (right y-axis) and the grey line indicates the subsolar latitude.

Figures fixedscap and fixedti show the surface pressure for the period 1900-2060, obtained with the model for different N_2 ice distributions and N_2 ice thermal inertia, while Figure 11 shows the latitudinal condensation-sublimation flux of N_2 during the period 1820-2060 for the four different extents of the northern cap explored.

The surface pressure is at its minimum during the 1880-1940 period (northern summer), when the subsolar point is above 15°N, because the northern cap is always smaller than the southern cap and therefore the condensation-dominated areas (most of the southern N_2 ice deposits) overcome the sublimation-dominated areas (the northern deposits). During the opposite season (southern summer), the pressure is at its maximum as the sublimation-dominated areas (most of the southern deposits) overcome the condensation-dominated areas (northern deposits), as shown by Figure 11 (all panels). In these simulations, the surface pressure peak occurs slightly after the southern summer solstice (2000) between year 2000-2010. The surface pressure evolutions obtained here are similar to those obtained by Spencer and Moore (1992) when they artificially maintained a permanent large southern cap of bright N_2 (see their Fig. 7).

As shown by Figure 9, the larger the northern cap, the more it can serve as a condensation area and buffer N_2 sublimation in the southern hemisphere, which results in a surface pressure peak that is lower and occurs sooner. In addition, the higher the thermal inertia of N_2 ice, the lower the amplitude of surface pressure over a seasonal cycle (higher minimum and lower maximum), and the earlier the surface pressure peaks.

We also tested different N_2 ice distributions in the southern hemisphere. Figure 10 shows that the amplitude of the surface pressure peak is strongly attenuated if N_2 ice remains between 30°S-0° (non-solid lines). This is because these latitudes are dominated by condensation rather than sublimation between the years 1980-2020, thus dampening the pressure peak (Figure 11, all panels). We also tested a scenario without N_2 ice between 90°S-80°S, leading to a pressure peak slightly lower as less N_2 is available for sublimation in southern summer (Figure 10, dotted lines).

These results suggest that a mid-to-high thermal inertia of N_2, coupled with a northern cap extending down to 45°N-60°N, is needed so that the surface pressure is ~1.4 Pa (back to Voyager 2 levels) in 2017, as observed from stellar occultations. If we assume no northern cap, then the modeled surface pressure remains higher than 1.6 Pa in 2017, which becomes inconsistent with the observations. A strong increase in surface pressure before 2000 cannot be obtained if N_2 ice is present between 30°S-0°. We also note that the surface pressure remains greater than 0.5 Pa even during the opposite season (southern winter) when a permanent northern cap extending down to 45°N is assumed. The presence of permanent southern and northern caps prevents Triton's atmosphere from collapsing.

Finally, as discussed in Section 2.3, IRTF/SpeX observations of Triton's near-IR spectrum in 2002 suggest that N_2 is undetectable or absent at high southern latitudes. Here, Figure 11 shows that about 30-50 cm of N_2 ice is removed at the south pole by sublimation during the period 1970-2000. It is not clear whether the removal of 30-50 cm of N_2 ice could have altered its detectability, even if N_2 is not completely removed. We discuss more on this point in Section 8.3.

7. VTM Simulations of the N_2 cycle

In this Section, we simulate the full volatile transport across Triton over the last 4 Myrs and explore a large range of parameters (bedrock albedo, thermal inertia, N_2 ice reservoir, internal flux and North-South asymmetry). The results (e.g., cap extents in 1989 and surface pressure in 2017) are compared to the available observations in order to better constrain these model parameters.

7.1 Initial state of the simulations and main model parameters

Section 3.3 and Table 1 summarize the initial state of the simulations. Note that all the results of this section are the outcome of 4-Myrs simulations in which the end state does not depend on the initial ice distribution and surface and subsurface temperatures, and in which the N_2 ice albedo is calculated by the model and constrained by the surface pressure in 1989 (~1.4 Pa). The N_2 ice albedo obtained in the model in 1989 usually ranges within 0.7-0.8, depending on the cap extents and on the internal heat flux. We first perform simulations with a spatially uniform N_2 ice albedo (Section 7.2) and then with a lower albedo in the northern hemisphere (Section 7.3, where the albedo of the northern cap is always lower than that of the southern cap by 0.1).

The bedrock and N_2 ice emissivities are fixed to ε=0.8, and the N_2 ice thermal inertia to TIN_2=1000 SI. We explore different values for the bedrock's thermal inertia TI_{bed} (Low: 200 SI; Moderate: 500 SI, 1000 SI; High: 2000 SI) and albedo A_{bed} (from 0.1 to 0.9), for the global N_2 ice reservoir R_{N2} (from 1 m to 650 m), and with and without a globally uniform internal heat flux of 30 mW m^{-2}.

7.2 Full volatile transport simulations with spatially uniform ice properties (no North-South asymmetries)

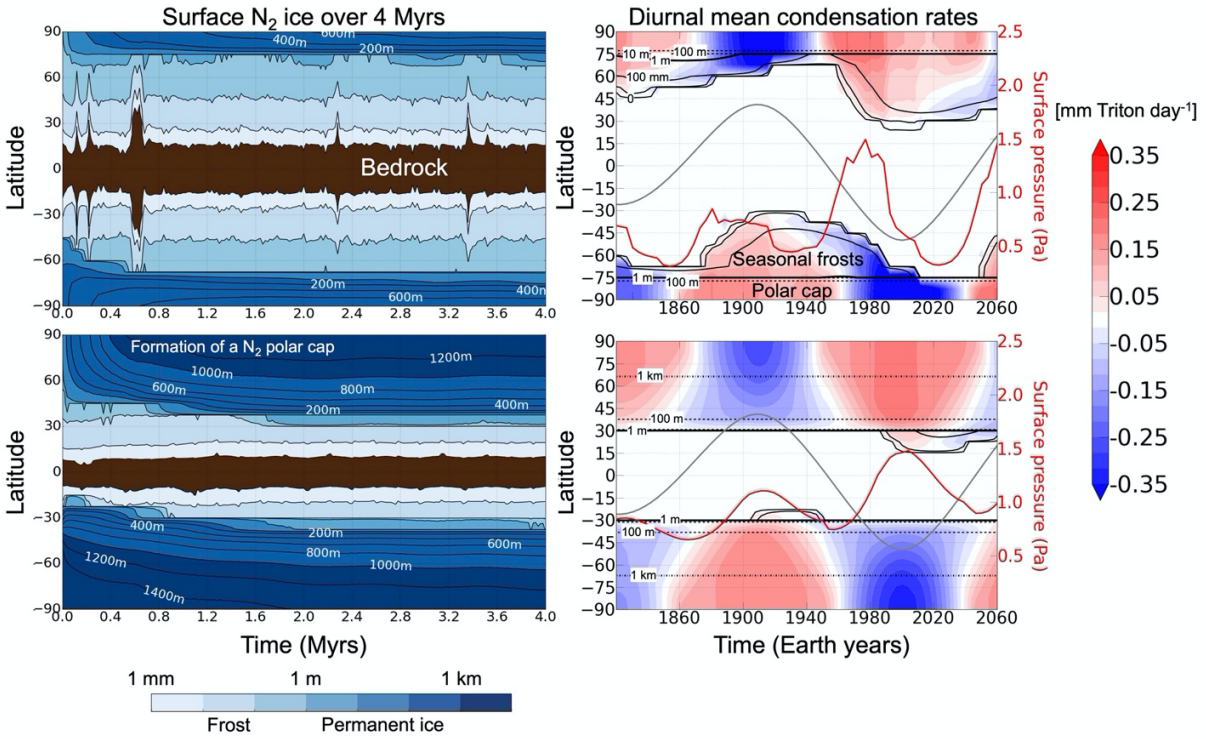

Figure 12: Results from a VTM simulation performed with spatially uniform N_2 ice properties. Top: Simulation with TI_{bed}=1000 SI, A_{bed}=0.8, R_{N2}=12 m. Bottom: TI_{bed}=500 SI, A_{bed}=0.7, R_{N2}=350 m.

Left: annual mean evolution of N_2 ice thickness (in zonal mean) over 4 Myrs. Right: Zonal and diurnal mean N_2 condensation-sublimation rate (mm per Triton day) during the period 1820-2060. The black contours indicate the extent of the caps (0-line, 10 mm, 100mm, solid), and where the ice is 1 m (thick solid line) and 1 km thick (dash-dotted line). The red line indicates the surface pressure (right y-axis) and the grey line indicates the subsolar latitude. Deposits thinner than 1 m tend to be seasonal.

Figure 12 shows examples of model results when a spatially uniform N_2 ice albedo is assumed, primarily in two formats: the long-term evolution of N_2 ice thickness over 4 Myrs (left panel) and the recent seasonal evolution of the diurnal mean N_2 condensation rates obtained during the 1820-2060 period (as the outcome of the 4-Myrs simulation).

First, in the long-term evolution, the northern hemisphere, initially warm and volatile-free, quickly cools down and allows the formation of a permanent northern cap, which stabilizes along with a symmetric southern cap after ~2 Myrs. The thickness and the extent of the caps depend on the global reservoir of N_2 ice. In the tropical regions, mm-to-m thick seasonal deposits can form and extend to the equatorial regions.

Second, the seasonal evolution (right panel) shows that the southern cap sublimates from ~1960 to ~2040, with N_2 condensing in the northern hemisphere. In the case of Figure 12 (top), the low amount of N_2 ice in the system reduces N_2 deposits to seasonal layers (mm-to-m thick) at latitudes equatorward of 70°N or of 75°S, and the southern cap retreats from 40°S to 75°S while the northern cap expands from 70°N to 20°N between 1960 and 2020. This leads to a strong decrease of surface pressure from 1989 as N_2 condensation-dominated areas increase in the north and as sublimation is limited in the south. In the case of Figure panel_uniform1 (bottom), there is enough N_2 ice on the surface so that the permanent northern and southern caps expand to 30°N and 30°S, respectively. The peak of surface pressure is reached around year 2000, when the sources of N_2 in the south balance the sinks in the north (~2-3 mm Triton day^{-1}).

In general, all simulations that assume spatially uniform subsurface and ice properties produce symmetric permanent caps. As shown by Figure 12, this results in either a northern cap that extends to latitudes southward of 45°N in 1989 (inconsistent with Voyager 2 observations) and/or a strong decrease of surface pressure between 1989 and 2017 (with values largely below the reported value of 1.41 Pa in 2017, inconsistent with stellar occultation observations).

In the next section, we impose a North-South asymmetry in N_2 ice albedo in order to force a smaller northern cap.

7.3 Full volatile transport simulations with a North-South asymmetry in N_2 ice albedo

In this section, we perform volatile transport simulations following the *Koyaanismuuyaw* model (Moore and Spencer, 1990): we assume that the N_2 ice albedo in the northern hemisphere is lower by 0.1 than that in the southern hemisphere, which leads to a larger permanent southern cap.

7.3.1. Comparison to the case without North-South asymmetry

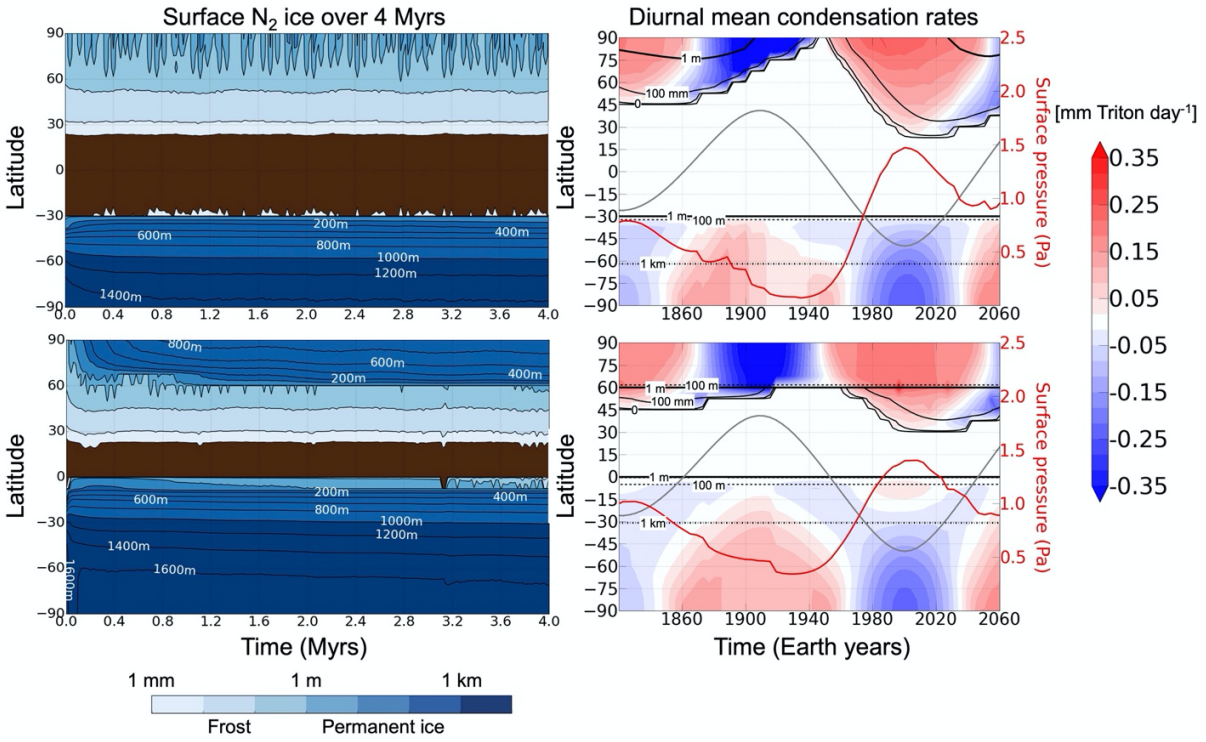

Figure 13: As Figure 12 but from a VTM simulation performed with a North-South asymmetry in N_2 ice albedo (ΔA_{N2}=0.1). Top: Simulation with TI_{bed}=1000 SI, A_{bed}=0.7, R_{N2}=200 m. Bottom: TI_{bed}=2000 SI, A_{bed}=0.7, R_{N2}=550 m.

Figure 13 (top) shows an example of a simulation performed with the North-South asymmetry in N_2 ice albedo and a global N_2 reservoir of 200 m. A permanent, 1-km thick southern cap forms and stabilizes with an extent to 30°S, due to the relatively high ice albedo and subsurface thermal inertia. In the northern hemisphere, only seasonal mm-to-m thick deposits form (Figure 13, top left). During the northern summer (1890-1940), these northern deposits entirely sublimate and disappear (Figure 13, top right). In this simulation, N_2 re-condenses in the northern hemisphere in the current southern summer, with a maximum extent of the frost to ~30°N, reached in 2000. The surface pressure peaks in ~2000, and is back to Voyager levels in 2017, consistent with the observations.

Figure 13 (bottom) describes a similar simulation but with a larger global N_2 ice reservoir of 550 m. In this simulation, the permanent southern cap extends to the equator and a smaller northern cap forms and extends to 60°N (Figure 13, bottom left). The seasonal frosts in the Northern hemisphere extend to ~30°N in 2000, and the pressure cycle is still consistent with the observations with a maximum reached in 2005 and a value close to that of 1989 in 2017. Note that N_2 re-condenses in the equatorial regions at the edge of the southern cap between 1980-2020 (Figure 13, bottom right), as also shown in Section 6.2. This may be related to the formation of the bright blue fringe observed in these regions by Voyager 2 (see discussion on this topic in Section 8.4).

7.3.2. Sensitivity of the results to surface properties, internal heat flux and ice reservoir

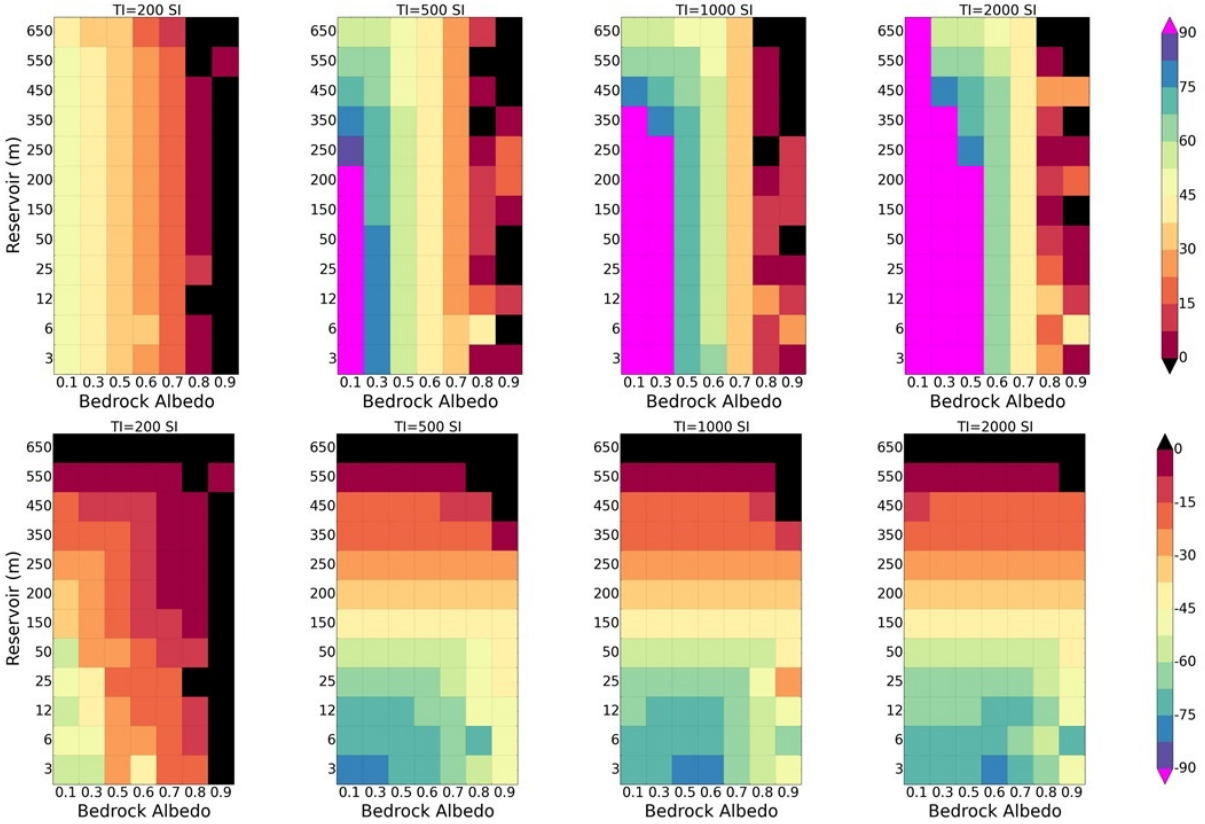

Figure 14: Latitude to which the northern (top) and southern (bottom) caps expand (from the pole) in 1989 as modeled by simulations with varying subsurface thermal inertia (columns, TI = 200, 500, 1000, and 2000 SI from left to right), N_2 global reservoir (y-axis) and bedrock albedo (x-axis). The simulations that best match Voyager 2 observations in 1989 are those that show a northern cap confined poleward of 45°N and a southern cap that extends to 30°S at least.

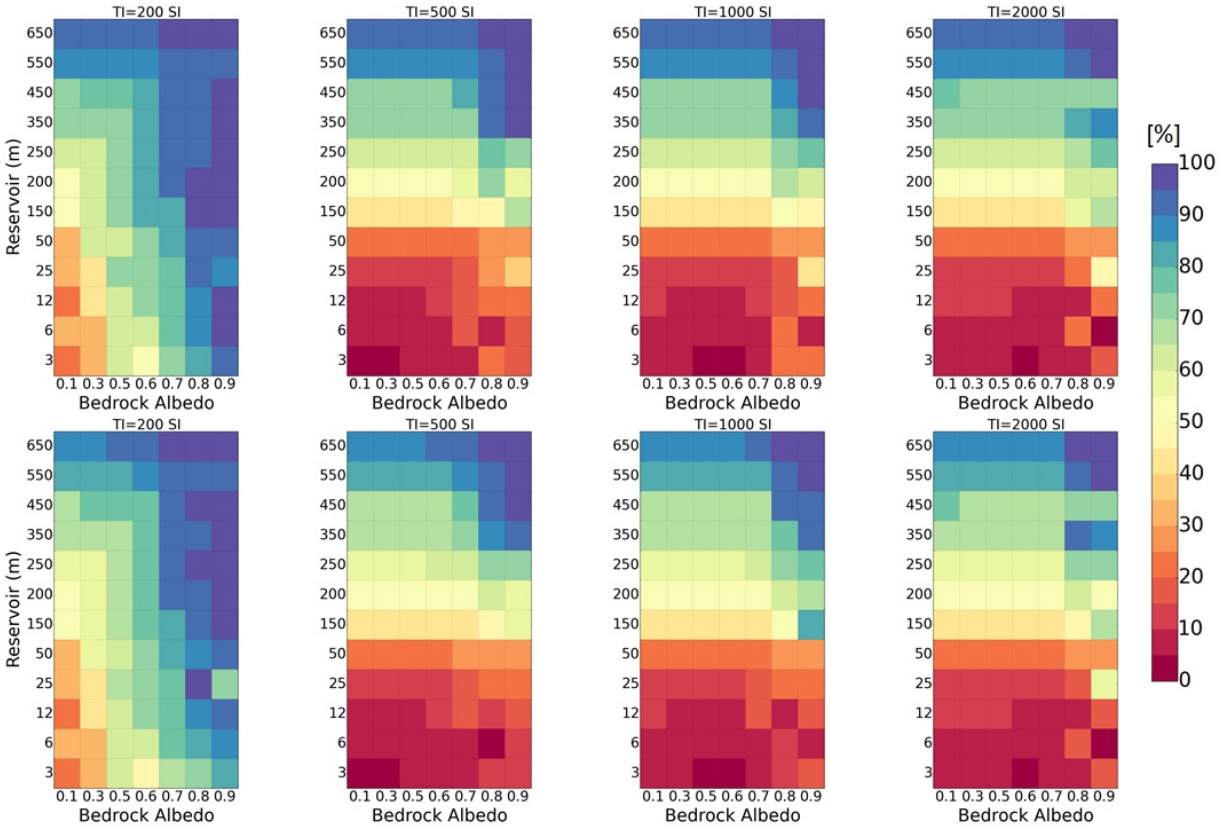

Figure 15: Modeled volatile fractional area (%) in 1995 (top) and 2010 (bottom), projected on the visible disk at these dates, with varying subsurface thermal inertia (columns, TI = 200, 500, 1000, and 2000 SI from left to right), N_2 global reservoir (y-axis) and bedrock albedo (x-axis). The simulations that best match Earth-based spectroscopic observations are those that show a volatile fractional area of 50-60% in 1995 (Quirico et al., 1995) and 60-70% in 2010 (Merlin et al., 2018). Note that the extent of the southern cap and the latitude of the subsolar point do not change much between 1995 and 2010, hence the relatively unchanged volatile fractional area during this period of time.

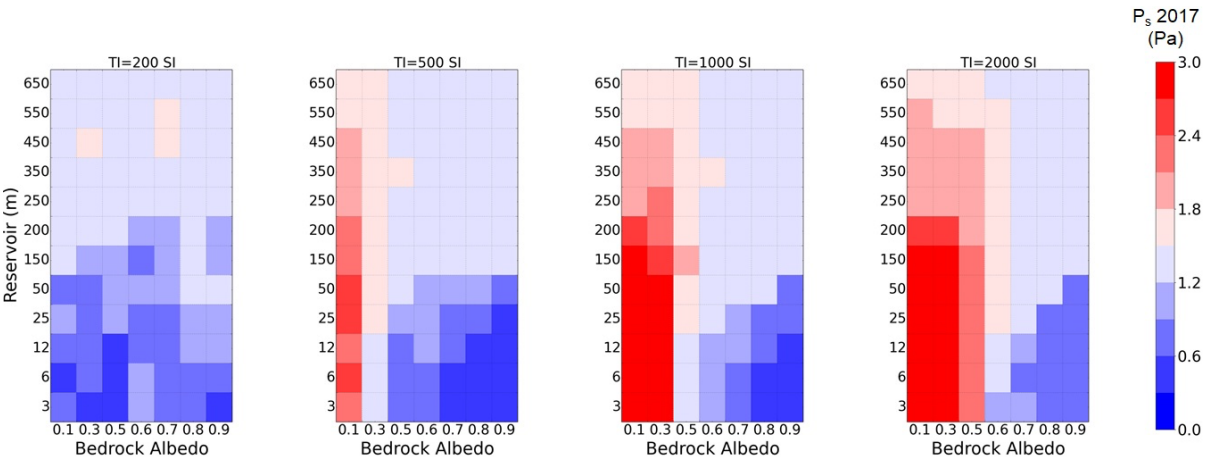

Figure 16: Surface pressure on Triton in 2017 as modeled by simulations with varying subsurface

thermal inertia (columns, TI = 200, 500, 1000, and 2000 SI from left to right), N_2 global reservoir (y-axis) and bedrock albedo (x-axis). The simulations that best match the 2017 stellar occultation data are those that show a surface pressure of ~1.41 Pa (Marques Oliveira et al., 2021).

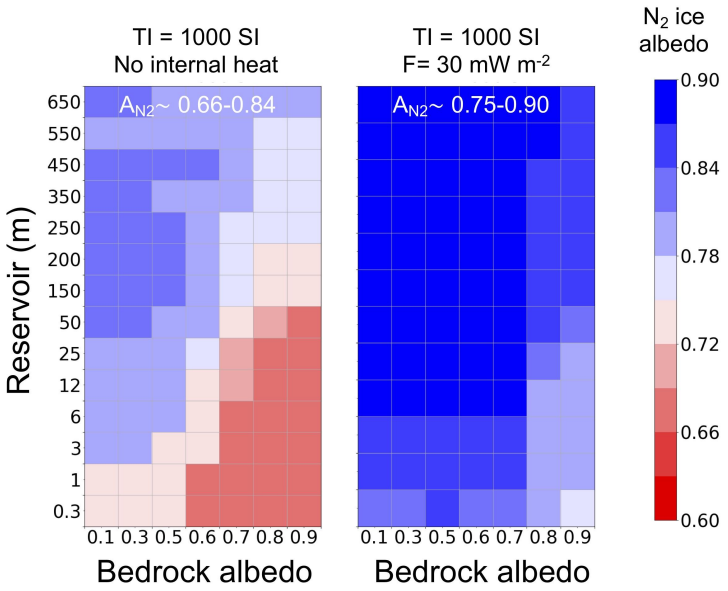

Figure 17: N_2 ice albedo in the southern hemisphere in 1989 as modeled by simulations without (left) and with internal heat flux (right), and for different N_2 global reservoir (y-axis) and bedrock albedo (x-axis). Albedos in the model are Bond albedos. The subsurface thermal inertia is set to 1000 SI.

We performed similar simulations with varying combinations of bedrock subsurface thermal inertias (TI = 200, 500, 1000, and 2000 SI), N_2 global reservoirs (from 0.3 m to 650 m) and bedrock albedos (from 0.1 to 0.9). We also explored how results are impacted by a uniform internal heat flux of 30 mW m^{-2}. The model sensitivity to these parameters is described by (1) Figure 14, which shows the extent of the caps in 1989, (2) Figure 15, which shows the modeled volatile fractional area as seen from Earth in 1995 and 2010, (3) Figure 16, which shows the surface pressure in 2017, and (4) Figure 17, which shows the value of the N_2 ice albedo in 1989 calculated by the model so that the surface pressure reached the observed value (~1.4 Pa). We also tested how the volatile cycle responds to a lower N_2 ice emissivity (ε_{N2}=0.3, 0.5, and taking into account the α-β phase transition) and higher values of thermal inertias (TI = 4000, 8000 SI).

Sensitivity to the N_2 reservoir

N_2 ice accumulation is always favored in the southern hemisphere, due to the north-south N_2 ice albedo asymmetry. As a result, the extent of the southern cap (and thus the volatile fractional area) strongly depends on the global N_2 reservoir and the viscous flow of N_2 (Figure 14, bottom). This is illustrated by Figure 18. The more N_2 in the system, the thicker the cap, the more it flows toward the equator, and the more the ice subsists through an extreme summer (larger perennial cap). On the other hand, a low reservoir would lead to a small and thin southern cap, with seasonal deposits that disappear during the recent extreme southern summer. As a result, simulations with low reservoirs also lead to a low volatile fraction area in 1995-2010 (except for the low thermal inertia case) and to surface pressures much lower in 2017 than in 1989 as condensation in the

north then dominates sublimation in the south. Reservoirs lower than 150 m coupled with moderate-to-high bedrock TI lead to a southern cap extending to latitudes poleward of 45°S in 1989, a volatile fraction area less than 40% in 1995-2010 (Figure 15) and surface pressure lower than 1.2 Pa in 2017 (Figure 16s), which is inconsistent with Earth-based spectroscopic observations and the 2017 stellar occultation. Very large reservoirs (> 350 m) tend to lead to a higher volatile fraction area than observed (>70%). They also lead to a higher seasonal minimum and a lower seasonal maximum in surface pressure, due to the fact that the caps extend to lower latitudes and are more perennial (limited amounts of seasonal deposits), which better balances the sources and sinks of N_2 (see Figure 9). A maximal surface pressure of ~2 Pa is reached during southern extreme summer for intermediate N_2 reservoirs of 12 m - 450 m coupled with intermediate thermal inertia (not shown).

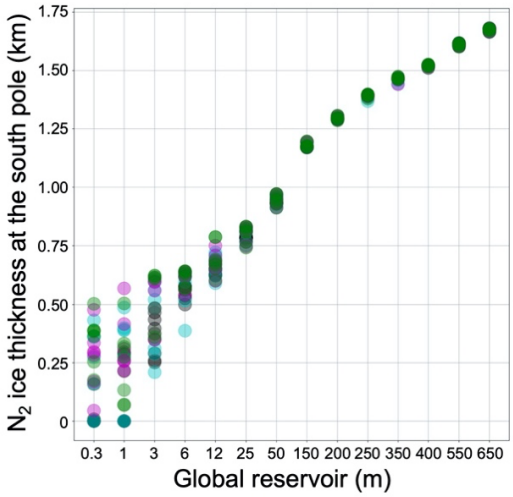

Figure 18: Modeled maximum N_2 ice thickness at the south pole in 1989 vs initial global N_2 ice reservoirs for all simulations performed with north-south N_2 ice albedo asymmetry, no internal heat flux. Colors indicate the thermal inertia (black: 200 SI; cyan: 500 SI; magenta: 1000 SI; green: 2000 SI). For large reservoirs greater than 25 m in global average, the maximum thickness of the ice at the south pole mostly depend on the reservoir (and not on the thermal inertia or albedo of the bedrock).

Sensitivity to the bedrock albedo

The extent of the northern cap does not strongly depend on the global N_2 reservoir but rather on the bedrock albedo (Figure 14). This is because N_2 ice is more stable within the southern cap and only allows a cap to form in the northern hemisphere if the surface is cold enough there (which, in our model, is driven by the bedrock albedo). As described in Section 7.1, our simulations are initialized with a warm northern hemisphere depleted of volatile ice. After several Myrs required to reach a steady state, most of these simulations present a permanent and/or seasonal northern cap in 1989, except when we assume a bedrock albedo much lower than 0.6 and a mid-to-high subsurface thermal inertia (Figure 14, top). Such a low albedo value for Triton's bedrock is unrealistic, as the surface was observed to be relatively bright in 1989 (with a bolometric Bond albedo at least greater than 0.5, McEwen, 1990). Furthermore, Figure 16 shows that a low bedrock albedo coupled with a mid-to-high thermal inertia tends to lead to a high surface pressure (as this would limit N_2 condensation in the northern hemisphere), greater than 1.8 Pa in 2017 (Figure 16), which is not consistent with the 2017 stellar occultation. On the other hand, a very

high bedrock albedo would favor more N_2 condensation in the north during southern summer, leading to a northern cap extending to the equator in 1989 and a low surface pressure in 2017, which is also inconsistent with observations (Figure 14, top, Figure 16). For instance, if the N_2 reservoir is lower than 150 m, the southern cap considerably shrinks during this season, leading to surface pressures lower than 1.2 Pa in 2017, inconsistent with the 2017 stellar occultation (Figure 16).

Sensitivity to the bedrock thermal inertia

The lower the bedrock thermal inertia, the higher the amplitude of bedrock surface and subsurface temperatures across the seasons (higher temperatures during summer, lower temperatures during winter), and, on average over seasonal cycles, the lower the temperatures, in particular at the poles. As a result, a lower bedrock thermal inertia leads to the formation of more mm-to-m seasonal frosts that extend to lower latitudes. In our simulations performed with the low TI = 200 SI and relatively high bedrock albedo (>0.5), the northern cap extends to 15°N in 1989 (Figure 14, top), which is inconsistent with Voyager 2 observations. However, the volatile fractional area is consistent with Earth-based spectroscopic observations for low thermal inertia coupled with low to moderate reservoirs and a surface albedo of ~0.6 (Figure 15). The increased presence of seasonal N_2 frosts forming in the northern hemisphere during winter in the case of low thermal inertia prevents an increase of surface pressure after 1989. As a result, low thermal inertia tends to lead to slightly low surface pressure (< 1.2 Pa) in 2017, especially when the N_2 reservoir is low (frosts would disappear in the southern hemisphere shortly after 1989). Moderate-to-large thermal inertia (500-2000 SI) limits the decrease of surface and subsurface temperature in the northern hemisphere during winter and thus allows for a limited extent of the northern cap in 1989. Surface pressure tends to increase from 1989 to ~2005-2010 and then decrease with a 2017 value close to that of 1989. Finally, we show on Figure 19.D two simulation cases performed with extremely (and possibly unrealistically; Ferrari and Lucas, 2016) high thermal inertias of 4000 SI and 8000 SI. Changes to the N_2 cycle are not significant in the case with TI=4000 SI. With TI=8000 SI, thicker deposits accumulate in the northern hemisphere and the seasonal changes of surface pressure are reduced, with a higher pressure minimum at 0.5 Pa.

Sensitivity to the internal heat flux

A higher internal heat flux (uniformly applied across the globe) increases the surface and subsurface temperature for a given insolation. In order to keep a surface pressure of ~1.4 Pa in 1989, the N_2 ice must thus remain at the same vapor-pressure equilibrium temperature and must therefore be brighter. In general, an internal heat flux of 30 mW m^{-2} leads to an increase in N_2 ice albedo of 0.1 compared to the case without internal heat flux (Figure 17) and as a result to slightly lower condensation and sublimation rates. The evolution of the surface pressure and the extent of the southern and northern caps remain relatively similar to the cases without internal heat flux.

Sensitivity to the N_2 ice emissivity

As detailed in Section 3.4.1, the N_2 ice emissivity on Triton may be lower than what is assumed in the model (ε_{N2}=0.8). Figure 19.A-B shows how the volatile cycle is impacted by a lower N_2 ice emissivity by comparing a reference simulation using a fixed emissivity ε_{N2}=0.8 with the same simulation but using ε_{N2}=0.3 and ε_{N2}=0.5. In addition, Figure 19.C shows the case of a temperature dependent N_2 ice emissivity, with an α-β phase transition for N_2 ice at $T_{\alpha-\beta}$=35.6 K, as implemented in the model and tested for Pluto in Bertrand et al., 2019 (see their equation 1). In all these “low

emissivity cases" (and as for all the other simulations of this section), the model had to adjust (increase by steps of 0.005, typically from 0.75 to 0.8) the N_2 ice albedo during the spin-up time so that the surface pressure remained close to 1.4 Pa in 1989.

Overall, the fixed lower emissivity induce higher pressure minima, which remain above 0.4 Pa in the case with ε_{N2}=0.3. Together with the subsequent increase of N_2 ice albedo needed to match the Voyager 2 pressure constraint, it induces lower condensation-sublimation rates and a smaller northern cap.

The cases with the α-transition are slightly different. The change of emissivity forces the ice surface temperature to remain at the transition temperature $T_{\alpha-\beta}$=35.6 K during the periods of low pressure (i.e., northern summers) and therefore the surface pressure during these periods also remains constant at ~0.5 Pa. However, ε_{N2} remains at 0.8 during most of time, and therefore the condensation-sublimation rates and the extension and thickness of the northern cap do not change much compared to the reference case.

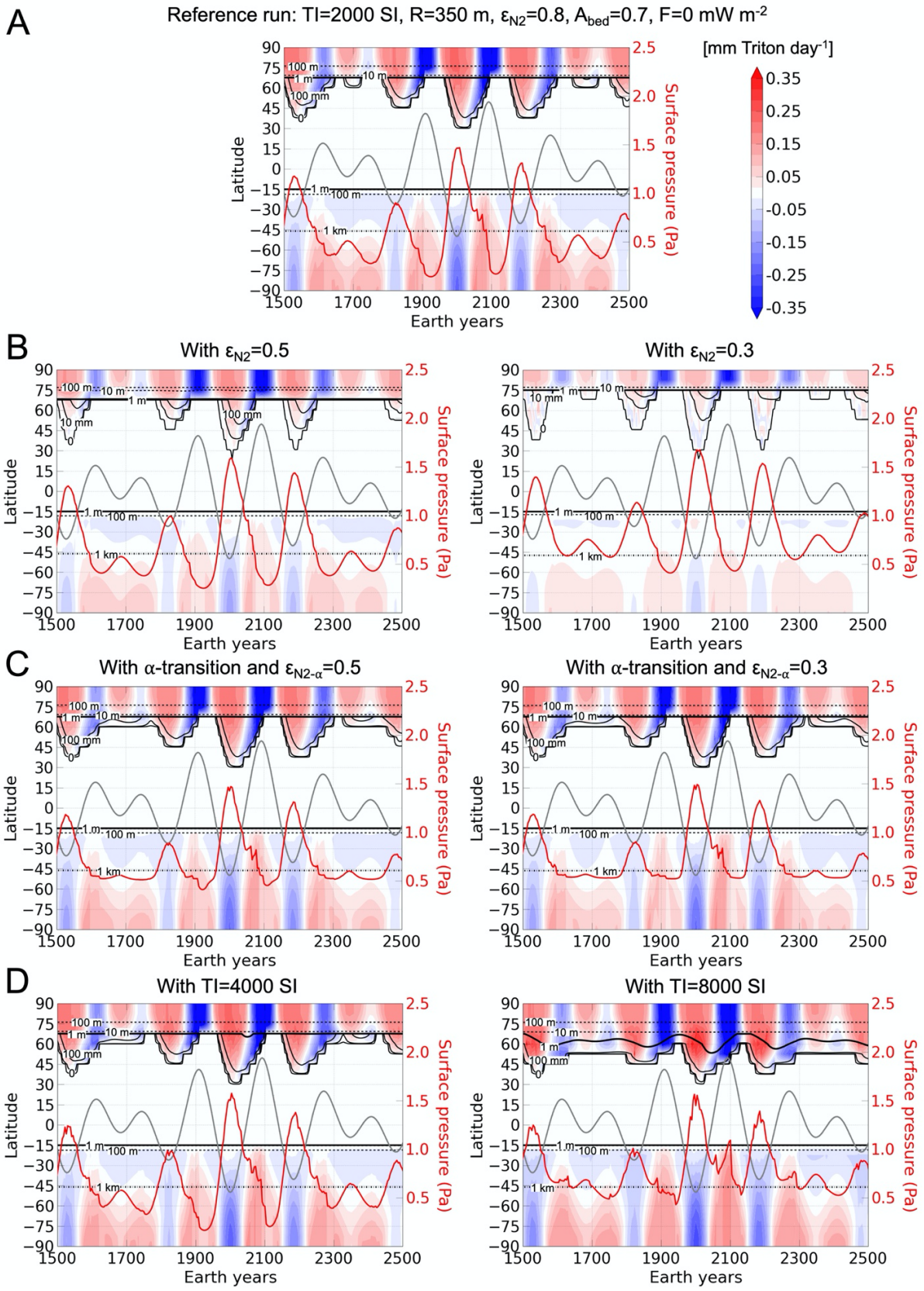
A
Reference run: TI=2000 SI, R=350 m, εN2=0.8, Abed=0.7, F=0 mW m-2
[mm Triton day-1]
0.35
0.25
0.15
0.05
-0.05
-0.15
-0.25
-0.35
Latitude
Surface pressure (Pa)
Earth years
B
With εN2=0.5
With εN2=0.3
C
With α-transition and εN2-α=0.5
With α-transition and εN2-α=0.3
D
With TI=4000 SI
With TI=8000 SI
100 m
10 m
1 m
100 mm
10 mm
1 km

Figure 19: Sensitivity of the volatile cycle to low N_2 ice emissivity and high thermal inertia. (A) Reference simulation among best-case runs, with the North-South asymmetry in N_2 ice albedo, TI=2000 SI, ε_{N2}=0.8, showing the zonal and diurnal mean N_2 condensation-sublimation rate (mm Triton day^{-1}) during the period 1500-2500 (about 7 seasonal cycles). The black contours indicate the extent of the caps (0-line, 10 mm, 100mm, solid), and where the ice is 1 m (thick solid line) and 1 km thick (dash-dotted line). The red line indicates the surface pressure (right y-axis) and the grey line indicates the subsolar latitude. (B) As in (A) but with ε_{N2}=0.5 (left) and ε_{N2}=0.3 (right). (C) As in (A) but with the α-β phase transition, $\varepsilon_{N2\text{-}\beta}$=0.8, $\varepsilon_{N2\text{-}\alpha}$=0.5 (left) and $\varepsilon_{N2\text{-}\alpha}$=0.3 (left). (D) As in (A) but with TI=4000 SI (left) and TI=8000 SI (right).

7.3.3. Best simulations matching observations

As defined in Section 3.5, realistic simulations must be consistent with the volatile fractional area retrieved from Earth-based spectroscopic observations, the relatively bright surface and the extent of the caps seen by Voyager 2 in 1989, and the surface pressure of ~1.41 Pa retrieved by stellar occultation in 2017 (all simulations match by construction the 1.4 Pa surface pressure measured by Voyager 2 in 1989).

Here we define four classes of simulations, summarized in Table 3. Simulations of Class #1 are consistent with the observed surface pressure in 2017 (1.41 Pa, with 30% margin, i.e. ±0.4 Pa) and with a relatively bright surface Bond albedo (A_{bed} >= 0.6). Note that all simulations of Class #1 satisfy the constraint of having a full-disk averaged surface temperature of 37-44 K in 1989 (although this constraint is not stringent enough to distinguish between best-case simulations). Simulations of Class #2.1 are of Class #1 and are in addition consistent with the volatile fractional area observed in 1995 and 2010, with relatively large margins (we assume 45-75% for both 1995 and 2010). Simulations of Class #2.2 are also of Class #1, but are consistent with the extent of the caps observed in 1989 by Voyager 2 (poleward of 45°N in the northern hemisphere and about 15°S in the southern hemisphere, with some margins on these values). Both Class #2.1 and Class #2.2 require a more constrained surface pressure in 2017 of 1.41 Pa ± 0.2 Pa. Finally, simulations of Class #3 are the most realistic ones. They are of Class #1, #2.1 and #2.2. Here we only analyze the simulations performed with the North-South N_2 albedo asymmetry (those without the asymmetry can match Class #1 criteria but do not match any of the Class #2 criteria, as shown in Section 7.2).

Class 1: Matching 2017 stellar occultations and surface albedo
Surface pressure in 2017: 1.41 ± 0.4 Pa
Surface albedo (all ices, including bedrock) ≥ 0.6 (relatively bright surface)
Class 2.1: Matching Earth-based spectroscopic observations
Must be of Class 1
Volatile fractional area within 45-75% in 1995 and in 2010
Surface pressure in 2017: 1.41 ± 0.2 Pa
Class 2.2: Matching cap extents seen by Voyager 2
Must be of Class 1
Southern cap extent within 35°S-5°N in 1989
Northern cap extent poleward of 35° in 1989
Surface pressure in 2017: 1.41 ± 0.2 Pa
Class 3: Best cases
Must be of Class 1, 2.1 and 2.2

Table 3: Classification of the simulations, based on the available observations and with some margins. Most realistic simulations are of Class #3.

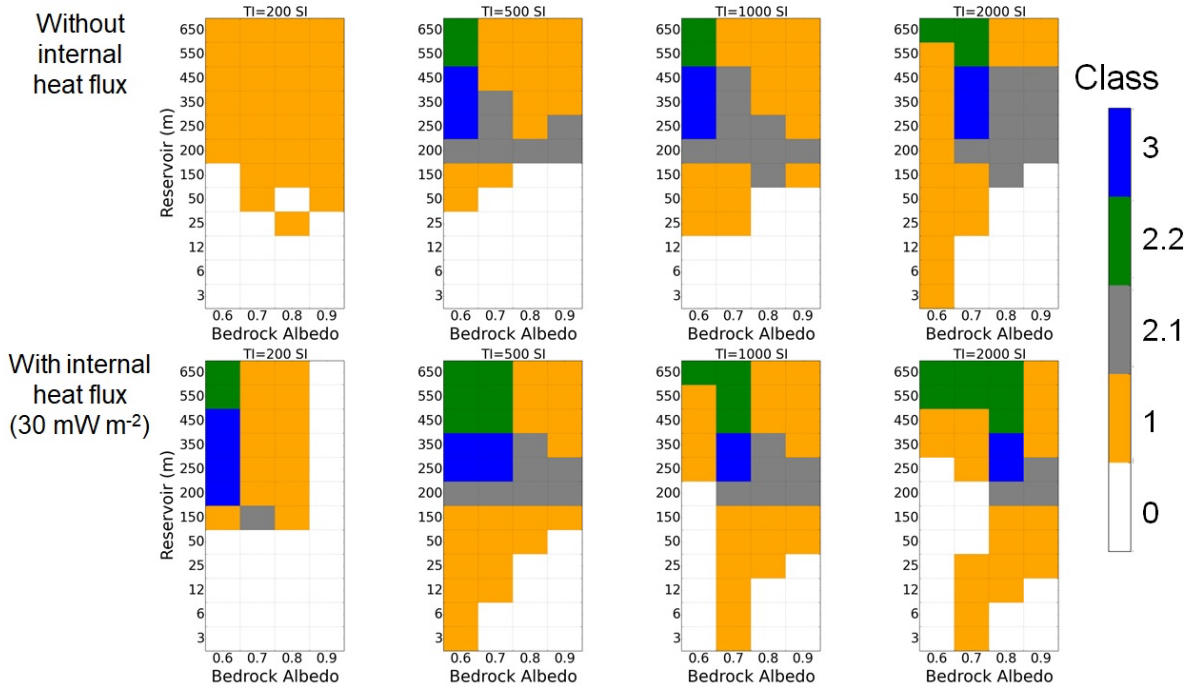

Figure 20: Classification of our simulations (with the North-South N_2 albedo asymmetry) without (top) and with (bottom) 30 mW m^{-2} internal flux as defined by Table 3, with varying subsurface thermal inertia (columns, TI = 200, 500, 1000, and 2000 SI from left to right), N_2 global reservoir (y-axis) and bedrock albedo (x-axis). Best case simulations (Class #3) are shown in blue. Class 0 does not meet any constraint.

Figure 20 shows the classification for all the simulations performed with the North-South N_2 albedo asymmetry. We note that:

- All simulations performed with a low TI of 200 SI are generally of Class #0 or #1 because they are inconsistent with the extent of the caps seen in 1989 and with the observed volatile fractional area (too large), except for the cases with an internal heat flux, a large reservoir and a bedrock surface albedo of 0.6 (Classe #3).
- The most realistic simulations in terms of surface pressure and N_2 ice distribution (extent in 1989 and fractional area in 1995-2010) have a bedrock albedo within 0.6-0.8 and a large N_2 ice reservoir greater than 200 m. In particular, the northern cap is confined to poleward of 45˚N in 1989 for moderate bedrock albedo (< 0.8) and mid-to-high bedrock thermal inertia, while the southern cap extends to at least 30˚S in 1989 for large N_2 reservoirs (> 200 m). As a result, these simulations are of Class #2 (2.1 or 2.2) at least.
- The fact that best case simulations are obtained for a bedrock albedo within 0.6-0.8 is consistent with Voyager 2 observations.
- Simulations of Class #3 that closely match all observations listed in Table 3 are generally obtained for mid-to-large reservoir (200-450m) coupled with (1) high thermal inertia (2000 SI) and a bedrock albedo of 0.7-0.8, or (2) intermediate thermal inertia (500-1000 SI) and

a bedrock albedo of 0.6-0.7, or (3) low thermal inertia (200 SI), a bedrock albedo of 0.6 and high internal heat flux.

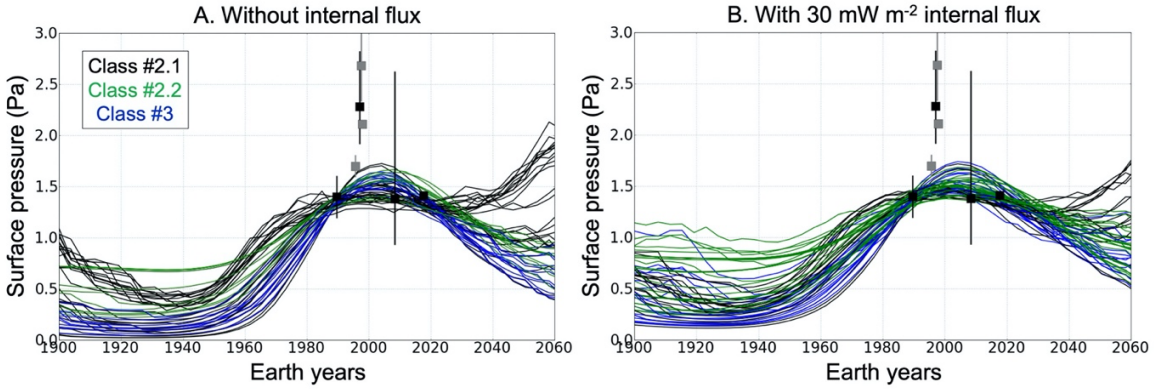

Figure 21: Surface pressure from 1900 to 2060 as obtained in the best case simulations, Classes #2.1 (black), #2.2 (green) and #3 (blue), without (A) and with internal heat flux (B). Black and grey data points and error bars represent the pressure observations as presented in Table 2 (black are for the data points that we consider are the strongest observational constraints).

Figure 21 shows the evolution of surface pressure in the best case simulations. The evolution is relatively similar for all these simulations: the surface pressure increases by a factor of 1.5-2 during the period 1980-2010, reaches a maximum of 1.5-1.8 Pa in ~2005-2010 and then decreases to reach 1-1.5 Pa in the period 2020-2040 and 0.5-1 Pa by 2060.

We note an increase in surface pressure between 2040-2060 in some Class #2.1 simulations. This is due to the fact that the seasonal northern cap is strongly extended (equatorward) in these simulations around year 2000, following a large accumulation of deposits at low latitude during southern summer. As a result, when the subsolar point moves northward (close to 0° in 2040-2060), there are large amounts of N_2 ice available for sublimation (at the equator and mid-latitudes) and sublimation tends to dominate condensation (at the poles) in global average, causing an increase in surface pressure.

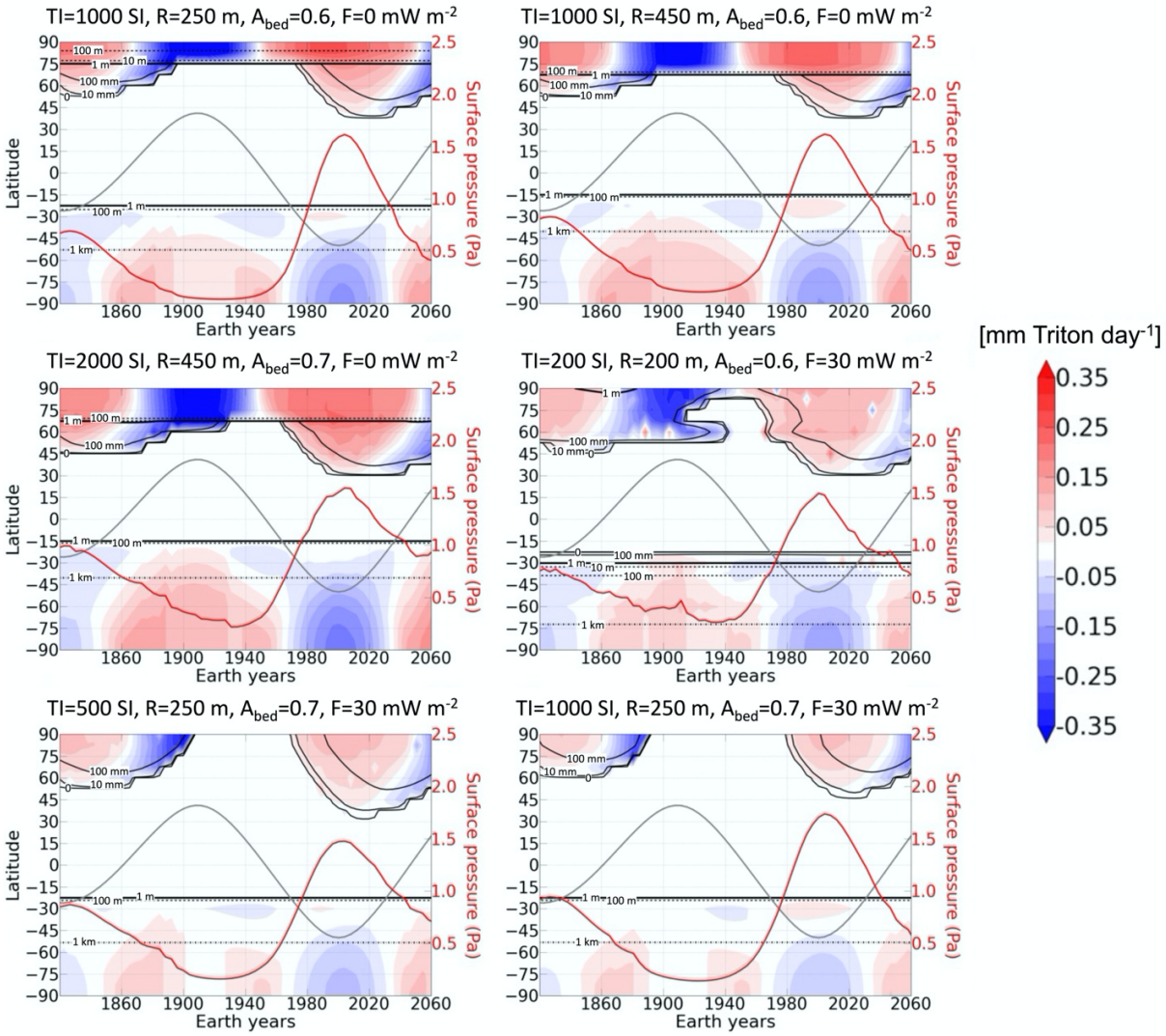

Figure 22: Best case simulations with the North-South asymmetry in N_2 ice albedo. Zonal and diurnal mean N_2 condensation-sublimation rate (mm Triton day^{-1}) during the period 1820-2060. The black contours indicate the extent of the caps (0-line, 10 mm, 100mm, solid), and where the ice is 1 m (thick solid line) and 1 km thick (dash-dotted line). The red line indicates the surface pressure (right y-axis) and the grey line indicates the subsolar latitude. Deposits thinner than 1 m tend to be seasonal.

Figure 22 shows the seasonal evolution of the N_2 condensation-sublimation rates for six of the best-case (class #3) simulations, while Figure 23 shows the latitudinal distribution of ice and surface temperatures as obtained for 1989 for the same simulations. The modeled southern cap is permanent and extends to ~15°S, with low latitudes being dominated by sublimation, but replenished in N_2 ice by viscous glacial flow. All best simulations suggest a southern cap that is >1 km thick poleward of 60°S. A small permanent northern polar cap is suggested for best-case simulations without internal heat flux, while only a seasonal northern cap is suggested for best-case simulations with 30 mW m^{-2} internal heat flux. In all simulations, the northern cap extends at least to 45°N in the period 2020-2040, and to ~30°N in some cases. At the southern summer

solstice, the sublimation and condensation rates are about ~0.1-0.2 mm per Triton day (i.e. 2-4x10^-7 mm s-1), and about 0.13-0.26 m if applied over 20 Earth years. Simulations performed with a high internal heat flux (F=30 mW m^{-2}) show reduced N_2 condensation-sublimation rates due to the higher N_2 ice albedo (~0.05-0.15 mm per Triton day), and smaller permanent caps. In all cases, N_2 recondenses in the low latitudes of the southern hemisphere during the period 1980-2020. Sublimation from the polar southern cap and condensation at the northern edge was also suggested by the thermal balance model of Grundy et al. (2010) and could help explain the longitudinal variation of the N_2 2.15 µm feature.

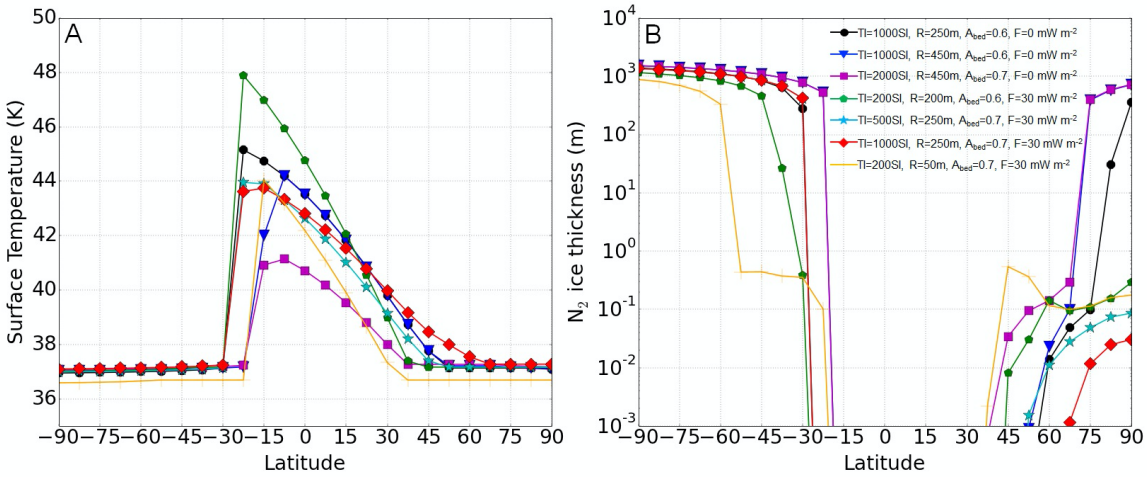

Figure 23: (A) Zonal mean surface temperature vs latitude for the best-case simulations in 1989, as shown by Figure best_flux1: Without internal heat flux : TI=1000 SI - R=250 m - A_{bed}=0.6 (black circle), TI=1000 SI - R=450 m - A_{bed}=0.6 (blue triangle), TI=2000 SI - R=450 m - A_{bed}=0.7 (purple square). With internal heat flux: TI=200 SI - R=200 m - A_{bed}=0.6 (green polygon), TI=500 SI - R=250 m - A_{bed}=0.7 (cyan star), TI=1000 SI - R=250 m - A_{bed}=0.7 (red losange). The orange solid line shows the cases of a low reservoir and low thermal inertia simulation (TI=200 SI - R=50 m - A_{bed}=0.7 - F=30 W m^{-2}) that is consistent with observed caps extent and volatile fractional area but inconsistent with the observed pressure in 2017 (too low, see text in Section 8.3). (B). Same as A but showing the surface N_2 ice thickness.

7.4 On the seasonal cycle of CO and CH_4

Our results show that CO and CH_4 remain mixed with N_2 and never form pure deposits (except for pure CH_4 frost residuals forming at the cap edge when N_2 ice sublimes and disappears, but these frosts quickly disappear within one Earth years or less). This contrasts with Pluto, where CH_4-rich ice deposits cover a large part of the surface (thick and permanent deposits in the equatorial regions, seasonal frosts or permanent mantle at mid-to-polar latitudes). This may be due to a difference in the global reservoir of CH_4 ice (which may be too small on Triton to form permanent CH_4-rich deposits). Another basic understanding of the absence of broad permanent CH_4-rich deposits on Triton is the following: on Pluto, N_2 and CH_4 ices tend to accumulate in the equatorial regions, which are colder than the mid-to-high latitudes, in average over a Pluto year and over several astronomical cycles, due to the relatively high obliquity of the spin axis (e.g., Bertrand et al., 2019). Whereas N_2 ice preferably accumulates in depressions, CH_4 ice preferably accumulates at high altitude (e.g., Bertrand and Forget, 2016, Bertrand et al., 2020b). The fact that the equatorial regions on Pluto correspond to a large area displaying a variegated topography, including deep depressions (such as the ~6-10 km deep Sputnik Planitia impact crater) and tall mountains (e.g. Pigafetta Montes, or the region of Tartarus dorsa) allows the

formation of both permanent N_2-rich (Sputnik Planitia ice sheet) and CH_4-rich (bladed terrain) deposits at different locations. On Triton, however, the coldest regions are the poles (maybe one pole in particular if one assumes an asymmetry in internal heat flux for instance), which correspond to a relatively small area where only small variations in topography may be displayed, thus not allowing the formation of both deposits (instead, the ice mix together at the poles).

Although we do not expect broad and thick CH_4-rich ice deposits to form on Triton, the formation of small and transitory CH_4-rich ice patches in our model may be limited by the spatial resolution used or the different assumptions made regarding the behavior of ice mixtures. Here we tested different scenarios for CO and CH_4 and describe the model predictions of CO and CH_4 atmosphere mixing ratios, and compare to observations. The various observations of CO and CH_4 surface ice and atmosphere mixing ratios are summarized in Section 2.3 and Section 2.5, respectively.

7.4.1. The CO seasonal cycle

In our model, when we impose a constant CO ice mixing ratio of 0.04% (respectively 0.08%) into N_2 ice and we assume that the vapour pressure equilibrium is controlled by Raoult's law, we obtain a mean CO gas volume mixing ratio of 0.006% (respectively 0.012%) during the period 2000-2020, in good agreement with the 2017 ALMA mm-observations (Gurwell et al. 2019), and therefore inconsistent with the 10x higher IR-derived value from Lellouch et al. (2010). The limited seasonal variation is due to the volatility of CO being close to that of N_2 and the absence of CO-rich ice deposits (Tegler et al., 2019, and absent on Pluto's surface as well, Bertrand and Forget 2016, Schmitt et al., 2017). In the model, CO tends to follow N_2 and condenses where N_2-rich deposits are already present. This is consistent with ground-based spectroscopic data of Triton (CO follows N_2 in longitude) and with observations of Pluto's surface by New Horizons. According to our model, the CO gas volume mixing ratio should remain very close to these values in the next decades (with a slight decrease in 2040 to 0.005% and 0.01%, respectively), although small variations in the CO gas volume mixing ratio are possible if the surface of some areas becomes enriched or depleted in CO ice as N_2 sublimates or condenses.

7.4.2. The CH_4 seasonal cycle

As detailed in Section 2.5, the observed CH_4 atmospheric mixing ratio is much larger (by three orders of magnitude) than expected for an ideal mixture, i.e. if CH_4 ice only exists on Triton as CH_4 diluted in a N_2-rich solid solution (Stansberry et al. 1996b), or for an intimate mixture. Instead, using the CH_4 patch model of Stansberry et al. (1996b), Merlin et al., 2018 (respectively, Quirico et al., 1999) estimated that CH_4-rich ice (at ~40 K) covered 2-3% in 2010-2013 (respectively, a maximal value of 10% in 1995) of the visible disk of Triton, which could be sufficient to maintain a CH_4 atmospheric volume mixing ratio around 0.03%, as observed by Voyager 2.

We tested this scenario in one of our reference simulations (TI=2000 SI, R=400 m, A_{bed}=0.6) by imposing pure CH_4 ice deposits on Triton's surface (with a fractional area consistent to the observations of Quirico et al., 1999 and Merlin et al., 2018), assuming that they follow Raoult's law and are a proxy for CH_4-rich ice (this assumption is good enough, as described in Young et al., 2021). We tested two different locations for these deposits:

(1) At the edges of the southern cap, thus forming a latitudinal band of CH_4 ice near the equator, with a fractional area of ~5% of the projected disk as seen from Earth at the time (~2010) of the observations of Merlin et al. (2018): these regions should contain seasonal volatile frosts, which would favor the formation of CH_4-rich ice by segregation as N_2 ice sublimates and disappears. Voyager 2 images showed features in these regions

suggestive of intense N_2 ice sublimation, which could lead to an enrichment in CH_4-rich ice on the surface.

(2) At the south pole (~2% of the disk surface seen from Earth in 2010): our simulations show that the N_2 ice sublimation rates are strongest at the south pole, which could favor the formation of CH_4-rich deposits on top of the surface.

Figure 24 shows the seasonal evolution of the global mean mixing ratio of atmospheric CH_4 over time for both scenarios, and assuming different albedos for the pure CH_4 ice. Note that the evolution of the surface pressure remains relatively unchanged for all cases compared to that in the reference simulation (without CH_4-rich ice).

The simulations with CH_4-rich ice at the cap edge produce a CH_4 partial pressure of 1-5x10^{-4} Pa in 1989, which is consistent with the 2.45x10^{-4} Pa observed by Voyager 2 (Figure 24, solid lines). Slightly larger amounts can be obtained with a lower CH_4 ice albedo and a higher surface CH_4 ice coverage (solid grey lines). The simulations with CH_4-rich ice at the south pole produce an increase in CH_4 partial pressure until 2005, followed by a decrease as the south pole exits polar day (Figure 24, dashed lines). A small fraction of the south pole covered by CH_4-rich ice is sufficient to produce a CH_4 partial pressure of a few nbar, as observed. The simulation including a CH_4-rich patch at the south pole with albedo of 0.7, is particularly promising to explain the factor of 4 (2.45 to 9.8x10^{-4} Pa) increase in the CH_4 partial pressure from 1989 to 2009, as reported by Lellouch et al. (2010). In contrast, the models in which CH_4-rich ice is concentrated at the N_2 cap edge do not reproduce this increase in the CH_4 atmospheric abundance over 1989-2009. However, a decrease in CH_4 ice albedo or increase in CH_4 ice coverage during this period can also explain the observed increase in CH_4 partial pressure. It is possible that both the pole and cap edge become enriched in CH_4 ice, with different amounts and timescales.

Note that here we assume that these modeled CH_4-rich deposits, exposed at the surface once N_2 ice locally disappeared, are permanent during southern summer. If CH_4 ice also disappears from the surface, the CH_4 atmospheric mixing ratio would slowly fall back to the levels expected for an ideal mixture (a few 10^{-5} %).

Also note that the relatively low CH_4 atmospheric mixing ratio observed (~0.03%) and simulated (>0.01%), would still be enough to block most of the incoming Lyman-α radiation (121.6 nm, 10.19 eV) from direct sunlight and from backscattering from the interplanetary medium, which has implication for the direct photolysis and subsequent darkening of the ices on the surface.

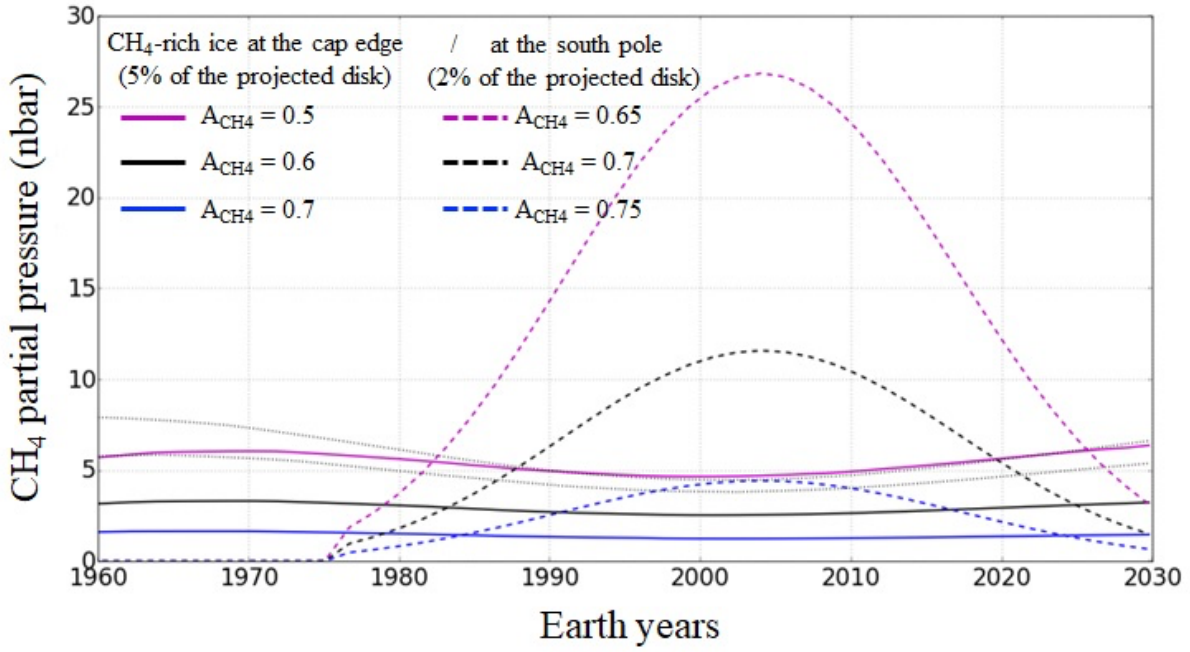

Figure 24: Global mean CH_4 partial pressure (nbar, or x10^{-4} Pa) over time, as obtained for the simulation TI=2000 SI, R=450 m, A_{bed}=0.6, with CH_4-rich ice at the cap edge (fractional area of 5% of the visible disk in 2010, solid lines) and at the south pole (2% of the visible disk, dashed lines), for different CH_4 ice albedos. The two grey curves are for a simulation with CH_4-rich ice at the cap edge (and A_{CH4}=0.6, as for the solid black curve) but covering 9% and 12% of Triton's visible surface area, respectively.

8. Discussion

8.1. On the formation of a northern (polar) cap

All long-term simulations performed in Section 5 with North-South asymmetries in internal heat flux, topography, and N_2 ice albedo, along with a global N_2 ice reservoir of 300 m, predict the formation of a permanent N_2 (polar) cap in the northern hemisphere (>100 m thick). Most of the best-case simulations (Class #1 to #3) performed in Section 7 also predict a permanent N_2 cap in the northern hemisphere. The northern cap is much smaller and thinner in the best-case simulations performed with an internal heat flux of 30 mW m^{-2}, due to the warmer subsurface. A few results with intermediate thermal inertia and moderate global N_2 reservoir (TI=1000 SI, R=250-350 m, A_{bed} = 0.6) predict no permanent cap. The northern cap is not permanent if a smaller global N_2 ice reservoir (< 250 m) is used along with large North-South asymmetries (see Figure 13, R=200 m, and ΔA_{N2} = 0.1). However, these low-reservoir simulations are not consistent with the available observations.

The formation of a permanent N_2 northern cap is primarily the result of two effects:

1. The northern polar night is long enough so that surface temperatures of the bedrock drop below 34 K for a bedrock surface albedo of 0.6. Consequently, N_2 condensation is easily triggered at the north pole if the surface pressure becomes higher than the pressure at solid-gas equilibrium (e.g., ~1 Pa at 37 K).

2. In the simulations, N_2 ice flows (slowly, on timescales longer than the seasonal timescales) from the southern cap towards the warmer sublimation-dominated mid-to-low latitudes, thus maintaining large amounts of ice in these regions, supplying N_2 for further sublimation and allowing the surface pressure to exceed that at solid-gas equilibrium at the north pole.

Note that all best-case simulations explored predict that N_2 condensation has been occurring in the northern hemisphere since 1980. They show that at least a seasonal deposit of a few mm of N_2 ice was covering the northern polar latitudes in 1989 and should cover the northern latitudes down to 30°N-45°N in the period 2010-2030 (see Figure 22). In general, the current extent of the northern cap is related to the extent of the southern cap by the surface pressure: a large extent of the northern cap down to 30°N-45°N (i.e., a large condensation-dominated area) is only possible if the southern cap remains extended to at least 15°S (i.e., a large sublimation-dominated area) during this period, and a smaller southern cap would imply little to no N_2 deposits in the northern hemisphere, otherwise northern condensation would largely dominate southern sublimation and the surface pressure would have significantly dropped in 2017 to levels inconsistent with observations. The scenario of a large permanent southern cap and the seasonal appearance of N_2 ice deposits in the northern hemisphere below the terminator could also explain the increase in N_2 band absorption observed with SpeX/IRTF during the period 2002-2020 (Holler et al., 2016, 2020).

8.2. On the evolution of surface pressure during the period 1989-2017

All best-case simulations show the same trend for the evolution of surface pressure, with an increase from 1920 to 2005-2010 (shortly after the southern summer solstice) followed by a decrease back to the 1920 levels in 2080.

Our results do not suggest a strong surge in surface pressure, as it has been reported for the period 1995-1997 (e.g., Elliot et al., 2000). During the 1989-2005 period, our best-case class #3 simulations suggest an increase in surface pressure by a factor of 1.1-1.2 only, with a peak around 1.5-1.7 Pa. Some of the Class #1 simulations show a peak in surface pressure reaching 2.3 Pa, i.e. a factor of 1.6 compared to the Voyager 2 epoch (these simulations typically predict a 2017 surface pressure that is above the 1.41+0.2 Pa constraint, not shown). These values are consistent with the 1995 occultation event and the derived pressure reported by Olkin et al. (1997), and also eventually with the 1997 occultation event and the derived pressure reported by Marques Oliveira et al. (2021), although the simulations only match this latter value at the 1σ significance level. However, they are inconsistent with the higher values reported in 1997 (Elliot et al., 2000, 2003). We note that a reanalysis of some of these data indicates that this pressure increase was not significant at the 3-σ level (Marques Oliveira et al., 2021). Such a strong increase in surface pressure could still have occurred if processes not taken into account in our model play an important role on Triton, such as strong surface albedo feedback for instance.

8.3. On the presence of volatile ice at the south pole

As detailed in Section 2.3, ground-based spectroscopy of Triton's surface performed with IRTF/SpeX in 2002-2014 and VLT/SINFONI in 2010-2013 showed little longitudinal variability for CO_2 and H_2O ice, unlike the three volatile ices N_2, CH_4, CO (Grundy et al. 2010, Holler et al., 2016, Merlin et al., 2018). To explain these observations, it has been suggested that CO_2 and H_2O ices are exposed at the south pole (the very southernmost latitudes, roughly 90°S-60°S), which would be bare of volatile ice (Grundy et al. 2010, Holler et al., 2016).

However, our volatile transport model challenges this scenario since it always predicts a permanent cap at the south pole, except if an extremely low N_2 reservoir, i.e. only seasonal frosts, is assumed, but these simulation cases typically present (at least for moderate to high thermal

inertias) a too low surface pressure in 2017 (< 1.41 Pa, Figure 16), a low volatile fractional area (< 40%, Figure 15) and a southern cap extent poleward of 45°S in 1989 (Figure 14). Our model, and its current modeled physical processes, cannot predict such a "hole" in volatile ice at the south pole (90°S-60°S). Physical processes not taken into account in the model may play an important role to mask the detection or completely remove N_2 ice at the south pole (see model uncertainties in Section 8.7). For instance, the predicted sublimation of 30-50 cm of N_2 ice at the south pole during the period 1970-2000 (Figure 11, Figure 22) could have led to an accumulation of CH_4-rich ice at the south pole could mask the detection of N_2 ice and be a possible scenario, although it would imply a relatively large CH_4-rich-covered area that would remain to be consistent with other observations.

The near-IR VLT/SINFONI observations and subsequent modeling of Merlin et al. (2018) showed that CO_2 ice is actually present in the form of very small grains and has two components (see their Table 9), one in which it is mixed into the N_2:CH_4:CO matrix (unit 1) and another in which it is mixed into H_2O ice (unit 2). These results suggest that CO_2 ice is present almost everywhere (with an equivalent area of 50% and very small grains). In addition, their model suggests that H_2O ice is present in unit 2 only (H_2O+CO_2+CH_4-rich) and does not need to be invoked in unit 1 (N_2:CH_4:CO). Based on these results, Merlin et al. (2018) imagined two scenarios that could reconcile the presence of both N_2 and CO_2 ices at the south pole: (1) A bedrock surface (CO_2 ice) covered by small CO_2 grains (regolith) covered by a transparent N_2-based matrix (allowing CO_2 to stay detectable), and (2) Small CO_2 particles on top or inside the N_2-based matrix, as the result of endogenous processes (e.g. active geysers tearing particles of CO_2 from the bedrock, transport and spatial redistribution of these particles by the winds, and deposition onto the surface).

Our model results are consistent with these two scenarios, since they do not prevent N_2 ice to be present at the south pole. However, in general, it remains difficult to be confident on the composition of Triton's south pole, given the limited amount of observational datasets, the relative simplicity of the VTM, and the large number of model parameters in both the VTM and the near-IR spectra analysis models.

8.4. On the different terrains observed at the cap edge by Voyager 2

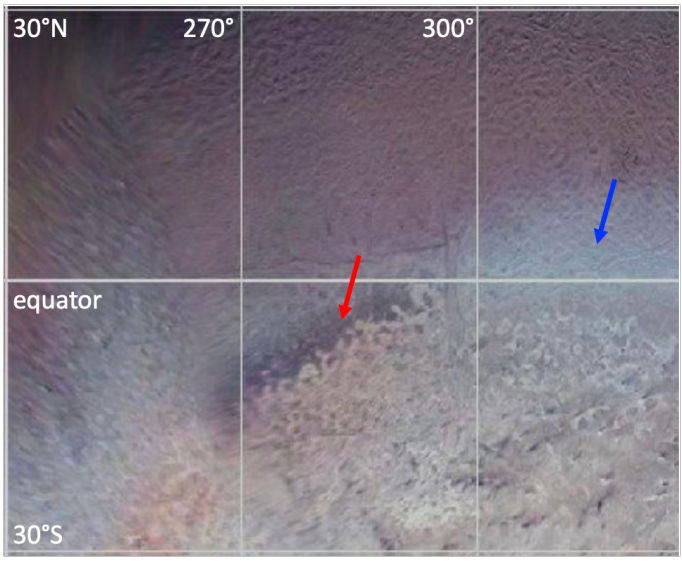

Figure 25: Equatorial regions on Triton at longitudes 240°E-330°E displaying alternation of relatively bright blue frosts (blue arrow, 240°E-270°E and 300°E-330°E) and relatively dark terrains without blue frost (red arrow, 270°E-300°E) at the edge of the southern cap.

Figure 25 highlights two different terrains observed in the equatorial regions at the cap edge: (1) a relatively bright blue (or less red) surface, with photometric properties consistent with a freshly deposited frost (McEwen, 1990); this terrain is seen at almost all longitudes and forms a fringe at the cap edge (Figure 2), and (2) a relatively dark surface, without much blue frost, around 270°E-300°E.

We hypothesize that this dark terrain is the result of a high concentration of dark materials (e.g. tholins-like haze deposits and/or irradiated ices) that had been mixed in N_2 ice and have now been revealed at the surface as the N_2 ice sublimates away. The composition of this unit may be similar to some degree to the dark N_2 ice plains located at the northern edge of Sputnik Planitia on Pluto, which are enriched in dark materials and in CH_4 ice due to intense N_2 ice sublimation (White et al., 2017). The fact that this unit on Triton may be enriched in CH_4 ice is consistent with IRTF/SpeX observations, which show a peak absorption for CH_4 near ~290°E and also a maximum of shift in the position of the CH_4 bands indicating an increased amount of CH_4-rich ice. However, these observations are for the period 2002-2014 only (Grundy et al., 2010, Holler et al., 2016). We also note that the formation of this dark terrain on Figure 25 could be related to topography (see Section 8.5).

This observed longitudinal asymmetry in CH_4 ice distribution could suggest the presence of CH_4-rich deposits at the cap edge, rather than at the south pole. Our simulations with CH_4-rich ice at the cap edge could explain the fourfold increase in CH_4 partial pressure from 1989 to 2009 reported by Lellouch et al. (2010) if the CH_4 ice albedo significantly lowered or if the CH_4 ice surface coverage significantly increased during this period. The latter would also be consistent with the observed increase in CH_4 band absorption during the period 2002-2020 (Holler et al., 2016, 2020). It should be noted that such a scenario of a variable-width ring of segregated less-volatile ice surrounding retreating volatile seasonal deposits has already been observed on Mars in the analogue case of water ice trapped in seasonal CO_2 ice deposits (Appéré et al. 2011). On Mars, this moving ring also triggers a strong seasonal increase in water vapor during its sublimation (e.g. Pankine et al., 2009, 2010).

Our simulations with CH_4-rich ice at the south pole also explain the fourfold increase in CH_4 partial pressure (suggested for the period 1989-2009) as being driven by insolation changes. However, it remains unclear how CH_4-rich ice would form there in the first place. The surface composition of the south pole on Triton in 1989 could also be comparable to the northern dark plains of Sputnik Planitia on Pluto in 2015, since these plains correspond to thick N_2 ice deposits experiencing the constant insolation of the polar day, as Triton's south pole. In Sputnik Planitia, the plains display darker N_2-rich ice deposits enriched in CH_4 ice. The permanent and cold N_2 ice layer located there may buffer the increase of surface temperatures and limit the formation of CH_4-rich deposits on top of the ice layer. On Pluto, CH_4-rich ice is mostly detected outside Sputnik Planitia, with more spatial variability in the CH_4:N_2 mixture at mid latitudes, where thinner seasonal deposits are found (Schmitt et al., 2017). By analogy, on Triton, CH_4-rich ice may tend to form primarily at mid-to-equatorial latitudes where volatile ice deposits are thinner, and at the cap edge where the deposits are seasonal.

The bright "blue" surface may be freshly deposited N_2 frost (relatively clean ice, hence the less red color). Our model suggests that N_2 recondenses in the equatorial regions after 1980 (and until 2020, Figure 22). This happens only if the exposed "bedrock" locally has a high surface albedo or if N_2 ice is already present or was recently present in these regions; in the latter case the exposed "bedrock" surface would have remained cold enough to permit N_2 recondensation. The locations of this hypothetical blue N_2 frost are relatively consistent with IRTF/SpeX observations, which show a minimal (respectively maximal) N_2 absorption roughly where the combined extent

of the cap and of the blue fringe is minimal (respectively maximal). The formation and expansion of this frost would also be consistent with the observed increase in N_2 band absorption during the period 2002-2020 (Holler et al., 2016, 2020).

Alternatively, the bright "blue" surface could be made of freshly-condensed CH_4-rich ice. As detailed in Section 2.3, the amount of CH_4 ice that is not diluted in N_2 ice is estimated to cover a relatively small area on Triton's surface: 2–3% of the surface projected on the visible disk in 2010 (Merlin et al., 2018) and a maximum of 10% in 1995. The blue fringe roughly covers a latitudinal band of 15° at the equator, which accounts for ~10% of the disk-projected surface, so exposed CH_4-rich frost at the location of the blue fringe would remain in the range of possible values (although close the highest possible value) consistent with surface spectroscopic observations. Would there be enough gaseous CH_4 in the atmosphere to permit CH_4 condensation onto the surface in the equatorial regions? We can estimate the saturation vapour pressure volume mixing ratio of CH_4 (above a volatile-free surface) by using equation 14 in Forget et al. (2017), derived from the thermodynamic relations computed by Fray and Schmitt (2009). For a surface temperature of 38 K, 39 K, 40 K and 41 K (i.e. slightly warmer than N_2 ice in 1989), we find a CH_4 saturation volume mixing ratio of 0.017%, 0.036%, 0.075% and 0.153% respectively. Consequently, a volume mixing ratio of CH_4 of ~0.03% (measured by Voyager 2 in 1989) would permit condensation onto a surface colder than ~39 K.

However, the hypothesis of CH_4-rich frost for the blue fringe faces three main issues: (1) In our model, the bedrock surface temperatures in 1989 in the equatorial regions at the cap edge are relatively warm at ~42-44 K and become colder than 39 K in the terrains poleward of 30°N (besttsurf1989), which is not consistent with a blue fringe made of freshly-condensed CH_4. We note that CH_4 condensation could still be favored at the cap edge by locally enhanced winds or if the bedrock surface is locally colder than modeled (e.g. with a higher albedo). (2) A CH_4 ice composition of that region does not match well the longitudinal trends seen in the near-IR spectra. (3) The scenario of a CH_4 ice deposit left after N_2 sublimation is not likely, as the remaining deposit would also contain a certain amount of tholins-like dark materials and therefore would not appear less red (i.e. cleaner) than the surrounding terrains.

Finally, on Pluto, it has been shown that albedo and composition positive feedback could further increase local contrasts in ice sublimation/condensation rates, which could explain the transition from bright to dark plains in Sputnik Planitia (Earle et al., 2018, Bertrand et al., 2020a). Such processes may also be operating on Triton and could explain the diversity of terrains and colors observed at the cap edge. For instance, N_2 sublimation and the subsequent darkening of the surface would lead to an amplifying positive feedback by increasing the absorption of incoming radiation and thus the sublimation rate, whereas N_2 condensation and the subsequent brightening of the surface would lead to further condensation.

8.5. On the topography and N_2 ice thickness in the southern hemisphere

Our best-case simulations have been obtained with a relatively large global reservoir of N_2 ice (>200 m), and suggest a thick southern cap (> 1 km at the south pole, > 100 m at the mid-latitudes and > 1 m at the equator, balanced by glacial flow). Interestingly, some simulations performed with a low bedrock thermal inertia of 200 SI have been able to produce a southern cap extended to the equatorial regions in 1989 with a lower N_2 global reservoir in the range 20 m - 200 m, leading to N_2 ice thickness of 0.1-1 m in the equatorial to mid-latitude regions and >100m at the south pole (Figure 14, and see solid orange line on Figure 23). In these simulations, the equatorial to mid-latitude deposits are not balanced by glacial flow (i.e., they are not connected to the polar deposits) but remain permanent due to the relatively cold bedrock, although in some of these cases a thin mid-latitude band of N_2 ice entirely sublimates in the period 2030-2050. However, these simulations with low bedrock thermal inertia are not among our best-case simulations (they

are only of Class #1 at best), see Figure 20), mostly because they predict N_2 ice deposits in the northern hemisphere extending from 90°N to at least 30°N in 1989 (due to the colder surface induced by lower thermal inertia, Figure 14), and consequently a surface pressure in 2017 much lower than the reported value of 1.41 Pa.

In general, the relatively coarse spatial resolution of Voyager 2 images and the lack of useful topography data above the southern cap do not allow us to determine with confidence the order of magnitude of the thickness of the bright southern deposits, which makes it difficult to conclude on the nature (less than 1 m thick seasonal vs. more than 1 m thick permanent) of these large-scale deposits. The spatial resolution also does not allow us to determine if glacial flow has occurred or not. However, the sharp dichotomy between the southern and northern terrains suggests that the northern bright deposit boundary is controlled by topography, possibly by a topographic barrier (e.g., scarps) of ~100 m to several 100 m (Figure 26), which reinforces our best-case model results suggesting thick and permanent volatile ice deposits in these regions.

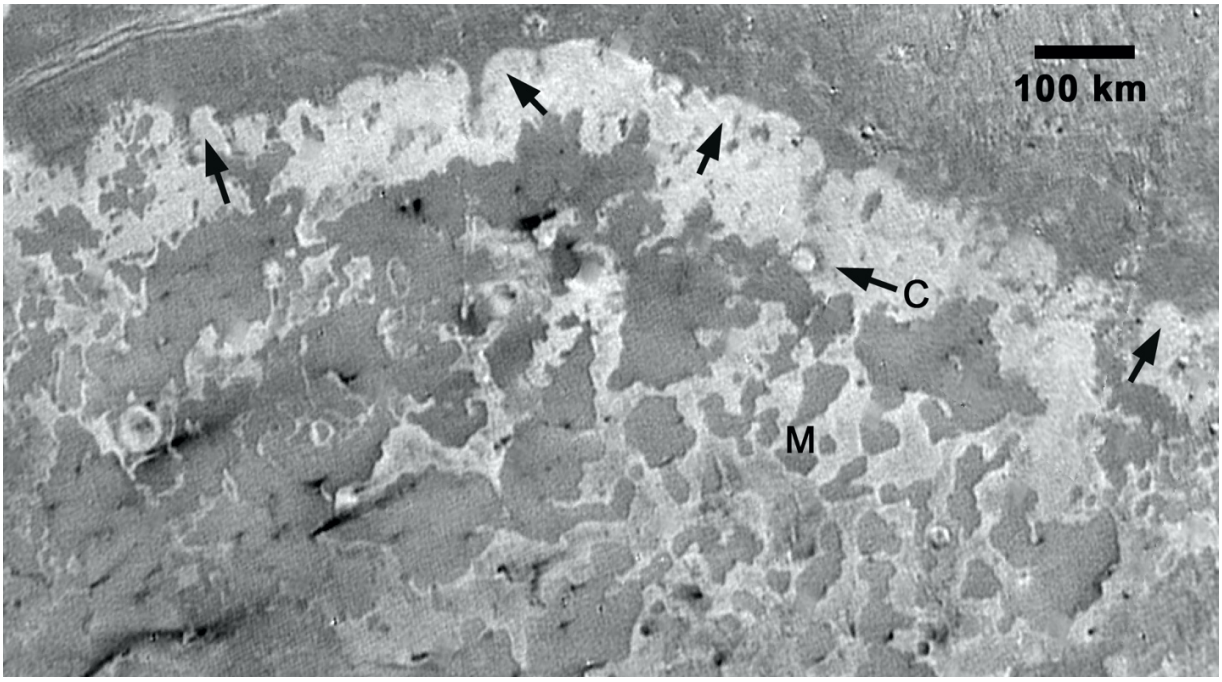

Figure 26: Enlargement of global cylindrical map showing macular southern terrains near the equator of Triton. Possible example of a topographic barrier in the form of scarps (arrows), possibly ~100 m to several 100 m in height, along the sharp dichotomy between the bright southern and northern terrains seen by Voyager 2. "M" denotes a region of mesas south of the main boundary. "C" shows a possible, partially buried crater. Image center ~15°S, 0°E. North is up.

Finally, the sigmoidal contact line of the edge of the dark terrain in Figure 25 seems to be related to topography (Paul Schenk, personal communication). This region forms the southwestern extent of the known region of cantaloupe terrain (Croft et al., 1995), which is characterized by closed topographic cells 20-50 km across and up to 500 m deep (Schenk et al., 2021). The dark material appears to occur mainly on the elevated boundaries between the cells, suggesting that these elevated terrains prevent volatile ice condensation or accelerate sublimation. These color and

topography contrasts between the northern and southern deposits at the cap edge could indicate a gradual decrease in elevation to the south.

8.6. Model predictions for the next decades

8.6.1. General climate predictions

Surface pressure and stellar occultations

Our best-case simulations that best match the observed surface pressure of the 2017 event suggest a slow decrease in surface pressure over the next decades, at least until 2080 when the subsolar point will be above 30°N and when northern sublimation should dominate over southern condensation (Figure 21). These simulations suggest a surface pressure of ~1-1.5 Pa in the period 2020-2040 and ~0.5-1 Pa by 2060. This is large enough for Triton's atmosphere to remain global during this period. In the next decades, stellar occultation events will be key to confirming or disproving the trend suggested by our model. The next Triton occultation will be on Oct. 6, 2022, and should indicate a surface pressure close to the 2017 value.

The southern and northern volatile ice deposits

Our results suggest that most of the N_2 deposits in the southern hemisphere are permanent, and the southern cap extent should therefore not change much over seasonal timescales (Figure 22, Figure 27.B). Our simulations performed with a low global N_2 reservoir (< 200 m) tend to predict a retreat of the southern cap, but they fail to meet the observational constraints on the northern cap extent in 1989 and on the surface pressure in 2017. In particular, the southern cap should not have retreated by more than 30° latitude since 1989 from its ~15°S extent at that time, otherwise the surface pressure would have dramatically collapsed since 1989, and would be inconsistent with the 2017 occultation (see Figure best_pres.B, Figure profile.B).

We obtained a large diversity of results regarding the thickness and the nature (perennial, seasonal, or non-existent) of the northern deposits. Our best-case simulations suggest that the N_2 northern cap will extend to at least 60°N in 2040 (and possibly down to 30°N, Figure 22, Figure 27). The extent of the seasonal northern N_2 deposits should be maximal during the period 2010-2030 (Figure 22). As the subsolar latitude currently increases with time, northern latitudes that were hidden in the polar night during the Voyager 2 flyby in 1989 start to be revealed. In the following decades, the northern cap at 60°N (at least its seasonal deposits), if existing, should therefore become visible below the northern limb in ~2025 (subsolar latitude ~30°S). Future observations of Triton with HST, JWST, and the Extremely Large Telescope (ELT) would be able to provide a new and rich dataset of Triton's surface (e.g., surface composition, rotational light-curves, and albedo maps at different wavelengths), which should give strong constraints on the extent of the northern and southern caps as well as on the surface properties of the different terrains (see examples in Section 8.6.2).

In our model, N_2 ice sublimation is more intense at the south pole than at the cap edge during the current season, and will continue until 2025-2030. The south pole may thus appear darker and to be enriched in CH_4 ice in the coming years. In 2030, the south pole should start to be dominated by N_2 condensation (Figure 22), which should reverse this trend. Finally, equatorial N_2 condensation is predicted until ~2025, possibly forming bright N_2-rich frosts. After 2025, N_2 sublimation should dominate in the equatorial regions, and any equatorial seasonal N_2 frost should start to disappear.

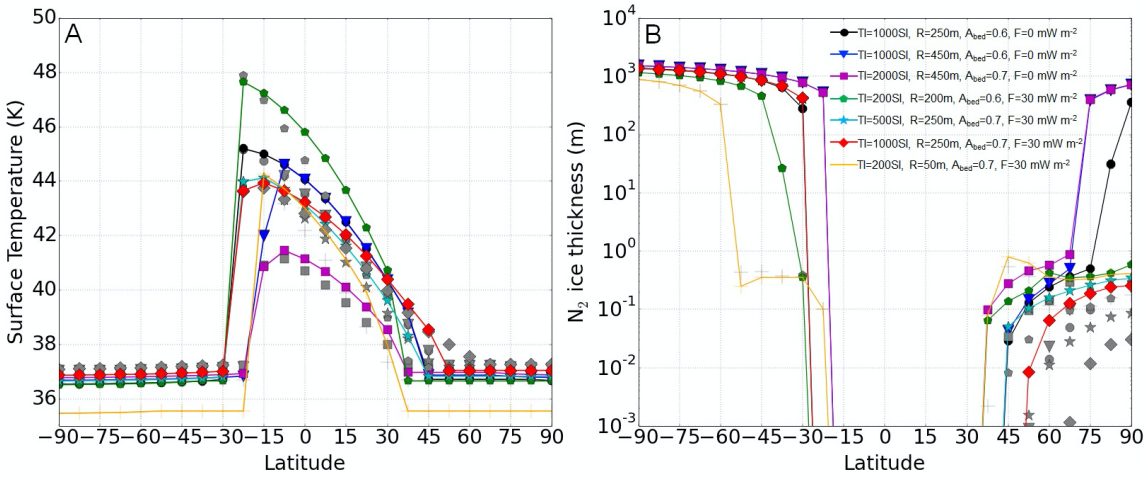

Figure 27: A. Surface temperature vs latitude for the best-case simulations in 1989 (grey symbols, as in Figure 23) and in 2030 (solid line with colored symbols). Without internal heat flux : TI=1000 SI - R=250 m - A_{bed}=0.6 (black circle), TI=1000 SI - R=450 m - A_{bed}=0.6 (blue triangle), TI=2000 SI - R=450 m - A_{bed}=0.7 (purple square). With internal heat flux: TI=200 SI - R=200 m - A_{bed}=0.6 (green polygon), TI=500 SI - R=250 m - A_{bed}=0.7 (cyan star), TI=1000 SI - R=250 m - A_{bed}=0.7 (red losange). The orange solid line shows the cases of a low reservoir and low thermal inertia simulation (TI=200 SI - R=50 m - A_{bed}=0.7 - F=30 W m^{-2}) that is consistent with observed caps extent and volatile fractional area but inconsistent with the observed pressure in 2017 (too low, see text in Section 8.3). Right. Same as A but showing the surface N_2 ice thickness.

Atmospheric abundances of CO and CH_4

According to our model and assuming a constant and uniform CO ice mixing ratio into N_2 ice of 0.04%-0.08%, the CO gas volume mixing ratio should remain relatively constant with time, with values around 0.005%-0.01% in 2040 (see Section 7.4.1). The evolution of the CH_4 atmospheric mixing ratio in the next decades remains uncertain (and very sensitive to the surface area covered by CH_4-rich deposits, see Section 7.4.2). It would tend to increase as the surface pressure decreases, in particular if new CH_4-rich deposits form in the mid-to-low latitudes at the edge of the southern cap. However, if most of the CH_4-rich deposits formed at the south pole, the CH_4 atmospheric mixing ratio would decrease in the next decades (see Figure 24) as the south pole will approach polar winter. CH_4 gas is relatively easy to observe from the ground (Lellouch et al. 2010) and could be further monitored with e.g. CRIRES+ at the VLT, and subsequently with HIRES on ELT.

8.6.2. Thermal lightcurve predictions for JWST

In this section, we model thermal lightcurves of Triton for different climate scenarios in 2022. Thermal lightcurves of Triton have never been observed before due to the inability of previous facilities (e.g., Spitzer, Herschel) to separate Triton from Neptune, given the maximum ~15" angular distance. Although ALMA can easily resolve Triton from Neptune, thermal radiation at mm wavelength is actually more sensitive to emissivity effects than to thermal inertia. JWST would be able to measure Triton's thermal lightcurve for the first time with the Mid-Infrared Instrument (MIRI, imaging mode), at 21 and 25.5 µm. We show here that future observations of Triton with JWST/MIRI would provide us with a one-of-a-kind dataset of Triton's surface that would strongly constrain the ice distribution and the surface properties (temperature, emissivity, roughness…) of

the volatile-covered vs. bedrock terrains. In addition, these observations would be able to test our model predictions and to discriminate between the climate scenarios presented in this section.

We designed and ran three simulations of the current seasonal cycle of Triton based on some of our best-case simulations (TI=1000 SI, no internal heat flux, R=200 and 650m, A=0.6 and 0.7). In these three simulations, we artificially prescribed the longitudinal asymmetry of the southern cap seen in the Voyager 2 images and inferred from the IRTF/SpeX spectra, with the bright deposits roughly extending to the equator on the sub-Neptunian hemisphere and to ~30°S in the opposite hemisphere (peak-to-peak magnitude of ±15° in latitude), and we assumed that the longitudinal variation of the spectrum has not changed since 1989. The three simulations are realistic in the sense that they are consistent with (1) a projected surface area of the volatile ice (given by NIR spectra) of ~60-70% in the period 1995-2010 (2) a southern cap extending to 15°S ±15° and no northern deposits south of 45°N in 1989 (consistent with Voyager 2 images), (3) a disk-averaged brightness temperature of 38-41 K at 45 μm in 1989 (consistent with the values retrieved from Voyager 2/IRIS), (4) relatively high Bond albedos for all terrains (0.6-0.8), and (5) a surface pressure of ~1.4 ± 0.2 Pa in 1989 and ~1.41 ± 0.4 Pa in 2017 (see Figure 29.A).

However, the three simulations differ in terms of bedrock surface albedo (A=0.6 vs. A=0.7) and of the extent of the southern cap in 2022 (large permanent cap to 7.5°S vs small cap to 37.5°S) as shown by Figure 28, which leads to three different climate scenarios (relatively cold, relatively warm, and intermediate):

(A) Warm scenario: Based on the simulation with TI=1000 SI, A=0.6, R=200m. In this scenario, we artificially set the thickness of N_2 ice to a few centimeters in the mid-to-equatorial southern regions so that these deposits become seasonal, undergo sublimation since 1989, and lead to a retreat of the southern cap from the equator in 1989 to 37.5°S in 2022. We also assume a warm bedrock surface (A=0.6) north of these deposits, which leads to a relatively warm global mean surface temperature.

(B) Intermediate scenario: Based on the simulation with TI=1000 SI, A=0.6, R=650m. This scenario assumes a large permanent N_2 southern cap (extending to 7.5°S) and a warm bedrock surface (A=0.6).

(C) Cold scenario: Based on the simulation with TI=1000 SI, A=0.7, R=650m. This scenario assumes a large permanent N_2 southern cap (extending to 7.5°S), a cold bedrock surface (A=0.7), and more extended N_2 ice in the northern hemisphere, which leads to a relatively cold global mean surface temperature.

We also performed similar simulations with no longitudinal asymmetry for the southern cap or with a longitudinal asymmetry amplified to a magnitude of ±25° latitude. The boundary of the cap edge in these cases is illustrated by the dashed lines on Figure 28.B.

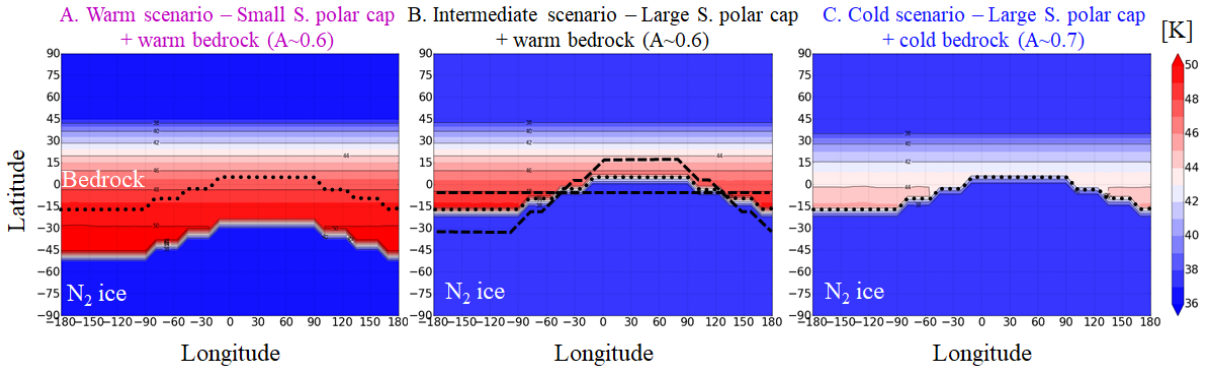

Figure 28: Modeled surface temperatures on Triton in 2022 (at local noon) for three climate scenarios with different extents for the southern cap and bedrock surface albedo. A. Warm scenario: reduced cap extent and warm bedrock (A=0.6). B. Intermediate scenario: large cap extent and warm bedrock (A=0.6). C. Cold scenario: large cap extent, cold bedrock (A=0.7), and more extended N_2 ice in the northern hemisphere. Dotted lines indicate the modeled cap extent in 1989 (the cap retreated only in scenario A). Dashed lines in panel B illustrate the cap extent in alternative simulations in which the longitudinal asymmetry disappeared or amplified to a magnitude of ±25° latitude (±15° is the reference case and roughly corresponds to the asymmetry seen by Voyager 2 in 1989).

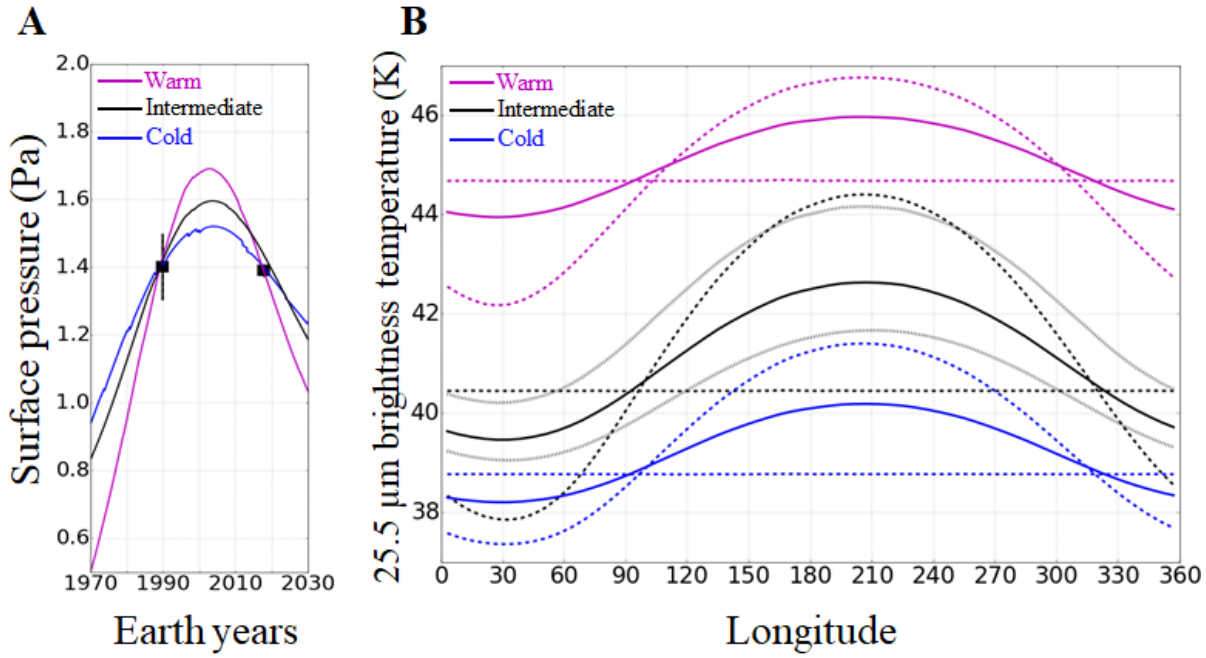

Figure 29: Triton climate model results. A. Surface pressure evolution for the 3 scenarios presented on Figure 28. Black squares indicate the Voyager 2 and 2017 occultation observations (Gurrola, 1995, Marques Oliveira et al., 2021). B. Triton 25.5 µm lightcurve for the 3 climate scenarios (with a 15° longitudinal asymmetry), with a diurnal thermal inertia of 20 SI (solid line). Dashed lines show the light curve for the alternative simulations with no or with ±25° longitudinal asymmetry. Grey lines for the intermediate scenario are for TI=10 (warmer) and TI=40 SI (colder).

Figure 28 shows that the N_2 southern cap surface temperature in 2022 is ~37 K (at solid-gas equilibrium) for the 3 cases while the equatorial volatile-free bedrock surface temperature (at local noon) is ~46 K for the warm and intermediate scenarios (A=0.6) and ~44 K for the cold scenario (A=0.7). In the case of a significant cap retreat since 1989, the volatile-free surface temperature in the mid-southern latitudes may reach ~50 K in 2022 (Figure 28.A). We note that locally, even warmer (resp. colder) patches could exist on Triton's surface due to subsurface heating activity (hot spots) or if the bedrock surface Bond albedo is significantly lower than 0.6 (resp. higher than 0.7). JWST/MIRI will be able to measure the thermal lightcurve of Triton (as seen from the Earth, i.e. of the projected disk) at 25.5 µm (and also at 21 µm) with its F2550W filter. Figure 29.B shows the modeled thermal lightcurves at 25.5 µm for the 3 climate scenarios in 2022. The thermal rotational variation on Triton is anti-correlated to the (subdued) optical light curve, with the warmest brightness temperatures being associated with the darkest regions (note that N_2-rich regions have a uniform temperature, ~37K, controlled by the surface pressure and the global albedo but not the local albedo). The thermal lightcurve variation and overall flux level therefore sensitively depend on ice distribution, mainly the presence/absence of volatile ice at the south pole, the southern cap extent, and the longitudinal variability between 45°S-20°N. Although N_2 ice deposits could cover the latitudes 90°N-30°N in 2022 and thus be seen by Earth-based telescopes in a small crescent below the terminator (56°N), they will have a weak quasi-negligible contribution to the lightcurves due to their cold surface and their small contribution (~ 3% in 2022, see Appendix A in Holler et al., 2016) to the total projected area relative to Triton's visible disk.

The thermal lightcurve is also sensitive to the thermal and energetic properties of the N_2-free terrains (thermal inertia, surface roughness, bolometric and spectral emissivity, Lellouch et al., 2011, 2016). In particular, the measured mean brightness temperature can discriminate between warm or cold scenarios (Figure 29.B). We expect generally low diurnal thermal inertias (TI=10-30 SI) as on Pluto (Lellouch et al., 2016), but this can be confirmed or disproved by thermal lightcurve measurements as the amplitude, general flux level and shape of the light curve will decrease for higher thermal inertia (see grey lines on Figure 29.B).

8.7. Uncertainties and future work

Although we explored the volatile cycles on Triton by using a large range of model parameters, other combinations may exist that also reproduce the observations. In particular, in the volatile transport simulations of this paper (Section 7), we fixed the diurnal and seasonal thermal inertia of N_2 ice to 20 SI and 800 SI respectively, and we only explored a north-south asymmetry in N_2 ice albedo (ΔA_{N2}=0.1). Other values for the thermal inertia are possible, although they should not impact the results to first order if they remain in the range of what has been suggested for Pluto (10-40 SI and 500-2000 SI, respectively). Other north-south or local asymmetries in albedo, emissivity, ice composition or internal heat flux are possible and may significantly impact the results. In particular, albedos and ice composition feedback probably have a significant role as geysers could deposit dark material (resp. bright ice grain) on top of the ice, and further darken (resp. brighten) the ice. Haze particle deposition and volatile ice sublimation could also contribute to darken the ice locally. We also consider that Triton's atmosphere remains always global, even when it hits a non-global limit in the past, with N_2 ice temperatures varying over the body. These processes are not taken into account in our model.

In addition, in our model, when both CH_4 and N_2 ices are present on the surface and CH_4 is sublimating, we assume that CH_4 is diluted in a solid solution N_2:CH_4 with a mole fraction of CH_4 in N_2 ice of 0.05% (Quirico et al. 1999, Merlin et al., 2018). We apply Raoult's law to compute the CH_4 atmospheric mixing ratio at saturation, as in Forget et al. (2017). We do not take into account possible variations and deviations from equilibrium. Tan and Kargel (2018) showed that these

volatile ices should not exhibit such ideal behavior and form solid solutions whose phases follow ternary phase equilibria (N_2, CO, CH_4). We note that sophisticated equations of state exist for the N_2-CO-CH_4 systems under Triton surface conditions (CRYOCHEM, Tan and Kargel, 2018). As these equations of state have not been coded for use in a climate model or been applied to the specific distribution of ices and temperatures seen on Triton, we have substituted the alternative of relying on Raoult's law.

Future work involving laboratory experiments, spectroscopic analyses, thermodynamic models, and global circulation models (GCMs) is strongly needed to improve the models, constrain the timescales for ice relaxation toward thermodynamic equilibrium, and explore in detail the effect of the ternary phase equilibrium on Triton and Pluto (and on other Trans-Neptunian objects). Lastly, coupling the volatile transport model with models of internal structure (including cryovolcanic activity, obliquity tides) and outgassing could also help us better understand the formation of geysers on Triton and atmospheric escape.

Conclusions

We simulated the long-term and seasonal volatile cycles of Triton, exploring a large range ofmodel parameters (thermal inertia, bedrock surface albedo, global reservoir of N_2 ice, internal heat flux) and comparing with available observations (Voyager 2 images and surface pressure, infrared surface emission measurements, albedo maps, volatile fractional area from Earth-based near-infrared spectra and surface pressure evolution from stellar occultations) to better constrain these parameters. In particular, we use an extremely high-quality occultation dataset obtained in 2017 to define our best-case simulations (Marques Oliveira et al., 2021). The following results were obtained:

1. Permanent volatile ice caps form at the poles and extend to low latitudes through glacial flow or through the formation of thinner seasonal deposits. North-South asymmetries in surface properties can favor the development of one cap over the other, as previously evidenced. A difference in topography has little impact on the North-South N_2 ice asymmetry.
2. Best-case simulations are obtained for a bedrock surface albedo of 0.6-0.7, a global reservoir of N_2 ice thicker than 200 m, and a bedrock thermal inertia larger than 500 SI or smaller but with a large internal heat flux (>30 mW m^{-2}). The large N_2 ice reservoir implies a permanent N_2 southern cap (several 100 m thick, and up to 1.5 km thick) extending to the equatorial regions with higher amounts of volatile ice at the south pole, which is not inconsistent with Voyager 2 images but does not reconcile well with observed full-disk near-infrared spectra. In particular, the lack of variability of the non-volatile ices (H_2O, CO_2, and ethane) with longitude (Holler et al., 2016) is not explained by our model.
3. Our results suggest that a small permanent polar cap should exist in the northern hemisphere, in particular if the internal heat flux remains relatively low (e.g. radiogenic, < 3 mW m^{-2}) and if the bedrock albedo is >0.7. A non-permanent northern polar cap was only obtained for simulations with high internal heat flux (30 mW m^{-2}). The northern cap will possibly extend to 30°N in the next decade, thus becoming visible by Earth-based telescopes. The southern cap should not significantly retreat in the next decades compared to what has been observed in 1989.
4. Our model predicts N_2 condensation at the northern edge of the southern cap in the period 1980-2020, which could explain the bright equatorial fringe observed by Voyager 2 in 1989. The model predicts that over the last 30 years, the southern polar

cap lost ~0.3 m of N_2 ice by sublimation, while ~0.1 m of ice deposited in the equatorial regions and mid northern latitudes.

5. Best-case surface pressures are consistent with a moderate increase of pressure during the 1990-2000 period. The model suggests that the peak of surface pressure occurred between 2000-2010 and did not exceed ~2 Pa (although albedo feedback may have increase the peak amplitude).
6. According to our model, the atmosphere of Triton never collapses. The surface pressure should slowly decrease but remain larger than 0.5 Pa by 2060. Simulations performed with low ice emissivity (ε_{N2}=0.3-0.5) show that the surface pressure could always remain larger than 0.5 Pa. Seasonal thin deposits play a significant role in the evolution of the surface pressure. The internal heat flux does not significantly impact the surface pressure curve since the ice albedo is adjusted to match the Voyager 2 pressure constraint (it impacts locally the sublimation-condensation rates but not the net mass balance of N_2).
7. In our model, CO tends to follow N_2 and condenses where N_2-rich deposits are already present. By using a CO/N_2 ice mixing ratio of 0.04%-0.08%, we obtain an atmospheric CO gas volume mixing ratio of 0.006%-0.012% during the period 2000-2020, and slightly slower values for the next decades (0.005%-0.01%).
8. Unlike for Pluto, no permanent CH_4-rich deposit form in our Triton model. We tested two scenarios with small CH_4-rich ice patches to explain the observed CH_4 atmospheric mixing ratio. Simulations with CH_4-rich ice at the cap edge (equatorial regions) produce a CH_4 partial pressure of 1-5x10^{-4} Pa that remains relatively constant during the period 1980-2030. Simulations with CH_4-rich ice at the south pole produce a strong increase in CH_4 partial pressure until 2005, followed by a decrease as the south pole exits polar day. Both “cap edge” and “south pole” scenarios could reconcile the 2.45x10^{-4} Pa partial pressure observed by Voyager 2 and the increase in the CH_4 partial pressure (factor of 4) observed from 1989 to 2009 (Lellouch et al., 2010), although the “cap edge” scenario would require a decrease in CH_4 ice albedo or increase in CH_4 ice coverage with time to lead to a significant increase in CH_4 partial pressure.
9. JWST/MIRI will be able to measure the thermal lightcurve of Triton at 25.5, 21μm, which will help in discriminating several possible climate scenarios, as well as in providing strong constraints on the thermal and energetic properties of the N_2-free terrains.

Triton remains relatively unexplored. In particular, we note that there is a strong need for more and continuing Earth-based observations (JWST, HST, VLT, Keck, ELT) of Triton’s surface and atmosphere in order to provide a temporal context and understand Triton’s seasonal evolution. Surface ice distribution has never been mapped, only inferred from disk integrated rotational curves of ice band depths, and except for very limited observations, surface temperatures have not been measured. This manifests as a substantial gap in our understanding of Triton’s climate evolution. Finally, an orbiter mission such as Neptune Odyssey or a flyby mission to Triton such as Trident would provide a rich science-breakthrough dataset with which to understand the physical and dynamical processes at play on Triton and their seasonal evolution (by comparison with existing Earth-based observations), which would be insightful to further understand this class of volatile-rich object, includingPluto, Eris, and Makemake.

Acknowledgments

T. B. was supported for this research by an appointment to the National Aeronautics and Space Administration (NASA) Postdoctoral Program at the Ames Research Center administered by Universities Space Research Association (USRA) through a contract with NASA. Part of the work leading to these results has received funding from the European Research Council under the European Community's H2020 2014-2021 ERC Grant Agreement n°669416 "Lucky Star". Under contract with NASA, part of this work was conducted at the Jet Propulsion Laboratory, California Institute of Technology.

References

- Agnor, C.B., Hamilton, D.P., 2006. Neptune's capture of its moon Triton in a binary-planet gravitational encounter. Nature 441, 192-194.
- Augé, B. and 12 colleagues, 2016. Irradiation of nitrogen-rich ices by swift heavy ions. Clues for the formation of ultracarbonaceous micrometeorites. Astronomy and Astrophysics 592. doi:10.1051/0004-6361/201527650.
- Bauer, J.M., Buratti, B.J., Li, J.-Y., Mosher, J.A., Hicks, M.D., Schmidt, B.E., Goguen, J.D., 2010. Direct detection of seasonal changes on Triton with Hubble Space Telescope. ApJL 723, L49-L52.
- Bertrand, T., & Forget, F., 2016. Observed glacier and volatile distribution on Pluto from atmosphere-topography processes. Nature, 540(7631). https://doi.org/10.1038/nature19337.
- Bertrand, T., Forget, F., Umurhan, O. M., Grundy, W. M., Schmitt, B., Protopapa, S., Zangari, A. M., White, O. L., Schenk, P. M., Singer, K. N., Stern, A., Weaver, H. A., Young, L. A., Ennico, K., & Olkin, C. B., 2018. The nitrogen cycles on Pluto over seasonal and astronomical timescales. Icarus, 309, 277–296. https://doi.org/10.1016/j.icarus.2018.03.012.
- Bertrand, T., Forget, F., Umurhan, O. M., Moore, J. M., Young, L. A., Protopapa, S., Grundy, W. M., Schmitt, B., Dhingra, R. D., Binzel, R. P., Earle, A. M., Cruikshank, D. P., Stern, S. A., Weaver, H. A., Ennico, K., & Olkin, C. B., 2019. The CH_4 cycles on Pluto over seasonal and astronomical timescales. Icarus. https://doi.org/10.1016/j.icarus.2019.02.007.
- Bertrand, T., Forget, F., White, O., Schmitt, B., Stern, S. A., Weaver, H. A., Young, L. A., Ennico, K., & Olkin, C. B., 2020a. Pluto's Beating Heart Regulates the Atmospheric Circulation: Results From High-Resolution and Multiyear Numerical Climate Simulations. Journal of Geophysical Research: Planets, 125(2), 1–24. https://doi.org/10.1029/2019JE006120.
- Bertrand, T., Forget, F., Schmitt, B., White, O. L., & Grundy, W. M., 2020b. Equatorial mountains on Pluto are covered by methane frosts resulting from a unique atmospheric process. Nature Communications, 11, 5056.
- Broadfoot, A. L., et al., 1989. Ultraviolet spectrometer observations of Neptune and Triton. Science 246, 1459-1466.
- Brown, R. H., Johnson, T. V., Goguen, J.D., Schubert, G., Ross, M. N., 1991. Triton's Global Heat Budget. Science 251, 1465–1467. doi:10.1126/science.251.5000.1465.
- Brown, R. H., Kirk, R. L., 1994. Coupling of volatile transport and internal heat flow on Triton. Journal of Geophysical Research 99, 1965–1982. doi:10.1029/93JE02618.

- Brown, R. H., Cruikshank, D. P., Veverka, J., Helfenstein, P., Eluszkiewicz, J., 1995. Surface composition and photometric properties of Triton. Neptune and Triton, 991–1030.
- Buratti, B. J., Goguen, J. D., Gibson, J., Mosher, J., 1994. Historical photometric evidence for volatile migration on Triton. Icarus 110, 303-314.
- Buratti, B. J., Bauer, J. M., Hicks, M. D., Hillier, J. K., Verbiscer, A., Hammel, H., Schmidt, B., Cobb, B., Herbert, B., Garsky, M., Ward, J., & Foust, J., 2011. Photometry of Triton 1992-2004: Surface volatile transport and discovery of a remarkable opposition surge. Icarus, 212(2), 835–846. https://doi.org/10.1016/j.icarus.2011.01.012.
- Chen, E. M. A., Nimmo, F., Glatzmaier, G. A., 2014. Tidal heating in icy satellite oceans. Icarus 229, 11–30. doi:10.1016/j.icarus.2013.10.024.
- Conrath, B. and 15 colleagues, 1989. Infrared Observations of the Neptunian System. Science 246, 1454–1459. doi:10.1126/science.246.4936.1454.
- Correia, A. C. M., 2009. Secular evolution of a satellite by tidal effect: Application to triton. Astrophysical Journal. https://doi.org/10.1088/0004-637X/704/1/L1.
- Croft, S. K., Kargel, J. S., Kirk, R. L., Moore, J. M., Schenk, P. M., Strom, R. G., 1995. The geology of Triton. In: Cruikshank (Ed.), Neptune and Triton. University of Arizona Press, Tucson, pp. 879–947.
- Cruikshank, D. P. and 7 colleagues, 1991. Tentative Detection of CO and CO2 Ices on Triton. Bulletin of the American Astronomical Society.
- Cruikshank, D. P., Roush, T. L., Owen, T. C., Geballe, T. R., de Bergh, C., Schmitt, B., Brown, R. H., Bartholomew, M. J., 1993. Ices on the surface of Triton. Science 261, 742-745.
- Cruikshank, D. P., Schmitt, B., Roush, T. L., Owen, T. C., Quirico, E., Geballe, T. R., de Bergh, C., Bartholomew, M. J., Dalle Ore, C. M., Douté, S., Meier, R., 2000. Water ice on Triton. Icarus 147, 309-316.
- DeMeo, F. E., Dumas, C., de Bergh, C., Protopapa, S., Cruikshank, D. P., Geballe, T.R., Alvarez-Candal, A., Merlin, F., Barucci, M. A., 2010. A search for ethane on Pluto and Triton. Icarus 208, 412-424.
- Douté, S., B. Schmitt, E. Quirico, T. C. Owen, D. P. Cruikshank, C. de Bergh, T. R. Geballe, and T.L. Roush, 1999. Evidence for methane segregation at the surface of Pluto. Icarus, 142, 421-444.
- Dubois, D. , Patthoff, D.A, Pappalardo, R.T., 2017. Diurnal, Nonsynchronous Rotation and Obliquity Tidal Effects on Triton Using a Viscoelastic Model: SatStressGUI. Implications for Ridge and Cycloid Formation. LPSC, LPI #1964, 2897.
- Duxbury, N. S., Brown, R. H., 1993. The Phase Composition of Triton's Polar Caps. Science 261, 748–751. doi:10.1126/science.261.5122.748.
- Earle, A. M., Binzel, R. P., Young, L. A., Stern, S. A., Ennico, K., Grundy, W., Olkin, C. B., Weaver, H. A. New Horizons Surface Composition Theme, 2018. Albedo matters: understanding runaway albedo variations on Pluto. Icarus 303, 1–9. doi: 10.1016/ j.icarus.2017.12.015.
- Elliot, J. L., et al., 1998. Global warming on Triton. Nature 393, 765-767.

- Elliot, J. L., Strobel, D. F., Zhu, X., Stansberry, J. A., Wasserman, L. H., & Franz, O. G., 2000. The thermal structure of triton's middle atmosphere. Icarus, 143(2), 425–428. https://doi.org/10.1006/icar.1999.6312.
- Elliot, J. L., Person, M. J., Qu, S., 2003. Analysis of Stellar Occultation Data. II. Inversion, with Application to Pluto and Triton.\ The Astronomical Journal 126, 1041–1079. doi:10.1086/375546
- Eluszkiewicz, J., 1991. On the microphysical state of the surface of Triton. J. Geophys. Res. 96, 19217-19229.
- Ferrari, C. & Lucas, A., 2016. Low thermal inertias of icy planetary surfaces. Evidence for amorphous ice? Astronomy and Astrophysics, 588, A133.
- Forget, F., Bertrand, T., Vangvichith, M., Leconte, J., Millour, E., & Lellouch, E., 2017. A post-New Horizons global climate model of Pluto including the N_2, CH_4 and CO cycles. Icarus, 287, 54–71. https://doi.org/10.1016/j.icarus.2016.11.038.
- Fray, N., Schmitt, B., 2009. Sublimation of ices of astrophysical interest: A bibliographic review. P&SS 57, 2053-2080.
- Gaeman, J., Hier-Majumder, S., Roberts, J. H., 2012. Sustainability of a subsurface ocean within Triton's interior. Icarus 220, 339–347. doi:10.1016/j.icarus.2012.05.006.
- Grundy, W. M., Fink, U., 1991. A new spectrum of Triton near the time of the Voyager encounter. Icarus 93, 379–385. doi:10.1016/0019-1035(91)90220-N.
- Grundy, W. M., & Young, L. A., 2004. Near-infrared spectral monitoring of Triton with IRTF/SpeX I: Establishing a baseline for rotational variability. Icarus, 172(2), 455–465. https://doi.org/10.1016/j.icarus.2004.07.013
- Grundy, W. M., Young, L. A., Stansberry, J. A., Buie, M. W., Olkin, C. B., Young, E. F., 2010. Near-infrared spectral monitoring of Triton with IRTF/SpeX II: Spatial distribution and evolution of ices. Icarus 205, 594-604.
- Grundy, W. M., Binzel, R. P., Buratti, B. J., Cook, J. C., Cruikshank, D. P., Dalle Ore, C. M., Earle, A. M., Ennico, K., Howett, C. J. A., Lunsford, A. W., Olkin, C. B., Parker, A. H., Philippe, S., Protopapa, S., Quirico, E., Reuter, D. C., Schmitt, B., Singer, K. N., Verbiscer, A. J., … Young, L. A., 2016. Surface compositions across Pluto and Charon. Science, 351(6279). https://doi.org/10.1126/science.aad9189.
- Gurrola, E. M., 1995. Interpretation of Radar Data from the Icy Galilean Satellites and Triton. Ph.D. thesis, Stanford University.
- Gurwell, M., Lellouch, E., Butler, B., Moreno, R., Moullet, A., Strobel, D., 2019. The Atmosphere of Triton Observed With ALMA. EPSC-DPS Joint Meeting 2019.
- Hansen, C.J., Paige, D.A., 1992. A thermal model for the seasonal nitrogen cycle on Triton. Icarus 99, 273-288.
- Herbert, F., Sandel, B.R., 1991. CH_4 and haze in Triton's lower atmosphere. JGR Supp. 96, 19241-19252.
- Hillier, J., Helfenstein, P., Verbiscer, A., & Veverka, J., 1991. Voyager photometry of Triton: Haze and surface photometric properties. Journal of Geophysical Research, 96(S01), 19203. https://doi.org/10.1029/91ja01736.

- Hillier, J., Veverka, J., Helfenstein, P., Lee, P., 1994. Photometric Diversity of Terrains on Triton. Icarus 109, 296–312. doi:10.1006/icar.1994.1095.
- Holler, B. J., Young, L. A., Grundy, W. M., & Olkin, C. B., 2016. On the surface composition of Triton's southern latitudes. Icarus, 267, 255–266. https://doi.org/10.1016/j.icarus.2015.12.027.
- Howard, A. D., Moore, J. M., White, O. L., Umurhan, O. M., Schenk, P. M., Grundy, W. M., Schmitt, B., Philippe, S., McKinnon, W. B., Spencer, J. R., Beyer, R. A., Stern, S. A., Ennico, K., Olkin, C. B., Weaver, H. A., & Young, L. A., 2017. Pluto: Pits and mantles on uplands north and east of Sputnik Planitia. Icarus, 293, 218–230. https://doi.org/10.1016/j.icarus.2017.02.027.
- Hussmann, H., Sohl, F., Spohn, T., 2006. Subsurface oceans and deep interiors of medium-sized outer planet satellites and large trans-neptunian objects. Icarus 185, 258–273. doi:10.1016/j.icarus.2006.06.005.
- Krasnopolsky, V. A., Cruikshank, D. P., 1999. Photochemistry of Pluto's atmosphere and ionosphere near perihelion. J. Geophys. Res. 104, 21979–21996. http://dx.doi.org/10.1029/1999JE001038.
- Johnson, P. E. and 8 colleagues, 2021. Modeling Pluto's minimum pressure: Implications for haze production. Icarus 356. doi:10.1016/j.icarus.2020.114070.
- Johnson, R.E., Oza, A. Young, L.A., Volkov, A. N., Schmidt, C. , 2015. Volatile Loss and Classification of Kuiper Belt Objects. ApJ, 809, 1, 43. doi:10.1088/0004-637X/809/1/43
- Jovanovic, L., Gautier, T., Vuitton, V., Wolters, C., Bourgalais, J., Buch, A., Orthous-Daunay, F., Vettier, L., Flandinet, L., Carrasco, N., 2020. Chemical composition of Pluto aerosol analogues. Icarus, 346, 113774, 10.1016/j.icarus.2020.113774.
- Laskar J, Robutel P, 1993. The chaotic obliquity of the planets. Nature 361:608–612.
- Lee, P., Helfenstein, P., Veverka, J., & McCarthy, D., 1992. Anomalous-scattering region on Triton. Icarus, 99(1), 82–97. https://doi.org/10.1016/0019-1035(92)90173-5.
- Lellouch, E., de Bergh, C., Sicardy, B., Ferron, S., Käufl, H.-U., 2010. Detection of CO in Triton's atmosphere and the nature of surface-atmosphere interactions. A&A 512, L8-L13.
- Lellouch, E., de Bergh, C., Sicardy, B., Käufl, H. U., Smette, A., 2011. High resolution spectroscopy of Pluto's atmosphere: detection of the 2.3 μm CH_4 bands and evidence for carbon monoxide. Astron. Astrophys. 530, L4. http://dx.doi.org/10.1051/0004-6361/201116954.
- Lellouch, E. and 11 colleagues, 2016. The long-wavelength thermal emission of the Pluto-Charon system from Herschel observations. Evidence for emissivity effects. Astronomy and Astrophysics 588. doi:10.1051/0004-6361/201527675.
- Lellouch, E., Gurwell, M., Butler, B., Fouchet, T., Lavvas, P., Strobel, D. F., Sicardy, B., Moullet, A., Moreno, R., Bockelée-Morvan, D., Biver, N., Young, L., Lis, D., Stansberry, J., Stern, A., Weaver, H., Young, E., Zhu, X., & Boissier, J., 2017. Detection of CO and HCN in Pluto's atmosphere with ALMA. Icarus, 286, 289–307. https://doi.org/10.1016/j.icarus.2016.10.013.
- Lewis, B. L. and 12 colleagues, 2021. Distribution and energy balance of Pluto's nitrogen ice, as seen by New Horizons in 2015. Icarus 356. doi:10.1016/j.icarus.2020.113633.

- Li, D., Johansen, A., Mustill, A. J., Davies, M. B., Christou, A. A., 2020. Capture of satellites during planetary encounters. A case study of the Neptunian moons Triton and Nereid. Astronomy and Astrophysics 638. doi:10.1051/0004-6361/201936672.
- Lunine, J, E., and Stevenson, D. J., 1985. Physical state of volatiles on the surface of Triton. Nature 317, 238-240.
- Mangold, N., 2011. Ice sublimation as a geomorphic process: A planetary perspective. Geomorphology 126, 1–17. doi:10.1016/j.geomorph.2010.11.009.
- Marques Oliveira, J. et al. 2021. Structure and evolution of Triton's atmosphere from the 5 October 2017 stellar occultation and previous observations. Submitted to A&A.
- Martin-Herrero, A., Romeo, I., & Ruiz, J., 2018. Heat flow in Triton: Implications for heat sources powering recent geologic activity. Planetary and Space Science, 160, 19–25. https://doi.org/10.1016/j.pss.2018.03.010.
- Materese, C. K., Cruikshank, D. P., Sandford, S. A., Imanaka, H., Nuevo, M. 2015. Ice Chemistry on Outer Solar System Bodies: Electron Radiolysis of N_2-, CH_4-, and CO-Containing Ices. The Astrophysical Journal 812. doi:10.1088/0004-637X/812/2/150.
- McCord, T. B., 1966. Dynamical evolution of the Neptunian system. Astron. J. 71, 585. http://dx.doi.org/10.1086/109967.
- McEwen, A. S., 1990. Global color and albedo variations on Triton. Geophys Res Lett 17, 1765–1768. http://dx.doi.org/10.1029/GL017i010p01765.
- McKinnon, W. B., 1984. On the origin of Triton and Pluto. Nature 311, 355–358. http:// dx.doi.org/10.1038/311355a0.
- McKinnon, W. B., Lunine, J. I., Banfield, D., 1995. Origin and evolution of Triton. In: Cruikshank (Ed.), Neptune and Triton. University of Arizona Press, Tucson, pp. 807–877.
- McKinnon W. B., Nimmo F., Wong T., et al., 2016. Convection in a volatile nitrogen-ice-rich layer drives Pluto's geological vigour. Nature, 534, 82-85.
- Merlin, F., 2015. New constraints on the surface of Pluto. Astron. Astrophys. 582, A39. http://dx.doi.org/10.1051/0004-6361/201526721.
- Merlin, F., E. Lellouch, E. Quirico, and B. Schmitt, 2018. Triton's surface ices: Distribution, temperature and mixing state from VLT/SINFONI observations. Icarus 314, 274-293.
- Meza, E., Sicardy, B., Assafin, M., Ortiz, J. L., Bertrand, T., Lellouch, E., Desmars, J., Forget, F., Bérard, D., Doressoundiram, A., Lecacheux, J., Oliveira, J. M., Roques, F., Widemann, T., Colas, F., Vachier, F., Renner, S., Leiva, R., Braga-Ribas, F., Benedetti-Rossi, G., Camargo, J. I. B., Dias-Oliveira, A., Morgado, B., Gomes-Júnior, A. R., Vieira-Martins, R., Behrend, R., Tirado, A. C., Duffard, R., Morales, N., Santos-Sanz, P., Jelínek, M., Cunniffe, R., Querel, R., Harnisch, M., Jansen, R., Pennell, A., Todd, S., Ivanov, V. D., Opitom, C., Gillon, M., Jehin, E., Manfroid, J., Pollock, J., Reichart, D. E., Haislip, J. B., Ivarsen, K. M., LaCluyze, A. P., Maury, A., Gil-Hutton, R., Dhillon, V., Littlefair, S., Marsh, T., Veillet, C., Bath, K.-L., Beisker, W., Bode, H.-J., Kretlow, M., Herald, D., Gault, D., Kerr, S., Pavlov, H., Faragó, O., Klös, O., Frappa, E., Lavayssière, M., Cole, A. A., Giles, A. B., Greenhill, J. G., Hill, K. M., Buie, M. W., Olkin, C. B., Young, E. F., Young, L. A., Wasserman, L. H., Devogèle, M., French, R. G., Bianco, F. B., Marchis, F., Brosch, N., Kaspi, S., Polishook, D., Manulis, I., Ait Moulay Larbi, M., Benkhaldoun, Z., Daassou, A., El Azhari, Y., Moulane, Y., Broughton, J., Milner, J., Dobosz, T., Bolt, G., Lade, B., Gilmore, A., Kilmartin, P., Allen, W. H., Graham, P. B., Loader, B., McKay, G., Talbot, J., Parker, S., Abe,

L., Bendjoya, P., Rivet, J.-P., Vernet, D., Di Fabrizio, L., Lorenzi, V., Magazzú, A., Molinari, E., Gazeas, K., Tzouganatos, L., Carbognani, A., Bonnoli, G., Marchini, A., Leto, G., Sanchez, R. Z., Mancini, L., Kattentidt, B., Dohrmann, M., Guhl, K., Rothe, W., Walzel, K., Wortmann, G., Eberle, A., Hampf, D., Ohlert, J., Krannich, G., Murawsky, G., Gährken, B., Gloistein, D., Alonso, S., Román, A., Communal, J.-E., Jabet, F., deVisscher, S., Sérot, J., Janik, T., Moravec, Z., Machado, P., Selva, A., Perelló, C., Rovira, J., Conti, M., Papini, R., Salvaggio, F., Noschese, A., Tsamis, V., Tigani, K., Barroy, P., Irzyk, M., Neel, D., Godard, J. P., Lanoiselée, D., Sogorb, P., Vérilhac, D., Bretton, M., Signoret, F., Ciabattari, F., Naves, R., Boutet, M., De Queiroz, J., Lindner, P., Lindner, K., Enskonatus, P., Dangl, G., Tordai, T., Eichler, H., Hattenbach, J., Peterson, C., Molnar, L. A., & Howell, R. R., 2019. Lower atmosphere and pressure evolution on Pluto from ground-based stellar occultations, 1988-2016. Astronomy and Astrophysics, 625, A42.

- Moore, J. M., Spencer, J. R., 1990. Koyaanismuuyaw - The hypothesis of a perenially dichotomous Triton. GRL 17, 1757-1760.
- Moore, M. H., Hudson, R. L., 2003. Infrared study of ion-irradiated N_2-dominated ices relevant to Triton and Pluto: formation of HCN and HNC. Icarus 161, 486–500. http://dx.doi.org/10.1016/S0019-1035(02)00037-4.
- Nimmo, F., & Spencer, J. R., 2015. Powering Triton's recent geological activity by obliquity tides: Implications for Pluto geology. Icarus, 246(C), 2–10. https://doi.org/10.1016/j.icarus.2014.01.044.
- Nogueira, E., Brasser, R., & Gomes, R., 2011. Reassessing the origin of Triton. Icarus. https://doi.org/10.1016/j.icarus.2011.05.003.
- Olkin, C. B., Elliot, J. L., Hammel, H. B., Cooray, A. R., McDonald, S. W., Foust, J. A., Bosh, A. S., Buie, M. W., Millis, R. L., Wasserman, L. H., Dunham, E. W., Young, L. A., Howell, R. R., Hubbard, W. B., Hill, R., Marcialis, R. L., McDonald, J. S., Rank, D. M., Holbrook, J. C., & Reitsema, H. J., 1997. The thermal structure of Triton's atmosphere: Results from the 1993 and 1995 occultations. Icarus, 129(1), 178–201. https://doi.org/10.1006/icar.1997.5757.
- Paige, D. A., 1985. The Annual Heat Balance of the Martian Polar Caps from Viking Observations. Ph.D. thesis, Calif. Inst. of Technol., Pasadena.
- Pankine, A. A., Tamppari, L. K., Smith, M. D., 2009. Water vapor variability in the north polar region of Mars from Viking MAWD and MGS TES datasets. Icarus 204, 87–102. doi:10.1016/j.icarus.2009.06.009.
- Pankine, A. A., Tamppari, L. K., Smith, M. D., 2010. MGS TES observations of the water vapor above the seasonal and perennial ice caps during northern spring and summer. Icarus 210, 58–71. doi:10.1016/j.icarus.2010.06.043.
- Prokhvatilov, A.I., Yantsevich, L.D., 1983. X-ray investigations of the equilibrium phase diagram of CH–N, solid mixtures. Sov. J. Low Temp. Phys. 9, 94–97.
- Protopapa, S., Grundy, W. M., Reuter, D. C., Hamilton, D. P., Dalle Ore, C. M., Cook, J. C., Cruikshank, D. P., Schmitt, B., Philippe, S., Quirico, E., Binzel, R. P., Earle, A. M., Ennico, K., Howett, C. J. A., Lunsford, A. W., Olkin, C. B., Parker, A., Singer, K. N., Stern, A., Young, L. A., 2017. Pluto's global surface composition through pixel-by-pixel Hapke modeling of New Horizons Ralph/LEISA data. Icarus, 287, 218–228. https://doi.org/10.1016/j.icarus.2016.11.028.

- Quirico, E., S. Douté, B. Schmitt, C. de Bergh, D.P. Cruikshank, T.C. Owen, T.R. Geballe, and T.L. Roush, 1999. Composition, physical state and distribution of ices at the surface of Triton. Icarus, 139, 159-178.
- Ruiz, J., 2003. Heat flow and depth to a possible internal ocean on Triton. Icarus 166, 436–439.
- Schenk, P. M., & Zahnle, K., 2007. On the negligible surface age of Triton. Icarus. https://doi.org/10.1016/j.icarus.2007.07.004.
- Schenk P. M., Beyer R. A., McKinnon W. B., et al., 2018. Basins, fractures and volcanoes: Global cartography and topography of Pluto from New Horizons. Icarus, 314, 400-433.
- Schenk, P. M., et al., 2021. Triton : Topography and Geology of a (Probable) Ocean World with Comparison to Pluto and Charon. Submitted.
- Schmitt, B., Philippe, S., Grundy, W. M., Reuter, D. C., Côte, R., Quirico, E., Protopapa, S., Young, L. A., Binzel, R. P., Cook, J. C., Cruikshank, D. P., Dalle Ore, C. M., Earle, A. M., Ennico, K., Howett, C. J. A., Jennings, D. E., Linscott, I. R., Lunsford, A. W., Olkin, C. B., … Weaver, H. A., 2017. Physical state and distribution of materials at the surface of Pluto from New Horizons LEISA imaging spectrometer. Icarus, 287, 229–260. https://doi.org/10.1016/j.icarus.2016.12.025.
- Smith, B. A., Soderblom, L. A., Banfield, D., Barnet, C., Basilevsky, A. T., Beebe, R. F., Bollinger, K., Boyce, J. M., Brahic, A., Briggs, G. A., Brown, R. H., Chyba, C., Collins, S. A., Colvin, T., Cook II, A. F., Crisp, D., Croft, S. K., Cruikshank, D., Cuzzi, J. N., Danielson, G. E., Davies, M. E., De Jong, E., Dones, L., Godfrey, D., Goguen, J., Grenier, I., Haemmerle, V. R., Hammel, H., Hansen, C. J., Helfenstein, C. P., Howell, C., Hunt, G. E., Ingersoll, A. P., Johnson, T. V., Kargel, J., Kirk, R., Kuehn, D.I., Limaye, S., Masursky, H., McEwen, A., Morrison, D., Owen, T., Owen, W., Pollack, J. B., Porco, C. C., Rages, K., Rogers, P., Rudy,D., Sagan, C.,Schwartz, J., Shoemaker, E. M., Showalter, M., Sicardy,B., Simonelli, D., Spencer, J.,Sromovsky, L. A., Stoker,C., Strom, R. G., Suomi,V.E., Synott, S. P., Terrile, R. J., Thomas, P., Thompson, W. R., Verbiscer, A., Veverka, J., 1989. Voyager 2 at Neptune – imaging science results. Science 246, 1422–1449.
- Soderblom, L. A., Kieffer, S. W., Becker, T. L., Brown, R. H., Cook II, A. F., Hansen, C. J., Johnson, T. V., Kirk, R. L., Shoemaker, E. M., 1990. Triton's geyser-like plumes: discovery and basic characterization. Science 250, 410–415.
- Spencer, J. R., 1990. NITROGEN FROST MIGRATION ON TRITON: A historical model. Geophysical Research Letters 17, 1769–1772. doi:10.1029/GL017i010p01769.
- Spencer, J. R., & Moore, J. M., 1992. The influence of thermal inertia on temperatures and frost stability on Triton. Icarus, 99(2), 261–272. https://doi.org/10.1016/0019-1035(92)90145-W.
- Stansberry, J. A., Lunine, J. I., Porco, C. C., McEwen, A. S., 1990. Zonally averaged thermal balance and stability models for nitrogen polar caps on Triton. Geophysical Research Letters 17, 1773–1776. doi:10.1029/GL017i010p01773.
- Stansberry, J. A., Yelle, R. V., Lunine, J. I., McEwen, A. S., 1992. Triton's surface-atmosphere energy balance. Icarus 99, 242–260. doi:10.1016/0019-1035(92)90144-V.
- Stansberry, J. A., Pisano, D. J., Yelle, R. V., 1996a. The emissivity of volatile ices on Triton and Pluto. Planetary and Space Science 44, 945–955. doi:10.1016/0032-0633(96)00001-3.

- Stansberry, J. A., Spencer, J. R., Schmitt, B., Benchkoura, A.-I., Yelle, R. V., & Lunine, J. I., 1996b. A model for the overabundance of methane in the atmospheres of Pluto and Triton. Planetary and Space Science, 44, 1051.
- Stern, S. A., McKinnon, W. B., 2000. Triton's Surface Age and Impactor Population Revisited in Light of Kuiper Belt Fluxes: Evidence for Small Kuiper Belt Objects and Recent Geological Activity. The Astronomical Journal 119, 945–952. doi:10.1086/301207.
- Stern, S. A., Bagenal, F., Ennico, K., Gladstone, G. R., Grundy, W. M., Mckinnon, W. B., Moore, J. M., Olkin, C. B., Spencer, J. R., Weaver, H. A., Young, L. A., Andert, T., Andrews, J., Banks, M., Bauer, B., Bauman, J., Barnouin, O. S., Bedini, P., Beisser, K., Versteeg, M. H., 2015. The Pluto system: Initial results from its exploration by New Horizons.
- Stone, E. C., Miner, E. D., 1989. The Voyager 2 encounter with the Neptunian system. Science 246, 1417-1421.
- Strobel, D. F., Summers, M. E., 1995. Triton's upper atmosphere and ionosphere. Neptune and Triton, 1107–1148.
- Tan, S. P., & Kargel, J. S., 2018. Solid-phase equilibria on Pluto's surface. Monthly Notices of the Royal Astronomical Society, 474(3), 4254–4263. https://doi.org/10.1093/mnras/stx3036.
- Tegler, S. C. and 13 colleagues, 2019. A New Two-molecule Combination Band as a Diagnostic of Carbon Monoxide Diluted in Nitrogen Ice on Triton. The Astronomical Journal 158. doi:10.3847/1538-3881/ab199f.
- Trafton, L., 1984. Large seasonal variations in Triton's atmosphere. Icarus 58, 312-324.
- Trafton, L. M., D. L. Matson, and J. A. Stansberry, 1998. Surface/atmosphere Interactions and Volatile Transport (triton, Pluto and Io). Solar System Ices 227, 773.
- Trafton, L. M., Stansberry, J. A., 2015. On the Departure from Isothermality of Pluto's Volatile Ice due to Local Insolation and Topography. AAS/Division for Planetary Sciences Meeting Abstracts #47.
- Trafton, L. M., 2015. On the state of methane and nitrogen ice on Pluto and Triton: Implications of the binary phase diagram. Icarus, 246(C), 197–205. https://doi.org/10.1016/j.icarus.2014.05.022.
- Tryka, K. A., Brown, R. H., Anicich, V., Cruikshank, D. P., Owen, T. C., 1993. Spectroscopic determination of the phase composition and temperature of nitrogen ice on Triton. Science 261, 751-754.
- Tryka, K. A., Brown, R. H., Chruikshank, D. P., Owen, T. C., Geballe, T. R., de Bergh, C., 1994. Temperature of nitrogen ice on Pluto and its implications for flux measurements. Icarus 112, 513–527. http://dx.doi.org/10.1006/icar.1994.1202.
- Tyler, G. L., Sweetnam, D. N., Anderson, J. D., Borutzki, S. E., Campbell, J. K., Kursinski, E. R., Levy, G. S., Lindal, G. F., Lyons, J. R., Wood, G. E., 1989. Voyager radio science observations of Neptune and Triton. Science 246, 1466-1473.
- Umurhan, O. M., Howard, A. D., Moore, J. M., Earle, A. M., White, O. L., Schenk, P. M., Binzel, R. P., Stern, S. A., Beyer, R. A., Nimmo, F., McKinnon, W. B., Ennico, K., Olkin, C. B., Weaver, H. A., & Young, L. A., 2017. Modeling glacial flow on and onto Pluto's Sputnik Planitia. Icarus, 287, 301–319. https://doi.org/10.1016/j.icarus.2017.01.017.

- Vetter, M., Jodl, H.-J., Brodyanski, A., 2007. From optical spectra to phase diagrams–the binary mixture N_2-CO. Low. Temp. Phys. 33, 1052-1060.
- White, O. L., Moore, J. M., McKinnon, W. B., Spencer, J. R., Howard, A. D., Schenk, P. M., Beyer, R. A., Nimmo, F., Singer, K. N., Umurhan, O. M., Stern, S. A., Ennico, K., Olkin, C. B., Weaver, H. A., Young, L. A., Cheng, A. F., Bertrand, T., Binzel, R. P., Earle, A. M., … Schmitt, B., 2017. Geological mapping of Sputnik Planitia on Pluto. Icarus, 287, 261–286. https://doi.org/10.1016/j.icarus.2017.01.011.
- Wood, S. E., and Paige, D. A., 1992. Modeling the martian seasonal CO2 cycle: Fitting the Viking lander pressure curves. Icarus 99, 1–14.
- Young, L. A., Bertrand, T., Trafton, L. M., Forget, F., Earle, A. M. and Sicardy, B., 2021. Pluto's Volatile and Climate Cycles on Short and Long Timescales. In *The Pluto System After New Horizons (S. A. Stern, J. M. Moore, W. M. Grundy, L. A. Young, and R. P. Binzel, eds)*, p.321-361. Univ. of Arizona, Tucson.
- Young, L. A., 2017. Volatile transport on inhomogeneous surfaces: II. Numerical calculations (VT3D). Icarus 284, 443–476. doi:10.1016/j.icarus.2016.07.021.
- Zent, A., et al., 1989, Grain size metamorphism in polar nitrogen ice on Triton. Geophys. Res. Lett. 16, 965-968.

Appendix - Calculation of the temporal variations of Triton's subsolar latitude

In our volatile transport model, the calculation of Triton's subsolar latitude is performed by using a trigonometric equation corresponding to a fit of a solution obtained by a dynamic model of Triton's motion.

The solution of the dynamic model was obtained over the period 06/09/-807 to 01/01/2100 using the *ephemph* application of the EPROC project (Berthier, 1998, Forget, 2000). The method, described by Le Guyader, 1993, includes the disturbances caused by Neptune's flatness at the poles (Peters, 1981), by the Sun and by the 8 other planets of the solar system, with their revised coordinates (Davies, 1996).

The trigonometric fit of this solution is based on the trigonometric equation proposed by Harris (1984) and Trafton (1984), from a suggestion by Dobrovolskis (1980). Changes in subsolar latitude λ are expressed as a sinus function, resulting from the superposition of 3 harmonics of different amplitudes and frequencies, as :

$$\sin(\lambda(t)) = A\cos(\alpha_0 - \alpha_1\mu) + B\sin(\alpha_0 - \beta_0 + (\beta_1 - \alpha_1)\mu) + C\sin(\alpha_0 + \beta_0 - (\alpha_1 + \beta_1)\mu)$$

With:

$$\mu = \frac{365.25\ t\ L_s}{D}$$

Where t is the time in Earth year from year 0 (i.e., t = 2000 corresponds to year 2000 A.D), L_s is the length of one Triton day in seconds (507773 s) and L_d is the length of one Triton day in Earth days (5.877 days).

Since the work of Harris (1984) and Trafton (1984), the angles and coefficients have been revised (Berthier, 1998, Forget, 2000) and the values are:

A = 0.429870

B = 0.370543

C = 0.0225091

D=31557595

α_0 = 241.52577°

α_1 = 0.038142 rad/year

β_0 = -100.79473°

β_1 = 0.009131 rad/year

The first harmonic evolves at the frequency α_1= 0.0381 rad/year, which corresponds to the sideral period of Neptune (165 Earth years). The second harmonic has a frequency equal to (β_1-α_1) with β_1 the frequency corresponding to the precession of Triton's orbit around Neptune's pole (period

= 650 Earth years). The period of this harmonic is ~221 Earth years. The third harmonic has a low amplitude compared to the others, and its frequency is equal to ($\alpha_1+\beta_1$), which corresponds to a period of 131.5 Earth years.

The error made on the subsolar latitude by using the trigonometric equation (compared to the dynamical solution) is always smaller than 0.5°, which is largely sufficient for the purpose of this paper (the latitudinal resolution of our model is 7.5°). In fact, the errors are periodic and their analysis in frequency (Laskar, 1999) show that the frequency peaks at 82.2, 93.4 and 683.4 years with an amplitude of the order of 0.1°, while other peaks have an amplitude at least 10 times smaller.

In conclusion, the trigonometric equation provides an excellent approximation of Triton's subsolar latitude that can be extrapolated in time. In our model, we compute the past climates of Triton by using these equations with t typically ranging from t=-9x10^6 (9 million years ago) to t=2100 (end of the current century). Note that over time, Triton's inclination is slowly increasing (getting closer to perfectly retrograde) and its precession period is slowly getting shorter as its orbit shrinks, but these are *very* long-term effects that are not significant over the timescale used in this paper (~10 Myrs). The obliquity of Neptune does not change significantly over this period either (it is suggested to be primordial, Laskar and Robutel, 1993).

- Berthier, J., 1998. Définitions relatives aux éphémérides pour l' observation physique des corps du système solaire. Notes scientifiques et techniques du Bureau des longitudes, S061.
- Davies, M.E., Abalakin, V.K., Bursa, M., Lieske, J.H., Morando, B., Morison, D., Seidelmann, P.K., Sinclair, A.T., Yallop, B., Tjuflin, Y.S., 1996. Report of the TAU/IAG/COSPAR working group on cartographic coordinates and rotational elements of the planets and satellites: 1994. Celes. Mech 63, 127-148.
- Forget, F., Decamp, N., Hourdin, F., 1999. A 3D general circulation model of Triton's atmosphere and surface. In "Piuto and Triton, comparisons and evolution over time", Lowell Observatory's fourth annual worshop, Flagstaff, Arizona.
- Laskar, J., 1999. Introduction to frequency map analysis. NATO ASI Hamiltonian Systems with Three or More Degrees of Freedom. C. Simd Ed. Kluwer, Dordrecht. 134-150.
- Le Guyader, C., 1993. Solution of the N-body problem expanded into Taylor series of high orders. Applications to the solar system over large time range. Astron. Astrophys. 272, 687-694.
- Harris, A. W., 1984. Physical characteristics of Neptune and Triton inferred from the orbital motion of Triton. Paper presented to I.A.U Colloquium 77, July 5-9, 1983 at Cornell Univ.
- Peters, C. F., 1981. Numerical integration of the satellites of the outer planets. Astron. Astrophys. 104, 37-41.

Bibliography

Abe, F., Airey, C., Barnard, E., Baudry, J., Botzler, C., Douchin, D., Freeman, M., Larsen, P., Niemiec, A., Perrott, Y., Philpott, L., Rattenbury, N., and Yock, P. (2013). Extending the planetary mass function to Earth mass by microlensing at moderately high magnification. *Monthly Notices of the Royal Astronomical Society*, 431:2975–2985.

Assafin, M., Camargo, J. I. B., Vieira Martins, R., Andrei, A. H., Sicardy, B., Young, L., da Silva Neto, D. N., and Braga-Ribas, F. (2010). Precise predictions of stellar occultations by Pluto, Charon, Nix, and Hydra for 2008-2015. *Astronomy & Astrophysics*, 515:A32.

Assafin, M., Camargo, J. I. B., Vieira Martins, R., Braga-Ribas, F., Sicardy, B., Andrei, A. H., and da Silva Neto, D. N. (2012). Candidate stellar occultations by large trans-Neptunian objects up to 2015. *Astronomy & Astrophysics*, 541:A142.

Assafin, M., Vieira Martins, R., Camargo, J. I. B., Andrei, A. H., Da Silva Neto, D. N., and Braga-Ribas, F. (2011). PRAIA - Platform for Reduction of Astronomical Images Automatically. In *Gaia follow-up network for the solar system objects : Gaia FUN-SSO workshop proceedings*, pages 85–88.

Baum, W. A. and Code, A. D. (1953). A photometric observation of the occultation of σ ARIETIS by Jupiter. *The Astronomical Journal*, 58:108–112.

Bertrand, T. and Forget, F. (2016). Observed glacier and volatile distribution on Pluto from atmosphere-topography processes. *Nature*, 540:86–89.

Bertrand, T., Lellouch, E., Holler, B. J., Young, L. A., Schmitt, B., Marques Oliveira, J., Sicardy, B., Forget, F., Grundy, W. M., Merlin, F., Vangvichith,

M., Millour, E., Schenk, P. M., Hansen, C. J., White, O. L., Moore, J. M., Stansberry, J. A., Oza, A. V., Dubois, D., Quirico, E., and Cruikshank, D. P. (2022). Volatile transport modeling on Triton with new observational constraints. *Icarus*, 373:114764.

Bouchez, A. H. (2004). *Seasonal trends in Titan's atmosphere: Haze, wind, and clouds*. PhD thesis, California Institute of Technology.

Braga-Ribas, F., Sicardy, B., Ortiz, J. L., Snodgrass, C., Roques, F., Vieira-Martins, R., Camargo, J. I. B., Assafin, M., Duffard, R., Jehin, E., Pollock, J., Leiva, R., Emilio, M., Machado, D. I., Colazo, C., Lellouch, E., Skottfelt, J., Gillon, M., Ligier, N., Maquet, L., Benedetti-Rossi, G., Gomes, A. R., Kervella, P., Monteiro, H., Sfair, R., El Moutamid, M., Tancredi, G., Spagnotto, J., Maury, A., Morales, N., Gil-Hutton, R., Roland, S., Ceretta, A., Gu, S. H., Wang, X. B., Harpsøe, K., Rabus, M., Manfroid, J., Opitom, C., Vanzi, L., Mehret, L., Lorenzini, L., Schneiter, E. M., Melia, R., Lecacheux, J., Colas, F., Vachier, F., Widemann, T., Almenares, L., Sandness, R. G., Char, F., Perez, V., Lemos, P., Martinez, N., Jørgensen, U. G., Dominik, M., Roig, F., Reichart, D. E., Lacluyze, A. P., Haislip, J. B., Ivarsen, K. M., Moore, J. P., Frank, N. R., and Lambas, D. G. (2014). A ring system detected around the Centaur (10199) Chariklo. *Nature*, 508(7494):72–75.

Broadfoot, A. L., Atreya, S. K., Bertaux, J. L., Blamont, J. E., Dessler, A. J., Donahue, T. M., Forrester, W. T., Hall, D. T., Herbert, F., Holberg, J. B., Hunten, D. M., Krasnopolsky, V. A., Linick, S., Lunine, J. I., Mcconnell, J. C., Moos, H. W., Sandel, B. R., Schneider, N. M., Shemansky, D. E., Smith, G. R., Strobel, D. F., and Yelle, R. V. (1989). Ultraviolet Spectrometer Observations of Neptune and Triton. *Science*, 246(4936):1459–1466.

Buratti, B. J., Bauer, J. M., Hicks, M. D., Hillier, J. K., Verbiscer, A., Hammel, H., Schmidt, B., Cobb, B., Herbert, B., Garsky, M., Ward, J., and Foust, J. (2011). Photometry of Triton 1992-2004: Surface volatile transport and discovery of a remarkable opposition surge. *Icarus*, 212(2):835–846.

Burns, J. A. (1986). *Some background about satellites.*, pages 1–38.

Camargo, J. I. B., Vieira-Martins, R., Assafin, M., Braga-Ribas, F., Sicardy, B., Desmars, J., Andrei, A. H., Benedetti-Rossi, G., and Dias-Oliveira, A. (2014).

Candidate stellar occultations by Centaurs and trans-Neptunian objects up to 2014. *Astronomy & Astrophysics*, 561:A37.

Carry, B. (2012). Density of asteroids. *Planetary and Space Science*, 73(1):98–118.

Cohen, C. J. and Hubbard, E. C. (1965). Libration of the close approaches of Pluto to Neptune. *The Astronomical Journal*, 70:10.

Conrath, B., Flasar, F. M., Hanel, R., Kunde, V., Maguire, W., Pearl, J., Pirraglia, J., Samuelson, R., Gierasch, P., Weir, A., Bezard, B., Gautier, D., Cruikshank, D., Horn, L., Springer, R., and Shaffer, W. (1989). Infrared Observations of the Neptunian System. *Science*, 246(4936):1454–1459.

Correia, A. C. M. (2009). Secular Evolution of a Satellite by Tidal Effect: Application to Triton. *The Astrophysical Journal Letters*, 704(1):L1–L4.

Cruikshank, D. P. and Silvaggio, P. M. (1979). Triton: a satellite with an atmosphere. *The Astrophysical Journal*, 233(3):1016–1020.

Davies, M. E., Abalakin, V. K., Bursa, M., Lieske, J. H., Morando, B., Morrison, D., Seidelmann, P. K., Sinclair, A. T., Yallop, B., and Tjuflin, Y. S. (1996). Report of the IAU/IAG/COSPAR Working Group on Cartographic Coordinates and Rotational Elements of the Planets and Satellites: 1994. *Celestial Mechanics and Dynamical Astronomy*, 63(2):127–148.

Dias-Oliveira, A., Sicardy, B., Lellouch, E., Vieira-Martins, R., Assafin, M., Camargo, J. I. B., Braga-Ribas, F., Gomes-Júnior, A. R., Benedetti-Rossi, G., Colas, F., Decock, A., Doressoundiram, A., Dumas, C., Emilio, M., Fabrega Polleri, J., Gil-Hutton, R., Gillon, M., Girard, J. H., Hau, G. K. T., Ivanov, V. D., Jehin, E., Lecacheux, J., Leiva, R., Lopez-Sisterna, C., Mancini, L., Manfroid, J., Maury, A., Meza, E., Morales, N., Nagy, L., Opitom, C., Ortiz, J. L., Pollock, J., Roques, F., Snodgrass, C., Soulier, J. F., Thirouin, A., Vanzi, L., Widemann, T., Reichart, D. E., LaCluyze, A. P., Haislip, J. B., Ivarsen, K. M., Dominik, M., Jørgensen, U., and Skottfelt, J. (2015). Pluto's Atmosphere from Stellar Occultations in 2012 and 2013. *The Astrophysical Journal*, 811:53.

Elliot, J. L. (1979). Stellar occultation studies of the solar system. *Annual review of astronomy and astrophysics*, 17:445–475.

Elliot, J. L., French, R. G., Dunham, E., Gierasch, P. J., Veverka, J., Church, C., and Sagan, C. (1977). Occultation of epsilon Geminorum by Mars. II. The structure and extinction of the Martian upper atmosphere. *The Astrophysical Journal*, 217:661–679.

Elliot, J. L. and Olkin, C. B. (1996). Probing Planetary Atmospheres with Stellar Occultations. *Annual Review of Earth and Planetary Sciences*, 24:89–124.

Elliot, J. L., Person, M. J., McDonald, S. W., Buie, M. W., Dunham, E. W., Millis, R. L., Nye, R. A., Olkin, C. B., Wasserman, L. H., Young, L. A., Hubbard, W. B., Hill, R., Reitsema, H. J., Pasachoff, J. M., McConnochie, T. H., Babcock, B. A., Stone, R. C., and Francis, P. (2000a). The Prediction and Observation of the 1997 July 18 Stellar Occultation by Triton: More Evidence for Distortion and Increasing Pressure in Triton's Atmosphere. *Icarus*, 148(2):347–369.

Elliot, J. L., Person, M. J., and Qu, S. (2003). Analysis of Stellar Occultation Data. II. Inversion, with Application to Pluto and Triton. *The Astronomical Journal*, 126(2):1041–1079.

Elliot, J. L., Stansberry, J. A., Olkin, C. B., Agner, M. A., and Davies, M. E. (1997). Triton's Distorted Atmosphere. *Science*, 278:436.

Elliot, J. L., Strobel, D. F., Zhu, X., Stansberry, J. A., Wasserman, L. H., and Franz, O. G. (2000b). NOTE: The Thermal Structure of Triton's Middle Atmosphere. *Icarus*, 143(2):425–428.

Elliot, J. L. and Young, L. A. (1992). Analysis of Stellar Occultation Data for Planetary Atmospheres. I. Model Fitting Application to Pluto. *Astronomical Journal*, 103:991.

Fjeldbo, G., Kliore, A. J., and Eshleman, V. R. (1971). The Neutral Atmosphere of Venus as Studied with the Mariner V Radio Occultation Experiments. *The Astronomical Journal*, 76:123.

Forget, F., Bertrand, T., Hinson, D., and Toigo, A. (2021). Dynamics of Pluto Atmosphere. In *Pluto System After New Horizons*.

Forget, F., Bertrand, T., Vangvichith, M., Leconte, J., Millour, E., and Lellouch, E. (2017). A post-new horizons global climate model of pluto including the n2, ch4 and co cycles. *Icarus*, 287:54 – 71. Special Issue: The Pluto System.

Forget, F., Decamp, N., Berthier, J., and Le Guyader, C. (2000). A New Model for the Seasonal Evolution of Triton. In *AAS/Division for Planetary Sciences Meeting Abstracts #32*, volume 32 of *AAS/Division for Planetary Sciences Meeting Abstracts*, page 45.01.

Fray, N. and Schmitt, B. (2009). Sublimation of ices of astrophysical interest: A bibliographic review. *Planetary and Space Science*, 57:2053–2080.

French, R. G., Elliot, J. L., and Gierasch, P. J. (1978). Analysis of stellar occultation data Effects of photon noise and initial conditions. *Icarus*, 33(1):186–202.

Gaia Collaboration, Brown, A. G. A., Vallenari, A., Prusti, T., de Bruijne, J. H. J., Babusiaux, C., Bailer-Jones, C. A. L., Biermann, M., Evans, D. W., Eyer, L., Jansen, F., Jordi, C., Klioner, S. A., Lammers, U., Lindegren, L., Luri, X., Mignard, F., Panem, C., Pourbaix, D., Randich, S., Sartoretti, P., Siddiqui, H. I., Soubiran, C., van Leeuwen, F., Walton, N. A., Arenou, F., Bastian, U., Cropper, M., Drimmel, R., Katz, D., Lattanzi, M. G., Bakker, J., Cacciari, C., Castañeda, J., Chaoul, L., Cheek, N., De Angeli, F., Fabricius, C., Guerra, R., Holl, B., Masana, E., Messineo, R., Mowlavi, N., Nienartowicz, K., Panuzzo, P., Portell, J., Riello, M., Seabroke, G. M., Tanga, P., Thévenin, F., Gracia-Abril, G., Comoretto, G., Garcia-Reinaldos, M., Teyssier, D., Altmann, M., Andrae, R., Audard, M., Bellas-Velidis, I., Benson, K., Berthier, J., Blomme, R., Burgess, P., Busso, G., Carry, B., Cellino, A., Clementini, G., Clotet, M., Creevey, O., Davidson, M., De Ridder, J., Delchambre, L., Dell'Oro, A., Ducourant, C., Fernández-Hernández, J., Fouesneau, M., Frémat, Y., Galluccio, L., García-Torres, M., González-Núñez, J., González-Vidal, J. J., Gosset, E., Guy, L. P., Halbwachs, J. L., Hambly, N. C., Harrison, D. L., Hernández, J., Hestroffer, D., Hodgkin, S. T., Hutton, A., Jasniewicz, G., Jean-Antoine-Piccolo, A., Jordan, S., Korn, A. J., Krone-Martins, A., Lanzafame, A. C., Lebzelter, T., Löffler, W., Manteiga, M., Marrese, P. M., Martín-Fleitas, J. M., Moitinho, A., Mora, A., Muinonen, K., Osinde, J., Pancino, E., Pauwels, T., Petit, J. M., Recio-Blanco, A., Richards, P. J., Rimoldini, L., Robin, A. C., Sarro, L. M., Siopis, C., Smith,

M., Sozzetti, A., Süveges, M., Torra, J., van Reeven, W., Abbas, U., Abreu Aramburu, A., Accart, S., Aerts, C., Altavilla, G., Álvarez, M. A., Alvarez, R., Alves, J., Anderson, R. I., Andrei, A. H., Anglada Varela, E., Antiche, E., Antoja, T., Arcay, B., Astraatmadja, T. L., Bach, N., Baker, S. G., Balaguer-Núñez, L., Balm, P., Barache, C., Barata, C., Barbato, D., Barblan, F., Barklem, P. S., Barrado, D., Barros, M., Barstow, M. A., Bartholomé Muñoz, S., Bassilana, J. L., Becciani, U., Bellazzini, M., Berihuete, A., Bertone, S., Bianchi, L., Bienaymé, O., Blanco-Cuaresma, S., Boch, T., Boeche, C., Bombrun, A., Borrachero, R., Bossini, D., Bouquillon, S., Bourda, G., Bragaglia, A., Bramante, L., Breddels, M. A., Bressan, A., Brouillet, N., Brüsemeister, T., Brugaletta, E., Bucciarelli, B., Burlacu, A., Busonero, D., Butkevich, A. G., Buzzi, R., Caffau, E., Cancelliere, R., Cannizzaro, G., Cantat-Gaudin, T., Carballo, R., Carlucci, T., Carrasco, J. M., Casamiquela, L., Castellani, M., Castro-Ginard, A., Charlot, P., Chemin, L., Chiavassa, A., Cocozza, G., Costigan, G., Cowell, S., Crifo, F., Crosta, M., Crowley, C., Cuypers, J., Dafonte, C., Damerdji, Y., Dapergolas, A., David, P., David, M., de Laverny, P., De Luise, F., De March, R., de Martino, D., de Souza, R., de Torres, A., Debosscher, J., del Pozo, E., Delbo, M., Delgado, A., Delgado, H. E., Di Matteo, P., Diakite, S., Diener, C., Distefano, E., Dolding, C., Drazinos, P., Durán, J., Edvardsson, B., Enke, H., Eriksson, K., Esquej, P., Eynard Bontemps, G., Fabre, C., Fabrizio, M., Faigler, S., Falcão, A. J., Farràs Casas, M., Federici, L., Fedorets, G., Fernique, P., Figueras, F., Filippi, F., Findeisen, K., Fonti, A., Fraile, E., Fraser, M., Frézouls, B., Gai, M., Galleti, S., Garabato, D., García-Sedano, F., Garofalo, A., Garralda, N., Gavel, A., Gavras, P., Gerssen, J., Geyer, R., Giacobbe, P., Gilmore, G., Girona, S., Giuffrida, G., Glass, F., Gomes, M., Granvik, M., Gueguen, A., Guerrier, A., Guiraud, J., Gutiérrez-Sánchez, R., Haigron, R., Hatzidimitriou, D., Hauser, M., Haywood, M., Heiter, U., Helmi, A., Heu, J., Hilger, T., Hobbs, D., Hofmann, W., Holland, G., Huckle, H. E., Hypki, A., Icardi, V., Janßen, K., Jevardat de Fombelle, G., Jonker, P. G., Juhász, Á. L., Julbe, F., Karampelas, A., Kewley, A., Klar, J., Kochoska, A., Kohley, R., Kolenberg, K., Kontizas, M., Kontizas, E., Koposov, S. E., Kordopatis, G., Kostrzewa-Rutkowska, Z., Koubsky, P., Lambert, S., Lanza, A. F., Lasne, Y., Lavigne, J. B., Le Fustec, Y., Le Poncin-Lafitte, C., Lebreton, Y., Leccia, S., Leclerc, N., Lecoeur-Taibi, I., Lenhardt, H., Leroux, F., Liao, S., Licata, E., Lindstrøm, H. E. P., Lister,

T. A., Livanou, E., Lobel, A., López, M., Managau, S., Mann, R. G., Mantelet, G., Marchal, O., Marchant, J. M., Marconi, M., Marinoni, S., Marschalkó, G., Marshall, D. J., Martino, M., Marton, G., Mary, N., Massari, D., Matijevič, G., Mazeh, T., McMillan, P. J., Messina, S., Michalik, D., Millar, N. R., Molina, D., Molinaro, R., Molnár, L., Montegriffo, P., Mor, R., Morbidelli, R., Morel, T., Morris, D., Mulone, A. F., Muraveva, T., Musella, I., Nelemans, G., Nicastro, L., Noval, L., O'Mullane, W., Ordénovic, C., Ordóñez-Blanco, D., Osborne, P., Pagani, C., Pagano, I., Pailler, F., Palacin, H., Palaversa, L., Panahi, A., Pawlak, M., Piersimoni, A. M., Pineau, F. X., Plachy, E., Plum, G., Poggio, E., Poujoulet, E., Prša, A., Pulone, L., Racero, E., Ragaini, S., Rambaux, N., Ramos-Lerate, M., Regibo, S., Reylé, C., Riclet, F., Ripepi, V., Riva, A., Rivard, A., Rixon, G., Roegiers, T., Roelens, M., Romero-Gómez, M., Rowell, N., Royer, F., Ruiz-Dern, L., Sadowski, G., Sagristà Sellés, T., Sahlmann, J., Salgado, J., Salguero, E., Sanna, N., Santana-Ros, T., Sarasso, M., Savietto, H., Schultheis, M., Sciacca, E., Segol, M., Segovia, J. C., Ségransan, D., Shih, I. C., Siltala, L., Silva, A. F., Smart, R. L., Smith, K. W., Solano, E., Solitro, F., Sordo, R., Soria Nieto, S., Souchay, J., Spagna, A., Spoto, F., Stampa, U., Steele, I. A., Steidelmüller, H., Stephenson, C. A., Stoev, H., Suess, F. F., Surdej, J., Szabados, L., Szegedi-Elek, E., Tapiador, D., Taris, F., Tauran, G., Taylor, M. B., Teixeira, R., Terrett, D., Teyssand ier, P., Thuillot, W., Titarenko, A., Torra Clotet, F., Turon, C., Ulla, A., Utrilla, E., Uzzi, S., Vaillant, M., Valentini, G., Valette, V., van Elteren, A., Van Hemelryck, E., van Leeuwen, M., Vaschetto, M., Vecchiato, A., Veljanoski, J., Viala, Y., Vicente, D., Vogt, S., von Essen, C., Voss, H., Votruba, V., Voutsinas, S., Walmsley, G., Weiler, M., Wertz, O., Wevers, T., Wyrzykowski, Ł., Yoldas, A., Žerjal, M., Ziaeepour, H., Zorec, J., Zschocke, S., Zucker, S., Zurbach, C., and Zwitter, T. (2018). Gaia Data Release 2. Summary of the contents and survey properties. *Astronomy & Astrophysics*, 616:A1.

Gaia Collaboration, Prusti, T., de Bruijne, J. H. J., Brown, A. G. A., Vallenari, A., Babusiaux, C., Bailer-Jones, C. A. L., Bastian, U., Biermann, M., Evans, D. W., Eyer, L., Jansen, F., Jordi, C., Klioner, S. A., Lammers, U., Lindegren, L., Luri, X., Mignard, F., Milligan, D. J., Panem, C., Poinsignon, V., Pourbaix, D., Randich, S., Sarri, G., Sartoretti, P., Siddiqui, H. I., Soubiran, C., Valette, V., van Leeuwen, F., Walton, N. A., Aerts, C., Arenou, F., Cropper, M., Drim-

mel, R., Høg, E., Katz, D., Lattanzi, M. G., O'Mullane, W., Grebel, E. K., Holland, A. D., Huc, C., Passot, X., Bramante, L., Cacciari, C., Castañeda, J., Chaoul, L., Cheek, N., De Angeli, F., Fabricius, C., Guerra, R., Hernández, J., Jean-Antoine-Piccolo, A., Masana, E., Messineo, R., Mowlavi, N., Nienartowicz, K., Ordóñez-Blanco, D., Panuzzo, P., Portell, J., Richards, P. J., Riello, M., Seabroke, G. M., Tanga, P., Thévenin, F., Torra, J., Els, S. G., Gracia-Abril, G., Comoretto, G., Garcia-Reinaldos, M., Lock, T., Mercier, E., Altmann, M., Andrae, R., Astraatmadja, T. L., Bellas-Velidis, I., Benson, K., Berthier, J., Blomme, R., Busso, G., Carry, B., Cellino, A., Clementini, G., Cowell, S., Creevey, O., Cuypers, J., Davidson, M., De Ridder, J., de Torres, A., Delchambre, L., Dell'Oro, A., Ducourant, C., Frémat, Y., García-Torres, M., Gosset, E., Halbwachs, J. L., Hambly, N. C., Harrison, D. L., Hauser, M., Hestroffer, D., Hodgkin, S. T., Huckle, H. E., Hutton, A., Jasniewicz, G., Jordan, S., Kontizas, M., Korn, A. J., Lanzafame, A. C., Manteiga, M., Moitinho, A., Muinonen, K., Osinde, J., Pancino, E., Pauwels, T., Petit, J. M., Recio-Blanco, A., Robin, A. C., Sarro, L. M., Siopis, C., Smith, M., Smith, K. W., Sozzetti, A., Thuillot, W., van Reeven, W., Viala, Y., Abbas, U., Abreu Aramburu, A., Accart, S., Aguado, J. J., Allan, P. M., Allasia, W., Altavilla, G., Álvarez, M. A., Alves, J., Anderson, R. I., Andrei, A. H., Anglada Varela, E., Antiche, E., Antoja, T., Antón, S., Arcay, B., Atzei, A., Ayache, L., Bach, N., Baker, S. G., Balaguer-Núñez, L., Barache, C., Barata, C., Barbier, A., Barblan, F., Baroni, M., Barrado y Navascués, D., Barros, M., Barstow, M. A., Becciani, U., Bellazzini, M., Bellei, G., Bello García, A., Belokurov, V., Bendjoya, P., Berihuete, A., Bianchi, L., Bienaymé, O., Billebaud, F., Blagorodnova, N., Blanco-Cuaresma, S., Boch, T., Bombrun, A., Borrachero, R., Bouquillon, S., Bourda, G., Bouy, H., Bragaglia, A., Breddels, M. A., Brouillet, N., Brüsemeister, T., Bucciarelli, B., Budnik, F., Burgess, P., Burgon, R., Burlacu, A., Busonero, D., Buzzi, R., Caffau, E., Cambras, J., Campbell, H., Cancelliere, R., Cantat-Gaudin, T., Carlucci, T., Carrasco, J. M., Castellani, M., Charlot, P., Charnas, J., Charvet, P., Chassat, F., Chiavassa, A., Clotet, M., Cocozza, G., Collins, R. S., Collins, P., Costigan, G., Crifo, F., Cross, N. J. G., Crosta, M., Crowley, C., Dafonte, C., Damerdji, Y., Dapergolas, A., David, P., David, M., De Cat, P., de Felice, F., de Laverny, P., De Luise, F., De March, R., de Martino, D., de Souza, R., Debosscher, J., del Pozo, E., Delbo, M., Delgado, A., Delgado, H. E., di Marco,

F., Di Matteo, P., Diakite, S., Distefano, E., Dolding, C., Dos Anjos, S., Drazinos, P., Durán, J., Dzigan, Y., Ecale, E., Edvardsson, B., Enke, H., Erdmann, M., Escolar, D., Espina, M., Evans, N. W., Eynard Bontemps, G., Fabre, C., Fabrizio, M., Faigler, S., Falcão, A. J., Farràs Casas, M., Faye, F., Federici, L., Fedorets, G., Fernández-Hernández, J., Fernique, P., Fienga, A., Figueras, F., Filippi, F., Findeisen, K., Fonti, A., Fouesneau, M., Fraile, E., Fraser, M., Fuchs, J., Furnell, R., Gai, M., Galleti, S., Galluccio, L., Garabato, D., García-Sedano, F., Garé, P., Garofalo, A., Garralda, N., Gavras, P., Gerssen, J., Geyer, R., Gilmore, G., Girona, S., Giuffrida, G., Gomes, M., González-Marcos, A., González-Núñez, J., González-Vidal, J. J., Granvik, M., Guerrier, A., Guillout, P., Guiraud, J., Gúrpide, A., Gutiérrez-Sánchez, R., Guy, L. P., Haigron, R., Hatzidimitriou, D., Haywood, M., Heiter, U., Helmi, A., Hobbs, D., Hofmann, W., Holl, B., Holland , G., Hunt, J. A. S., Hypki, A., Icardi, V., Irwin, M., Jevardat de Fombelle, G., Jofré, P., Jonker, P. G., Jorissen, A., Julbe, F., Karampelas, A., Kochoska, A., Kohley, R., Kolenberg, K., Kontizas, E., Koposov, S. E., Kordopatis, G., Koubsky, P., Kowalczyk, A., Krone-Martins, A., Kudryashova, M., Kull, I., Bachchan, R. K., Lacoste-Seris, F., Lanza, A. F., Lavigne, J. B., Le Poncin-Lafitte, C., Lebreton, Y., Lebzelter, T., Leccia, S., Leclerc, N., Lecoeur-Taibi, I., Lemaitre, V., Lenhardt, H., Leroux, F., Liao, S., Licata, E., Lindstrøm, H. E. P., Lister, T. A., Livanou, E., Lobel, A., Löffler, W., López, M., Lopez-Lozano, A., Lorenz, D., Loureiro, T., MacDonald, I., Magalhães Fernandes, T., Managau, S., Mann, R. G., Mantelet, G., Marchal, O., Marchant, J. M., Marconi, M., Marie, J., Marinoni, S., Marrese, P. M., Marschalkó, G., Marshall, D. J., Martín-Fleitas, J. M., Martino, M., Mary, N., Matijevič, G., Mazeh, T., McMillan, P. J., Messina, S., Mestre, A., Michalik, D., Millar, N. R., Miranda, B. M. H., Molina, D., Molinaro, R., Molinaro, M., Molnár, L., Moniez, M., Montegriffo, P., Monteiro, D., Mor, R., Mora, A., Morbidelli, R., Morel, T., Morgenthaler, S., Morley, T., Morris, D., Mulone, A. F., Muraveva, T., Musella, I., Narbonne, J., Nelemans, G., Nicastro, L., Noval, L., Ordénovic, C., Ordieres-Meré, J., Osborne, P., Pagani, C., Pagano, I., Pailler, F., Palacin, H., Palaversa, L., Parsons, P., Paulsen, T., Pecoraro, M., Pedrosa, R., Pentikäinen, H., Pereira, J., Pichon, B., Piersimoni, A. M., Pineau, F. X., Plachy, E., Plum, G., Poujoulet, E., Prša, A., Pulone, L., Ragaini, S., Rago, S., Rambaux, N., Ramos-Lerate, M., Ranalli, P., Rauw, G., Read, A., Regibo,

S., Renk, F., Reylé, C., Ribeiro, R. A., Rimoldini, L., Ripepi, V., Riva, A., Rixon, G., Roelens, M., Romero-Gómez, M., Rowell, N., Royer, F., Rudolph, A., Ruiz-Dern, L., Sadowski, G., Sagristà Sellés, T., Sahlmann, J., Salgado, J., Salguero, E., Sarasso, M., Savietto, H., Schnorhk, A., Schultheis, M., Sciacca, E., Segol, M., Segovia, J. C., Segransan, D., Serpell, E., Shih, I. C., Smareglia, R., Smart, R. L., Smith, C., Solano, E., Solitro, F., Sordo, R., Soria Nieto, S., Souchay, J., Spagna, A., Spoto, F., Stampa, U., Steele, I. A., Steidelmüller, H., Stephenson, C. A., Stoev, H., Suess, F. F., Süveges, M., Surdej, J., Szabados, L., Szegedi-Elek, E., Tapiador, D., Taris, F., Tauran, G., Taylor, M. B., Teixeira, R., Terrett, D., Tingley, B., Trager, S. C., Turon, C., Ulla, A., Utrilla, E., Valentini, G., van Elteren, A., Van Hemelryck, E., van Leeuwen, M., Varadi, M., Vecchiato, A., Veljanoski, J., Via, T., Vicente, D., Vogt, S., Voss, H., Votruba, V., Voutsinas, S., Walmsley, G., Weiler, M., Weingrill, K., Werner, D., Wevers, T., Whitehead, G., Wyrzykowski, Ł., Yoldas, A., Žerjal, M., Zucker, S., Zurbach, C., Zwitter, T., Alecu, A., Allen, M., Allende Prieto, C., Amorim, A., Anglada-Escudé, G., Arsenijevic, V., Azaz, S., Balm, P., Beck, M., Bernstein, H. H., Bigot, L., Bijaoui, A., Blasco, C., Bonfigli, M., Bono, G., Boudreault, S., Bressan, A., Brown, S., Brunet, P. M., Bunclark, P., Buonanno, R., Butkevich, A. G., Carret, C., Carrion, C., Chemin, L., Chéreau, F., Corcione, L., Darmigny, E., de Boer, K. S., de Teodoro, P., de Zeeuw, P. T., Delle Luche, C., Domingues, C. D., Dubath, P., Fodor, F., Frézouls, B., Fries, A., Fustes, D., Fyfe, D., Gallardo, E., Gallegos, J., Gardiol, D., Gebran, M., Gomboc, A., Gómez, A., Grux, E., Gueguen, A., Heyrovsky, A., Hoar, J., Iannicola, G., Isasi Parache, Y., Janotto, A. M., Joliet, E., Jonckheere, A., Keil, R., Kim, D. W., Klagyivik, P., Klar, J., Knude, J., Kochukhov, O., Kolka, I., Kos, J., Kutka, A., Lainey, V., LeBouquin, D., Liu, C., Loreggia, D., Makarov, V. V., Marseille, M. G., Martayan, C., Martinez-Rubi, O., Massart, B., Meynadier, F., Mignot, S., Munari, U., Nguyen, A. T., Nordlander, T., Ocvirk, P., O'Flaherty, K. S., Olias Sanz, A., Ortiz, P., Osorio, J., Oszkiewicz, D., Ouzounis, A., Palmer, M., Park, P., Pasquato, E., Peltzer, C., Peralta, J., Péturaud, F., Pieniluoma, T., Pigozzi, E., Poels, J., Prat, G., Prod'homme, T., Raison, F., Rebordao, J. M., Risquez, D., Rocca-Volmerange, B., Rosen, S., Ruiz-Fuertes, M. I., Russo, F., Sembay, S., Serraller Vizcaino, I., Short, A., Siebert, A., Silva, H., Sinachopoulos, D., Slezak, E., Soffel, M., Sosnowska, D., Straižys, V., ter Linden, M.,

Terrell, D., Theil, S., Tiede, C., Troisi, L., Tsalmantza, P., Tur, D., Vaccari, M., Vachier, F., Valles, P., Van Hamme, W., Veltz, L., Virtanen, J., Wallut, J. M., Wichmann, R., Wilkinson, M. I., Ziaeepour, H., and Zschocke, S. (2016). The Gaia mission. *Astronomy & Astrophysics*, 595:A1.

Galle, J. G. (1846). Account of the discovery of Le Verrier's planet Neptune, at Berlin, Sept. 23, 1846. *Monthly Notices of the Royal Astronomical Society*, 7:153.

Goldreich, P., Murray, N., Longaretti, P. Y., and Banfield, D. (1989). Neptune's Story. *Science*, 245(4917):500–504.

Grundy, W. M., Schmitt, B., and Quirico, E. (1993). The Temperature-Dependent Spectra of α and β Nitrogen Ice with Application to Triton. *Icarus*, 105(1):254–258.

Gurrola, E. M. (1995). *Interpretation of Radar Data from the Icy Galilean Satellites and Triton*. PhD thesis, Stanford University.

Gurwell, M., Lellouch, E., Butler, B., Moreno, R., Moullet, A., and Strobel, D. (2019). The Atmosphere of Triton Observed With ALMA. In *EPSC-DPS Joint Meeting 2019*, volume 2019, pages EPSC–DPS2019–806.

Hansen, C. J., Castillo-Rogez, J., Grundy, W., Hofgartner, J. D., Martin, E. S., Mitchell, K., Nimmo, F., Nordheim, T. A., Paty, C., Quick, L. C., Roberts, J. H., Runyon, K., Schenk, P., Stern, A., and Umurhan, O. (2021). Triton: Fascinating Moon, Likely Ocean World, Compelling Destination! *The Planetary Science Journal*, 2(4):137.

Hansen, C. J., McEwen, A. S., Ingersoll, A. P., and Terrile, R. J. (1990). Surface and Airborne Evidence for Plumes and Winds on Triton. *Science*, 250(4979):421–424.

Herbert, F. and Sandel, B. R. (1991). CH_4 and haze in Triton's lower atmosphere. *Journal of Geophysical Research*, 96:19241–19252.

Hinson, D. P., Linscott, I. R., Young, L. A., Tyler, G. L., Stern, S. A., Beyer, R. A., Bird, M. K., Ennico, K., Gladstone, G. R., Olkin, C. B., Pätzold, M., Schenk, P. M., Strobel, D. F., Summers, M. E., Weaver, H. A., and Woods,

W. W. (2017). Radio occultation measurements of Pluto's neutral atmosphere with New Horizons. *Icarus*, 290:96–111.

Hubbard, W. B., Brahic, A., Sicardy, B., Elicer, L. R., Roques, F., and Vilas, F. (1986). Occultation detection of a neptunian ring-like arc. *Nature*, 319(6055):636–640.

Hubbard, W. B., Lellouch, E., Sicardy, B., Brahic, A., Vilas, F., Bouchet, P., McLaren, R. A., and Perrier, C. (1988). Structure of Scintillations in Neptune's Occultation Shadow. *The Astrophysical Journal*, 325:490.

Hubbard, W. B., Sicardy, B., Miles, R., Hollis, A. J., Forrest, R. W., Nicolson, I. K. M., Appleby, G., Beisker, W., Bittner, C., Bode, H. J., Bruns, M., Denzau, H., Nezel, M., Riedel, E., Struckmann, H., Arlot, J. E., Roques, F., Sevre, F., Thuillot, W., Hoffmann, M., Geyer, E. H., Buil, C., Colas, F., Lecacheux, J., Klotz, A., Thouvenot, E., Vidal, J. L., Carreira, E., Rossi, F., Blanco, C., Cristaldi, S., Nevo, Y., Reitsema, H. J., Brosch, N., Cernis, K., Zdanavicius, K., Wasserman, L. H., Hunten, D. M., Gautier, D., Lellouch, E., Yelle, R. V., Rizk, B., Flasar, F. M., Porco, C. C., Toublanc, D., and Corugedo, G. (1993). The occultation of 28 SGR by Titan. *Astronomy & Astrophysics*, 269:541–563.

Ingersoll, A. P. (1990). Dynamics of Triton's atmosphere. *Nature*, 344(6264):315–317.

Johnson, P. E., Young, L. A., Protopapa, S., Schmitt, B., Gabasova, L. R., Lewis, B. L., Stansberry, J. A., Mandt, K. E., and White, O. L. (2020). Modeling Pluto's Minimum Pressure: Implications for Haze Production. *arXiv e-prints*, page arXiv:2008.10716.

Krasnopolsky, V. A. and Cruikshank, D. P. (1995). Photochemistry of Triton's atmosphere and ionosphere. *Journal of Geophysical Research*, 100(E10):21271–21286.

Krasnopolsky, V. A., Sandel, B. R., and Herbert, F. (1992). Properties of haze in the atmosphere of Triton. *Journal of Geophysical Research*, 97(E7):11695–11700.

Krasnopolsky, V. A., Sandel, B. R., Herbert, F., and Vervack, R. J. (1993). Temperature, N_2, and N density profiles of Triton's atmosphere: Observations and model. *Journal of Geophysical Research*, 98(E2):3065–3078.

Lassell, W. (1846). Discovery of supposed ring and satellite of Neptune. *Monthly Notices of the Royal Astronomical Society*, 7:157.

Lellouch, E., de Bergh, C., Sicardy, B., Ferron, S., and Käufl, H. U. (2010). Detection of CO in Triton's atmosphere and the nature of surface-atmosphere interactions. *Astronomy & Astrophysics*, 512:L8.

Lellouch, E., Gurwell, M., Butler, B., Fouchet, T., Lavvas, P., Strobel, D. F., Sicardy, B., Moullet, A., Moreno, R., Bockelée-Morvan, D., Biver, N., Young, L., Lis, D., Stansberry, J., Stern, A., Weaver, H., Young, E., Zhu, X., and Boissier, J. (2017). Detection of CO and HCN in Pluto's atmosphere with ALMA. *Icarus*, 286:289–307.

Lellouch, E., Santos-Sanz, P., Fornasier, S., Lim, T., Stansberry, J., Vilenius, E., Kiss, C., Müller, T., Marton, G., Protopapa, S., Panuzzo, P., and Moreno, R. (2016). The long-wavelength thermal emission of the Pluto-Charon system from Herschel observations. Evidence for emissivity effects. *Astronomy & Astrophysics*, 588:A2.

Lellouch, E., Stansberry, J., Emery, J., Grundy, W., and Cruikshank, D. P. (2011). Thermal properties of Pluto's and Charon's surfaces from Spitzer observations. *Icarus*, 214(2):701–716.

Lewis, B. L., Stansberry, J. A., Holler, B. J., Grundy, W. M., Schmitt, B., Protopapa, S., Lisse, C., Stern, S. A., Young, L., Weaver, H. A., Olkin, C., Ennico, K., and New Horizons Science Team (2021). Distribution and energy balance of Pluto's nitrogen ice, as seen by New Horizons in 2015. *Icarus*, 356:113633.

Lyttleton, R. A. (1936). On the possible results of an encounter of Pluto with the Neptunian system. *Monthly Notices of the Royal Astronomical Society*, 97:108.

Manfroid, J., Haefner, R., and Bouchet, P. (1986). New evidence for a ring around Neptune. *Astronomy and Astrophysics*, 157(1):L3–L5.

McCord, T. B. (1966). Dynamical evolution of the Neptunian system. *The Astronomical Journal*, 71:585.

McKinnon, W. B. (1984). On the origin of Triton and Pluto. *Nature*, 311(5984):355–358.

McKinnon, W. B., Lunine, J. I., and Banfield, D. (1995). Origin and evolution of Triton. In *Neptune and Triton*, pages 807–877.

Merlin, F., Lellouch, E., Quirico, E., and Schmitt, B. (2018). Triton's surface ices: Distribution, temperature and mixing state from VLT/SINFONI observations. *Icarus*, 314:274–293.

Meza, E., Sicardy, B., Assafin, M., Ortiz, J. L., Bertrand, T., Lellouch, E., Desmars, J., Forget, F., Bérard, D., Doressoundiram, A., Lecacheux, J., Marques Oliveira, J., Roques, F., Widemann, T., Colas, F., Vachier, F., Renner, S., Leiva, R., Braga-Ribas, F., Benedetti-Rossi, G., Camargo, J. I. B., Dias-Oliveira, A., Morgado, B., Gomes-Júnior, A. R., Vieira-Martins, R., Behrend, R., Tirado, A. C., Duffard, R., Morales, N., Santos-Sanz, P., Jelínek, M., Cunniffe, R., Querel, R., Harnisch, M., Jansen, R., Pennell, A., Todd, S., Ivanov, V. D., Opitom, C., Gillon, M., Jehin, E., Manfroid, J., Pollock, J., Reichart, D. E., Haislip, J. B., Ivarsen, K. M., LaCluyze, A. P., Maury, A., Gil-Hutton, R., Dhillon, V., Littlefair, S., Marsh, T., Veillet, C., Bath, K. L., Beisker, W., Bode, H. J., Kretlow, M., Herald, D., Gault, D., Kerr, S., Pavlov, H., Faragó, O., Klös, O., Frappa, E., Lavayssière, M., Cole, A. A., Giles, A. B., Greenhill, J. G., Hill, K. M., Buie, M. W., Olkin, C. B., Young, E. F., Young, L. A., Wasserman, L. H., Devogèle, M., French, R. G., Bianco, F. B., Marchis, F., Brosch, N., Kaspi, S., Polishook, D., Manulis, I., Ait Moulay Larbi, M., Benkhaldoun, Z., Daassou, A., El Azhari, Y., Moulane, Y., Broughton, J., Milner, J., Dobosz, T., Bolt, G., Lade, B., Gilmore, A., Kilmartin, P., Allen, W. H., Graham, P. B., Loader, B., McKay, G., Talbot, J., Parker, S., Abe, L., Bendjoya, P., Rivet, J. P., Vernet, D., Di Fabrizio, L., Lorenzi, V., Magazzú, A., Molinari, E., Gazeas, K., Tzouganatos, L., Carbognani, A., Bonnoli, G., Marchini, A., Leto, G., Sanchez, R. Z., Mancini, L., Kattentidt, B., Dohrmann, M., Guhl, K., Rothe, W., Walzel, K., Wortmann, G., Eberle, A., Hampf, D., Ohlert, J., Krannich, G., Murawsky, G., Gährken, B., Gloistein, D., Alonso, S., Román, A., Communal, J. E., Jabet, F., deVisscher, S., Sérot, J., Janik, T., Moravec, Z., Machado, P., Selva,

A., Perelló, C., Rovira, J., Conti, M., Papini, R., Salvaggio, F., Noschese, A., Tsamis, V., Tigani, K., Barroy, P., Irzyk, M., Neel, D., Godard, J. P., Lanoiselée, D., Sogorb, P., Vérilhac, D., Bretton, M., Signoret, F., Ciabattari, F., Naves, R., Boutet, M., De Queiroz, J., Lindner, P., Lindner, K., Enskonatus, P., Dangl, G., Tordai, T., Eichler, H., Hattenbach, J., Peterson, C., Molnar, L. A., and Howell, R. R. (2019). Lower atmosphere and pressure evolution on Pluto from ground-based stellar occultations, 1988-2016. *Astronomy & Astrophysics*, 625:A42.

Millis, R. L., Wasserman, L. H., and Birch, P. V. (1977). Detection of rings around Uranus. *Nature*, 267(5609):330–331.

Moore, P. (1995). The discoveries of Neptune and Triton. In *Neptune and Triton*, pages 15–36.

Nogueira, E., Brasser, R., and Gomes, R. (2011). Reassessing the origin of Triton. *Icarus*, 214(1):113–130.

Ohno, K., Zhang, X., Tazaki, R., and Okuzumi, S. (2020). Haze Formation on Triton. *arXiv e-prints*, page arXiv:2012.11932.

Olkin, C. B., Elliot, J. L., Hammel, H. B., Cooray, A. R., McDonald, S. W., Foust, J. A., Bosh, A. S., Buie, M. W., Millis, R. L., Wasserman, L. H., Dunham, E. W., Young, L. A., Howell, R. R., Hubbard, W. B., Hill, R., Marcialis, R. L., McDonald, J. S., Rank, D. M., Holbrook, J. C., and Reitsema, H. J. (1997). The Thermal Structure of Triton's Atmosphere: Results from the 1993 and 1995 Occultations. *Icarus*, 129(1):178–201.

Ortiz, J. L., Santos-Sanz, P., Sicardy, B., Benedetti-Rossi, G., Bérard, D., Morales, N., Duffard, R., Braga-Ribas, F., Hopp, U., Ries, C., Nascimbeni, V., Marzari, F., Granata, V., Pál, A., Kiss, C., Pribulla, T., Komžík, R., Hornoch, K., Pravec, P., Bacci, P., Maestripieri, M., Nerli, L., Mazzei, L., Bachini, M., Martinelli, F., Succi, G., Ciabattari, F., Mikuz, H., Carbognani, A., Gaehrken, B., Mottola, S., Hellmich, S., Rommel, F. L., Fernández-Valenzuela, E., Campo Bagatin, A., Cikota, S., Cikota, A., Lecacheux, J., Vieira-Martins, R., Camargo, J. I. B., Assafin, M., Colas, F., Behrend, R., Desmars, J., Meza, E., Alvarez-Candal, A., Beisker, W., Gomes-Junior, A. R., Morgado, B. E., Roques, F., Vachier, F., Berthier, J., Mueller, T. G., Madiedo, J. M., Unsalan, O., Sonbas, E., Karaman,

N., Erece, O., Koseoglu, D. T., Ozisik, T., Kalkan, S., Guney, Y., Niaei, M. S., Satir, O., Yesilyaprak, C., Puskullu, C., Kabas, A., Demircan, O., Alikakos, J., Charmandaris, V., Leto, G., Ohlert, J., Christille, J. M., Szakáts, R., Takácsné Farkas, A., Varga-Verebélyi, E., Marton, G., Marciniak, A., Bartczak, P., Santana-Ros, T., Butkiewicz-Bak, M., Dudziński, G., Alí-Lagoa, V., Gazeas, K., Tzouganatos, L., Paschalis, N., Tsamis, V., Sánchez-Lavega, A., Pérez-Hoyos, S., Hueso, R., Guirado, J. C., Peris, V., and Iglesias-Marzoa, R. (2017). The size, shape, density and ring of the dwarf planet Haumea from a stellar occultation. *Nature*, 550(7675):219–223.

Phinney, R. A. and Anderson, D. L. (1968). On the radio occultation method for studying planetary atmospheres. *J. Geophys. Res.*, 73:1819.

Press, W. H., Teukolsky, S. A., Vetterling, W. T., and Flannery, B. P. (1992). *Numerical Recipes in C., The Art of Scientific Computing,*. New York: Cambridge Univ. Press,.

Rages, K. and Pollack, J. B. (1992). Voyager imaging of Triton's clouds and hazes. *Icarus*, 99(2):289–301.

Rymer, A. M., Clyde, B., Runyon, K., and Neptune-Odyssey team (2020). Neptune Odyssey: Mission to the Neptune-Triton System. *LPI Contributions*, 2547:6031.

Santos-Sanz, P., French, R. G., Pinilla-Alonso, N., Stansberry, J., Lin, Z. Y., Zhang, Z. W., Vilenius, E., Müller, T., Ortiz, J. L., Braga-Ribas, F., Bosh, A., Duffard, R., Lellouch, E., Tancredi, G., Young, L., Milam, S. N., and JWST "Occultations" Focus Group (2016). James Webb Space Telescope Observations of Stellar Occultations by Solar System Bodies and Rings. *Publications of the Astronomical Society of the Pacific*, 128(959):018011.

Schmude, Richard W., J., Baker, R. E., Fox, J., Krobusek, B. A., Pavlov, H., and Mallama, A. (2016). The Secular and Rotational Brightness Variations of Neptune. *arXiv e-prints*, page arXiv:1604.00518.

Sicardy, B., Colas, F., Widemann, T., Bellucci, A., Beisker, W., Kretlow, M., Ferri, F., Lacour, S., Lecacheux, J., Lellouch, E., Pau, S., Renner, S., Roques, F., Fienga, A., Etienne, C., Martinez, C., Glass, I. S., Baba, D., Nagayama,

T., Nagata, T., Itting-Enke, S., Bath, K.-L., Bode, H.-J., Bode, F., Lüdemann, H., Lüdemann, J., Neubauer, D., Tegtmeier, A., Tegtmeier, C., Thomé, B., Hund, F., deWitt, C., Fraser, B., Jansen, A., Jones, T., Schoenau, P., Turk, C., Meintjies, P., Hernandez, M., Fiel, D., Frappa, E., Peyrot, A., Teng, J. P., Vignand, M., Hesler, G., Payet, T., Howell, R. R., Kidger, M., Ortiz, J. L., Naranjo, O., Rosenzweig, P., and Rapaport, M. (2006). The two Titan stellar occultations of 14 November 2003. *Journal of Geophysical Research (Planets)*, 111(E11):E11S91.

Spencer, J. R. and Moore, J. M. (1992). The influence of thermal inertia on temperatures and frost stability on Triton. *Icarus*, 99(2):261–272.

Stansberry, J. A., Pisano, D. J., and Yelle, R. V. (1996). The emissivity of volatile ices on Triton and Pluto. *Planetary and Space Science*, 44(9):945–955.

Stansberry, J. A., Yelle, R. V., Lunine, J. I., and McEwen, A. S. (1992). Triton's surface-atmosphere energy balance. *Icarus*, 99(2):242–260.

Stone, E. C. and Miner, E. D. (1989). The Voyager 2 Encounter with the Neptunian System. *Science*, 246(4936):1417–1421.

Strobel, D. F. and Summers, M. E. (1995). Triton's upper atmosphere and ionosphere. In *Neptune and Triton*, pages 1107–1148.

Strobel, D. F., Summers, M. E., Herbert, F., and Sandel, B. R. (1990). The photochemistry of methane in the atmosphere of Triton. *Geophysical Research Letters*, 17(10):1729–1732.

Strobel, D. F. and Zhu, X. (2017). Comparative planetary nitrogen atmospheres: Density and thermal structures of Pluto and Triton. *Icarus*, 291:55–64.

Sánchez-Lavega, A. (2010). *An Introduction to Planetary Atmospheres*.

Thomas, P. C. (2000). NOTE: The Shape of Triton from Limb Profiles. *Icarus*, 148(2):587–588.

Tryka, K. A., Brown, R. H., Anicich, V., Cruikshank, D. P., and Owen, T. C. (1993). Spectroscopic Determination of the Phase Composition and Temperature of Nitrogen Ice on Triton. *Science*, 261(5122):751–754.

Tyler, G. L., Sweetnam, D. N., Anderson, J. D., Borutzki, S. E., Campbell, J. K., Eshleman, V. R., Gresh, D. L., Gurrola, E. M., Hinson, D. P., Kawashima, N., Kursinski, E. R., Levy, G. S., Lindal, G. F., Lyons, J. R., Marouf, E. A., Rosen, P. A., Simpson, R. A., and Wood, G. E. (1989). Voyager Radio Science Observations of Neptune and Triton. *Science*, 246(4936):1466–1473.

Vangvichith, M. (2013). *Modélisation des Atmosphères et des Glaces de Pluton et Triton*. PhD thesis, Ecole Polytechnique France, available online at http://www.sudoc.fr/17695547X.

Vapillon, L., Combes, M., and Lecacheux, J. (1973). The beta Scorpii occultation by Jupiter. II. The temperature and density profiles of the Jupiter upper atmosphere. *Astronomy & Astrophysics*, 29:135.

Washburn, E. W. (1930). *International Critical Tables of Numerical Data: Physics, Chemistry and Technology, Vol. 7*. McGraw-Hill, New York.

Yelle, R. V., Lunine, J. I., and Hunten, D. M. (1991). Energy balance and plume dynamics in Triton's lower atmosphere. *Icarus*, 89(2):347–358.

Yelle, R. V., Lunine, J. I., Pollack, J. B., and Brown, R. H. (1995). Lower atmospheric structure and surface-atmosphere interactions on Triton. In *Neptune and Triton*, pages 1031–1105.

Young, L. A., Kammer, J. A., Steffl, A. J., Gladstone, G. R., Summers, M. E., Strobel, D. F., Hinson, D. P., Stern, S. A., Weaver, H. A., Olkin, C. B., Ennico, K., McComas, D. J., Cheng, A. F., Gao, P., Lavvas, P., Linscott, I. R., Wong, M. L., Yung, Y. L., Cunningham, N., Davis, M., Parker, J. W., Schindhelm, E., Siegmund, O. H. W., Stone, J., Retherford, K., and Versteeg, M. (2018). Structure and composition of Pluto's atmosphere from the New Horizons solar ultraviolet occultation. *Icarus*, 300:174–199.